POLISH ANATOMICAL SOCIETY

FOLIA MORPHOLOGICA

Vol. 81   *2022*   *No. 1*

VM
VIA MEDICA

FOLIA
MORPHOLOGICA

VM VIA MEDICA

REVIEW ARTICLE

CLARITY techniques based tissue clearing: types and differences

Z. Guo[1], Y. Zheng[2], Y. Zhang[1]

[1]*Department of General Surgery, Hepatic-biliary-pancreatic Institute, Lanzhou University Second Hospital, Lanzhou University, Lanzhou, China*
[2]*Department of Plastic Surgery, Lanzhou University Second Hospital, Lanzhou University, Lanzhou, China*

CLARITY is a tissue imaging technique that uses hydrogel embedded tissue to remove lipids while maintaining the intactness of protein and tissue fine structure. CLARITY has been widely used in the field of three-dimensional reconstruction of intact tissues and biomolecular information analysis, which enhances the ability to obtain biological structural and molecular information from intact systems. Therefore, many modified tissue clearing methods based on CLARITY have emerged. However, the variety and complexity of modified CLARITY techniques, as well as such challenges as low tissue clearing efficiency, tissue damage, and expensive experimental equipment significantly limited popular application. This review systematically summarises the progress of CLARITY techniques from the perspective of tissue clearing and classifies them into active CLARITY, passive CLARITY, and the method of merging active CLARITY with passive CLARITY according to different tissue clearing methods, which helps researchers to select a suitable tissue clearing method for the experimental samples more quickly and effectively based on balancing the removal speed and tissue transparency of different tissue clearing methods. In addition, combing through the advantage and highlighting the limitations of CLARITY techniques may be beneficial for the ideas building of different research and enlighten to improve the details of the techniques. (Folia Morphol 2022; 81, 1: 1–12)

Key words: CLARITY, three-dimensional imaging, tissue clearing, lipid removal, electrophoresis, brain, histology

INTRODUCTION

Biological tissue is a three-dimensional (3D) structure with complex detailed structures and vast molecular information, and how to acquire these data has always been a critical challenge [14, 20, 28, 35, 37, 43, 44, 54]. This task has mainly relied on cutting the tissue into thin slices and providing cellular information at the 3D level. Such conventional tissue imaging inevitably loses crucial molecular information after tissue slicing and also artificially segment interconnection and function of tissues, which is particularly important for neurological studies. Therefore, how to transform intact tissues and organs into optically transparent structures has attracted people's attention. Tissue optical clearing, a unique large volume imaging method, enable tissue structures to be visualized in the whole tissue or in the whole body that has not been sliced. Tissue clearing methods achieve

deeper imaging in large volumes by reducing scattering and increasing the depth of light penetration [29, 45–47, 53]. Furthermore, these methods can adapt to various optical imaging techniques and show great potential to acquire 3D high-resolution images of intact tissue [5, 32].

At present, there are mainly three types of tissue clearing methods: hydrophobic, hydrophilic and hydrogel methods [39, 41]. Hydrophobic tissue clearing methods use organic solvents to achieve rapid transparency of intact tissue by reducing light scattering [44]. 3DISCO, a hydrophobic tissue clearing method, can completely clear the intact adult mouse brain within 2 days. However, the storage time of samples is short owing to fluorescence quenching [10, 11]. The hydrophilic tissue clearing methods are carried out by using water-soluble reagents. Although the tissue clearing ability of hydrophilic tissue clearing methods (such as Scale, Scales, SeeDB, CUBIC, etc.) was sometimes inferior to that of hydrophobic tissue clearing methods, they offer unique advantages, including preservation of protein function and high levels of biosafety and biocompatibility [16, 17, 19, 38]. The hydrogel-based tissue clearing method is similar to the hydrophilic tissue clearing method, but the lipids are extracted from the hydrogel-tissue hybrid in a more aggressive way.

CLARITY (Clear Lipid-exchanged Acrylamide-hybridised Rigid Imaging/Immunostaining/*In situ* hybridisation-compatible Tissue-hYdrogel) proposed in 2013 is a hydrogel-based tissue clearing method, and its necessary steps are as follows: tissue fixation, hydrogel formation, lipid extraction, staining, and imaging [3]. By crosslinking acrylamide with intact tissue to form a reticular hydrogel structure, this technique provides a physical framework for tissue without destroying biomolecules and fine structure characteristics of removing lipids from intact tissue to turn it into optically transparent and permeable transparent tissue. Therefore, it can be stained and de-stained for multiple rounds without tissue sections, and then the 3D structure of the tissue can be observed and constructed under an optical microscope. CLARITY was initially applied to construct the structure of brain tissue, showing neurotransmitters, cellular relationships, subcellular structures intact-tissue imaging of long-range projections, local circuit wiring, etc. It has been widely used in the basic research of the pathological structure of nervous system-related diseases, transparent processing of intact organs (such

as pancreas, lung, intestine, liver, and kidney), the relationship between organ structure and function and dynamic changes of blood vessels, 3D imaging of plant organs, 3D biogeography and metabolic status of microorganisms and other scientific research [1, 3, 4, 12, 25, 31, 36]. Furthermore, CLARITY can also be combined with traditional imaging techniques, which brings new opportunities for the fundamental study of disease pathology [36].

However, the variety and complexity of the improved techniques for CLARITY, as well as such challenges as complicated steps, low tissue clearing efficiency, tissue damage, and expensive experimental equipment significantly limited popular application. This review systematically summarises the research progress of CLARITY techniques from the perspective of tissue clearing. The brief schematic representation of CLARITY and its modifications is shown in Figure 1. In addition, since the lipids in the tissue affect the tissue transparency to a great extent, the focus of CLARITY is the extraction of lipids from the tissue [22]. Lipid extraction can be passive thermal diffusion, with lipids captured in the detergent micelle diffusing, or active by applying an electric field. The two different methods of lipid extraction are compared in Table 1. According to the way of lipid extraction, these modified CLARITY are classified as active CLARITY, passive CLARITY, and the method of merging active CLARITY with passive CLARITY to select the appropriate tissue clearing method more quickly and effectively based on the balance of tissue clearing speed and tissue transparency of different tissue clearing methods. Furthermore, combing through the advantages of CLARITY and highlighting limitations may be conducive to the construction of different research ideas and enlighten to improve the details of the techniques.

PASSIVE CLARITY

The diffusion barrier properties caused by the lipid bilayer of cells are related to chemical penetration and light scattering properties of the lipid-water interface, making the tissue difficult to visualise [3, 40, 54]. Therefore, lipid extraction is critical for the optical transparency of tissue. The original CLARITY used 4% sodium dodecyl sulphate (SDS) (sodium borate buffer, pH 8.5) at 37–50°C for electrophoretic tissue clearing. However, this may be difficult to implement and may lead to variability in the final tissue quality, including epitopes loss, damage to fine structure and tissue damage caused by heating. Fortunately, lipid extrac-

Figure 1. Schematic representation of CLARITY and its modifications. An outline of the individual steps involved in each of the CLARITY and its modifications is provided alongside the reagents required for each step. Each method has three rows of boxes. The first row presents the simplified steps of the protocol; the second row shows the required reagents; the third row displays the recommended working temperature; RT — room temperature; other abbreviations — see text.

Table 1. Comparison of electrophoresis and passive thermal diffusion

Methods	Electrophoresis	Passive thermal diffusion
Clearing speed	Rapid (several hours to days)	Slow (several days to weeks)
Sample damage	Severe	Mild
The loss of biological information	More	Less
Cost and complexity	Expensive and difficult	Cheap and easy
Circulation	Need (to control the flow rate and temperature)	Needless
Clearing buffer	4% SDS (in PBS buffer, pH 8.5)	8% SDS (in PBS buffer, pH 7.5)

SDS — sodium dodecyl sulphate; PBS — phosphate buffered saline

tion can be passive: lipids captured in the detergent micelles can slowly diffuse out of the tissue into the detergent solution. Temperature and solution affect the rate of lipid clearing, tissue homogeneity and protein loss, but excessive temperature can also lead to tissue damage and fluorescence quenching. Tissue clearing can also accelerate the removal process by gentle shaking and constantly changing the clearing solution. Poguzhelskaya et al. proposed a simplified diffusion-based method, omitting the electrophoresis chamber, called CLARITY2 [33]. The sample (1–1.5 mm thickness) can be completely cleared by incubating it in the clearing solution for 1–2 weeks, with gentle shaking at 37°C. Passive tissue clearing omits the

time-consuming and laborious electrophoresis step and avoids the risk of tissue damage. Moreover, it was reported that there was no significant difference in protein concentration before and after between active and passive clearing [8].

However, several limitations and challenges are facing passive tissue clearing. The main weakness of passive clearing methods is the slow clearing speed, which makes them unsuitable for the clearing of large tissue volumes or whole organisms. Moreover, excessive clearing time leads to a decrease in the signal of fluorescent proteins and an increase in the loss of biomolecules. Therefore, passive CLARITY is an excellent choice for poor laboratory conditions, small samples

(tissue thickness < 3 mm), or high requirements for the integrity of tissue structure and molecular information. However, in recent years, how to promote rapid, whole-brain, and whole-body passive clearing has gradually become the focus of research, and some new modified techniques have emerged that have dramatically improved the scope of application of passive CLARITY technique.

PACT and its variants

In the original CLARITY, the experimental animals were transcardially perfused with hydrogel monomer solution (including 4% paraformaldehyde [PFA], 4% acrylamide, and 0.05% bis-acrylamide in phosphate buffered saline [PBS] supplemented with 0.25% VA-044 initiator). The interesting parts were selected and incubated in 4°C hydrogel monomer solution for 3 days and then polymerised into a hydrogel mesh [3]. Although hydrogel-tissue hybrid avoids tissue damage and the loss of biological information, the dense hydrogel mesh structure leads to low SDS transport efficiency and slow down the speed of lipid extraction. Therefore, Yang et al. [52] developed a simple version of CLARITY based on the passive lipids extraction and termed it PACT (passive clarity technique) to increase the efficiency of SDS transportation and retain the fine structure of the tissue. They perfused and fixed tissue with 4% PFA, and then the tissue was incubated in A4P0 (4% acrylamide in PBS supplemented with 0.25% VA-044 initiator) at 4°C overnight. Compared with original CLARITY, the tissue treated with A4P0 increased the hydrogel mesh porosity, which significantly improves the SDS transport speed, but the tissue was also more easily to swell, and the changes of the tissue weight and volume were 174% and 223%, respectively. Fortunately, the tissue will gradually shrink to the original size in the following steps, and this change of tissue volume expansion-contraction has little effect on the tissue structure, even providing an advantage for the application of some dense tissues, such as bone [15]. Moreover, since the hydrogel cross-linking inside and outside the tissue is reduced by removing bis-acrylamide from the hydrogel monomer solution during the hydrogel tissue embedding process, the tissue can simply be removed from the surrounding hydrogel, reducing the physical damage to the sample. Besides, they emphasized that increasing the concentration of the SDS clearing buffer from the original 4% to 8% can achieve uniform tissue clearing, and called

8% SDS buffer as PACT reagents. PACT increases the efficiency of passive lipid extraction and is suitable for clearing small or particularly fragile samples and organs, which can clear 1–3 mm thick samples (including the brain, spinal cord, kidney, heart, lung and intestine, etc.) within 2–5 days.

However, PACT is still slow to clear large volumes of tissues, which limits its scope of application. The PACT reagents can be delivered either intracranially or *via* the vasculature to clear and label whole-brain and whole-body. A4P0 and PACT reagents were continuously circulated in the fixed animal vasculature by the peristaltic pump for tissue clearing *in situ*. This method, similar to cardiac perfusion, was named PARS (perfusion-assisted agent release *in situ*) by Yang et al. [13, 52]. PARS increases the contact area between clearing buffer and tissue, so the rate of tissue clearing becomes faster. Furthermore, the tissue swell of PARS is reduced due to the limitation of physiological structure in the process of tissue clearing. Unfortunately, the implementation complexity of PARS limits its further application. Moreover, PACT/PARS needs more time to get maximal tissue transparency. Therefore, there are some PACT-based tissue clearing methods emerged.

Woo et al. [49, 50] modified PACT by treating tissues in 4% acrylamide and 0.25% VA-044 in two separate steps during hydrogel formation to improve the lipid removal speed, called psPACT (process separation PACT). This separation process avoids the removal of the remaining unpolymerised hydrogel monomers surround the tissue and the time required for lipid extraction of psPACT is also 10% less than that of PACT. Meanwhile, based on the psPACT, Woo et al. [49, 50] added 0.5% a-thioglycerol, a un-browning agent, to the PACT reagent to increase the lipid removal speed of most tissues by 25%, and called this method mPACT (modified PACT). The addition of 0.5% a-thioglycerol to PACT reagent accelerated optical transparency but increased tissue fragility. Therefore, Woo et al. [48] proposed the process separation PACT-Acrylamide (psPACT-A) and modified PACT-Acrylamide (mPACT-A) protocols, which avoid increasing tissue fragility without reducing optical transparency and can be used to remove mouse embryos. In the modified methods, after the tissue was embedded in 0.25% VA-044, the sample was reincubated in the A4P0 solution to improve the firmness of hydrogel. Both psPACT-A and mPACT-A can achieve rapid optical tissue clearing within the same clearing time as the original protocols.

PACT and its variants expanded the application of CLARITY, which can be used to achieve whole-brain and whole-body clearing and labelling. Moreover, these modified methods provide a powerful tool to study the mechanism of disease onset and progression, and can reflect detailed changes in a part of the observed sample as a whole to fully understand its biological characteristics.

Free of acrylamide SDS-based tissue clearing

The original CLARITY includes a hydrogel embedding step based on two hypotheses:

— The process of the extraction of lipids from tissues removes the lipid bilayers that are critical to cell integrity, but cell integrity is different from tissue integrity. Although the former may be mainly maintained by the plasma membrane, the tissue has mechanical strength, and its integrity is maintained by the intracellular cytoskeleton, cooperative transmembrane adhesion junctions, and extracellular junctions [18];

— The tissue is crosslinked with formaldehyde in the presence of hydrogel monomers, covalently linking tissue elements to monomers that are then polymerised into a hydrogel mesh. It forms a physical framework that prevents proteins from being removed from the tissue during SDS-micelle clearing, while lipids can be washed away [3]. However, the use of acrylamide hydrogel in CLARITY caused many problems. The process of hydrogel tissue embedded causes the tissue to swell and become more fragile with the loss of structural integrity [3, 26, 30]. Moreover, although the pores of hydrogel-tissue hybrid help to promote lipid extraction and antibody penetration, antibody penetration appears to be better in unhybridized, formaldehyde-fixed tissue [42, 52]. Therefore, Lai et al. [23] questioned whether acrylamide was cross-linked with formaldehyde-modified proteins. They believed that tissue-PFA-acrylamide was not cross-linked and that when the tissue was fully fixed, the use of hydrogel can be avoided in the process of lipid removal. Compared with the lipid removal process of SDS-micelles in hydrogel embedded tissue and hydrogel non-embedded tissue, there was no visible tissue swelling in the unembedded tissue of the hydrogel. Furthermore, protein loss in unembedded tissue only increased slightly, which was probably due to the diffusion limitation of hydrogel on protein leakage, rather than the sta-

ble fixation of proteins in the framework formed by hydrogels. Therefore, as long as the tissue is well fixed, the use of acrylamide hydrogel can be omitted to simplify tissue clearing.

For these reasons, Liu et al. [27] developed an improved CLARITY named FASTClear (Free-of-acrylamide SDS-based Tissue Clearing). 4% PFA/10% neutral-buffered formalin fixed tissue, avoiding the use of hydrogel, is directly immersed in 4% SDS for degreasing and at a temperature of 50°C to increase the removal rate. However, prolonged PFA fixation time will hinder the clearing rate and immune labelling due to excessive PFA cross-linking on the tissue [26]. Moreover, some tissues (such as spinal cord and cortical white matter) are difficult to become transparent after SDS delipidation. Fortunately, iDISCO can permeate optically opaque, PFA-fixed tissue in a cocktail of detergent to immunostain the tissue [34]. Then, the tissue can be optically transparent with organic solvents using the 3DISCO [9]. FASTClear is a simplified and rapid method of tissue clearing, which simplifies the process and adds potential additional benefits, including avoiding the use of toxic acrylamide, increasing antibody penetration, reducing tissue swelling, and increasing compatibility with other tissue treatment techniques. Furthermore, FASTClear can be applied to the imaging of tissues that are difficult to become transparent with traditional tissue clearing techniques, such as fresh spinal cord tissue. However, the FASTClear is limited to antibody labelling, and the penetration depth of the antibody is not uniform, which may be related to the local tissue structure.

Thus, Xu et al. [51] developed a rapid free of acrylamide SDS-based tissue clearing method by modifying and merging PACT and FASTClear to reduce tissue clearing time and preserve fluorescent signals. In the step of lipid extraction, FACT used 8% SDS to remove lipids and removed the process of hydrogel perfusion and embedding from PACT to improve the speed of clearing. The staining step of FASTClear was used for reference, but the working temperature was reduced to 37 °C and the pH 7.5 clearing buffer was used, which could reduce the fluorescence quenching rate. The FACT is a simple and low-cost method of tissue clearing, which improves the preservation of cell structure, the penetration depth of antibody and the long-term retention of the fluorescence signal. Moreover, FACT avoids the use of hydrogel and reduces tissue swelling, which can be applied to the study of fine cytoarchitectural details such as microglia.

Table 2. Electrophoretic tissue clearing with various protocols

Methods	CLARITY	Stochastic electrotransport	Active clarity technique	PRE-CLARITY (NCES)
Electrodes	Wire-electrodes	Wire-electrodes	Platinum plate-electrodes	Wire-electrodes
Electric field	Static	Rotational	Static	Static
Clearing speed*	++ (2 weeks)	+++ (3 days)	++++ (5–6 h)	+
Sample damage	++	+	+++	++
Complexity	++	+++	++	+
Circulation	Yes	Yes	Yes	No

*The time required to clear the mouse brain; NCES — non-circulation electrophoresis system

ACTIVE CLARITY

Accelerating the extraction of lipids from intact tissue is the key to obtain better tissue imaging. Passive lipid removal has been greatly improved, such as CLARITY2, PACT, PARS, mPACT and other modified methods, which greatly shorten the time of tissue clearing. However, the lipid extraction speed of passive clearing methods is still slow. Therefore, improvements in active clearing methods have been underway. In the original CLARITY, the SDS detergent can capture lipids in SDS micelles, which are negatively charged at alkaline solutions (pH 7.5–8.5), so they can be removed under the action of an electric field in a customized electrophoresis chamber. The electrophoretic tissue clearing (ETC) system of the original CLARITY has four elements [3]:
— a power supply;
— an electrophoresis chamber containing electrodes and samples;
— a circulator used to provide fresh clearing solutions and to control the flow rate and temperature;
— a buffer filter to filter larger particles in the clearing solution.

Electrophoretic tissue clearing increases the lipid extraction speed by several orders of magnitude compared with passive clearing, and make larger samples (such as mouse brain) transparent in a few hours to days, rather than a few days to weeks, significantly increasing the rate of lipid extraction and reducing tissue swelling.

Although ETC enhances the speed of lipid extraction, it also faces some challenges. First, the too strong electric field of ETC will lead to the formation of bubbles, discoloration, and deposition of black particles on the surface of samples, making the hydrogel opaque, and larger bubbles may cause the hydrogel to break. Moreover, the electrophoresis chamber used by the active CLARITY is heated up due to the effect of Joule heating. Although the ETC clears the tissue more thoroughly at higher temperatures, samples tend to lose structural integrity due to high temperature, just like passive CLARITY. In addition, ETC uses a static electrostatic field to cause lipids to be extracted in one direction, resulting in uneven tissue clearing. Furthermore, expensive electrophoresis equipment and complex implementation steps limit the application of electrophoretic tissue clearing. In response to these challenges, there have been many modified methods about ETC in recent years. These methods are summarized in Table 2 and diagrams of these ETC systems are presented in Figure 2.

Stochastic electrotransport

The electric field can drive the movement of charged particles in the tissue with pores (such as hydrogel–tissue hybridisation), but if the tissue contains charged molecules, the electric field can also destroy the tissue. Moreover, the electrical properties in different parts of the tissue are not uniform, and different regions have different electrical properties, which may lead to the emergence of a concentrated electric field in the tissue. Therefore, when lipids are extracted using the static electric field (an electric field that is constant along a certain direction), different parts of the tissue are extracted to different degrees of lipids, which also results in uneven penetration of antibodies in the subsequent steps of staining [21]. The excessive electric field can cause tissue deformation or even tissue structural damage, and may cause bubbles to form inside the hydrogel, reducing the transparency of the tissue and even causing the hydrogel to rupture [3, 21]. Therefore, ETC can accelerate lipid removal in a non-destructive way only at a low electric field, and dense or larger tissue cannot be effectively removed in the low electric field.

Kim et al. [21] proved that the rotational electric field could improve the diffusivity of charged molecules in porous samples, and there is a quadratic
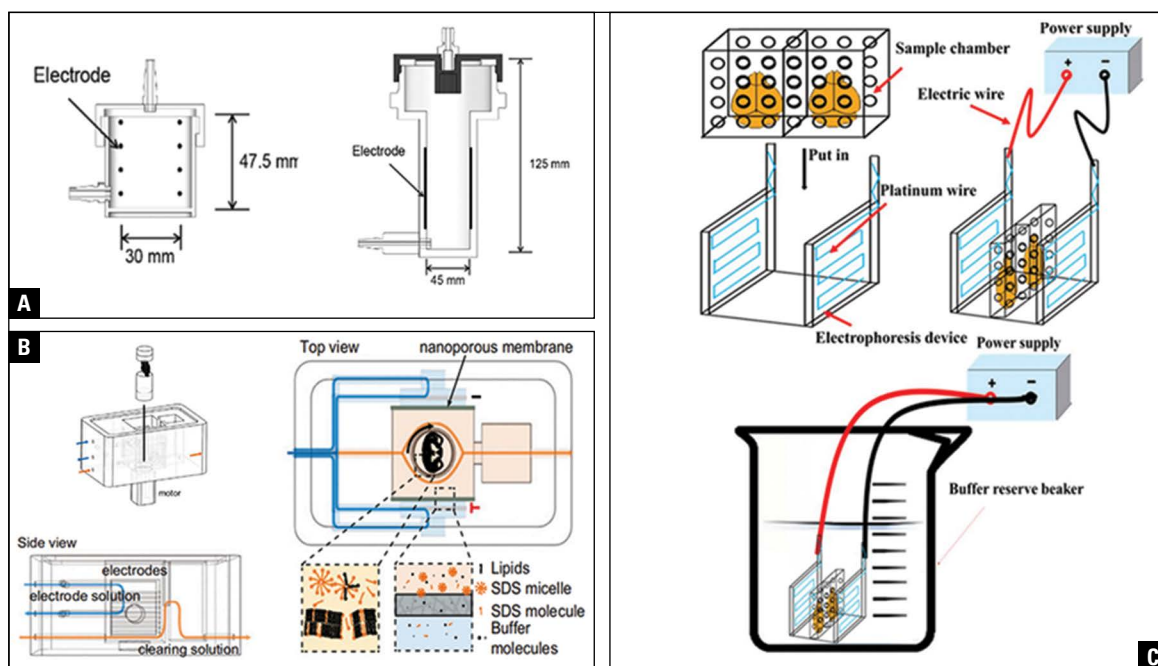
Figure 2. Comparison of electrophoretic tissue clearing (ETC) systems; **A.** Simplified device diagrams of the original ETC chamber (left) and ACT chamber (right), including the electrode area, electrode-electrode distance and inner-chamber dimensions. This picture is cited from the article of Lee et al. [24]; **B.** The device for clearing tissues using stochastic electrotransport. The sample tissue is constantly rotating relative to the electric field. This picture is cited from the article of Kim et al. [21]; **C.** Simplified device diagram of the non-circulation electrophoresis system (NCES). This picture is cited from the article of Du et al. [6].

correlation between the diffusivity and the electrical properties of charged molecules. Moreover, this electrophoresis-driven diffusion transport method can selectively promote the dispersion of free-moving molecules with high electromobility and inhibit the dispersion of endogenous cross-linked biomolecules with low electromobility in the samples. Therefore, Kim et al. [21] improved the method of transportation called stochastic electrotransport, which does not use the unidirectional field but uses a rotational electric field that changes the direction of the electric field over time. The rotational electric field is achieved by continuously rotating the sample chamber between the two electrodes to generate an external rotational electric field relative to the sample, which enhances the random diffusivity of charged molecules, thereby enhancing the efficiency of lipid extraction and staining of large and dense tissues with nuclear dyes, proteins, and antibodies. Moreover, stochastic electrotransport used nanoporous membranes to contain samples, preventing samples from directly contacting electrodes or electrolytic by-products. Stochastic electrotransport can completely remove the mouse organs within 1–3 days and stain them within 1 day.

The advantage of stochastic electrotransport is that it can quickly transport charged molecules out of the tissue without causing significant damage to the tissue structure. Comparing the deformation degree of tissue before and after optical clearing, there is no significant difference in the degree of tissue deformation caused by diffusion and stochastic electrotransport. On the contrary, the extraction of lipids by the static electric field may cause severe damage to the tissue, especially in the tissues with poor conductivity. Although the use of electrophoresis to remove tissue may not use an almost high voltage, the speed of electrophoresis will eventually be limited by tissue damage. Therefore, stochastic electrotransport has apparent advantages in clearing large and dense samples.

However, stochastic electrotransport has the potential for rapid lipid removal and staining, but the temperature increases with the strength of the electric field due to the effect of joule-heating. As mentioned before, the intact tissue structure and biological information will be gradually destroyed and lost as the temperature increases, which limits the further improvement of the clearing efficiency [8]. Therefore, it is significant to explore the balance point

between the efficiency of lipid removal, temperature and electric field strength for finding the appropriate temperature and electric field strength of different tissues and organs in the following studies.

Active clarity technique

The use of electrophoresis has dramatically increased the speed of tissue clearing, but the whole process is slow and requires complex procedures. Therefore, Lee et al. [24] improved CLARITY by optimising the composition of hydrogel and electrophoresis and called this method active clarity technique (ACT). As for lipid extraction, there are two specific improvements in the ACT:

— in the process of hydrogel tissue embedding, the two-step fixation method mentioned in passive CLARITY was used [52]: 4% PFA fixation, and then acrylamide perfusion without bisacrylamide. This method reduced the cross-linking of protein-acrylamide and obtained hydrogels with higher porosity so that lipids can be extracted quickly and staining can be better performed;

— an improved version of the ETC chamber (a dense current ETC system) was designed: the platinum plate was used to replace the thin platinum wire to produce a dense and regular current, which kept the PH and colour of the clearing solution unchanged during the clearing process. Moreover, the addition of an active cooling system significantly reduced the heat generation, thereby reducing the limitation of joule-heating, and can quickly obtain optically transparent tissue without causing tissue damage and protein loss. In addition, expanding the length of the ETC chamber allows all the air bubbles to float on the surface, and then all the bubbles are removed through the upper outlet of the ETC chamber, which increases the light transmittance of the hydrogel and avoids the risk that larger bubbles may cause the hydrogel to break. These improvements can quickly make large tissue samples optically transparent without causing tissue burning, collapse and protein loss.

Active clarity technique can clear most adult mouse tissues within 2–20 hours, and can expand to large organs (such as the brains of rats or rabbits) and even the whole bodies of adult animals (such as adult mouse, zebrafish and Xenopus) [24]. Comparing the clearing efficiency of ACT with other tissue clearing methods, it has been found that ACT takes 2 hours to achieve almost complete optical transparency of a 1 mm thick brain slice, but it takes 3 days for other methods to achieve similar optical transparency. Therefore, ACT has a great advantage in clearing thick tissues and large organs, even adult animals. The tissue cleared by ACT also showed a high contrast between connective tissue and soft tissue in PBS buffer, and the tissue structure could be distinguished even under a standard anatomical microscope. ACT, a reliable and rapid method for clearing large samples, accelerates the speed of tissue clearing and has promising applications in the field of cellular and molecular functions. However, when ACT is applied to the whole body clearing, the clearing efficiency of different tissues varies with size and density. Moreover, under conventional conditions, ACT clears some tissue with significant swelling, which requires further improvement.

Fix-Clear

The original CLARITY creatively applied hydrogel mesh to bind tissue proteins and nucleic acids to preserve the biological information of the tissue when using detergent to clear lipids. However, subsequent studies have found that hydrogel embedding is not essential for tissue clearing, and some protocols, such as SWITCH, FASTClear and FACT, use SDS for delipidation without hydrogel embedding [27, 30, 51]. Although the formation of hydrogel-tissue complexes provides lasting physical strength in the degreasing process and provides expandability, dry-ability, and the ability to selectively bind to functional chemicals, the process of hydrogel embedding has some drawbacks [7]:

— during the clearing process, the super-hydrophilic property of acrylamide causes the tissue to swell, which is not desirable for the maintenance of subcellular structures;

— crosslinking of acrylamide to proteins increases the risk of protein inactivation when immunolabelled [23, 34];

— the infiltration of acrylamide monomer into the tissue increases the complexity of the method.

Passive CLARITY first tried the method of SDS--based tissue clearing without acrylamide and made some progress. Therefore, whether this method can be applied to active CLARITY to improve tissue clearing method has attracted attention. Choi et al. [2] merged the acrylamide-free tissue clearing technique with ETC and named it Fix-Clear (FxClear). FxClear has some advantages:

— by removal of the transcardial perfusion with hydrogel solution and hydrogel tissue embedding steps, shorter reaction time, smaller tissue expansion, and higher immunoreactivity can be achieved. Compared with ACT, FxClear provides stronger immunolabelling for most antibodies due to the absence of acrylamide;

— using a tan electrophoretic mechanism with SDS for delipidation, the lipids in the tissue can be removed quickly. However, the tissue expansion of FxClear is smaller than that in the ACT due to the absence of acrylamide, so lipids are not extracted completely, which may have a particular impact on subsequent imaging.

Furthermore, one potential problem with FxClear is that ETC can damage the tissues. Quantitative analysis of protein loss shows that ETC > 1 day can lead to protein loss, which may be caused by tissue damage, so long-term use of ETC is not recommended. On the contrary, only a small amount (< 2%) of protein loss was detected in a safe time (< 1 day). FxClear is particularly suitable for the 3D pathological examination of small samples (such as brain samples of 1~2 mm). Furthermore, FxClear can be applied to some studies that require precise preservation of sample size due to the small tissue swelling.

THE METHOD OF MERGING ACTIVE AND PASSIVE CLARITY

Lipid extraction is essential for obtaining optically transparent tissue. Although electrophoresis is faster than passive thermal perfusion, it needs to establish a professional circulatory system, which makes electrophoresis difficult to manipulate. Therefore, how to design a simplified electrophoresis device to facilitate implementation has become a challenge. Du et al. [6] separates the electrode from the electrophoresis chamber and designs a mobile electrophoresis device named non-circulation electrophoresis system (NCES). Furthermore, Du et al. [6] also reported a new tissue clearing method called PRE-CLARITY (Passive pRe-electrographysics CLARITY) by merging passive thermal perfusion and electrophoretic lipid extraction for the first time. First, the A4P0B0 (4% PFA in PBS) treated brain was cleared by NCES for 1 day with 4% SDS clearing buffer containing 1% alpha-thioglycerol. Then, the passive clearing was conducted in 4% SDS clearing buffer with 5% alpha-thioglycerol at 50°C, with gentle shaking. PRE-CLARITY can make the brain
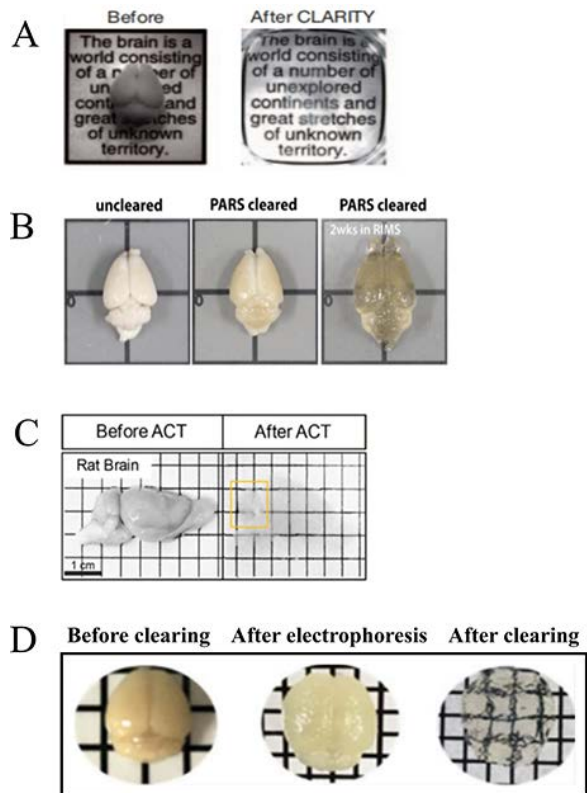
Figure 3. Brain imaging of intact adult mice and rats prepared by different methods; **A.** Images of mouse brains prepared using CLARITY. The first box (from left) is the uncleared brain, and the second box is the brain processed with 8 days of CLARITY. This picture is cited from the article of Chung et al. [3]; **B.** Images of mouse brain before (first box, from left), after (second box) 2 weeks of PARS clearing and after immersion in RIMS (third box). This picture is cited from the article of Yang et al. [52]; **C.** Images of rat brain hemisphere before (first box, from left), after (second box) 15 hours of active clarity technique clearing. This picture is cited from the article of Lee et al. [24]; **D.** Images of mouse brains prepared using PRE-CLARITY. The first box (from left) is the A4P4B0.05-processed brain, the second box is the brain after 1 day electrophoresis at 25 V/37°C, and the last box is the brain after 15 days passive clearing at 50°C. This picture is cited from the article of Du et al. [6].

completely transparent in 5 days. They had three main findings:

— when electrophoresis or passive clearing is used, A4P0B0 embedding method and adding alpha-thioglycerol could achieve faster clearing and higher transparency than the A4P4B0.05 (4% PFA, 4% acrylamide, 0.05% bis-acrylamide and 0.25% VA-044 initiator in PBS) treated brains;

— when different PFA post-fixation times are used, the cleaning speed is different. The shorter the PFA post-fixation time, the faster the clearing speed, but when using a post-fixation time less than

10 hours, the sample is more likely to be damaged in the electrophoresis.
— compared with electrophoresis or passive clearing alone, PRE-CLARITY improved the transparency of tissue. It showed improvements in transparency over electrophoresis clearing and shortened the clearing time to half compared with passive tissue clearing (Fig. 3).

However, PRE-CLARITY also has some challenges. A4P4B0.05 treated sample was not well cleared in NCES, which may be related to the short electrophoresis time. It may also be related to the flow-assisted dissociation of lipid molecules because the main difference between the original electrophoresis system and the NCES system lies in the flow of clearing buffer. Moreover, NCES uses platinum wire to make electrodes. Platinum plates are reported to generate denser currents, thus speeding up tissue clearing, which can be improved in follow-up research. In short, PRE-CLARITY provides a simplified electrophoresis system and a faster and more transparent method of tissue clearing. The attempt to merge different tissue clearing methods also provides a new perspective for tissue optical clearing method and facilitates the development of tissue clearing method.

CONCLUSIONS

With the deepening of biomolecular information research, CLARITY and its variants will be increasingly applied to fine structure imaging of tissues and the function of cells or biomolecules in intact tissues, which has a broad application prospect. A list of variants of the CLARITY simplify and improve the experimental conditions, equipment, and concrete steps of the original CLARITY. By classifying these modified CLARITY techniques and comparing the similarities and differences between them, it is easier to find the areas where these protocols need to be improved, and we can also learn some improved ideas from them. For example, the hydrogel matrix for passive tissue clearing was optimised to the A4P0 in the PACT protocol, but this formula was later used in active tissue clearing methods. These modified methods increase the speed of tissue clearing and tissue transparency and maintain the fine structure of tissue, which is helpful to the study of different tissue types. Moreover, these improvements also break the limitation of original CLARITY. Optical clearing of intact tissues can be carried out even in ordinary laboratories, making it easier for researchers to obtain detailed biological information. Furthermore, the classification and summary of the modified CLARITY techniques will help researchers to choose a suitable tissue clearing method more quickly and effectively.

In short, passive CLARITY is a right choice for poor laboratory conditions, small samples (tissue thickness < 3 mm), or high requirements for the integrity of tissue structure and molecular information. Of course, passive CLARITY can also be used to clear large samples or even whole mice, but it takes a long time, which puts forward higher requirements for the preservation of tissue and fluorescent staining. The use of active CLARITY can accelerate this process, but the high requirements of laboratory equipment limit its application. In addition, although many improvements have been made to ETC, the tissue damage caused by the current is still the main factor limiting its application. The suitable electric field intensity and electrophoresis time should be strictly selected for different texture tissues.

For the improvement of active CLARITY, the electric field conditions have been optimised in the past, whether active CLARITY can be optimised from its power source. At present, the power that drives lipids to extract from the tissue quickly is electricity, whether it can be replaced with other types of power to avoid tissue damage, such as magnetic energy or hydrodynamic pressure for molecular transport or even centrifugation. Besides, whether active or passive CLARITY, as noted by the researchers who initially developed CLARITY, the subsequent acquisition of high-resolution 3D image and how to analyse these data remains a challenge, which is a common problem in all tissue clearing methods. The improvement of image acquisition and data analysis and exploring how to combine with other technologies will not only make us more skilled in the application of CLARITY but also re-recognise the physiological characteristics of tissue or even a species as a whole for the first time from a 3D perspective.

Conflict of interest: None declared

REFERENCES

1. Ando K, Laborde Q, Lazar A, et al. Inside Alzheimer brain with CLARITY: senile plaques, neurofibrillary tangles and axons in 3-D. Acta Neuropathol. 2014; 128(3): 457–459, doi: 10.1007/s00401-014-1322-y, indexed in Pubmed: 25069432.

2. Choi J, Lee E, Kim JH, et al. FxClear, a free-hydrogel electrophoretic tissue clearing method for rapid de-lipidation of tissues with high preservation of immunoreactivity. Exp Neurobiol. 2019; 28(3): 436–445, doi: 10.5607/en.2019.28.3.436, indexed in Pubmed: 31308802.

3. Chung K, Wallace J, Kim SY, et al. Structural and molecular interrogation of intact biological systems. Nature. 2013; 497(7449): 332–337, doi: 10.1038/nature12107, indexed in Pubmed: 23575631.

4. DePas WH, Starwalt-Lee R, Van Sambeek L, et al. Exposing the three-dimensional biogeography and metabolic states of pathogens in cystic fibrosis sputum via hydrogel embedding, clearing, and rRNA labeling. mBio. 2016; 7(5), doi: 10.1128/mBio.00796-16, indexed in Pubmed: 27677788.

5. Dodt HU, Leischner U, Schierloh A, et al. Ultramicroscopy: three-dimensional visualization of neuronal networks in the whole mouse brain. Nat Methods. 2007; 4(4): 331–336, doi: 10.1038/nmeth1036, indexed in Pubmed: 17384643.

6. Du H, Hou P, Wang L, et al. Modified CLARITY achieving faster and better intact mouse brain clearing and immunostaining. Sci Rep. 2019; 9(1): 10571, doi: 10.1038/s41598-019-46814-4, indexed in Pubmed: 31332235.

7. El-Sherbiny IM, Yacoub MH. Hydrogel scaffolds for tissue engineering: Progress and challenges. Glob Cardiol Sci Pract. 2013; 2013(3): 316–342, doi: 10.5339/gcsp.2013.38, indexed in Pubmed: 24689032.

8. Epp JR, Niibori Y, Liz Hsiang HL, et al. Optimization of CLARITY for clearing whole-brain and other intact organs. eNeuro. 2015; 2(3), doi: 10.1523/ENEURO.0022-15.2015, indexed in Pubmed: 26464982.

9. Ertürk A, Becker K, Jährling N, et al. Three-dimensional imaging of solvent-cleared organs using 3DISCO. Nat Protoc. 2012; 7(11): 1983–1995, doi: 10.1038/nprot.2012.119, indexed in Pubmed: 23060243.

10. Ertürk A, Bradke F. High-resolution imaging of entire organs by 3-dimensional imaging of solvent cleared organs (3DISCO). Exp Neurol. 2013; 242: 57–64, doi: 10.1016/j.expneurol.2012.10.018, indexed in Pubmed: 23124097.

11. Ertürk A, Mauch CP, Hellal F, et al. Three-dimensional imaging of the unsectioned adult spinal cord to assess axon regeneration and glial responses after injury. Nat Med. 2011; 18(1): 166–171, doi: 10.1038/nm.2600, indexed in Pubmed: 22198277.

12. Feng Yi, Cui P, Lu X, et al. CLARITY reveals dynamics of ovarian follicular architecture and vasculature in three-dimensions. Sci Rep. 2017; 7: 44810, doi: 10.1038/srep44810, indexed in Pubmed: 28333125.

13. Gage GJ, Kipke DR, Shain W. Whole animal perfusion fixation for rodents. J Vis Exp. 2012(65), doi: 10.3791/3564, indexed in Pubmed: 22871843.

14. Gradinaru V, Treweek J, Overton K, et al. Hydrogel-Tissue chemistry: principles and applications. Annu Rev Biophys. 2018; 47: 355–376, doi: 10.1146/annurev-biophys-070317-032905, indexed in Pubmed: 29792820.

15. Greenbaum A, Chan KY, Dobreva T, et al. Bone CLARITY: Clearing, imaging, and computational analysis of osteoprogenitors within intact bone marrow. Sci Transl Med. 2017; 9(387), doi: 10.1126/scitranslmed.aah6518, indexed in Pubmed: 28446689.

16. Hama H, Hioki H, Namiki K, et al. ScaleS: an optical clearing palette for biological imaging. Nat Neurosci. 2015; 18(10): 1518–1529, doi: 10.1038/nn.4107, indexed in Pubmed: 26368944.

17. Hama H, Kurokawa H, Kawano H, et al. Scale: a chemical approach for fluorescence imaging and reconstruction of transparent mouse brain. Nat Neurosci. 2011; 14(11): 1481–1488, doi: 10.1038/nn.2928, indexed in Pubmed: 21878933.

18. Humphrey JD, Dufresne ER, Schwartz MA. Mechanotransduction and extracellular matrix homeostasis. Nat Rev Mol Cell Biol. 2014; 15(12): 802–812, doi: 10.1038/nrm3896, indexed in Pubmed: 25355505.

19. Ke MT, Fujimoto S, Imai T. SeeDB: a simple and morphology-preserving optical clearing agent for neuronal circuit reconstruction. Nat Neurosci. 2013; 16(8): 1154–1161, doi: 10.1038/nn.3447, indexed in Pubmed: 23792946.

20. Kim JH, Jang MJ, Choi J, et al. Optimizing tissue-clearing conditions based on analysis of the critical factors affecting tissue-clearing procedures. Sci Rep. 2018; 8(1): 12815, doi: 10.1038/s41598-018-31153-7, indexed in Pubmed: 30143733.

21. Kim SY, Cho JH, Murray E, et al. Stochastic electrotransport selectively enhances the transport of highly electromobile molecules. Proc Natl Acad Sci U S A. 2015; 112(46): E6274–E6283, doi: 10.1073/pnas.1510133112, indexed in Pubmed: 26578787.

22. Kim SY, Chung K, Deisseroth K. Light microscopy mapping of connections in the intact brain. Trends Cogn Sci. 2013; 17(12): 596–599, doi: 10.1016/j.tics.2013.10.005, indexed in Pubmed: 24210964.

23. Lai HM, Liu AK, Ng WL, et al. Rationalisation and validation of an acrylamide-free procedure in three-dimensional histological imaging. PLoS One. 2016; 11(6): e0158628, doi: 10.1371/journal.pone.0158628, indexed in Pubmed: 27359336.

24. Lee E, Choi J, Jo Y, et al. ACT-PRESTO: Rapid and consistent tissue clearing and labeling method for 3-dimensional (3D) imaging. Sci Rep. 2016; 6: 18631, doi: 10.1038/srep18631, indexed in Pubmed: 26750588.

25. Lee H, Park JH, Seo I, et al. Improved application of the electrophoretic tissue clearing technology, CLARITY, to intact solid organs including brain, pancreas, liver, kidney, lung, and intestine. BMC Dev Biol. 2014; 14: 48, doi: 10.1186/s12861-014-0048-3, indexed in Pubmed: 25528649.

26. Liu AKL, Hurry MED, Ng OTW, et al. Bringing CLARITY to the human brain: visualization of Lewy pathology in three dimensions. Neuropathol Appl Neurobiol. 2016; 42(6): 573–587, doi: 10.1111/nan.12293, indexed in Pubmed: 26526972.

27. Liu AKL, Lai HM, Chang RCC, et al. Free of acrylamide sodium dodecyl sulphate (SDS)-based tissue clearing (FASTClear): a novel protocol of tissue clearing for

three-dimensional visualization of human brain tissues. Neuropathol Appl Neurobiol. 2017; 43(4): 346–351, doi: 10.1111/nan.12361, indexed in Pubmed: 27627784.

28. Mano T, Albanese A, Dodt HU, et al. Whole-Brain analysis of cells and circuits by tissue clearing and light-sheet microscopy. J Neurosci. 2018; 38(44): 9330–9337, doi: 10.1523/JNEUROSCI.1677-18.2018, indexed in Pubmed: 30381424.

29. Mao Z, Zhu D, Hu Y, et al. Influence of alcohols on the optical clearing effect of skin in vitro. J Biomed Opt. 2008; 13(2): 021104, doi: 10.1117/1.2892684, indexed in Pubmed: 18465953.

30. Murray E, Cho JH, Goodwin D, et al. Simple, scalable proteomic imaging for high-dimensional profiling of intact systems. Cell. 2015; 163(6): 1500–1514, doi: 10.1016/j.cell.2015.11.025, indexed in Pubmed: 26638076.

31. Palmer WM, Martin AP, Flynn JR, et al. PEA-CLARITY: 3D molecular imaging of whole plant organs. Sci Rep. 2015; 5: 13492, doi: 10.1038/srep13492, indexed in Pubmed: 26328508.

32. Parra SG, Chia TH, Zinter JP, et al. Multiphoton microscopy of cleared mouse organs. J Biomed Opt. 2010; 15(3): 036017, doi: 10.1117/1.3454391, indexed in Pubmed: 20615019.

33. Poguzhelskaya E, Artamonov D, Bolshakova A, et al. Simplified method to perform CLARITY imaging. Mol Neurodegener. 2014; 9: 19, doi: 10.1186/1750-1326-9-19, indexed in Pubmed: 24885504.

34. Renier N, Wu Z, Simon DJ, et al. iDISCO: a simple, rapid method to immunolabel large tissue samples for volume imaging. Cell. 2014; 159(4): 896–910, doi: 10.1016/j.cell.2014.10.010, indexed in Pubmed: 25417164.

35. Rocha MD, Düring DN, Bethge P, et al. Tissue clearing and light sheet microscopy: imaging the unsectioned adult zebra finch brain at cellular resolution. Front Neuroanat. 2019; 13: 13, doi: 10.3389/fnana.2019.00013, indexed in Pubmed: 30837847.

36. Spence RD, Kurth F, Itoh N, et al. Bringing CLARITY to gray matter atrophy. Neuroimage. 2014; 101: 625–632, doi: 10.1016/j.neuroimage.2014.07.017, indexed in Pubmed: 25038439.

37. Sung K, Ding Y, Ma J, et al. Simplified three-dimensional tissue clearing and incorporation of colorimetric phenotyping. Sci Rep. 2016; 6: 30736, doi: 10.1038/srep30736, indexed in Pubmed: 27498769.

38. Susaki EA, Tainaka K, Perrin D, et al. Whole-brain imaging with single-cell resolution using chemical cocktails and computational analysis. Cell. 2014; 157(3): 726–739, doi: 10.1016/j.cell.2014.03.042, indexed in Pubmed: 24746791.

39. Susaki EA, Ueda HR. Whole-body and whole-organ clearing and imaging techniques with single-cell resolution: toward organism-level systems biology in mammals. Cell Chem Biol. 2016; 23(1): 137–157, doi: 10.1016/j.chembiol.2015.11.009, indexed in Pubmed: 26933741.

40. Syková E, Nicholson C. Diffusion in brain extracellular space. Physiol Rev. 2008; 88(4): 1277–1340, doi: 10.1152/physrev.00027.2007.

41. Tainaka K, Kuno A, Kubota SI, et al. Chemical principles in tissue clearing and staining protocols for whole-body cell profiling. Annu Rev Cell Dev Biol. 2016; 32: 713–741, doi: 10.1146/annurev-cellbio-111315-125001, indexed in Pubmed: 27298088.

42. Treweek JB, Chan KY, Flytzanis NC, et al. Whole-body tissue stabilization and selective extractions via tissue-hydrogel hybrids for high-resolution intact circuit mapping and phenotyping. Nat Protoc. 2015; 10(11): 1860–1896, doi: 10.1038/nprot.2015.122, indexed in Pubmed: 26492141.

43. Ueda HR, Ertürk A, Chung K, et al. Tissue clearing and its applications in neuroscience. Nat Rev Neurosci. 2020; 21(2): 61–79, doi: 10.1038/s41583-019-0250-1, indexed in Pubmed: 31896771.

44. Vigouroux RJ, Belle M, Chédotal A. Neuroscience in the third dimension: shedding new light on the brain with tissue clearing. Mol Brain. 2017; 10(1): 33, doi: 10.1186/s13041-017-0314-y, indexed in Pubmed: 28728585.

45. Wang J, Zhang Y, Xu TH, et al. An innovative transparent cranial window based on skull optical clearing. Laser Physics Letters. 2012; 9(6): 469–473, doi: 10.7452/lapl.201210017.

46. Wen X, Mao Z, Han Z, et al. In vivo skin optical clearing by glycerol solutions: mechanism. J Biophotonics. 2010; 3(1-2): 44–52, doi: 10.1002/jbio.200910080, indexed in Pubmed: 19937846.

47. Wen X, Tuchin VV, Luo Q, et al. Controling the scattering of intralipid by using optical clearing agents. Phys Med Biol. 2009; 54(22): 6917–6930, doi: 10.1088/0031-9155/54/22/011, indexed in Pubmed: 19887711.

48. Woo J, Kang H, Lee EY, et al. Investigation of PRDM7 and PRDM12 expression pattern during mouse embryonic development by using a modified passive clearing technique. Biochem Biophys Res Commun. 2020; 524(2): 346–353, doi: 10.1016/j.bbrc.2019.12.133, indexed in Pubmed: 32000999.

49. Woo J, Lee EY, Park HS, et al. Novel passive clearing methods for the rapid production of optical transparency in whole CNS tissue. J Vis Exp. 2018(135), doi: 10.3791/57123, indexed in Pubmed: 29806831.

50. Woo J, Lee M, Seo JM, et al. Optimization of the optical transparency of rodent tissues by modified PACT-based passive clearing. Exp Mol Med. 2016; 48(12): e274, doi: 10.1038/emm.2016.105, indexed in Pubmed: 27909337.

51. Xu Na, Tamadon A, Liu Y, et al. Fast free-of-acrylamide clearing tissue (FACT)-an optimized new protocol for rapid, high-resolution imaging of three-dimensional brain tissue. Sci Rep. 2017; 7(1): 9895, doi: 10.1038/s41598-017-10204-5, indexed in Pubmed: 28852046.

52. Yang B, Treweek JB, Kulkarni RP, et al. Single-cell phenotyping within transparent intact tissue through whole-body clearing. Cell. 2014; 158(4): 945–958, doi: 10.1016/j.cell.2014.07.017, indexed in Pubmed: 25088144.

53. Zhu D, Larin KV, Luo Q, et al. Recent progress in tissue optical clearing. Laser Photon Rev. 2013; 7(5): 732–757, doi: 10.1002/lpor.201200056, indexed in Pubmed: 24348874.

54. Zhu X, Xia Y, Wang X, et al. Optical brain imaging: a powerful tool for neuroscience. Neurosci Bull. 2017; 33(1): 95–102, doi: 10.1007/s12264-016-0053-6, indexed in Pubmed: 27535148.

ORIGINAL ARTICLE

Expression of the ionotropic glutamate receptors on neuronostatin neurons in the periventricular nucleus of the hypothalamus

S. Serter Kocoglu[1], C. Cakir[2], Z. Minbay[2], O. Eyigor[2]

[1]Department of Histology and Embryology, Balikesir University School of Medicine, Balikesir, Turkey
[2]Department of Histology and Embryology, Bursa Uludag University School of Medicine, Bursa, Turkey

Background: Neuronostatin, a newly identified peptide, is accepted as an anorexigenic peptide since it suppresses food intake when given intracerebroventricularly. Although the effect mechanisms of neuronostatin have been shown in different studies, there are no reports in the literature describing the mechanisms controlling neuronostatin neurons. In this study, we aimed to determine the presence of the ionotropic glutamate receptor subunits (iGluRs) in neuronostatin neurons in the periventricular nucleus of the hypothalamus.

Materials and methods: The presence of glutamate receptors in neuronostatin neurons was investigated by dual immunohistochemistry. Immunohistochemistry was performed on 40 μm thick coronal brain sections with antibodies against AMPA (GluA1-4), kainate (GluK1/2/3, and GluK5), and NMDA (GluN1 and GluN2A) receptor subunits.

Results: The results showed that the neuronostatin neurons expressed most of the NMDA and non-NMDA receptor subunits. The neuronostatin neurons in the anterior hypothalamic periventricular nucleus were particularly immunopositive for GluA1, GluA4, GluK1/2/3, GluK5 and GluN1 antibodies. No expression was observed for GluA2, GluA3 and GluN2A antibodies.

Conclusions: For the first time in the literature, our study demonstrated that the neuronostatin neurons express glutamate receptor subunits which may form homomeric or heteromeric functional receptor complexes. Taken together, these results suggest that multiple subunits of iGluRs are responsible for glutamate transmission on neuronostatin neurons in the anterior hypothalamic periventricular nucleus. (Folia Morphol 2022; 81, 1: 13–19)

Key words: neuronostatin, glutamate, NMDA, kainate, AMPA

INTRODUCTION

Glutamate is the major excitatory amino acid neurotransmitter in the mammalian central nervous system [1, 2]. Glutamate mediated neurotransmission occurs via metabotropic and ionotropic glutamate receptors [13]. Ionotropic glutamate receptors are classified according to their agonists: N-methyl-D-aspartate (NMDA), alpha-amino-3-hydroxy-5-methyl-4-isoazolpropionic acid (AMPA) and 2-carboxy-3-carboxymethyl-4-isopropenylpyrrolidine (kainate) receptors [13, 16, 31]. NMDA receptors are composed of subunits named GluN1, GluN2A–D and GluN3A–B [3, 14]. These

Address for correspondence: Assis. Prof. S. Serter Koçoğlu, PhD, Balikesir University Faculty of Medicine, Department of Histology and Embryology, Balıkesir, Turkey, e-mail: serter_bio@hotmail.com

receptors have a critical function in excitatory synaptic transmission, plasticity and neurotoxicity [4, 19, 21–23]. NMDA receptors can participate in very different processes because they have different characteristics from AMPA and kainate receptors. In addition to glutamate, an agonist, glycine or D-serine, is required for NMDA activation. AMPA receptors are composed of four subunits named GluA1–4 [19]. Kainate receptors consist of five subunits named GluK1–5 [17]. While GluK1–3 form functional homomeric receptors, GluK4 and GluK5 only form functional receptors when combined with one of the other subunits (GluK1–3), which generates kainic acid receptors with varying kinetics and agonist affinities [9, 16]. The other receptors, kainate receptors have presynaptic and postsynaptic localisations usually on the same neuron [12].

Neuronostatin is a newly identified anorexigenic peptide encoded by the somatostatin gene [28]. Immunohistochemical studies have shown that neuronostatin positive neurons are localised in the anterior hypothalamic periventricular nucleus and suprachiasmatic nucleus, while neuronostatin immunoreactive axon terminations are localised in the arcuate nucleus with median eminence. There are fewer and less densely-marked neuronostatin-expressing cells in the polymorphic layer of the dentate gyrus and motor cortex, amygdala and cerebellum [5]. These areas where neuronostatin neurons are localised in the hypothalamus play a role in the control of food intake [28]. Also, neuronostatin has regulatory effects on energy consumption [28], cardiovascular system [11], and digestive system [27]. In the literature, experimental studies investigating central regulators (such as glutamate) involved in the control of neuronostatin neurons have not been found.

To better understand glutamatergic function in the neuronostatin neurons localised in the anterior hypothalamic periventricular nucleus, it is necessary to determine the localisation of various iGluR subunits in neuronostatin neurons. In the present study, we examined the cellular localisation of protein expression of AMPA (GluA1, GluA2, GluA3, and GluA4), kainate (GluK1/2/3 and GluK5), and NMDA (GluN1 and GluN2A) receptor subunits in the neuronostatin neurons in the periventricular nucleus of the hypothalamus by immunofluorescence.

MATERIALS AND METHODS

Animals

All animal experiments were carried out under the instructions of the National Institute of Health Guide for the Care and Use of Laboratory Animals and approved by the Experimental Ethical Committee of Bursa Uludag University (Approval No: 2016-4/4). Sixty-day-old male Sprague-Dawley rats (200–250 g) (n = 10) were used in this study. The rats were maintained at the Bursa Uludag University Experimental Animals Breeding and Research Centre and were housed two per cage in a temperature-controlled environment (21°C) with a 12:12-hour light/ /dark cycle. The animals were allowed to access food and water ad libitum. All the experiments were carried out between 9:00 am and 11:00 am.

Tissue preparation

The animals were deeply anesthetised and fixed by trans-cardiac perfusion with 4% paraformaldehyde in phosphate buffer, pH 7.4 (300 mL per animal). Brains and brainstems were carefully removed and post-fixed overnight in the same fixative. Forty-micrometre-thick coronal serial sections throughout the brains were cut with a vibratome and collected into Tris-HCl buffer (0.05 M, pH 7.6). The sections were kept in the cryoprotectant solution at –20°C until use.

Immunohistochemistry

Tris-HCl buffer was used for all washing steps. Blocking buffer (10% normal horse serum, 0.2% triton X-100, and 0.1% sodium azide in Tris-HCl buffer) was used for incubations to prevent non-specific binding and to dilute the antibodies. All incubation steps were carried out on an orbital shaker with appropriate agitation.

Free-floating sections were equilibrated to room temperature and washed 3 times in Tris-HCl buffer to remove cryoprotectant and blocked in blocking buffer for 2 hours. Following the washing step, tissues were incubated in preheated Antigen Retrieval (AR) solution (final solution temperature 73–75°C) for 30 minutes. 50 mM trisodium citrate buffer (pH 6, for neuronostatin, GluK1/2/3 and GluA4) or 1 mM EDTA solution (pH 8, for GluN1 and GluN2A) was used in the AR process. The sections were washed 3 times. Tissues were treated with 3% H_2O_2 to quench endogenous peroxidase, washed 3 times and blocked with 10% normal horse serum for 2 hours. The sections were incubated in rabbit anti-neuronostatin (1/4000 dilution, H-060-50, Phoenix Pharmaceuticals, Inc., USA) and mouse anti-GluA1 (1/500 dilution, AM-60040PU-N, Acris, USA), mouse anti-GluA2 (1/500 dilution, MAB397, Millipore, USA), mouse anti--GluA3 (1/250 dilution, MAB5416, Millipore, USA),
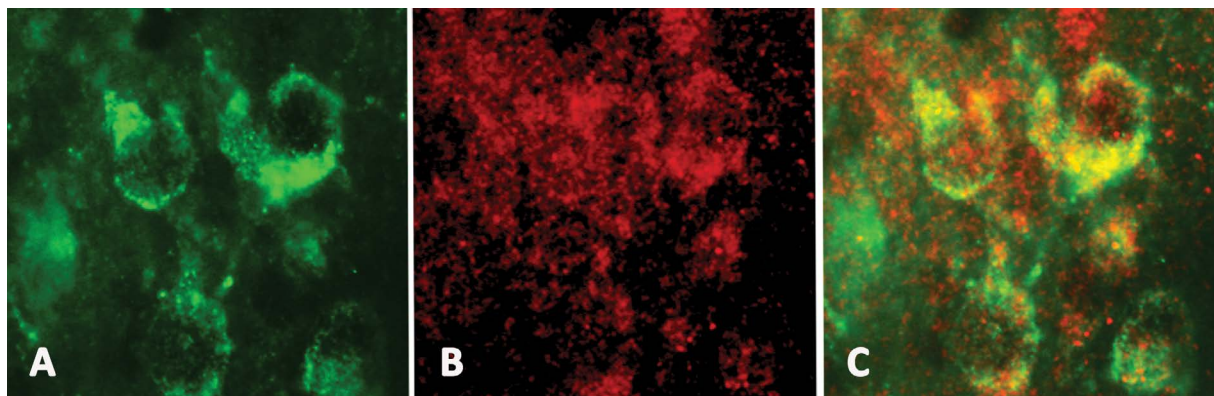
Figure 1. Evaluation of dual immunohistochemical staining; **A.** Neurons expressing the peptide labelled with green fluorochrome; **B.** Neurons expressing glutamate receptor subunit protein labelled with red fluorochrome; **C.** Neurons expressing the glutamate receptor subunit protein together with the peptide are monitored in yellow.

goat anti-GluA4 (1/250 dilution, LS-B3606, LifeSpan BioSciences, Inc., USA), mouse anti-GluK1/2/3 IgM (1/500 dilution, MAB379, Chemican Int., USA), goat anti-GluK5 (1/250 dilution, sc-8915, Santa Cruz Biotechnology, Inc., USA), mouse anti-GluN1 (1/500 dilution, 556308, BD Pharmingen, USA), and mouse anti-GluN2A (1/3000 dilution, H-060-50, Millipore, USA). The washed sections were processed with donkey anti-goat IgG-Alexa-Fluor (1/500 dilution), donkey anti-mouse IgG-Alexa-Fluor (1/500 dilution), donkey anti-mouse IgM-biotin-conjugate (1/200 dilution), donkey anti-rabbit IgG-Alexa-Fluor 488 (1/500 dilution) and streptavidin-TR (1/100 dilution) for 2 hours. After washes, the sections were mounted on glass slides, dried and coverslipped with antifade medium.

Neuronostatin antibodies used in this study have been used in many reports in the literature as well as in our previous studies [6, 30]. The antibody specificity of ionotropic glutamate receptors in the rat red nucleus was shown in our previous studies in the literature [20].

Analysis

Sections were analysed and photographed with Olympus BX-50 photomicroscope attached to a CCD camera (Olympus DP71, CCD colour camera, 1.5 million pixels, Olympus Corporation, Japan). Sections between the coordinates determined according to the rat brain atlas (bregma –0.24 mm to –3.60 mm for periventricular nucleus) were used for single and double immunohistochemical labelling [24]. Cross-sections were taken at 5 different levels at the same coordinate and an equal distance for each animal. Immunofluorescent staining intensities of neuronostatin neurons co-localised with kainic acid, AMPA and NMDA receptor subunits in the anterior hypothalamic periventricular nucleus were graded by the following scale: '+' was used for a small number of double immunoreactive neuronostatin neurons, '++' for a moderate number of double immunoreactive neuronostatin neurons, and '+++' for a high number of double immunoreactive neuronostatin neurons.

RESULTS

The results showed that ionotropic glutamate receptor subunits (iGluRs) subunits were expressed in neuronostatin neurons localised in the anterior hypothalamic periventricular nucleus. Specific staining was localised in neuronal perikarya. The number of stained neuronostatin neurons changed depending on the type of iGluRs subunits. The neuronostatin neurons in the anterior hypothalamic periventricular nucleus were particularly immunopositive for GluA1, GluA4, GluK1/2/3, GluK5 and GluN1 antibodies. No expression was observed for GluA2, GluA3 and GluN2A antibodies. The highest expression was detected for GluN1-positive neuronostatin neurons.

Neuronostatin protein positivity was visualised by green reaction product with a fluorochrome (Alexa 488) (Fig. 1A) and glutamate receptor subunit protein positivity was labelled by red fluorochromes (Alexa 594 or streptavidin-conjugated Texas-Red) (Fig. 1B) in the cytoplasm. In digitally overlapped images, neurons expressing both proteins were visualised in yellow (Fig. 1C).
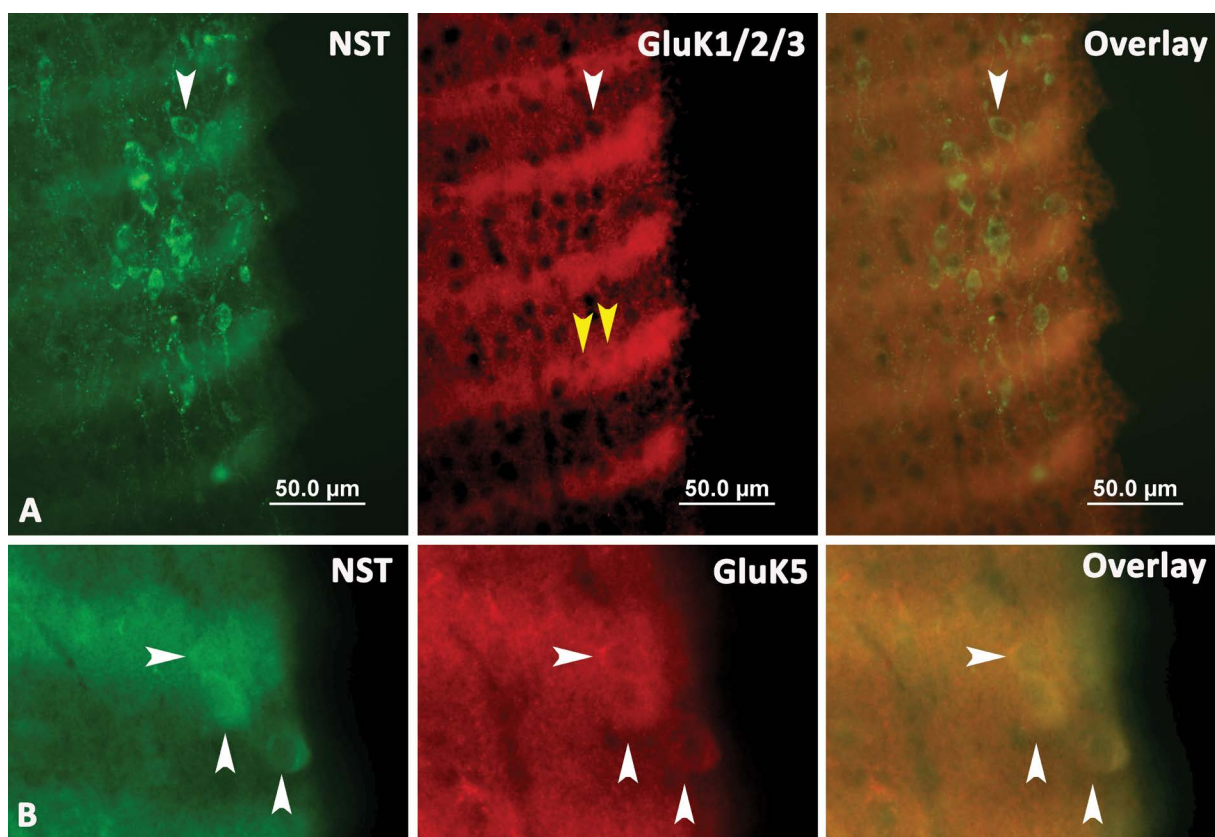
Figure 2. Immunofluorescence image of GluK1/2/3-positive neuronostatin (NST) neurons in the anterior hypothalamic periventricular nucleus (**A**). Immunofluorescence image of GluK5-positive neuronostatin neurons in the anterior hypothalamic periventricular nucleus (**B**). Neurons co-expressing both proteins (white arrowhead), only GluK1/2/3-positive neurons (yellow arrowhead).

Table 1. The distribution of the staining intensity of ionotropic glutamate receptor subunits in neuronostatin neurons localised in the anterior hypothalamic periventricular nucleus

Neuronostatin neurons							
GluK1/2/3	GluK5	GluA1	GluA2	GluA3	GluA4	GluN1	GluN2A
+	+	++	–	–	++	++/+++	–

The expression of kainic acid receptor subunits in neuronostatin neurons (GluK1–3 and GluK5)

Dual immunofluorescence studies showed that GluK1-, GluK2-, GluK3- and GluK5-positive neuronostatin neurons were expressed in the anterior hypothalamic periventricular nucleus. However, a small number of GluK1-, GluK2-, GluK3- (Fig. 2A) and GluK5-positive neuronostatin neurons (Fig. 2B) was observed in the anterior hypothalamic periventricular nucleus (Table 1).

The expression of AMPA receptor subunits in neuronostatin neurons (GluA1–4)

GluA1 (Fig. 3A) and GluA4 subunit protein (Fig. 3B) from the AMPA receptor family were co-expressed in

neuronostatin neurons. However, GluA2 and GluA3 subunit proteins were not expressed in neuronostatin neurons.

GluA1, GluA4 and neuronostatin neurons were expressed in the anterior hypothalamic periventricular nucleus. A moderate number of neuronostatin neurons expressing GluA1 and GluA4 were detected in the anterior hypothalamic periventricular nucleus (Table 1).

The expression of NMDA receptor subunits in neuronostatin neurons (GluN1 and GluN2A)

GluN1-positive neuronostatin neurons were ob-served in the anterior hypothalamic periventricular
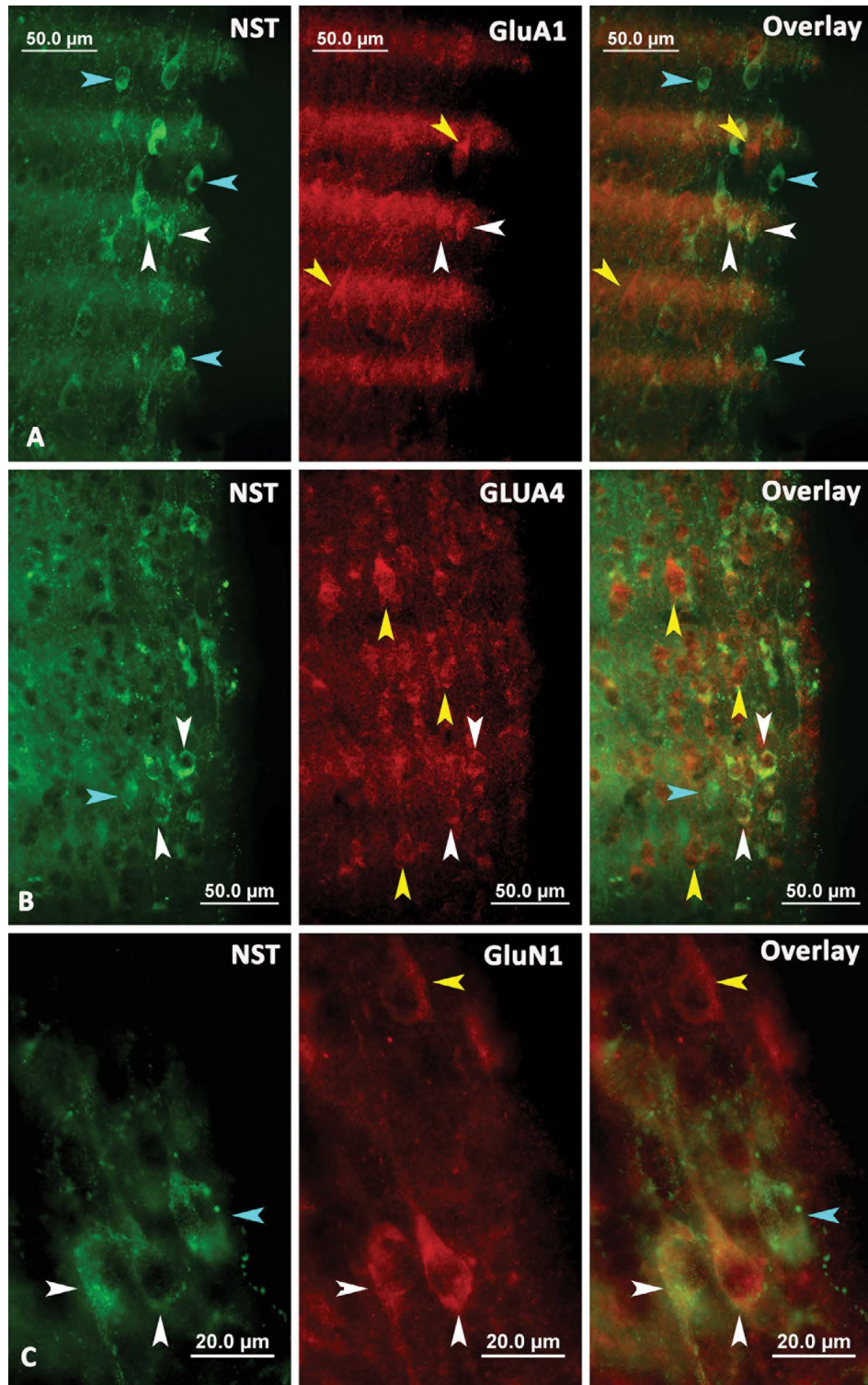
Figure 3. Immunofluorescence image of GluA1-positive neuronostatin (NST) neurons in the anterior hypothalamic periventricular nucleus (**A**). Immunofluorescence image of GluA4-positive neuronostatin neurons in the anterior hypothalamic periventricular nucleus (**B**). Immunofluorescence image of GluN1-positive neuronostatin neurons in the anterior hypothalamic periventricular nucleus (**C**). Neurons co-expressing both proteins (white arrowhead), only GluA1-positive neurons, only GluA4-positive neurons, only GluN1-positive neurons (yellow arrowhead) and only neuronostatin-immunoreactive neurons (blue arrowhead).

nucleus (Fig. 3C). However, no expression of GluN2A subunit protein was detected in neuronostatin neu-

rons. The number of GluN1-positive neuronostatin neurons varied from moderate to high (Table 1).

17

DISCUSSION

The present study showed that both NMDA and non-NMDA glutamate receptor proteins were synthesised by neuronostatin neurons. Our results indicated that neuronostatin neurons express iGluRs subunits in varying quantities and intensities. To the best of our knowledge, this is the first descriptive study on the differential expression pattern of iGluRs in the neuronostatin neurons localised in the anterior hypothalamic periventricular nucleus. GluA1, GluA4, GluK1/2/3, GluK5 and GluN1 receptor proteins were expressed in neuronostatin neurons, but no immunoreactivity indicating the presence of GluA2, GluA3 and GluN2A proteins was detected.

Localisation of ionotropic glutamate receptors in the anterior hypothalamic periventricular nucleus

Studies showing the distribution at mRNA and protein levels of glutamate receptors in the central nervous system and hypothalamus are available in the literature [7, 8, 18, 25, 26, 29]. In studies on immunohistochemistry and in-situ hybridisation in the anterior hypothalamic periventricular nucleus, GluA1 and GluA2 proteins from the AMPA receptor family were moderately high in density; GluA3 and GluA4 have been reported to be expressed at low intensity [18, 29]. In another in-situ hybridisation study, the presence at the mRNA level of kainate receptor subunits was determined in the anterior hypothalamic periventricular nucleus and it was shown that GluK5 expression was high and that other subunits (GluK1, GluK2 and GluK3) were expressed at low-medium density [7]. In the same study, mRNA signals of NMDA receptor subunits were also determined and the most intense signal was shown to belong to GluN2A. mRNA signals of GluN1, GluN2B and GluN2D subunits were reported to be moderate, and at low density for GluN2C [7]. Results of the present study show that some NMDA and non-NMDA glutamate receptor signals belong to neuronostatin neurons in the anterior hypothalamic periventricular nucleus.

Kainic acid receptor subunits in neuronostatin neurons (GluK1–3 and GluK5)

Glutamate receptor subunits combine to form functional receptor complexes. These receptor complexes may be homomeric or heteromeric. Homomeric ion channels are formed by combining the same subunits, heteromeric functional ion channels are formed by combining different subunits [10, 15, 19]. The present study demonstrated that neuronostatin neurons express receptor subunit proteins of the kainate receptor family.

The present study suggests two ideas about the kainate receptor proteins expressed in neuronostatin neurons: 1) The GluK5 subunit cannot form a stand-alone channel; it can form a functional heteromeric kainate receptor complex combined with one of the GluK1, GluK2 or GluK3 subunits; 2) GluK1, GluK2 or GluK3, which are low-affinity kainate receptor subunits, may form functional homomeric kainate receptor complexes.

AMPA receptor subunits in neuronostatin neurons (GluA1–4)

AMPA receptor complexes may form homomeric ion channels but are mostly present in the form of heteromers [10, 19]. GluA1 and GluA4 subunits, which were determined to be expressed in neuronostatin neurons, were thought to form functional cation channels either individually or together. The results of the present study showed that the activating effect of glutamate on neuronostatin neurons was mediated by AMPA-selective ionotropic glutamate receptors along with kainate receptors.

NMDA receptor subunits in neuronostatin neurons (GluN1 and GluN2A)

NMDA receptor subunits can only form functional receptor complexes of heteromeric structure [23]. The essential subunit of NMDA receptor complexes is GluN1 [15]. The present study showed that GluN1, a NMDA receptor subunit protein, was expressed in neuronostatin neurons.

Although GluN2A immunoreactivity was not determined in neuronostatin neurons, they were still thought to carry functional NMDA-selective glutamate receptors. This is because: 1) Expression of GluN1, the indispensable subunit of NMDA receptor complexes, was positive in neuronostatin neurons; 2) The GluN1 subunit forms functional receptor channels with other types of GluN2. In the present study, the expressions of GluN2B, GluN2C and GluN2D subunits in neuronostatin neurons were not investigated. Even so, the GluN2B, C and D receptor types are expressed in the anterior hypothalamic periventricular nucleus. The results suggest that neuronostatin neurons localised in the anterior hypothalamic periventricular nucleus may also express these receptor types and therefore may be regulated by NMDA receptors.

For the first time in the literature, our study demonstrated that the neuronostatin neurons express glutamate receptor subunits which may form homomeric or heteromeric functional receptor complexes.

CONCLUSIONS

As conclusion, glutamate plays an effective role in regulating the functions of neurons synthesising neuronostatin and glutamate shows its effectiveness through NMDA and non-NMDA receptors.

Conflict of interest: None declared

REFERENCES

1. Brann DW. Glutamate: a major excitatory transmitter in neuroendocrine regulation. Neuroendocrinology. 1995; 61(3): 213–225, doi: 10.1159/000126843, indexed in Pubmed: 7898626.
2. Brann D, Mahesh V. Excitatory amino acids: function and significance in reproduction and neuroendocrine regulation. Front Neuroendocrinol. 1994; 15(1): 3–49, doi: 10.1006/frne.1994.1002.
3. Collingridge GL, Olsen RW, Peters J, et al. A nomenclature for ligand-gated ion channels. Neuropharmacology. 2009; 56(1): 2–5, doi: 10.1016/j.neuropharm.2008.06.063, indexed in Pubmed: 18655795.
4. Cull-Candy S, Brickley S, Farrant M. NMDA receptor subunits: diversity, development and disease. Curr Opin Neurobiol. 2001; 11(3): 327–335, doi: 10.1016/s0959-4388(00)00215-4, indexed in Pubmed: 11399431.
5. Dun SL, Brailoiu GC, Tica AA, et al. Neuronostatin is co-expressed with somatostatin and mobilizes calcium in cultured rat hypothalamic neurons. Neuroscience. 2010; 166(2): 455–463, doi: 10.1016/j.neuroscience.2009.12.059, indexed in Pubmed: 20056135.
6. Ekizceli G, Halk KZ, Minbay Z, et al. Nesfatin-1 and neuronostatin neurons are co-expressed with glucocorticoid receptors in the hypothalamus. Biotech Histochem. 2021; 96(7): 555–561, doi: 10.1080/10520295.2020.1832703, indexed in Pubmed: 33054452.
7. Eyigor O, Centers A, Jennes L. Distribution of ionotropic glutamate receptor subunit mRNAs in the rat hypothalamus. J Comp Neurol. 2001; 434(1): 101–124, doi: 10.1002/cne.1167, indexed in Pubmed: 11329132.
8. Eyigor O, Minbay Z, Cavusoglu I, et al. Localization of kainate receptor subunit GluR5-immunoreactive cells in the rat hypothalamus. Brain Res Mol Brain Res. 2005; 136(1-2): 38–44, doi: 10.1016/j.molbrainres.2005.01.015, indexed in Pubmed: 15893585.
9. Frerking M, Nicoll RA. Synaptic kainate receptors. Curr Opin Neurobiol. 2000; 10(3): 342–351, doi: 10.1016/s0959-4388(00)00094-5, indexed in Pubmed: 10851174.
10. Herguedas B, García-Nafría J, Cais O, et al. Structure and organization of heteromeric AMPA-type glutamate receptors. Science. 2016; 352(6285): aad3873, doi: 10.1126/science.aad3873, indexed in Pubmed: 26966189.
11. Hua Y, Ma H, Samson WK, et al. Neuronostatin inhibits cardiac contractile function via a protein kinase A- and JNK-dependent mechanism in murine hearts. Am J Physiol Regul Integr Comp Physiol. 2009; 297(3): R682–R689, doi: 10.1152/ajpregu.00196.2009, indexed in Pubmed: 19553502.
12. Kamiya H. Kainate receptor-dependent presynaptic modulation and plasticity. Neurosci Res. 2002; 42(1): 1–6, doi: 10.1016/s0168-0102(01)00303-0, indexed in Pubmed: 11814603.
13. Kew JNC, Kemp JA. Ionotropic and metabotropic glutamate receptor structure and pharmacology. Psychopharmacology (Berl). 2005; 179(1): 4–29, doi: 10.1007/s00213-005-2200-z, indexed in Pubmed: 15731895.
14. Köles L, Wirkner K, Illes P. Modulation of ionotropic glutamate receptor channels. Neurochem Res. 2001; 26(8-9): 925–932, doi: 10.1023/a:1012380416876, indexed in Pubmed: 11699944.
15. Kumar J, Schuck P, Mayer ML. Structure and assembly mechanism for heteromeric kainate receptors. Neuron. 2011; 71(2): 319–331, doi: 10.1016/j.neuron.2011.05.038, indexed in Pubmed: 21791290.
16. Lerma J, Paternain AV, Rodríguez-Moreno A, et al. Molecular physiology of kainate receptors. Physiol Rev. 2001; 81(3): 971–998, doi: 10.1152/physrev.2001.81.3.971, indexed in Pubmed: 11427689.
17. Lomeli H, Wisden W, Köhler M, et al. High-affinity kainate and domoate receptors in rat brain. FEBS Lett. 1992; 307(2): 139–143, doi: 10.1016/0014-5793(92)80753-4, indexed in Pubmed: 1322826.
18. Martin LJ, Blackstone CD, Levey AI, et al. AMPA glutamate receptor subunits are differentially distributed in rat brain. Neuroscience. 1993; 53(2): 327–358, doi: 10.1016/0306-4522(93)90199-p, indexed in Pubmed: 8388083.
19. Mayer ML. Structural biology of glutamate receptor ion channel complexes. Curr Opin Struct Biol. 2016; 41: 119–127, doi: 10.1016/j.sbi.2016.07.002, indexed in Pubmed: 27454049.
20. Minbay Z, Kocoglu SS, Yurtseven DG, et al. Immunohistochemical localization of ionotropic glutamate receptors in the rat red nucleus. Bosnian J Basic Med Sci. 2017; 17(1): 29–37.
21. Ozawa S, Kamiya H, Tsuzuki K. Glutamate receptors in the mammalian central nervous system. Prog Neurobiol. 1998; 54(5): 581–618, doi: 10.1016/s0301-0082(97)00085-3, indexed in Pubmed: 9550192.
22. Pachernegg S, Strutz-Seebohm N, Hollmann M. GluN3 subunit-containing NMDA receptors: not just one-trick ponies. Trends Neurosci. 2012; 35(4): 240–249, doi: 10.1016/j.tins.2011.11.010, indexed in Pubmed: 22240240.
23. Paoletti P. Molecular basis of NMDA receptor functional diversity. Eur J Neurosci. 2011; 33(8): 1351–1365, doi: 10.1111/j.1460-9568.2011.07628.x, indexed in Pubmed: 21395862.
24. Paxinos G, Watson C. The rat brain in stereotaxic coordinates. London Acad Press, London 2009.
25. Petralia RS, Wenthold RJ. Light and electron immunocytochemical localization of AMPA-selective glutamate receptors in the rat brain. J Comp Neurol. 1992; 318(3): 329–354, doi: 10.1002/cne.903180309, indexed in Pubmed: 1374769.
26. Petralia RS, Yokotani N, Wenthold RJ. Light and electron microscope distribution of the NMDA receptor subunit NMDAR1 in the rat nervous system using a selective anti-peptide antibody. J Neurosci. 1994; 14(2): 667–696, indexed in Pubmed: 8301357.
27. Salvatori AS, Elrick MM, Samson WK, et al. Neuronostatin inhibits glucose-stimulated insulin secretion via direct action on the pancreatic α-cell. Am J Physiol Endocrinol Metab. 2014; 306(11): E1257–E1263, doi: 10.1152/ajpendo.00599.2013, indexed in Pubmed: 24735892.
28. Samson WK, Zhang JV, Avsian-Kretchmer O, et al. Neuronostatin encoded by the somatostatin gene regulates neuronal, cardiovascular, and metabolic functions. J Biol Chem. 2008; 283(46): 31949–31959, doi: 10.1074/jbc.M804784200, indexed in Pubmed: 18753129.
29. Sato K, Kiyama H, Tohyama M. The differential expression patterns of messenger RNAs encoding non-N-methyl-D-aspartate glutamate receptor subunits (GluR1-4) in the rat brain. Neuroscience. 1993; 52(3): 515–539, doi: 10.1016/0306-4522(93)90403-3, indexed in Pubmed: 8450957.
30. Serter Kocoglu S, Gok Yurtseven D, Cakir C, et al. Glutamatergic activation of neuronostatin neurons in the periventricular nucleus of the hypothalamus. Brain Sci. 2020; 10(4), doi: 10.3390/brainsci10040217, indexed in Pubmed: 32268550.
31. Tse YC, Yung KK. Cellular expression of ionotropic glutamate receptor subunits in subpopulations of neurons in the rat substantia nigra pars reticulata. Brain Res. 2000; 854(1-2): 57–69, doi: 10.1016/s0006-8993(99)02292-1, indexed in Pubmed: 10784107.

V M
VIA MEDICA

O R I G I N A L   A R T I C L E

Cervicothoracic sympathetic system in the dog: new insights by the gross morphological description of each ganglion with its branches on each side

M.M.A. Abumandour[1] , B.G. Hanafy[1], K. Morsy[2, 3], A. El-kott[2, 4], A. Shati[2], E. Salah EL-Din[3, 5], N.F. Bassuoni[1]

[1]Anatomy and Embryology Department, Faculty of Veterinary Medicine, Alexandria University, Alexandria, Egypt
[2]Biology Department, College of Science, King Khalid University, Abha, Saudi Arabia
[3]Zoology Department, Faculty of Science, Cairo University, Cairo, Egypt
[4]Zoology Department, Faculty of Science, Damanhour University, Damanhour, Egypt
[5]Biology Department, Faculty of Science, Bisha University, Bisha, Saudi Arabia

Background: Much published data exists on the position of cervicothoracic ganglion, but a little published research has been done on the cervicothoracic system of dog. Herein, we illustrated topographical position and shape of each ganglion of cervicothoracic system to determine the distribution of nerves dispersing from them on two sides, left and right.

Materials and methods: Our work designed on the usage of 10 healthy adult dogs. Left cervicothoracic sympathetic system is represented by two ganglia: caudal and middle ganglion, while the right system is represented by three ganglia: caudal, middle cervical and small accessory ganglia.

Results: Left caudal cervical ganglion was elongated triangular, while the right one was elongated spindle in shape. Left caudal cervical ganglion was located on lateral surface of longus colli muscle, at the first intercostal space, while the right one was located at the level of the second rib. Left middle cervical ganglion was ovoid in shape and located at the first intercostal space, while the right one was located at the level of the second rib. There were two nerve trunks forming ansa subclavian trunk on both sides. There were three sympathetic-parasympathetic communicating branches on both sides.

Conclusions: Our study recorded the first observation of left pericardial branch in dog, which originated from the caudal angle of middle cervical ganglion. There was a small ganglion located on the lateral surface of trachea at the level of the first rib. (Folia Morphol. 2022; 81, 1: 20–30)

Key words: caudal cervical ganglion, middle cervical ganglion, accessory cervical ganglion, ansa subclavia, dog

INTRODUCTION

The accumulating body of evidence recorded that the autonomic sympathetic nervous system is formed from nerves and ganglia [6]. Furthermore, several reports have described that the ganglia make communication between the central nervous system from one

side to the viscera on the other side of the body. In the cervical region, the ganglia of the sympathetic chain are classified into three bilaterally situated ganglia: cranial, middle, and caudal cervical ganglion [1, 6, 9, 13, 22]. Sometimes, another ganglia may be present on the vertebral nerve named vertebral ganglion [22].

The caudal cervical or the stellate ganglion was described previously in many published articles in different animals [1, 6, 8, 14, 17, 19]. Moreover, as recorded in several reports, the cervicothoracic system with its all nerves give an autonomic sympathetic innervation of the forelimb, cervical region, and the organs included in the chest region [1, 10, 21].

There were several published anatomical books mentioning the position of the cervicothoracic ganglia in the dog. However, to date, a scanty report recorded the cervicothoracic ganglia in Baladi dogs. The current investigation was prepared to illustrate the cervicothoracic system and describe the topographical position, shape of the caudal and middle cervical ganglion on each side and their relationship with the surrounding structures and the nerves dispersing from them. Finally, the obtained data were compared to those reported in other animal species.

MATERIALS AND METHODS

Animals

Ten healthy adult dogs of both sexes (sexes and body weights were not recorded) were collected from the Kafrelsheikh Governorate and transported to the anatomical lab of the Anatomy and Embryology Department of the Faculty of Veterinary Medicine, Alexandria University, Egypt to make the anatomical studies. The dog considered the famous canine species. The Baladi dog is the famous dog in Egyptian street. The dog belongs to *carnivore* order, *Canidae* family, *canis* genus, *canis iupus* species, and *canis iupus familiaris* (Linnaeus, 1758) subspecies [4, 23].

This study followed the guidelines for the care and use of laboratory animals and the animal welfare and was approved by the Ethics Committee of the Faculty of Veterinary Medicine, Alexandria University according the Egyptian laws. Adequate measures were taken to minimize pain or discomfort of examined animals.

Preparation of animals

The collected dogs were given an injection of acepromazine (0.05 mg/kg/IM), and after 10 min injection of xylazine (0.2 mg/kg of body weight/IM) and atropine (0.04 mg/kg). All dogs were well bled via a cannula placed in the common carotid artery; the cannula was subsequently used as an inflow port for injection of 10% formalin solution through the common carotid artery to fix the specimens, and then, after specimens had been stored for 2 weeks, the fixation process was completed. The anatomical dissection technique was carried out on both sides of all dogs to describe the topographical position, shape, and branches of the ganglia. The dissected dogs were photographed by means of a digital camera (Canon IXY 325, Japan). The measurements were carried out by utilising digital callipers. The quantitative results were expressed as mean ± standard deviation. The anatomical terms followed the Nomina Anatomica Veterinaria [18].

RESULTS

Anatomical description of the left cervicothoracic sympathetic system

The left cervicothoracic sympathetic system was represented by the presence of the two ganglia: the caudal (cervicothoracic) and the middle cervical ganglion (Figs. 1–5; G and M), in addition to one or more thoracic ganglia. The caudal cervical (cervicothoracic) ganglion was elongated triangular in shape with its apex ventrally and located on the lateral surface of the longus colli muscle, at the first intercostal space. The cranial 1/4 of the examined ganglion was crossed laterally by the first thoracic spinal nerve of the brachial plexus and the costocervical artery (Figs. 1 and 2).

In all examined dogs, the formation of the caudal cervical ganglion (cervicothoracic) achieved by the union of the last (eighth) cervical sympathetic nerve and the first two thoracic sympathetic ganglia. There were several rami communicantes received by the caudal cervical ganglion, which were originated from the eight cervical and the first two thoracic spinal segments. These rami communicantes originating from the first two thoracic spinal segments were united with the sympathetic trunk to combine with the caudal cervical ganglion at its caudodorsal angle (Figs. 1–5; b and c). The ramus communicans named the eight cervical spinal segments was combined with the caudal cervical ganglion at its craniodorsal border (Figs. 1–5; a).

Middle cervical ganglion (Figs. 1–5; M) was ovoid or, in some cases, spindle in shape. It was located at the same level of the caudal cervical ganglion, at the first intercostal space or at the level of the second rib (2 cases).

21
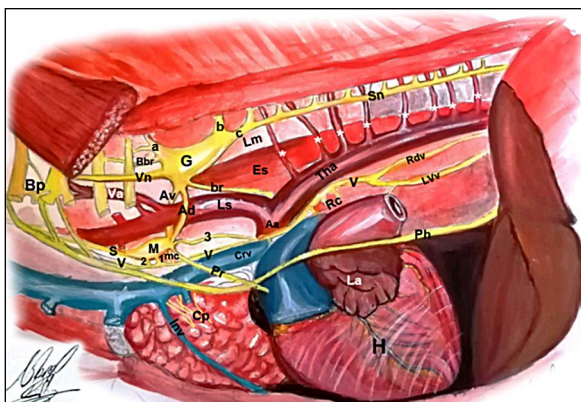
Figure 1. Illustrated image to describe the left cervicothoracic system of dog; G — left cervicothoracic ganglion; M — middle cervical ganglion; a — last (eighth) cervical sympathetic nerve; b — first thoracic sympathetic ganglion; c — second thoracic sympathetic ganglion; br — the nerve to brachiocephalic trunk; Bbr — ramus communicans combined with the thoracic spinal nerve to share in the formation of the brachial plexus; Ad — lateral small ansa subclavia nerve; Av — medial large ansa subclavia nerve; Pr — pericardial branch; 3 — the long caudally directed sympathetic-parasympathetic communicating branch; mc — cardiac nerves; Aa — aortic arch; Ls — left subclavian artery; Tha — thoracic aorta; white stars refer to the intercostal arteries; Es — oesophagus; Lm — longus colli muscle; Va — vertebral artery; Vn — vertebral nerve; Sn — sympathetic nerve; Inv — internal thoracic vein; V — vagus nerve; Ldv — left dorsal vagus nerve; Lvv — left ventral vagus nerve; Ph — phrenic nerve; H — heart; La — left atrium; Crv — cranial venea cavae.

Its dorsal 1/4 was covered laterally by the left subclavian artery before its bifurcation into common carotid, internal thoracic and axillary arteries. The middle cervical ganglion communicated with the caudal cervical ganglion by two nerve trunks forming the left ansa subclavia. After it left the vagosympathetic nerve trunk, the cervical part of the sympathetic nerve trunk was combined with the middle cervical ganglion at its cranial angle.

Branches dispersing from the left caudal cervical ganglion

The vertebral nerve

The vertebral nerve (Figs. 1 and 2; Vn) was a large nerve that originated from the cranial angle of the triangular caudal cervical ganglion. Then, it passed in the craniodorsal direction on the lateral surface of the longus colli muscle and was covered laterally by the last cervical and the first thoracic spinal nerve. During its course, it was corresponding with the vertebral artery and vein (Figs. 1–3; Va and Vv), after that, they passed under the transverse process of the seventh cervical vertebrae and entered the transverse foramen of the sixth cervical vertebrae.
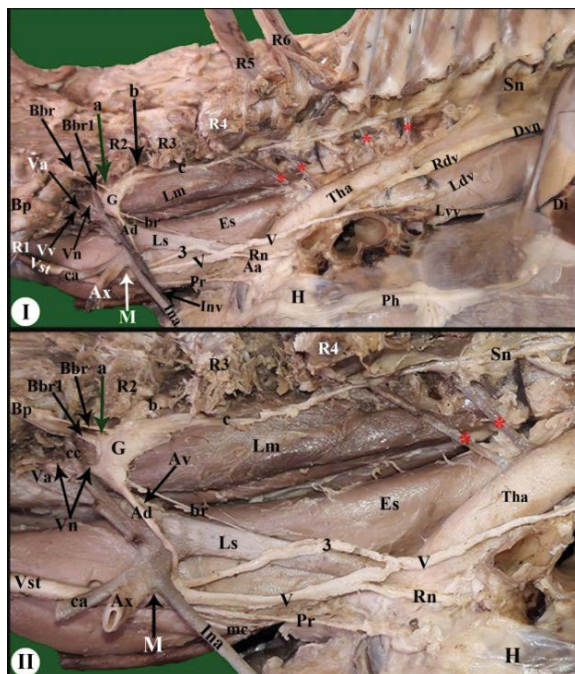
Figure 2. Gross anatomical photographs of the lateral macroscopic appearance of left cervicothoracic ganglion after the cranial reflection of the first rib (R1), removal of succeeding three ribs (R2–R4), reflection of fifth and sixth ribs (R5 and R6), and elevation of brachial plexus (Bp): **View I** with the presence of left subclavian vein and its branches and **view II** after removal of left subclavian vein and its branches; G — left cervicothoracic ganglion; M — middle cervical ganglion; a — last (eighth) cervical sympathetic nerve; b — first thoracic sympathetic ganglion; c — second thoracic sympathetic ganglion; br — the nerve to brachiocephalic trunk; Bbr — a long ramus communicans combined with the first thoracic spinal nerve to share in the formation of the brachial plexus; Bbr1 — short ramus communicans combined with the first thoracic spinal nerve to share in the formation of the brachial plexus; Ad — lateral small ansa subclavia nerve; Av — medial large ansa subclavia nerve; Pr — pericardial branch; 3 — the long caudally directed sympathetic-parasympathetic communicating branch; mc — cardiac nerves; Aa — aortic arch; Ls — left subclavian artery; Tha — thoracic aorta; Es — oesophagus; Lm — longus colli muscle; cc — costocervical artery; Va — vertebral artery; Vv — vertebral vein; Vn — vertebral nerve; ca — common carotid artery; Vst — vagosympathetic trunk; Sn — sympathetic nerve; Ax — axillary artery; Ina — internal thoracic artery; Inv — internal thoracic vein; red asterisk — intercostal arteries; V — vagus nerve; Ldv — left dorsal vagus nerve; Rdv — left dorsal vagus nerve; Lvv — left ventral vagus nerve; Dvn — dorsal vagal nerve trunk; Di — diaphragm; Ph — phrenic nerve; H — heart; Rn — recurrent laryngeal nerve.

The ansa subclavian nerve

The ansa subclavia was the nerve dispersing from the caudal cervical ganglion and wrapped around the left subclavian artery. The left ansa subclavia consisted of two nerve trunks originating from the caudoventral angle of the caudal cervical ganglion and named: the lateral small branch and the medial large branch (Figs. 1–5; Ad and Av).
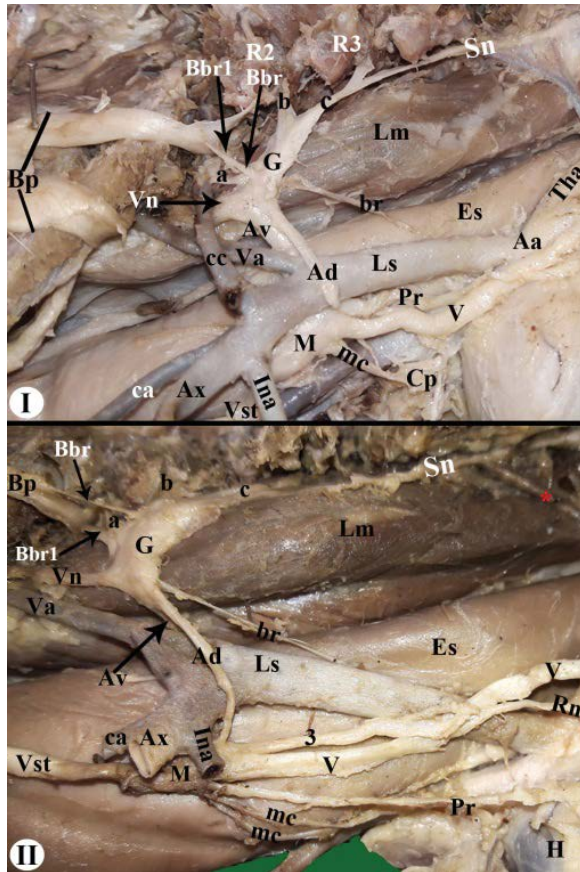
Figure 3. Gross anatomical photographs of lateral macroscopic appearance of the left cervicothoracic ganglion after the removal of first four ribs (R1–R4), and the elevation of brachial plexus (Bp); **View I** revelaed the presence of left subclavian vein and its branches while; **View II** revealed the removal of left subclavian vein and its branches; G — left cervicothoracic ganglion; M — middle cervical ganglion; a — last (eighth) cervical sympathetic nerve; b — first thoracic sympathetic ganglion; c — second thoracic sympathetic ganglion; br — nerve to brachiocephalic trunk; Bbr — a long ramus communicans combined with the first thoracic spinal nerve to share in the formation of the brachial plexus; Bbr1 — short ramus communicans combined with the first thoracic spinal nerve to share in the formation of the brachial plexus; br — nerve to the brachiocephalic trunk; Ad — lateral small ansa subclavia nerve; Av — medial large ansa subclavia nerve; Pr — pericardial branch; 3 — the long caudally directed sympathetic-parasympathetic communicating branch; mc — cardiac nerves; Cp — cardiac plexus; Aa — aortic arch; Ls — left subclavian artery; Tha — thoracic aorta; Es — oesophagus; Lm — longus colli muscle; cc — costocervical artery; Va — vertebral artery; Vn — vertebral nerve; ca — common carotid artery; Vst — vagosympathetic trunk; Sn — sympathetic nerve; Ax — axillary artery; Ina — internal thoracic artery; red star — intercostal artery; V — vagus nerve; H — heart; Rn — recurrent laryngeal nerve.

Figure 4. Gross anatomical photographs of lateral macroscopic appearance of the left cervicothoracic ganglion after the removal of first four ribs (R1–R4), and the elevation of brachial plexus (Bp); **View I** revelaed the presence of left subclavian vein and its branches while; **View II** revealed the removal of left subclavian vein and its branches; G — left cervicothoracic ganglion; M — middle cervical ganglion; a — last (eighth) cervical sympathetic nerve; b — first thoracic sympathetic ganglion; c — second thoracic sympathetic ganglion; br — the nerve to brachiocephalic trunk; Bbr — a long ramus communicans combined with the first thoracic spinal nerve to share in the formation of the brachial plexus; Bbr1 — short ramus communicans combined with the first thoracic spinal nerve to share in the formation of the brachial plexus; Ad — lateral small ansa subclavia nerve; Av — medial large ansa subclavia nerve; CAV — common ansa subclavia nerve; Vn — vertebral nerve; Pr — pericardial branch; 1 and 2 — represent the two-short sympathetic-parasympathetic communicating branch; 3 — the long caudally directed sympathetic-parasympathetic communicating branch; mc — cardiac nerves; Cp — cardiac plexus; Ls — left subclavian artery; Tha — thoracic aorta; Es — oesophagus; Lm — longus colli muscle; Vst — vagosympathetic trunk; S — sympathetic trunk; Sn — sympathetic nerve; red asterisk — intercostal arteries; V — vagus nerve; H — heart; Rn — recurrent laryngeal nerve.

The lateral small branch (Figs. 1–5; Ad) was directed oblique ventrally and passed on the lateral surface of the left subclavian artery, and then fused with the medial large branch of the ansa subclavia, entered the middle cervical ganglion as one nerve trunk from its dorsal arch and embedded directly in the body of the middle cervical ganglion (Figs. 1–4; CAV). While the medial large branch of the ansa subclavia passed medially to the left subclavian artery and on the lateral surface of the oesophagus (Figs. 1–5; Ad and Av)

Figure 5. Gross anatomical photographs of lateral macroscopic appearance of the left cervicothoracic ganglion; G — left cervicothoracic ganglion; M — middle cervical ganglion; b — first thoracic sympathetic ganglion; c — second thoracic sympathetic ganglion; br — the nerve to brachiocephalic trunk; Ad — lateral small ansa subclavia nerve; Av — medial large ansa subclavia nerve; Vn — vertebral nerve; Pr — pericardial branch; 1 and 2 — represent the two-short sympathetic-parasympathetic communicating branch; 3 — the long caudally directed sympathetic-parasympathetic communicating branch; mc — cardiac nerves; Cp — cardiac plexus; Ls — left subclavian artery; Tha — thoracic aorta; Es — oesophagus; Lm — longus colli muscle; Sn — sympathetic nerve; red asterisk — intercostal arteries; V — vagus nerve; H — heart; Rn — recurrent laryngeal nerve; pi — pericardium; La — left atrium.
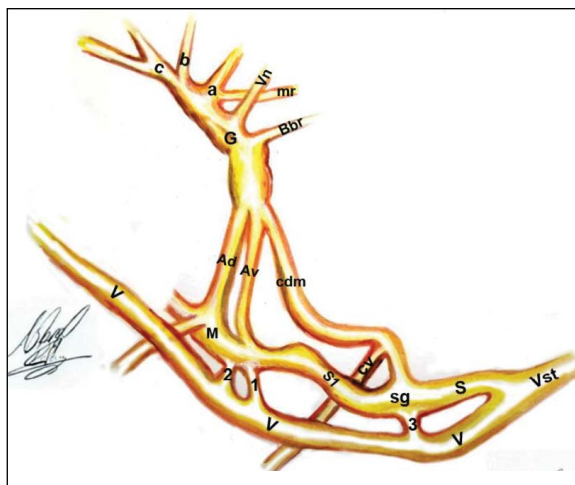
Figure 6. Illustrated image to describe the right cervicothoracic system of dog; G — right cervicothoracic ganglion; M — middle cervical ganglion; a — last (eighth) cervical sympathetic nerve; b — first thoracic sympathetic ganglia; c — second thoracic sympathetic ganglia; mr — muscular branch from right cervicothoracic ganglia; Bbr — the ramus communicans combined with the last cervical spinal nerve to share in the formation of the brachial plexus; Ad — lateral small ansa subclavia nerve; Av — medial large ansa subclavia nerve; cdm — the cranioventrally directed nerve; Vn — vertebral nerve; Cr — the caudal cardiac nerve; V — vagus nerve; Vst — vagosympathetic trunk; Sn — sympathetic nerve; S1 — communicating sympathetic branch between the middle and the small ganglia; sg — small ganglion; cv — caudoventrally directed branch from the cranioventrally directed nerve.

until it united with the lateral one forming the common trunk that embedded directly in the body of the middle cervical ganglion.

The nerve to the brachiocephalic trunk

It was the smaller branch dispersing from the caudoventral border of the caudal cervical ganglion near to its caudoventral angle, and then directed caudoventrally to the medial surface of the brachiocephalic and the left subclavian artery (Figs. 1–5; br).

The rami communicants

There were two rami communicants combined with the first thoracic spinal nerve to share in the formation of the brachial plexus. These two rami communicants originated from the craniodorsal border of the caudal cervical ganglion. These two rami communicants were described as: a short and long one (Figs. 1–3; Bbr and Bbr1). In 2 cases of the examined dogs, there was only one ramus communicans to the first thoracic spinal nerve.

Branches dispersing from the middle cervical ganglion
Cardiac nerves

There were two or three cardiac nerves originating from the ventral and medial surface of the middle cervical ganglion. These cardiac nerves coursed ventrally or slightly caudoventrally to combine with other cardiac nerves forming a cardiac plexus (Figs. 1–5; mc and Cp).

The sympathetic-parasympathetic communicating branch

There were three sympathetic–parasympathetic communicating branches joining the vagus nerve; two short branches directed ventrally and one long branch directed caudally. The two short ventrally directed branches originated from the ventral arch of the ovoid middle cervical ganglion to join the vagus nerve (Figs. 1–5; 1 and 2), and these two nerves are 5 cm long, 2 cm wide and 1 cm thick.
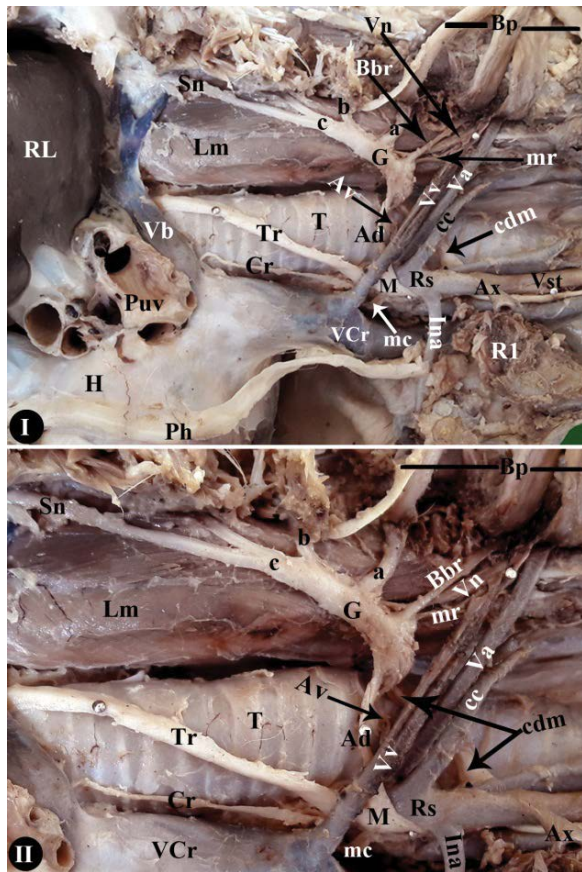
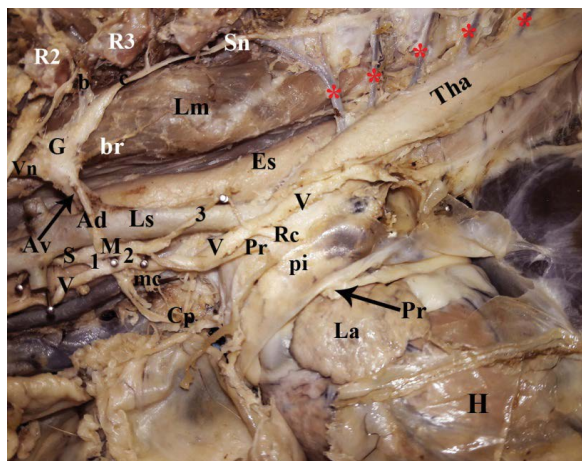**Figure 7.** Gross anatomical photographs of lateral macroscopic appearance of the right cervicothoracic ganglion after the elevation of the brachial plexus (Bp); **View I** revelaed the presence of left subclavian vein and its branches while; **View II** revelaed the removal of left subclavian vein and its branches; G — right cervicothoracic ganglion; M — middle cervical ganglion; a — last (eighth) cervical sympathetic nerve; b — first thoracic sympathetic ganglia; c — second thoracic sympathetic ganglia; mr — muscular branch from right cervicothoracic ganglia; Bbr — the ramus communicans combined with the last cervical spinal nerve to share in the formation of the brachial plexus; Ad — lateral small ansa subclavian nerve; Av — medial large ansa subclavia nerve; cdm — the cranioventrally directed nerve; Vn — vertebral nerve; Cr — the caudal cardiac nerve; mc — cardiac nerves; Rs — right subclavian artery; Ax — axillary artery; Ina — internal thoracic artery; cc — costocervical trunk; Lm — longus colli muscle; Vst — vagosympathetic trunk; Sn — sympathetic nerve; Vv — vertebral vein; Va — vertebral artery; Sn — sympathetic nerve; VCr — cranial venea cavae; H — heart; Ph — phrenic nerve; T — trachea; Vb — azygos vein; RL — right lung; Puv — pulmonary veins; R1 — first rib.

Figure 8. Gross anatomical photographs of lateral macroscopic appearance of the right cervicothoracic ganglion after the elevation of the brachial plexus (Bp); **View I** revealed the presence of left subclavian vein and its branches while; **View II** revealed the removal of left subclavian vein and its branches; G — right cervicothoracic ganglion; M — middle cervical ganglion; a — last (eighth) cervical sympathetic nerve; b — first thoracic sympathetic ganglion; c — second thoracic sympathetic ganglion; mr — muscular branch from right cervicothoracic ganglion; Bbr — the ramus communicans combined with the last cervical spinal nerve to share in the formation of the brachial plexus; Ad — lateral small ansa subclavia nerve; Av — medial large ansa subclavia nerve; cdm — the cranioventrally directed nerve; Vn — vertebral nerve; Cr — the caudal cardiac nerve; cm — cardiac nerves; Cp — cardiac plexus; Rs — right subclavian artery; ca — common carotid artery; Ax — axillary artery; Ina — internal thoracic artery; cc — costocervical trunk; Lm — longus colli muscle; Vst — vagosympathetic trunk; V — vagus nerve; S — sympathetic nerve trunk; Sn — sympathetic nerve; Vv — vertebral vein; Va — vertebral artery; Sn — sympathetic nerve; VCr — cranial venea cavae; H — heart; Ph — phrenic nerve; T — trachea; Vb — azygos vein; RL — right lung; Puv — pulmonary veins; R1 — first rib.

The long caudally directed branch measured about 5 cm in length, 2 cm in breadth and 1.5 cm in thickness and originated from the caudal angle of the middle cervical ganglion together with the pericardial branch (Figs. 1–5; 3 and Pr), and then directed caudally for 5 cm and united with the vagus nerve before the origin of the recurrent laryngeal nerve from the vagus

nerve by 1 cm (Fig. 4; 3, V and Rc), except in one case where it united with the vagus nerve after the origin of the recurrent laryngeal nerve by 1.5 cm

Pericardial branch

It originated from the caudal angle of the middle cervical ganglion together with the long caudally
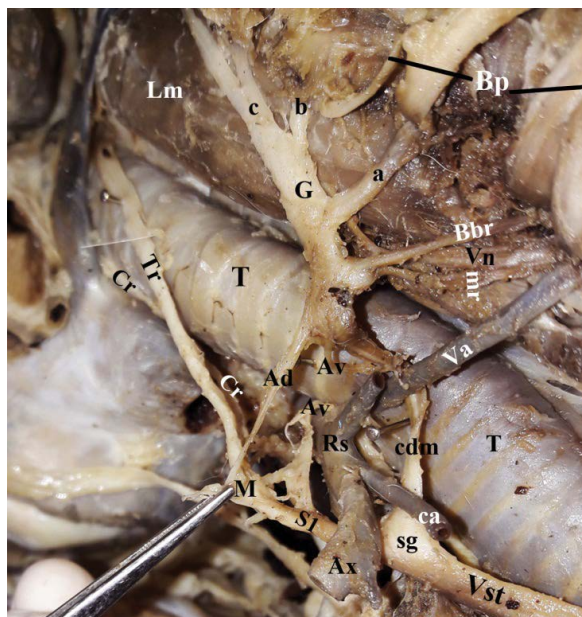
Figure 9. Gross anatomical photographs of the cranial macroscopic view of the right cervicothoracic ganglion after the elevation of the brachial plexus (Bp); G — right cervicothoracic ganglion; M — middle cervical ganglion; sg — small ganglion; a — last (eighth) cervical sympathetic nerve; b — first thoracic sympathetic ganglion; c — second thoracic sympathetic ganglion; mr — muscular branch from right cervicothoracic ganglia; Bbr — the ramus communicans combined with the last cervical spinal nerve to share in the formation of the brachial plexus; Ad — lateral small ansa subclavian nerve; Av — medial large ansa subclavia nerve; cdm — the cranioventrally directed nerve; Vn — vertebral nerve; Cr — the caudal cardiac nerve; mc — cardiac nerves; S1 — communicating sympathetic branch between the middle and the small ganglia; Rs — right subclavian artery; ca — common carotid artery; Ax — axillary artery; Ina — internal thoracic artery; cc — costocervical trunk; Lm — longus colli muscle; Vst — vagosympathetic trunk; V — vagus nerve; Va — vertebral artery; S — sympathetic nerve trunk; Sn — sympathetic nerve; T — trachea.

directed branch of the sympathetic–parasympathetic communicating branches (Figs. 1–4; 3 and Pr), and then directed caudoventrally to reach the pericardium above the left auricle, then it penetrates the pericardium to reach the wall of the left auricle (Fig. 5; Pr, pi and La).

Anatomical description of the right cervicothoracic sympathetic system

The right cervicothoracic sympathetic system was represented by two sympathetic ganglia: the caudal (cervicothoracic) and the middle cervical ganglion (Figs. 6–10; G and M). The caudal cervical ganglion was elongated, spindle in shape and located at the level of the second rib on the lateral surface of the longus colli muscle (Figs. 6–10; G and Lm), while the cranial 1/4 of the ganglion was located in the groove
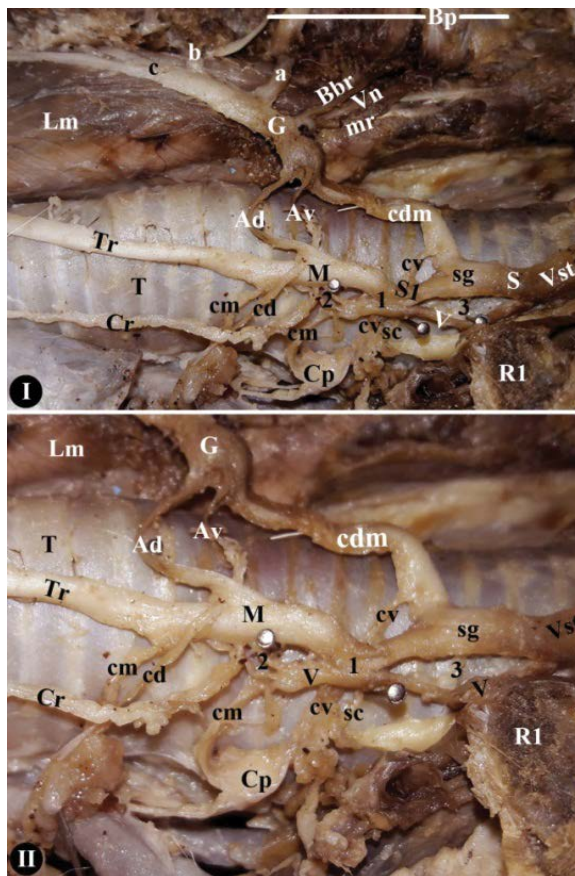
Figure 10. Gross anatomical photographs of lateral macroscopic appearance of the right cervicothoracic ganglion after elevation of brachial plexus (Bp); **View I** revealed the presence of left subclavian vein and its branches while; **View II** revealed the removal of left subclavian vein and its branches; G — right cervicothoracic ganglion; M — middle cervical ganglion; sg — small ganglion; a — last (eighth) cervical sympathetic nerve; b — first thoracic sympathetic ganglion; c — second thoracic sympathetic ganglion; mr — muscular branch from right cervicothoracic ganglion; Bbr — the ramus communicans combined with the last cervical spinal nerve to share in the formation of the brachial plexus; Ad — lateral small ansa subclavia nerve; Av — medial large ansa subclavia nerve; cdm — the cranioventrally directed nerve; Vn — vertebral nerve; Cr — the caudal cardiac nerve; mc — cardiac nerves; Cp — cardiac plexus; 1 and 2 — the two small sympathetic-parasympathetic communicating branches which originated from the middle cervical ganglion and directed ventrally to join with the vagus nerve; 3 — the sympathetic-parasympathetic communicating branch of the accessory small ganglion; cv — caudoventrally directed branch from the cranioventrally directed nerve; sc — the ventrally directed cardiac nerve from the small ganglia; S1 — communicating sympathetic branch between the middle and the small ganglia; Lm — longus colli muscle; Vst — vagosympathetic trunk; V — vagus nerve; S — sympathetic nerve trunk; Sn — sympathetic nerve; Sn — sympathetic nerve; VCr — cranial venea cavae; T — trachea; Bbr — the ramus communicans combined with the last cervical spinal nerve to share in the formation of the brachial plexus.

between the longus colli muscle and the trachea (Figs. 6–10; G, Lm and T). The cranial 1/2 of the examined ganglion was covered laterally by the second and

third thoracic spinal nerve of the brachial plexus (Figs. 6–10; G, Bp and R2).

The right caudal cervical ganglion was located in the cranial 1/4 of the quadrilateral venous area. This quadrilateral area was formed by: vertebral veins cranially, the right vena azygous caudally, the cranial vena cava ventrally, and the vertebral column dorsally (Figs. 7I and 8I; G, Vv, VCr and Vb).

In all examined dogs, the formation of the caudal cervical ganglion was achieved by the union of the last (eighth) cervical sympathetic nerve and the first two thoracic sympathetic ganglia. There were several rami communicants received by the caudal cervical ganglion, which originated from the eight cervical and the first two thoracic spinal segments. These rami communicants that originated from the first two thoracic spinal segments were united with the sympathetic trunk to combine with the caudal cervical ganglion at its craniodorsal angle (Figs. 6–10; b and c). The ramus communicans named eight cervical spinal segment was combined with the caudal cervical ganglion at its craniodorsal border (Figs. 6–10; a).

Middle cervical ganglion (Figs. 6–10; M) was ovoid in shape, and it was located at the same level of the caudal cervical ganglion, at the level of the second rib, nearly the ventrolateral surface of the trachea. The middle cervical ganglion was located on the lateral surface of the right subclavian artery and its caudal 1/4 was covered laterally by the vertebral vein (Figs. 6–10; Rs and Vv). The middle cervical ganglion was communicated with the caudal cervical ganglion by the two-nerve loop trunk named the ansa subclavia: the lateral and the medial nerve loop trunk (Figs. 6–10; Ad and Av). Furthermore, the middle cervical ganglion was communicated with the accessory small ganglion by the cranially directed nerve branch originated from the cranial angle of the middle cervical ganglion (Figs. 6–10; S1).

Branches of the right caudal cervical ganglion
The vertebral nerve

The vertebral nerve (Figs. 6, 7; Vn) originated from the cranial part of the craniodorsal border of the caudal cervical (cervicothoracic) ganglion. Then, it passed under the last cervical spinal nerve in the craniodorsal direction. During its course, it was corresponding with the vertebral artery and vein (Fig. 7; Va and VV). After that, they passed under the transverse process of the seventh cervical vertebrae and enter the transverse foramen of the sixth cervical vertebrae.

The ansa subclavian nerve

The nerve loop trunk named the ansa subclavia consists of two nerve loops: the lateral and the media nerve trunk loop. The lateral nerve loop of the ansa subclavia (Figs. 6–10; Ad) originated from the cranial part of the caudoventral border of the caudal cervical ganglion and ran caudal to the origin of the medial nerve loop of the ansa subclavia by 0.3 cm, and then it directed ventrally on the lateral surface of the trachea to enter the dorsal arch of the middle cervical ganglion.

The medial nerve loop of the ansa subclavia (Figs. 6–10; Av) originated from the cranial part of the caudoventral border of the caudal cervical ganglion, and then it directed ventrally directly on the lateral surface of the trachea and passed under the right subclavian artery to join the middle cervical ganglion at its medial surface. This nerve loop measured about 3.5 cm in length and 0.1 cm in width.

The cranioventrally directed nerve

This nerve originated from the cranial part of the caudoventral border of the caudal cervical ganglion (Figs. 6–10; cdm), and then it ran directed cranioventrally on the lateral surface of the trachea and joined the sympathetic nerve trunk before its union with the middle cervical ganglion forming a small sympathetic ganglion (Figs. 6–10; sg). The cranioventrally directed nerve measured about 4.5 cm in length and 0.3 cm in width and before its sharing in the formation of the small sympathetic ganglion by 1 cm it gave off a caudoventrally directed cardiac branch (Figs. 6–10; cv) of 4 cm in length to share in the cardiac plexus formation with other cardiac branches originating from the ansa subclavia and the middle cervical ganglion.

The ramus communicans

There was only one ramus communicans that was combined with the last cervical spinal nerve which sharing in the formation of the brachial plexus (Figs. 6–10; Bbr). This ramus communicans originated from the craniodorsal angle of the caudal cervical ganglion.

Muscular branch

There was only one muscular branch that originated from the craniodorsal angle of the caudal cervical ganglion (Figs. 6–10; mr). This branch was directed craniodorsally in corresponding with the vertebral nerve and ramus communicans and was combined

with the last cervical spinal nerve, in which these three branches had the same origin from the craniodorsal angle of the caudal cervical ganglion.

Branches of the middle cervical ganglion
The sympathetic–parasympathetic communicating branch of the middle cervical ganglion

There were two smalls sympathetic–parasympathetic communicating branches of 0.7 cm in length (Figs. 6 and 10; 1 and 2), which originated from the middle cervical ganglion and directed ventrally to join the vagus nerve.

The caudal cardiac nerve

There were two or three cardiac nerves originating from the ventral and medial surface of the middle cervical ganglion (Figs. 6–10; mc). These cardiac nerves coursed slightly caudoventrally to combine with other cardiac nerves originating from the lateral loop of ansa subclavia, cranioventrally directed nerve and small ganglia to form a cardiac plexus (Figs. 6–10; CP).

Anatomical description of the accessory small ganglion

There was a small ganglion located on the lateral surface of the trachea at the level of the first rib and cranial to the middle cervical ganglion by 1.2 cm (Figs. 6–10; sg). This ganglion formed by the union of the cranial sympathetic branch that originated from the cranial angle of the middle cervical ganglion with the cranioventrally directed nerve that originated from the caudal cervical ganglion (Figs. 6–10; cdm and S1). The sympathetic nerve trunk was joining the cranial angle of the accessory small ganglion.

Branches of the accessory small ganglion
The sympathetic–parasympathetic communicating branch of the accessory small ganglion

This was a small ventrally directed branch of 1cm in length that originated from the ventral border of the accessory small ganglion to join the vagus nerve (Figs. 6 and 10; 3).

The caudoventrally directed cardiac branch

This was a small caudoventrally directed branch that originated from the caudal angle of the accessory small ganglion to share in the formation of the cardiac plexus (Figs. 6 and 10; sc).

DISCUSSION

The present study clarified that the Baladi dog had some anatomical variations in the position of the ganglia forming the cervicothoracic system on two sides; the left caudal cervical ganglion was located at the first intercostal space on the lateral surface of the longus colli muscle, while the right caudal cervical ganglion was located at the level of the second rib. This variation in the position of the ganglia forming the cervicothoracic system was reported previously by Ozgel et al. [19] in the donkey in which the left and right caudal cervical ganglia of the four examined donkeys were located at the level of the first intercostal space, but in one examined donkey, the left one was situated at the level of the second intercostal space, and in the area between the first and second intercostal spaces on the right side. In the horse [1], it was reported that the location of the left caudal cervical ganglion was cranial to the level of the first rib, but the right examined ganglion was located at the level of the first rib. However, there are numerous articles that noted that the left and right caudal cervical ganglia were located at the level of the first intercostal space [8, 12, 19, 20], while in the domestic animals König and Liebich [15] observed that the cervicothoracic ganglion was located at the level of the first rib.

The previously published articles reported the presence of the some anatomical variations about the presence the middle cervical ganglion [6, 10, 15]. The current work observed the presence of the middle cervical ganglion on both sides; this result is similar to that noted by Ozgel et al. [19] in the donkey, while in the horse [1] it was observed that the middle cervical ganglion was present on the right side and absent on the left side.

The current work agree with the observation noted by many authors that the caudal cervical ganglion was situated on the lateral surface of the longus colli muscle [8, 19, 21]; however, in the horse [1] it was reported that the left-sided caudal cervical ganglion was located on the lateral surface of the oesophagus, while the right-sided caudal cervical ganglion was located on the ventrolateral surface of the longus colli muscle and trachea. In the roe deer [12] it was noted that the caudal cervical ganglion was located on the border of the longus colli muscle.

There are various appearances of the caudal cervical ganglion observed in the numerous published articles [1, 11, 13, 16, 19–21]. The current study reported that, the left caudal cervical ganglion was elongated triangular in shape with its apex directed ventrally, while the right one is elongated spindle in shape. The general appearance of the caudal cervical ganglion is a spindle-shape or star shape, similar to that observed by [1, 6, 8, 10, 12, 19, 20]. In the donkey, there were five different appearance of the caudal cervical ganglion (fusiform, star, oval, lunate, and irregular) described by Ozgel et al. [19], but only three different appearance were noted by Kabak et al. [12] and Pather et al. [20]. In the horse [1] it was reported that the left caudal cervical ganglion was stellate in shape and compressed from its centre, while the right caudal cervical ganglion was stellate and middle cervical ganglion was star.

Some published anatomical articles described the formation of the caudal cervical ganglion and observed some variations between different animals. The caudal cervical ganglion consisted of union of the last (eighth) cervical and the first thoracic sympathetic nerves [5, 19]. However, the present study noted that the examined caudal cervical ganglion consisted of the union of the last (eighth) cervical and first two thoracic sympathetic nerves, this result was similar to those observed in roe deer and donkey [12, 19]. It consisted of the union of the last (eighth) cervical and first three thoracic sympathetic nerves as reported in the dog [7] and horse [1]. Moreover, Chung et al. [3] and Evans and Lahunta [8] reported that the caudal cervical ganglion consisted of the union of the last (eighth) cervical and first four thoracic sympathetic nerves. However, in the human [20] it was reported that the caudal cervical ganglion consisted of the union of the last two cervical and the first thoracic sympathetic nerve, and in some cases the second [13] or occasionally the third and the fourth thoracic sympathetic nerves [2].

The present study observed that the left caudal cervical ganglion gave off the following branches: the vertebral nerve, the two branches forming the ansa subclavia, the nerve to the brachiocephalic trunk, muscular branches, and the ramus communicans to the first thoracic spinal nerve. However, the previous literature reports [1, 13, 19, 20] described that the caudal cervical ganglion gave the following branches: the vertebral nerve, the two branches forming the ansa subclavia, and the caudal cardiac nerve. The

rami communicants joining the brachial plexus were also reported by [1, 19, 20].

There are some minor variations in the origin of the vertebral nerve from the caudal cervical ganglion [5, 13]. The present study observed that the left vertebral nerve originated from the cranial angle of the left caudal cervical ganglion, while the right vertebral nerve originated from the cranial part of the craniodorsal border of the caudal cervical ganglion. Abumadour and El-defrawy [1] and Ozgel et al. [19] observed that the vertebral nerve radiating from the craniodorsal angle of the caudal cervical ganglion.

The cardiac nerves were derived from the caudal cervical ganglion and sharing in the cardiac plexus formation [1, 13, 19]. In the present study, the cardiac nerves originated directly from the caudal and middle cervical ganglion. In addition, there were some cardiac nerves that originated from ansa subclavia, accessory cervical ganglion.

The present study reports the first record of the presence of the pericardial branch in the dog that originated from the caudal angle of the middle cervical ganglion, and then penetrated the pericardium to reach the wall of the left auricle. The pericardial branch was only reported previously in the horse [1].

The present study presents the first record of the sympathetic–parasympathetic communications branches, in which on the left side, there were three sympathetic–parasympathetic communicating branches that originated from the middle cervical ganglion to join the vagus nerve, while on the right side there were sympathetic–parasympathetic communicating branches to join the vagus nerve; two branches originated from the middle cervical ganglion, in addition to only one sympathetic–parasympathetic communications branch that originated from the accessory cervical ganglion. The sympathetic–parasympathetic communications branch was previous reported only by Ozgel et al. [19] in one donkey on the right side and by Abumadour and El-defrawy [1] on both sides of all examined horse.

CONCLUSIONS

In the current work, there was a right small ganglion in addition to the other three cervical ganglia: cranial, middle and caudal. The right small ganglion named the accessory cervical ganglion was found on the right side only and absent on the left. This right accessory ganglion was located on the lateral surface of the trachea at the level of the first rib. This gangli-

on formed by the union of the cranial sympathetic branch that originated from the cranial angle of the middle cervical ganglion with the cranioventrally directed nerve that originated from the caudal cervical ganglion. In the roe deer [12] the presence of two accessory ganglions was observed, one on each side; the left one was located at the origin of the brachiocephalic trunk from the aortic arch, while the right one was located on the dorsal side of the trachea.

Compliance with ethical standards

The authors confirmed that the article do not contain any studies with human participants.

This study followed the guidelines for the care and use of laboratory animals and the animal welfare and was approved by the Ethics Committee of the Faculty of Veterinary Medicine, Alexandria University according the Egyptian laws. Adequate measures were taken to minimise pain or discomfort.

Acknowledgements

Conflict of interest: None declared

REFERENCES

1. Abumandour M, El-defrawy F. Morphological Investigations of the Cervicothoracic Sympathetic System in the Horse (Equus ferrus caballus) in Egypt. Int J Morphol. 2016; 34(3).
2. Arıncı K and Elhan A. Anatomi, 2. Cilt, Guneş Kitabevi LTD. STI, Ankara 1995.
3. Chung IH, Oh CS, Koh KS, et al. Anatomic variations of the T2 nerve root (including the nerve of Kuntz) and their implications for sympathectomy. J Thorac Cardiovasc Surg. 2002; 123(3): 498–501, doi: 10.1067/mtc.2002.119340, indexed in Pubmed: 11882821.
4. Daniels TJ, Bekoff M. Population and social biology of free-ranging dogs, Canis familiaris. J Mammalogy. 1989; 70(4): 754–762.
5. Dursun N. Veteriner Anatomi II. Medisan Yayınevi, Ankara 2000.
6. Dyce KM, Sack WO, Wensing CJG. Text book of Veterinary anatomy. W.B. Saunders Company, Philadelphia, London and Toronto 2010.
7. Evans HE, Lahunta A. Guide to the dissection of the dog. 7th ed. Saunders Company, Philadelphia 2010.
8. Evans HE, Lahunta A. Miller's anatomy of the dog. 4th ed. W.B. Saunders Company, Philadelphia 2013: 1181.
9. Fioretto E, Guidi W, Oliveira P, et al. Macrostructure of the cranial cervical ganglionar complex and distal vagal ganglion during post natal development in dogs. Braz J Vet Res Animal Sci. 2003; 40(3), doi: 10.1590/s1413-95962003000300006.
10. Getty R. The anatomy of the domestic animals. Vol. 1, 5th ed. W.B. Saunders Company, Philadelpshia 1975.
11. Hogan QH, Erickson SJ. MR imaging of the stellate ganglion: normal appearance. AJR Am J Roentgenol. 1992; 158(3): 655–659, doi: 10.2214/ajr.158.3.1739014, indexed in Pubmed: 1739014.
12. Kabak M, Onuk B, Demirci B. Macroanatomical Investigation of the Cervicothoracic Ganglion in Roe Deer, Capreolus capreolus. Pakistan J Zool. 2015; 47(6): 1555–1561.
13. Kalsey G, Mukherjee RN, and Pa. A comparative study of cervical sympathetic chain. J Anat Soc India. 2000; 49: 26–30.
14. Klećkowska J, Janeczek M, and Po. Analiza morfologiczna zwoju szyjno-piersiowego (ganglion cervicothoracicum) u 9-tygodniowych płodów świni. Medicina Veterinaria. 2003; 2(1): 41–47.
15. König HE, Liebich HG. Veterinary anatomy of domestic mammals. 3rd ed. Schattauer gimH, Holderlinstrabe, Germany 2007.
16. Marcer N, Bergmann M, Klie A, et al. An anatomical investigation of the cervicothoracic ganglion. Clin Anat. 2012; 25(4): 444–451, doi: 10.1002/ca.21266, indexed in Pubmed: 22488995.
17. Masliukov PM, Pankov VA, Strelkov AA, et al. Morphological features of neurons innervating different viscera in the cat stellate ganglion in postnatal ontogenesis. Auton Neurosci. 2000; 84(3): 169–175, doi: 10.1016/S1566-0702(00)00208-3, indexed in Pubmed: 11111849.
18. Nomina Anatomica Veterinaria N. International Committee on Veterinary Gross Anatomical Nomenclature and authorized by the general assembly of the world Association of veterinary Anatomist. Knoxville, 3rd Ed. Ghent. Published by the Editorial Committee Hanover (Germany), Ghent (Belgium), Columbia, MO (U.S.A.), Rio de Janeiro (Brazil). 2017.
19. Ozgel O, Duzler A, Dursun N, et al. The morphology of the cervico-thoracic sympathetic system in donkeys (Equus asinus L.). Anat Histol Embryol. 2009; 38(2): 139–144, doi: 10.1111/j.1439-0264.2008.00912.x, indexed in Pubmed: 19183351.
20. Pather N, Partab P, Singh B, et al. Cervico-thoracic ganglion: its clinical implications. Clin Anat. 2006; 19(4): 323–326, doi: 10.1002/ca.20214, indexed in Pubmed: 16317739.
21. Phillips JG, Randall WC, Armour JA. Functional anatomy of the major cardiac nerves in cats. Anat Rec. 1986; 214(4): 365–371, doi: 10.1002/ar.1092140405, indexed in Pubmed: 3706781.
22. Rosse C, Gaddum-Rosse P. Hollinshead's Textbook of Anatomy. 5th Ed. Lippincott-Raven, Philadelphia 1997: 728–729.
23. Young J, Olson K, Reading R, et al. Is wildlife going to the dogs? Impacts of feral and free-roaming dogs on wildlife populations. BioScience. 2011; 61(2): 125–132, doi: 10.1525/bio.2011.61.2.7.

ORIGINAL ARTICLE

VIA MEDICA

The ulnar nerve in the cubital tunnel: a foetal study

D.N. Bailey[1], S. Ishwarkumar[2] , B.Z. De Gama[1], P. Pillay[1]

[1]Department of Clinical Anatomy, School of Laboratory Medicine and Medical Sciences, College of Health Sciences, University of KwaZulu-Natal, Westville Campus, Durban, South Africa
[2]Department of Human Anatomy and Physiology, Faculty of Health Sciences, University of Johannesburg, Doornfontein Campus, South Africa

Background: The ulnar nerve (UN), a terminal branch of the medial cord of the brachial plexus, is located posteromedial to brachial artery coursing along medially in the arm from the anterior to the posterior compartment through the arcade of Struthers. It passes posterior to medial epicondyle of humerus and enters the cubital tunnel. Then, it exits through the distal part of the cubital fossa to enter the medial side of the forearm between the two heads of the flexor carpi ulnaris muscle underneath Osborne's ligament to enter the anterior compartment of the forearm. Entrapment of the UN at the cubital tunnel results in a pain and a tingling sensation on the medial side of the forearm and fourth and fifth digits.

Materials and methods: This foetal study documented the course of the UN within the cubital tunnel and its anatomical relations utilising bilateral microscopic dissection of 25 foetuses (gestational age: 19–36 weeks).

Results: The UN followed the standard anatomical course in 96% (48/50) of the specimens, however it was found to lie deep to the muscles of the cubital tunnel in 6% (3/50). The radial artery joined the UN distal to the cubital tunnel in 8% (4/50), while the superior ulnar collateral artery was posteriorly related to the UN in 32% (16/50) of specimens. The Osborne's ligament (crossed between the two heads of the flexor carpi ulnaris muscle, posterior to the medial epicondyle of the humerus) was present in all specimens 100% (50/50). It had a mean length of 6.32 ± 0.97 mm and 6.30 ± 1.10 mm on the left and right sides, respectively. The current study observed that the flexor pronator aponeurosis was present in 2% (1/50) of specimens.

Conclusions: Knowledge of the normal and variable anatomical course of the UN in the cubital tunnel in this study may assist in the diagnosis and treatment of compressive neuropathy of the UN in the cubital tunnel. (Folia Morphol 2022; 81, 1: 31–36)

Key words: ulnar nerve, cubital fossa, foetal study and anatomical course

---

Address for correspondence: Dr. P. Pillay, Department of Clinical Anatomy, School of Laboratory Medicine and Medical Sciences, College of Health Sciences, University of KwaZulu-Natal, Private Bag X54001, Durban, 4000, South Africa, tel: + 27 31 260 7789, fax: + 27 31 260 7890, e-mail: soobramoneypa@ukzn.ac.za

INTRODUCTION

The ulnar nerve (UN) is the larger terminal branch of the medial cord of the brachial plexus formed by the ventral rami of C8 and T1, with occasional branches from C7 [4, 23]. In its course, it runs on the medial side of the brachial artery in the middle-third of the arm, pierces the medial intermuscular septum with the superior ulnar collateral artery (SUCA), runs in the arcade of Struthers between the septum and the medial head of the triceps [5, 18]. The arcade of Struthers is described as a musculotendinous band, located at variable distances superior to the medial epicondyle of the humerus between the medial intermuscular septa and the medial head of the triceps brachii muscle [5, 8, 16]. The UN then passes posterior to the medial epicondyle of humerus, to enter the forearm medial to the olecranon of the ulna [15, 18]. At this juncture, a tendinous ligamentous arch is stated to span between the humeral and ulnar heads of flexor carpi ulnaris (FCU) muscle which is referred to as the Osborne's ligament [10, 19]. The cubital tunnel is a fibromuscular canal beneath the Osborne's ligament [20]. The Osborne's ligament forms the roof of the canal laterally, and the floor is formed by the medial collateral ligament, the joint capsule of elbow and olecranon process [19]. This tunnel can be divided into three parts: *viz.* (i) the entrance posterior to the medial epicondyle; (ii) the fascial aponeurosis joining two heads of the FCU, and (iii) at the muscular bellies [22].

The UN slopes postero-medially together with the ulnar vessels in the forearm deep to anterior margin of FCU and flexor digitorum profundus (FDP), giving motor branches to both muscles [21].

Typically, compression of the UN occurs at the cubital tunnel; however, the nerve is also vulnerable at other sites around the elbow [15, 20]. These sites are classified as either pre-cubital, cubital tunnel or post-cubital tunnel compression sites [6, 20]. Since, the compression sites are variable, anatomical knowledge of the relations of the UN is important [4, 15, 20].

Therefore, this study aimed at documenting the course of the UN with a focus on the anatomical relations within the cubital tunnel.

MATERIALS AND METHODS

A bilateral dissection of 25 foetal cadavers (n = 50), 11 females and 14 males between 19 and 36 gestational weeks, was performed to expose muscles of the forearm and reveal the UN in the cubital tunnel, in order to document its course and relations. The presence of the arcade of Struthers, anconeus epitrochlearis muscle, flexor-pronator aponeurosis (FPA), Osborne's ligament, the SUCA, radial artery and ulnar artery was also documented together with anatomical variations (if present). A morphometric analysis of the Osborne's ligament was performed by measuring the distance between the medial epicondyle and the lateral border of the olecranon process using a digital sliding calliper in order to determine the size of the cubital tunnel. The foetal cadavers were sourced from the Department of Clinical Anatomy at the University of KwaZulu-Natal (Westville Campus). Ethical clearance was obtained (BE397/17). Foetuses whose forearms were deformed by traumas, malformations, scars or any other macroscopic evidence of pathology were excluded from this study. The data was captured and analysed using the Statistical Package for Social Sciences (SPSS version 23.0) software. A p-value of less than 0.05 was deemed statistically significant.

Reliability and validity

Morphometric analysis of the Osborne's ligaments was performed by an inter-observer on 5 random cadavers using the sliding digital calliper. The intra-class correlation coefficient test was then employed to assess the inter-observer reliability. A 0.989 significance for the mean Osborne's ligament length between both observers was found which denotes excellent agreement.

RESULTS

The course and relations of the ulnar nerve

The UN passed through the cubital tunnel in 96% (48/50) of the specimens, while it was absent in 4% (2/50) (Fig. 1). In its course through the cubital tunnel, the UN was located deep to the FCU and supero-lateral to the FDP in 6% (3/50) (Fig. 2). The SUCA accompanied the UN into the cubital tunnel in 32% (16/50) in at least one side of the present study prior to its anastomoses with the ulnar recurrent arteries (Figs. 3, 4; Table 1). A statistically significant correlation between the course of the UN and SUCA was documented in this study with a p-value of 0.042.

The ulnar artery accompanied the UN as it passes through the cubital fossa in 34% (17/50) (Figs. 5, 6). In 2% (1/50) of the specimens, the UN was covered medially by a common flexor pronator aponeurosis (Fig. 7). The radial artery followed the standard anatomical course in 92% (46/50) of the specimens;
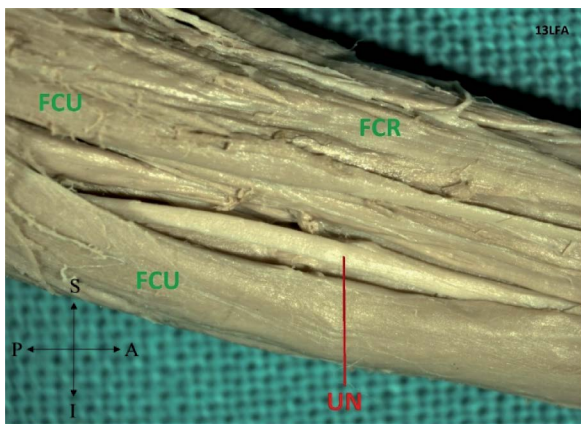
Figure 1. The standard description of ulnar nerve (UN) in the cubital tunnel; FCR — flexor carpi radialis; FCU — flexor carpi ulnaris.

Figure 2. The ulnar nerve (UN) lies deep to the cubital tunnel muscles; FCR — flexor carpi radialis; FCU — flexor carpi ulnaris; FDP — flexor digitorum profundus.
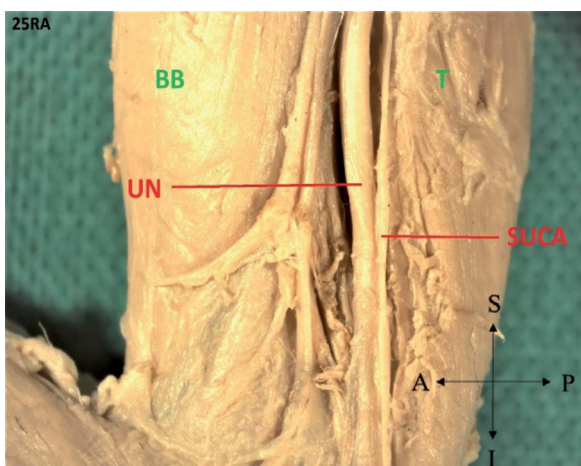
Figure 3. The ulnar nerve (UN) in the arm accompanied by the superior ulnar collateral artery (SUCA); BB — biceps brachii; T — triceps muscle.

Figure 4. The ulnar nerve (UN) in arm without the superior ulnar collateral artery (SUCA); BB — biceps brachii; T — triceps muscle.

Table 1. Presence/absence of the superior ulnar collateral artery in relation to laterality (n = 50)

	Incidence	Percentage
Present on left side only	5	10%
Present on right side only	3	6%
Bilaterally present	8	16%
Bilaterally absent	26	52%
Absent on left side only	5	10%
Absent on right side only	3	6%

however, it accompanied the UN distal to the cubital tunnel in 8% (4/50) (Fig. 8).

Arcade of Struthers

All specimens sampled in this study showed that the arcade of Struthers was absent. This may be due to the developmental stages of foetuses used.

Osborne's ligament

The Osborne's ligament was found in 100% of specimens (50/50) (Fig. 9), but varied from a thin aponeurotic structure to a thickened fascial band. The anconeus epitrochlearis muscle, an analogue to the Osborne's ligament was found in 2% (1/50) of the specimens (Fig. 10). The Osborne's ligament had a mean length of 6.32 ± 0.97 and 6.30 ± 1.10 mm on the left and right sides, respectively (Table 2). This study found no statistically significant relationship between the length of Osborne's ligament and laterality (right: p = 0.55 and left p = 0.65).

33
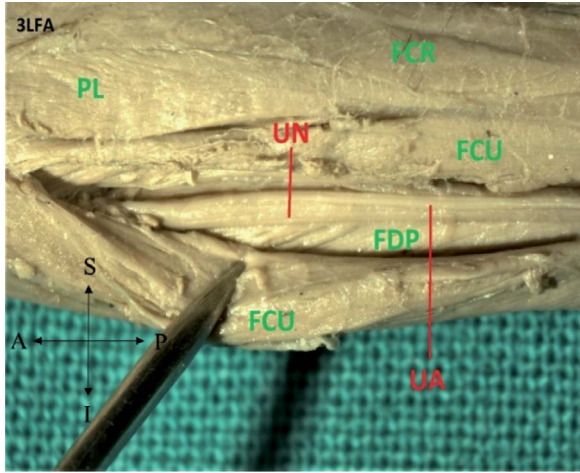
Figure 5. The ulnar nerve (UN) in the cubital tunnel and forearm accompanied by the ulnar artery (UA); FCR — flexor carpi radials; FCU — flexor carpi ulnaris; FDP — flexor digitorum profundus; PL — palmaris longus.
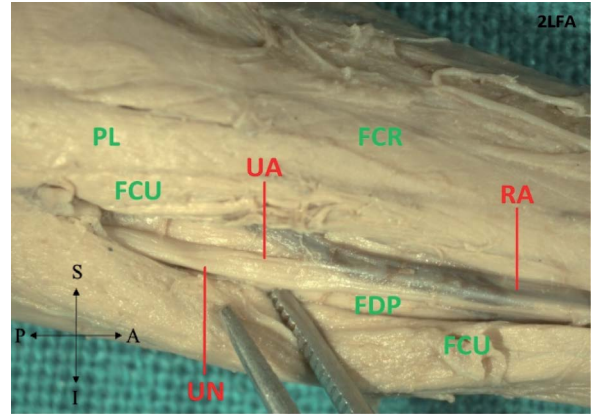
Figure 8. The ulnar nerve (UN) accompanied by the radial artery (RA); FCR — flexor carpi radialis; FCU — flexor carpi ulnaris; FDP — flexor digitorum profundus; PL — palmaris longus; UA — ulnar artery.
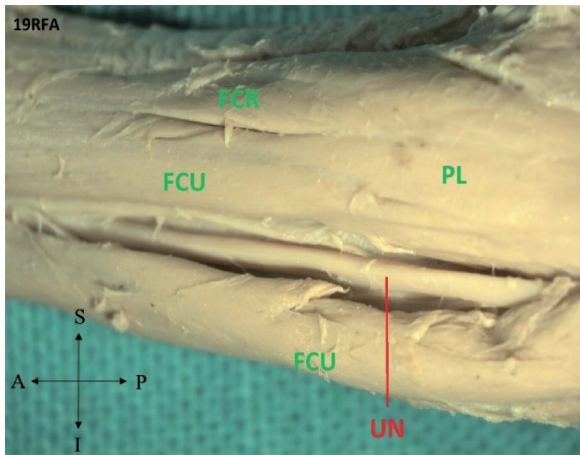
Figure 6. The ulnar nerve (UN) in the cubital tunnel without the ulnar artery; FCR — flexor carpi radialis; PL — palmaris longus; FCU — flexor carpi ulnaris.
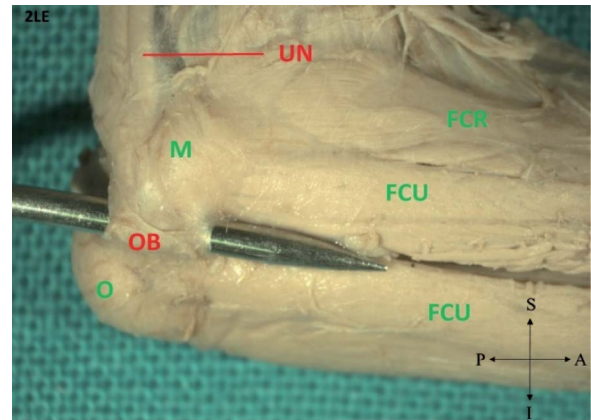
Figure 9. The Osborne's ligament between the two heads of flexor carpi ulnaris (FCU); UN — ulnar nerve; M — medial epicondyle; OB — Osborne's band; O — olecranon process; FCR — flexor carpi radialis.
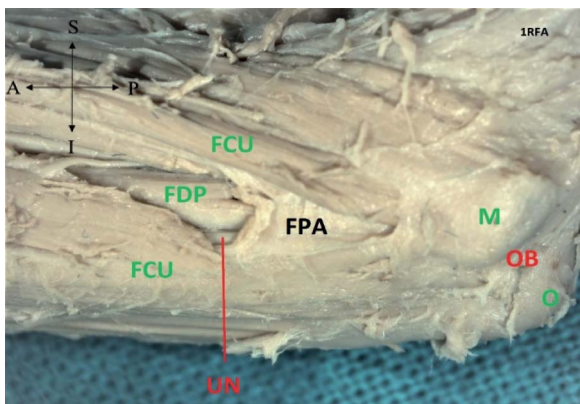
Figure 7. The flexor pronator aponeurosis (FPA) underneath heads of flexor carpi ulnaris (FCU); FDP — flexor digitorum profundus; OB — Osborne's band; UN — ulnar nerve; M — medial epicondyle; O — olecranon process.
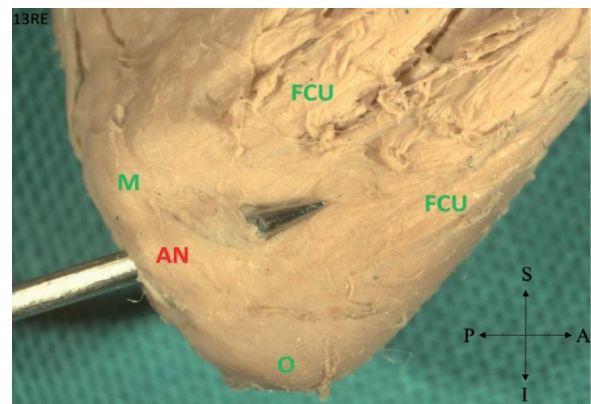
Figure 10. The anconeus epitrochlearis (AN) muscle between the two heads of the flexor carpi ulnaris (FCU); M — medial epicondyle; O — olecranon process.

34

Table 2. Mean length and standard deviations of Osborne's ligament

	Minimum length [mm]	Maximum length [mm]	Mean length [mm]	Standard deviation
Age [weeks]	19.49	36.93	26.55	3.73
Right Osborne's ligament	4.64	8.82	6.30	1.09
Left Osborne's ligament	4.48	8.69	6.32	0.97

Table 3. Descriptions of the flexor-pronator aponeurosis (FPA) in the cadaver studies

Author	Year	Sample size	FPA (present/absent)	Length [cm]
Inserra and Spinner [13]	1986	10	Absent	1.5–2.0
Amadio and Beckenbaugh [1]	1986	20	100%	5
Green and Rayan [11]	1999	19	100%	2.9
Gonzalez et al. [9]	2001	38	43.5%	4.2
Degeorges and Masquelet [7]	2002	24	45.8%	6
Siemionow et al. [20]	2007	28	100%	5.6
Present study	2017	50	2%	Not measured

DISCUSSION

The course and relations of the ulnar nerve

This study found that in 96% (48/50) of the specimens, the standard course of the UN was documented, *viz.* the nerve crosses the medial collateral ligament of the elbow and enters the flexor compartment of the forearm between the two heads of the FCU, then travelled distally between the FCU and FDP muscles [12, 15, 17].

However, the course of the UN can vary. Assmus et al. [2] documented the UN in the cubital tunnel whereby the nerve had a superficial course, anterior to the medial epicondyle but did not penetrate the fascia between the FCU muscles. In this study, the radial artery accompanied the UN, distal to the cubital tunnel, from the middle third of the forearm was documented as a unique finding.

An elliptically shaped fibrous tunnel formed by the flexor pronator aponeurosis was observed (2%); however, previous literature indicated the incidence of the FPA to range between 43.5% and 100% (Table 3) [1, 7, 9, 11, 13, 20]. Siemionow et al. [20] documented that the elliptically shaped tunnel may be a cause of UN compression.

Arcade of Struthers

The arcade of Struthers was observed in previous literature [15, 20], however it was not present in the specimens used in this study. This could be due to the sample size or the use of foetuses instead of adult cadavers. Furthermore, Bartels et al. [3] and Caetano et al. [5] stated that the occurrence of the arcade of Struthers is rare and observed in 0.7% to 2.5% of the population. Furthermore, Mizia et al. [16] found that the arcade of Struthers is a valid anatomical structure that is present in most individuals; however, its presence is highly variable.

Osborne's ligament

An Osborne's ligament was documented in 100% of specimens; however, the ligament varied from a very thin aponeurotic structure to a thickened muscle. An anconeus epitrochlearis muscle found in one of the specimens, has been described as the cause of UN neuritis [14]. The mean length of the Osborne's ligament in this study was 6.32 ± 0.97 mm on the left side and 6.30 ± 1.10 mm on the right side (Table 2). The length of the Osborne's ligament differed with previous reports such as Gonzalez et al. [9] who found its average length as 4.6 mm. Variations in the length of the Osborne's ligament to a previous study can be attributed to the fact that previous studies were conducted on adult cadavers, while the current study was conducted on foetuses.

The SUCA accompanied the UN into the cubital tunnel in 32% and a significant correlation was observed between presence of the superior ulnar collateral artery and the course of UN.

Limitations of the study

The present study only included foetal specimens, as there is a shortage of adult cadavers. A further study is required to document the histology of the Osborne's ligament as this was not done in this study.

CONCLUSIONS

The understanding of the anatomy of the UN is important for the diagnosis and treatment of conservative and surgical lesions of the UN in the cubital region. In this study, the potential sites of UN compression may be at the cubital tunnel; beneath the FCU; FPA (elliptically shaped tunnel) and the Osborne's ligament. Knowledge of the anatomy of the UN in the cubital tunnel may be essential to mitigate the risk of injury during the now increasingly performed endoscopically assisted decompression surgery [2].

Acknowledgements

Conflict of interest: None declared

REFERENCES

1. Amadio P, Beckenbaugh R. Entrapment of the ulnar nerve by the deep flexorpronator aponeurosis. J Hand Surg. 1986; 11(1): 83–87, doi: 10.1016/s0363-5023(86)80110-1.
2. Assmus H, Antoniadis G, Bischoff C. Carpal and cubital tunnel and other, rarer nerve compression syndromes. Dtsch Arztebl Int. 2015; 112(1-2): 14–25; quiz 26, doi: 10.3238/arztebl.2015.0014, indexed in Pubmed: 25613452.
3. Bartels RH, Grotenhuis JA, Kauer JMG. The arcade of Struthers: an anatomical study. Acta Neurochir (Wien). 2003; 145(4): 295–300; discussion 300, doi: 10.1007/s00701-003-0006-5, indexed in Pubmed: 12748890.
4. Becker R, Manna B. Anatomy, upper limb, elbow, nerves, ulnar. StatPearls Publishing, Treasure Island (FL) 2018.
5. Caetano EB, Sabongi Neto JJ, Vieira LA, et al. The arcade of Struthers: an anatomical study and clinical implications. Rev Bras Ortop. 2017; 52(3): 331–336, doi: 10.1016/j.rboe.2016.07.006, indexed in Pubmed: 28702393.
6. Cutts S. Cubital tunnel syndrome. Postgrad Med J. 2007; 83(975): 28–31, doi: 10.1136/pgmj.2006.047456, indexed in Pubmed: 17267675.
7. Degeorges R, Masquelet AC. The cubital tunnel: anatomical study of its distal part. Surg Radiol Anat. 2002; 24(3-4): 169–176, doi: 10.1007/s00276-002-0032-7, indexed in Pubmed: 12375068.
8. Depukat P, Mizia E, Zwinczewska H, et al. Topography of ulnar nerve and its variations with special respect to carpal region. Folia Med Cracov. 2014; 54(4): 45–58, indexed in Pubmed: 25891242.
9. Gonzalez MH, Lotfi P, Bendre A, et al. The ulnar nerve at the elbow and its local branching: an anatomic study. J Hand Surg Br. 2001; 26(2): 142–144, doi: 10.1054/jhsb.2000.0532, indexed in Pubmed: 11281666.
10. Granger A, Sardi JP, Iwanaga J, et al. Osborne's ligament: a review of its history, anatomy, and surgical importance. Cureus. 2017; 9(3): e1080, doi: 10.7759/cureus.1080, indexed in Pubmed: 28405530.
11. Green JR, Rayan GM. The cubital tunnel: anatomic, histologic, and biomechanical study. J Shoulder Elbow Surg. 1999; 8(5): 466–470, doi: 10.1016/s1058-2746(99)90078-2, indexed in Pubmed: 10543601.
12. Heithoff SJ. Cubital tunnel syndrome: ulnar nerve subluxation. J Hand Surg Am. 2010; 35(9): 1556; author reply 1556–7, doi: 10.1016/j.jhsa.2010.06.027, indexed in Pubmed: 20807635.
13. Inserra S, Spinner M. An anatomic factor significant in transposition of the ulnar nerve. J Hand Surg. 1986; 11(1): 80–82, doi: 10.1016/s0363-5023(86)80109-5.
14. Joshi SD, Joshi SS. Study of cubital tunnel. J Anat Soc India. 2002; 51(2): 173–175.
15. Macchi V, Tiengo C, Porzionato A, et al. The cubital tunnel: a radiologic and histotopographic study. J Anat. 2014; 225(2): 262–269, doi: 10.1111/joa.12206, indexed in Pubmed: 24917209.
16. Mizia E, Zarzecki MP, Pekala JR, et al. An anatomical investigation of rare upper limb neuropathies due to the Struthers' ligament or arcade: a meta-analysis. Folia Morphol. 2021; 80(2): 255–266, doi: 10.5603/FM.a2020.0050, indexed in Pubmed: 32394418.
17. Moore KL. Clinically Oriented Anatomy 6th Ed. Lippincott, Williams and Wilkins, Baltimore, MD 2010: 770.
18. Moore KL, Dalley AF, Agur AMR. Clinically orientated anatomy. Lippincott, Williams and Wilkins 2014: 514–516.
19. Sawardeker P, Kindt KE, Baratz NE. Nerve Compression: Ulnar Nerve of the Elbow. 2015.
20. Siemionow M, Agaoglu G, Hoffmann R. Anatomic characteristics of a fascia and its bands overlying the ulnar nerve in the proximal forearm: a cadaver study. J Hand Surg Eur Vol. 2007; 32(3): 302–307, doi: 10.1016/J.JHSB.2006.12.015, indexed in Pubmed: 17321018.
21. Standring S. Gray's Anatomy E-Book: The Anatomical Basis of Clinical Practice. Elsevier Health Sciences 2015.
22. Xarchas KC, Psillakis I, Koukou O, et al. Ulnar nerve dislocation at the elbow: review of the literature and report of three cases. Open Orthop J. 2007; 1: 1–3, doi: 10.2174/1874325000701010001, indexed in Pubmed: 19461901.
23. Yamada K, Nagaoka M, Nagao S, et al. Anatomical study of osborne ligament elongation in relation to elbow flexion. J Nihon University Med Ass. 2013; 72(3): 154–158, doi: 10.4264/numa.72.154.

VIA MEDICA

ORIGINAL ARTICLE

Topography of the common fibular nerve terminal division in human foetuses

A. Karykowska[1], Z.A. Domagała[2], B. Gworys[3]

[1]Department of Anthropology, Wroclaw University of Environmental and Life Sciences, Wroclaw, Poland
[2]Division of Anatomy, Department of Human Morphology and Embryology, Faculty of Medicine,
Wroclaw Medical University, Wroclaw, Poland
[3]Faculty of Health Science and Physical Education, The Witelon State University of Applied Sciences, Legnica, Poland

Background: The progress of paediatric surgery and increasingly better diagnosis of foetal defects require detailed knowledge of human developmental anatomy. Precise knowledge of the anatomy of innervation of the lower extremities corresponds to this subject and is not only cognitive but also clinically important. The end of the common fibular nerve is superficially located in the area exposed to frequent injuries as well as in the area subject to possible surgical repair procedures.
Materials and methods: The analysis was carried out on 200 human foetuses aged from the 113th day to 222nd day of foetal life. The study material is a part of local foetal collection. The study incorporated the following methods: anthropological, preparational and image acquisition which was acquired with the use of high-resolution digital camera. Statistical analysis was carried out with the use of STATISTICA package.
Results: Based on the research results the new typology of the examined nerve was determined. The head of the fibula was the criterion: (i) high division — above the head of the fibula (1%); (ii) intermediate division — at the height of the head of the fibula (34%); (iii) low division — below the head of the fibula (65%). The mathematical analysis did not reveal statistically significant bilateral and gender differences. Moreover the additional branch was observed in 30% of foetuses, regardless of age class. This branch occurred in 50% of cases in both sides of the foetus. This nerve was defined as the accessory fibular nerve (nervous fibularis/peroneus accessorius).
Conclusions: The created unique typology of the terminal division of common fibular nerve is an important supplement to the anatomical knowledge and at the same time, due to the peripheral and superficial location of the described structures, it has a relatively high clinical significance. (Folia Morphol 2022; 81, 1: 37–43)

Key words: common peroneal nerve, dissection, human foetuses, accessory fibular nerve

INTRODUCTION

The common fibular nerve (*nervus peroneus communis*) is formed as a branch of the sciatic nerve (*nervus ischiadicus*) at thigh level or in the area of the popliteal fossa [37, 38]. It runs in the distal and lateral direction, towards the head of the fibula. It then bends around the fibula neck (*collum fibulae*) and divides into superficial and deep fibular nerves

Address for correspondence: Z. Domagała, MD, PhD, Division of Anatomy, Department of Human Morphology and Embrology, Faculty of Medicine, Wroclaw Medical University, ul. Chałubińskiego 6a, 50–367 Wrocław, Poland, tel: +48 71 784 13 30, e-mail: zygmunt.domagala@umed.wroc.pl

(*nervus peroneus superficialis et profundus*) within the fibularis longus muscle (*musculus peroneus longus*) belly [3, 34, 38]. Both nerves, which are branches of the common fibular nerve, supply the anterior and lateral compartment of the leg and dorsal foot structures [7, 8, 38]. Many articles in the scientific literature have highlighted diseases and injuries to these nerves and their branches. One of the most common postoperative complications in the leg area is neuroma of the common or superficial fibular nerve [4, 6, 22, 32]. Damage to the common fibular nerve and its branches as a result of fibula fracture or superficial sports injuries are also frequent [1, 8, 38]. In addition, there are often various medical procedures carried out in the area near to the nerve trunk, which may cause iatrogenic damage to the nerve or its final branches [2, 19, 21, 41]. Therefore, it is of anatomical and clinical importance to know the variability of the final division of the common fibular nerve (FDCFN).

The course, branching pattern, and relationships of the common fibular nerve and its terminal branches with bony landmarks have been well demonstrated in adults by many authors [5, 11, 12, 25, 37, 38]. However, no information has yet been identified that would indicate a detailed bifurcation topography pattern in the foetus, which may be important in tumour surgery and treatment of early deformities [16, 29, 33, 36]. Therefore, the aim of this study was to develop a typology of the FDCFN in relation to the head of the fibula based on the available foetal material.

MATERIALS AND METHODS

Preparatory analysis was performed on 200 human foetuses aged from 113 to 222 days of foetal life. Foetal specimens were divided into age classes based on lunar months (Table 1).

The analysed foetal material comes from the collection of the Department of Anatomy in Wroclaw, Poland. It was obtained from maternity wards of local gynaecological clinics as a result of preterm and early deliveries and miscarriages between 1960 and 1996. The foetuses were stored in a suitable preservative solution containing ethanol, glycerol, and formalin in constant proportions [18, 31, 42]. Foetuses with visible developmental malformations and those that did not have complete clinical documentation were excluded from the study. The value of the foetal collection was confirmed in numerous previously published scientific studies [10, 13, 14, 17, 18, 24, 40]. The scientific experience of the team has been

Table 1. The quantity of examined foetuses in subsequent age classes with the gender division

Calendar age [months]	N	Males	Females
4 + 5	69	34	35
6	78	39	39
7	40	18	22
8 + 9	13	8	5

confirmed in many works using anatomical scientific methodology and anatomical techniques used for statistical analysis [9, 15, 27].

The preparation was performed using classical preparatory methods. In order to visualise the FDCFN, it was necessary to use the binocular surgical microscope Leica Provido (Leica Microsystems, Germany).

The prepared common fibular nerve and its two final branches were described using schematic drawings. In addition, photographs were taken using a Sony Alpha (Sony Corporation, Japan) camera and a suitable Manfrotto (Manfrotto, Italy) tripod to ensure that the angle and height of the lens in relation to the foetuses were constant.

Statistical analysis

The mean values and standard deviations (± SD), minimum and maximum variability range were determined on the basis of the collected research material. In order to examine the independence of two qualitative features, the χ^2 independence test was applied. All analyses were performed using the STATISTICA 10.0 (TIBCO Software Inc., USA) package. The work and whole study protocol was approved by the Bioethics Committee No. KB-708/2017

RESULTS

Based on sectional studies, three types of FDCFN positions were determined. The head of the fibula was the criterion: (i) type A: high division — above the head of the fibula (Fig. 1); (ii) type B: intermediate division — at the height of the head of the fibula (Fig. 2); (iii) type C: low division — below the head of the fibula (Fig. 3). Prevalence of individual types is shown in Figure 4.

The following concepts have been introduced: symmetrical division, which means that in the case of both limbs the division of the common fibular nerve into terminal branches occurs at the same level; adjacent division, which means that from one extremity
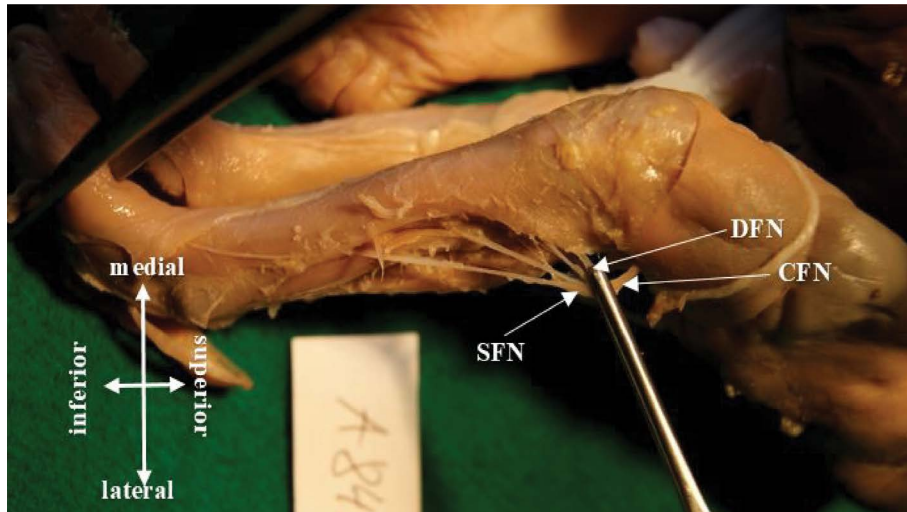
Figure 1. Type high of the common fibular nerve final division; DFN — deep fibular neve; CFN — common fibular nerve; SFN — superficial fibular nerve.
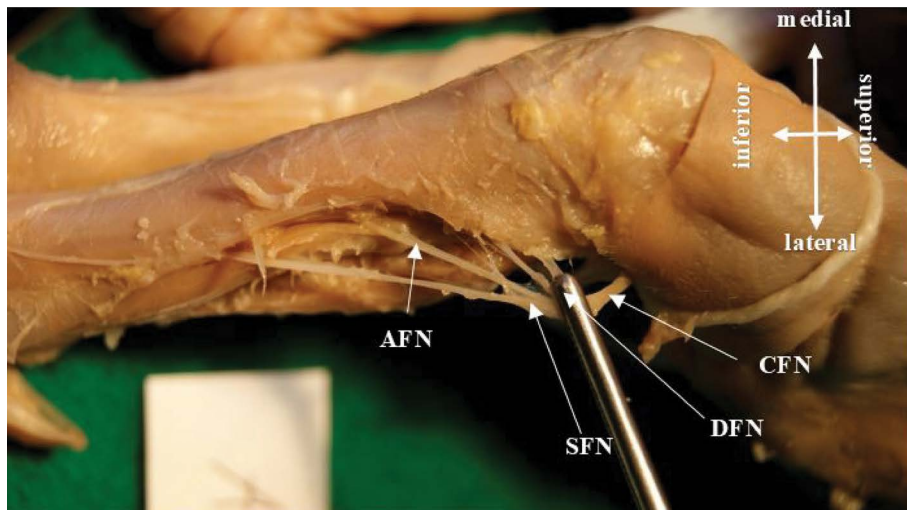
Figure 2. Intermediate type; DFN — deep fibular neve; CFN — common fibular nerve; SFN — superficial fibular nerve; AFN — accessory fibular nerve.
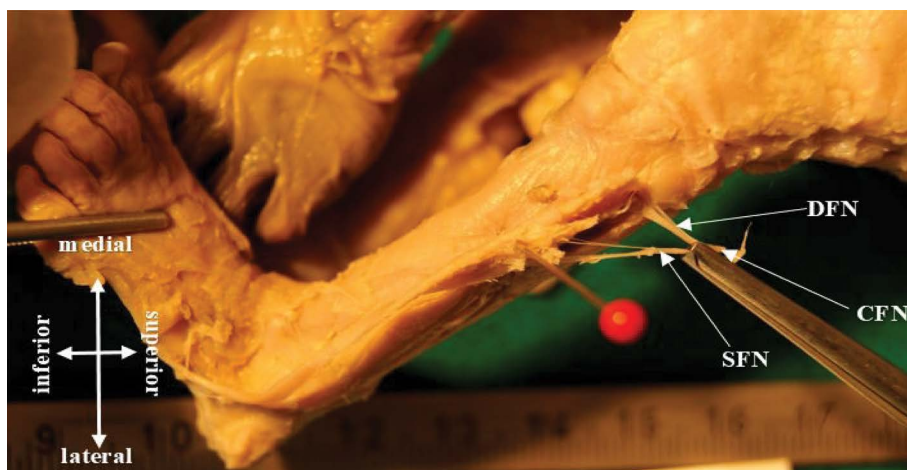
Figure 3. Low type; DFN — deep fibular neve; CFN — common fibular nerve; SFN — superficial fibular nerve.
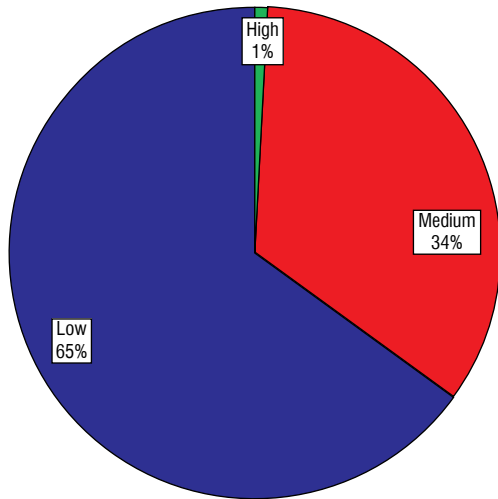
Figure 4. Percentage of individual types of end division of the examined nerve.

there is, e.g. high division, and intermediate division into the other extremity; and distant division, which refers to the extreme opposite position of the final nerve division on both limbs of one specimen (Table 2). Despite the examples of asymmetry shown (Table 2), analysis did not reveal statistically significant differences (χ^2 = 30.67, p = 0.43), which means that there are no branch variants observed more frequently in particular age classes. Additionally, there was no asymmetry in the occurrence of FDCFN branches (χ^2 = 6.67, p = 0.15) and no relationship between

symmetrical/adjacent and distant division and foetal sex (Table 3).

A more detailed evaluation of the data showed no statistically significant differences in the right limb final division of the common fibular nerve (p = 0.21). Similarly, no statistically significant differences were found for the left limb (p = 0.06). A schematic drawing was also created for the right and left common fibular nerve, illustrating the course of this nerve and its division into subsequent branches.

Along with the superficial and deep fibular branches of the common fibular nerve, an additional branch was observed in 30% of foetuses, regardless of age class. This branch occurred in 50% of cases in both sides of the foetus. This nerve was defined as the accessory fibular nerve (*nervus fibularis/peroneus accessorius*) in a previous work [12]. Statistical analysis did not reveal any bilateral (p = 0.07) or dimorphic differences (p = 0.16) in the incidence of that additional branch of common fibular nerve in human foetuses.

DISCUSSION

The present work is based on unique material of high cognitive value [17, 23]. An important novelty of this analysis is the evaluation of variability of the FDCFN based on extensive foetal material, which is difficult to obtain. The available literature analysing the subject area is relatively poor in the case of foetal

Table 2. Frequency of occurrence of particular types of common fibular nerve terminal division (FDCFN) in selected age classes and symmetry of occurrence of given types depending on the age class

Month	A + B	A + C	B + A	B + B	B + C	C + B	C + C	Total
4 + 5	0	0	1	7	11	16	36	69
6	0	1	0	15	15	10	37	78
7	1	0	0	7	5	10	17	40
8 + 9	0	0	0	2	1	4	4	13
Total	1	1	1	31	32	40	94	200

A — high division: above the head of the fibula; B — intermediate division: at the height of the head of the fibula; C — low division: below the head of the fibula; Total — number of examined foetuses; the first letter in the first row describes the position of FDCFN on left limb, and the second one — on the right

Table 3. The relationship between symmetrical/adjacent and distant division and foetal sex (χ^2 = 9.45, p = 0.15)

Sex	A + B	A + C	B + A	B + B	B + C	C + B	C + C	Total
Male	0	1	0	13	16	15	54	99
Female	1	0	1	18	16	25	40	101
Total	1	1	1	31	32	40	94	200

A — high division: above the head of the fibula; B — intermediate division: at the height of the head of the fibula; C — low division: below the head of the fibula; Total — number of examined foetuses; the first letter in the first row describes the position of FDCFN on left limb, and the second one — on the right).

anatomy. It is based on the analysis of a small number of cases, without a division into age classes [12, 28].

It is worth emphasizing that the variability of the fibular nerves arouses great interest in the scientific world, as evidenced by numerous anatomical publications and clinical papers describing the relationship between the neurological complications of surgical procedures or injuries and the variability of the position of nerve trunks and branches [1, 4, 6, 22, 32, 37, 39]. The terminal section of the common fibular nerve trunk is particularly vulnerable to injury due to its course just above the fibula [1]. Complicated fractures or direct-acting other types of injury (blow, cut) require the implementation of surgical treatment, the success of which depends upon the anatomical competence of the performing physician in this area

For this reason, a new typology has been proposed to assess the position of FDCFN in relation to the fibula head. The head of the fibula is easily palpable in a physical examination regardless of age, and can also be easily visualised in radiological examinations. It therefore seems to be the best reference point for the final division *nervus peroneus communis.*

The proposed typology is partly inspired by a paper published by authors from South Africa, where the fibular tubercle was used as a landmark [7]. Interestingly, there is no such a structure in the anatomical nomenclature. The authors suspect that the described point is an incorrectly defined point *fibulare*, which is an anthropological determinant of the detectable fragment of *apex capitis fibulae*.

Based on the proposed typology it has been established that type 3, i.e. low division of the common fibular nerve into end branches, is the most common typology present in the population of the examined foetuses.

Very similar characteristics are presented by Turkish researchers [28] who analysed the final division of sciatic nerve and common fibular nerve based on 20 foetuses and showed relatively low nerve division in both cases. In the available literature based on adult material, the division of common fibular nerve usually takes place above the head of the fibula [3, 8, 34].

The presented data support the thesis of a different location of bifurcation *nervus peroneus communis* in human foetuses. The cause of this phenomenon has not been clearly identified. Kurtoglu et al. [28] suggest that the different location of nervous divisions is the result of limb elongation after the end of foetal development. This process affects the fascia and can thus modify the position of important anatomical points such as the final division of the common fibular nerve. On the other hand, Kołaczkowski and Stachura [26] suggest that the "climbing" of nervous divisions may be caused by a process of physical activity that significantly modifies the ratio between the length of the tendon and the length of the muscle belly by shortening the belly and lengthening the tendon, which hypothetically is supposed to change the position of the nervous branches.

Most importantly, this work aimed to demonstrate the presence of *nervus peroneus superficialis accessorius*. The available literature very rarely indicates the presence of an additional branch of the common fibular nerve [20, 35]. This additional branch occurred among as many as 30% of the examined foetuses, of which as much as 50% of the cases appeared on both sides. Similar observations can be found in a study by Domagała et al. [12], who also indicate the presence of an additional branch of the common fibular nerve, which penetrates the anterior compartment of leg in 12% of examined foetuses. The authors defined this nerve as *nervus peroneus accessorius* because of its origin, which makes it impossible to define this additional branch as an element originating from *nervus peroneus superficialis* or *nervus peroneus profundus*. The sample was much less numerous, so it is probable that this frequency would increase as the size of the examined cohort increases. While these branches are fascinating for anatomists, they are also of great clinical importance. Their unusual localisation may lead to unpredictable complications, especially as it is likely that, in addition to the sensory fibres, they may also conduct motor fibres to *musculus peroneus tertius* [14] or *musculus extensor digitorum brevis* [30].

Conflict of interest: None declared

REFERENCES

1. Aigner F, Longato S, Gardetto A, et al. Anatomic survey of the common fibular nerve and its branching pattern with regard to the intermuscular septa of the leg. Clin Anat. 2004; 17(6): 503–512, doi: 10.1002/ca.20007, indexed in Pubmed: 15300871.

2. Alentorn-Geli E, Stuart JJ, James Choi JH, et al. Postero-lateral portal tibial tunnel drilling for posterior cruciate ligament reconstruction: technique and evaluation of safety and tunnel position. Knee Surg Sports Traumatol Arthrosc. 2017; 25(8): 2474–2480, doi: 10.1007/s00167-015-3958-0, indexed in Pubmed: 26718637.

3. Arora AK, Abrol S, Verma P. An anomalous variation in the division pattern of the common peroneal nerve. Int J Appl Basic Med Res. 2011; 1(2): 118–119, doi: 10.4103/2229-516X.91159, indexed in Pubmed: 23776791.

4. Baima J, Krivickas L. Evaluation and treatment of peroneal neuropathy. Curr Rev Musculoskelet Med. 2008; 1(2): 147–153, doi: 10.1007/s12178-008-9023-6, indexed in Pubmed: 19468889.

5. Bogacka U, Dziedzic D, Komarnitki I, et al. Anatomy of the long peroneal muscle of the leg. Folia Morphol. 2017; 76(2): 284–288, doi: 10.5603/FM.a2016.0054, indexed in Pubmed: 27714727.

6. Bowley MP, Doughty CT. Entrament Neuroathies of the Lower Extremity. Vol. 103. Medical Clinics of North America 2019: 371–382.

7. Chetty D, Pillay P, Lazarus L, et al. The common fibular nerve (and its branches) in fetuses. Int J Morphol. 2014; 32(2): 455–460, doi: 10.4067/s0717-95022014000200013.

8. Dellon AL, Ebmer J, Swier P. Anatomic variations related to decompression of the common peroneal nerve at the fibular head. Ann Plast Surg. 2002; 48(1): 30–34, doi: 10.1097/00000637-200201000-00004, indexed in Pubmed: 11773727.

9. Domagała Z, Dąbrowski P, Kurlej W, et al. The sequence of lanugo pattern development on the trunk wall in human fetuses. Adv Clin Exp Med. 2017; 26(6): 967–972, doi: 10.17219/acem/61440, indexed in Pubmed: 29068598.

10. Domagała Z, Dąbrowski P, Porwolik M, et al. Is the secular trend reflected in early stages of human ontogenesis? Anthropol Rev. 2014; 77(1): 77–86, doi: 10.2478/anre-2014-0007.

11. Domagała Z, Gworys B, Kreczyńska B, et al. contribution to the discussion concerning the variability of the third peroneal muscle: An anatomical analysis on the basis of foetal material. Folia Morphol. 2006; 65(4): 329–336, indexed in Pubmed: 17171612.

12. Domagała Z, Gworys B, Porwolik K. Preliminary assessment of anatomical variability of nervus peroneus superficialis in the foetal period. Folia Morphol. 2003; 62(4): 401–403, indexed in Pubmed: 14655126.

13. Dudek K, Kędzia W, Kędzia E, et al. Mathematical model-ling of the growth of human fetus anatomical structures. Anat Sci Int. 2017; 92(4): 521–529, doi: 10.1007/s12565-016-0353-y, indexed in Pubmed: 27393150.

14. Dudek K, Nowakowska-Kotas M, Kędzia A. Mathematical models of human cerebellar development in the fetal period. J Anat. 2018; 232(4): 596–603, doi: 10.1111/joa.12767, indexed in Pubmed: 29315634.

15. Gawlikowska-Sroka A, Dabrowski P, Szczurowski J, et al. Influence of physiological stress on the presence of hypo-plasia and fluctuating asymmetry in a medieval population from the village of Sypniewo. Int J Paleopathol. 2017; 19: 43–52, doi: 10.1016/j.ijpp.2017.10.002, indexed in Pubmed: 29198399.

16. Giannakopoulou C, Korakaki E, Hatzidaki E, et al. Per-oneal nerve palsy: a complication of umbilical artery catheterization in the full-term newborn of a mother with diabetes. Pediatrics. 2002; 109(4): e66, doi: 10.1542/peds.109.4.e66, indexed in Pubmed: 11927739.

17. Gworys B, Domagala Z. The typology of the human fetal lanugo on the thorax. Ann Anat. 2003; 185(4): 383–386, doi: 10.1016/S0940-9602(03)80066-3, indexed in Pubmed: 12924478.

18. Gworys B, Jeka S, Brukiewa R, et al. Dinámica de crecimiento del estómago en el período fetal humano: un estudio post-mortem. Int J Morphol. 2012; 30(2): 461–6.

19. Hall MP, Ryzewicz M, Walsh PJ, et al. Risk of iatrogenic injury to the peroneal nerve during posterolateral femo-ral tunnel placement in double-bundle anterior cruciate ligament reconstruction. Am J Sports Med. 2009; 37(1): 109–113, doi: 10.1177/0363546508324177, indexed in Pubmed: 18952904.

20. Infante E, Kennedy WR. Anomalous branch of the peroneal nerve detected by electromyography. Arch Neurol. 1970; 22(2): 162–165, doi: 10.1001/arch-neur.1970.00480200068007, indexed in Pubmed: 5409772.

21. Jenkins MJ, Farhat M, Hwang P, et al. The distance of the common peroneal nerve to the posterolateral structures of the knee. J Arthroplasty. 2016; 31(12): 2907–2911, doi: 10.1016/j.arth.2016.05.005, indexed in Pubmed: 27267229.

22. Kang J, Yang P, Zang Q, et al. Traumatic neuroma of the superficial peroneal nerve in a patient: a case report and review of the literature. World J Surg Oncol. 2016; 14(1): 242, doi: 10.1186/s12957-016-0990-6, indexed in Pubmed: 27613606.

23. Kedzia A, Andrzejak R, Dudek K, et al. Analysis of human scapula morphometry in the fetal period. Adv Clin Exp Med. 2009; 18(3): 197–204.

24. Kedzia A, Woźniak W. The long colic nerves in human fe-tuses. I. Macroscopic studies. Folia Morphol. 1992; 51(3): 225–40, indexed in Pubmed: 1339778.

25. Khan AA, Asari MA, Pasha MA. The sciatic nerve in human cadavers: high division or low formation? Folia Morphol. 2016; 75(3): 306–310, doi: 10.5603/FM.a2015.0130, indexed in Pubmed: 26711654.

26. Kołaczkowski Z, Stachura D. Antropomorfologia mięśnia piszczelowego przedniego w ontogenezie człowieka. Przegl Antrop. 1974; 40: 77–84.

27. Kulus M, Dąbrowski P. How to calculate the age at for-mation of Harris lines? A step-by-step review of current methods and a proposal for modifications to Byers' for-mulas. Archaeol Anthropol Sci. 2019; 11(4): 1169–1185, doi: 10.1007/s12520-018-00773-5.

28. Kurtoglu Z, Aktekin M, Uluutku MH. Branching patterns of the common and superficial fibular nerves in fetus. Clin Anat. 2006; 19(7): 621–626, doi: 10.1002/ca.20235, indexed in Pubmed: 16302233.

29. Mathis J, Raio L, Baud D. Fetal laser therapy: applications in the management of fetal pathologies. Prenat Diagn. 2015; 35(7): 623–636, doi: 10.1002/pd.4587, indexed in Pubmed: 25736523.

30. Murad H, Neal P, Katirji B. Total innervation of the extensor digitorum brevis by the accessory deep peroneal nerve. Eur J Neurol. 1999; 6(3): 371–373, doi: 10.1046/j.1468-1331.1999.630371.x, indexed in Pubmed: 10210922.

31. Nizankowski C, Ziółkowski M. Studies on the sciatic nerve course in man in the fetal period. Folia Morphol. 1979; 38(4): 481–488, indexed in Pubmed: 317585.

32. Poage C, Roth C, Scott B. Peroneal nerve palsy: evaluation and management. J Am Acad Orthop Surg. 2016; 24(1): 1–10, doi: 10.5435/JAAOS-D-14-00420, indexed in Pubmed: 26700629.

33. Popkov A, Aranovich A, Popkov D. Prevention of recurrence of tibia and ankle deformities after bone lengthening in children with type II fibular hemimelia. Int Orthop. 2015; 39(7): 1365–1370, doi: 10.1007/s00264-015-2752-4, indexed in Pubmed: 25832175.

34. Rausch V, Hackl M, Oppermann J, et al. Peroneal nerve location at the fibular head: an anatomic study using 3D imaging. Arch Orthop Trauma Surg. 2019; 139(7): 921–926, doi: 10.1007/s00402-019-03141-7, indexed in Pubmed: 30737594.

35. Reimann R. [Accessory peroneal nerves in man]. Anat Anz. 1984; 155(1-5): 257–267, indexed in Pubmed: 6721189.

36. Senes FM, Campus R, Becchetti F, et al. Sciatic nerve injection palsy in the child: early microsurgical treatment and long-term results. Microsurgery. 2009; 29(6): 443–448, doi: 10.1002/micr.20632, indexed in Pubmed: 19306387.

37. Tomaszewski KA, Graves MJ, Henry BM, et al. Surgical anatomy of the sciatic nerve: A meta-analysis. J Orthop Res. 2016; 34(10): 1820–1827, doi: 10.1002/jor.23186, indexed in Pubmed: 26856540.

38. Tomaszewski KA, Graves MJ, Vikse J, et al. Superficial fibular nerve variations of fascial piercing: A meta-analysis and clinical consideration. Clin Anat. 2017; 30(1): 120–125, doi: 10.1002/ca.22741, indexed in Pubmed: 27271092.

39. Tomaszewski KA, Roy J, Vikse J, et al. Prevalence of the accessory deep peroneal nerve: A cadaveric study and meta-analysis. Clin Neurol Neurosurg. 2016; 144: 105–111, doi: 10.1016/j.clineuro.2016.03.026, indexed in Pubmed: 27038872.

40. Wozniak S, Pytrus T, Kobierzycki C, et al. The large intestine from fetal period to adulthood and its impact on the course of colonoscopy. Ann Anat. 2019; 224: 17–22, doi: 10.1016/j.aanat.2019.02.004, indexed in Pubmed: 30914345.

41. Yacub JN, Rice JB, Dillingham TR. Nerve injury in patients after hip and knee arthroplasties and knee arthroscopy. Am J Phys Med Rehabil. 2009; 88(8): 635–41; quiz 642, doi: 10.1097/PHM.0b013e3181ae0c9d, indexed in Pubmed: 19620828.

42. Ziółkowski M, Gworys B, Kurlej W. Estimation of fetal age on the basis of certain measurements and ossification of the sternum. Folia Morphol. 1988; 47(1-4): 145–151, indexed in Pubmed: 3267621.

Morphometric study of sciatic nerve and its topographic anatomical variations in relation to landmark structures around pelvis: a Nigerian population study

G. Mbaka[1], A. Osinubi[2]

[1]Department of Anatomy, Lagos State University College of Medicine, Ikeja, Nigeria
[2]Department of Anatomy, College of Medicine of the University of Lagos, Idi-Araba, Lagos, Nigeria

Background: Sciatic nerve (SN) presents significant variations that pertain to its topography and divisions. The topographic variation shows sex effect due to differences in the dimension of pelvis that makes for the adaptability of female pelvis for pregnancy and childbirth. The objective therefore was to evaluate the SN morphology and its topographical variations in relation to landmark structures in the pelvis of both sexes.
Materials and methods: Ninety-eight lower limb adult cadavers, 66 males and 32 females devoid of any gross pathology from Nigerians were used for the study. The cadavers were dissected to expose the SNs and the variations recorded. Anthropological measurements were taken and analysed using a Spearman's rank-order correlation model.
Results: The relationships between SN and the piriformis muscle shows five varied types with the typical type comprising 83.0%. The largest thickness of SN in males and females were 18.5 cm and 17.3 cm, respectively while the smallest thickness were 8.6 cm and 11.9 cm, respectively. The dimensions between posterior superior iliac spine and greater trochanter (PSIS-GT) and between lateral edges of SN intersection with piriformis to the tip of greater trochanter (LESN-GT) shows inverse correlation relationship between the two sexes. In males, there was a weak positive correlation ($r_s = 0.165$) between LESN-GT (4.75 ± 1.52) and PSIS-GT (15.3 ± 2.90) which was not statistically significant at 0.01 level ($p = 0.989$). In females, the relationship between LESN-GT (6.39 ± 0.59) and PSIS-GT (12.2 ± 3.70) shows moderate negative correlation ($r_s = -0.476$) which was not statistically significant at 0.01 level ($p = 0.195$).
Conclusions: The dimension of LESN-GT which was observed to be longer in females was deemed to account for the deviation of sciatic nerve of females from the males' topographic anatomical relations. (Folia Morphol 2022; 81, 1: 44–51)

Key words: sciatic nerve, morphometry, topography, variations

INTRODUCTION

The word sciatic has Greek origin. Sciatic nerve (SN) is unique because it is not only the longest but also the thickest nerve in the body [19, 25]. It has an extensive origin from lumbosacral plexus formed by the ventral rami of L4-S3 spinal nerves in the pelvic region. It has two components, the tibia and common peroneal. The tibia component is formed from

the ventral branches of ventral rami of L4-S3 spinal nerves, while the common peroneal component is formed from the dorsal branches of ventral rami of L4-S2 spinal nerves [28]. Usually the nerve enters the gluteal region by passing through the greater sciatic foramen beneath the piriformis. In the gluteal region it lies beneath gluteal maximus muscle descending downward between ischial tuberosity and greater trochanter of femur to reach the back of thigh. More often the nerve terminates by dividing into two branches, tibial nerve and common peroneal nerve usually at the superior angle of popliteal fossa [1, 19]. SN is essentially the nerve supply to the muscles of the leg, foot and back of the thigh. It also provides cutaneous innervation to nearly the entire skin of the leg [25, 28].

The understanding of the course of SN is important because it presents significant variations that pertains to its topography and divisions. More so large number of invasive procedures are performed in the gluteal region. Therefore, the knowledge of the typical and variant anatomical patterns in relation to landmark structures is crucial to avoid accidental iatrogenic injuries during surgical procedures. Piriformis is a key muscle of the gluteal region that has remarkable landmark relations with SN [17]. The high bifurcation of SN in the pelvis with the varied exit of its component parts through greater sciatic notch in relation to piriformis might lead to the compression of the nerve or nerves which could also result to piriformis syndrome [2]. There are reports on varied anatomical relations with piriformis where the undivided nerve may emerge above or through the muscle while other variables include the division of the nerve which may lie above or partly demarcated by the muscle [3, 4, 18]. These variable relationships different from what is considered the normal with piriformis have been suggested to increase the chances of the nerve entrapment at the location [15].

At the lower part of gluteal region, the land mark structures of SN are the ischial tuberosity and greater trochanter of femur where the nerve location corresponds to a line drawn slightly medial to the midpoint between ischial tuberosity and the greater trochanter to the apex of popliteal fossa. In between the two bony tuberosities the nerve crosses posterior to obturator internus, gameli and quadratus femoris muscles that form its muscular bed [5]. The SN descends to the back of thigh and it is commonly reported to bifurcate into tibial and common peroneal

nerves at the superior angle of popliteal fossa [25]. Its bifurcation, however, has shown wide topographic variations [20, 27, 28].

This study was designed to evaluate the sciatic nerve morphology and its topographical variations in relation to landmark structures in the pelvis of both sexes in adults with the view to establishing sexual differences in its orientation.

MATERIALS AND METHODS

Ninety-eight lower limb adult cadavers, 66 males and 32 females devoid of any gross pathology were used for the study. The cadavers were formalin-fixed in the Anatomy Department of three Medical Schools in Nigeria. The fixation was carried out by pouring the prepared formalin solution into the embalming pressure cylinder fitted with a pipe with a pair of cannulas attached to its end. Each of the cadavers was transfused with formalin solution through the femoral artery. Some quantity was also conveyed through the carotid artery for the brain tissues to be adequately fixed. After the embalment, the cadavers were kept in the storage tanks containing formalin solution for 3 weeks before the dissections. The gluteus maximus was cut midway with each half reflected medially and laterally to expose the underlying sciatic nerve partially covered at the lower part of gluteal region. The biceps femoris was also cut and retracted to expose the nerve at the upper part of the thigh. The fatty and connective tissues were removed for the nerve to be fully appreciated. SN was followed down to its point of bifurcation. The emergence of the nerve from the greater sciatic foramen and its relations to the piriformis was recorded. Also images of anatomical variations of SN were captured with digital camera and documented. Illustrations were also made to further elucidate the variations. The measurements presented in Table 1 were made in accordance with established guidelines [14] with modifications using digital calliper and stainless meter rule.

Statistical analysis

The data collected was analysed using STATA software version 14.0. A Spearman's rank-order correlation model was used in assessing the statistical significance of associations at 0.05 and 0.01 confidence levels. The rationale for correlation coefficient analytical model in this study was to ascertain parameters positively and negatively correlated with connection to sexual dimorphism of adult human pelvis.

Table 1. Measured parameters

S/N	Measured parameters	Abbreviations
1	The width of sciatic nerve at the lower margin of the piriformis	WSN-LMP
2	The width of sciatic nerve at the level of lesser trochanter	WSN-LLT
3	The vertical distance between medial edge of sciatic nerve intersection with piriformis to ischial tuberosity	MESN-IT
4	The vertical distance between lateral edge of sciatic nerve intersection with piriformis to the tip of greater trochanter	LESN-GT
5	The length of sciatic nerve from the lower edge of piriformis to the point of its bifurcation	LSNLP-SNB
6	The width of common peroneal nerve at sciatic nerve bifurcation	WCP-SNB
7	The width of tibia nerve at sciatic nerve bifurcation	WTN-SNB
8	The vertical distance between the lateral edge of sciatic nerve intersection with piriformis to the posterior superior iliac spine	LSN-PPSS
9	The thigh length from the tip of greater trochanter to knee joint fusion	TL
10	Distance between apex of ischial tuberosity and greater trochanter	IT-GT
11	Distance between posterior superior iliac spine and greater trochanter	PSIS-GT
12	Distance between posterior superior iliac spine and ischial tuberosity	PSIS-IT
13	Length of the lower extremity	LLE

S/N — serial number

Table 2. Relationship between sciatic nerve and the piriformis

Types	Description	Percentage proportion
A	Sciatic nerve emerging below piriformis (common type)	83.0% (81)
B	Sciatic nerve divisions passing through and below piriformis uniting inferior	7.1% (7)
C	Sciatic nerve divisions emerging above and below piriformis uniting inferior	2.0% (2)
D	Two sciatic nerve divisions emerging below piriformis not uniting inferior	6.0% (6)
E	Sciatic nerve divisions passing through and below piriformis not uniting inferior	2.0% (2)

RESULTS

A total of five varied types of SN relationships with piriformis was observed in this study. The summary is shown in Table 2. Type A is the most frequently occurring and it is the typical type. Besides type A, four variable types were observed. The total number of the variable types were not significant compared to the typical type (type A).

In Figure 1A, SN gains access into the gluteal region beneath the lower border of piriformis as an undivided nerve which was the most common type showing a prevalence of 81 (83.0%). In males the incidence was 54 (55.1%) while in females, 27 (27.6%). Figure 1B shows a bifurcated nerve entering the gluteal region comprising 7 (7.1%) cases. In males the occurrence was 5 (5.1%) and in females, 2 (2.0%). This variation shows the common peroneal nerve piercing the piriformis while the tibial nerve emerging at the lower border of piriformis with both uniting inferiorly. Figure 1C was observed in 2 (2.0%) cases all in males. The pattern shows two divisions from sacral plexus emerging above and below the piriformis muscle respectively in the gluteal region which united into a common trunk at the inferior part of the muscle. In Figure 1D, the bifurcated nerves separately entered the gluteal region below the piriformis muscle and continuing separately throughout their course. This variation comprises 6 (6.0%) cases. In males it had incidence of 4 (4.1%) whereas in females the incidence was 2 (2.0%). Figure 1E shows a bifurcated nerve with the common peroneal component piercing the piriformis while the tibial component emerging at the lower border of the piriformis muscle with both continuing separately throughout their course. The variation had a prevalence of 2 (2.0%) cases with one (1.0%) each in male and female respectively. Apart from the pictures, the five varied types were also illustrated as depicted in Figure 2A–E.

The statistical data in Tables 3 and 4 did not vary markedly in their mean probably because most of the parameters considered were not affected by the anomalous types or due to their insignificant number. Further analysis on the data was conducted to identify the parameters positively and negatively correlated with connection to sexual dimorphism of human pelvis.

A Spearman's rank-order correlation was run to determine the relationship between WSN-LMP in males and in females respectively (Table 5). There was a moderate, positive correlation between WSN-LMP in males and in females which was not statistically significant $r_s = -0.465$, p = 0.052.

Table 6 presents a Spearman's correlation that was run to assess the relationship between LESN-GT and
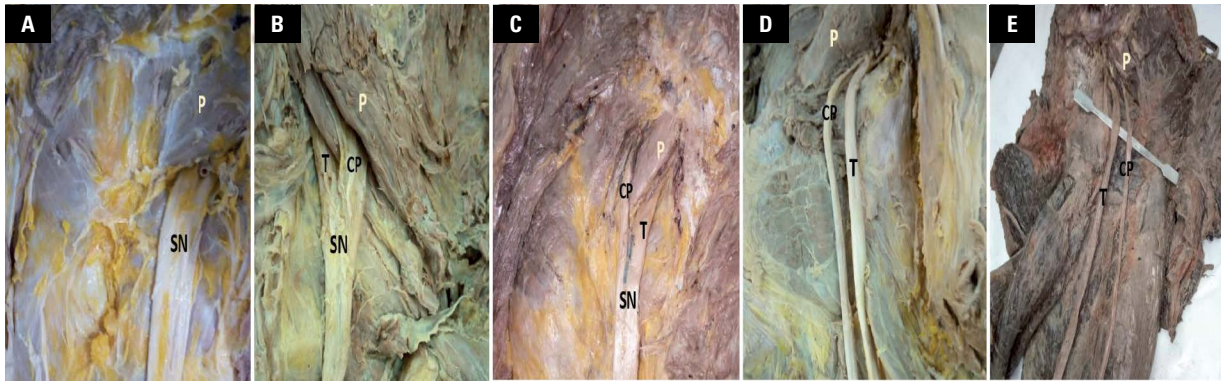
Figure 1. A–E. Variations in sciatic nerve (SN) divisions into tibial nerve (TN) and common peroneal nerve (CPN); **A.** SN passes beneath the lower border of piriformis into the gluteal region as an undivided nerve; **B.** CPN entered gluteal region by piercing the piriformis while the TN emerged at the lower border of piriformis with both uniting inferiorly; **C.** CPN entered the gluteal region above the piriformis while TN emerged below the piriformis into gluteal region with both uniting inferiorly; **D.** CPN and TN separately entered the gluteal region below the piriformis muscle and continuing separately throughout their course; **E.** CPN pierced the piriformis while the TN emerged at the lower border of piriformis with both continuing separately throughout their course; CP — common peroneal (nerve); P — Piriformis; T — Tibia (nerve).
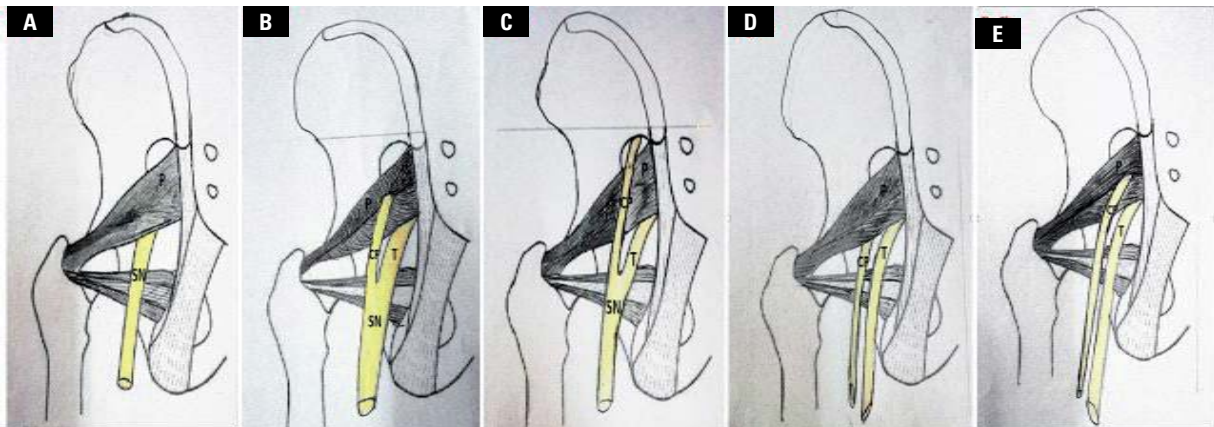
Figures 2. A–E. Illustration on the variations in sciatic nerve (SN) into tibial nerve and common peroneal nerve; CP — common peroneal (nerve); P — Piriformis; T — Tibia (nerve).

IT-GT in the examined male and female cadavers. In the males, there was a very weak positive correlation (r_s = 0.005) between LESN-GT and IT-GT. However, there was no statistically significant correlation between them at 0.01 level (p = 0.989). In females, the relationship between LESN-GT and IT-GT shows moderate positive correlation (r_s = 0.399) which was not statistically significant at 0.01 level (p = 0.302).

Spearman's correlation was run to assess the relationship between LESN-GT and PSIS-GT in male and female cadavers as presented in Table 7. In males, there was a weak positive correlation (r_s = 0.165) between LESN-GT and PSIS-GT which was not statistically significant at 0.01 level (p = 0.989). In females, the relationship between LESN-GT and PSIS-GT shows moderate negative correlation (r_s = –0.476)

which was not statistically significant at 0.01 level (p = 0.195).

DISCUSSION

Sciatic nerve shows substantial variations with landmark structures in the gluteal region. Different population studies have highlighted some of these variations most of which are variations in relation with piriformis [12, 23, 24]. The major interest with the variations is because of the clinical event associated with the abnormalities. More often, variation in the exit of SN in relation to piriformis may cause its compression resulting to piriformis syndrome [11, 12]. The variable relations of SN to piriformis was also noted as the probable cause of nondiscogenic sciatica and other pain aetiologies [31]. Variations such as high

47

Table 3. Basic descriptive statistics for the analysed variables in males

N	Abbreviations	Mean [cm]	Median [cm]	Maximum [cm]	Minimum [cm]	Standard deviation [cm]
1	WSN-LMP	15.20	13.55	18.50	8.60	± 2.93
2	WSN-LLT	13.32	13.10	18.10	8.09	± 3.07
3	MESN-IT	4.55	4.33	6.60	2.06	± 1.18
4	LESN-GT	4.75	5.15	7.00	2.50	± 1.52
5	LSNLP-SNB	37.58	35.50	44.00	27.00	± 5.26
6	WCP-SNB	3.69	3.67	5.08	2.25	± 0.86
7	WTN-SNB	6.42	6.58	8.66	4.50	± 1.49
8	LSN-PPSS	7.15	7.25	9.00	5.50	± 1.22
9	TL	39.72	37.50	45.00	30.00	± 3.11
10	IT-GT	6.50	7.00	7.50	5.00	± 0.60
11	PSIS-GT	15.30	14.00	16.50	12.50	± 2.90
12	PSIS-IT	28.20	12.00	14.50	10.00	± 2.73
13	LLE	82.72	82.00	93.00	70.00	± 3.20

Table 4. Basic descriptive statistics for the analysed variables in females

N	Abbreviations	Mean [cm]	Median [cm]	Maximum [cm]	Minimum [cm]	Standard deviation [cm]
1	WSN-LMP	14.05	14.60	17.30	11.90	± 1.60
2	WSN-LLT	9.88	11.38	16.40	6.36	± 3.64
3	MESN-IT	5.48	5.45	5.90	5.00	± 0.32
4	LESN-GT	6.39	6.60	7.70	5.50	± 0.59
5	LSNLP-SNB	31.50	32.75	38.50	27.00	± 3.37
6	WCP-SNB	3.12	2.66	3.59	1.72	± 0.54
7	WTN-SNB	4.78	5.63	7.07	4.19	± 0.84
8	LSN-PPSS	6.91	7.30	8.50	6.10	± 0.78
9	TL	34.52	35.00	39.00	31.00	± 2.50
10	IT-GT	11.10	11.00	7.00	6.00	± 0.30
11	PSIS-GT	12.20	12.00	15.00	10.00	± 3.70
12	PSIS-IT	11.10	11.00	14.00	10.00	± 1.90
13	LLE	72.10	70.00	80.00	65.00	± 4.10

division of SN can lead to nerve injury during deep intramuscular injections. It is also the major factor responsible for the failure of SN block when performing popliteal block anaesthesia [1]. Nonetheless, each of the anatomical variations may reflect a different and specific clinical presentation. In this study, five types of relationship of SN with piriformis was recorded. The typical type (type A) shows very high prevalence constituting 83% of the population examined. Other population reports corroborated with similar high frequency [1, 5, 21]. In the other observed variable types, SN exhibited high bifurcation with its component parts having varied relations with piriformis muscle. However, they constituted a small fraction of the over-

all number examined. They formed 17% cumulative of the entire population. None of the unusual types was unique compared to other population studies. The most prevalent of the variations was type B. The high prevalence shows consistency with the report of many population studies [2, 21, 22, 26]. Type C and type E were the least occurring variables, each accounting for 2% of cases. Type C was also shown as least frequently occurring in many population studies [1, 21, 30]. It is pertinent to establish the prevalence rate of SN variable types because more often they lead to inadvertent injury during surgical procedures in the gluteal region. Besides they are often exposed to compression resulting to 'piriformis syndrome'.

Table 5. Correlation between width of sciatic nerve at the lower margin of the piriformis (WSN-LMP) in males and in female cadavers. Correlation is significant at the 0.01 level (2-tailed)

Spearman's rho		WSN-LMP — male	WSN-LMP — female
WSN-LMP — male	Correlation coefficient	1.000	−0.465
	Sig. (2-tailed)	–	0.052
	N	60	30
WSN-LMP — female	Correlation coefficient	−0.465	1.000
	Sig. (2-tailed)	0.052	–
	N	60	30

Table 6. Correlation between the vertical distance between lateral edge of sciatic nerve intersection with piriformis to the tip of greater trochanter (LESN-GT) and distance between apex of ischial tuberosity and greater trochanter (IT-GT); in male and female cadavers. Correlation is significant at the 0.01 level (2-tailed)

Spearman's rho		LESN-GT		IT-GT	
		Male	Female	Male	Female
LESN-GT	Correlation coefficient	1.000	1.000	0.005	0.388
	Sig. (2-tailed)	–	–	0.989	0.302
	N	66	32	66	32
IT-GT	Correlation coefficient	0.005	0.388	1.000	1.000
	Sig. (2-tailed)	0.989	0.302	–	–
	N	66	32	66	32

Table 7. Correlation between the vertical distance between lateral edge of sciatic nerve intersection with piriformis to the tip of greater trochanter (LESN-GT) and Distance between posterior superior iliac spine and greater trochanter (PSIS-GT) in male female cadavers. Correlation is significant at the 0.01 level (2-tailed)

Spearman's rho		LESN-GT		PSIS-GT	
		Male	Female	Male	Female
LESN-GT	Correlation coefficient	1.000	1.000	0.165	−0.476
	Sig. (2-tailed)	–	–	0.628	0.195
	N	66	32	66	32
PSIS-GT	Correlation coefficient	0.165	−0.476	1.000	1.000
	Sig. (2-tailed)	0.628	0.195	–	–
	N	66	32	66	32

It is observed that limited number of articles centred on the morphometric analysis of SN structure as well as its relations with some landmark structures [13, 32]. Its morphometric studies that relates to sex dimension began to emerge just in the recent past [10, 14, 16]. There has been an increase in curiosity due to diversity in topographic anatomical relations of the nerve in the females which is of clinical concern.

The width of SN that was assessed at the lower margin of piriformis muscle shows values that did not vary markedly between the two sexes. In both legs of each specimen, the values were not varied; however, it only applied to cases where the nerve emerges as a single trunk beneath the lower border of piriformis muscle. Nonetheless, a population study in Brazil has documented a significant difference in the width size of SN between both legs of the same spacemen [6]. In a correlation coefficient analysis between the two sexes, a moderate, positive correlation was observed between WSN-LMP in males and in females. The analysis was indicative that sex variation showed cumulatively very little differential in the nerve width of the two sexes. The sizes of WSN-LMP and WSN-LLT in each specimen varied considerably with WSN-LLT showing reduction in size that was more remarkable in females.

The relationship of SN with piriformis muscle and also with selected bony landmarks in the pelvis was examined in both sexes. In typical anatomical relations between SN and piriformis and selected bony landmarks, certain regularities can be established in

the two sexes. The relationship between LESN-GT and IT-GT in both sexes shows positive correlation nonetheless in males it exhibited weak correlation ($r_s = 0.005$) whereas in females it was moderately correlated ($r_s = 0.399$).

The female's pelvis serves multiple roles that include providing support, locomotion, childbirth, etc. [10]. The adaptability to these multiple roles is responsible for its sexual dimorphism. Pelvis dimorphism has been used variably for sex determination in various anthropological contexts [7, 29]. The path of SN has been described in relation to ischial tuberosity (IT), greater trochanter (GT) and PSIS [8, 27]. The information provided was a clear guide in this contextual view of SN topography in the two sexes. It is noted in a recent study that the sexual differences in distances and angulation between clinically relevant pelvis and hip bone landmark show that only the angle at PSIS and GT are significantly larger in males [32]. Huseynov et al. [16] had earlier reported that the obstetric adaptation of female pelvis makes for wider pelvic cavity influenced by hormonal changes at puberty. Apparently, the sexual dimorphism is viewed as the major factor responsible for topographic variation of SN in females. Pregnancy also constitutes a key consideration in this regard which, however, borders outside this investigation. In this study, however, the angulation between LESN-GT and PSIS-GT were ascertained and analysed. The analysis of relationship between LESN-GT and PSIS-GT in male cadavers shows weak positive correlation ($r_s = 0.165$). However, in females the relationship between LESN-GT and PSIS-GT exhibited moderate negative correlation ($r_s = -0.476$). Between the two sexes the correlation analysis indicated inverse relationship between LESN-GT and PSIS-GT in males and in females. The negative correlation of LESN-GT and PSIS-GT recorded in females has a strong bearing to obstetric adaptation of pelvis for child birth. The result of the morphometric analysis buttresses orientation alteration of ileum in females in which there is a considerable reduction in angulation between PSIS and GT. Based on this study findings, the authors strongly agree with the report that the angle at PSIS and GT are significantly larger in males [9]. However, the remark [9] that there are no sex differences in the orientation of the ileum is not in tandem with our findings. The dimension of LESN-GT in both sexes show considerable variations. LESN-GT is longer (significantly) in females than in males thus accounting in part to SN varied topographic relations

and to a larger extent deemed to be responsible for inverse correlation between LESN-GT and PSIS-GT in the two sexes. The considerable deviation of SN of females from the males' topographic anatomical relations is of clinical concern because of the sexual dimorphism of the pelvis. The implications in females include greater risk of SN injury during intramuscular injections and during invasive medical procedures at the gluteal region [9, 14].

CONCLUSIONS

The morphometric analysis of the anatomical relationships between SN and the landmark structures of the hip bone shows variations due to the sexual differences in the dimension of the pelvis. The deviation of SN of females from the males' topographic anatomical relations is of clinical concern requiring for diligence during surgical procedures in the gluteal region to avoid damage to the nerve.

Acknowledgements

Conflict of interest: None declared

REFERENCES

1. Adibatti M, V S. Study on variant anatomy of sciatic nerve. J Clin Diagn Res. 2014; 8(8): AC07–AC09, doi: 10.7860/JCDR/2014/9116.4725, indexed in Pubmed: 25302181.
2. Anbumani TL, Selvi TA, Ammal AS, et al. Sciatic nerve and its variations: an anatomical study. Int J Anat Res. 2015; 3(2): 1121–1127, doi: 10.16965/ijar.2015.175.
3. Arifoglu Y, Sargon MF, Tanyeli E, et al. Double superior gemellus together with double piriformis and high division of the sciatic nerve. Surg Radiol Anat. 1997; 19(6): 407–408, doi: 10.1007/BF01628510, indexed in Pubmed: 9479716.
4. Babinski MA, Machado FA, Costa WS. A rare variation in the high division of the sciatic nerve surrounding the superior gemellus muscle. Eur J Morphol. 2003; 41(1): 41–42, doi: 10.1076/ejom.41.1.41.28099, indexed in Pubmed: 15121548.
5. Berihu BA, Debeb YG. Anatomical variation in bifurcation and trifurcations of sciatic nerve and its clinical implications: in selected university in Ethiopia. BMC Res Notes. 2015; 8: 633, doi: 10.1186/s13104-015-1626-6, indexed in Pubmed: 26526618.
6. Brooks J, Silva C, Soares S, et al. Variações anatômicas do nervo ciático em um grupo de cadáveres brasileiros.

Revista Dor. 2011; 12(4): 332–336, doi: 10.1590/s1806-00132011000400009.

7. Bruzek J. A method for visual determination of sex, using the human hip bone. Am J Phys Anthropol. 2002; 117(2): 157–168, doi: 10.1002/ajpa.10012, indexed in Pubmed: 11815949.

8. Currin S, Mirjalili S, Meikle G, et al. Revisiting the surface anatomy of the sciatic nerve in the gluteal region. Clin Anat. 2014; 28(1): 144–149, doi: 10.1002/ca.22449.

9. Elgellaie A, Ashcroft E, Larkin TA. Morphology and anatomical relations of iliac and femoral bony landmarks, gluteal muscles and the sciatic nerve: Sex differences and clinical implications. Eur J Anat. 2019; 23(5): 377–382.

10. Fischer B, Mitteroecker P. Allometry and sexual dimorphism in the human pelvis. Anat Rec (Hoboken). 2017; 300(4): 698–705, doi: 10.1002/ar.23549, indexed in Pubmed: 28297185.

11. Foster M. Piriformis syndrome. Orthopedics. 2002; 25(8): 821–825, doi: 10.3928/0147-7447-20020801-12.

12. Güvençer M, Akyer P, Iyem C, et al. Anatomic considerations and the relationship between the piriformis muscle and the sciatic nerve. Surg Radiol Anat. 2008; 30(6): 467–474, doi: 10.1007/s00276-008-0350-5, indexed in Pubmed: 18458807.

13. Güvençer M, Iyem C, Akyer P, et al. Variations in the high division of the sciatic nerve and relationship between the sciatic nerve and the piriformis. Turk Neurosurg. 2009; 19(2): 139–144, indexed in Pubmed: 19431123.

14. Haładaj R, Pingot M, Polguj M, et al. Anthropometric study of the piriformis muscle and sciatic nerve: a morphological analysis in a polish population. Med Sci Monit. 2015; 21: 3760–3768, doi: 10.12659/msm.894353, indexed in Pubmed: 26629744.

15. Halpin RJ, Ganju A. Piriformis syndrome: a real pain in the buttock? Neurosurgery. 2009; 65(4 Suppl): A197–A202, doi: 10.1227/01.NEU.0000335788.45495.0C, indexed in Pubmed: 19927068.

16. Huseynov A, Zollikofer CPE, Coudyzer W, et al. Developmental evidence for obstetric adaptation of the human female pelvis. Proc Natl Acad Sci U S A. 2016; 113(19): 5227–5232, doi: 10.1073/pnas.1517085113, indexed in Pubmed: 27114515.

17. Kirschner JS, Foye PM, Cole JL. Piriformis syndrome, diagnosis and treatment. Muscle Nerve. 2009; 40(1): 10–18, doi: 10.1002/mus.21318, indexed in Pubmed: 19466717.

18. Mas N, Ozekşi P, Ozdemir B, et al. case of bilateral high division of the sciatic nerves, together with a unilateral unusual course of the tibial nerve. Neuroanatomy. 2003; 2: 13–15.

19. Moore KL, Dalley AF, Agur AMR. Clinically Oriented Anatomy. 8th ed. Wolters Kluwer 2018: 709–716.

20. Ndiaye A, Sakho Y, Fall F, et al. [Sciatic nerve in gluteal portion: application of sciatic nerve post injection lesion]. Morphologie. 2004; 88(282): 135–138, doi: 10.1016/s1286-0115(04)98136-2, indexed in Pubmed: 15641650.

21. Ogeng'o JA, El-Busaidy H, Mwika PM, et al. Variant anatomy of sciatic nerve in a black Kenyan population. Folia Morphol. 2011; 70(3): 175–179, indexed in Pubmed: 21866528.

22. Pecina M. Contribution to the etiological explanation of the piriformis syndrome. Acta Anat (Basel. 1979; 105: 181–187.

23. Pokorný D, Jahoda D, Veigl D, et al. Topographic variations of the relationship of the sciatic nerve and the piriformis muscle and its relevance to palsy after total hip arthroplasty. Surg Radiol Anat. 2006; 28(1): 88–91, doi: 10.1007/s00276-005-0056-x, indexed in Pubmed: 16311716.

24. Prakash BAK, Devi MN, Sridevi NS, et al. Sciatic nerve division: a cadaver study in the Indian population and review of literature. Singapore Med J. 2010; 51: 721–723.

25. Saritha S, Praveen KM, Supriya G. Anatomical variations in the bifurcation of the sciatic nerve. A cadaveric study and its clinical implications. Anat Physiol. 2012; 2: 111, doi: 10.4172/2161-0940.1000111.

26. Sinha MB, Aggarwal A, Sahni D, et al. Morphological variations of sciatic nerve and piriformis muscle in gluteal region during fetal period. Eur J Anat. 2014; 18(4): 261–266.

27. Sinnatamby CS, Last RJ. Last's Anatomy Regional and Applied, 12th ed. Churchill Livingstone 2011.

28. Standring S. Gray's anatomy: the anatomical basis of clinical practice. 39th ed. Churchill Livingstone, London 2005: 1364–1458.

29. Steyn M, Işcan MY. Metric sex determination from the pelvis in modern Greeks. Forensic Sci Int. 2008; 179(1): 86.e1–86.e6, doi: 10.1016/j.forsciint.2008.04.022, indexed in Pubmed: 18554832.

30. Ugrenović S, Jovanović I, Krstić V, et al. [The level of the sciatic nerve division and its relations to the piriform muscle]. Vojnosanit Pregl. 2005; 62(1): 45–49, doi: 10.2298/vsp0501045u, indexed in Pubmed: 15715349.

31. Van Erdewyk and I. Jonathan. Anatomical variations of the sciatic nerve divisions in relation to the piriformis muscle and clinical implications, University of Nebraska Medical Center, Theses and Dissertations, Omaha, Nebraska, 2017.

32. Vicente E, Viotto M, Barbosa C, et al. Estudo das relações anatômicas e suas variações entre o nervo ciático e o músculo piriforme. Rev Bras Fisioter. 2007; 11(3): 227–232, doi: 10.1590/s1413-35552007000300009.

Effect of preservative-free and preserved prostaglandin analogues on the histology of cornea of adult male guinea pigs following repeated exposure

A.F. Ali[1], R.M. Salama[2] , M.A. Soliman[1]

[1]Department of Histology, Faculty of Medicine, Menoufia University, Egypt
[2]Department of Anatomy and Embryology, Faculty of Medicine, Menoufia University, Egypt

Background: Glaucoma is a group of eye diseases that can cause vision loss. Prostaglandin analogues (PGAs) are known to be first-line treatment for patients with glaucoma. Latanoprost is a good, efficient and well-tolerated PGA that is currently available as latanoprost with benzalkonium chloride (BAC) (Xalatan) and preservative-free (PF) prostaglandin analogue latanoprost (Monopost). Lately, using PF anti-glaucoma agents has been considered an essential procedure for enhancing glaucoma care. This study aimed to analyse the histological changes within the corneal tissue with the use of currently available preserved prostaglandins-derived eye drops and PF prostaglandin analogue.

Materials and methods: In this study, 40 male guinea pigs were divided into four equal groups. Control group, Latanoprost with 0.02% BAC-treated group, Recovery group and PF latanoprost-treated group. After 2 months, the corneal tissues of guinea pigs were prepared for light and electron microscopic studies; morphometric and statistical studies were performed.

Results: Our results indicated that guinea pigs treated with latanoprost with BAC exhibited ocular surface changes: there was epithelial thinning with desquamation, the stroma showed irregularly arranged collagen fibres and small keratocytes. Morphometrically, there was a marked decrease in the thickness of epithelium and number of keratocytes. Negative periodic acid Schiff (PAS) reaction was observed in some parts of the epithelial basement membrane. The epithelium gave a strong positive immunoreactivity for Bcl-2-associated X protein (BAX). Guinea pigs left to recover exhibited improvement, while treatment of animals with PF latanoprost resulted in nearly normal corneal structure.

Conclusions: In conclusion, PF prostaglandin anti-glaucoma medication seems to be better and have protective effect on cornea of male guinea pigs than prostaglandins with BAC preservative. (Folia Morphol 2022; 81, 1: 52–64)

Key words: glaucoma, cornea, guinea pigs, prostaglandins analogues, periodic acid Schiff (PAS), Bcl-2-associated X protein (BAX)

Address for correspondence: Dr. R.M. Salama, Department of Anatomy and Embryology, Faculty of Medicine, Menoufia University, Smouha, Alexandria, Egypt, tel: 00201005240928, e-mail: drrashasalama@yahoo.com

INTRODUCTION

Glaucoma is an optic neuropathy that is considered the main cause of blindness in the world, affecting approximately 67 million people worldwide [6, 30]. Glaucoma often occurs due to elevated intraocular pressure (IOP) that leads to damage of the optic nerve which can progress to irreversible vision loss, when left without treatment [36].

Intraocular pressure is an essential risk factor and is the main aim for the currently approved glaucoma treatment through the use of topical ocular hypotensive drops [21] that should be taken through life to inhibit or stop loss of retinal ganglion cells and visual impairment [31].

Prostaglandin analogues (PGAs) are one of the most important drugs utilised for ocular hypertension and glaucoma treatment [26]. These compounds are known to be highly effective in decreasing IOP [19].

Uzunel [39] reported that PGAs stimulated drainage of aqueous humour through the uveo-scleral outflow pathway and facilitated the trabecular outflow resulting in reducing IOP. Five different prostaglandins (PGs) are known to be used for treatment of glaucoma, namely, isopropyl unoprostone, latanoprost, travoprost, bimatoprost, and tafluprost [16].

Long-term local treatment with these anti-glaucoma drugs is always associated with ocular surface disease such eye colour change, darkening of eyelid skin, droopy eyelids, sunken eyes, eye redness, and itching [32].

Kim et al. [16] referred these side effects to the components of these topical hypotensive drops such as benzalkonium chloride (BAC) preservative. BAC is the most commonly applied preservative in eye drops having highly effective anti-microbial features. It is a quaternary ammonium salt, a cationic surfactant and tension-active compound. It breaks up the lipid layer of tear film and cell membranes of corneal surface. BAC acts also by denaturing proteins and disrupting the cell membrane, thus improving the active compounds penetration; so, it could be employed as a penetration enhancer [2, 25]. It has the advantage of being relatively well tolerated with few allergic side effects [6]. Having very slow turnover, BAC remains within the ocular tissues after a single drop administration about 48 hours [16].

BAC side effects seemed to be time- and dose-dependent, rising with larger amounts utilised over prolonged periods [22, 42]. With rising attention to the ocular surface side effects of this preservative, other types of preservatives-containing PGs and new preservative-free (PF) PGs have been advanced [38].

So, this current study was designed to analyse the histological alterations within the corneal tissue with the use of currently available (PGs)-derived eye drops, namely latanoprost with BAC (Xalatan) and PF PGA latanoprost (Monopost), in male guinea pigs.

MATERIALS AND METHODS

Animals and experimental protocol

The present experimental study was conducted at Research Centre in Menoufia University, Egypt. Study protocol was reviewed and observed via the Animal Ethics Committee of the Research Laboratory of Experimental Animals at Faculty of Medicine, Menoufia University, Egypt. Forty male adult guinea pigs, weighting 400–450 g were employed in the current work. They were kept in cages at room temperature. The water and food were available. Strict hygiene was followed to keep a healthy medium for the guinea pigs.

Animal groups

The animals were distributed randomly into four groups, each included 10 guinea pigs:
— group I (Control group): the guinea pigs were left without treatment during the experimental period;
— group II (Latanoprost with BAC treated group): they were treated topically with latanoprost preserved with 0.02% benzalkonium chloride (0.005% Xalatan 125 μg/2.5 mL, Pfizer, New York, USA);
— group III (Recovery group): they were treated as group II and left for 2 weeks without treatment for recovery;
— group IV (PF latanoprost-treated group): the guinea pigs in this group were treated topically with preservative free latanoprost (Monopost 50 μg/mL, Thea Pharmaceuticals Ltd., UK).

All guinea pigs received treatment as a single eye drop (1.5 μg latanoprost) in both eyes daily for 2 months [14].

At the assigned time of scarification for each group, cardiac perfusion was done under anaesthesia using sodium pentobarbital, 40 mg/kg by intraperitoneal injection [15]. From each animal, both eyeballs were enucleated rapidly and the corneal tissues were prepared for light and transmission electron microscopic studies.

Light microscopic study

From each animal, the right eye ball was fixed in 10% formaldehyde solution and processed for paraffin sections of about 7 μm thick. Sections were obtained and stained with haematoxylin and eosin (H&E) to demonstrate the histological details and Mallory's trichrome stain to detect the collagen fibres [3]. For histochemical study, the corneal sections were processed to be stained by periodic acid Schiff (PAS) reaction for determination of carbohydrate (epithelial basement membrane) [3]. For immunohistochemical study, Bcl-2-associated X protein (BAX) immune-staining was carried out (a marker of apoptosis), paraffin sections were put within monoclonal BAX antibody (Ab-14 Golden, Lab Vision Clone B-9; Santa Cruz Biotechnology Inc., USA). Negative control sections were processed by replacing the primary antibody with buffer alone. Hodgkin's lymphoma was used as a positive control. Brown cytoplasmic staining was scored as a positive reaction. Counterstaining was performed by using Meyer's haematoxylin [29].

Transmission electron microscopic study

The cornea of the left eye was dissected. Small corneal specimens were obtained and rapidly fixed in 3% glutaraldehyde with 0.1 M phosphate buffer at pH 7.4, and then, processed for examination, using a Jeol electron microscope (Seo-Russia) in Tanta E.M. Centre at Faculty of Medicine, Tanta University [12].

Morphometric study and statistical analysis

From each animal in all groups, the cornea was examined under light microscope using objective lens ×40. Thickness of corneal epithelium in μm and keratocytes number was measured in 10 high power fields in each specimen.

The morphometric results were analysed and compared by Student's t-test. P-value was utilised to estimate the significant change in each parameter in the experimental animals in comparison with the control group. Then, the data were tabulated as mean ± standard deviation and then, analysed utilising statistical package for the Social Science Software (SPSS). P value was set at 0.05; p > 0.05 was considered non-significant, p value < 0.05 was considered significant and p value < 0.001 was considered highly significant [28].

RESULTS

Effects of preservative-free and preserved prostaglandin analogues on corneal morphology

Seven μm paraffin corneal sections stained with H&E of the different experimental groups to analyse the histological alterations with the use of latanoprost with BAC (Xalatan) and PF PGA latanoprost (Monopost) in male guinea pigs was done. Group I (Control group) showed well defined corneal layers, these were: the outer epithelium, Bowman's membrane, stroma, Descemet's membrane and inner endothelium. The corneal epithelium was stratified squamous non-keratinised epithelium with smooth upper surface. It consisted of basal layer of single columnar cells with basal oval nuclei, intermediate layer consisting of polyhedral cells with central rounded nuclei arranged in 2 to 3 rows and superficial layer consisting of one to two rows of flattened squamous cells with flat nuclei. Under the epithelium, an acidophilic homogenous membrane appeared, Bowman's membrane. The stroma constituting the most corneal thickness was formed of bundles of collagen fibres which were arranged regularly and keratocytes appeared as flat cells with flattened nuclei, scattered between collagen fibres (Fig. 1A). While, the corneal sections from group II (Latanoprost with BAC treated group) exhibited epithelial thinning with flat nuclei (Fig. 1B). The thickness of corneal epithelium showed a highly significant decrease as compared with control group (p < 0.001) (Table 1, Fig. 3A). Some surface epithelial cells were exfoliated and desquamated and other epithelial cells exhibited vacuolated cytoplasm and their nuclei revealed variable degrees of degeneration, karyolysis and pyknosis (Fig. 1C). The stroma demonstrated irregularly arranged collagen fibres which were separated by wide spaces (Figs. 1B, C) and small dark keratocytes were seen (Fig. 1C). The mean number of keratocytes was highly significantly decreased in comparison with the control group (p < 0.001) (Table 1, Fig. 3B). Cellular infiltration, neovascularisation (Fig. 2B) and congested blood vessels (Fig. 1C) were also observed in the stroma. Group III (Recovery group) revealed less degenerative changes in the form of slight superficial epithelial cells desquamation and corrugated basement membrane. The stroma consisted of collagen bundles arranged regularly and spindle-shaped keratocytes with pale nuclei in between. Some keratocytes appeared small in size
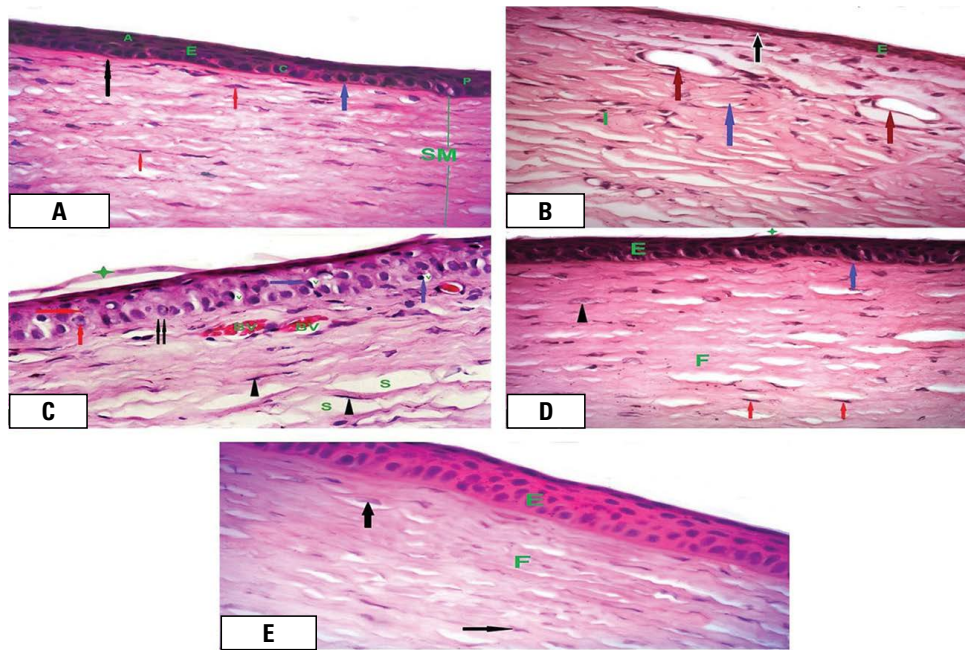
Figure 1. Photomicrographs of haematoxylin and eosin (H&E) stained corneal sections of the different experimental groups; **A.** Control group: illustrating non-keratinized stratified squamous epithelium (E) resting on clear basement membrane (blue arrow) and consists of basal layer of columnar cells (C) with basal oval nuclei, intermediate layers of polyhedral cells (P) with central rounded nuclei and superficial layer of flattened cells (A) with flat nuclei. The Bowman's membrane (black arrow) appears as an acidophilic homogenous layer under the epithelium. The stroma (SM) consists of collagen fibres arranged regularly with spindle-shaped keratocytes with flat nuclei (red arrows) in-between; **B.** Group II: illustrating all epithelial layers (E) appear with flattened nuclei (black arrow). The stroma shows irregularly arranged collagen fibres (blue arrow) and neovascularisation (red arrows). Notice, cellular infiltration (I) within the stroma; **C.** Group II: illustrating desquamation of the superficial epithelium (star) is observed, the epithelial cells appear with vacuolated cytoplasm (V) and their nuclei show variable degrees of degeneration, karyolysis (red arrows) and pyknosis (blue arrows). The stroma shows wide spaces (S) in between collagen fibres, congested blood vessels (BV) and small dark keratocytes (arrow heads). Notice, discontinuation of basement membrane (double arrow); **D.** Group III: illustrating stratified squamous non-keratinised epithelium (E) resting on corrugated basement membrane (blue arrow). The superficial cells appear with slight desquamation (star). The stroma is formed of parallel arranged collagen fibres (F) with spindle shaped keratocytes with pale nuclei in between (arrow head). Notice, some keratocytes appear small with condensed nuclei (red nuclei); **E.** Group IV: illustrating preserved corneal epithelium (E). The stroma appears with regularly arranged collagen fibres (F) with keratocytes (arrows) in between. H&E ×400.

Table 1. Comparison between control group and other studied groups

	Group I	Group II	Group III	Group IV	P value
Corneal epithelial thickness	41.1 ± 1.2	38.4 ± 3.8	26.1 ± 1.2	41.2 ± 1.2	P1 = 0.000 P2 = 0.010 P3 = 0.713 P4 = 0.000
Number of keratocytes	23.7 ± 0.6	20.9 ± 5.2	16.5 ± 2.5	24.3 ± 1.7	P1 = 0.000 P2 = 0.022 P3 = 0.157 P4 = 0.000

P1 — comparison was done between group 1 (Control group) and group II (Latanoprost with BAC-treated group); P2 — comparison was done between group I (Control group) and group III (Recovery group); P3 — comparison was done between group I (Control group) and group IV (PF latanoprost-treated group); P4 — comparison was done between group IV (PF latanoprost group) and group II (Latanoprost with BAC-treated group); $p < 0.001$ was considered highly significant; $p < 0.05$ was considered significant; $p > 0.05$ was considered non-significant

with condensed nuclei (Fig. 1D). The corneal epithelial thickness and the mean number of keratocytes were improved compared with group II ($p < 0.05$) (Table 1, Fig. 3A, B). Group IV (PF latanoprost treated group) revealed better corneal structure that appeared almost similar to that of the control group (Fig. 1E). There was a nonsignificant difference ($p > 0.05$) in corneal epithelial thickness and the
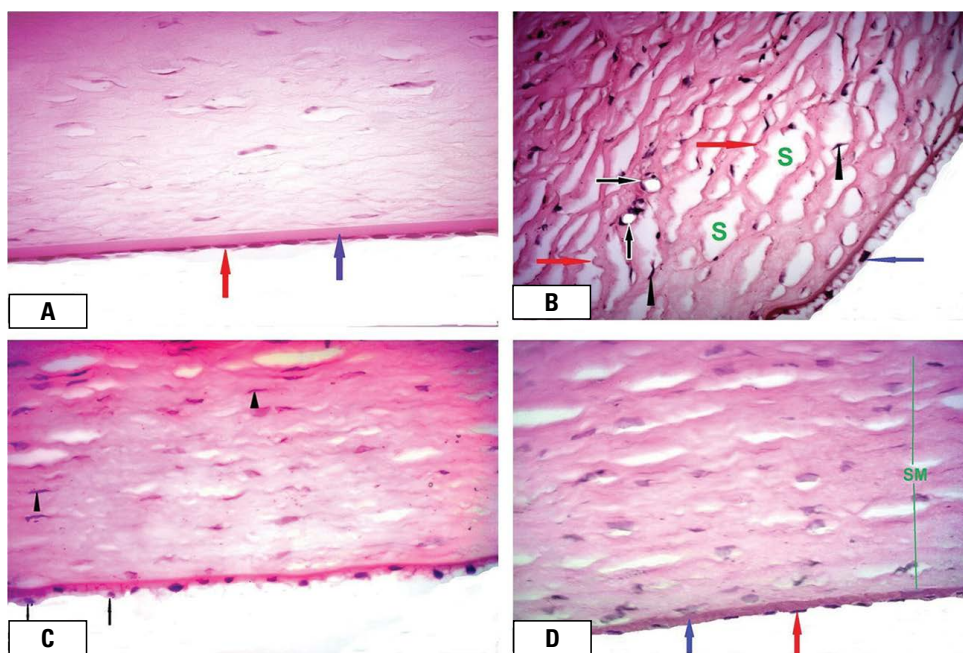
Figure 2. Photomicrographs of haematoxylin and eosin (H&E) stained corneal sections of the different experimental groups; **A.** Control group: illustrating the posterior aspect of the cornea Descemet's membrane (blue arrow) appears as a homogenous acellular membrane and lined by a single layer of endothelial cells with flat nuclei (red arrow); **B.** Group II: illustrating apparently few endothelial cells with small pyknotic nuclei (blue arrow). The stroma appears with irregularly arranged collagen fibres (red arrows) with wide spaces in between (S). Small keratocytes (arrow heads) with dark nuclei are observed. Note, appearance of neovascularisation (black arrows) in the stroma; **C.** Group III: illustrating some endothelial cells (arrows) separated from the Descemet's membrane. Notice, some small-sized keratocytes (arrow heads) with condensed nuclei in the stroma; **D.** Group IV: illustrating Descemet's membrane (blue arrow) which appears as a homogenous acellular membrane and lined by a single layer of endothelial cells (red arrow). Notice, normal appearance of stroma (SM). H&E ×400.
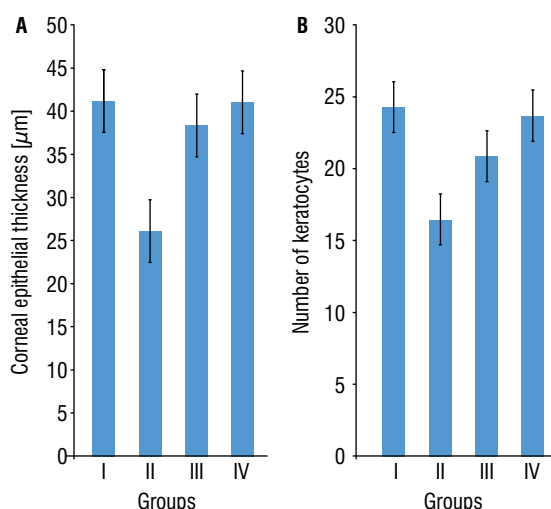
Figure 3. A histogram showing mean values of the corneal epithelial thickness (**A**) and keratocyte number (**B**) of the different experimental groups.

mean number of keratocytes when compared with control group. While at the same time, these animals showed a highly significant decrease in these parameters in comparison with group II (p < 0.001) (Table 1, Fig. 3A, B). Regarding to the posterior aspect of the cornea, group I displayed flat endothelial cells arranged in one layer and supported via a homogenous acellular Descemet's membrane (Fig. 2A). Group II showed apparently few endothelial cells with small pyknotic nuclei. Stroma with irregularly arranged collagen fibres and with wide spaces in between was seen. The keratocytes appeared small in size with dark nuclei (Fig. 2B). Group III revealed few endothelial cells separated from the Descemet's membrane (Fig. 2C). Moreover, group IV displayed acellular Descemet's membrane lined by a single layer of endothelial cells (Fig. 2D).

In order to visualise changes in collagen fibre architecture Mallory trichrome-stained corneal sections of the different experimental groups were performed. Group I (Control group) revealed regularly arranged collagen fibres (Fig. 4A). However, in group II (Latanoprost with BAC treated group), there were widely separated and irregularly arranged collagen fibres (Fig. 4B). Group III (Recovery group) exhibited regularly arranged collagen fibres. Wide space between collagen fibres was observed (Fig. 4C). In group IV (PF latanoprost treated group), there was regular arrangement of collagen fibres similar to control (Fig. 4D).
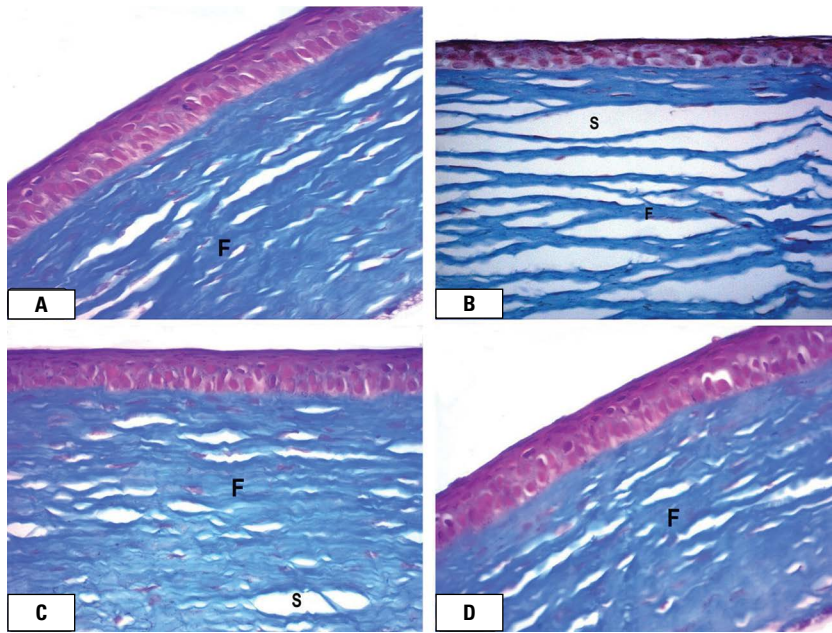
Figure 4. Photomicrographs of Mallory's trichrome-stained corneal sections of the different experimental groups; **A.** Control group: illustrating regularly arranged collagen fibres (F); **B.** Group II: illustrating, widely separated (S) and irregularly arranged collagen fibres (F); **C.** Group III: illustrating, regularly arranged collagen fibres (F). Notice, wide space between collagen fibres (S); **D.** Group IV: illustrating, regular arrangement of collagen fibres (F) similar to control group. Mallory's trichrome ×400.
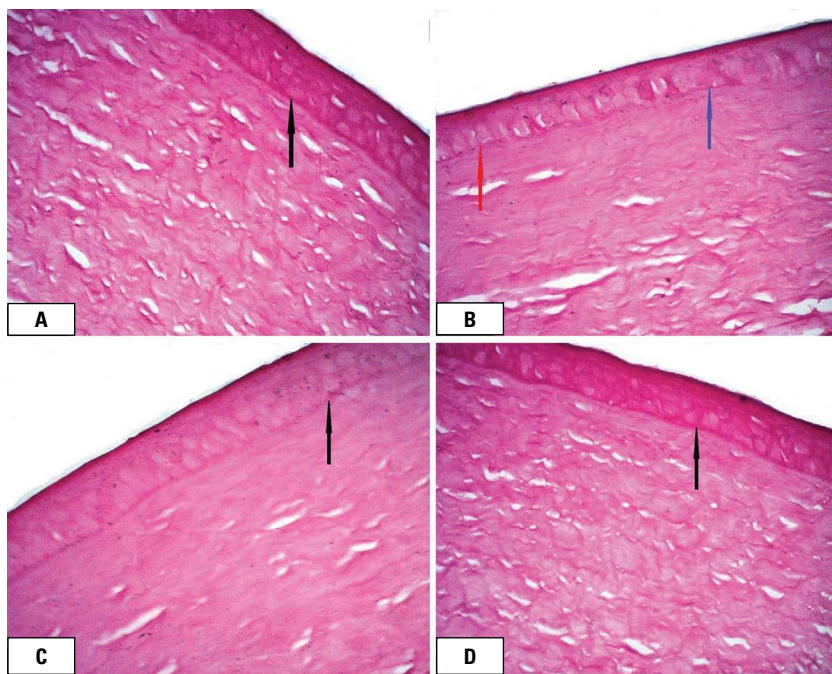
Figure 5. Photomicrographs of periodic acid Schiff (PAS) stained corneal sections of the different experimental groups; **A.** Control group: illustrating strong positive PAS reaction in the epithelial basement membrane (arrow); **B.** Group II: illustrating, mild positive PAS reaction in some parts (blue arrow) and negative in other parts (red arrow) of the epithelial basement membrane; **C.** Group III: illustrating, mild positive PAS reaction in the basement membrane (arrow); **D.** Group IV: illustrating, strong positive PAS reaction in the basement membrane (arrow). PAS ×400.

For determination of carbohydrate (epithelial basement membrane), PAS stained corneal sections of the different experimental groups were done. Group I (Control group) exhibited strong positive reaction in the epithelial basement membrane (Fig. 5A). However, mild positive PAS reaction in some parts and negative in other parts of the basement membrane were seen in group II (Latanoprost with BAC treated group) (Fig. 5B). Group III (Recovery group) revealed mild positive reaction (Fig. 5C). In group IV (PF latanoprost treated group), there was strong positive PAS reaction in the basement membrane similar to control group (Fig. 5D).

For detection of apoptosis immunohistochemically in corneal tissue, BAX immune-marker expression was determined. There was a negative BAX expression in the corneal tissue of group I (Fig. 6A), whereas in group II, strong positive cytoplasmic BAX reaction
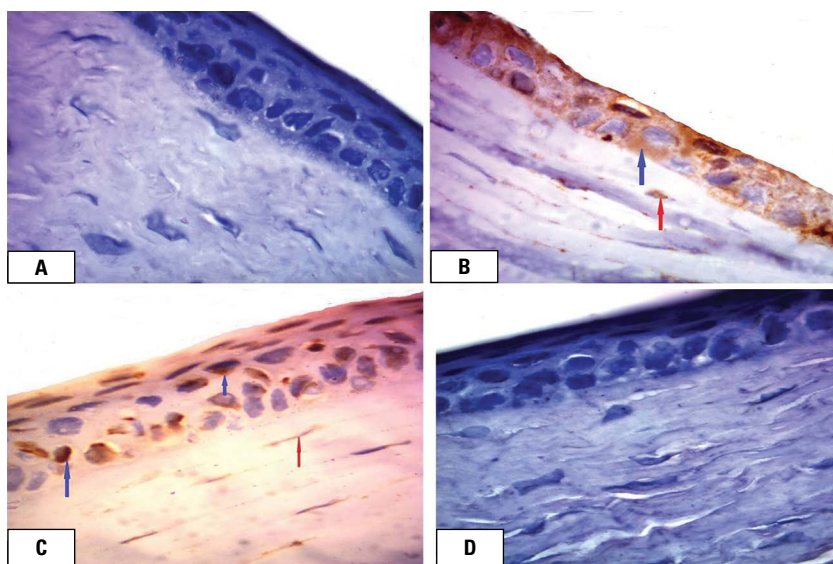
Figure 6. Photomicrographs of Bcl-2-associated X protein (BAX) immune-stained corneal sections of the different experimental groups; **A.** Control group: illustrating negative BAX reaction in the epithelium and stroma; **B.** Group II: illustrating, strong positive cytoplasmic BAX reaction in the epithelium (blue arrow) and mild reaction (red arrow) in the keratocytes; **C.** Group III: illustrating, moderate BAX reactivity in the corneal epithelial cells (blue arrows) and mild reaction in the keratocytes (red arrow); **D.** Group IV: illustrating, negative BAX reaction in the epithelium and stroma. BAX ×1000.

in the epithelium and mild reaction in keratocytes were observed (Fig. 6B). However, group III, exhibited moderate BAX reactivity in the corneal epithelial cells and mild reaction in keratocytes (Fig. 6C). In group IV, there was negative reaction in the epithelium and stroma similar to control animals (Fig. 6D).

Effects of preservative-free and preserved prostaglandin analogues on corneal ultrastructure

Electron microscopic examination was done to confirm the light microscopic findings.

Group I (Control group), the corneal epithelium had basal columnar cells with euchromatic rounded nuclei. Hemi-desmosomes appeared as electron dense spots and were seen on the basal sides of these cells, facing the basement membrane. The intermediate cells had rounded euchromatic nuclei. The superficial cells were flattened with flat nuclei. All epithelial cells were connected together by many electron dense desmosomes, allowing narrow intercellular spaces. Under the epithelium, there was the Bowman's membrane which appeared as a thick collagen fibre layer (Fig. 7A, B). The stroma had regularly arranged collagen fibres parallel to the corneal surface. The keratocytes appeared as spindle-shaped cells with scanty cytoplasm and moderately electron dense oval nucleus. They appeared squeezed in-between collagen fibres (Fig. 7C). The Descemet's membrane displayed as homogenous acellular electron-dense layer and lined by a single layer of endothelial cell which appeared as flat cells having oval nuclei and their cytoplasm contained

rough endoplasmic reticulum cisterna and mitochondria (Fig. 7D).

Group II (Latanoprost with BAC treated group), marked alterations including the various corneal layers were seen. The basal and intermediate epithelial cells appeared with cytoplasmic vacuoles, free ribosomes, distorted mitochondria, wide perinuclear space and shrunken nuclei (Fig. 8A, B). Moreover, the cells were separated by wide intercellular space (Fig. 8B). The superficial epithelial cells showed flat euchromatic nuclei with irregular contour. Wide intercellular spaces with partial loss of desmosomal junctions between some superficial epithelial cells were seen (Fig. 8C). The stroma exhibited keratocytes which were widely separated from the collagen fibres. The keratocytes appeared with cytoplasmic processes and their cytoplasm contained shrunken nuclei, dilated rough endoplasmic reticulum cisterna and lysosomes (Fig. 8D). Moreover, small areas in the stroma contained little amount of collagen fibres (Fig. 9A, B) and appearance of blood vessel was found (Fig. 9A). The endothelial cells had discontinued cell membrane and distorted mitochondria (Fig. 9B).

Group III (Recovery group) exhibited superficial epithelial cells with euchromatic nuclei and desmosomal junctions in between. Wide intercellular spaces with loss of desmosomes between some superficial epithelial cells were observed (Fig. 9C). The stroma exhibited regularly arranged collagen fibres. The keratocytes appeared with indented nucleus and abundant cytoplasm containing rough endoplasmic reticulum. Wide space between collagen fibres and keratocytes was
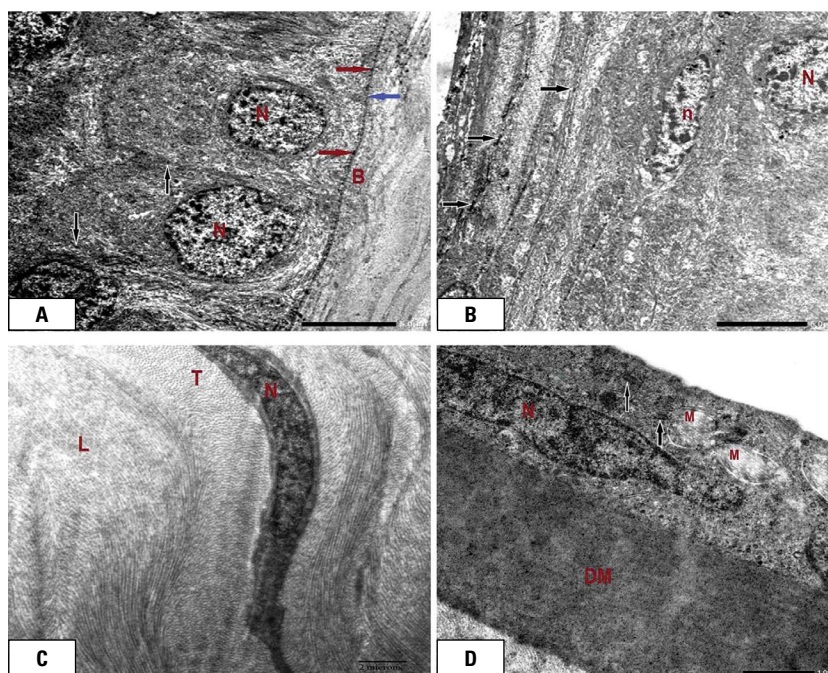
Figure 7. Electron micrographs of the cornea of control group illustrating: **A.** A basal columnar epithelial cells with euchromatic rounded nuclei (N) resting on clear intact Bowman's membrane (B). The epithelial cells are connected to each other by numerous desmosomes (black arrows) with narrow intercellular spaces. Notice, hemi-desmosomes appear as electron dense spots (red arrow) fixing the basal cells to the underlying basement membrane (blue arrow); ×4000; **B.** The intermediate cells have rounded euchromatic nuclei (N). The superficial cells are flattened with flat nuclei (n). All epithelial cells are connected with each other by electron dense desmosomes (arrows); ×4000; **C.** A spindle-shaped keratocyte with scanty cytoplasm and moderately electron dense oval nucleus (N) is seen squeezed between regularly arranged collagen fibres in longitudinal (L) and transverse (T) directions; ×5000; **D.** A single endothelial cell layer with flat nucleus (N) and abundant cytoplasm containing mitochondria (M) and rough endoplasmic reticulum cisterna (arrows) is observed. The endothelial cells line thick homogenous electron-dense Descemet's membrane (DM); ×15000.

observed (Fig. 9D). The Descemet's endothelial cells appeared with cytoplasmic vacuoles and distorted mitochondria (Fig. 10A).

Group IV (PF latanoprost treated group) showed corneal structure similar to that of the control group. The superficial epithelial cells were well organized with preserved desmosomal junctions (Fig. 10B). The stroma showed regularly arranged collagen fibres. The keratocytes with oval nucleus and rough endoplasmic reticulum in their cytoplasm were observed. The Descemet's endothelial cells appeared with flat nucleus and mitochondria (Fig. 10C).

DISCUSSION

Prostaglandin analogues are the first treatment used for glaucoma as a monotherapy or with other hypotensive agents. PGAs are preferable to other ocular hypotensive agents, because during long-term clinical use, there were no systemic side effects [16].

Among all the types of available PGAs, latanoprost was chosen in the present study, because this drug has good efficacy. Latanoprost is an esterified pro-

drug of prostaglandin F2-alpha, more lipophilic than other PGAs, which means that it is better absorbed through the cornea. Latanoprost is well tolerated. So, patients receiving latanoprost treatment are more persistent than other ocular prostaglandins hypotensive medications [35]. Latanoprost is the first PGA that has an improved, recently produced formulation without BAC [1].

In this study, the histological changes within the corneal tissue with the use of currently available PG-derived eye drops, namely latanoprost (Xalatan) and PF PGA latanoprost (Monopost), in male guinea pigs were evaluated by light and electron microscope.

In the current study, the light microscopic corneal changes were confirmed by electron microscope. Corneal tissue from guinea pigs treated with latanoprost with BAC showed toxic changes that were considered to be related to the preservative, BAC, as previously reported by Trzeciecka et al. [38].

Epstein et al. [9] demonstrated that preservatives which exist in eye drops, such as BAC, change the permeability of the ocular surface epithelium, even
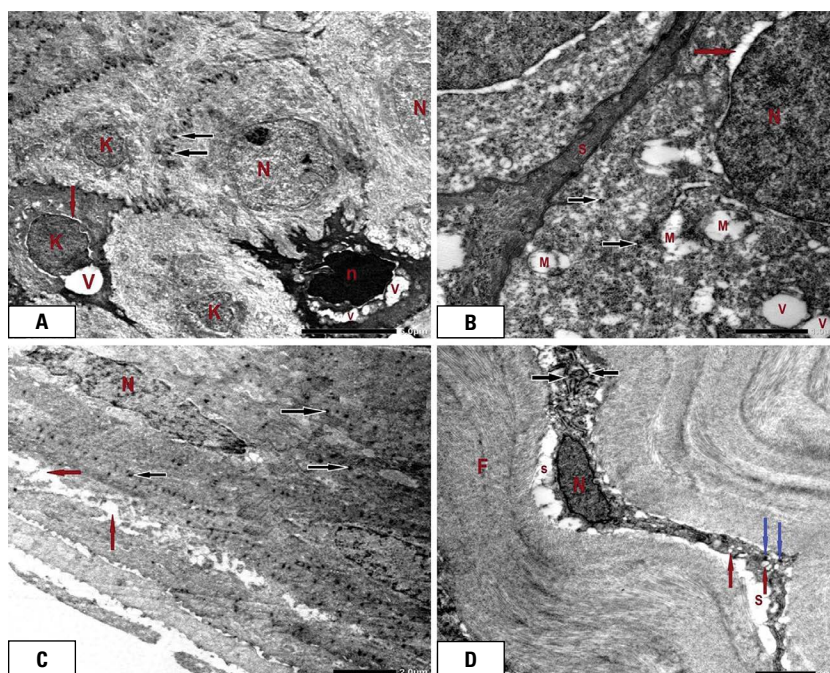
Figure 8. Electron micrographs of the cornea of group II illustrating: **A.** Basal and intermediate epithelial cells. One cell appears with cytoplasmic vacuoles (V) and condensed nuclei (n). Some cells have a euchromatic nuclei (N), whereas others have shrunken nuclei (K) and wide perinuclear space (red arrow). Notice, the cell membranes are interdigitated and connected by desmosomal junctions (black arrows); ×4000; **B.** Epithelial cells with euchromatic nucleus (N) and wide perinuclear space (red arrow) are seen. The cytoplasm shows multiple vacuoles (V), free ribosomes (arrows) and distorted mitochondria (M). The cells are separated by wide intercellular space (S); ×15000; **C.** The superficial epithelial cells have flat euchromatic nuclei (N) with irregular contour, some cells show preserved desmosomal junctions (black arrows). Notice, wide intercellular spaces with loss of junctions between some epithelial cells (red arrows); ×5000; **D.** The keratocyte has shrunken nucleus (N), variable sized cytoplasmic vacuoles (red arrows), dilated rough endoplasmic reticulum cisterna (black arrows) and lysosomes (blue arrow). The keratocyte is widely separated (S) from regularly arranged collagen fibres (F) of stroma; ×5000.

at very low doses. BAC gives rise to cell membranes lysis at the ocular surface.

Thinning of epithelial covering with desquamation of some surface cells was detected in the present study; this finding was confirmed morphometrically by showing highly significant decrease within the corneal epithelial thickness in comparison with the control animals. These results coincided with other authors [10, 22, 39] who reported a decrease in the number of corneal epithelial layers with highly significant decrease in the central corneal thickness following long term treatment with BAC-containing eye drops. This might be due to degeneration of corneal epithelial cells with dead cells loss and failure of cellular regeneration and proliferation following long term treatment with BAC containing eye drops.

Guo et al. [13] and Soliman et al. [37] illustrated that the corneal epithelial cells desquamation with intracellular adenozyno-5'-trifosforan (ATP) depletion is accelerated by BAC. Among the various effects of ATP depletion, regulatory light chain of myosin II (MLC) phosphorylation has been detected. It is proven that

the corneal epithelial cells exposure to BAC results in MLC phosphorylation that leads to contraction of the cytoskeleton of the epithelial cells leading to distortion the corneal barrier integrity.

Latanoprost with BAC-treated guinea pigs showed variable degrees of degeneration within the nuclei of the epithelial cells, endothelial cells and stromal keratocytes. This might be due to deoxyribonucleic acid (DNA) damage occurring in corneal cells after treatment of BAC-containing eye drops, as previously demonstrated with Kobayashi et al. [17] and Soliman et al. [37].

These results were also, in accordance with Barzilai and Yamamoto [4] and Baudouin et al. [5] who stated that BAC caused oxidative stress leading to free radicals generation, such as hydroxyl radicals and superoxide anion, and reactive oxygen species (ROS), such as singlet oxygen and hydrogen peroxide. Overproduction of ROS can induce cellular damage, particularly the DNA through the mitochondrial damage, which causes activation of endonuclease and apoptogenic proteases resulting in apoptosis.
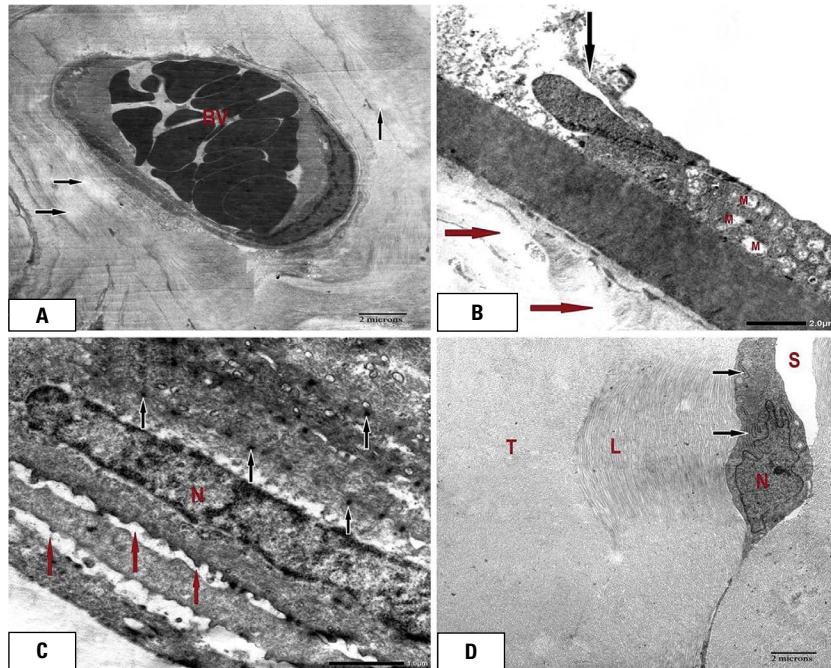
Figure 9. Electron micrographs of the cornea of group II (A, B) and group III (C, D); **A.** Group II: illustrating small areas in the stroma containing little amount of collagen fibres (black arrows) with appearance of blood vessel (BV); ×5000; **B.** Group II: illustrating, discontinued endothelial cell membrane (black arrow) with distorted mitochondria (M). The stroma displays little amount of collagen fibres (red arrow); ×5000; **C.** Group III: illustrating, superficial epithelial cells with flat euchromatic nuclei (N) and preserved desmosomal junctions in between (black arrows). Wide intercellular spaces between some superficial cells with loss of desmosomes are observed (red arrows); ×15000; **D.** Group III: illustrating stroma with regularly arranged collagen fibres in longitudinal (L) and transverse (T) directions. The keratocyte appears with indented nucleus (N) and abundant cytoplasm containing rough endoplasmic reticulum cisterna (black arrow). Notice, wide space (S) between keratocyte and collagen fibres; ×5000.
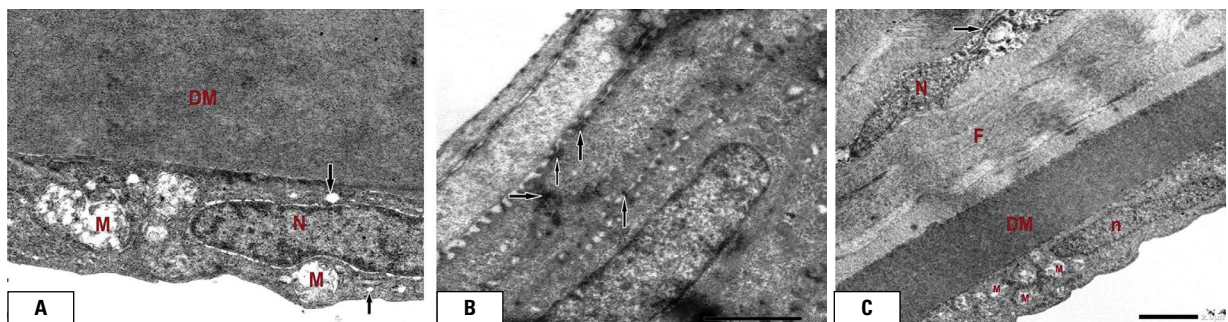
Figure 10. Electron micrographs of the cornea of group III (A) and group IV (B, C); **A.** Group III: Descemet's membrane (DM) lined by a single endothelial cell layer. The endothelial cell appears with flat nucleus (N) and abundant cytoplasm containing distorted mitochondria (M) and vacuoles (black arrows); ×15000; **B.** Group IV: illustrating normal appearance of superficial epithelial cells with preserved desmosomal junctions (black arrows); ×5000; **C.** Group IV: illustrating stroma with regularly arranged collagen fibres (F). The keratocyte appears with oval nucleus (N) and rough endoplasmic reticulum (black arrow). The Descemet's membrane (DM) is lined by endothelial cells having flat nucleus (n) and mitochondria (M); ×5000.

Rosin and Bell [33] referred decreasing number of keratocytes within the stroma detected within corneal tissues from guinea pigs treated with latanoprost with BAC to their contraction, apoptosis and death of these cells after exposure to BAC. This finding was supported morphometrically as showing a highly significant decrease in the keratocytes number as compared with that of the control animals.

Disarrangement and loss of collagen fibres in some areas within the stroma in this study may be due to keratocytes loss as they synthesize and preserve stromal collagen; thus, keratocytes loss leads to

less collagen secretion [23]. Another explanation of damaged corneal stromal cells following prolonged BAC exposure was that PGAs are known to reduce IOP by upregulation of matrix metalloproteinases (MMPs), which are collagen degradation enzymes induced by prostaglandin F2-alpha [34, 39], causing connective tissue remodelling and degeneration of extracellular matrix, involving collagens of the sclera and ciliary muscle, resulting in lowering resistance of uveo-scleral outflow, thus improving aqueous humour outflow [18].

Stromal neovascularisation and congested blood vessels detected in the present study might be due to corneal stromal cells activation and migration to the site of injury following exposure to BAC. These stromal cells express vascular endothelial growth factor (VEGF) that induces angiogenesis with new blood vessels formation as previously explained by Mahmoud et al. [20].

It was also suggested by DeStafeno and Kim [8] that stromal neovascularisation might be due to unbalancing between angiogenic factors such as VEGF, fibroblast growth factor and anti-angiogenic ones such as angiostatin in the cornea.

Inflammatory cellular infiltration of the stroma detected within corneal sections from guinea pigs treated with latanoprost with BAC may be considered as a trial for healing and protection against infection which become easier with disturbance of the normal corneal epithelial barrier with prolonged treatment of BAC containing hypotensive eye drops.

Yang et al. [41] reported that inflammatory cellular infiltration of the stroma might be due to the expression of several inflammatory factors, such as chemotactic factors: monocyte chemo-attractant protein 1, macrophage inflammatory protein-1 alpha and growth-regulated protein alpha, which increased after treatment with BAC within a week. These inflammatory factors have chemotactic activity for eosinophils monocytes and neutrophils, either separately or together.

Negri et al. [24] referred the inflammatory cellular infiltration of corneal stroma to the effect of BAC in lipoxygenase activation and secretion of inflammatory mediators, and multiple cytokines such as interleukin-la, tumour necrosis factor alpha, interleukin-8, leading to irritation and allergic reaction.

In the current study, widely separated irregularly arranged collagen fibres in Mallory's trichrome-stained corneal sections from guinea pigs treated with latanoprost with BAC might be due to degradation of its collagen fibres by active MMPs which are produced by prolonged exposure to BAC. These findings were in agreement with Gaton et al. [11] and Park et al. [26] who reported that PGAs cause up-regulation of MMPs that leads to degradation of extracellular matrix, including collagens of the ciliary muscle and sclera.

Another explanation of wide spaces in-between collagen fibres is that prolonged treatment with hypotensive eye drops containing BAC resulted in intracellular and extracellular oedema, as previously explained by Collin and Collin [7].

Histochemically, corneal sections of this group revealed mild positive PAS reaction in some parts and negative in other parts of the basement membrane. These results indicated reduction or even depletion of carbohydrates within the basement membrane of corneal epithelium.

Immunohistochemically, a marked immune positive cytoplasmic reaction for BAX in the covering epithelial cells and stromal keratocytes within corneal sections from guinea pigs treated with latanoprost with BAC was observed. This could be due to apoptosis of these cells. BAX is a nuclear-encoded protein that can penetrate the mitochondrial membrane and, thus, mediate cell death via apoptosis. So, increase reactivity for BAX indicates cellular apoptosis [40].

Guinea pigs left to recover without treatment for 2 weeks after treatment with latanoprost with BAC showed mild improvement of the histological changes of the cornea. However, some histological alterations were still persisting as desquamation of the superficial epithelial cells and corrugated Bowman's membrane. Small keratocytes with dark nuclei were noticed. Few endothelial cells appeared separated from the Descemet's membrane. These findings were in harmony with Soliman et al. [37] who demonstrated that there was mild recovery within the corneal sections of rats left for recovery after 0.02% BAC treatment with minimal decrease of the thickness of corneal epithelium and stromal degeneration.

On the other hand, light and electron microscopic studies of corneal sections from guinea pigs treated with PF latanoprost revealed nearly normal corneal structure. Moreover, these results were in harmony with Pauly et al. [27] and Yang et al. [41] who reported that rat corneal tissue presented better tolerance with PF latanoprost therapy. This improvement could be referred to absence of the BAC preservative from PGAs which in turn might improve the structure and function of the corneal epithelial barrier.

CONCLUSIONS

Prostaglandins with BAC preservative derived eye drops result in many histological alterations in the corneal tissue. These alterations might be improved by withdrawal of the preservative. PF prostaglandin medication seems to be alternative to those preserved with BAC formulations.

Conflict of interest: None declared

REFERENCES

1. Alm A. Latanoprost in the treatment of glaucoma. Clin Ophthalmol. 2014; 8: 1967–1985, doi: 10.2147/OPTH.S59162, indexed in Pubmed: 25328381.
2. Ammar DA, Noecker RJ, Kahook MY. Effects of benzalkonium chloride-preserved, polyquad-preserved, and sofZia-preserved topical glaucoma medications on human ocular epithelial cells. Adv Ther. 2010; 27(11): 837–845, doi: 10.1007/s12325-010-0070-1, indexed in Pubmed: 20931366.
3. Bancroft JD, Layton C. Theory and practice of histological technique. 7th ed. Churchill Livingstone, London 2010: 173–214.
4. Barzilai A, Yamamoto KI. DNA damage responses to oxidative stress. DNA Repair (Amst). 2004; 3(8-9): 1109–1115, doi: 10.1016/j.dnarep.2004.03.002, indexed in Pubmed: 15279799.
5. Baudouin C, Labbé A, Liang H, et al. Preservatives in eyedrops: the good, the bad and the ugly. Prog Retin Eye Res. 2010; 29(4): 312–334, doi: 10.1016/j.preteyeres.2010.03.001, indexed in Pubmed: 20302969.
6. Brignole-Baudouin F, Desbenoit N, Hamm G, et al. A new safety concern for glaucoma treatment demonstrated by mass spectrometry imaging of benzalkonium chloride distribution in the eye, an experimental study in rabbits. PLoS One. 2012; 7(11): e50180, doi: 10.1371/journal.pone.0050180, indexed in Pubmed: 23209668.
7. Collin SP, Collin HB. The corneal epithelial surface in the eyes of vertebrates: environmental and evolutionary influences on structure and function. J Morphol. 2006; 267(3): 273–291, doi: 10.1002/jmor.10400, indexed in Pubmed: 16323209.
8. DeStafeno JJ, Kim T. Topical bevacizumab therapy for corneal neovascularization. Arch Ophthalmol. 2007; 125(6): 834–836, doi: 10.1001/archopht.125.6.834, indexed in Pubmed: 17562998.
9. Epstein SP, Chen D, Asbell PA. Evaluation of biomarkers of inflammation in response to benzalkonium chloride on corneal and conjunctival epithelial cells. J Ocul Pharmacol Ther. 2009; 25(5): 415–424, doi: 10.1089/jop.2008.0140, indexed in Pubmed: 19857103.
10. Fasce F, Spinelli A, Bolognesi G, et al. Comparison of BD Multivisc with the soft shell technique in cases with hard lens nucleus and Fuchs endothelial dystrophy. Eur J Ophthalmol. 2007; 17(5): 709–713, doi: 10.1177/112067210701700504, indexed in Pubmed: 17932844.
11. Gaton DD, Sagara T, Lindsey JD, et al. Increased matrix metalloproteinases 1, 2, and 3 in the monkey uveo-scleral outflow pathway after topical prostaglandin F(2 alpha)-isopropyl ester treatment. Arch Ophthalmol. 2001; 119(8): 1165–1170, doi: 10.1001/archopht.119.8.1165, indexed in Pubmed: 11483084.
12. Glauert AM, Lewis PR. Biological specimen preparation for transmission electron microscope. 1st ed. Princeton University Press, London 1999.
13. Guo Y, Satpathy M, Wilson G, et al. Benzalkonium chloride induces dephosphorylation of Myosin light chain in cultured corneal epithelial cells. Invest Ophthalmol Vis Sci. 2007; 48(5): 2001–2008, doi: 10.1167/iovs.06-0613, indexed in Pubmed: 17460253.
14. Hae-Young L, Jie HK, Kyung ML, et al. Effect of prostaglandin analogues on tear proteomics and expression of cytokines and matrix metalloproteinases in the conjunctiva and cornea. Experimental Eye Res. 2011; 94(1): 13–21, doi: 10.1016/j.exer.2011.10.017.
15. Kalleny N, Soliman N. Light and electron microscopic study on the effect of topically applied hyaluronic acid on experimentally induced corneal alkali burn in albino rats. Egyptian J Histol. 2011; 34(4): 829–848, doi: 10.1097/01.ehx.0000407699.63226.2a.
16. Kim JH, Kim EJ, Kim YH, et al. In vivo effects of preservative-free and preserved prostaglandin analogs: mouse ocular surface study. Korean J Ophthalmol. 2015; 29(4): 270–279, doi: 10.3341/kjo.2015.29.4.270, indexed in Pubmed: 26240512.
17. Kobayashi N, Katsumi S, Imoto K, et al. Quantitation and visualization of ultraviolet-induced DNA damage using specific antibodies: application to pigment cell biology. Pigment Cell Res. 2001; 14(2): 94–102, doi: 10.1034/j.1600-0749.2001.140204.x, indexed in Pubmed: 11310797.
18. Lazcano-Gomez G, Ancona-Lezama D, Gil-Carrasco F, et al. Effects of topical travoprost 0.004% on intraocular pressure and corneal biomechanical properties in an animal model. Digit J Ophthalmol. 2016; 22(1): 1–5, doi: 10.5693/djo.01.2015.03.001, indexed in Pubmed: 27330476.
19. Lee AJ, Goldberg I. Emerging drugs for ocular hypertension. Expert Opin Emerg Drugs. 2011; 16(1): 137–161, doi: 10.1517/14728214.2011.521631, indexed in Pubmed: 21352074.
20. Mahmoud B, Shady A, Meleegy UEl, et al. Effects of ultraviolet B radiation on the cornea of adult male albino rats and the possible role of lornoxicam. Egypt J Histol. 2010; 33(1): 156–167, doi: 10.1097/00767537-201003000-00015.
21. Meda R, Wang Q, Paoloni D, et al. The impact of chronic use of prostaglandin analogues on the biomechanical properties of the cornea in patients with primary open-angle glaucoma. Br J Ophthalmol. 2017; 101(2): 120–125, doi: 10.1136/bjophthalmol-2016-308432, indexed in Pubmed: 27162226.
22. Nada S, Elgendy M, Morcos M, et al. Histological study on conjunctival and corneal reactions in rabbits induced by chronic topical application of latanoprost and travoprost. Egyptian J Histol. 2013; 36(1): 139–148, doi: 10.1097/01.ehx.0000423477.48372.05.
23. Naroo S. Refractive surgery: a guide to assessment and management. 1st ed. Elsevier Health Sciences 2003: 96.
24. Negri L, Ferreras A, Iester M. Timolol 0.1% in glaucomatous patients: efficacy, tolerance, and quality of life. J Ophthalmol. 2019; 2019: 4146124, doi: 10.1155/2019/4146124, indexed in Pubmed: 31191995.

25. Okabe K, Kimura H, Okabe J, et al. Effect of benzalkonium chloride on transscleral drug delivery. Invest Ophthalmol Vis Sci. 2005; 46(2): 703–708, doi: 10.1167/iovs.03-0934, indexed in Pubmed: 15671302.

26. Park HL, Kim JH, Lee KM, et al. Effect of prostaglandin analogues on tear proteomics and expression of cytokines and matrix metalloproteinases in the conjunctiva and cornea. Exp Eye Res. 2012; 94(1): 13–21, doi: 10.1016/j.exer.2011.10.017, indexed in Pubmed: 22067128.

27. Pauly A, Roubeix C, Liang H, et al. In vitro and in vivo comparative toxicological study of a new preservative-free latanoprost formulation. Invest Ophthalmol Vis Sci. 2012; 53(13): 8172–8180, doi: 10.1167/iovs.12-10766, indexed in Pubmed: 23150620.

28. Peat J, Barton B. Medical statistics. A Guid to data analysis and critical appraisal. 1st ed. Wiley-Blackwell 2005: 113–119.

29. Penault-Llorca F, Bouabdallah R, Devilard E, et al. Analysis of BAX expression in human tissues using the anti-BAX, 4F11 monoclonal antibody on paraffin sections. Pathol Res Pract. 1998; 194(7): 457–464, doi: 10.1016/s0344-0338(98)80114-3, indexed in Pubmed: 9728362.

30. Quigley HA, Broman AT. The number of people with glaucoma worldwide in 2010 and 2020. Br J Ophthalmol. 2006; 90(3): 262–267, doi: 10.1136/bjo.2005.081224, indexed in Pubmed: 16488940.

31. Quigley H. Glaucoma. Lancet. 2011; 377(9774): 1367––1377, doi: 10.1016/s0140-6736(10)61423-7.

32. Ramli N, Supramaniam G, Samsudin A, et al. Ocular surface disease in glaucoma: effect of polypharmacy and preservatives. Optom Vis Sci. 2015; 92(9): e222–e226, doi: 10.1097/OPX.0000000000000542, indexed in Pubmed: 25730335.

33. Rosin LM, Bell NP. Preservative toxicity in glaucoma medication: clinical evaluation of benzalkonium chloride-free 0.5% timolol eye drops. Clin Ophthalmol. 2013; 7: 2131–2135, doi: 10.2147/OPTH.S41358, indexed in Pubmed: 24204115.

34. Saika S, Ohnishi Y, Ooshima A, et al. Epithelial repair: roles of extracellular matrix. Cornea. 2002; 21(2 Suppl 1): S23–S29, doi: 10.1097/00003226-200203001-00006, indexed in Pubmed: 11995806.

35. Shafranov G. Comparing prostaglandins. Glaucoma Today. 2005: 37–39.

36. Smith M. Medication review: prostaglandin analogs for glaucoma. Pharmacy Times. 2015; 19(6): 949–956.

37. Soliman ME, Mahmoud BL, Kafafy MA. Histological changes in cornea following repeated exposure to Benzalkoniumatoms Chlorid and the possible protective effect of topically applied sodium hyaluronate. Nature Science. 2015; 13(5): 64–76.

38. Trzeciecka A, Paterno JJ, Toropainen E, et al. Long-term topical application of preservative-free prostaglandin analogues evokes macrophage infiltration in the ocular adnexa. Eur J Pharmacol. 2016; 788: 12–20, doi: 10.1016/j.ejphar.2016.06.014, indexed in Pubmed: 27288881.

39. Uzunel UD. The effect of prostaglandin analogues on central corneal thickness. Int J OphthalmolClin Res. 2018; 5(1), doi: 10.23937/2378-346x/1410084.

40. Westphal D, Dewson G, Czabotar PE, et al. Molecular biology of Bax and Bak activation and action. Biochim Biophys Acta. 2011; 1813(4): 521–531, doi: 10.1016/j.bbamcr.2010.12.019, indexed in Pubmed: 21195116.

41. Yang Q, Zhang Y, Liu X, et al. A comparison of the effects of benzalkonium chloride on ocular surfaces between C57BL/6 and BALB/c mice. Int J Mol Sci. 2017; 18(3), doi: 10.3390/ijms18030509, indexed in Pubmed: 28245636.

42. Yee RW, Norcom EG, Zhao XC. Comparison of the relative toxicity of travoprost 0.004% without benzalkonium chloride and latanoprost 0.005% in an immortalized human cornea epithelial cell culture system. Adv Ther. 2006; 23(4): 511–519, doi: 10.1007/BF02850039, indexed in Pubmed: 17050493.

ORIGINAL ARTICLE

VIA MEDICA

Comparative study on the therapeutic effects of bone marrow mesenchymal stem cells versus platelet rich plasma on the pancreas of adult male albino rats with streptozotocin-induced type 1 diabetes mellitus

H. El-Haroun[1], R.M. Salama[2]

[1]Department of Histology, Faculty of Medicine, Menoufia University, Egypt
[2]Department of Anatomy and Embryology, Faculty of Medicine, Menoufia University, Egypt

Background: The optimal treatment for autoimmune type 1 diabetes mellitus (T1DM) is endogenous regeneration of the pancreatic beta-cell. This can be achieved either by transplanting bone marrow mesenchymal stem cells (BMSCs) or injecting platelet-rich plasma (PRP). Current research reviewed a T1DM model and compared the effect of BMSCs on exocrine and endocrine pancreas portions versus PRP.

Materials and methods: Rats were divided into four groups: Control group, Diabetic group (single streptozotocin dose 60 mg/kg IP), Diabetic + PRP group (PRP, 0.5 mL/kg SC twice weekly/4 weeks given to diabetic rats) and Diabetic + BMSCs group (1 mL of PKH26 labelled MSCs suspension in buffer phosphate solution, 3×10^6 cells/mL IV to diabetic rats). Glucose, amylase and lipase levels were calculated and pancreases were designed for light, electron microscopic, immunohistochemistry, morphometry and statistical analysis.

Results: Diabetic rats exhibited elevated glucose, decreased amylase and lipase compared to control rats. In addition, variable histological degenerative changes in the form of congested blood vessels have been identified with a significant increase in the mean area percentage of collagen, a significant decrease in the diameter of the islets, the number of cells in the islets of Langerhans and the number of zymogen granules. Ultrastructural findings exhibited distorted Golgi apparatus morphology, degenerated mitochondria, pyknotic nuclei, and few secretory beta-cell granules.

Conclusions: Administration of BMSCs to diabetic group significantly increased the number of cells and diameter of Langerhans islets and the number of zymogen granules compared to Diabetic group as well as Diabetic + PRP group. BMSCs could be considered more efficient than PRP in the treatment of type 1 diabetes. (Folia Morphol 2022; 81, 1: 65–81)

Key words: type 1 diabetes mellitus, streptozotocin, bone marrow mesenchymal stem cells, platelet-rich plasma, anti-insulin antibody

Address for correspondence: Dr. R.M. Salama, Department of Anatomy and Embryology, Faculty of Medicine, Menoufia University, Smouha, Alexandria, Egypt, tel: 00201005240928, e-mail: drrashasalama@yahoo.com

INTRODUCTION

As a major health concern in the 21st century, diabetes mellitus (DM) is a chronic metabolic disease causing hyperglycaemia; it is categorised into two major types (1 and 2). Type 1 diabetes mellitus (T1DM) is an autoimmune disease distinguished by an absolute insulin deficiency due to immune-mediated beta-cell-decimation of the islet pancreas [34]. Type 2 diabetes mellitus (T2DM) is distinguished by insulin resistance, reduced insulin production, and pancreatic beta-cell failure [44].

Diabetes has the potential to cause severe morbidity associated with microvascular damage and neuropathy affecting the retina, kidney, peripheral arteries and peripheral nerves due to numerous organ and body system complications [5, 10].

Insulin injections, hormone replacement, and oral hypoglycaemic drugs are main treatment choices for diabetic patients to stabilise their blood glucose [6] and to prevent deterioration of the condition [39]. However, these available treatments only manage symptoms or patient's condition and can only ameliorate hyperglycaemia [32]. Consequently, they are less effective in reversing insulin resistance, and in altering the progression of DM, and they do not prevent the progressive islet beta-cell degeneration, and cannot cure diabetes [27].

Another way of treatment was reliance on beta-cell renewal therapy utilising either the pancreas or the islet transplantation [46]. However, these procedures were constrained by risks of major invasive surgery, donor shortages and rejection complications [43].

Therefore, regeneration of the endogenous beta-cells would be the ideal therapeutic approach for DM control [36].

Platelet-rich plasma (PRP), other names, growth factor-rich plasma or autologous concentrated plasma is now a low-cost procedure and has acted as an attractive area for clinicians and researchers over the two last decades in tissue repair [47]. PRP is an aggregation of the homologous platelets that is 3 to 5 times exceeding physiological constituent of thrombocytes suspended in a small volume of plasma in the entire blood [31]. Marx et al. [38] was the first to research PRP, suggested that plasma can only be called platelet-rich if the concentration of condensed platelets exceeds the baseline (150–400 thousand per microliter). For autologous plasma to have high healing properties, the platelet levels should be at least 1 million in 5 mL of plasma.

Growth factors (GFs) are among the innate biological peace-makers that have a role in regulating processes of tissue repair and regeneration, growth, and differentiation [35]. Platelets contain not only proteins needed for haemostasis but also convey many GFs [53], related to vasculature and tissue repair such as transforming growth factor (TGF), platelet-derived growth factor (PDGF), vascular endothelial growth factor (VEGF), epidermal growth factor (EGF), cytokines and insulin-like growth factor (IGF) [37].

Platelet-rich plasma can be used as an inexpensive technique for delivering high levels of homologous GFs [14]. It has been used in a number of medical and surgical specialties, including orthopaedics, neurosurgery, ophthalmology, maxillofacial surgery, cosmetic surgery and dentistry [58]. Nevertheless, there was a dearth of research that detected the influence of PRP injection on diabetic rat pancreas.

Mesenchymal stem cells (MSCs) have recently attracted considerable attention as a more promising method of treating DM. MSC are multipotent stem cells found in bone marrow, adipose tissue, umbilical cord blood and many other tissues. Such cells are used in regenerative medicine as they are capable of renewing themselves and differentiating into a wide range of cells and have a high capacity for cultural expansion [50, 59].

Stem cell transplantation can delay diabetes progression and prevent the complications of hyperglycaemia side effects and was successfully implemented in diabetes [62]. Similarly, bone marrow mesenchymal stem cells (BMSCs) transplant could retrieve pancreatic beta-cells and control blood glucose levels [42]. In addition, there are angiogenic, anti-apoptotic, anti-inflammatory and immunomodulatory effects [13].

The purpose of this study was to compare the impact of BMSCs and PRP on the biochemical and structural changes in the pancreas of adult male albino rats with streptozotocin (STZ)-induced T1DM in order to shed light on the potential for clinical use of such applications.

MATERIALS AND METHODS

Animals

In this study, 70 adult male albino rats were used, each weighing 180–200 g. The animals were purchased from and kept in the Medical Research Institute's animal house, Alexandria University, Egypt, and the experiment was carried out there. Until the beginning of the experiment, animals were housed in
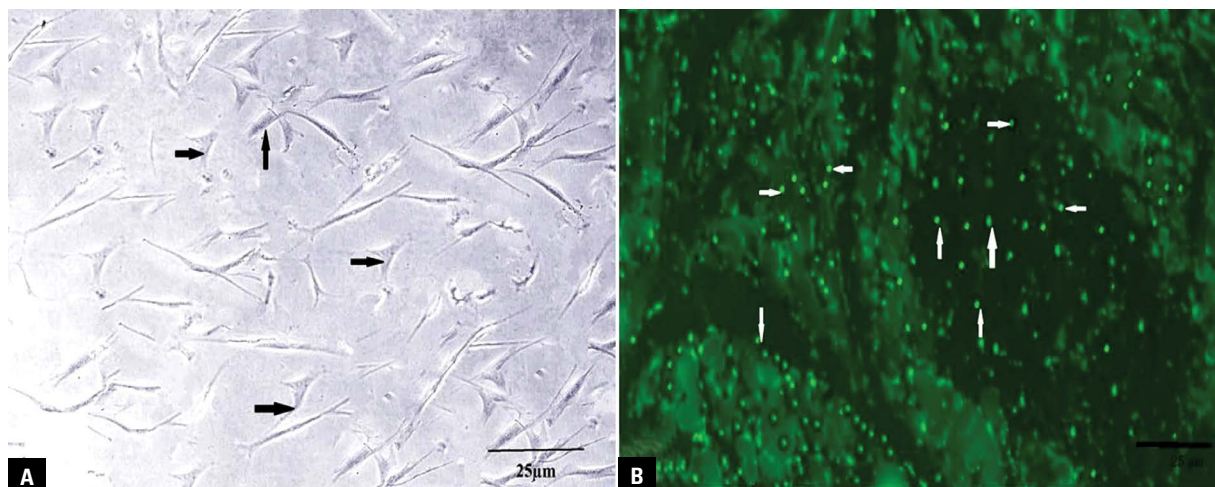
Figure 1. A. Ten-day culture, inverted microscope micrograph of bone marrow mesenchymal stem cells (BMSCs). The cells are adherent spindle-shaped cells; **B**. An image of a fluorescent microscope showing BMSCs labelled with fluorescent PKH67 appearing inside acini and pancreas islets as bright dots. Scale bar: 25 μm.

separate wire mesh cages and acclimatised at room temperature for 1 week, with a light and dark duration of 12:12, with access to food and water ad libitum. In this research, ethical principles for the treatment of animals were applied and monitored by an animal facility, Medical Research Institute, Alexandria University.

Chemicals

Streptozotocin (STZ): a vial of 1.5 g STZ powder and 220 mg citric acid (Sigma Aldrich, Egypt), dissolved in 0.1 M sodium citrate buffer (pH 6) in accordance with the directions of manufacture and was used within 5 min of preparation.

Platelet-rich plasma

PRP preparation. At the Medical Research Institute's animal house, Alexandria University, Egypt, PRP was freshly prepared. The preparation method was accomplished by adjusting the protocol of the double centrifugation tube [48]. With the rats under ether anaesthesia, 2 mL of blood was collected from the retro-orbital plexus under sterilisation. The blood was submitted for 10 min centrifugation at 1600 revolutions/minute, resulting in 3 different layers; red blood cells below, white blood cells buffy coat in the middle, and plasma above. The plasma was then pipetted and the part over the buffy coat was gained. After that, the plasma was submitted for 10 min centrifugation at 2000 rpm, resulting in 2 portions: platelet poor plasma (PPP) above and platelet button at the bottom. To allow platelet resuspension, a portion of

the PPP was removed and another portion remained with platelets that were slightly agitated. To verify the platelet concentration, 80 μL of the PRP was counted in an automatic apparatus to ensure that the platelet number was greater than 1,000,000/μL.

Finally, aspirate 0.5 mL/kg PRP with micropipette and dissolute into the saline phosphate buffer (PBS) (PRP 1:1 PBS), and subcutaneously injected with a sterile insulin syringe.

Bone narrow mesenchymal stem cells

BM-MSCs (labelled PKH67; Green Fluorescent Cell Linker) were supplied from the stem cell research unit of the Department of Biochemistry of the Faculty of Medicine, Cairo University, Egypt. According to Augello et al. [9], BM-MSCs were harvested from the bone marrow of femurs and tibiae of 6-week-old male rats.

In Dulbecco's Modified Eagle Medium (DMEM) purchased from Sigma, the isolated MSCs were cultured. 10% foetal calf serum (FCS) and 1% 100 U/mL penicillin, 100 mg/mL streptomycin and 2 mM L-glutamine were supplemented with DMEM. In humidified CO_2 — 5% air at 37°C, the cells were cultured to confluence (80–90%). Experiments were conducted on confluent cultures that were usually acquired on the 12th to 14th day of culture. In the next 3 passages, this process was repeated. For all experiments, cells at passage 3 were used. In vitro detection of MSCs was performed by culture research, using an inverted microscope (Olympus CKX53) to appear as spindle-shaped cells (Fig. 1A).

The cells were centrifuged and washed twice in a serum-free medium prior to the experiment. Pancreatic tissue was studied with a fluorescent microscope (Olympus BX50F4, No. 7M03285, Tokyo, Japan) to detect and track PKH67-stained cells (Fig. 1B). The extracted cells in the third passage were labelled with the green fluorescent protein (PKH67-Sigma) [17].

Induction of diabetes

Overnight-fasted rats received a single intra-peritoneal (IP) injection of STZ (60 mg/kg body weight) dissolved in 0.1 M sodium citrate buffer for T1DM induction. 48 hours after STZ injection (day 0 of experiment), animals were fasted overnight and blood samples were collected from the tail vein for glucose level monitoring. Rats are considered diabetic when glucose level exceeds 250 mg/dL [58].

Experimental design

In order to obtain PRP, 20 of the 70 male rats were used and the other 50 were randomly divided into four groups:
— Group I (Control group, n = 20 rats): four equal subgroups were subdivided into: (5 rats each):
  • Subgroup Ia: rats were retained and acted as negative control without medication,
  • Subgroup Ib: rats obtained an IP injection of a single 0.1 M sodium citrate buffer,
  • Subgroup Ic: rats were subcutaneously injected on a bi-weekly basis with PRP at a dose of 0.5 mL/kg for 4 weeks,
  • Subgroup Id: rats received 1 mL of PKH26 labelled MSC suspension in buffer phosphate solution (3×10^6 cells/mL) IV via tail vein [25] for 2 successive days;
— Group II (Diabetic group, n = 10 rats): a single STZ (60 mg/kg body weight) IP injection dissolved in a 0.1 M sodium citrate buffer was administered to rats;
— Group III (Diabetic + PRP group, n = 10 rats): PRP was administered bi-weekly to rats at a dose of 0.5 mL/kg by SC injection for 4 weeks on day 0 following STZ diabetes induction assurance;
— Group IV (Diabetic + BMSCs group, n = 10 rats): 1 mL of PKH26-labeled MSC suspension in buffer phosphate solution was administered to rats on day 0 after induction of STZ diabetes for 2 consecutive days (3×10^6 cells/mL) IV via the tail vein [25].

Biochemical study

Blood samples collected from the tail vein of overnight fasting rats at the end of the 4th week to measure.

Fasting glucose level, use one-touch Accu-Check glucometer and compatible blood glucose test strips, prior to grouping at the beginning of the experiment, all animals were subjected to blood glucose level measurement to ensure that they were normoglycaemic. Then, for the different sample types, the measuring method was conducted with statistical analysis.

Serum pancreatic amylase was performed by Landt et al. [33], an immunoabsorbent prepared by coating latex beads with a monoclonal antibody unique for pancreatic amylase. Serum pancreatic lipase was prepared by the enzyme-colorimetric method using Automated Hitachi Analyser [56].

Experiments in histology, immunohistochemistry and electron microscopy

Rats from all groups were sacrificed at the end of the 4th week by being decapitated under light halothane anaesthesia. Pancreases were rapidly dissected out and divided into two parts: one for light microscopic examination and the other for electron microscopic examination.

Specimens subjected for light microscopic inspection were fixed in 10% formol saline for 24 h and subsequently processed for the preparation of 5-μm-thick paraffin sections for haematoxylin and eosin (H&E) for histological validation [11], Mallory's trichrome stain for collagen fibre indication, and toluidine blue stain [57].

Immunohistochemical study of anti-insulin antibody

The immune-localisation technique was performed on pancreatic paraffin sections of 5 μm thickness with the streptavidin-biotin-peroxidase staining method [15]. Anti-sera containing rat insulin polyclonal primary antibody (Bio-Genex, case no.: AR.295-R.) were then incubated with these parts for 1 h. Dako-K0690; Dako Universal LSAB Kit (bio-tinylated secondary antibody) and Dako-K0690 (streptavidin horseradish peroxidase) were incubated in the components for 30 min. Then, they were incubated with a 3,30-di-aminobenzidine-4-hydrochloride (Sigma-D5905; Sigma Aldrich Company Ltd., Gillingham, UK) substrate

Table 1. Biochemical reaction (fasting glucose level, serum amylase, serum lipase)

	Control	Sodium citrate	PRP	BMSCs	STZ	STZ + PRP	STZ + BMSCs	P value
Fasting blood glucose	80.7 ± 3.2	82.8 ± 2.3	80.8 ± 2.78	81.5 ± 2.46	414.6 ± 17.61	118.7 ± 4.74	82.3 ± 4.03	P1: 0.153; P2: 0.95; P3: 0.49; P4: 0.001**; P5: 0.001**; P6: 0.38
Serum amylase	63.1 ± 2.77	62.1 ± 4.07	62.4 ± 2.63	63.5 ± 2.17	31.9 ± 2.85	59.4 ± 2.72	61.5 ± 1.78	P1: 0.45; P2: 0.41; P3: 0.65; P4: 0.001**; P5: 0.004**; P6: 0.11
Serum lipase	85.3 ± 4.45	83 ± 3.37	86.5 ± 2.46	87.9 ± 2.02	36 ± 2.87	64.1 ± 4.82	84.3 ± 6.52	P1: 0.067; P2: 0.494; P3: 0.119; P4: 0.001**; P5: 0.001**; P6: 0.578

**Highly significant difference: $p < 0.001$. Data are shown as mean ± standard deviation; BMSCs — bone marrow mesenchymal stem cells; PRP — platelet-rich plasma; STZ — streptozotocin; P1 = control vs. sodium citrate; P2 = control vs. PRP; P3 = control vs. BMSCs; P4 = control vs. STZ; P5 = control vs. STZ + PRP; P6 = control vs. STZ + BMSCs

package for 10 min to obtain the immune label. Lastly, the nuclei were stained by Harry's haematoxylin stain and a light microscope was used to examine the binding antibody [2].

Morphometrical studies

Using a light microscopic examination of the ×400 images of the Mallory trichrome stain and anti-insulin antibody, the mean area percentage of collagen fibres and the number of insulin-positive beta-cells of all the animal groups were counted. By light microscopic inspection of the ×400 H&E, the diameter of the Langerhans islets was determined. Light microscope analyses of the toluidine blue stained section of ×400 were used to count the number of zymogen granules. In the Department of Histology, Faculty of Medicine, Menoufia University (Leica Q 500 MC programme, Wechsler, Germany), all measurements were taken using the image analyser. Examinations in 10 high-power fields in each sample were carried out.

Statistical studies

The statistical analysis was conducted in the mean ± standard error of mean (SEM) format using SPSS version 17 software (IBM Corporation, Somers, New York, USA). Using a one-way analysis of variance with post hoc analysis, the average of each group was compared with that of the other groups. In terms of chance, less than 0.01 at the p-value was the least significant quantity used.

RESULTS

General observation

Rats displayed normal behaviour in all groups, with the exception of excessive urination in diabetic rats, 2 days after the injection of STZ.

Biochemical results

Fasting blood glucose, serum lipase and amylase. In the control group, there was no significant difference between the rats (subgroups Ia, Ib, Ic, and Id). In the diabetic group, administration of STZ significantly increased blood glucose levels and decreased serum amylase and lipase levels relative to control rats ($p < 0.001$). Important rises in glucose levels and decreases in amylase and lipase levels in the Diabetic + PRP group were also observed relative to the Control group ($p < 0.001$). PRP triggered a significant decrease in glucose and a rise in the amount of amylase and lipase, relative to the diabetic group ($p < 0.001$). The Diabetic + BMSCs group displayed negligible variations in contrast to the Control group (Table 1, Fig. 2A–C).

Histological results

The histological and immunohistochemical findings of all group I (Control group) subgroups were similar. So, group I (Control group) applied to them.

Haematoxylin and eosin

All control subgroups displayed regular pancreatic architecture; the gland is covered by a capsule of thin connective tissue that sends septae separating it into lobes and lobules. The pancreatic lobules were formed of crowded acini separated by thin connective tissue septa. Acinar cell cytoplasm revealed both basal basophilia and apical acidophilia. Langerhans islets appeared among pancreatic acini as lightly stained areas (Figs. 3A, 4A).

Diabetic group showed loss of normal lobular architecture with congested dilated blood vessels. Some acinar cells showed vacuolation with pyknosis of their nuclei. Islets of Langerhans showed multiple
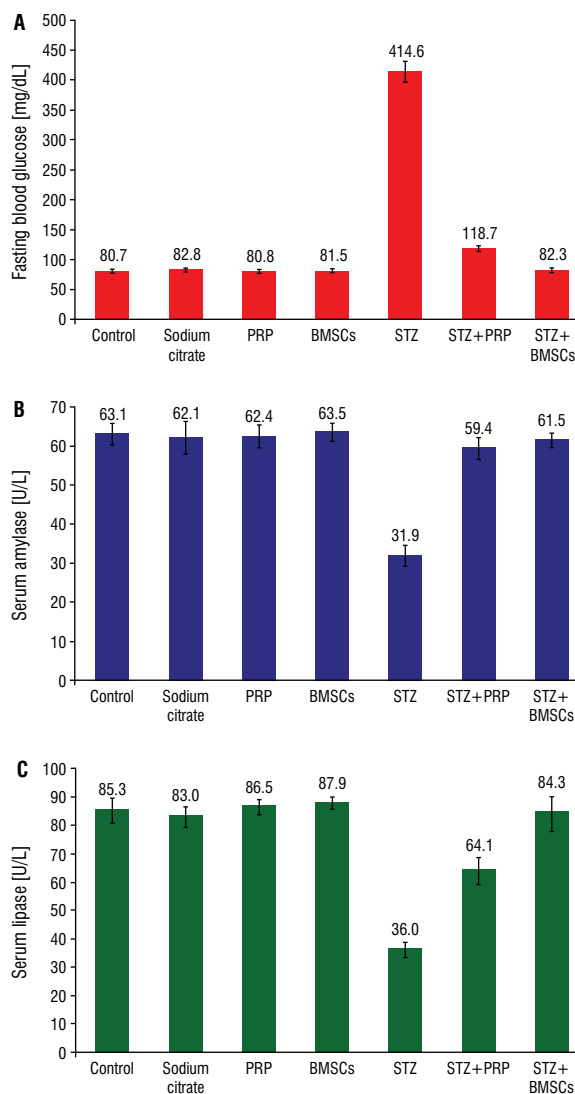
Figure 2. Fasting glucose (**A**), serum pancreatic amylase (**B**) and lipase levels (**C**) are illustrated in the graph; BMSCs — bone marrow mesenchymal stem cells; PRP — platelet-rich plasma; STZ — streptozotocin.

empty spaces, congested blood vessels and degenerative changes in some cells in the form of pyknosis of their nuclei and vacuolation of their cytoplasm (Figs. 3B, 4B).

Diabetic + PRP group pancreatic lobular architecture appeared almost identical to the Control group. However, there were still congested blood vessels and vacuolation of some acinar cells (Figs. 3C, 4C).

The group of Diabetic+ BMSCs displayed almost normal lobular pancreatic architecture. Acinar cells appeared in the nuclei of the vesicles. Normal Langerhans islet was found surrounded by normal acinar pancreatic tissue (Figs. 3D, 4D).

Mallory's trichrome stain

Sections of Control group showed thin connective tissue around blood vessels, in septae, in between pancreatic lobules and in islets of Langerhans (Fig. 5A).

Diabetic group showed excessive deposition of collagen fibres around thickened hypertrophied congested dilated blood vessels. Furthermore, islets of Langerhans showed massive deposition of collagen fibres (Fig. 5B).

The group treated with PRP showed moderate collagen fibres deposition between the pancreatic lobules (Fig. 5C). On the other hand, the injection of BMSCs showed a marked decrease in the value of collagen deposition (Fig. 5D).

Toluidine reaction

Sections of Control group showed abundant dark zymogen granules in the apical part of pancreatic acinar cells with normal features of their cells (Fig. 6A), while Diabetic group showed few apical zymogen granules in pancreatic acinar cells (Fig. 6B).

Meanwhile, PRP administration to diabetic rats (Diabetic + PRP group) induced an increase in number of zymogen granules in pancreatic acinar cells (Fig. 6C). Diabetic + BMSCs group showed normal distribution of zymogen granules in pancreatic acinar cells (Fig. 6D).

Immunohistochemical results

Strong positively stained insulin secretory granules of the beta-cells comprising the most common cell population of the islets were seen in sections of the control group (Fig. 7A).

Streptozotocin administration in diabetic group resulted in a decrease in the intensity of stained secretory granules of beta-cells, as well as a decrease in the number of cells and in the diameter of Langerhans islets (Fig. 7B).

Platelet-rich plasma administration to diabetic rats caused the positive stained secretory granules of beta-cells to increase moderately, primarily in the central core. There were also a few groups of unstained cells still present in the periphery of the islets (Fig. 7C).

The group of Diabetic + BMSCs displayed normal numbers of strong positively stained beta-cell secretory granules predominantly in the central core (Fig. 7D).

Electron microscopic results

With respect to electron microscopic results, subgroup Ia, Ib, Ic, and Id showed no significant difference, so they were represented as control group.
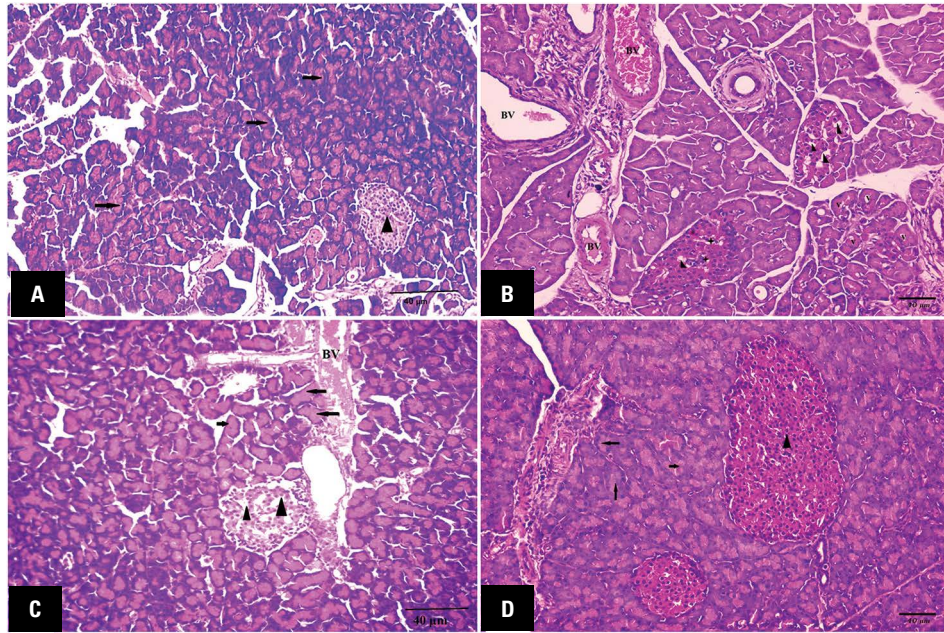
Figure 3. A. Stained pancreatic section of haematoxylin and eosin of the Control group showing pancreatic acinar cells (arrow). In between pancreatic acini, formed by cords of pale stained cells with foamy, the islet of Langerhans (arrow head) is also seen; **B**. Group II (Diabetic group) demonstrating congested dilated blood vessels (BV). Some acinar cells showed vacuolation (v) with their nuclei pyknosis. The Langerhans islets showed empty spaces (arrow head) and degenerative changes in some cells in the form of pyknotic nucleus and cytoplasm vacuolation (star); **C**. Group III (Diabetic + PRP group) showing congested blood vessels and certain acinar cells with pyknotic nucleus (arrow). The Langerhans Islets showed empty spaces (arrow head); **D**. Group IV (Diabetic + BMSCs group) reveals normal pancreatic lobular architecture. The acinar cells appear with vesicular nuclei (arrow). Normal pancreatic islet of Langerhans (arrow head) surrounded by normal pancreatic acini is seen. Scale bar: 40 μm.
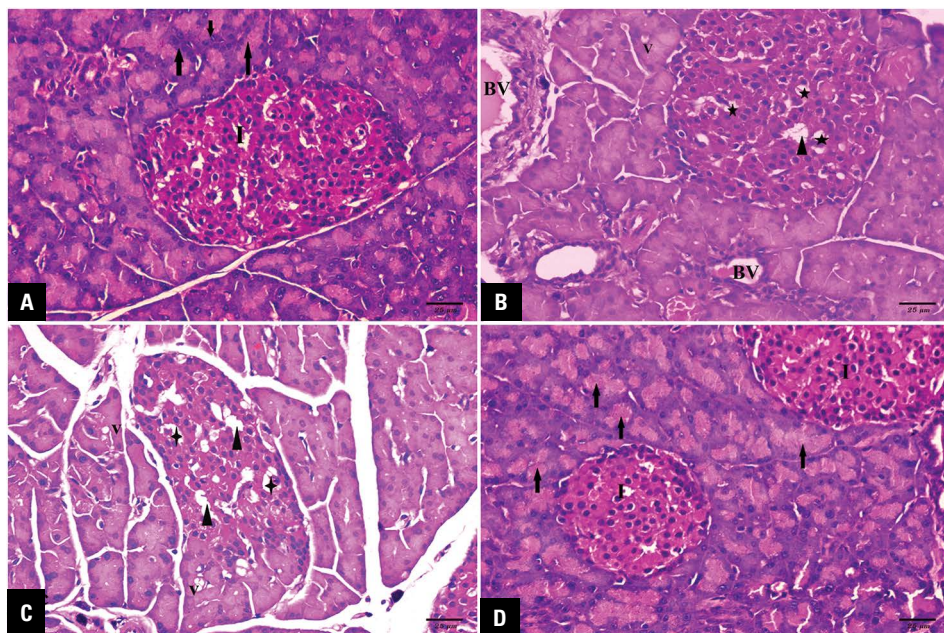
Figure 4. A. Stained pancreatic section haematoxylin and eosin of the Control group exhibiting pancreatic acinar cells appearing pyramidal with basal rounded vesicular nuclei (arrow). Between pancreatic acini, formed of cords of pale stained cells with foamy cytoplasm, the islet of Langerhans (I) is also seen; **B**. Group II (Diabetic group) showing dilated congested blood vessels (BV). Some acinar cells showed vacuolation (V) with their pyknotic nuclei. Langerhans islets showed empty spaces (arrow head) and degenerative changes in some cells in the form of cytoplasmic vacuolation (star); **C**. Group III (Diabetic + PRP group) showing vacuolation (v) of some acinar cells with pyknotic nucleus. The islets of Langerhans showed empty spaces in their cells (arrow head) and vacuolation (star); **D**. Group IV (Diabetic + BMSCs group) showing normal pancreatic lobular architecture, normal pancreatic islet of Langerhans (I) surrounded by normal pancreatic acini (arrow). Scale bar: 25 μm.
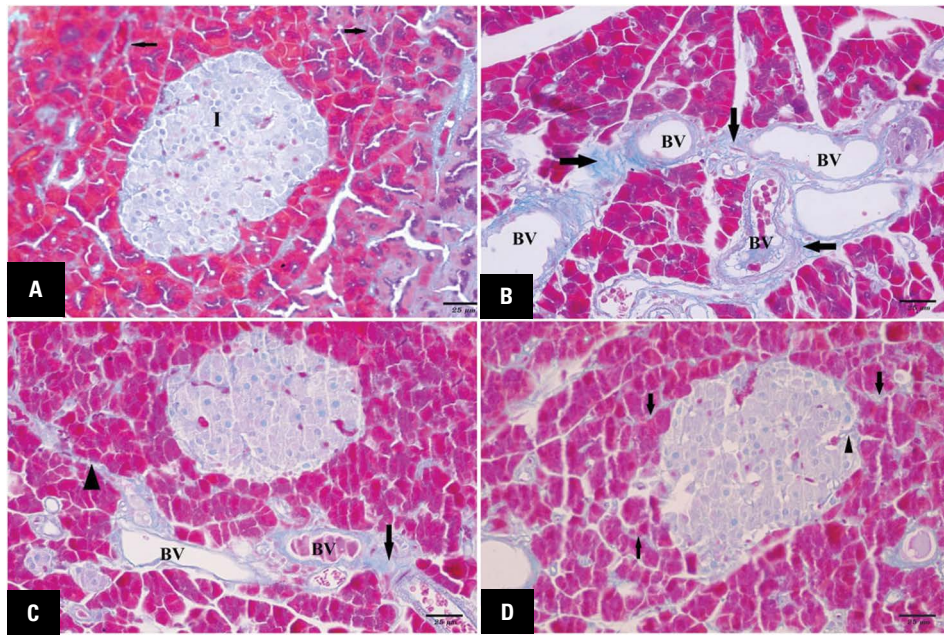
Figure 5. A. Mallory's trichrome stained portion of the control group pancreas showing thin connective tissue septae (arrow) between pancreatic acini and lobules; **B**. Group II (Diabetic group) exhibiting dilated blood vessels (BV) with large deposition of collagen fibres around blood vessels (arrow); **C**. Group III (Diabetic + PRP group) exhibiting mild deposition of collagen fibres between pancreatic acini (arrow head) and around blood vessels (arrow); **D**. Group IV (Diabetic + BMSCs group) exhibiting thin collagen fibres between pancreatic acini (arrow) and cells of islets of Langerhans (arrow head). Scale bar: 25 μm.
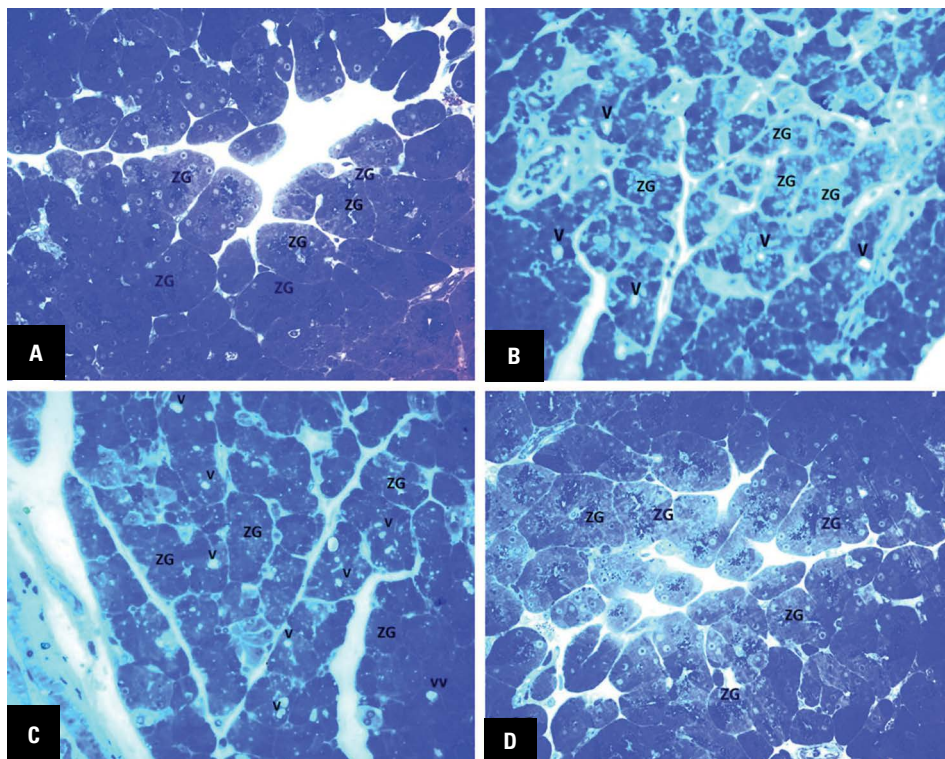
Figure 6. A. Toluidine blue stained pancreatic section of the control group displaying zymogen granules (ZG) in the apical part of the pancreatic acini-lined cells; **B**. Group II (Diabetic group) showing few apical ZG in most pancreatic acini with multiple vacuoles (v); **C**. Group III (Diabetic + + PRP group) showing increase in number of apical ZG with several vacuolations (v) of their cytoplasm in most acinar cells; **D**. Group IV (Diabetic + BMSCs group) displaying ZG in the apical portion of the cells lining pancreatic acini.
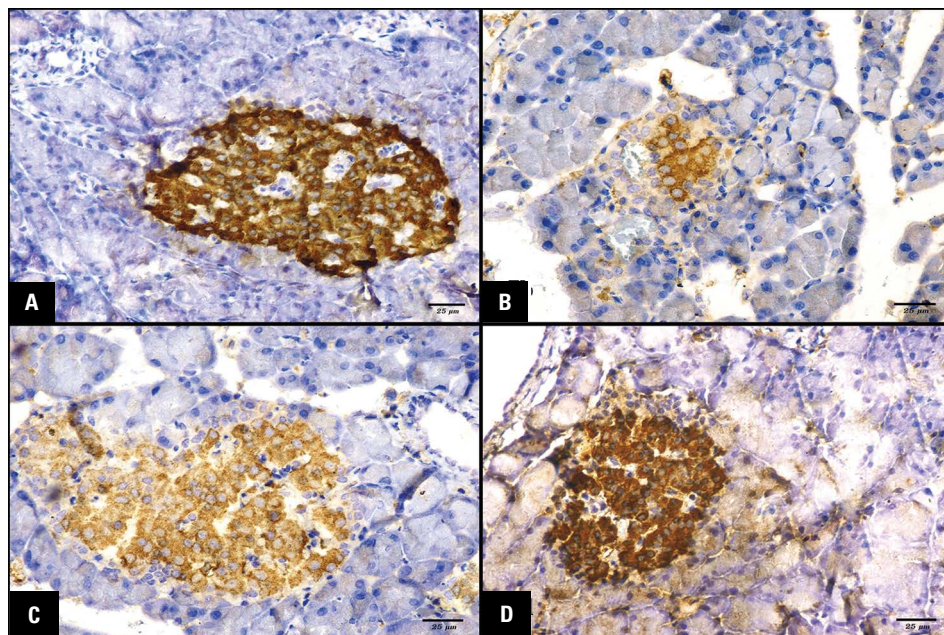
Figure 7. A. Pancreatic section stained anti-insulin antibodies of the control group exhibiting strong positively stained beta-cells for anti-insulin antibodies constituted by the main population of the Langerhans islet, leaving few central unstained cells; **B**. Group II (Diabetic group) with very few weak positive stained beta-cells exhibiting anti-insulin antibodies located mainly in the central part of the islet; **C**. Group III (Diabetic + + PRP group) with a moderate positive reaction of stained beta-cells to anti-insulin antibodies. The majority of unstained cell groups are located in the peripheral portion of the islet; **D**. Group IV (Diabetic + BMSCs group) showing strong positively stained beta-cells for anti-insulin antibodies which constitute the largest population of the Langerhans islet leaving few unstained central cells.

Pancreatic acinar cells with basal rounded vesicular nuclei and prominent nucleoli were shown by electron microscopic analysis of the control rat's pancreas. Acinar cells displayed packed cisterns of the rough endoplasmic reticulum (RER) and variable mitochondria in their cytoplasm. Apically, electron dense zymogen granules of variable sizes were located (Fig. 8A).

There were primarily beta-cells in the Langerhans islets. Many electron dense secretory granules surrounded by large lucent halo, mitochondria, and euchromatic nucleus accommodate their cytoplasm. Alpha-cell granules were small and electron dense (Fig. 8B).

Ultrathin sections of Diabetic group (group II) showed pancreatic acini with irregular electron dense nuclei, dilated RER, degenerated (balloon-shaped) mitochondria and phagosomes, some acinar cells were degenerated (Fig. 9A, B). Langerhans islets primarily contain beta-cells with few secretory granules displaying distorted Golgi apparatus morphology, degenerated mitochondria and pyknotic nucleus (Fig. 9C).

Platelet-rich plasma-treated rat pancreas (group III) with acinar cells displayed euchromatic nuclei surrounded by disrupted RER focal area and normal mitochondria (Fig. 10A). There are many electron dense secretory granules in the cytoplasm of islets beta-cells surrounded by large lucent halos, mitochondria, euchromatic nucleus, and mildly dilated Golgi cisternae (Fig. 10B).

As shown by the presence of regular pancreatic acinar cells, the pancreatic acini of the Diabetic + + BMSCs group showed marked improvement. Cytoplasm of acinar cells revealed regularly organised cisternae of RER, typical mitochondria and variable sized electron dense granules (Fig. 11A). The nuclei appeared vesicular and rounded. Cytoplasm beta-cells containing several dense electron secretory granules surrounded by wide lucent halos, mitochondria, and euchromatic nucleus were shown (Fig. 11B).

Morphometric results

Mean area percentage of collagen fibre deposition in pancreatic tissues. The Diabetic group (group II) reported a marked increase in the mean area percentage of pancreatic collagen deposition, which was significantly higher compared to the mean value of the control subgroups (Ia, Ib, Ic, and Id). The mean area percentage of collagen fibres displaying an increased value was seen in group III, which was statistically significant compared to the Control group ($p > 0.05$).
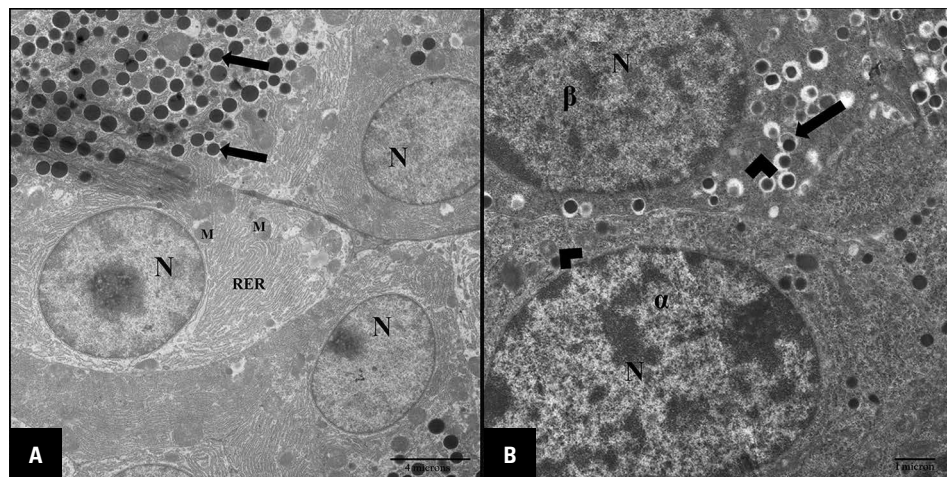
Figure 8. A. Group I (Control group) demonstrating acinar cells with euchromatic nuclei (N) and many electron dense secretory granules (arrow) of variable size, more or less normal mitochondria (M) and rough endoplasmic reticulum (RER) (×8000); **B**. Group I (Control group) showing Langerhans islets incorporating beta-cells (β) and alpha-cells (α). Many electron-dense secretory granules of beta-cells surrounded by a large light halo (arrow), mitochondria (arrow head), and euchromatic nucleus (N), while alpha-cell granules were small and electron-dense (×17500).
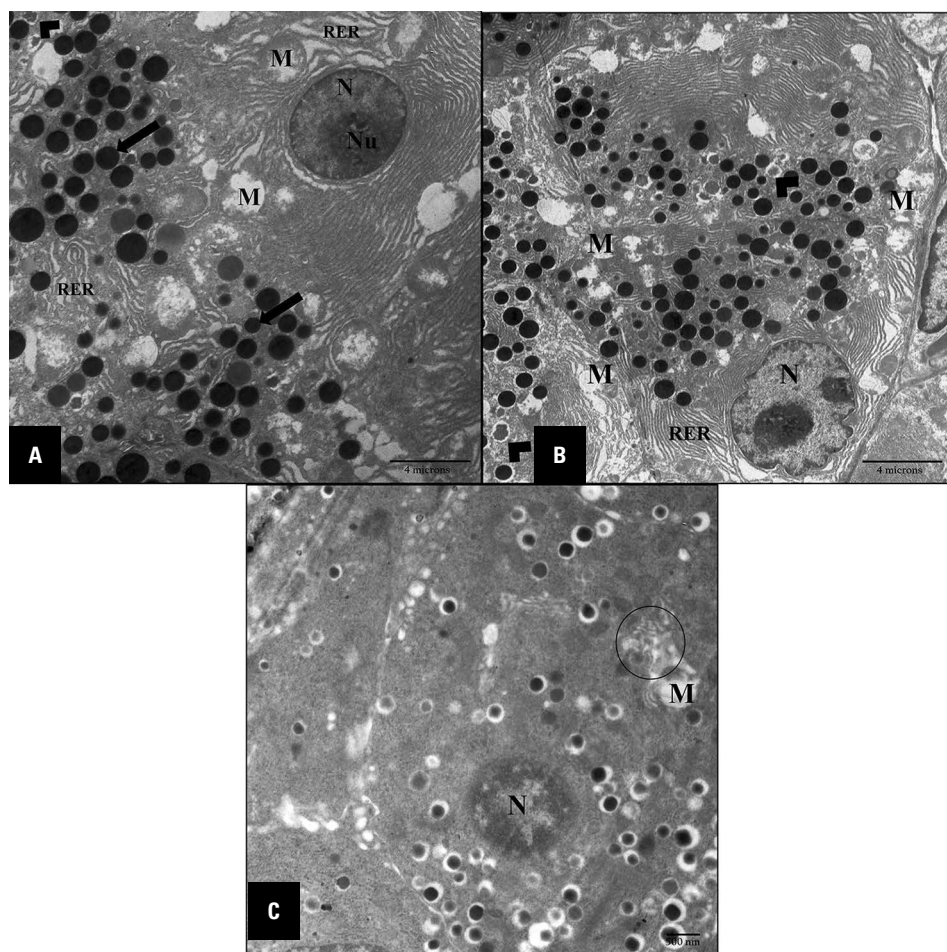
Figure 9. A. Group II (Diabetic group) displaying a large central nucleolus (Nu) hyperchromatic nucleus (N), massive dilated rough endoplasmic reticulum (RER), balloon-shaped mitochondria (M) and phagosomes (arrow head). Note the variable-sized apical secretory granules (arrow) (×8000); **B**. Pancreatic acinar cells of group II (Diabetic group) with abnormal pancreatic acinar nucleus (N) surrounded by dilated rough endoplasmic reticulum (RER) with distorted mitochondria (M) and phagosomes (arrow head) (×8000); **C**. Group II (Diabetic group) Langerhans islets include distorted Golgi apparatus morphology (circle), degenerated mitochondria (M) and non-clear and swollen nuclear membrane (N) of beta-cells (×17500).
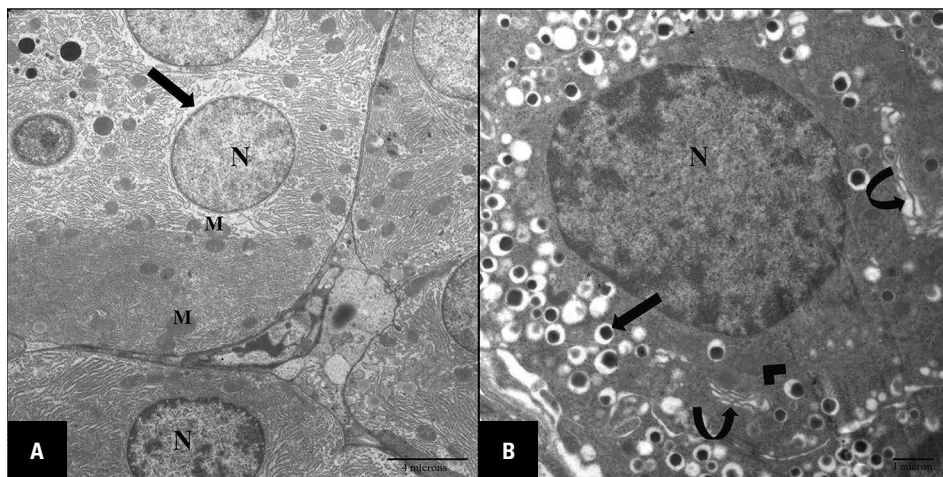
Figure 10. A. Group III (Diabetic + PRP group) showing euchromatic nucleus (N), acinar cells surrounded by focal disrupted rough endoplasmic reticulum (arrow), most likely normal mitochondria (M) (×8000); **B**. Group III showing beta-cell-containing islets of Langerhans with several dense electron secretory granules surrounded by a large light halo (arrow), mitochondria (arrow head), euchromatic nucleus (N), and mildly dilated Golgi flattened vesicles (curved arrow) (×17500).
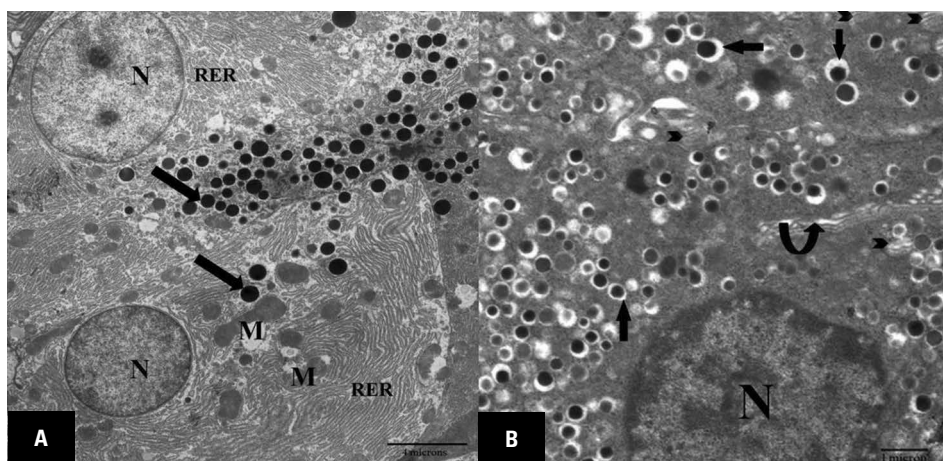
Figure 11. A. Group IV (Diabetic + BMSC group) displaying euchromatic nucleus (N) acinar cells and multiple electron dense secretory granules of variable size (arrow), mild degenerated mitochondria (M) and most likely regular rough endoplasmic reticulum (RER) (×8000); **B**. Group IV (Diabetic + BMSCs group) showing Langerhans islets incorporate beta-cells with several dense secretory granules surrounded by a large light halo (arrow), mitochondria (arrow head) and euchromatic nucleus (N), normal Golgi apparatus morphology (curved arrow) (×17500).

Group IV, on the other hand, displayed normal value with no noticeable difference relative to Control group.

Number of beta-cells/islet, diameter of islets and number of zymogen granules. In the control subgroups (Ia, Ib, Ic, and Id), there were no substantial variations between the rats in the number of cells of the Langerhans islets, the diameter of the Langerhans islets and the number of zymogen granules. The administration of STZ in the Diabetic group resulted in a substantial decrease in the number of cells of the Langerhans islets, in the diameter of the Langerhans islets, as well as in the number of gran-

ules of zymogen. Meanwhile, the administration of PRP to diabetic rats (Diabetic + PRP group) has led to a significant decrease in the number of Langerhans islet cells, the diameter of Langerhans islets and the number of zymogen granules compared to the control group, and a significant increase in the number of Langerhans islet cells, the diameter of Langerhans islets and the number of zymogen granules compared to diabetic rats (p < 0.001).

The Diabetic + BMSCs group showed a noticeable increase in the number of Langerhans islet cells, the diameter of Langerhans islets and the number of zymogen

Table 2. Morphometric results: number of beta-cells/islet, diameter of islets, number of zymogen granules and mean area percentage of collagen fibres

	Control	Sodium citrate	PRP	BMSCs	STZ	STZ + PRP	STZ + BMSCs	P value
Mean area percentage of collagen fibres	8.21 ± 0.66	8.5 ± 0.419	8.52 ± 0.48	8.41 ± 0.55	29.4 ± 2.27	20.6 ± 2.07	8.4 ± 0.66	P1: 0.4; P2: 0.06; P3: 0.13; P4: 0.001**; P5: 0.001**; P6: 0.41
Number of beta-cells/islet	212.9 ± 3.14	210.1 ± 3.7	210.7 ± 2.1	213.2 ± 3.16	75 ± 4.29	142.7 ± 5.54	215.8 ± 3.52	P1: 0.12; P2: 0.06; P3: 0.797; P4: 0.001**; P5: 0.001**; P6: 0.046*
Diameter of islets	309.8 ± 2.3	305.9 ± 5.4	309.2 ± 2.3	312.1 ± 2.96	171 ± 6.2	219 ± 6.6	312.3 ± 3.97	P1: 0.037; P2: 0.616; P3: 0.102; P4: 0.001**; P5: 0.001**; P6: 0.12
Number of zymogen granules	53.1 ± 2.77	52.1 ± 4.07	52.4 ± 2.63	53.5 ± 2.17	23.9 ± 5.7	51.3 ± 2.5	52.9 ± 1.85	P1: 0.45; P2: 0.41; P3: 0.65; P4: 0.001**; P5: 0.15; P6: 0.81

*Significant difference: p < 0.01; **Highly significant difference: p < 0.001. Data are shown as mean ± standard deviation; BMSCs — bone marrow mesenchymal stem cells; PRP — platelet-rich plasma; STZ — streptozotocin; P1 = control vs. sodium citrate; P2 = control vs. PRP; P3 = control vs. BMSCs; P4 = control vs. STZ; P5 = control vs. STZ + PRP; P6 = control vs. STZ + BMSCs
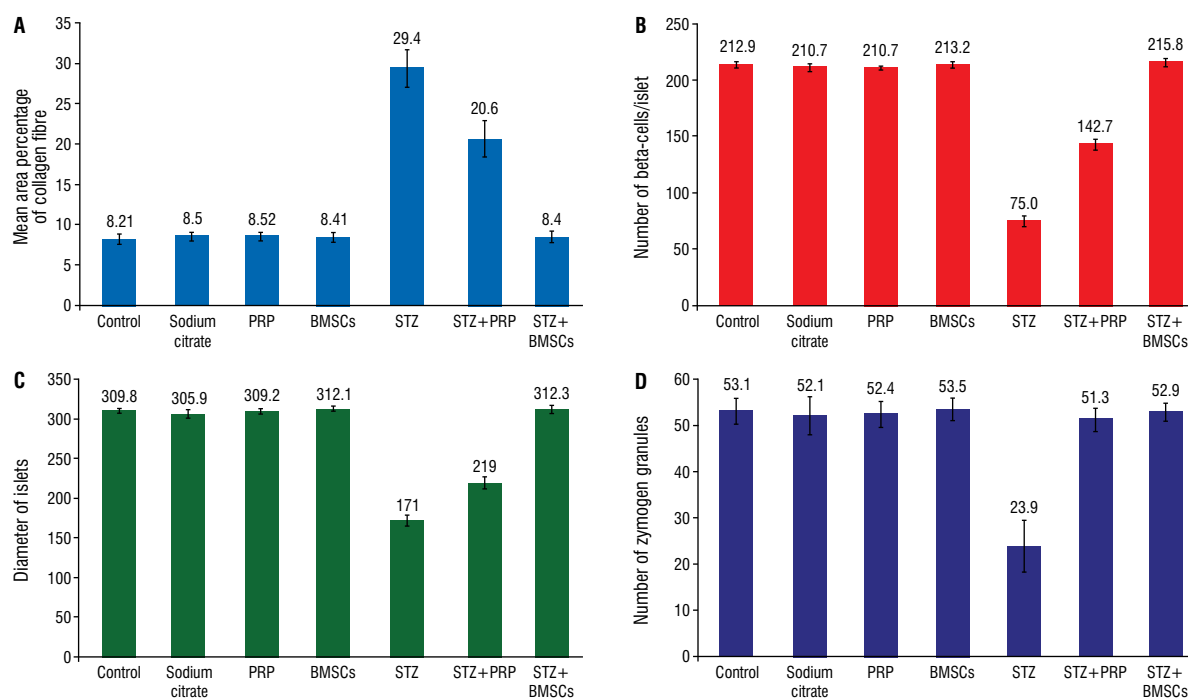
Figure 12. View graphs; **A**. Mean area percentage of collagen; **B**. Number of beta-cells/islet; **C**. Islet diameter; **D**. Number of granules of zymogen; BMSCs — bone marrow mesenchymal stem cells; PRP — platelet-rich plasma; STZ — streptozotocin.

granules (p < 0.001) compared to Diabetic and Diabetic + PRP groups, and showed an insignificant difference compared to the Control group (Table 2, Fig. 12A–D).

DISCUSSION

In this study, 48 hours after STZ administration, T1DM was induced when blood glucose levels exceeded 250 mg/dL [58]. This correlates with previous studies demonstrating that a single 60 mg/kg dose of STZ can minimise the secretion of insulin and destruct pancreatic beta-cells in rats [3].

In this study, H&E in the Diabetic group of exocrine pancreatic acini as well as the Langerhans islets showed loss of normal lobular architecture, congested dilated blood vessels, necrosis, vacuolation and apoptotic pyknotic nuclei.

These changes are close to the observations of the congested blood vessels and darkly stained pyknotic

nuclei of some diabetic rat acinar cells [41, 45] that observed nearly all acinar cells in diabetic rats were swollen with small vacuoles. These results are consistent with Nurdiana et al. [41] that revealed histological destruction of the pancreatic islets of diabetic rats. Our findings coincide with Omar and Aboulkhair [45] who documented cell necrosis with congested blood capillaries, apoptosis in beta-cell of Langerhans and vacuolations in their cytoplasm. Ismail et al. [26] documented damage to the beta-cell of Langerhans due to STZ injection. Vacuolation has been described as one of the membrane permeability disorders that led to the transport of water and electrolytes into the cell. Significant cellular membrane damage resulting from lipid peroxidation mediating reactive oxygen species can be referred to as a permeability disorder [22].

The effect of STZ on the pancreas was explained by a decrease in cellular NAD+ and adenosine triphosphate (ATP) and an increase in the release of reactive oxygen species secondary to the passage of STZ through the cell membranes, causing alkylation and DNA damage, as well as the release of nitric oxide inside the cells which inhibits the action of aconitase, causing further DNA damage [3]. In addition, chronic diabetes hyperglycaemia contributes to increased development of oxygen-free radicals through glucose autoxidation, lipid peroxidation, and protein glycosylation, resulting in disruption of the oxidative/anti-oxidative balance, resulting in oxidative stress and cellular harm in turn. These effects could result in the degeneration after STZ injection of islet beta-cells and pancreatic acinar cells [52].

The previous histological results of the destruction of islet beta-cells in the present study could explain the substantial increase in blood glucose levels and the apparent decrease in the number of Langerhans islet cells and the diameter of Langerhans islet cells in the diabetic group compared to the control group. This interpretation is agreed by others [40] who have explained that the drop in plasma insulin levels caused by selective pancreatic beta-cell necrosis is the cause of hyperglycaemia.

There was a decrease in serum amylase and lipase in the Diabetic group in this study.

These results are in agreement with Sano et al. [51] who documented damage to beta-cells with decreased synthesis of amylase and release from the exocrine pancreas of diabetic rats, pointing to the close connection between the endocrine and exocrine sections of the pancreas of the vascular network. In addition, marked decrease in amylase enzyme has been documented in STZ-diabetic mouse pancreatic acinar cells [4]. These findings suggest that the presence of insulin receptors on acinar cells is involved in the control of insulin function. In order to control cytosolic Ca^{2+} signals in acinar cells, ATP is well recognized and ATP production in acinar cells was inhibited by glucose metabolism in DM. Therefore, decreased cytosolic Ca^{2+} signals secondary to DM may be linked in reducing the secretion of digestive enzymes [30]. However, elevations in serum pancreatic amylase and lipase were reported for paediatric diabetic ketoacidosis [49].

Excessive deposition of collagen fibres was detected by Mallory's trichrome stain inspection of the Diabetic group. These results coincide with El-Desouki et al. [18] and Sorour et al. [55] that revealed increased collagen fibres around the islands of Langerhans, the pancreatic acini, the blood vessels and intercalated ducts in the diabetic group. Pancreatic fibrosis may be caused by pancreatic stellate cells (PSCs). Hyperglycaemia leads to the activation of PSCs in diabetes, resulting in fibrotic changes. In addition, stellate cell invasions of the pancreatic islets contribute to the destruction of fibrotic islets, resulting in a decline in beta-cell proliferation and a rush to apoptosis in diabetic patients [29]. Localised PSCs have begun to proliferate, morphologically turn into myofibroblast-like cells, and secrete components of the extracellular matrix once activated [8]. Moreover, collagen fibres were found allowing inadequate oxygen to enter the tissue, leading to degenerative changes and necrosis [3]. Furthermore, severe tissue damage following cytotoxic STZ-induced diabetes has caused lymphocytic depletion to increase reticular fibres [1].

Diabetic group showed few apical zymogen granules, which documented in agreement with other findings, that related decreased zymogen granules significantly to decrease serum amylase and acinar cell atrophy in diabetic rats [51]. Likewise, ultrastructural changes of acinar cells, such as electron dense nuclei, dilated RER, degenerated mitochondria and phagosomes, were detected. These findings agreed with others [18] that recorded dilatation and vesiculation of exocrine acinar cells with RER cisternae and mitochondrial disruption in diabetic rats due to disorganisation of cytoskeleton and integral proteins on the RER and the accumulation of iso-osmotic fluid in the injured cell.

Langerhans islets beta-cells revealed degenerative changes such as distorted Golgi apparatus morphology, degenerated mitochondria and pyknotic nucleus with few secretory granules ultrastructurally. Similar findings have been documented in pancreatic beta-cells of diabetic rats with alloxan or STZ [28]. Moreover, El-Desouki et al. [18] showed that pancreatic beta-cells were degenerated with a pronounced decreased and breakdown of their granules. STZ caused damage to both the exocrine and endocrine portions of the pancreas. The most promising methods for the treatment of DM have recently been targeting the pancreatic beta-cell [60].

Current findings of the Diabetic + PRP group have shown an improvement in the histological picture of pancreatic islet cells and acini. These improvements have been confirmed by a decrease in blood glucose, increase in serum amylase and lipase levels with a modest increase in the amount of positively stained beta-cell secretory granules. These findings coincided with El-Tahawy et al. [19] who found improvement in the morphology of the pancreas, several healthy islets with an increase in the number of beta-cells, and a substantial decrease in blood glucose levels in the Diabetic + PRP treated group. The biological characteristics of PRP depend on the platelets concentration; convenient PRP preparations can provide high concentrations of many GFs, including IGF, EGF, and TGFβ. PRP should contain at least one million platelets per microliter to be value for tissue repair [21]. GFs originated from PRP may be used as prospective therapies for diabetes as it can induce in vivo pancreatic beta-cell proliferation, regeneration and insulin production [36]. Moreover, a substantial elevation in GFs molecules, like VEGF, was noticed after treatment with a single dose of leukocyte-rich PRP [7]. In addition, Bonner-Weir et al. [12] clarified the production of new islet cells from progenitors in postnatal rodents via the neo-genesis process. Some cells derived from hormone progenitors present near the ducts in the adult pancreas and are transformed in adult mice into hormone-positive islet cells [63]. In both rodents and humans, endocrine cells can also be discovered in exocrine cells. Similarly, the long-term low dose administration of EGF induced beta-cell neogenesis in diabetic mice and resulted in ductal cell differentiation into beta-cells [64].

From the current study, it could be inferred that BMSCs could alleviate the degeneration of beta-cells and acinar cells induced by STZ. These findings were confirmed by the results of Omar and Aboulkhair [45] that showed normal histological structure of the Langerhans islets and the pancreatic acini with a substantial decrease in the mean random blood sugar level value, abundant positive insulin immunoreaction, with a significant increase in the mean area of islets beta-cells in the treated BMSCs group compared to the Diabetic group.

These assumptions in the histological and biochemical improvement of the Diabetic + BMSCs group in the current study were coincided with the findings that BMSCs have a crucial role in repairing injured tissues. They may differentiate, to replace the dead cells and to stimulate surrounding cells in the microenvironment, by secreting stimulant factors to boost the tissue repair process [61]. Consequently, BMSCs may be applied to treat tissue dysfunction in chronic hyperglycaemia. By replacing T1DM with either in vitro or in vivo differentiation, local microenvironment modulation by cytokines, chemokines and factors that promote endogenous regeneration, and by reducing or preventing autoimmunity of beta-cells, MSC transplantation may increase the mass of beta-cells [20]. Similarly, Ianus et al. [24] found that the stem cells survived and differentiated into beta-cells resulting in an increase in the number and size of islets of Langerhans. Similarly, by observing normal blood glucose levels and neovascular formation after co-transplantation of pancreatic MSCs and islet mass, Sordi et al. [54] suggested the role of MSCs as helper cells. In comparison, other authors [16, 23] have found that the hyperglycaemic environment of diabetic patients reduces the proliferative capacity of MSCs, thus increasing cell apoptosis.

CONCLUSIONS

The present study reveals a model by STZ for T1DM. Promising treatments for diabetics are BMSCs and PRP. Their results are clearly visible. Due to their improved histological and ultrastructural protection of the pancreas and their ability to increase the number of cells in the islets of Langerhans, to decrease the amount of glucose and to increase serum amylase and lipase enzymes, the use of BMSCs may be more successful than PRP. PRP, however, is much less expensive than BMSC.

Conflict of interest: None declared

REFERENCES

1. Abdel-Wahab MH, Abd-Allah AR. Possible protective effect of melatonin and/or desferrioxamine against streptozotocin-induced hyperglycaemia in mice. Pharmacol Res. 2000; 41(5): 533–537, doi: 10.1006/phrs.1999.0614, indexed in Pubmed: 10753552.

2. Abdul-Hamid M, Moustafa N. Protective effect of curcumin on histopathology and ultrastructure of pancreas in the alloxan treated rats for induction of diabetes. J Basic Applied Zool. 2013; 66(4): 169–179, doi: 10.1016/j. jobaz.2013.07.003.

3. Abu-nasef SK, Amin HA, Abdel-Hamid GA. A histological and immunohistochemical study of beta cells in streptozotocin diabetic rats treated with caffeine. Folia Histochem Cytobiol. 2014; 52(1): 42–50, doi: 10.5603/FHC.2014.0005, indexed in Pubmed: 24802960.

4. Akpan OU, Bassey RB, Agba BS, et al. Elevation of serum pancreatic amylase and distortion of pancreatic cyto-architecture in type 1 diabetes mellitus rats treated with Ocimum gratissimum. Niger Med J. 2014; 55(1): 34–38, doi: 10.4103/0300-1652.128157, indexed in Pubmed: 24970967.

5. Alshehri AM. Metabolic syndrome and cardiovascular risk. J Family Community Med. 2010; 17(2): 73–78, doi: 10.4103/1319-1683.71987, indexed in Pubmed: 21359028.

6. American Diabetes Association. Diagnosis and classification of diabetes mellitus. Diabetes Care. 2005; 28 (Suppl 1): S37–S42, doi: 10.2337/diacare.28.suppl_1.s37, indexed in Pubmed: 15618111.

7. Amy SW, Hillary B, Alex HS, et al. The systemic effects of platelet-rich plasma injection. Am J Sports Med. 2013; 41(1): 186–193, doi: 10.1177/0363546512466383, indexed in Pubmed: 23211708.

8. Apte M, Pirola R, Wilson J. New insights into alcoholic pancreatitis and pancreatic cancer. J Gastroenterol Hepatol. 2009; 24 Suppl 3: S51–S56, doi: 10.1111/j.1440-1746.2009.06071.x, indexed in Pubmed: 19799699.

9. Augello A, Kurth TB, De Bari C. Mesenchymal stem cells: a perspective from in vitro cultures to in vivo migration and niches. Eur Cell Mater. 2010; 20: 121–133, doi: 10.22203/ecm.v020a11, indexed in Pubmed: 21249629.

10. Bainbridge KE, Hoffman HJ, Cowie CC. Diabetes and hearing impairment in the United States: audiometric evidence from the National Health and Nutrition Examination Survey, 1999 to 2004. Ann Intern Med. 2008; 149(1): 1–10, doi: 10.7326/0003-4819-149-1-200807010-00231, indexed in Pubmed: 18559825.

11. Bancroft JD, Layton C. Theory and practice of histological technique. 7th ed. Churchill Livingstone, London 2010: 173–214.

12. Bonner-Weir S, Li WC, Ouziel-Yahalom L, et al. Beta-cell growth and regeneration: replication is only part of the story. Diabetes. 2010; 59(10): 2340–2348, doi: 10.2337/db10-0084, indexed in Pubmed: 20876724.

13. Cao M, Pan Q, Dong H, et al. Adipose-derived mesenchymal stem cells improve glucose homeostasis in high-fat diet-induced obese mice. Stem Cell Res Ther. 2015; 6: 208, doi: 10.1186/s13287-015-0201-3, indexed in Pubmed: 26519255.

14. Cavallo C, Roffi A, Grigolo B, et al. Platelet-rich plasma: the choice of activation method affects the release of bioactive molecules. Biomed Res Int. 2016; 2016: 6591717, doi: 10.1155/2016/6591717, indexed in Pubmed: 27672658.

15. Cemek M, Kağa S, Simşek N, et al. Antihyperglycemic and antioxidative potential of Matricaria chamomilla L. in streptozotocin-induced diabetic rats. J Nat Med. 2008; 62(3): 284–293, doi: 10.1007/s11418-008-0228-1, indexed in Pubmed: 18404309.

16. Cheng NC, Hsieh TY, Lai HS, et al. High glucose-induced reactive oxygen species generation promotes stemness in human adipose-derived stem cells. Cytotherapy. 2016; 18(3): 371–383, doi: 10.1016/j.jcyt.2015.11.012, indexed in Pubmed: 26780864.

17. Chudakov DM, Matz MV, Lukyanov S, et al. Fluorescent proteins and their applications in imaging living cells and tissues. Physiol Rev. 2010; 90(3): 1103–1163, doi: 10.1152/physrev.00038.2009, indexed in Pubmed: 20664080.

18. El-Desouki NI, Basyony M, El-Nenaey M, et al. Histological and cytological studies on the effect of melatonin on experimentally induced pancreatic diabetes in rats. Egypt J Exp Biol (Zoo.). 2007; 3: 69–82.

19. El-Tahawy NF, Rifaai R, Saber E, et al. Effect of platelet rich plasma (PRP) injection on the endocrine pancreas of the experimentally induced diabetes in male albino rats: a histological and immunohistochemical study. J Diab Metab. 2017; 08(03), doi: 10.4172/2155-6156.1000730.

20. Ezquer M, Arango-Rodriguez M, Giraud-Billoud M. Mesenchymal stem cell therapy in type 1 diabetes mellitus and its main complications: from experimental findings to clinical practice. J Stem Cell Res Ther. 2014; 4(8), doi: 10.4172/2157-7633.1000227.

21. Gandhi A, Bibbo C, Pinzur M, et al. The role of platelet-rich plasma in foot and ankle surgery. Foot Ankle Clin. 2005; 10(4): 621–37, viii, doi: 10.1016/j.fcl.2005.06.009, indexed in Pubmed: 16297823.

22. Halliwell B, Chirico S. Lipid peroxidation: its mechanism, measurement, and significance. Am J Clin Nutr. 1993; 57(5 Suppl): 715S–724S; discussion 724S, doi: 10.1093/ajcn/57.5.715S, indexed in Pubmed: 8475889.

23. Hankamolsiri W, Manochantr S, Tantrawatpan C, et al. The effects of high glucose on adipogenic and osteogenic differentiation of gestational tissue-derived mscs. Stem Cells Int. 2016; 2016: 9674614, doi: 10.1155/2016/9674614, indexed in Pubmed: 27057179.

24. Ianus A, Holz GG, Theise ND, et al. In vivo derivation of glucose-competent pancreatic endocrine cells from bone marrow without evidence of cell fusion. J Clin Invest. 2003; 111(6): 843–850, doi: 10.1172/JCI16502, indexed in Pubmed: 12639990.

25. Isik AT, Celik T, Ural AU, et al. Mesenchymal stem cell therapy for the streptozotocin-induced neurodegeneration in rats. Neurol Res. 2016; 38(4): 364–372, doi: 10.1080/01616412.2016.1139292, indexed in Pubmed: 27078696.

26. Ismail ZM, Kamel AM, Yacoub MF, et al. The effect of in vivo mobilization of bone marrow stem cells on the pancreas of diabetic albino rats (a histological & immunohistochemical study). Int J Stem Cells. 2013; 6(1): 1–11, doi: 10.15283/ijsc.2013.6.1.1, indexed in Pubmed: 24298369.

27. Kahn S, Cooper M, Del Prato S. Pathophysiology and treatment of type 2 diabetes: perspectives on the past, present, and future. Lancet. 2014; 383(9922): 1068–1083, doi: 10.1016/s0140-6736(13)62154-6.

28. Kanter M, Uysal H, Karaca T, et al. Depression of glucose levels and partial restoration of pancreatic beta-cell damage by melatonin in streptozotocin-induced diabetic rats. Arch Toxicol. 2006; 80(6): 362–369, doi: 10.1007/s00204-005-0055-z, indexed in Pubmed: 16341692.

29. Kim JW, Ko SH, Cho JH, et al. Loss of beta-cells with fibrotic islet destruction in type 2 diabetes mellitus. Front Biosci. 2008; 13: 6022–6033, doi: 10.2741/3133, indexed in Pubmed: 18508639.

30. Kluge R, Scherneck S, Schürmann A, et al. Pathophysiology and genetics of obesity and diabetes in the New Zealand obese mouse: a model of the human metabolic syndrome. Methods Mol Biol. 2012; 933: 59–73, doi: 10.1007/978-1-62703-068-7_5, indexed in Pubmed: 22893401.

31. Knezevic NN, Candido KD, Desai R, et al. Is platelet-rich plasma a future therapy in pain management? Med Clin North Am. 2016; 100(1): 199–217, doi: 10.1016/j.mcna.2015.08.014, indexed in Pubmed: 26614728.

32. Lambrinoudaki I, Vlachou SA, Creatsas G. Genetics in gestational diabetes mellitus: association with incidence, severity, pregnancy outcome and response to treatment. Curr Diabetes Rev. 2010; 6(6): 393–399, doi: 10.2174/157339910793499155, indexed in Pubmed: 20879971.

33. Landt M, Hortin GL, Smith CH, et al. Rapid measurement of serum pancreatic amylase. J Clin Lab Anal. 1994; 8(1): 10–15, doi: 10.1002/jcla.1860080104, indexed in Pubmed: 7513020.

34. Maahs DM, West NA, Lawrence JM, et al. Epidemiology of type 1 diabetes. Endocrinol Metab Clin North Am. 2010; 39(3): 481–497, doi: 10.1016/j.ecl.2010.05.011, indexed in Pubmed: 20723815.

35. Mani R, Mahantesha S, Nandini S, et al. Growth factors in periodontal regeneration. J Adv Oral Res. 2018; 5(2): 1–5, doi: 10.1177/2229411220140201.

36. Márquez-Aguirre AL, Canales-Aguirre AA, Padilla-Camberos E, et al. Development of the endocrine pancreas and novel strategies for beta-cell mass restoration and diabetes therapy. Braz J Med Biol Res. 2015; 48(9): 765–776, doi: 10.1590/1414-431X20154363, indexed in Pubmed: 26176316.

37. Marx RE. Platelet-rich plasma: evidence to support its use. J Oral Maxillofac Surg. 2004; 62(4): 489–496, doi: 10.1016/j.joms.2003.12.003, indexed in Pubmed: 15085519.

38. Marx RE, Carlson ER, Eichstaedt RM, et al. Platelet-rich plasma: growth factor enhancement for bone grafts. Oral Surg Oral Med Oral Pathol Oral Radiol Endod. 1998; 85(6): 638–646, doi: 10.1016/s1079-2104(98)90029-4, indexed in Pubmed: 9638695.

39. Monnier L, Colette C, Dunseath GJ, et al. The loss of postprandial glycemic control precedes stepwise deterioration of fasting with worsening diabetes. Diabetes Care. 2007; 30(2): 263–269, doi: 10.2337/dc06-1612, indexed in Pubmed: 17259492.

40. Najafian M, Jahromi MZ, Nowroznejhad MJ, et al. Phloridzin reduces blood glucose levels and improves lipids metabolism in streptozotocin-induced diabetic rats. Mol Biol Rep. 2012; 39(5): 5299–5306, doi: 10.1007/s11033-011-1328-7, indexed in Pubmed: 22167331.

41. Nurdiana S, Goh YM, Ahmad H, et al. Changes in pancreatic histology, insulin secretion and oxidative status in diabetic rats following treatment with Ficus deltoidea and vitexin. BMC Complement Altern Med. 2017; 17(1): 290, doi: 10.1186/s12906-017-1762-8, indexed in Pubmed: 28576138.

42. Oh SH, Muzzonigro TM, Bae SH, et al. Adult bone marrow-derived cells trans-differentiating into insulin-producing cells for the treatment of type I diabetes. Lab Invest. 2004; 84(5): 607–617, doi: 10.1038/labinvest.3700074, indexed in Pubmed: 15034596.

43. Okere B, Lucaccioni L, Dominici M, et al. Cell therapies for pancreatic beta-cell replenishment. Ital J Pediatr. 2016; 42(1): 62, doi: 10.1186/s13052-016-0273-4, indexed in Pubmed: 27400873.

44. Olokoba AB, Obateru OA, Olokoba LB. Type 2 diabetes mellitus: a review of current trends. Oman Med J. 2012; 27(4): 269–273, doi: 10.5001/omj.2012.68, indexed in Pubmed: 23071876.

45. Omar A, Aboulkhair A. Effect of bone marrow versus adipose tissue derived mesenchymal stem cells on the pancreas of streptozotocin-induced diabetes mellitus type i in adult male rats (histological study). Egypt J Histol. 2017; 40(1): 12–24, doi: 10.21608/ejh.2017.3693.

46. Pagliuca FW, Millman JR, Gürtler M, et al. Generation of functional human pancreatic beta cells in vitro. Cell. 2014; 159(2): 428–439, doi: 10.1016/j.cell.2014.09.040, indexed in Pubmed: 25303535.

47. Pavlovic V, Ciric M, Jovanovic V, et al. Platelet rich plasma: a short overview of certain bioactive components. Open Med (Wars). 2016; 11(1): 242–247, doi: 10.1515/med-2016-0048, indexed in Pubmed: 28352802.

48. Pazzini J, De Nardi AB, Huppes RR, et al. Method to obtain platelet-rich plasma from rabbits (Oryctolagus cuniculus). Pesq Vet Bras. 2016; 36(1): 39–44, doi: 10.1590/s0100-736x2016000100007.

49. Quiros JA, Marcin JP, Kuppermann N, et al. Elevated serum amylase and lipase in pediatric diabetic ketoacidosis. Pediatr Crit Care Med. 2008; 9(4): 418–422, doi: 10.1097/PCC.0b013e318172e99b, indexed in Pubmed: 18496406.

50. Ren H, Sang Y, Zhang F, et al. Comparative analysis of human mesenchymal stem cells from umbilical cord, dental pulp, and menstrual blood as sources for cell therapy. Stem Cells Int. 2016; 2016: 3516574, doi: 10.1155/2016/3516574, indexed in Pubmed: 26880954.

51. Sano T, Ozaki K, Matsuura T, et al. Giant mitochondria in pancreatic acinar cells of alloxan-induced diabetic rats. Toxicol Pathol. 2010; 38(4): 658–665, doi: 10.1177/0192623310368982, indexed in Pubmed: 20448086.

52. Sheweita SA, Mashaly S, Newairy AA, et al. Changes in oxidative stress and antioxidant enzyme activities in streptozotocin-induced diabetes mellitus in rats: role of alhagi maurorum extracts. Oxid Med Cell Longev. 2016; 2016: 5264064, doi: 10.1155/2016/5264064, indexed in Pubmed: 26885249.

53. Sonker A, Dubey A, Bhatnagar A, et al. Platelet growth factors from allogeneic platelet-rich plasma for clinical improvement in split-thickness skin graft. Asian J Transfus Sci. 2015; 9(2): 155–158, doi: 10.4103/0973-6247.162712, indexed in Pubmed: 26420935.

54. Sordi V, Melzi R, Mercalli A, et al. Mesenchymal cells appearing in pancreatic tissue culture are bone marrow-derived stem cells with the capacity to improve transplanted

islet function. Stem Cells. 2010; 28(1): 140–151, doi: 10.1002/stem.259, indexed in Pubmed: 19924826.

55. Sorour H, Selim m, EL-Moselhy LS, et al. Ameliorative effect of watermelon rind ingestion on the pancreas of diabetic female albino rat (histological, immunohistochemical and morphometric study). Egypt J Histol. 2019; 42(1): 10–22, doi: 10.21608/ejh.2018.4243.1018.

56. Stoytcheva M, Montero G, Zlatev R, et al. Analytical Methods for Lipases Activity Determination: A Review. Curr Analyt Chem. 2012; 8(3): 400–407, doi: 10.2174/157341112801264879.

57. Suvarna K, Layton CH, Bancroft J. Bancroft's theory and practice of histological techniques. 8th ed. Churchill Livingstone, Philadelphia 2013: 373–391.

58. Ukwenya V, Ashaolu O, Adeyemi D, et al. Experimental diabetes and the epididymis of Wistar rats: The protective effects of Anacardium occidentale (Linn.). J Exp Clini Anat. 2015; 14(2): 57, doi: 10.4103/1596-2393.177029.

59. Van Pham P, Vu NB, Phan N. Umbilical cord-derived stem cells (ModulatistTM) show strong immuno-modulation capacity compared to adipose tissue--derived or bone marrow-derived mesenchymal stem cells. Biomed Res Ther. 2016; 3(6), doi: 10.7603/s40730-016-0029-1.

60. Vetere A, Choudhary A, Burns SM, et al. Targeting the pancreatic beta-cell to treat diabetes. Nat Rev Drug Discov. 2014; 13(4): 278–289, doi: 10.1038/nrd4231, indexed in Pubmed: 24525781.

61. Wang Y, Chen X, Cao W, et al. Plasticity of mesenchymal stem cells in immunomodulation: pathological and therapeutic implications. Nat Immunol. 2014; 15(11): 1009–1016, doi: 10.1038/ni.3002, indexed in Pubmed: 25329189.

62. Xie Z, Hao H, Tong C, et al. Human umbilical cord-derived mesenchymal stem cells elicit macrophages into an anti-inflammatory phenotype to alleviate insulin resistance in type 2 diabetic rats. Stem Cells. 2016; 34(3): 627–639, doi: 10.1002/stem.2238, indexed in Pubmed: 26523620.

63. Xu X, D'Hoker J, Stangé G, et al. Beta cells can be generated from endogenous progenitors in injured adult mouse pancreas. Cell. 2008; 132(2): 197–207, doi: 10.1016/j.cell.2007.12.015, indexed in Pubmed: 18243096.

64. Zhang M, Lin Q, Qi T, et al. Growth factors and medium hyperglycemia induce Sox9+ ductal cell differentiation into beta cells in mice with reversal of diabetes. Proc Natl Acad Sci U S A. 2016; 113(3): 650–655, doi: 10.1073/pnas.1524200113, indexed in Pubmed: 26733677.

V M

VIA MEDICA

ORIGINAL ARTICLE

Lymphocyte subsets in the small intestine of piglets fed with probiotic and zinc: a qualitative and quantitative micro-anatomical study

A. Kalita[1], M. Talukdar[2], K. Sarma[2], P.C. Kalita[1], N.N. Barman[3], P. Roychoudhury[4], G. Kalita[5], O.P. Choudhary[1] , P.J. Doley[1], S. Debroy[1], K. Keneisenuo[1], R. Sarkar[1]

[1]Department of Veterinary Anatomy and Histology, College of Veterinary Sciences and Animal Husbandry, Central Agricultural University (I), Selesih, Aizawl, Mizoram, India
[2]Department of Veterinary Anatomy and Histology, College of Veterinary Science, Assam Agricultural University, Khanapara, Guwahati, Assam, India
[3]Department of Veterinary Microbiology, College of Veterinary Science, Assam Agricultural University, Khanapara, Guwahati, Assam, Indi
[4]Department of Veterinary Microbiology, College of Veterinary Sciences and Animal Husbandry, Central Agricultural University (I), Selesih, Aizawl, Mizoram, India
[5]Department of Livestock Production and Management, College of Veterinary Sciences and Animal Husbandry, Central Agricultural University (I), Selesih, Aizawl, Mizoram, India

Background: Piglet mortality is a real concern to the pig farmers. The major cause is due to the late maturation of the immune system and dietary changes in post-weaned piglets. The potential role of probiotic and zinc in the stimulation of the immune system is well established. Hence, the present study was undertaken to evaluate alterations of T and B cells in the small intestine after dietary inclusion of probiotic and zinc in pre and post-weaned piglets.

Materials and methods: A total of 18 healthy Large White Yorkshire (LWY) piglets, irrespective of sex obtained from 3 litters at the age-group of 20, 30 and 60 days. They were divided into a control group fed with basal diet and a treatment group fed with probiotic and zinc supplement along with the basal diet, consisting of three animals in each group. The piglets were weaned at 28 days of age. After sacrificing the animals at day 20, 30 and 60 from both the groups, the abdominal cavity was opened and small intestinal tissue samples were collected, processed and stained by indirect immunofluorescence technique. The slides were evaluated under the fluorescent light microscope. The data were statistically analysed.

Results: The different T and B cell subsets were recorded in the lining epithelium, core of villus, crypt area of lamina propria and Peyer's patch area. The number of $CD4^+$, $CD8^+$, IgA^+ and IgM^+ cells was higher in the treated piglets than the control group of animals, irrespective of segments of intestine and age-group.

Conclusions: It can be concluded that the dietary supplementation of probiotic and zinc was found to be good additives as they can stimulate the immune response in piglets, especially during the critical early post-weaning period. (Folia Morphol 2022; 81, 1: 82–90)

Key words: probiotic, zinc, lymphocyte, small intestine, piglet

---

Address for correspondence: Dr. O.P. Choudhary, Department of Veterinary Anatomy and Histology, College of Veterinary Sciences and Animal Husbandry, Central Agricultural University (I), Selesih, Aizawl, Mizoram-796015, India, tel: 91-9928099090, e-mail: dr.om.choudhary@gmail.com

INTRODUCTION

Pre-weaning piglet mortality ranges from 5% to 35%, which causes major economic issues in pig production [18]. Similarly, weaning is a critical stage in pig production because the piglets have to face many challenges such as low feed intake, acute diarrhoea and body weight loss, which causes nutritional, immunological and psychological disruptions [15]. The innate immune cells and gut-associated lymphoid tissue are not functionally developed until 4–7 weeks of age [9]. Diet plays an important role in the maturation and modification of the gut-associated immune system and the development of gut function [5]. Probiotics particularly lactic acid bacteria have beneficial effects on the health of the host [20]. These probiotics bacteria can able to induce natural and acquired immunity in healthy mice [10]. The beneficial effect of probiotics in respect of immunity was also recorded in sows and piglets [22]. In addition, zinc supplementation has been responsible for maintaining nonspecific defence mechanisms [21]. Kalita et al. [14] already described the probiotic and zinc effects on the small intestinal mucosal cells in piglets.

In this communication, we assessed the effects of probiotic and zinc supplementation in pre- and post-weaned piglets on the qualitative and quantitative development of the gut-associated immune system by the use of the indirect immunofluorescence technique. The objective of the present study was to examine the effect of feeding probiotic (*Lactobacillus acidophilus*, *Lactobacillus rhamnosus* and *Bifidobacterium longum*) and zinc on T and B cells subsets that demonstrate the immune status in the small intestine of critical pre and post-weaned piglets.

MATERIALS AND METHODS

The present study was conducted in the pig farm of the College, Central Agricultural University (I), Mizoram, India. The Institutional Animal Ethics Committee ethically approved the animals used for the experiment. The experiment was carried out from February, 2017 to May, 2019.

Animals

The present study was conducted on eighteen healthy Large White Yorkshire (LWY) piglets, irrespective of sex at different stages of development as age-group of 20, 30 and 60 days. Each of six numbers of these piglets was selected from three sows. The piglets were divided into control group (C) fed with basal diet and treatment group (T) fed with combined probiotic and zinc oral supplement along with the basal diet. The basal diet used in this experiment was in pellet form and formulated to provide the nutrient requirements as per National Research Council (NRC) [19]. The piglets were weaned at 28 days of age.

Selection, dose and period of treatment

A mixture of probiotic bacteria consisted of *Lactobacillus acidophilus* (0.65×10^9), *Lactobacillus rhamnosus* (0.4×10^9) and *Bifidobacterium longum* (0.2×10^9) reconstituted in 1 mL of normal saline solution, were orally administered to each treatment group of piglets individually from birth to 10 days, so that each animal received probiotic mixture at a final concentration of 1.25×10^9 colony forming unit/day [17]. The ZnO was given orally to the treatment group of piglets at the rate of 2000 ppm/day from birth to 10 days of age [4]. The piglets of the control group were given the same volume of sterilised saline solution.

Sample preparation

The experimental animals were anesthetised using diazepam at the rate of 2 mg/kg body weight followed by ketamine at the rate of 10 mg/kg body weight intravenously in the peripheral ear vein and then exsanguinated the animals. The animals were sacrificed on days 20, 30 and 60 from both the groups. After sacrifice, the animal's abdominal cavity was exposed, and parts of the small intestine were dissected out [12]. Tissue samples were taken immediately after sacrifice from the duodenum (5 cm caudal to the pylorus), jejunum (in the middle of the jejunum) and ileum (5 cm cranial to the ileocaecal valve).

Monoclonal antibodies

The murine monoclonal antibodies (mAbs) reactive with porcine leukocyte surface molecules, i.e., cluster of differentiation (CD) antigens or immunoglobulin A (IgA) molecule on plasma cells, used as the primary antibodies (pAbs) to study *in situ* identification, distribution and quantification patterns of respective lymphoid and non-lymphoid cell subsets residing small intestine of experimental piglets are listed in Table 1.

Immunofluorescence

Different cell populations of the immune system were identified by indirect immunofluorescence (Indi-

Table 1. List of primary antibodies and secondary antibody conjugates (conjugated with FITC) used for immunofluorescence identification/localisation and morphometric quantification of T and B cell subsets in the small intestine

Antibody	Isotype	Antibody specificity	Cytochrome	Target cells/Molecules	Origin
Primary					
MIL 17	IgG2b	CD4α	None	Helper T lymphocytes	Bio-Rad Laboratories, USA
MIL 12	IgG2a	CD8α	None	Cytotoxic T lymphocytes	Bio-Rad Laboratories, USA
K61 1B4	IgG1	IgA	None	IgA$^+$ plasma cell	Bio-Rad Laboratories, USA
K52 1C3	IgG1	IgM	None	IgM$^+$ plasma cell	Bio-Rad Laboratories, USA
Secondary					
Goat anti-mouse IgG- FITC	IgG	Mouse IgG	FITC	Mouse IgG	Sigma-Aldrich, USA

rect-IF) technique [22]. Briefly, small intestinal sections that had been cut to a thickness of 5 μm were deparaffinised, dehydrated and hydrated to water. After antigen retrieval in sodium citrate buffer (10 mM, pH 6.0), the nonspecific binding sites were blocked by 1% bovine serum albumin (30 min at room temperature). Then, sections were flooded with a primary monoclonal antibody (BIORAD, Table 1) at a dilution of 1:100 and incubated overnight (4°C). Sections were washed 3 times (5-min each) with washing buffer (phosphate buffer saline mixed with 0.035% Tween 20) and stained with secondary antibody (anti-mouse IgG--FITC) conjugated with FITC (Sigma-Aldrich, Table 1) at a dilution of 1:200 for 60 minutes at room temperature. The excess secondary antibody was removed by washing the sections with a wash buffer 3 times for 5 minutes each. Finally, the sections were mounted with mounting media (glycerol). The immunostained slides were visualised and photographed under the fluorescent light microscope at 400× magnification (Olympus BX 51, Japan).

Cells counts of the sections were performed at 400-fold magnification. Histomorphometric analysis of targeted immunopositive cells was counted in 10 fields (representing a tissue area of about 0.24 mm^2) from each of the three sampled piglets per group [24]. Such counting included villus epithelium, crypt epithelium, villus and crypt lamina propria, submucosa and Peyer's patches. Results were expressed as mean counts per unit area.

Statistical analysis

The data obtained were analysed using statistical package SPSS version 20. Differences in cell counts were accessed using the Student's t-test and differences between experimental groups by one-way ANOVA.

RESULTS

The distribution and number of CD4$^+$, CD8$^+$, IgA$^+$ and IgM$^+$ cells in the small intestine of control and treated piglets were analysed by indirect immunofluorescence technique.

CD4$^+$ lymphocytes

The CD4$^+$ T lymphocytes were located in the core of the villus (Fig. 1A), crypt area of the lamina propria (LP) (Fig. 1B) and Peyer's patch (PP) area (Fig. 1C) of the small intestine in both the group of piglets. However, these lymphocytes were concentrated in the core of the villus and crypt area of the LP in the duodenum as the PP were found to be absent in this segment of the intestine. The CD4$^+$ T lymphocytes were highly concentrated in the crypt area, followed by the PP area and the core of the villus (Fig. 1D). These lymphocytes were not observed in the epithelium. The total number of CD4$^+$ T lymphocytes exhibited an increasing trend in LP and PP areas towards the higher age in both the groups. In the LP area of the current study, the number of cells expressing the CD4 co-receptor was increased significantly at day 60 (p < 0.05) in the duodenum; at day 20 (p < 0.01), day 30 (p < 0.05) and day 60 (p < 0.01) in jejunum; and day 30 (p < 0.01) and day 60 (p < 0.01) in the ileum of piglets fed with probiotic and zinc in compared to the control group of piglets (Fig. 2A). Similarly, in PP area of this study showed a significant increased (p < 0.01) in CD4$^+$ immunopositive cells at day 20, day 30 and day 60 in the jejunum of treated piglets (Fig. 2B).

CD8$^+$ lymphocytes

The immunopositive CD8$^+$ cells were consistently present within the epithelium (Fig. 3A), the core of LP (Fig. 3B) and the crypt area (Fig. 3C) of the intestinal
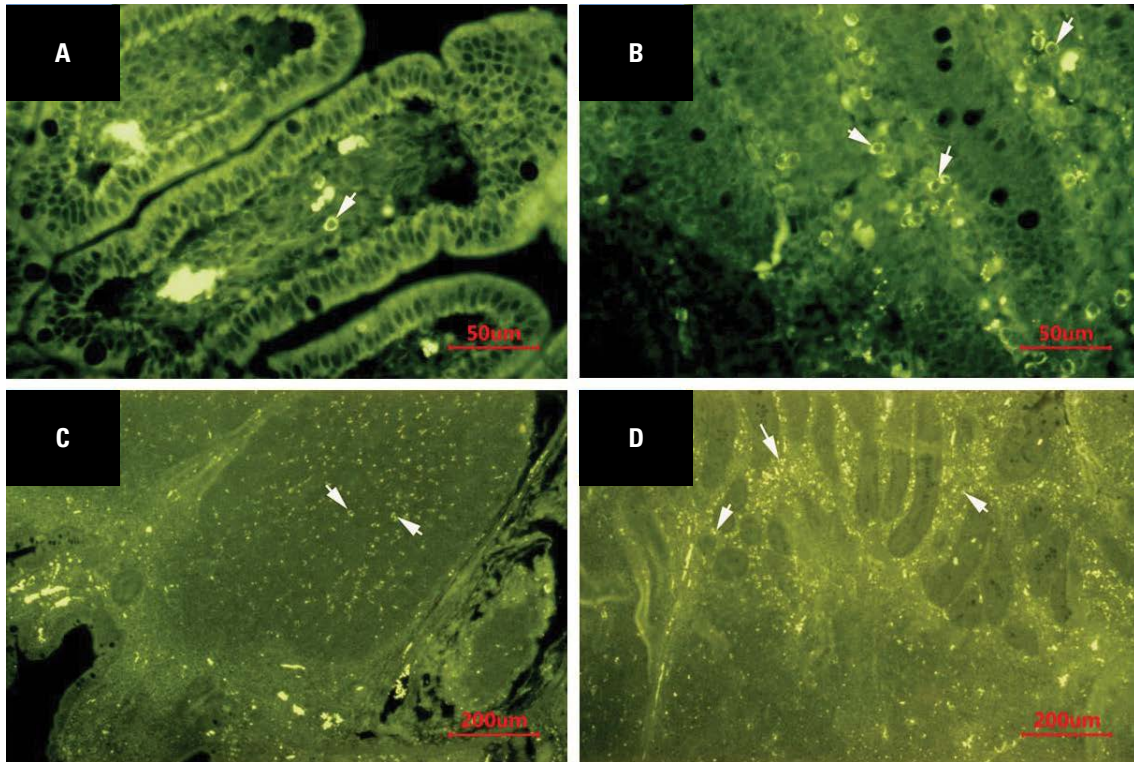
Figure 1. CD4$^+$ T lymphocytes in 30-day-old treated piglets; **A.** Core of the villus (arrow) in duodenum; **B.** Crypt lamina propria area (arrow) of jejunum (Indirect-IF method, ×400); **C.** Peyer's patch area (arrow) of ileum; **D.** Rich population (arrow) in the crypt area of ileum (Indirect-IF method, ×100)**.**
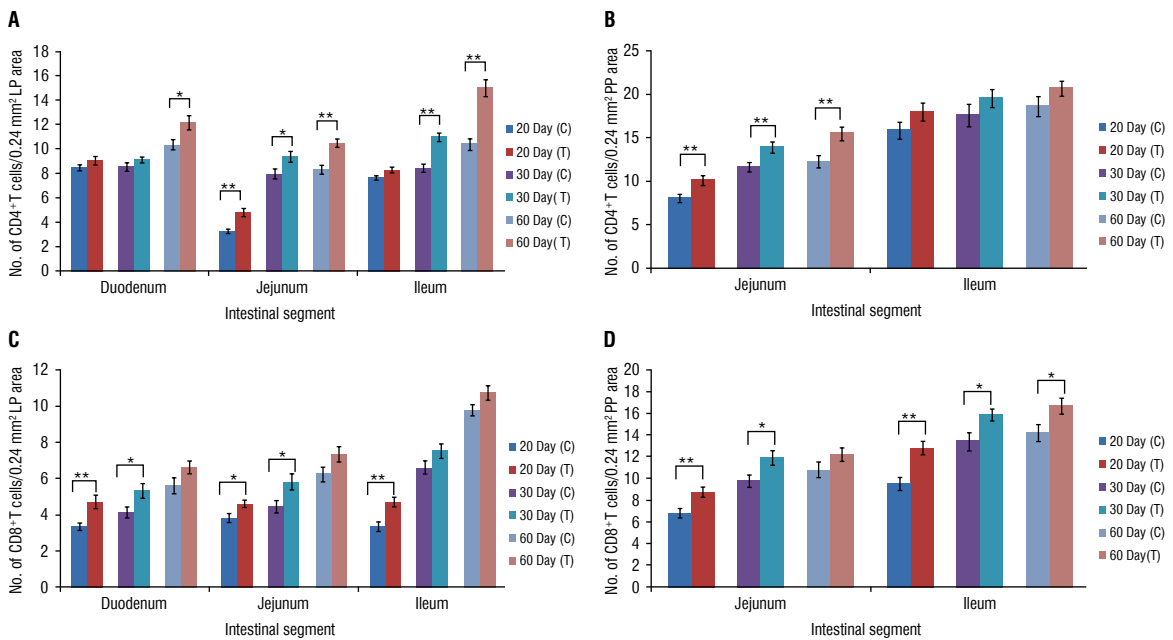
Figure 2. Localisation of T lymphocytes in the small intestine of control and treatment group of piglets (*p < 0.05, **p < 0.01); **A, B.** CD4$^+$ T lymphocytes in lamina propria (LP) and Peyer's patch (PP) area; **C, D.** CD8$^+$ T lymphocytes in LP and PP area.
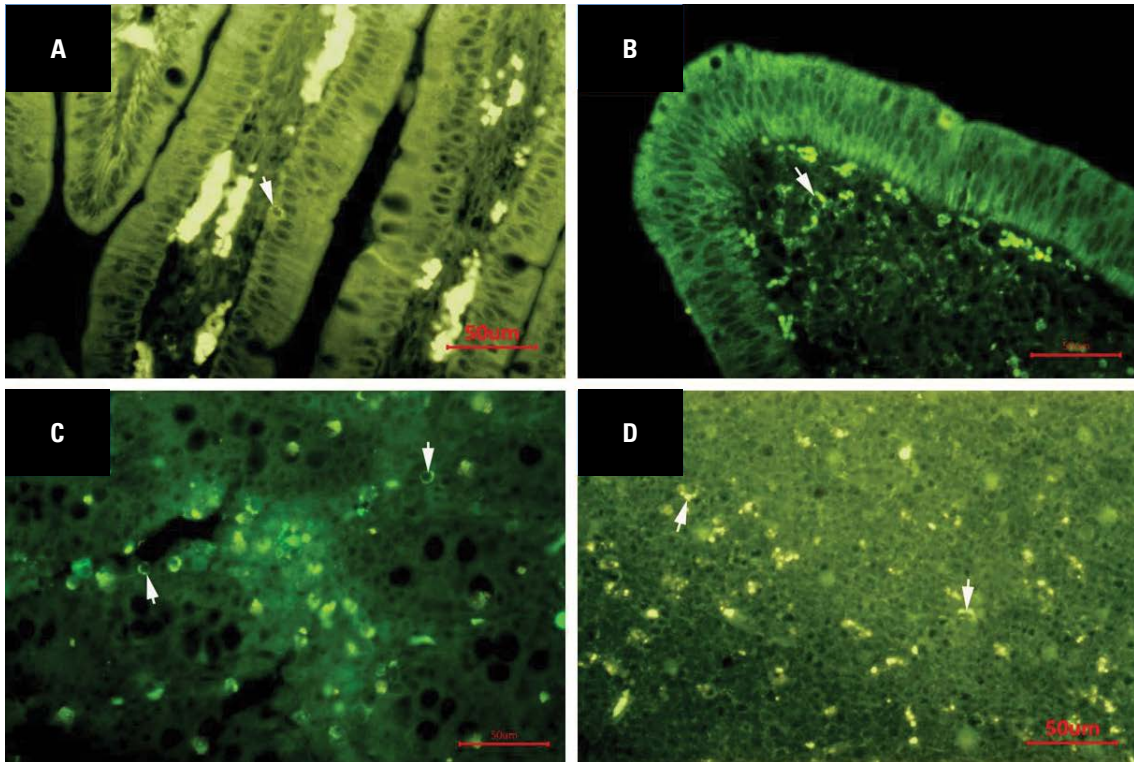
Figure 3. CD8$^+$ T lymphocytes in 20-day-old treated piglets (Indirect-IF method, ×400); **A.** Lining epithelium (arrow) of duodenum; **B.** Core of lamina propria area (arrow) in duodenum; **C.** Crypt area (arrow) of jejunum; **D.** Peyer's patch area (arrow) of ileum.
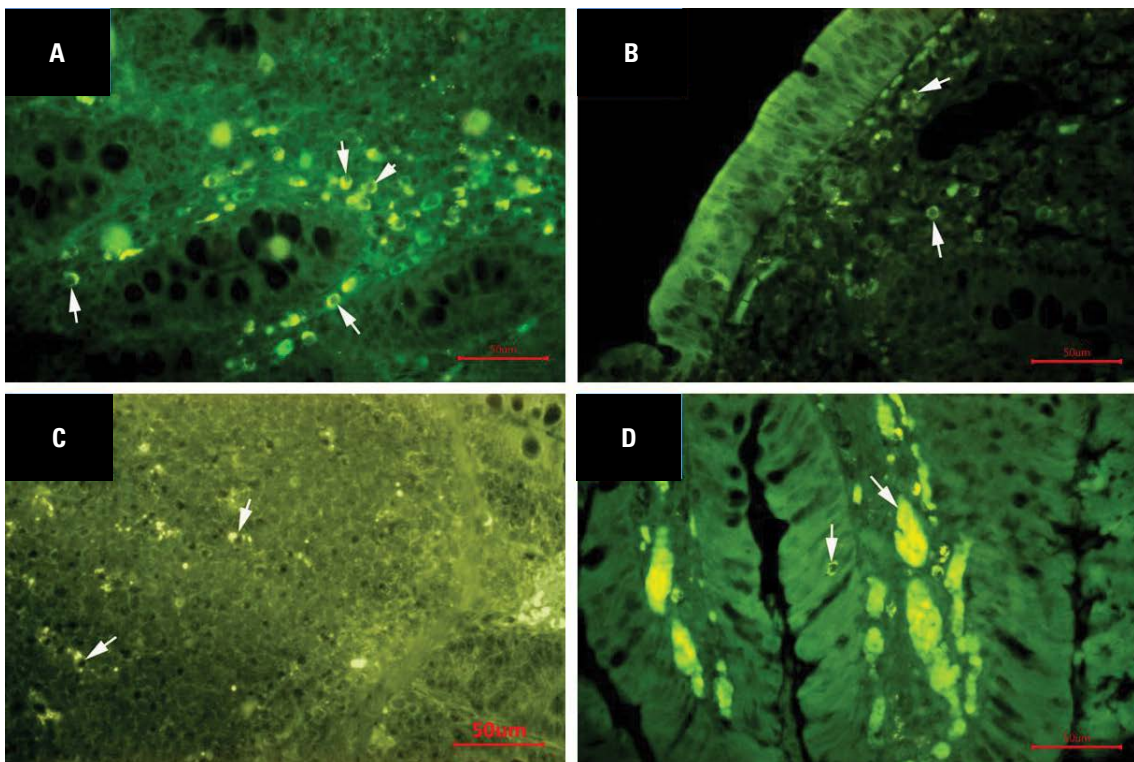
Figure 4. IgA$^+$ B lymphocytes in 60-day-old treated piglets (Indirect-IF method, ×400); **A.** Crypt area (arrow) of duodenum; **B.** Core of lamina propria (LP) area (arrow) in jejunum; **C.** Peyer's patch area of ileum; **D.** Lining epithelium and LP area along with their secretions (arrow) in jejunum.
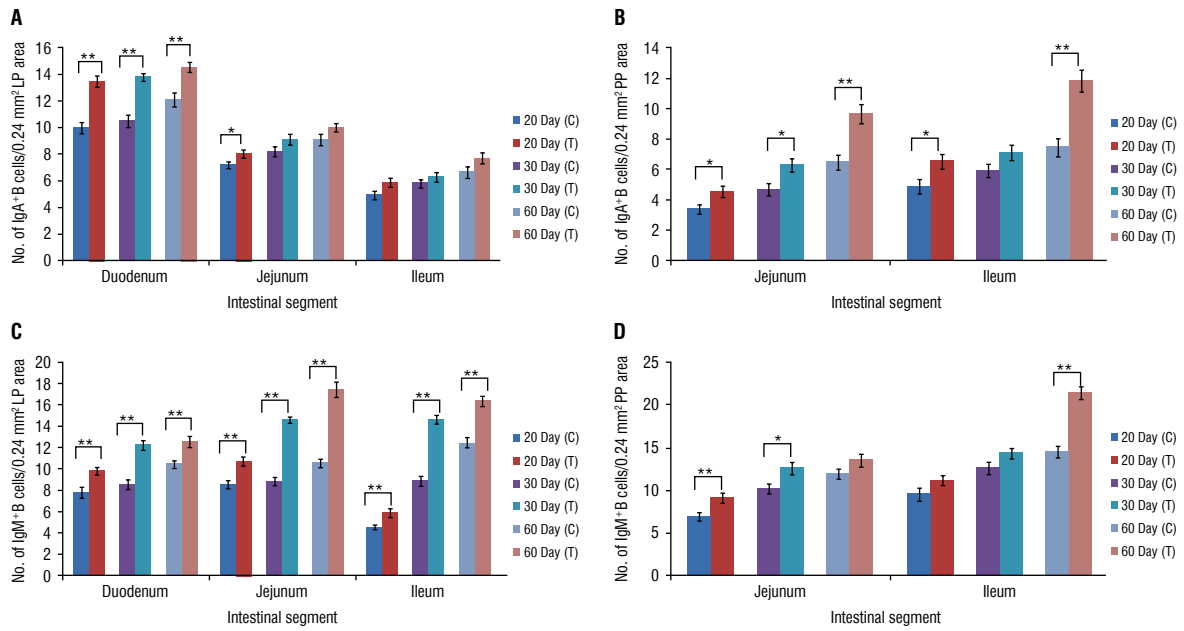
Figure 5. Localisation of B lymphocytes in the small intestine of control and treatment group of piglets (*p < 0.05, **p < 0.01); **A, B.** IgA[+] B lymphocytes in lamina propria (LP) and Peyer's patch (PP) area; **C, D.** IgM[+] B lymphocytes in LP and PP area.
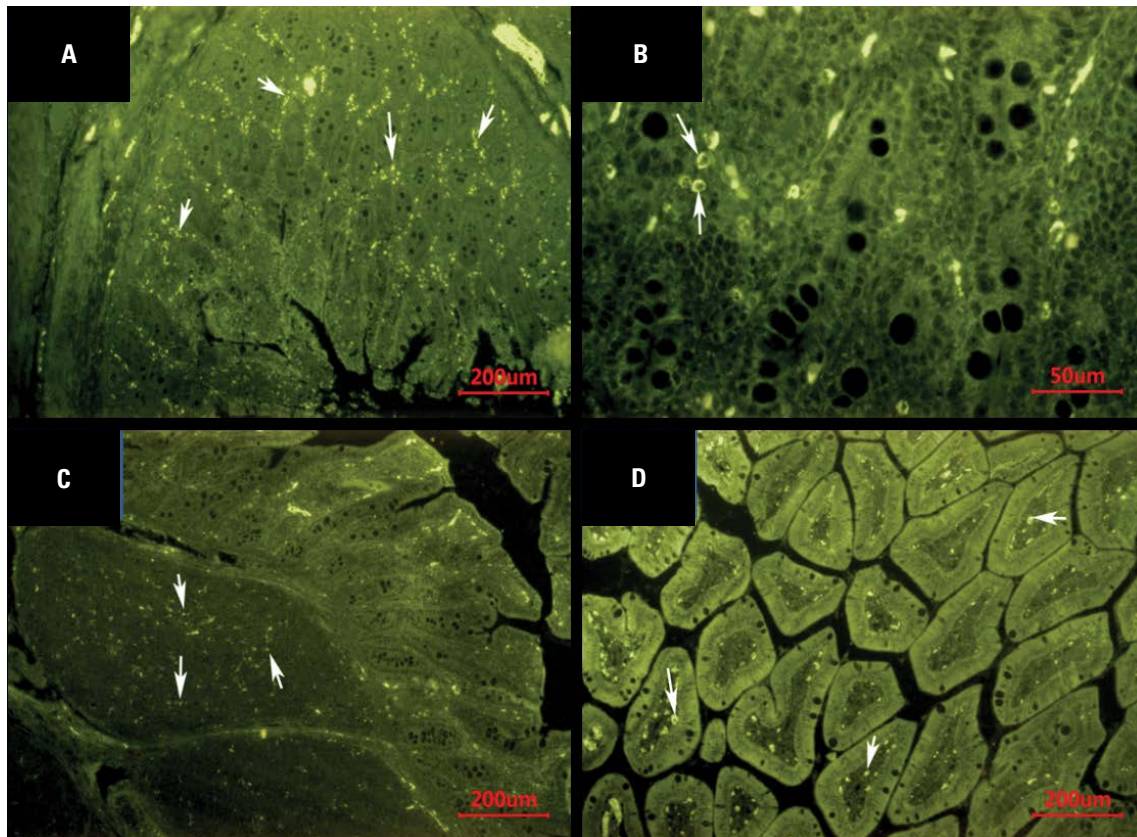
Figure 6. IgM[+] B lymphocytes in treated piglets; **A.** Predominant location in the crypt area (arrow) of 60-day-old jejunum (Indirect-IF method, ×100): **B.** Crypt area (arrow) in 60-day-old duodenum (Indirect-IF method, ×400); **C.** Peyer's patch (PP) area (arrow) in 30-day-old ileum; **D.** Core of the villi (arrow) in 30-day-old jejunum (Indirect-IF method, ×100).

mucosa in both the groups. Moreover, their presence was also revealed in the PP area of jejunum and ileum (Fig. 3D). The total number of CD8$^+$ cells in the current study showed an elevated pattern as per the age advancement in both groups. In the LP area, the number of CD8$^+$ cells significantly increased at day 20 (p < 0.01) and day 30 (p < 0.05) in the duodenum; at day 20 (p < 0.05) and day 30 (p < 0.05) in the jejunum; and at day 20 (p < 0.01) in the ileum of the treatment group of piglets (Fig. 2C). Similarly, in the PP area of treated piglets, their number increased significantly at day 20 (p < 0.01) and day 30 (p < 0.05) in the jejunum and, day 20 (p < 0.01), day 30 (p < 0.05) and day 60 (p < 0.05) in the ileum (Fig. 2D).

IgA$^+$ lymphocytes

IgA expressing plasma cells were predominantly found in the LP of the crypts (Fig. 4A) irrespective of group and age. However, their presence was also observed in the cores of the villi (Fig. 4B) and the PP area (Fig. 4C). Some of the IgA$^+$ cells were also observed in the epithelium along with their secretion in the LP area (Fig. 4D) of treated piglets. In all experimental animals, the largest populations of these immunoglobulin containing cells were found in the duodenum, followed by jejunum and ileum in the LP area. However, these counts were more in the ileum than jejunum in the PP area of this study. The total number of IgA$^+$ cells was increased with the advancement of age in both the control and treatment groups of piglets under study. In the LP area, the mean number of IgA$^+$ cells was significantly increased (p < 0.01) in all age-groups of the duodenum and significantly higher (p < 0.05) at day 20 of jejunum in the treatment group of piglets than in the control group (Fig. 5A). Similarly, in the PP area of the present study, these immunopositive cells were increased significantly (p < 0.05) at day 20 and day 30 in the jejunum and day 20 in the ileum (Fig. 5B). Furthermore, dietary inclusion of probiotic and zinc showed significantly higher (p < 0.01) IgA$^+$ cells at the PP area of day 60 in jejunum and ileum (Fig. 4C).

IgM$^+$ lymphocytes

The IgM$^+$ containing cells were predominantly located in the LP region of the crypt area (Fig. 6A, B) followed by the PP area (Fig. 6C) and the core of the villi (Fig. 6D) irrespective of group and age. The IgM$^+$ cells were increased as per the advancement of age in both groups. The number of these cells varied depending upon segments of the small intestine and age-groups in the LP area. However, in the PP area, they were more predominantly located in the ileum than jejunum irrespective of group and age. In the LP area of the current study, the mean number of IgM$^+$ cells was significantly increased (p < 0.01) in the treatment group of piglets irrespective of segments of the small intestine (Fig. 5C). Furthermore, in the PP area, these cells were significantly higher (p < 0.01) in the treated piglets at day 20 of jejunum and day 60 of the ileum (Fig. 6D). In addition, in the treated piglets, they were increased significantly (p < 0.05) at day 30 of the jejunum (Fig. 6D).

DISCUSSION

In the present investigation, the CD4$^+$ T lymphocytes were mainly concentrated in the crypt area followed by the PP area (jejunum and ileum) and the core of the villus. The number of these cells was higher in piglets fed with probiotic and zinc than in the control group of piglets. In one of the previous studies, it was reported that the CD4$^+$ T cells were mainly located in the lamina propria and played a central role in regulating the immune system [6]. From the present findings, it could be concluded that the probiotic and zinc might be the main influencing factor for the changes of CD4$^+$ T cells. Increased CD4$^+$ T cells in the treatment group could modulate the production and secretion of secretory IgA (SIgA) by secreting cytokines [3] and provide better and effective immunity to this group of piglets. The total number of CD8$^+$ cells in the current study was higher in the treated group of piglets in all the segments of the small intestine. The higher number of CD8$^+$ subpopulations present in the treatment group piglets might enhance defence against pathogens by cytotoxic CD8$^+$ cells or maintenance and enhancement of the epithelial integrity by $\gamma\delta$ CD8$^+$ cells [7]. As per a previous study conducted by Galina et al. [8] probiotics have been found to increase (p < 0.05) the number of intraepithelial lymphocytes and the density of CD3$^+$ cells in Peyer's patches and lamina propria. The CD19 marker assists the expression of all B lineage cells [23] and a study proved that the supplementation of zinc showed a higher percentage of CD19$^+$ lymphocytes in human [11]. However, analysis of the CD3$^+$ and CD19$^+$ lymphocytes was not performed in the present investigation.

In the present study, IgA expressing plasma cells were predominantly found in the LP of the crypts, irrespective of group and age. In addition, some of the

IgA+ cells were also observed in the epithelium along with their secretion in the LP area of treated piglets. In agreement with our findings, the other authors reported more populations of these immunoglobulin containing cells in the LP area of the duodenum, followed by jejunum and ileum [2]. However, these counts were more in the ileum than jejunum in the PP area of this current study. The mean number of IgA+ cells was higher in the treatment group of piglets compared to control animals in all segments of the small intestine. The highly significant increase of IgA+ cells of the duodenum in all age-groups of treated piglets might be correlated with more immunoglobulin-producing cells in the duodenum, which might ensure a fast reaction to potential pathogens [6]. The secretory IgA of gut mucosa was an antibody isotype specialised in mucosal protection that played an essential role as the first line of defence and aided in regulating bacteria-host interaction [16]. The antigen uptake of probiotic bacteria in the treatment group of piglets of the present study could be carried out by M cells or might be sampled by dendritic cells. Furthermore, the microenvironment cytokines would favour the clonal expansion of IgA B lymphocytes, increasing the number of IgA-producing cells and their passage to plasmatic cells in the different intestinal tissue of the gut. The higher number of IgA+ cells present in the treatment group could be concluded with better mucosal protection by boosting the immune system. In the current study, the number of IgM+ cells was found to be more in the PP area as compared to IgA+ cells, which was correlated with the findings of the previous study in pigs [2]. The more number of IgM+ cells in the PP area observed in the present study might be indicated that IgM was the first antibody to appear in response to initial exposure to an antigen [1]. In the present observation, the mean number of IgM+ cells was higher in treated piglets irrespective of segments of the small intestine. In the previous study, it was documented that IgM bound to the polyimmunoglobulin receptor, which was an Fc receptor that facilitated the transcytosis of the soluble polymeric isoforms of IgA [13]. Polyimmunoglobulin receptor were mainly located on the epithelial lining of mucosal surfaces of the gastrointestinal tract. In this way, the IgM reached the mucosal surface and enhanced mucosal immunity. In the treatment group of the present study, an increased number of IgA+ cells provided the environment to bind with IgM+ cells by the pIgR and transported the IgM+ cells to the apical mucosal epithelial cell surface. This might lead to better mucosal immunity in the treatment group of piglets.

CONCLUSIONS

The findings of the present study indicate that dietary supplementation of probiotic and zinc positively affected immune response in piglets that might help in promoting intestinal health, and improving piglet growth in pre and post-weaned period of life.

Conflict of interest: None declared

REFERENCES

1. Alberts B, Johnson A, Lewis J. Molecular Biology of the Cell. 4th ed. Garland Science, New York, UK 2002.
2. Allen WD, Porter P. The relative distribution of IgM and IgA cells in intestinal mucosa and lymphoid tissues of the young unweaned pig and their significance in ontogenesis of secretory immunity. Immunol. 1973; 24(3): 493–501.
3. Blum S, Alvarez S, Haller D, et al. Interactions between commensal bacteria and mucosal immunocompetent cells. Int Dairy J. 1999; 9(1): 63–68, doi: 10.1016/s0958-6946(99)00045-x.
4. Case CL, Carlson MS. Effect of feeding organic and inorganic sources of additional zinc on growth performance and zinc balance in nursery pigs. J Anim Sci. 2002; 80(7): 1917–1924, doi: 10.2527/2002.8071917x, indexed in Pubmed: 12162660.
5. Castillo M, Martín-Orúe SM, Taylor-Pickard JA, et al. Use of mannanoligosaccharides and zinc chelate as growth promoters and diarrhea preventative in weaning pigs: Effects on microbiota and gut function. J Anim Sci. 2008; 86(1): 94–101, doi: 10.2527/jas.2005-686, indexed in Pubmed: 17911238.
6. Che C, Pang X, Hua X, et al. Effects of human fecal flora on intestinal morphology and mucosal immunity in human flora-associated piglet. Scand J Immunol. 2009; 69(3): 223–233, doi: 10.1111/j.1365-3083.2008.02211.x, indexed in Pubmed: 19281534.
7. Chen Y, Chou K, Fuchs E, et al. Protection of the intestinal mucosa by intraepithelial gamma delta T cells. Proc Natl Acad Sci U S A. 2002; 99(22): 14338–14343, doi: 10.1073/pnas.212290499, indexed in Pubmed: 12376619.
8. Gāliņa D, Ansonska L, Valdovska A. Effect of probiotics and herbal products on intestinal histomorphological and immunological development in piglets. Vet Med Int. 2020; 2020: 3461768, doi: 10.1155/2020/3461768, indexed in Pubmed: 32373310.
9. Gaskins HR, Kelly KW. Immunology and neonatal mortality. In: Varley MA (editor). The Neonatal Pig Development and Survival. CAB International, Wallingford, UK 1995.
10. Gill HS, Rutherfurd KJ, Prasad J, et al. Enhancement of natural and acquired immunity by Lactobacillus rhamnosus (HN001), Lactobacillus acidophilus (HN017) and Bifidobacterium lactis (HN019). Br J Nutr. 2000; 83(2): 167–176, doi: 10.1017/s0007114500000210, indexed in Pubmed: 10743496.

11. Guo CH, Wang CL. Effects of zinc supplementation on plasma copper/zinc ratios, oxidative stress, and immunological status in hemodialysis patients. Int J Med Sci. 2013; 10(1): 79–89, doi: 10.7150/ijms.5291, indexed in Pubmed: 23289009.

12. Habel RE. Guide to the dissection of domestic ruminants. Michigan, Edwards Brother Inc. Ann Arbor, USA 1964.

13. Johansen FE, Braathen R, Brandtzaeg P. Role of J chain in secretory immunoglobulin formation. Scand J Immunol. 2000; 52(3): 240–248, doi: 10.1046/j.1365-3083.2000.00790.x, indexed in Pubmed: 10972899.

14. Kalita A, Talukdar M, Sarma K, et al. Small intestinal mucosal cells in piglets fed with probiotic and zinc: a qualitative and quantitative microanatomical study. Folia Morphol. 2021; 80(3): 605–617, doi: 10.5603/FM.a2020.0091, indexed in Pubmed: 32789842.

15. Lallès JP, Bosi P, Smidt H, et al. Weaning — a challenge to gut physiologists. Livestock Sci. 2007; 108(1-3): 82–93, doi: 10.1016/j.livsci.2007.01.091.

16. Lemme-Dumit JM, Polti MA, Perdigón G, et al. Probiotic bacteria cell walls stimulate the activity of the intestinal epithelial cells and macrophage functionality. Benef Microbes. 2018; 9(1): 153–164, doi: 10.3920/BM2016.0220, indexed in Pubmed: 29124968.

17. Liu H, Zhang J, Zhang S, et al. Oral administration of Lactobacillus fermentum I5007 favors intestinal development and alters the intestinal microbiota in formula-fed piglets. J Agric Food Chem. 2014; 62(4): 860–866, doi: 10.1021/jf403288r, indexed in Pubmed: 24404892.

18. Mainau E, Temple D, Manteca X. Pre-weaning mortality in piglets. University of Barcelona, USA: Farm Animal Welfare Education Centre (FAWEC); Nº11/January 2015.

19. National Research Council (NRC). Nutrient requirements of swine. In: Computer model program for predicting nutrient requirements. 10th ed. National Academy of Sciences, Washington DC, USA. 1998.

20. Reid G, Jass J, Sebulsky MT, et al. Potential uses of probiotics in clinical practice. Clin Microbiol Rev. 2003; 16(4): 658–672, doi: 10.1128/CMR.16.4.658-672.2003, indexed in Pubmed: 14557292.

21. Sargeant HR, McDowall KJ, Miller HM, et al. Dietary zinc oxide affects the expression of genes associated with inflammation: Transcriptome analysis in piglets challenged with ETEC K88. Vet Immunol Immunopathol. 2010; 137(1-2): 120–129, doi: 10.1016/j.vetimm.2010.05.001, indexed in Pubmed: 20605641.

22. Scharek L, Altherr BJ, Tölke C, et al. Influence of the probiotic Bacillus cereus var. toyoi on the intestinal immunity of piglets. Vet Immunol Immunopathol. 2007; 120(3-4): 136–147, doi: 10.1016/j.vetimm.2007.07.015, indexed in Pubmed: 17870185.

23. Scheuermann RH, Racila E. CD19 antigen in leukemia and lymphoma diagnosis and immunotherapy. Leuk Lymphoma. 1995; 18(5-6): 385–397, doi: 10.3109/10428199509059636, indexed in Pubmed: 8528044.

24. Sozmen M, Brown PJ, Cripps PJ. IgA, IgG and IgM immunohistochemical staining in dormal dog salivary glands and in cases of chronic sialoadenitis. Vet Res. 1996; 27: 285–294, indexed in Pubmed: 8767890.

ORIGINAL ARTICLE

Immune cells in the small intestinal mucosa of newborn yaks

Q. Zhang[1], Y. Cui[1], S.J. Yu[2], Y.F. Huang[1], Y.Y. Pan[2], Z.C. Bai[1]

[1]College of Veterinary Medicine, Gansu Agricultural University, Lanzhou, Gansu, China
[2]Gansu Province Livestock Embryo Engineering Research Centre, College of Veterinary Medicine, Gansu Agricultural University, Lanzhou, Gansu, China

Background: This study aimed to characterise and evaluate the main markers of T lymphocytes, B lymphocytes, immunoglobulin (Ig) A and IgG plasmocytes, macrophages, and dendritic cells of the intestinal mucosa of newborn yaks.
Materials and methods: Ten newborn yaks (2–4 weeks old) were chosen. Immunohistochemistry and real-time quantitative polymerase chain reaction were used to analyse the immune cell distribution and specific markers at the mRNA expression level in the duodenum, jejunum, and ileum.
Results: The results showed in the epithelium, CD3ε-positive T lymphocyte levels were higher than other immune cell levels (p < 0.05). Additionally, in the lamina propria, the number of cells positive for CD3ε, CD68, and signal inhibitory regulatory protein alpha (SIRPα) were higher in the villi, while CD79α, IgA and IgG cells were more common at the base of the crypt. Moreover, both in the epithelium and lamina propria, the number of CD3ε, CD68 and SIRPα were decreased from the duodenum to the ileum (p < 0.05), additionally the number of CD79α, IgA and IgG positive cells were increased from the duodenum to the ileum of newborn yaks (p < 0.05). Furthermore, the mRNA expression levels of CD3ε, CD68, and SIRPα increased from the duodenum to the ileum (p < 0.05), while the mRNA expression levels of CD79α, IgA and IgG decreased from the duodenum to the ileum.
Conclusions: Immunohistochemical characterisation and expression levels of immune factors in the small intestinal mucosa of newborn yaks suggest that the intestinal mucosa is an important part of the natural barrier and provides useful references for immunity functions of newborn yak intestinal mucosa. (Folia Morphol 2022; 81, 1: 91–100)

Key words: newborn yaks, small intestine, mucosa, immunity cell

INTRODUCTION

Domesticated yaks are a valuable breed resource in the Qinghai-Tibet Plateau. They have unique ecological characteristics and are valued for their meat, draft and milk [19]. Highland pastoral areas are currently dominated by traditional grazing yak breeding; however, due to the harsh plateau environment, extensive management, and the influence of pathogenic factors, the intestinal mucosal immune barrier of yaks is highly susceptible to damage. Therefore,

Address for correspondence: Prof. Y. Cui, Faculty of Veterinary Medicine, Gansu Agricultural University, Lanzhou, Gansu, China, fax: +86-0931-7631220, e-mail: cuiyan369@sina.com

the incidence of gastrointestinal function disorder, inflammatory bowel disease, and infectious diarrhoea disease is high. These illnesses increase the length of the growth cycle and, as a result, the yak develops slowly. The mortality rate of newborn yaks is as high as 30% [9], which causes serious damage to the development of agriculture. Therefore, in order to improve yak survival and productivity, it is imperative to understand the characteristics of the small intestinal mucosal immune cells of yaks.

The small intestinal tract contains the largest number of immune cells, comprising a heterogeneous population of T and B lymphocytes, plasmocytes, macrophages, dendritic cells and a variety of non-professional antigen-presenting cells [8, 18]. Appropriate interactions between these different cell types are essential for generating immune responsiveness or tolerance to a large array of environmental antigens. The previous study analysed the distribution and population of immunocompetent cells in the small intestine of sheep, pigs, calves and mice [4, 6, 21, 22]. However, due to the limitation of the global yak distribution, there are few reports on the immune cells of yaks.

The aim of the present study was to provide basic data on the characteristics of immune cells and factors in the small intestine of healthy newborn yaks. We used CD3ε, CD79α, immunoglobulin (Ig) A, IgG, CD68, and signal inhibitory regulatory protein alpha (SIRPα) to characterise T and B lymphocytes, plasmocytes, macrophages, and dendritic cells in the small intestine of newborn yaks, and assayed the mRNA expression levels of immune cell-specific markers.

MATERIALS AND METHODS
Animals and tissues collection

All experimental animals were handled according to the Animal Ethics Procedures and Guidelines of the People's Republic of China and were approved by the Institutional Animal Care and Use Committee of the College of Veterinary Medicine of Gansu Agricultural University. All yaks were considered healthy based on the results of physical examination and serum biochemical analysis. The animals were euthanased with an intravenous injection of pentobarbital sodium (200 mg/kg). To maintain the original habitat of the animals, the yaks were sacrificed, and samples were collected from local farms.

Ten newborn yaks (2–4 weeks old) were obtained on a local farmer in Xining City, Qinghai Province. The small intestinal regions (duodenum, jejunum, and ileum) were excised from each animal and samples were taken for immunohistochemical and polymerase chain reaction (PCR) analysis. All specimens intended for immunohistochemical analysis were fixed in 4% neutral paraformaldehyde phosphate buffer (pH 7.3). Specimens intended for real-time quantitative PCR (RT-qPCR) were flash frozen and stored in liquid nitrogen until further processing.

Relative RT-qPCR

Total RNA was isolated from the small intestine using TRIzol reagent (Invitrogen, Carlsbad, CA, USA). RNA was reverse transcribed to single-stranded cDNA using a reverse transcription kit (MBI Fermentas, Burlington, ON, Canada) according to the manufacturer's instructions. The RT-qPCR primers were designed according to the *Bos grunniens* CD3ε, CD79α, IgA, IgG, CD68, SIRPα, and β-actin gene sequences (GenBank accession numbers: KY911279, KY911280, MG432919, MF099643, KY921959, MH347358, and DQ838049, respectively) using Primer 5 software and synthesised by the Beijing Genomics Institute BGI Company (China). The RT-qPCR primer sequences are presented in Table 1. RT-qPCR was conducted using a Light-Cycler480 thermocycler (Roche, Manheim, Germany) in 20-μL reaction volumes consisting of 1 μL cDNA, 1 μL forward primer, 1 μL reverse primer, 10 μL 2$\times$ SYBR Green II PCR Master Mix (TaKaRa, Shiga, Japan), 0.4 μL Rox, and 6.4 μL nuclease-free H$_2$O. Four replicates were set for each sample to ensure the accuracy of the relative expression of the target genes in the sample. After amplification, according to the system-generated Ct value, the $2^{-\Delta\Delta Ct}$ method was used with β-actin as an internal standard to obtain the relative expression of CD3ε, CD79α, IgA, IgG, CD68 and SIRPα mRNA.

Immunohistochemical examination

The spatial distribution of cells positive for CD3ε, CD79α, IgA, IgG, CD68 and SIRPα in the small intestine of newborn yaks was evaluated by immunohistochemical staining. Fixed tissue sections were mounted on microscope slides in a routine manner and exposed to primary antibodies against CD3ε (monoclonal rabbit anti-cow CD3ε, Abcam, Cambridge, UK; ab16669, 1:200 dilution), CD79α (monoclonal mouse anti-cow CD79α, Abcam; ab199001, 1:100 dilution), IgA (polyclonal rabbit anti-cow IgA, Abcam; ab112630, 1:100 dilution), IgG (polyclonal rabbit anti-cow IgG, Abcam; ab6692, 1:100 dilution), SIRPα (polyclonal rabbit an-

Table 1. Primers used in this study

Genes	Primer names	Primer sequences (5′-3′)	Length (bp)	Annealing (℃)
CD3ε	P1	F: GGGCTCATAGTCTGGATTGG	155	57
	P2	R: TGTGTCACTCTGGGCTTGC		
CD79α	P3	F: ACGGCAAGAAGATTCAGCG	182	60
	P4	R: CCAAGGAGGCAATAGGAG		
IgA	P5	F: GGTTCACAGGACCCAGA	227	57
	P6	R: AGCACCTAGTGAAGCCC		
IgG	P7	F: AACCAACACCACAGGAAC	208	60
	P8	R: AGTGTAGTCTCCTATTGCCT		
CD68	P9	F: TGAGAGGAGCAAGTGGGA	194	56
	P10	R: GTGGACATCATCCTGGCTGG		
SIRPα	P11	F: ATCCTGCTGCCCGCTGTA	215	60
	P12	R: AACAGTTGGGCGGCGAG		
β-actin	P13	F: AGGCTGTGCTGTCCCTGTATG	207	60
	P14	R: GCTCGGCTGTGGTGGTAAA		

ti-cow SIRPα, Abcam; ab116254, 1:100 dilution), and CD68 (polyclonal rabbit anti-cow CD68, Abbiotec, San Diego, USA; No:252281, 1:100 dilution) for 2 h at 37℃ in a moist chamber. Biotinylated secondary antibodies were applied for 10 min. Streptavidin-conjugated peroxidase was then applied to the slides for 10 min. The reaction products were formed using 3,3-diaminobenzidine tetrahydrochloride. The sections were lightly counterstained with haematoxylin. The negative control for each sample was created by replacing the primary antibody with serum albumin; all other steps and conditions remained the same.

Examination of sections

The sections were examined under a light microscope with image analysis software (Image-Pro Plus, Media Cybemetics, Silver Spring, MD, USA). Cells positive for CD3ε, CD79α, IgA, IgG, SIRPα and CD68 in the small intestine of newborn yaks were evaluated. Subjective analysis of the distribution of positively labelled cells in the lamina propria and epithelial compartments was performed using a ×40 objective.

In each tissue sample, the number of positively labelled cells was determined in three standard areas (Fig. 1) of the lamina propria: the villi, the upper crypt, and the base of the crypt. Five images were randomly chosen for each of these areas. Results were expressed as cells per 10000 μm^2 of lamina propria tissue [7]. Intraepithelial immune cells were assessed by counting positively labelled cells in five areas (each of 100 enterocytes) of the epithelium, and the results were
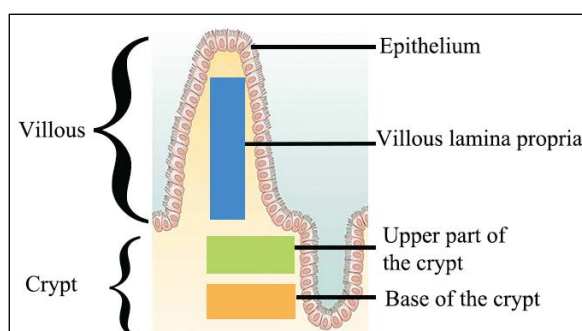
Figure 1. Diagram of small intestinal epithelium and lamina propria to demonstrate the areas used for counting.

expressed as the mean number of cells/100 enterocytes. Repeated independent counts were performed on five serial sections from the same tissue block to assess the precision of both the lamina propria and epithelial cell counting techniques.

Statistical analysis

All statistical analyses were performed using SPSS (version 21.0; IBM Corp., Armonk, NY, USA). The relative mRNA levels and positive cell numbers among the study groups are expressed as mean ± standard error. Statistical significance was determined using one-way analysis of variance and was set at $p < 0.05$.

RESULTS
Morphological analysis of the crypt-villus axis

The small intestinal mucosa of newborn yaks can be divided into three layers: the epithelium, lamina
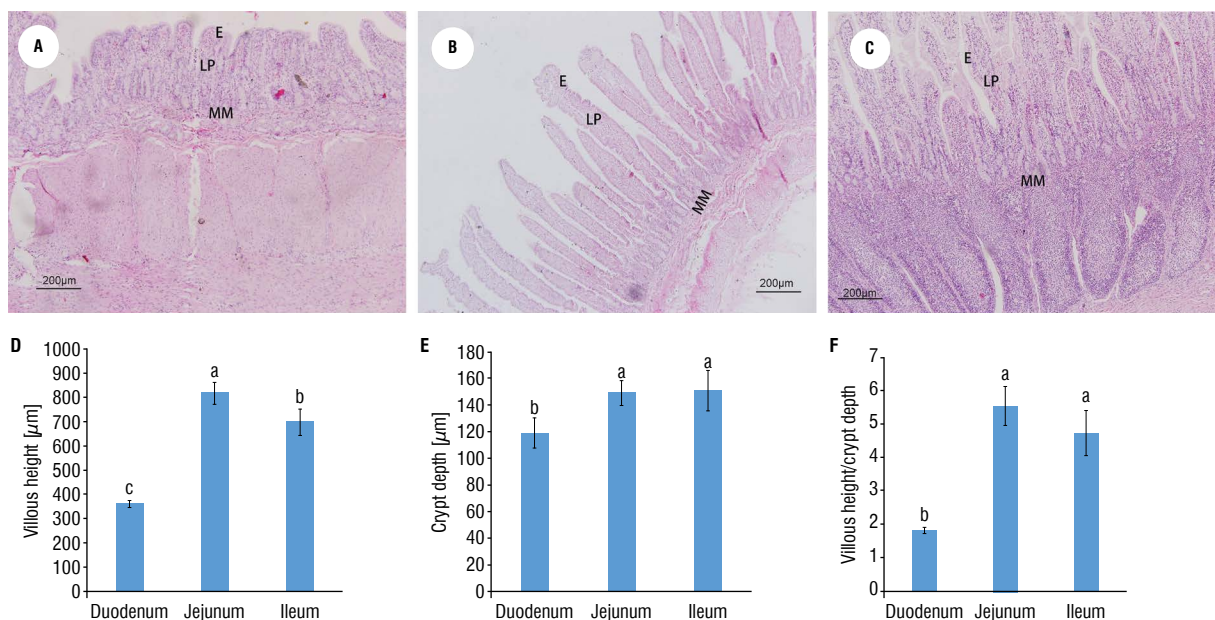
Figure 2. Morphological characteristics and analysis (including villous height, crypt depth, and ratio of villous height to crypt depth) of the small intestinal mucosa in newborn yaks; **A–C.** The histological section of the duodenum, jejunum and ileum in newborn yaks (HE, ×100); **D.** The villous height of the duodenum, jejunum and ileum in newborn yaks; **E.** The crypt depth of the duodenum, jejunum and ileum in newborn yaks; **F.** Ratio of villous height to crypt depth of the duodenum, jejunum and ileum in newborn yaks. Bars with different superscripts are significantly different (p < 0.05). The results were presented as mean ± standard error; E — mucosal epithelium; LP — lamina propria; MM — muscularis mucosa.

propria and mucosal muscle. The morphological parameters of the crypt-villus axis in the small intestine include villous height, crypt depth, and the ratio of villous height to crypt depth (Fig. 2A–C). The villous height was highest in the jejunum, followed by the ileum and the duodenum (p < 0.05) (Fig. 2D). Crypt depth was higher in the jejunum and ileum than in the duodenum (p < 0.05) (Fig. 2E). Moreover, there were no differences between the jejunum and ileum (p > 0.05). Furthermore, the ratio of villous height to crypt depth was higher in the jejunum and ileum than in the duodenum (p < 0.05) (Fig. 2F).

CD3ε, CD79α, IgA, IgG, CD68 and SIRPα mRNA expression

The relative expression levels of CD3ε, CD79α, IgG, IgA, CD68 and SIRPα mRNA differed between the duodenum, jejunum and ileum of newborn yaks (Fig. 3). Within the same intestinal region, the expression levels of CD3ε, CD68 and SIRPα mRNA were significantly higher than those of CD79α, IgA and IgG. Additionally, in the different intestinal regions, CD3ε, CD68 and SIRPα mRNA expression levels increased from the duodenum to the ileum (p < 0.05), while the mRNA expression levels of CD79α, IgA and IgG decreased from the duodenum to the ileum.
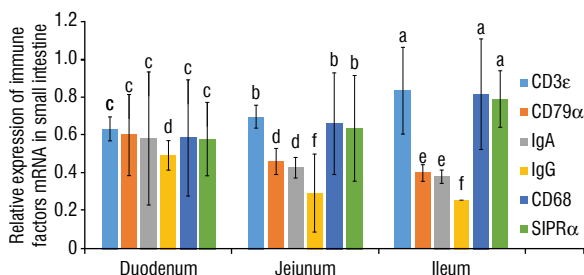
Figure 3. Relative abundance of CD3ε, CD79α, immunoglobulin A (IgA), immunoglobulin G (IgG), CD68 and signal inhibitory regulatory protein alpha (SIRPα) mRNA in the duodenum, jejunum and ileum of newborn yaks. Bars with different superscripts are significantly different (p < 0.05). Data are normalised and presented as ratio mean ± standard error, with β-actin as an internal control.

CD3ε-positive T lymphocytes in the small intestinal mucosa

The membrane staining of CD3ε-positive cells was located in the epithelium and lamina propria of the small intestinal mucosa of newborn yaks (Fig. 4A–C). In the epithelium, the number of CD3ε-positive T lymphocytes increased from the duodenum to the ileum, peaking at the ileum (p < 0.05) (Fig. 5). The difference between the duodenum and jejunum was not significant (p > 0.05). In the lamina propria, CD3-positive T lymphocytes increased from the basal
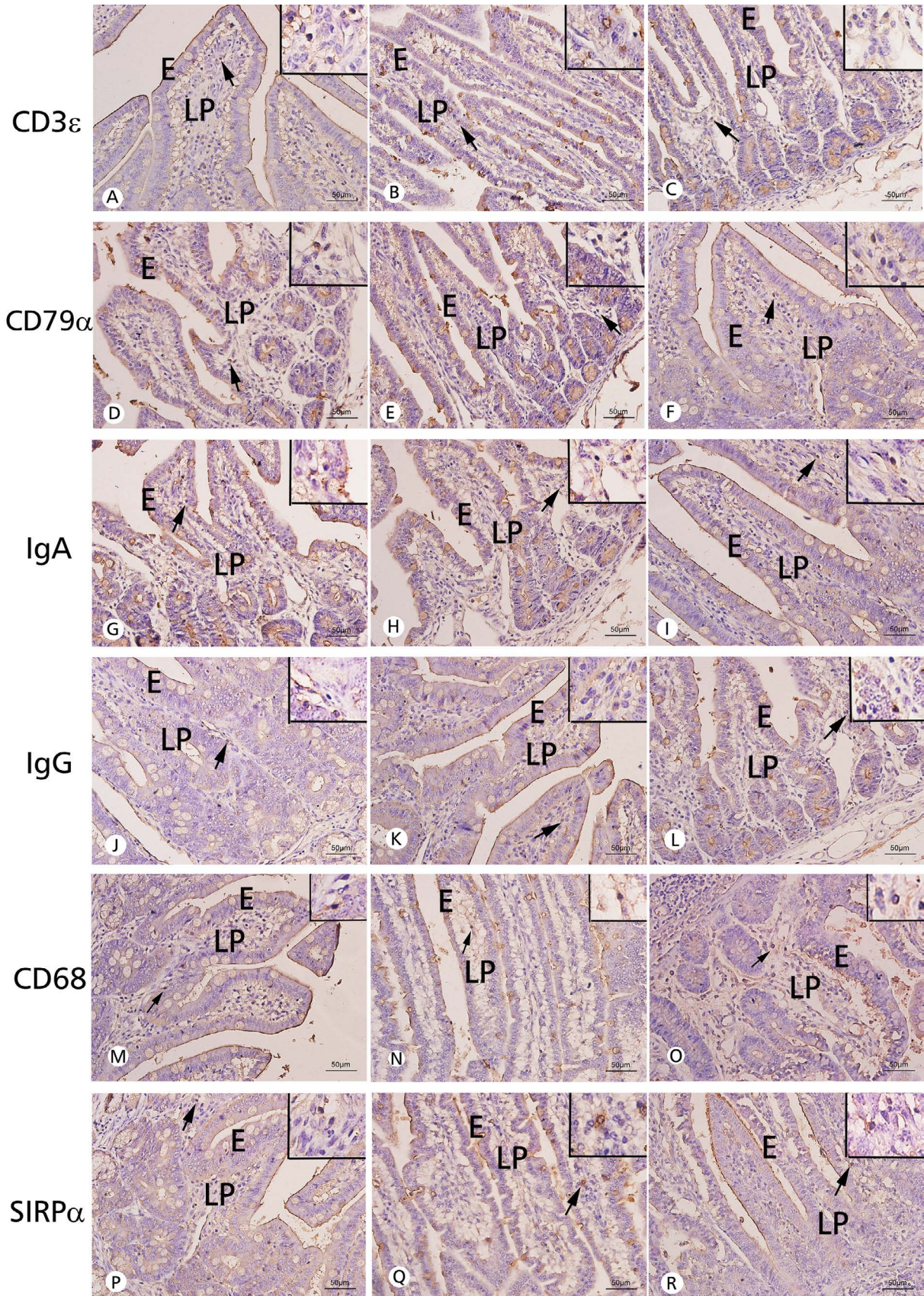
Figure 4. A–R. Immunohistochemical staining of cells expressing CD3ε, CD79α, immunoglobulin A (IgA), immunoglobulin G (IgG), CD68 and signal inhibitory regulatory protein alpha (SIRPα) in the duodenum, jejunum and ileum of newborn yaks; E — mucosal epithelium; LP — lamina propria. Arrows show the positive cells (brown). Bar = 50 μm (low-power lens), bar = 20 μm (high-power lens on the upper right).
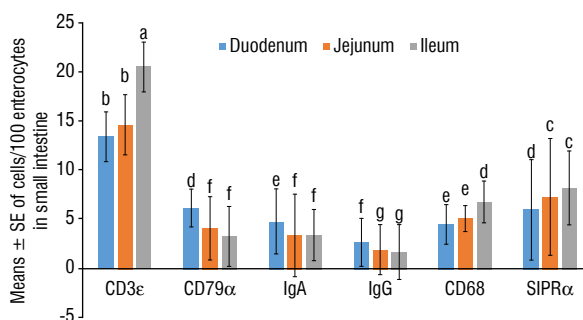
Figure 5. The number of CD3ε, CD79α, immunoglobulin A (IgA), immunoglobulin G (IgG), CD68 and signal inhibitory regulatory protein alpha (SIRPα) positive cells in mucosal epithelium from the duodenum, jejunum and ileum of newborn yaks. Bars with different superscripts are significantly different ($p < 0.05$). Data are normalised and presented as mean $\pm$ standard error (SE) of cells//100 enterocytes.

crypt to the villi (Fig. 6A). Additionally, the number of CD3-positive cells in the lamina propria was higher in the ileum than in the duodenum and jejunum.

CD79α-positive B lymphocytes in the small intestinal mucosa

The membrane staining of CD79α-positive B lymphocytes was localised to the epithelium and lamina propria of the small intestinal mucosa of newborn yaks (Fig. 3D–F). CD79α-positive B lymphocyte levels were highest in the epithelium of the duodenum and then decreased from the duodenum to the ileum ($p < 0.05$) (Fig. 5). Additionally, in the lamina propria, CD79α-positive B lymphocytes increased from the villi to the basal crypt. Moreover, the number of CD79α-positive B lymphocytes in the lamina propria was higher in the duodenum than in the ileum and jejunum ($p < 0.05$) (Fig. 6B).

IgA- and IgG-positive plasmocytes in the small intestinal mucosa

IgA and IgG markers stained the cytoplasm of the plasmocytes. Positive cells appeared in the epithelium and lamina propria of the small intestinal mucosa of newborn yaks (Fig. 3G–L). IgA- and IgG-positive plasmocytes were highest in the epithelium of the duodenum but decreased from the duodenum to the ileum ($p < 0.05$) (Fig. 5). There were no significant differences between the duodenum and the ileum. Furthermore, in the lamina propria, IgA- and IgG-positive plasmocytes increased from the villi to the basal crypt in all regions of the intestine, peaking in the basal crypt ($p < 0.05$) (Fig. 6C, D). Moreover,

the number of IgA- and IgG-positive plasmocytes in the lamina propria was higher in the duodenum than in the ileum and jejunum.

CD68-positive macrophages in the small intestinal mucosa

CD68-positive macrophages presented as large, irregular, or elongated cells scattered in the epithelium and lamina propria of the small intestinal mucosa of newborn yaks (Fig. 3M–O). In the epithelium, CD68-positive macrophages increased from the duodenum to the ileum, peaking in the ileum ($p < 0.05$) (Fig. 5). The difference between the duodenum and jejunum was not significant ($p > 0.05$). Furthermore, in the lamina propria, CD68-positive macrophages increased from the basal crypt to the villi in all regions of the intestine, peaking in the villi ($p < 0.05$) (Fig. 6E). Additionally, the number of CD68 positive macrophages in the lamina propria was higher in the ileum than in the duodenum and jejunum ($p < 0.05$).

SIRPα-positive dendritic cells in the small intestinal mucosa

Strong SIRPα cytoplasmic staining of dendritic cells was observed in the epithelium and lamina propria of the small intestinal mucosa of newborn yaks (Fig. 3P–R). SIRPα-positive dendritic cell numbers were higher in the epithelium of the ileum and jejunum than in the epithelium of the duodenum ($p < 0.05$) (Fig. 5). Furthermore, in the lamina propria, SIRPα-positive dendritic cells increased from the basal crypt to the villi, peaking in the villi ($p < 0.05$) (Fig. 6F). Moreover, the number of SIRPα-positive dendritic cells in the lamina propria was higher in the ileum than in the duodenum and jejunum.

DISCUSSION

Many studies have focused on immunocompetent cells in various species, including lambs [4], calves [6], pigs [21], and mice [22]. However, there are limited data available on the small intestine of newborn yaks. To our knowledge, this is the first study to investigate the distribution of immunocompetent cells of the mucosa and to characterise the changes in these cell markers in the small intestine of newborn yak.

The inner surface of the small intestine is covered with finger-like projections called villi that increase the surface area available for the absorption of nutrients from the gut content. The villi increase the length of
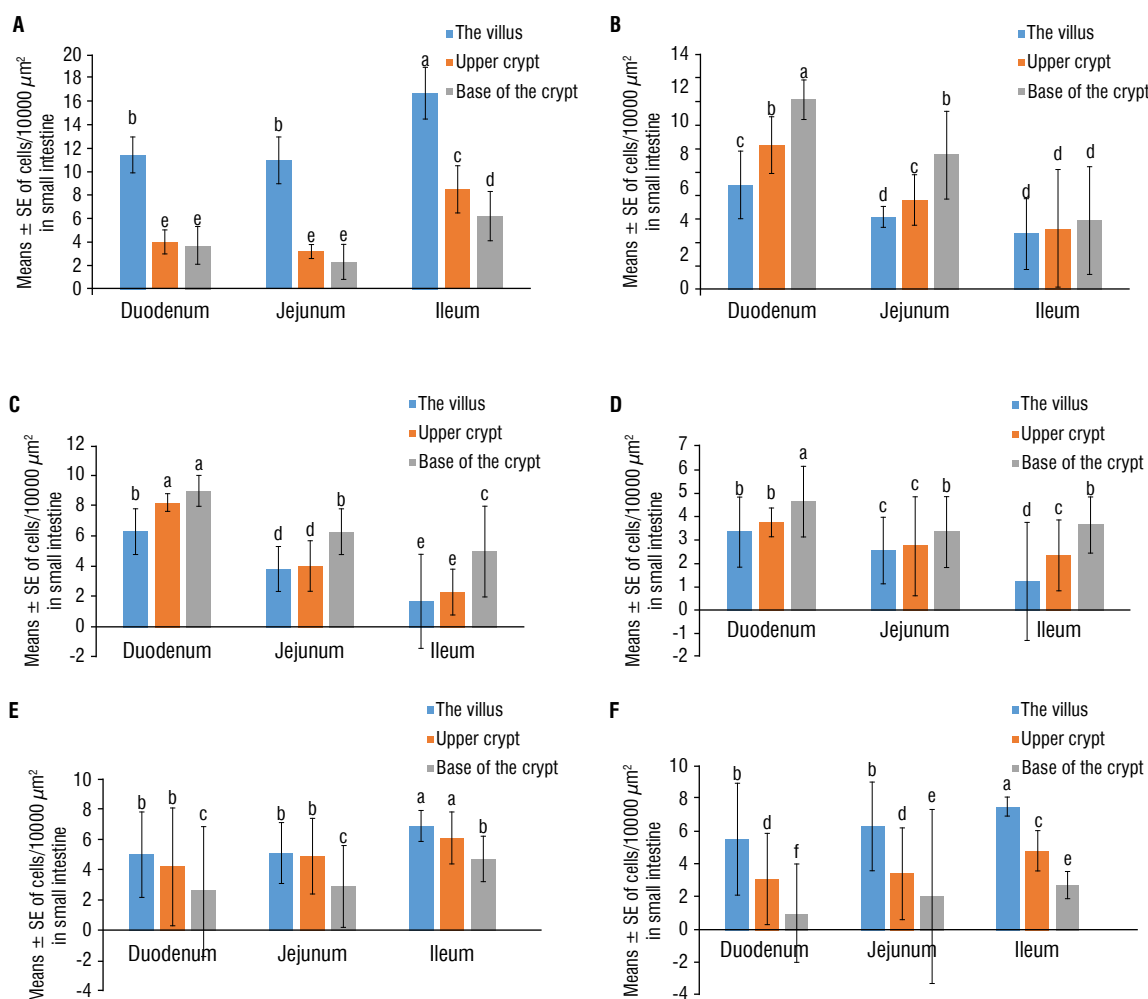
Figure 6. The number of CD3ε (**A**), CD79α (**B**), immunoglobulin A (IgA) (**C**), immunoglobulin G (IgG) (**D**), CD68 (**E**) and signal inhibitory regulatory protein alpha (SIRPα) (**F**) positive cells in mucosal lamina propria from duodenum, jejunum and ileum of newborn yaks. Bars with different superscripts are significantly different (p < 0.05). Data are normalised and presented as mean $\pm$ standard error (SE) of cells/10000 μm^2.

the small intestine and therefore increase the likelihood of a food particle encountering a digestive enzyme and being absorbed across the epithelium and into the bloodstream [13]. In the present study, the largest villous height was observed in the jejunum of newborn yaks; thus, the highest rate of absorption may occur in the jejunum. On the other hand, Zhou [28] reported crypts are formed by secretory epithelial cells. In this study, the deepest crypt depths were located in the jejunum and ileum of the newborn yaks, indicating the highest rate of digestion occurs in the jejunum and ileum of newborn yaks. Furthermore, the ratio of villous height to crypt depth reflected the functional state of the small intestine, with a high ratio indicating a high elimination and absorption function [28]. We also found that the ratio of villous height to crypt depth was higher in the jejunum and ileum than in the duodenum. This may indicate that

the highest rate of absorption and digestion occurs in the jejunum and ileum of newborn yaks.

Possessing the characteristics of both innate and adaptive immunity, T lymphocytes in the mucosa serve as an effective first-line defence against invasive microorganisms [23]. CD3ε is an important differentiation antigen on the surface of the T lymphocyte membrane and a characteristic marker of mature T lymphocytes [10]. We found that the number of CD3ε-positive T lymphocytes was higher in the epithelium and lamina propria of the ileum than those of the duodenum. Consistently, in cats, calves, and goats, the total number of T lymphocytes is greatest in the ileum [4, 6, 24]. Ma reported that CD3ε-positive T lymphocytes in the mucosa of the small intestine can rapidly respond to microbial invasion by activating host defence responses, including the production of mucus and antimicrobial peptides, which

help prevent microbes from reaching the epithelial surface [14]. Additionally, during active infection, T lymphocytes in the mucosa promote epithelial cytolysis and cytokine and chemokine production, which serve to limit pathogen invasion, replication, and dissemination [17]. The distribution characteristics of CD3ε-positive T lymphocytes in the intestinal mucosa in this study suggest that cellular immunity of the intestinal mucosa of newborn yaks mainly occurs in the ileum. Furthermore, we found that the number of CD3ε-positive cells in the lamina propria was higher in the villi than in either of the two crypt regions in newborn yaks. The increase in T lymphocyte density towards the villous tip likely reflects the increased exposure to luminal antigens at this site.

CD79α is a common marker of B lymphocytes that plays a key role in B lymphocyte antigen receptor signal transduction, development, stabilisation, and function [20]. In the present study, a significant number of CD79α-positive cells were observed in the basal crypt area of the lamina propria. Wang reported that B cells of the lamina propria have an increased expression of surface activation markers and exhibit spontaneous immunoglobulin secretion [25]. This indicates that the basal crypt area may be the site of B cell terminal differentiation in the development of immune responses against intestinal antigens. The present study showed a higher number of B lymphocytes in the duodenal epithelium and lamina propria of newborn yaks than in the ileum; similar results have been obtained in lambs and calves [4, 6]. We speculated that the duodenum is likely the first site to come into contact with foreign antigens and activate immune responses. Therefore, the duodenum contains a higher number of B lymphocytes which are stimulated by antigens and involved in humoral immunity.

IgA- and IgG-positive cells are important immunoglobulin secretory cells. Yasuda et al. [27] reported the distribution and quantity of IgA and IgG have been reported to be directly related to the antibody secretion level, and thus reflect the local cellular immune function, of the small intestinal mucosa. In the present study, a greater number of plasmocytes were found in the base of the crypt than in the villi and upper crypt. This indicates that the base of the crypt is a potential site of B lymphocyte terminal differentiation into plasma cells. In both the epithelium and lamina propria, the total number of IgA- and IgG-positive plasma cells was higher in the duodenum than in the jejunum and ileum of newborn yaks. These results

are in general agreement with those found in calves, where the total number of plasmocytes is greatest in the duodenum [27]. Wu et al. [26] reported that, by binding to and entrapping antigens in the mucus layer, IgA and IgG limit their access to the mucosa and promote antigen degradation by enzymes within the lumen. Thus, IgA and IgG may provide a backup system in which antigens that have penetrated the mucosal barrier may be cleared by secretory component-mediated transport in the liver [26]. These findings also reflect that the duodenum is a potential major site of effector function for plasma B lymphocytes. It was likely related to duodenal antigens, bile salts, pancreatic secretions, and other local factors that stimulate the production and maturation of antibody-secreting cells.

CD68 is widely used as a marker for intestinal macrophages [16]. Muller reported that, in non-inflamed intestinal mucosa, the lamina propria extracellular matrix releases transforming growth factor beta and interleukin-8, which then recruit blood monocytes to the lamina propria to become resident macrophages [16]. Farache et al. [5] previously showed that functions of intestinal macrophages include antigen presentation, phagocytosis, and production of immune-regulatory factors. In the present study, CD68-positive macrophages were observed in the epithelium. Mowat reported that the main function of most lamina propria macrophages is to phagocytose bacteria (both commensals and pathogens) crossing the epithelium without evoking a strong inflammatory response [15]. Thus, we speculated that epithelial macrophages in the small intestine of yaks may capture and present antigens to lymphocytes, and may also be engaged in the phagocytosis of senescent intestinal epithelial cells. The number of CD68-positive macrophages in the lamina propria was higher in the villi than in the other regions of newborn yaks. Similarly, Bain and Schridde [1] reported that macrophage concentrations were highest in the villi of the intestinal lamina propria. This result suggests that the villi may play a larger role in antigen stimulation and macrophage recruitment than other areas of the lamina propria. Interestingly, macrophages positive for CD68 were more commonly found in the epithelium and the lamina propria of the ileum than in other regions of the intestine. This suggests that the ileal mucosa of newborn yaks may be more susceptible to antigen capture and processing than the mucosa of the duodenum and jejunum.

Dendritic cells express SIRPα [2]. Mucosal dendritic cells are a key link between innate and acquired

immunity via their roles in antigen presentation and regulation of T cell activation [2]. In the present study, SIRPα-positive dendritic cells were observed in the epithelium of the small intestine of newborn yaks. It has been previously suggested that dendritic cells can extend their dendrites into the lumen between epithelial cells to handle antigens. In this study, we found a higher number of SIRPα-positive cells in the villi of the lamina propria. We believe the appearance of abundant SIRPα-positive cells in the villi of the lamina propria was because the site is easily exposed to lymphocytes and bacterial or dietary antigens. Furthermore, we found that SIRPα-positive cell concentrations were higher in the epithelium and lamina propria of the ileum and jejunum of newborn yaks. The distribution trend was similar to that for T lymphocytes. Coombes and Powrie [3] showed that dendritic cells expressing the chemokine receptor CCR6 could activate T lymphocytes in response to bacterial invasion. Previous reports have indicated that the wide distribution of dendritic cells in the ileum and jejunum play critical roles in the regulation of intestinal immunity, antigen uptake, and T lymphocyte activation [3, 11, 12].

In this study, RT-qPCR was used to detect specific immune cell markers. The mRNA expression levels of CD3ε, CD68, and SIRPα were significantly higher than those of CD79α, IgA, and IgG in the same intestinal regions. Thus, we speculate that in the small intestine of newborn yaks, T lymphocytes, macrophages, and dendritic cells may be more abundant than B lymphocytes and plasmocytes. Additionally, we also found that the mRNA expression levels of CD3ε, CD68, and SIRPα were higher in the ileum, whereas CD79α, IgA, and IgG mRNA expression levels were higher in the duodenum. These observations indicate that local humoral immunity may occur more commonly in the ileum, while cellular immunity may occur more commonly in the duodenum.

CONCLUSIONS

In summary, we immunohistochemically characterised immune cells in the small intestinal mucosa and analysed the mRNA expression level of immune factors in the small intestine of newborn yaks. In the epithelium CD3ε-positive T lymphocytes were more popular than the other immune cells. In the lamina propria, CD3ε-positive T lymphocytes, CD68-positive macrophages and SIRPα-positive dendritic cells were more highly concentrated in the villi, while CD79α-positive B lymphocytes, and IgA- and IgG-pos-

itive plasmocytes were more prevalent in the base of the crypt. Furthermore, a higher number of T lymphocytes, macrophages and dendritic cells were located in the epithelium and lamina propria of the ileum than those of the duodenum and jejunum; B lymphocytes, and IgA and IgG plasmocytes were more likely to be observed in the epithelium and lamina propria of the duodenum of newborn yaks than those of the jejunum and ileum. These findings suggest that cellular immunity and antigen presentation are more readily activated in the epithelium, the villi of the lamina propria, and the ileal mucosa of the small intestine of newborn yaks, while humoral immune cells are mostly concentrated in the base of the crypt of the lamina propria and duodenal mucosa. The results from this study will provide information on the baseline characteristics of immune cells in the small intestine of newborn yaks and serve as a reference for future studies on various immunologic reactions in both healthy yaks and those with digestive diseases.

Conflict of interest: None declared

REFERENCES

1. Bain CC, Schridde A. Origin, differentiation, and function of intestinal macrophages. Front Immunol. 2018; 9: 2733, doi: 10.3389/fimmu.2018.02733, indexed in Pubmed: 30538701.

2. Bekiaris V, Persson EK, Agace WW. Intestinal dendritic cells in the regulation of mucosal immunity. Immunol Rev. 2014; 260(1): 86–101, doi: 10.1111/imr.12194, indexed in Pubmed: 24942684.

3. Coombes JL, Powrie F. Dendritic cells in intestinal immune regulation. Nat Rev Immunol. 2008; 8(6): 435–446, doi: 10.1038/nri2335, indexed in Pubmed: 18500229.

4. Corpa JM, Juste RA, García Marín JF, et al. Distribution of lymphocyte subsets in the small intestine lymphoid tissue of 1-month-old lambs. Anat Histol Embryol. 2001; 30(2): 121–127, indexed in Pubmed: 11379367.

5. Farache J, Zigmond E, Shakhar G, et al. Contributions of dendritic cells and macrophages to intestinal homeostasis and immune defense. Immunol Cell Biol. 2013; 91(3):

232–239, doi: 10.1038/icb.2012.79, indexed in Pubmed: 23399695.

6. Fries PN, Popowych YI, Guan LeL, et al. Age-related changes in the distribution and frequency of myeloid and T cell populations in the small intestine of calves. Cell Immunol. 2011; 271(2): 428–437, doi: 10.1016/j.cellimm.2011.08.012, indexed in Pubmed: 21917242.

7. German AJ, Hall EJ, Day MJ. Analysis of leucocyte subsets in the canine intestine. J Comp Pathol. 1999; 120(2): 129–145, doi: 10.1053/jcpa.1998.0262, indexed in Pubmed: 10087487.

8. Hitotsumatsu O, Hamada H, Naganuma M, et al. Identification and characterization of novel gut-associated lymphoid tissues in rat small intestine. J Gastroenterol. 2005; 40(10): 956–963, doi: 10.1007/s00535-005-1679-8, indexed in Pubmed: 16261432.

9. Hou HW, Wen Y. Investigation and control of diarrhea in yak calf in Gannan alpine grazing area. Chin J Vet Med. 2007; 43(3): 26, doi: CNKI:SUN:ZSYZ.0.2007-03-012.

10. Hu MD, Jia L, Edelblum KL. Policing the intestinal epithelial barrier: Innate immune functions of intraepithelial lymphocytes. Curr Pathobiol Rep. 2018; 6(1): 35–46, indexed in Pubmed: 29755893.

11. Iwasaki A. Mucosal Dendritic Cells. Ann Rev Immunol. 2007; 25(1): 381–418, doi: 10.1146/annurev.immunol.25.022106.141634.

12. Johansson C, Kelsall BL. Phenotype and function of intestinal dendritic cells. Semin Immunol. 2005; 17(4): 284–294, doi: 10.1016/j.smim.2005.05.010, indexed in Pubmed: 15978836.

13. Korkmaz D, Kum S. A histological and histochemical study of the small intestine of the dromedary camel (Camelus dromedarius). J Camel Pract Res. 2016; 23(1): 111, doi: 10.5958/2277-8934.2016.00018.7.

14. Ma H, Tao W, Zhu S. T lymphocytes in the intestinal mucosa: defense and tolerance. Cell Mol Immunol. 2019; 16(3): 216–224, doi: 10.1038/s41423-019-0208-2, indexed in Pubmed: 30787416.

15. Mowat AM, Bain CC. Mucosal macrophages in intestinal homeostasis and inflammation. J Innate Immun. 2011; 3(6): 550–564, doi: 10.1159/000329099, indexed in Pubmed: 22025201.

16. Muller PA, Matheis F, Mucida D. Gut macrophages: key players in intestinal immunity and tissue physiology. Curr Opin Immunol. 2020; 62: 54–61, doi: 10.1016/j.coi.2019.11.011, indexed in Pubmed: 31841704.

17. Pérez-Cano FJ, Castellote C, González-Castro AM, et al. Developmental changes in intraepithelial T lymphocytes and NK cells in the small intestine of neonatal rats. Pediatr Res. 2005; 58(5): 885–891, doi: 10.1203/01.pdr.0000182187.88505.49, indexed in Pubmed: 16257927.

18. Powell N, MacDonald TT. Recent advances in gut immunology. Parasite Immunol. 2017; 39(6), doi: 10.1111/pim.12430, indexed in Pubmed: 28370104.

19. Qiu Q, Zhang G, Ma T, et al. The yak genome and adaptation to life at high altitude. Nat Genet. 2012; 44(8): 946–949, doi: 10.1038/ng.2343, indexed in Pubmed: 22751099.

20. Ratcliffe M. B cell development in gut associated lymphoid tissues. Vet Immunol Immunopathol. 2002; 87(3-4): 337–340, doi: 10.1016/s0165-2427(02)00061-2.

21. Solano-Aguilar G, Vengroski K, Beshah E, et al. Characterization of lymphocyte subsets from mucosal tissues in neonatal swine. Develop Comp Immunol. 2001; 25(3): 245–263, doi: 10.1016/s0145-305x(00)00053-7.

22. Suzuki H. Age-dependent changes in intraepithelial lymphocytes (IELs) of the small intestine, cecum, and colon from young adult to aged mice. Arch Gerontol Geriatr. 2012; 55(2): 261–270, doi: 10.1016/j.archger.2011.07.009, indexed in Pubmed: 21840070.

23. Tamura A, Soga H, Yaguchi K, et al. Distribution of two types of lymphocytes (intraepithelial and lamina-propria-associated) in the murine small intestine. Cell Tissue Res. 2003; 313(1): 47–53, doi: 10.1007/s00441-003-0706-4, indexed in Pubmed: 12827490.

24. Waly N, Gruffydd-Jones TJ, Stokes CR, et al. The distribution of leucocyte subsets in the small intestine of healthy cats. J Comp Pathol. 2001; 124(2-3): 172–182, doi: 10.1053/jcpa.2000.0450, indexed in Pubmed: 11222015.

25. Wang Z, Wang L, Qian T, et al. Chemokines and receptors in intestinal B lymphocytes. J Leukocyte Biol. 2018; 103(5): 807–819, doi: 10.1002/jlb.1ru0717-299rr.

26. Wu CT, Davis PA, Luketic VA, et al. A review of the physiological and immunological functions of biliary epithelial cells: targets for primary biliary cirrhosis, primary sclerosing cholangitis and drug-induced ductopenias. Clin Dev Immunol. 2004; 11(3-4): 205–213, doi: 10.1080/17402520400004177, indexed in Pubmed: 15559365.

27. Yasuda M, Fujino M, Nasu T, et al. Histological studies on the ontogeny of bovine gut-associated lymphoid tissue: appearance of T cells and development of IgG+ and IgA+ cells in lymphoid follicles. Dev Comp Immunol. 2004; 28(4): 357–369, doi: 10.1016/j.dci.2003.09.013, indexed in Pubmed: 14698221.

28. Zhou YJ, Gao J, Yang HM, et al. Morphology and ontogeny of dendritic cells in rats at different development periods. World J Gastroenterol. 2009; 15(10): 1246––1253, doi: 10.3748/wjg.15.1246, indexed in Pubmed: 19291826.

V M
VIA MEDICA

 O R I G I N A L   A R T I C L E

Decay score: a guide to the immunoreactivity of human pancreatic islets in autopsy specimen

P.K. Ravi[1], S. Purkait[2], S.R. Singh[3], P.R. Mishra[1]

[1]Department of Anatomy, All India Institute of Medical Sciences, Bhubaneswar, Odisha, India
[2]Department of Pathology, All India Institute of Medical Sciences, Bhubaneswar, Odisha, India
[3]Department of Forensic Medicine and Toxicology, All India Institute of Medical Sciences, Bhubaneswar, Odisha, India

Background: The pancreas is an exo-endocrine organ that undergoes rapid autolysis soon after death, which limits its utility in academics and research. The timeline of autolytic changes of pancreatic islets and its immunoreactivity is limited in the literature. Decay score has been used to grade the autolytic changes in organs like the brain, lung and liver. However, reports are not available in the pancreas/pancreatic islets. Knowledge regarding the decay score may be used as a torchbearer for the immunoreactivity of human pancreatic islets in autopsy cases. The present study is aimed to provide an optimal cut-off time based on the decay score before which pancreatic specimens should be collected for the purpose of immunohistochemical studies (IHC) of pancreatic islets.

Materials and methods: Serial sections of 20 adult human pancreases obtained from the autopsy were subjected to haematoxylin and eosin (H&E) and immunohistochemical staining. Autolytic changes of pancreatic islets were graded by using decay score in H&E sections, which was compared with the results of the immunohistochemical reactivity of pancreatic islets in IHC sections.

Results and Conclusions: Pancreatic islets immunoreactivity was found to be well preserved in the samples collected early within 9 hours with a decay score of less than 1.4. There was an inverse relation of decay score and immunoreactivity of pancreatic islets. The decay score of less than 1.4 has better-preserved immunoreactivity than having more than 1.4. This knowledge will help researchers working in the field of the endocrine pancreas. (Folia Morphol 2022; 81, 1: 101–106)

Key words: autolysis, pancreatic islets, immunohistochemistry, decay score, human pancreas

INTRODUCTION

Brain-dead organ donors and autopsy are the two major sources of whole human pancreatic tissue for academics and research [8, 10, 15, 17]. The availability of brain-dead donor pancreas is limited in developing countries. Thus, the autopsy is the only source of the whole pancreatic tissue, yet its utility is limited by the appearance of early autolytic changes following death [4, 6, 13]. Well-preserved micro-architecture and immunogenicity are the integral part of any histological and immunohistochemical studies (IHC) on pancreas, including islets. A review of studies on the human pancreas did not reveal any standardised cut off time following death within which the specimen

Table 1. Information about the subjects

Case no.	Age [years]	Gender	Body mass index [kg/m²]	Time since death [h]
1	45	Male	29.30	13.5
2	52	Male	28.73	4.5
3	28	Male	21.10	9
4	60	Male	22.20	7.5
5	43	Female	18.49	7.25
6	30	Female	20.57	8.5
7	34	Female	20.89	13
8	34	Female	22.22	10
9	35	Male	24.28	5
10	75	Male	18.33	5.25
11	45	Male	19.08	9
12	27	Male	19.77	12
13	25	Male	28.48	7
14	62	Male	21.47	5.5
15	45	Female	21.32	4.5
16	28	Male	25.79	7.5
17	23	Female	23.61	7.25
18	42	Female	33.25	12
19	34	Female	18.92	10.5
20	35	Male	27.28	10

has to be collected for IHC of pancreatic islets. Decay score has been used to grade the autolytic changes in organs like the brain, lung and liver. However, decay score grading of autolytic changes is not performed in the pancreas/pancreatic islets. The present study is aimed to provide an optimal cut-off time based on the decay score before which pancreatic specimens should be collected from autopsy for the purpose of IHC of pancreatic islets.

MATERIALS AND METHODS

Pancreas collection:

A total of 20 autopsy specimens of the adult human (age range 23–75 years) pancreas were collected after the approval of the Institutional Ethical Committee (vide approval No. IEC/AIIMS BBSR/PG Thesis/2017-18/22). The cause of death, time since death and existence of other co-morbid conditions were documented (Table 1). In most of the cases, the cause of death was road traffic accident and none of the cases were associated with chronic diseases like diabetes. Pancreatic specimens with congenital anomalies or showing gross abnormalities like a cyst, tumour was excluded.

The incision was made over the constricted neck region of the pancreas (in relation to portal vein) to divide the head from the rest of the pancreas. Then the rest of the pancreas was divided into two equal parts (body and tail) as described in the previous studies [3, 12]. After overnight fixation in 10% neutral buffered formalin solution, the whole coronal section and horizontal section of the pancreatic head, body and tail were again subdivided into small sub-blocks (approximately 40 sub-blocks were obtained from each pancreas). All the well-labelled sub-blocks were fixed in 10% neutral buffered formalin followed by automated tissue processing by Leica automated tissue processor. Sections from the first tissue block of each part of the pancreas (one each from head, body and tail region; first coronal section) were utilized for this study, the rest of the paraffin-embedded pancreatic tissue blocks were preserved for further studies. Serial sections from the selected block were stained with haematoxylin and eosin (H&E) and immunohistochemically with anti-synaptophysin and anti-insulin antibodies. Cases showing features of occult pancreatitis in H&E staining were also excluded and no IHC was done.
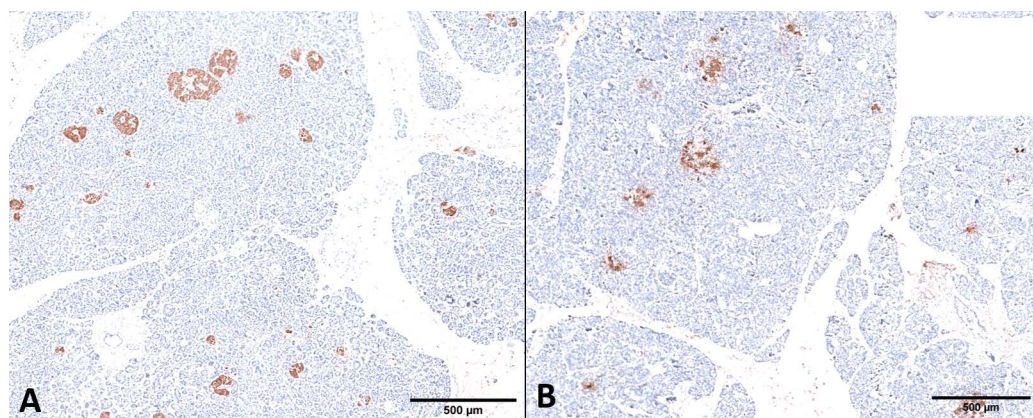
Figure 1. Photographs of immunohistochemistry slides showing sharp and strong positivity (**A**) in the islets with decay score of less than 1.4; **B.** The diffused immunoreactivity.

Immunohistochemistry

Immunohistochemical studies were done on two consecutive 4 μm thick paraffin sections. Antigen retrieval was done with citrate buffer by using the heat antigen retrieval method under pressure. Serial sections of each block were stained using a rabbit monoclonal anti-synaptophysin antibody (1:300) (PathnSitu, Livermore, California) (45 min incubation) for identifying islets and rabbit monoclonal anti-insulin (1:200) (PathnSitu, Livermore, California) (45 min incubation) for identifying beta-cells. The primary antibody was detected by a secondary antibody labelled with Horseradish peroxidase (HRP) and DAB (3,3-diaminobenzidine) chromogen (DAKO, Carpinteria, CA). Immunohistochemical positivity was assessed under 40× in a bright-field microscope (Olympus BX43 microscope) based on the rate of positivity and its sharpness (Fig. 1).

Grading of autolysis

All the H&E slides were screened at lower power to identify the areas which showing maximum autolytic changes. Those identified areas were examined under a 40× bright field microscope (Olympus BX43 microscope). Five high power fields from each slide were used for the assessment of autolytic changes based on the cellular and nuclear architecture: normal nucleus (grade 1), pyknosis and minimal karyorrhexis (grade 2), prominent karyorrhexis (grade 3), no nucleus visible (grade 4) and no cell visible (grade 5) [9]. Autolytic changes will be heterogeneous even in single islets; i.e. cells within single islets will show different grades of nuclear changes. To maintain the uniform standard of scoring the autolytic changes we adapted the decay score for each high-power

field from previous literature [9]. The decay score is calculated by multiplying the percentage of cells with a certain grade of nuclear changes by the value of grades (1–5) and summing these values. For example, within a single islet, 25% of cells showing features of grade 1 (normal), 50% of cells with grade 2 and 25% of cells with grade 3 autolytic changes, the overall decay score was calculated as (0.25 × 1) + + (0.5 × 2) + (0.25 × 3) = 2.0. The final decay score of each slide will be calculated from the mean of five high-power fields. Decay score grading was done by three independent observers in different time period, the average score of the three observers was taken as the final score.

Statistical analysis

Data were summarised and expressed as mean ± standard error of mean (SEM). One-way ANOVA was used to compare the data between more than two groups. Paired 't' test was used to compare the data of means decay score in head, body and tail of the pancreas. P value < 0.05 taken as significant. Spearman correlation was used to compare the relation between decay score with time since death and immunoreactivity. Statistical test was performed by the using SPSS software version 25 and graphs were plotted by Microsoft Excel 2019 software.

RESULTS

The pancreatic samples were categorised into three groups based on the time since death: group 1 — less than 6 hours of death, group 2 — from 6 hours to 9 hours of the death and group 3 — more than 9 hours of death to 14 hours.

Micro-architectural changes in H&E

The decay score of all the individual pancreas was plotted in Figure 2 with its immunohistochemical reactivity status. Mean decay score of group 1, group 2 and group 3 are 1.351 ± 0.715, 1.409 ± 0.225 and 1.895 ± 0.793, respectively. The statistical significance was observed between group 1 and group 3 with a p-value of < 0.042. The statistically significant positive correlation (r = 0.479) was observed between decay score and the time since death with the p-value of 0.033. The mean decay score of head, body and tail of all the cases was 1.54 ± 0.655, 1.543 ± 0.604 and 1.56 ± 0.645. There was no statistically significant difference in the histological appearance of autolytic changes in various parts of the pancreas.

Immunohistochemical reactivity

Decay score and time since death were inversely proportional to the immunoreactivity of the pancreatic islets (Fig. 2). Strong immunoreactivity of pancreatic islets in groups 1, 2 and 3 was 80%, 72% and 42.85%, respectively (Fig. 3). The mean decay score of the pancreatic islets with strong immunoreactivity was 1.22 ± 0.182 and 2.205 ± 0.652 for specimens with poor immunoreactivity. The statistically significant negative correlation (r = –0.736) was observed between the decay score and immune reactivity of pancreatic islets with the p-value of < 0.0001. Furthermore, all the strong IHC positive tissue has decay score less than 1.4 except sample no. 20 which had weak immune reactivity and a decay score of 1.39. Samples showing strong immunoreactivity for islets also shown similar reactivity for beta-cells.

DISCUSSION

Most of the studies on pancreatic islets have used animal models [1]. The studies involving microscopic analysis of human pancreatic islets are limited and the majority of these are from developed countries where tissue samples from the brain-dead donor are easily available [7, 11, 16]. The critical factor limiting the use of human pancreatic samples from the autopsy is the appearance of early autolytic changes in the pancreatic tissue (exocrine and endocrine) within an hour of death [13]. As the pancreas contains a high number of proteolytic enzymes, it undergoes rapid autodigestion soon after death. The autopsy done after 12 hours of death renders the pancreatic tissue unusable [13]. The various components of pancreatic tissue like exocrine, endocrine and stromal parts may
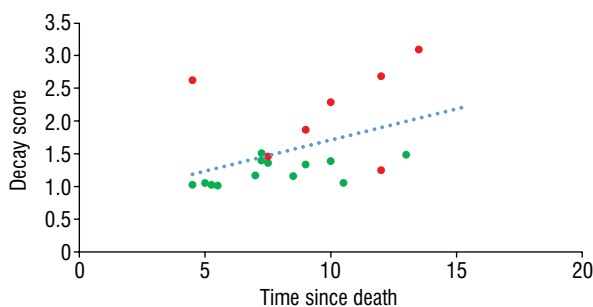
Figure 2. Scatter plot showing the comparison of decay score with time since death ($R^2 = 0.185$) and immunoreactivity status; red dot — poor immunoreactivity; green dot — good immunoreactivity
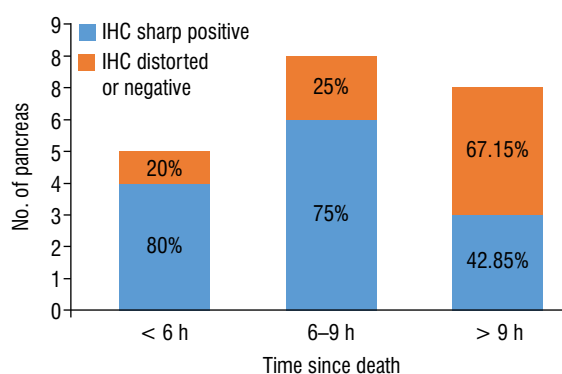
Figure 3. The percentage of pancreatic sample having preserved and diffused immunoreactivity in relation to time since death; IHC — immunohistochemical studies.

show a variable timeline of autolytic changes, i.e. the exocrine part undergoes autolysis earlier than endocrine and stromal components [4]. Siriwardana et al. [13], given the timeline of autolytic changes in the pancreas as a whole, which may not be useful for endocrine study. The current study is focused on the autolytic changes of endocrine pancreas (islets) to guide the IHC on pancreatic islets specifically.

As there is a paucity of data regarding time since death and an acceptable amount of autolytic changes in pancreatic islets, many studies in the literature have used a wide range of cut-off time varying from 6 hours to 24 hours after death or cold ischaemia. The present study shows that autolytic changes increase with time, which in turn inversely affects the immunoreactivity of the pancreatic islets. Authors found that 67.15% of pancreatic samples collected after 9 hours of death were showed diffused or absent immunoreactivity, but similar findings were found only in 23% of samples which were collected within

9 hours of death. Thus, if the pancreatic tissue is preserved in formalin within 9 hours of death, its immunoreactivity is highly maintained (75% to 80%). The finding of the present study is consistent with the existing literature in which the author graded the autolytic changes with H&E staining without mentioning its immunoreactivity [5].

The autolytic changes of a particular islet will be heterogeneous in nature, i.e. all the cells in the islet may not show a similar grade of autolysis. The decay score system helps us to objectively score the autolytic changes in a particular islet. We observed an increasing trend of decay score with time. Higher the decay score of pancreatic islets represents the greater degree of tissue destruction, which in turn results in poor immunoreactivity of the tissue. We found that slides with a decay score of less than 1.4 had good immunoreactivity and this value (decay score 1.4) may be used as the cut off to proceed for IHC. Immunoreactivity of samples obtained from surgeries and the brain-dead donors were mainly influenced by the cold ischaemia time. The cold ischaemia time is the interval between the removal of tissue from the body and its contact with formalin. Autolytic changes still occur even in the period of cold ischaemia [5]. Autolytic changes may be delayed in the foetal pancreas (under 5-month) due to underdeveloped exocrine part (less proteolytic enzymes) when compared with adult pancreas [2].

Even though most of the cases showed a consistent relation between degree of autolysis and time since death; in 1 case severe autolytic changes (decay score of 2.63) was observed in less than 6 hours of death but in few other specimens well-preserved micro-architectures (decay score of 1.49) and staining immunogenicity were seen even after 12 hours of death. Similar findings have also been reported in post-mortem studies of lung, liver and brain tissue, in which authors justified that the above variation as a pattern of normal distribution [9]. Apart from that, the inaccurate record of the time of death in cases where the death occurred outside the hospital setup may explain the confounding results. In spite of the controversial observation between time since death and immunoreactivity, the relationship between the decay score and immunoreactivity of pancreatic tissue is maintained. Thus, the decay score might be used as a tool to know the antigenic status of the tissue prior to the immunohistochemistry of autopsy specimens.

Immunoreactivity is not only affected by time since death, but also by any defect in the tissue processing and staining procedure. Studies have reported that factors like fixation time, dehydration, clearing, paraffin impregnation, antigen retrieval and IHC staining procedures also play a significant role in the optimal expression of tissue antigenicity [9, 14]. The authors believe that the factors involving tissue processing and staining have a very insignificant role in the present study as all the samples used here were processed and stained by using the standard protocol in the same laboratory setup.

CONCLUSIONS

Pancreatic islets immunoreactivity was found to be well preserved in the samples collected early within 9 hours with a decay score of less than 1.4. There is an inverse relationship between the decay score and immunoreactivity of islets, i.e. smaller the decay score, better the immunoreactivity. To the best of our knowledge, no literature is available on the autolytic changes and immunoreactivity of human pancreatic islets. The present study concludes that the time since death may not be the sole criterion to determine the immunoreactivity of the pancreatic islets. The decay score of pancreatic islets must be taken into consideration prior to the IHC. This knowledge will help the researchers working in the field of the endocrine pancreas.

Conflict of interest: None declared

REFERENCES

1. Abunasef SK, Amin HA, Abdel-Hamid GA. A histological and immunohistochemical study of beta cells in streptozotocin diabetic rats treated with caffeine. Folia Histochem Cytobiol. 2014; 52(1): 42–50, doi: 10.5603/FHC.2014.0005, indexed in Pubmed: 24802960.
2. Banting FG, Best CH, Collip JB, et al. Pancreatic extracts in the treatment of diabetes mellitus. Can Med Assoc J. 1922; 12(3): 141–146, indexed in Pubmed: 20314060.
3. Campbell-Thompson ML, Montgomery EL, Foss RM, et al. Collection protocol for human pancreas. J Vis Exp. 2012(63): e4039, doi: 10.3791/4039, indexed in Pubmed: 22665046.
4. Cocariu EA, Mageriu V, Stăniceanu F, et al. Correlations between the autolytic changes and postmortem interval in refrigerated cadavers. Rom J Intern Med. 2016; 54(2):

105–112, doi: 10.1515/rjim-2016-0012, indexed in Pubmed: 27352439.

5. Hilling DE, Bouwman E, Terpstra OT, et al. Effects of donor-, pancreas-, and isolation-related variables on human islet isolation outcome: a systematic review. Cell Transplant. 2014; 23(8): 921–928, doi: 10.3727/096368913X666412, indexed in Pubmed: 23635354.

6. Holtzer RL, Van Lancker JL. Early changes in pancreas autolysis. Am J Pathol. 1962; 40: 331–336, indexed in Pubmed: 13908608.

7. Ionescu-Tirgoviste C, Gagniuc PA, Gubceac E, et al. A 3D map of the islet routes throughout the healthy human pancreas. Sci Rep. 2015; 5: 14634, doi: 10.1038/srep14634, indexed in Pubmed: 26417671.

8. Jones LC, Clark A. Beta-cell neogenesis in type 2 diabetes. Diabetes. 2001; 50 Suppl 1: S186–S187, doi: 10.2337/diabetes.50.2007.s186, indexed in Pubmed: 11272189.

9. Lesnikova I, Schreckenbach MN, Kristensen MP, et al. Usability of Immunohistochemistry in Forensic Samples With Varying Decomposition. Am J Forensic Med Pathol. 2018; 39(3): 185–191, doi: 10.1097/PAF.0000000000000408, indexed in Pubmed: 29794805.

10. Olehnik SK, Fowler JL, Avramovich G, et al. Quantitative analysis of intra- and inter-individual variability of human beta-cell mass. Sci Rep. 2017; 7(1): 16398, doi: 10.1038/s41598-017-16300-w, indexed in Pubmed: 29180621.

11. Poudel A, Fowler JL, Zielinski MC, et al. Stereological analyses of the whole human pancreas. Sci Rep. 2016; 6: 34049, doi: 10.1038/srep34049, indexed in Pubmed: 27658965.

12. Ravi PK, Purkait S, Agrawal U, et al. Regional variation of human pancreatic islets dimension and its impact on beta cells in Indian population. Islets. 2019; 11(6): 141–151, doi: 10.1080/19382014.2019.1686323, indexed in Pubmed: 31743072.

13. Siriwardana RC, Deen KI, Hevawesenthi J. Postmortem sampling of the pancreas for histological examination: what is the optimum cut-off time? JOP. 2010; 11(1): 87–88, indexed in Pubmed: 20065563.

14. Suvarna S, Layton C, Bancroft JD. Bancroft's Theory and Practice of Histology Techniques. 7th ed. Churchill Livingstone, China 2013.

15. Wang X, Misawa R, Zielinski MC, et al. Regional differences in islet distribution in the human pancreas — preferential beta-cell loss in the head region in patients with type 2 diabetes. PLoS One. 2013; 8(6): e67454, doi: 10.1371/journal.pone.0067454, indexed in Pubmed: 23826303.

16. Wang X, Zielinski MC, Misawa R, et al. Quantitative analysis of pancreatic polypeptide cell distribution in the human pancreas. PLoS One. 2013; 8(1): e55501, doi: 10.1371/journal.pone.0055501, indexed in Pubmed: 23383206.

17. Yagihashi S, Inaba W, Mizukami H. Dynamic pathology of islet endocrine cells in type 2 diabetes: beta-cell growth, death, regeneration and their clinical implications. J Diabetes Investig. 2016; 7(2): 155–165, doi: 10.1111/jdi.12424, indexed in Pubmed: 27042265.

V M
VIA MEDICA

ORIGINAL ARTICLE

Effect of seasonal changes on the innate immunity of wild *Pseudois nayaur*: potential reason for its endangerment

B. Song[2], B. Wu[1, 2]

[1]*Key Laboratory of Southwest China Wildlife Resources Conservation, Ministry of Education, Sichuan, PR China*
[2]*College of Life Science, China West Normal University, Sichuan, PR China*

Background: Seasonal climate change may impose stress on mammal's immune system, but this has never been connected to wildlife endangerment reasons. This study focuses on Pseudois nayaur, a rare Chinese sheep facing a severe situation of disappearing.
Materials and methods: Wild Pseudois nayaurs in Sichuan, China were observed in this research by an integrated method including habitat environment, foraging rules, and breeding activities investigation in ecology filed, accompanied with immunity research by peripheral blood, including erythrocyte, neutrophils, natural killer cells, and macrophages immunity by means of erythrocyte rosette, phagocytosis, lactate dehydrogenase release and acid alpha-naphthyl acetate esterase method, respectively.
Results: The results show that Pseudois nayaurs's innate and red blood cell immunity in autumn and winter Pseudois nayaurs and it may be the results of energy reallocation between reproduction and the immune system. In addition, the environment pressure found in Zhu Balong, Sichuan, China including food reduction, human disturbance, low temperature, and severe drought still existed, which may prevent the Pseudois nayaur from normal immunity enhancement before winter.
Conclusions: In conclusion, the innate immunosuppression found in this study especially at their breeding season in autumn and winter may be the ignored cause of wild Pseudois nayaur's endangerment and should be considered in their protection strategy. (Folia Morphol 2022; 81, 1: 107–116)

Key words: *Pseudois nayaur*, ecological immunity, immunosuppression, seasonal change, reproductive coercion

INTRODUCTION

Pseudois nayaur, a cherished wild species in China under the protection of Chinese government by the law of State Protection of China and the International Union for Conservation of Nature, is in danger of extinction. From 1988 to 2003, their habitat area had decreased about 48,000 km[2] in Batang, Sichuan. For the protection of this species, many studied their behavioural traits and living habits. For instance, some mentioned that the group behaviours of them were too

vulnerable to escape from the predators [19, 28]. Moreover, the skin-based trade was revealed by researches and the *Pseudois nayaurs* were always easily caught by both human and predators because of the changeless water-drinking places [20, 28]. As the protection law executed strictly, these predictable factors had been removed. However, the number of the *Pseudois nayaurs* has not increased as expected; only 500–700 ones were speculated to exist in this area [13]. This indicates that the main reasons for its endangerment are still unknown and unresolved, which asks for more attention to its physiology features, especially for the immune system that determines individuals' death directly.

Animal ecological immunology was defined in the 1990s, covering the study of animal immunity changes under certain environment conditions which were used to wide-ranged science research from physiology to molecular biology [26, 27]. One of the most important phenomenons to wildlife in the field is the periodic changes in immune system controlled by hormone and innate immunity. It was found that some mammals tend to enhance their innate immunity to get through the living challenges in winter [23], which is mainly correlated to temperature-controlled gene regulation [31]. However, Harshman and Zera [11] studied that a decrease of immunity also existed when the reproduction time is coming up, which means there may be a trade-off relationship between immunity and reproduction [2, 7], but few studies have targeted so far the ones whose reproductive time is between autumn and winter which also asks for energy in immunity enhancement. So, what's the body choice when facing both challenges in reproduction and immunity? Through *Pseudois nayaur*, the remained questions can be answered, and the relationship between its endangerment and this body choice could also be revealed.

To understand the trade-off relationship between immunity and reproduction in winter-reproduction mammals, and help protect *Pseudois nayaur* in a more scientific way. The study investigated *Pseudois nayaur* by the ecological immunology method. Seasonal changes of the immunity were studied by their peripheral blood (PB), mainly reflected by innate and red blood cell (RBC) immunity. Meanwhile, habitat environment, foraging rules were studied to evaluate the environment pressure, and the breeding activities were observed additionally to be combined with immunity research and understand the trade-off choices that the body has made.

MATERIALS AND METHODS

Experimental animals and ecological research

Zhu Balong Nature Reserve, Sichuan, China was chosen to be the research area. Thirteen *Pseudois nayaurs* which were females and healthy were captured first and given a GPS-position collar. Every season (May, August, November, February in the next year), the same individuals were caught again without neutering for the PB (anticoagulated and cooled in ice bag with temperature 0–4°C immediately before transfer to a laboratory nearby in 24 h, the total number of samples was 156, 3 replicates × 13 individuals × 4 seasons) from the vena jugularis externa. The manipulating process of animals were supervised by Animal Welfare Committee and Tangjiahe Government under the guidance of the Law of the People's Republic of China on the Protection of Wildlife, 2016, and the blood storage process followed the rules of International Committee standard of haematology, ICSH,1993, using EDTA-2K. Their living habits including foraging rules, reproductive and clustering activities were also trailed through the GPS collar and faeces, before sighted.

Immunological examination

Routine blood test. The prepared PB transferred to the laboratory was used for routine blood test by the animal haematology analyser (RR-29103302, Mindray); included indexes were white blood cell (WBC), monocytes (Mon), lymphocyte (Lymph), lymphocyte% (Lymph%), granulocyte% (Gran%), RBC, haematocrit (HCT), mean corpuscular volume (MCV), mean corpuscular haemoglobin (MCH), red blood cell volume distribution width (RDW), mean corpuscular haemoglobin concentration (MCHC), platelet (PLT), platelet count (PCT), mean platelet volume (MPV), haemoglobin (HGB), platelet distribution width (PDW), and monocytes% (Mon%). Every data conducted then were recorded and analysed to see the differences between seasons.

Blood smear analysis. The blood smear was made according to the methods used by Ndao et al. [24]. PB slides were made firstly, followed by Wright's-Giemsa solution (G1020, solarbio) staining. Then, the stained slides were pictured through microscope (MF53, Mshot), after which WBC, and RBC were calculated by image-pro plus (HGB can also be reflected by the measurement of light-stained area in blood cell) (Fig. 1).

Detection of the erythrocyte immunity. The erythrocyte rosette rate was measured by the method
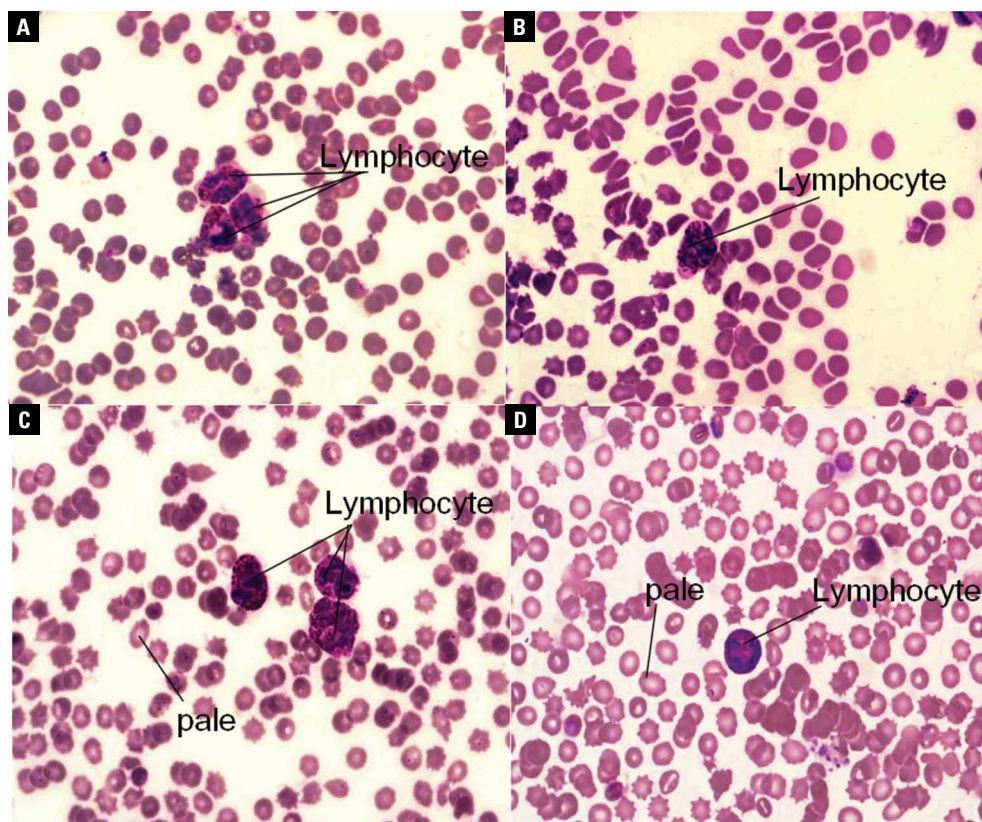
Figure 1. Representative blood smear figures between four seasons. Panels **A**, **B**, **C**, and **D** are the blood smears in spring, summer, autumn and winter, respectively (×1000, stained with Wright's-Giemsa staining). The light stained part of red blood cells in autumn and winter was more obvious than that in spring and summer, and the least obvious in summer, indicating that the haemoglobin content in autumn and winter was lower than in spring and summer, while the haemoglobin content in summer was the highest.

which was introduced by Chu et al. [4]. In brief, 4 mL of yeast solution was taken, and an equal amount of serum was added to make 1×10^8/mL concentration of bacterial suspension. Then, the red blood cell suspension was prepared and mixed to make the blood smear. After staining with Wright's-Giemsa, they were detected on a microscopic level. One hundred erythrocytes in each season were calculated. The erythrocyte rosette rate = number of RBCs forming rosette/total number.

Detection of the immune function of neutrophils. Under the condition of sterile operation, 5 drops diluted staphylococcus aureus was added into 1 mL anticoagulant, mixed and placed in carbon dioxide incubator at 37°C for 30 min, and shaken every 10 min. Then, the solution was used to make blood smears, before dried and observed with the microscope (MF53, Mshot). In each season, 100 neutrophils of every individuals were counted, after which the staphylococcus aureus-contained-neutrophils were recorded. The immune function of neutrophils was reflected by this way, and the phagocyte rate = the

number of staphylococcus aureus-contained-neutrophils in every 100 neutrophils.

Determination of the NK cell immunological killing function by LDH. Lactate dehydrogenase (LDH) release method was used in the study to the detection of natural kill (NK) cell immunological killing function, as described by Konjević et al. [15]. Briefly, 0.1 mL of the prepared NK cells of *Pseudois nayaur* (taken in PB) and 0.1 mL of the K562 cells (K562 cells were cultured for 28 h in logarithmic phase and washed twice with RPMI-1640 medium). Then, they were suspended in 10% FCS-RPMI-1640 medium at the concentration of 1×10^5 cells per mL and detected by 0.5% trypan blue staining. Then, among the experimental group, target cell natural release group (0.1 mL target cell + 0.1 mL 10% FCS-RPMI-1640 medium) and maximum release group (0.1 mL target cell + 0.1 mL 1% NP40 solution) were set up. After adding LDH substrate liquid for 15 min, the value A was measured by Enzyme Linked Monitor (ELx800, Bio-Tek, USA) under 570 nm. NK cell activity % = [(value A of the experimental group – value A of

natural release control group)/(value A of maximum – release control group)] × 100%.

Detection of the phagocytosis of macrophages. Each blood smear slide of four seasons was prepared in the same way as mentioned above. After that, they were fixed with the solution of alpha-naphthalene acetic acid (α-NAE) for 15 min, then washed with distilled water for 5 min and dried under 25°C. Then, the α-NAE incubation solution was added, before put the smears into the humid cabinet at 37°C (avoiding light to incubate for 1 h). To the next, after cleaning with water, the solution of methyl green dye was added to the droplet and then restained with water, after which the positive rate of macrophages was calculated under the microscope (MF53, Mshot) by the image-pro plus. (All reagents were purchased from the α-NAE assay kit, CAT#G2390, Solarbio, Japan).

Statistical analysis

The data collected from PB experiments mentioned above were analysed with t-test, one-way ANOVA. The data passed the homogeneity test for variance went through the Least-Significant Difference (LSD) test, and others were compared by Tamhane's T2 test to keep the findings about the impact of seasons on *Pseudois nayaurs'* immunity in accuracy. For the calculation process, it was done by SPSS20, and the outcomes were displayed as means ± standard deviation (x ± SD), p-value, df, F, and MS figures.

RESULTS

Ecological results

Research area. The *Pseudois nayaurs* lived in Zhubalong preserve with an altitude between 2,600 and 3,500 m. This area is a mountain valley landform and locates in the south-eastern edge of the Qinghai-Tibet plateau. It was found that a large number of *Pseudois nayaurs* prefer staying at the places with cliff to be able to escape from their natural enemies. In addition, the climate here was obviously divided into dry season (from October to the next April) and rainy season (from May to September) every year, which makes winter harder to get through. To cope with the unfriendly climate, the concave hillside was used by them, which was both helpful for the cover under the rain and the warming up under the sunshine. For instance, in summer, the *Pseudois nayaur* would move their sleeping place to a cool place to avoid the high temperature, strong sunshine, or rain. In winter, they tended to choose steep slopes under the sun as resting points.

Foraging rules. In this research, we observed that the foraging time of the *Pseudois nayaurs* was mainly on the morning and evening. Meadows, thickets, rocky escarpments with sparse grasses, and tall oak forests were the usual foraging sites. It was found that the main vegetation coverage was spiny roses and annual herbs, which accorded with the characteristics of vegetation coverage in dry-hot valley climate. However, the amount of the available food for *Pseudois nayaurs* was not in lacking. Dry environments and low temperatures limited the growth of vegetation, besides, grazing activities led by human were also found, which imposed threats to their living conditions, especially in autumn and winter.

Breeding activities. In the aspect of breeding activities, we found that the time was mainly in November, which is at the boundary time of autumn and winter. Pregnant females give birth to offspring in May of the following year after about 6 months of gestation. Due to the harsh winter environment during pregnancy and the influence of natural enemies on the offspring, both the pregnancy success rate and the survival rate of the offspring were low, we speculated that this was an important reason why the species is in the danger of extinction and was ignored by most scholars.

Cluster activities. For group behaviours, the cluster types were observed in mixed group, separated female group and male group. The number of mixed groups was the largest, mostly 20 to 30 individuals per group. This might be the strategy of them to survival from predators and harsh climates, while it became harder and harder to keep that group number.

Immunological detection

Blood routine. The results of blood routine are shown in Tables 1–3. For the immune system related cells figures in Table 1, there was no significant difference between seasons for WBC and Mon (p > 0.05). However, the number of Lymphs decreased rapidly in autumn, compared with the figures in spring (p < 0.01) and summer (p < 0.05), before climbed to the highest in winter (p < 0.01, compared with the figure in autumn). For the figure of Gran, it was seen a decrease in autumn compared with the figure in winter (p < 0.05).

To RBCs related figures shown in Table 2, everyone except for RDW and MCV was significantly low in autumn and increased at different levels in winter. It should be noticed that MCH, MCHC, and HGB had apparently

Table 1. Immunity related cells' blood routine results

Project	Spring	Summer	Autumn	Winter	df	F	MS
WBC [10⁹/L]	8.62 ± 0.76	7.69 ± 0.22	7.28 ± 3.74	8.80 ± 0.22	155	0.146	1.604
Monocytes [10⁹/L]	2.33 ± 0.28	1.83 ± 0.15	0.59 ± 0.55	2.50 ± 0.1	155	7.109	2.231
Lymphocyte [10⁹/L]	8.17 ± 1.53^c	7.13 ± 0.46^c	2.57 ± 1.21^{AbD}	9.27 ± 0.40^c	155	8.243	25.983
Granulocyte [10⁹/L]	7.57 ± 0.58	6.84 ± 0.16	6.47 ± 0.22^d	7.62 ± 0.23^c	155	2.717	0.955

WBC — white blood cell; Data are expressed as mean and standard deviation (sample number = 156); a, b, c, d means different from those data in spring, summer, autumn and winter respectively. Capitalisation means significant difference $p < 0.01$, while lowercase represent extremely significant $p < 0.05$. Overall, severe immunosuppression occurred in autumn, followed by winter, but in a resistant state.

Table 2. Red blood cells related blood routine results

Project	Spring	Summer	Autumn	Winter	df	F	MS
RBC [10¹²/L]	5.86 ± 0.49	5.94 ± 0.07	3.30 ± 1.62^d	6.34 ± 0.36^c	155	2.580	5.807
HCT [%]	35.63 ± 2.90	37.40 ± 1.04	21.23 ± 10.53^c	39.87 ± 1.68^d	155	2.282	210.762
MCV [fL]	60.97 ± 0.62^a	62.80 ± 1.23	65.53 ± 1.81^c	63.00 ± 0.96	155	2.266	10.570
MCH [pg]	50.27 ± 0.96^c	50.63 ± 0.52^{Cd}	24.00 ± 0.17^{ABD}	48.33 ± 0.37^{abC}	155	489.131	500.136
RDW [%]	13.23 ± 0.55	13.47 ± 0.98	16.17 ± 1.84	13.47 ± 1.05	155	1.346	5.823
MCHC [g/L]	826.00 ± 7.55^{Cd}	806.67 ± 25.33^c	373.33 ± 4.91^{ABD}	768.33 ± 5.46^{aC}	155	245.296	138469.639
HGB [g/L]	294.33 ± 22.67^c	302.67 ± 0.67^c	117.33 ± 6.06^{ABD}	306.67 ± 15.01^c	155	43.668	25440.528

RBC — red blood cell; HCT — haematocrit; MCV — mean corpuscular volume; MCH — mean corpuscular haemoglobin; RDW — red blood cell volume distribution width; MCHC — mean corpuscular haemoglobin concentration; HGB — haemoglobin; Data are expressed as mean and standard deviation (sample number = 156); a, b, c, d means different from those data in spring, summer, autumn and winter respectively. Capitalisation means significant difference, $p < 0.01$, while lowercase represent extremely significant $p < 0.05$. Overall, severe immuno-suppression occurred in autumn, followed by winter, but in a resistant state.

Table 3. Platelet related blood routine results

Project	Spring	Summer	Autumn	Winter	df	F	MS
PLT [%]	524.33 ± 152.4^{bd}	1016.33 ± 215.48^{ac}	396.67 ± 117.32^{bD}	1132.00 ± 56.08^{aC}	155	6.028	391425.556
PCT [%]	0.25 ± 0.07^{bd}	0.52 ± 0.09^a	0.29 ± 0.09^d	0.57 ± 0.03^{ac}	155	4.746	0.078
MPV [fL]	4.87 ± 0.23	4.83 ± 0.09	5.37 ± 0.37	5.00 ± 0.10	155	1.136	0.179
PDW [fL]	16.33 ± 0.33^c	15.67 ± 0.33^c	12.63 ± 0.59^{ABD}	16.00 ± 0.00^c	155	20.286	8.723

PLT — platelet; PCT — platelet count; MPV — mean platelet volume; PDW — platelet distribution width; Data are expressed as mean and standard deviation (sample number = 156); a, b, c, d means different from those data in spring, summer, autumn and winter respectively. Capitalisation means significant difference $p < 0.01$, while lowercase represent extremely significant $p < 0.05$. Overall, severe immunosuppression occurred in autumn, followed by winter, but in a resistant state.

significant decreases ($p < 0.01$) in autumn since spring, and then, recovered with an inadequate level in winter.

As for PLT related indexes, the figure for PLT was at the lowest level in autumn, compared to the highest one in winter ($p < 0.01$). In addition, the trend for the change of PDW was dramatic; it decreased considerably from spring to autumn ($p < 0.01$), which reached the bottom, and increased steadily at winter. For MPV, no evidence had shown the changes between seasons ($p > 0.05$), and there were both relatively low figures found in spring and autumn for PCT.

Overall, whether indexes in RBCs, PLT, or immune related cells, wide-range decreases were found. Meanwhile, the recovery seemed to happen in winter but in a sign of weakness.

Blood smear analysis. The light stained part of RBCs in autumn and winter was more obvious than that in spring and summer (least obvious), indicating that the HGB contents in autumn and winter were lower in spring and summer, shown in the Table 4.

Erythrocyte immunity. The results are shown in Figure 2. The rosette rate of RBCs decreased significantly in winter ($p < 0.05$) when compared with the figures in spring, summer, and autumn. The results showed that the immune function of erythrocytes was inhibited in winter.

Immune function of neutrophils. As shown in Figures 3 and 4, seasonal changes had a significant impact on the number of neutrophils ($p < 0.01$). The phagocytosis rate of neutrophils in summer was

Table 4. Blood smear cell count analysis

Project	Spring	Summer	Autumn	Winter	df	F	MS
WBC [10⁹/L]	8.58 ± 0.76	7.51 ± 0.22	7.27 ± 3.74	8.86 ± 0.22	155	0.165	1.625
RBC [10¹²/L]	5.71 ± 0.49	5.91 ± 0.07	3.46 ± 1.62^d	6.82 ± 0.36^c	155	2.731	5.994

RBC — red blood cell; WBC — white blood cell; Data are expressed as mean and standard deviation (sample number = 156); a, b, c, d means different from those data in spring, summer, autumn and winter, respectively. Capitalization means significant difference p < 0.01, while lowercase represent extremely significant p < 0.05. Table 4 shows that red blood cells decreased significantly in autumn which indicated the reproduction stress in that time. And increased in winter, which was thought to be relevant to the compensatory strategies.
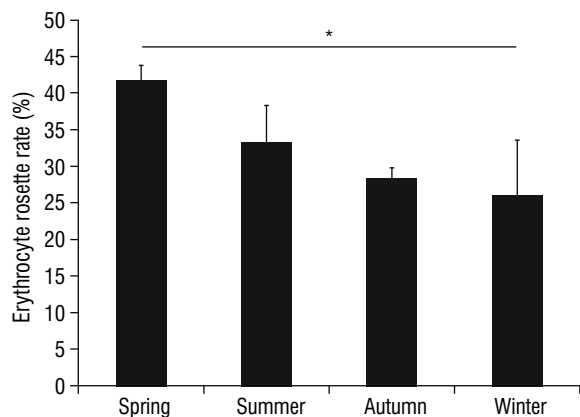
Figure 2. Statistical chart of the seasonal changes of the erythrocyte wreath rate. *In the figure represents a significant difference between the two groups (p < 0.05). The comparison between each group and the winter group was conducted before pairwise comparison. The rosette rate of red blood cells significantly decreased in winter (p < 0.05) when compared with the spring, was low summer and autumn. The results showed that the immune function of erythrocytes was inhibited in winter.
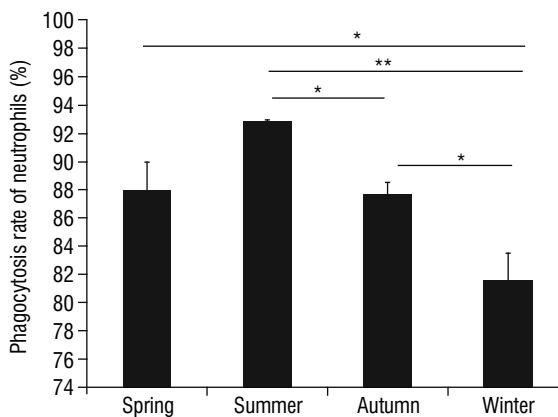
Figure 4. The statistical diagram of the seasonal changes of staphylococcus aureus phagocytised by neutrophils. *In the figure represents a significant difference between the two groups (p < 0.05), and **represents a very significant difference (p < 0.01). The figure suggests that the function of neutrophils was affected by the seasonal changes. It is better in summer than in spring and autumn, while the suppression was found in winter.
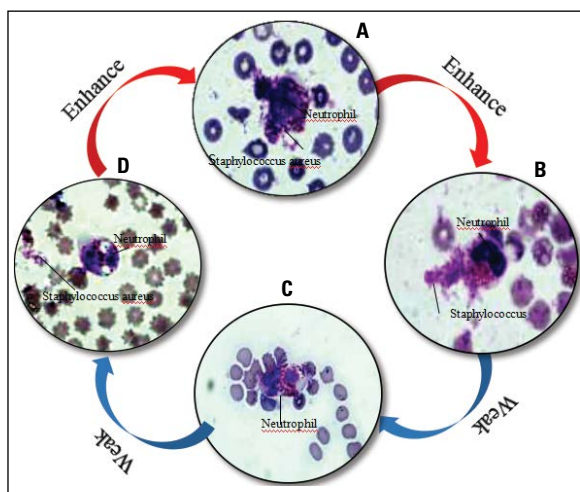
Figure 3. Seasonal changes of staphylococcus aureus phagocytised by neutrophils. Panels **A**, **B**, **C**, and **D** are the blood smears in spring, summer, autumn and winter, respectively (×1000, stained with Wright's-Giemsa staining). Phagocytosis rate of neutrophils in summer was significantly higher than in winter (p < 0.01), the indexes in summer and autumn were higher than those in spring and winter, respectively (p < 0.05).

significantly higher than that in winter (p < 0.01), and the indexes in summer and autumn were higher than those in spring and winter, respectively (p < 0.05). The results showed that the bactericidal function of neutrophils was inhibited in winter, and was the strongest in summer, followed by spring and autumn.

Phagocytosis of macrophages. As shown in Figure 5, there were significant differences between seasons (except for them between autumn and winter) of the figures (p < 0.01), and the figures were the lowest in autumn and winter. The results showed that the function of macrophages was inhibited in autumn and winter, while it was relatively stronger in spring and especially in summer.

NK cell immunological killing function. As shown in Figure 6, seasonal changes had imposed great influence of the function for NK cells, they could only played the weakest role in autumn and winter, compared with that in spring and summer.
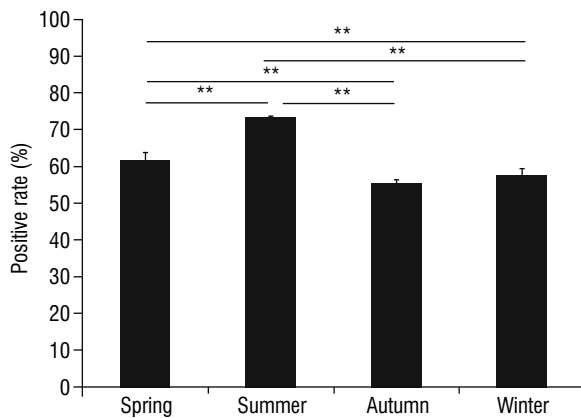
Figure 5. Seasonal variation of macrophage positive rate. **In the figure represents a very significant difference (p < 0.01). It can be concluded in the figure that the macrophage positive rate was also in change with the period of seasons, but it was in the autumn that the rate declined more significantly instead of winter, which was speculated to be relevant to the reproduction matter.
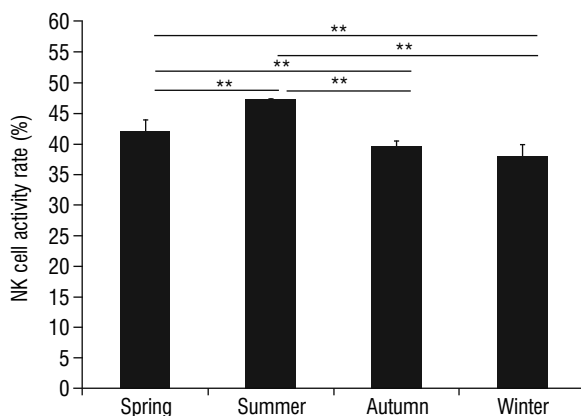
Figure 6. Statistical diagram of the activity rate of natural kill (NK) cells in four seasons. **In the figure represents a very significant difference (p < 0.01). NK cell activity rate was shown in an increase in summer which was consistent to above indexes, and the rate in spring and autumn, was familiar but declined in winter.

DISCUSSION

Challenging living conditions

In this research, four aspects of living conditions were studied, including habitat environment, foraging rules, breeding and cluster activities. Firstly, the places that *Pseudois nayaur* lives in locate in the south-eastern edge of the Qinghai-Tibet plateau, where mountain valley and cliffs are usually to be seen. It was found that they could take good advantages of the landform to escape from predators, and achieve the possibility of keeping safe from harmful sunshine and pour rain. However,

step down to the bottom of the valley for water was unpreventable when the dry season (autumn and winter) was coming, which had been become the most risky movement of *Pseudois nayaurs* because of the awaiting hunter traps and natural enemies. What's more, although the food available for the *Pseudois nayaur* was relatively enough in spring and summer, dry season had again made the vegetation in degradation especially for the higher but safer place. When facing such pressure, clusters got its own strategy, mainly expressed by acting together. As a result, more strong and healthy individuals would survive, but apparently, most females whose pregnancy period of time were from November to May are not among the group, which was proved by the low survival rate of cubs and the mothers found by Liu et al. [19].

Trade-off between immune and reproduction of *Pseudois nayaur*

In addition to the external challenges, the energy cost of reproduction and immunity in autumn and winter also should be noticed. It has been found that, body usually make choices between reproduction and immunity, because the energy gained is limited. For most of the time, the immunity would be the suppressed one [6, 8, 14]. This hypothesis can be the reason why *Pseudois nayaur*'s immunity was found in a sigh of weakness in autumn. Among them, PLT and PCT, shown in Table 2, were at a low condition. Kuter and Rosenberg [18] did a correlation analysis about the reason why PLT was low, the factors leading to the destruction of PLT in the experiment, such as diseases of the *Pseudois nayaur*, were excluded. We believed that this phenomenon may be related to the reduction of megakaryocytic cells and growth factors in bone marrow, resulting in the weakened proliferation and differentiation of PLT, thus the function of wound healing was reduced. Then, MCH, MCHC, and HGB indexes showed seasonal suppression which indicated that malnutrition was exist and also suggested that the blood's ability to transport oxygen decreased obviously in autumn, and in this period *Pseudois nayaur* may face to the risk of anaemia disorders [3, 9]. These findings also provided evidence of food shortages and the effects of overgrazing in the results. In terms of innate immune function, NK cells was inhibited, indicating the rising risk of infection, transformation or stress and decreased target cells kill function [30], even much
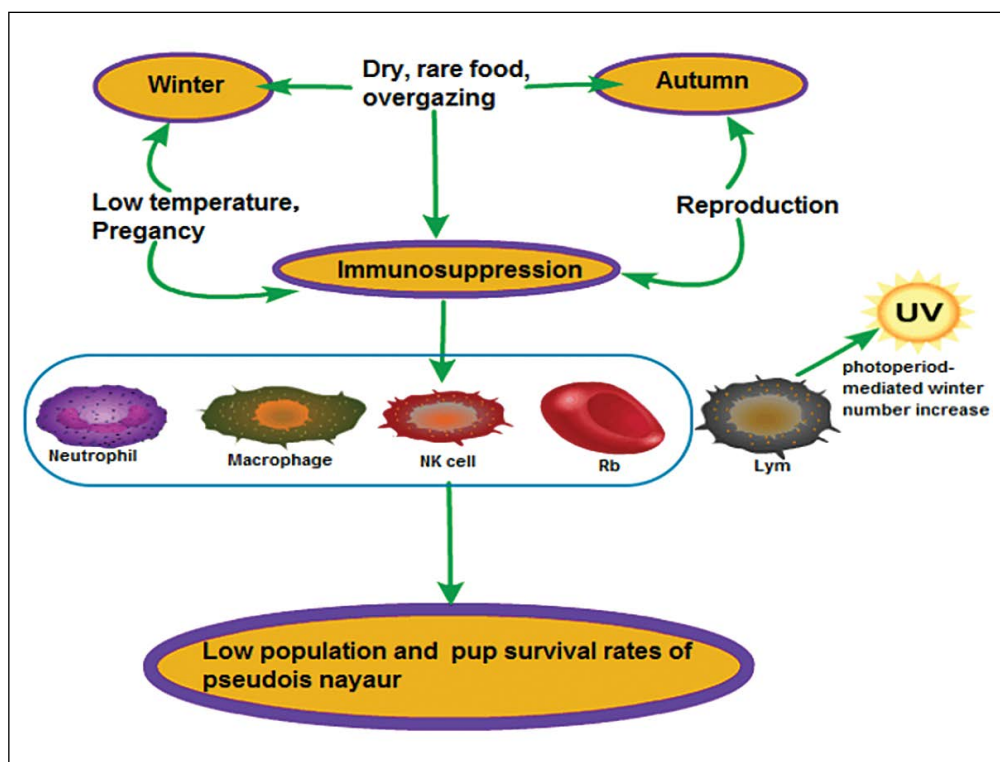
Figure 7. Eco-immune pathway of endangered of *Pseudois nayaur*. The immunosuppression may be due to the seasonal changes and reproduction hobby. The harsh climates and human activities causes the immunosuppression against the evolutionary strategies that *Pseudois nayaur* owns to enhance the immunity, and it may finally result in low survival rates.

higher probability of getting cancer [1]. Moreover, the macrophages and neutrophils functions were inhibited, which meant the second line of immune defence decreased and bacterial resistance was declined [10, 22]. In addition, erythrocyte rosette rate's suppression in results was also a good proof of that, because the erythrocyte plays an important part in immune complex clearing, tumour, and innate immune [5, 21].

Winter immunity recovery

In winter, the immunity suppression was also found but in a lower level. However, the food and water pressure were bigger than that in autumn, and the effects of low temperature were also beginning to emerge. So, the results were thought to be an evidence for the winter immunoenhancement hypothesis.

Through ecological investigation, it was found that cliffs and concave hillside were used by *Pseudois nayaur* gaining appropriate sunshine, and it is believed that many small mammals have evolved a set of life-cycle strategies that can increase their immune function by using seasonal variation signals such as sunshine

trait (length and strength) to improve their survival in winter [25, 29]. In this study, WBC was found the highest in winter and the upward trend was also obvious for the recovery of immunity in many other immunology findings, which are complied with similar phenomenon found previously in root voles. The rising number of WBC and other indexes would make them survive better in winter [16, 17]. The rise of MCV in autumn might suggest the mechanism of resistance to the reduction of MCH and MCHC. For the further evidence to the phenomenon, studies in molecular level are needed. Although, the phenomenon of resistant immunosuppression was found, the future of the *Pseudois nayaur* was not encouraging. After the trade-off choice has been made in autumn to enhance the ability to reproduce at the expense of immunity, winter resistance seemed very important for their survival, and therefore, more efficient steps needs to be taken at this very season. The key point of its protection then turns to environment again, but in more specific to winter. We need to stop the agricultural overgrazing [12] and other human interference or wild *Pseudois nayaur's* extinction would be destination.

CONCLUSIONS

As a conclusion, we suggest that the habitat pressure of this species keeps increasing, and it is also found that these species have a large-scale immunosuppression when it is close to the special autumn breeding period in winter (Table 1), which confirms the trade-off between immunity and reproduction. At the same time, due to the challenge of winter climate, the immunity has not recovered quickly though there is a phenomenon of winter immunoenhancement. As shown in results, the survival of female *Pseudois nayaur* during pregnancy was difficult. Therefore, we conclude that the immune suppression of *Pseudois nayaur* is more threatening than other species. They are facing an immunosuppression for up to 6 months which is also the time for reproduction in population (Fig. 7).

Acknowledgements

Conflict of interest: None declared

REFERENCES

1. Albertsson PA, Basse PH, Hokland M, et al. NK cells and the tumour microenvironment: implications for NK-cell function and anti-tumour activity. Trends Immunol. 2003; 24(11): 603–609, doi: 10.1016/j.it.2003.09.007, indexed in Pubmed: 14596885.
2. Amdam GV, Aase AL, Seehuus SC, et al. Social reversal of immunosenescence in honey bee workers. Exp Gerontol. 2005; 40(12): 939–947, doi: 10.1016/j.exger.2005.08.004, indexed in Pubmed: 16169181.
3. Cartwright GE, Lee GR. The anaemia of chronic disorders. Br J Haematol. 1971; 21(2): 147–152, doi: 10.1111/j.1365-2141.1971.tb03424.x, indexed in Pubmed: 4934605.
4. Chu Y, Haigh T, Nash GB. Rheological analysis of the formation of rosettes by red blood cells parasitized by Plasmodium falciparum. Br J Haematol. 1997; 99(4): 773–783, doi: 10.1046/j.1365-2141.1997.4643268.x, indexed in Pubmed: 9432021.
5. Cornacoff JB, Hebert LA, Smead WL, et al. Primate erythrocyte-immune complex-clearing mechanism. J Clin Invest. 1983; 71(2): 236–247, doi: 10.1172/jci110764, indexed in Pubmed: 6822663.
6. Deerenberg C, Arpanius V, Daan S, et al. Reproductive effort decreases antibody responsiveness. P Roy Soc B-Biol Sci. 1997; 264(1384): 1021–1029, doi: 10.1098/rspb.1997.0141.
7. Fedorka KM, Zuk M, Mousseau TA. Immune suppression and the cost of reproduction in the ground cricket, Allonemobius socius. Evolution. 2004; 58(11): 2478–2485, doi: 10.1111/j.0014-3820.2004.tb00877.x, indexed in Pubmed: 15612291.
8. French SS, DeNardo DF, Moore MC. Trade-offs between the reproductive and immune systems: facultative responses to resources or obligate responses to reproduction? Am Nat. 2007; 170(1): 79–89, doi: 10.1086/518569, indexed in Pubmed: 17853993.
9. Fuchs D, Hausen A, Reibnegger G, et al. Immune activation and the anaemia associated with chronic inflammatory disorders. Eur J Haematol. 1991; 46(2): 65–70, doi: 10.1111/j.1600-0609.1991.tb00524.x, indexed in Pubmed: 1899833.
10. Gordon S, Martinez FO. Alternative activation of macrophages: mechanism and functions. Immunity. 2010; 32(5): 593–604, doi: 10.1016/j.immuni.2010.05.007, indexed in Pubmed: 20510870.
11. Harshman LG, Zera AJ. The cost of reproduction: the devil in the details. Trends Ecol Evol. 2007; 22(2): 80–86, doi: 10.1016/j.tree.2006.10.008, indexed in Pubmed: 17056152.
12. Homewood K, Rodgers WA. Pastoralism, conservation and the overgrazing controversy; In Conservation in Africa: people, policies and practice. (eds) Anderson D and Grove R. Cambridge University Press, London 1987: 111–128.
13. Hu JC. Dwarf rock sheep in urgent need of protection. China Nat. 1997; 1: 34–35.
14. Knowles S, Nakagawa S, Sheldon B. Elevated reproductive effort increases blood parasitaemia and decreases immune function in birds: a meta-regression approach. Funct Ecol. 2009; 23(2): 405–415, doi: 10.1111/j.1365-2435.2008.01507.x.
15. Konjević G, Jurišić V, Spužić I. Corrections to the original lactate dehydrogenase (LDH) release assay for the evaluation of NK cell cytotoxicity. J Immunol Methods. 1997; 200(1-2): 199–201, doi: 10.1016/s0022-1759(96)00194-9.
16. Książek A, Zub K, Szafrańska PA, et al. The nexus of hair corticosterone level, immunocompetence, metabolic rates and overwinter survival in the root vole, Microtus oeconomus. Gen Comp Endocrinol. 2017; 250: 46–53, doi: 10.1016/j.ygcen.2017.05.021, indexed in Pubmed: 28577898.
17. Książek A, Zub K, Szafrańska PA, et al. Immunocompetence and high metabolic rates enhance overwinter survival in the root vole, Microtus oeconomus. Biol Lett. 2014; 10(12): 20140684, doi: 10.1098/rsbl.2014.0684, indexed in Pubmed: 25519753.
18. Kuter DJ, Rosenberg RD. Appearance of a megakaryocyte growth-promoting activity, megapoietin, during acute

thrombocytopenia in the rabbit. Blood. 1994; 84(5): 1464–1472, indexed in Pubmed: 8068941.

19. Liu G, Zhou C, Yang Z, et al. Diurnal activity rhythm and time budgets of the Dwarf Blue Sheep (Pseus schaeferi) in Zhubalong Nature Reserve. Acta Ecol Sinica. 2011; 31(4): 00197–0981, doi: 10.3724/SP.J.1011.2011.00197.

20. Long S, Zhou CQ, Wang WK, et al. Behavior coding and ethogram of the pseudois nayaur. Acta Ecol Sinica. 2008; 28(11): 5632–5640.

21. Lutz HU. nnate immune and non-immune mediators of erythrocyte clearance. Cell Mol Biol. 2004; 50(2): 107––116, doi: 10.1379/1466-1268(2004)009<0088: AOHIVI>2.0.CO;2.

22. MacMicking J, Xie QW, Nathan C. Nitric oxide and macrophage function. Annu Rev Immunol. 1997; 15: 323–350, doi: 10.1146/annurev.immunol.15.1.323, indexed in Pubmed: 9143691.

23. Martin LB, Weil ZM, Nelson RJ. Seasonal changes in vertebrate immune activity: mediation by physiological trade-offs. Philos Trans R Soc Lond B Biol Sci. 2008; 363(1490): 321–339, doi: 10.1098/rstb.2007.2142, indexed in Pubmed: 17638690.

24. Ndao M, Bandyayera E, Kokoskin E, et al. Comparison of blood smear, antigen detection, and nested-PCR methods for screening refugees from regions where malaria is endemic after a malaria outbreak in Quebec, Canada. J Clin Microbiol. 2004; 42(6): 2694–2700, doi: 10.1128/JCM.42.6.2694-2700.2004, indexed in Pubmed: 15184454.

25. Nelson R, Demas G. Seasonal changes in immune function. Quarterly Rev Biol. 1996; 71(4): 511–548, doi: 10.1086/419555.

26. Rolff J, Siva-Jothy MT. Invertebrate ecological immunology. Science. 2003; 301(5632): 472–475, doi: 10.1126/science.1080623, indexed in Pubmed: 12881560.

27. Sheldon BC, Verhulst S. Ecological immunology: costly parasite defences and trade-offs in evolutionary ecology. Trends Ecol Evol. 1996; 11(8): 317–321, doi: 10.1016/0169-5347(96)10039-2, indexed in Pubmed: 21237861.

28. Shen DJ, Wang Y, Zeren J, et al. Primary study on behavior of dwarf blue sheep (pseus schaeferi). Sichuan J Zool; 2007: 26-4 doi org/10 1016/0169. 2007; 2007(26-4), doi: 10.1016/0169-5347(96)10039-2.

29. Sinclair JA, Lochmiller RL. The winter immunoenhancement hypothesis: associations among immunity, density, and survival in prairie vole (Microtus ochrogaster) populations. Can J Zool. 2000; 78(2): 254–264, doi: 10.1139/z99-203.

30. Sun JC, Lanier LL. NK cell development, homeostasis and function: parallels with CD8+ T cells. Nat Rev Immunol. 2011; 11(10): 645–657, doi: 10.1038/nri3044, indexed in Pubmed: 21869816.

31. Xaquin CD, Marina E, Ricardo CF, et al. Widespread seasonal gene expression reveals annual differences in human immunity and physiology. Nat Commun. 2015; 6(1), doi: 10.1038/ncomms8000.

V M
VIA MEDICA

ORIGINAL ARTICLE

The role of congenital malformations of the thoracic outlet in the development of the syndrome

M. Artico[1]*, M.T. Santarelli[1]*, G. Stevanato[2], R. Cirocchi[3], V. D'Andrea[4],
A. Nicolai[1], G. Cialone[5], G. Monteleone[6], I. Pindinello[7]*, S. Taurone[1]*

[1]Department of Sensory Organs, "Sapienza" University of Rome, Italy
[2]Neurosurgery Unit, Dell'Angelo Hospital, Mestre, Venice, Italy
[3]Department of Surgical Sciences, University of Perugia, Italy
[4]Department of Surgical Sciences, Sapienza University of Rome, Italy
[5]Unit of Radiology Regina Coeli, Rome, Italy
[6]Department of Biomedicine and Preventive Medicine, Tor Vergata University of Rome, Italy
[7]Department of Drug Chemistry and Technology, "Sapienza" University of Rome, Italy

Background: Thoracic outlet syndrome (TOS) represents a clinical condition caused by compression of the neurovascular structures that cross the thoracic outlet. TOS can be classified in: 1) neurogenic TOS (NTOS), 2) venous TOS (VTOS), 3) arterial TOS (ATOS). Many different causes can determine the syndrome: congenital malformations, traumas, and functional impairments.

Materials and methods: This manuscript reviews how the congenital malformations play an important role in adult age; however, TOS also affects patients of all ages.

Results: Radiological imaging like X-ray (radiography), magnetic resonance and computed tomography can provide useful information to assess TOS causes and decide a potential surgery. 79% of the patients included in the first two stages of nerve, artery, vein (NAV) staging experienced excellent results with kinesio-therapy; whereas patients included in the third and fourth stage of NAV staging were subject to surgery.

Conclusions: The treatment of acute forms of TOS involves thrombolysis and anti-coagulant therapy; surgery is appropriate for true NTOS, vascular TOS and in some cases when conservative treatment fails. (Folia Morphol 2022; 81, 1: 117–123)

Key words: brachial plexus, subclavian artery, subclavian vein, neuromuscular bundle, first rib, anterior and middle scalene muscle, congenital malformation, clinical grading, interscalene triangle, costoclavicular triangle

INTRODUCTION

Thoracic outlet syndrome (TOS) manifests with signs and symptoms that depend on the structure of the neurovascular bundle being compressed: the bra- chial plexus, the subclavian artery and the subclavian vein (Fig. 1) [4, 12]. The neurovascular dysfunction depends on three factors: 1) The space between the neck and the axilla is very limited; 2) Physiological
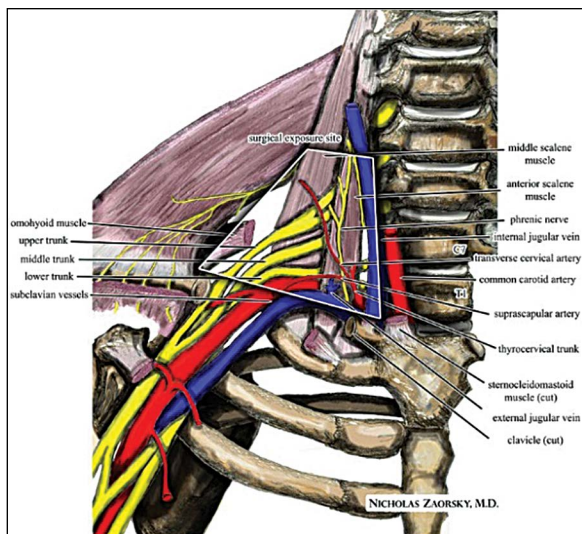
Figure 1. An illustration of the relevant neurovascular anatomy in anterior supraclavicular neurosurgical approach to the brachial plexus and subclavian vessels for thoracic outlet syndrome.
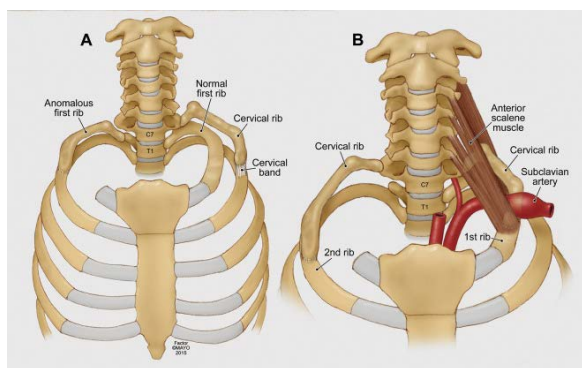
Figure 2. Arterial thoracic outlet syndrome; **A.** Right side: an anomalous first rib inserting into the mid portion of the right second rib, left side: a cervical rib originating from the transverse process of C7; **B.** Cervical ribs may insert on either the first rib or second rib.

conditions may cause intermittent compression to the neurovascular bundle; 3) Congenital malformations of bones and of muscles may trigger the symptoms. The classic subjects affected by TOS are young asthenic women with a thin neck and weak muscles. The structural anomalies involved in the TOS are: 1) Anomalous ribs, 2) Anomalous scalene tendon insertion, 3) Fibrous band insertion of the first rib, 4) Clavicular abnormalities (Fig. 2) [1, 6, 15].

MATERIALS AND METHODS

Thoracic outlet syndrome includes three different syndromes: 1) Neurogenic TOS (NTOS) with compression of the brachial plexus; 2) Venous TOS (VTOS)

with compression of the subclavian vein; 3) Arterial TOS (ATOS) with compression of the subclavian artery [10, 11, 14, 18]. The estimate of a suspected TOS may be assessed via medical history, medical examination and diagnostic tests that have, however, low sensitivity and low specificity but may support the diagnosis. To diagnose cervical ribs and anomalous first ribs one may use X-rays of the cervical spine and shoulder girdle and also computed tomography (CT), magnetic resonance (MR) and electromyography. Patients present symptoms of venous obstruction, arterial insufficiency, paraesthesia and pain [2, 8, 14, 16, 17]. The therapy is often conservative, including exercises and physical therapy. If it fails, it may be necessary to use surgical approaches such as supraclavicular exposure and the first rib resection. In this study we present a study of 181 clinical cases classified according to: 1) Type of malformation (cervical rib, anomalous first rib, scalenus medius insertion, scalenus minimus [Sibson's muscle] hypertrophy, Sibson's fascia band, fibrous band arising from incomplete cervical rib and elongated C7 transverse process, anomalous scalenus anticus insertion, anomalous vessels, hypertrophy of little pectoral); 2) Physical structure of the patient; 3) Gender. Any single case is classified through three parameters: nerve (N), artery (A), and vein (V). There are four grades for each parameter according to clinical and instrumental severity (Table 1) [2]

Neurogenic TOS

The aetiopathogenesis of the neurogenic TOS includes various aspects: 1) Presence of thick fibrous band from the apex of sketch of cervical rib; 2) A work task that involves the prolonged abduction of the arms; 3) Physical characteristics; 4) Dominant limb [3, 5, 9].

Clinical case 1

Young woman, 19 years old (Figs. 3–5).

Task performed (job) at the time of the diagnosis: at the counter (Table 2).

Clinical malformation: fibrous band from sketch of accessory rib.

Clinical condition of NTOS: N3 (advanced neurological lesions), V1 (early venous lesions), A1 (early arterial lesions). The neurological disturbances depend on lesion of the fibres of the lower trunk of the brachial plexus; sensory symptoms appear in advance of motor signs and are often subject to pain and paraesthesia. The pain is diffuse in the su-

Table 1. Pang grades; see Busetto et al. [2]

Pang grades	NAV (nerve [N], artery [A], vein [V]) stages
1 = pain and paraesthesia ± intermittent postural ischaemia ± sympathetic instability	1th stage = N0–1 A0–1 V0–1 — Intermittent neurovascular compression without anatomical damage
2 = sensory deficits in ulnar distribution	2th stage = N2 A0–1 V0–1 — Anatomical damage: early and reversible neurological lesions
3 = intrinsic hand muscle weakness ± atrophy	3th stage = N3 A2 V2 — Anatomical damage: advanced neurological lesions ± early arterial lesions ± advanced venous lesions
4 = persistent ischaemic changes in hand (gangrene, skin necrosis) resulting from emboli or subclavian thrombosis	4th stage = every N with A3 or V3 — Anatomical damage: advanced irreversible neuro-vascular lesions

Figure 3. The image shows a young woman affected by bilateral accessory rib.

Figure 5. The contrast-enhanced computed tomography scan was reconstructed with volume-rendering algorithms and documents the compression by the accessory cervical rib on the neurovascular bundle.
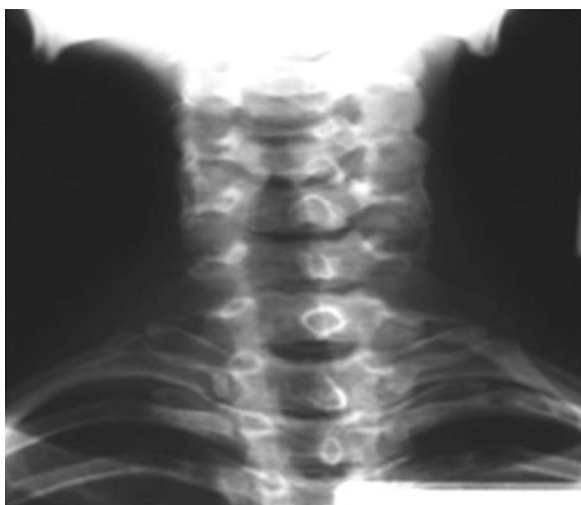
Figure 4. The X-ray of the cervical spine demonstrates the presence of right and left cervical rib.

praclavicular and shoulder region and widespread along the arm, and sometimes affects face and neck.

The pain does not respect a C8-T1 dermatomal pattern, whereas the paraesthesia is usually localised to the C8-T1 ulnar side of the forearm. After some time the patient loses sensitivity in the ulnar fingers and show objective signs of sensory axonopathy in the C8-T1 dermatomes. The symptoms may be triggered by trauma to the shoulder and the pain gets worse after many hours of work. Motor disturbances: a testable weakness may indicate a motor axonopathy that manifests after some time from the beginning of sensory disturbance and means a worsening of the disease. The thenar muscles are affected first, followed by the hypothenar group (ulnar muscles). There is often consumption in the side part of thenar eminence giving a roughened appearance to the side outline of the hand (Fig. 6).

Stress tests

Experiments were performed in compliance with the Italian laws and guidelines concerning the in-

Table 2. Homogeneous group of patients with the same malformation and a similar clinical stage (neurogenic thoracic outlet syndrome [TOS], positive electromyography, stage III)

Sex	Congenital malformation	Clinical picture (neurogenic TOS, positivity to electromyography)	Age at diagnosis	Period between the onset of symptoms and the diagnosis	Task carried out at the diagnosis
Female	Fibrous band from sketch of accessory rib	N3, V1, A1	19	36 months	At the counter
Female	Fibrous band from sketch of accessory rib	N3, V1, A1	24	43 months	Traffic warden
Female	Fibrous band from a prominent transversus	N3, V1, A1	41	32 months	Hair dresser
Male	Fibrous band from sketch of accessory rib	N3, V1, A1	38	83 months	Mechanical motorcycle
Female	Fibrous band from sketch of accessory rib	N3, V1, A3	22	17 months	Cashier — warehouse worker
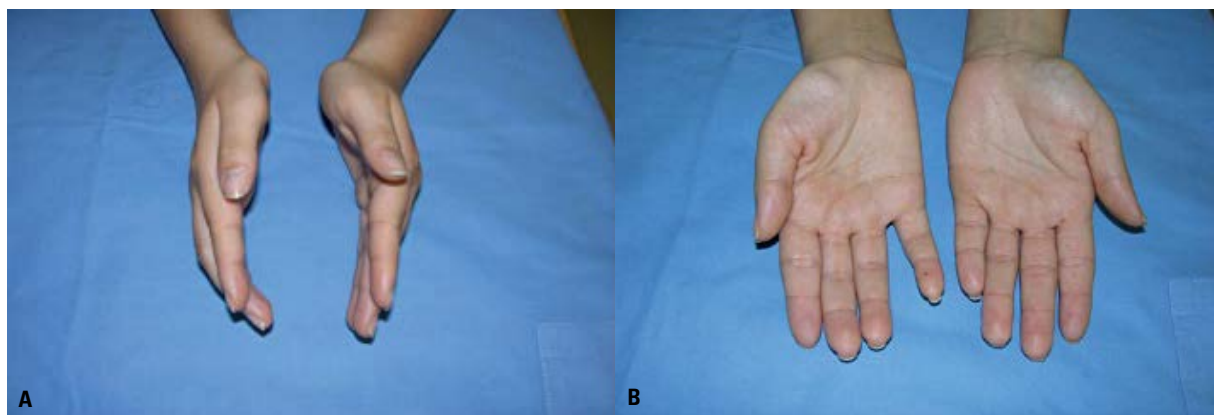
Figure 6. A, **B**. Thenar consumption in thoracic outlet syndrome. Note the severe thenar consumption especially with respect to the abductor pollicis brevis.

formed consent of patient (Dir.2001/20/CE). Stress tests are useful to diagnose the TOS because they increase the neurovascular compression at the thoracic outlet. There are many tests, each for a specific site of compression but the only reliable one is the 90 grades abduction external rotation test where the arm is abducted to a right angle and externally rotated while the head is turned to the opposite side. If the brachial plexus and the subclavian artery are compressed, the pain and paraesthesia are felt by the patient first in the ulnar area and then in the whole hand. If pain and tingling are extended without decreasing their intensity we can infer a purely neurogenic TOS [3]. The diagnosis is confirmed if by dropping the arm the discomfort is relieved and, also, if pain and tingling increase when opening and closing the fist for 3 minutes in the abduction external rotation position. The objective physical findings are very important for the diagnosis, e.g. weakness or atrophy of the hand, ulnar hypoesthesia, abnormalities of ribs and a positive electromyography. The radiological imaging cannot always lead to the diagnosis of TOS. Besides X-rays,

CT may also help to identify congenital malformation such as scalene muscle hypertrophy. CT angiography with the arm in hyperabduction may confirm the compression of neuromuscular bundle. Cervical spine MR images help to discover scalene muscle abnormalities. MR angiography with arms in different positions may confirm neurovascular compression. To discover deviations in the usual course of the nerves we can perform MR neurography by injecting a dye around the brachial plexus. Some patients affected by NTOS have anomalous nerve conduction velocities though this exam has low sensitivity and low specificity in the diagnosis of NTOS. Somatosensory-evoked potential may be useful in some cases of neurogenic TOS but have low specificity and can't locate abnormalities. The stimulation of the eighth cervical nerve is useful during a surgery but it is too invasive for outpatients. We can also use a combination of medial antebrachial cutaneous nerve conduction and C8 nerve root stimulation tests to do the diagnosis of NTOS [2, 3, 5, 9, 19]. Medial antebrachial cutaneous assessment is useful to reveal little alterations in the transmission

of the lower trunk of the brachial plexus. Botulinum toxin injection into the anterior scalene muscle has been used for the diagnosis of NTOS and to reduce the symptoms (Fig. 7).

Clinical staging and classification of TOS

Thoracic outlet syndrome may be staged by its temporal sequence for severity and chronicity. In the first three stages there are weakness, pain and tingling in the whole hand (symptoms of intermittent ischaemia). In the fourth stage there are persistent ischaemic changes in the hands like gangrene and skin necrosis from thromboembolism in the subclavian territory.

Management of TOS

Patients with NTOS should have a conservative treatment for three months and then a surgery can be taken into consideration. Conservative treatment includes soft physical therapy, muscle relaxants, anti-inflammatory drugs that determine an improvement of symptoms in many patients with a better function and return to work. Surgery is necessary when there are neurological dysfunctions and acute vascular insufficiency and functional impairments. Surgical procedures concern lysis of fibrotic band, scalenectomy and first rib excision.

Arterial TOS

ATOS is the least common type of TOS and is caused by a congenital malformation that determines a compression of subclavian artery. Possible malformations are: cervical or anomalous first rib, fibromuscular bands, scalene muscle [13].

Clinical Case 2

Young woman, 22 years old.

Tasks performed (job) at the time of the diagnosis: cashier (Table 2).

Clinical malformation: Fibrous band from sketch of accessory rib (Table 2)

Clinical condition of TOS: N3-V1-A3 (advanced neurological lesions, early venous lesions, advanced arterial lesions). The patient has persistent ischaemic changes in the hands (gangrene and skin necrosis) resulting from subclavian thrombosis (Figs. 8, 9). The arterial compression can determine aneurysm formation, growth of thrombi and embolization. Abnormalities of ribs are often involved in ATOS (74% of cases). There are arterial damage, thrombus production and symptoms of claudication. Clavicle injury deformities

Figure 7. Antero-posterior cervical spine X-ray shows the presence of bilateral cervical accessory rib.
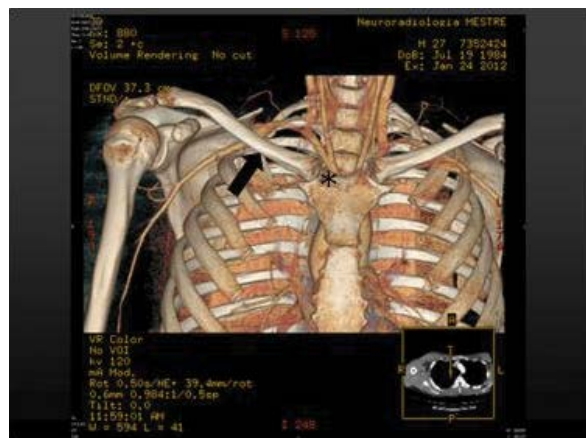
Figure 8. The contrast-enhanced computed tomography scan was reconstructed with volume-rendering algorithms. It documents thoracic outlet syndrome caused by the cervical rib compressing right subclavian artery (→). The right subclavian artery originates from the brachiocephalic trunk (*), then bends laterally passing between the scalene muscles. The image shows the backstage section of the right subclavian artery which contracts inferiorly with the first rib which is compressed by.

and compression may also determine ATOS by causing thrombosis and embolisation of the artery.

Clinical presentation

Arterial TOS is asymptomatic and symptoms like pain, tingling, cyanosis and changes of colour of the hands (until gangrene) may appear when embolization occurs. There is absence of radial pulse and signs of ischaemia of the distal phalanges. The objective examination of the patient can reveal a bony prominence and is possible to palpate pulsation of the supraclavicular artery

Figure 9. The contrast-enhanced computed tomography (CT) scan was reconstructed with volume-rendering algorithms. It documents the costo-clavicular triangle delimited anteriorly by the middle third of the clavicle, posteromedially by the first rib and posterolaterally by the upper profile of the scapula. The CT shows the irregularity of the profile of the subclavian artery with an evident dilation (*) upstream of its compression at the level of the costo-clavicular triangle.
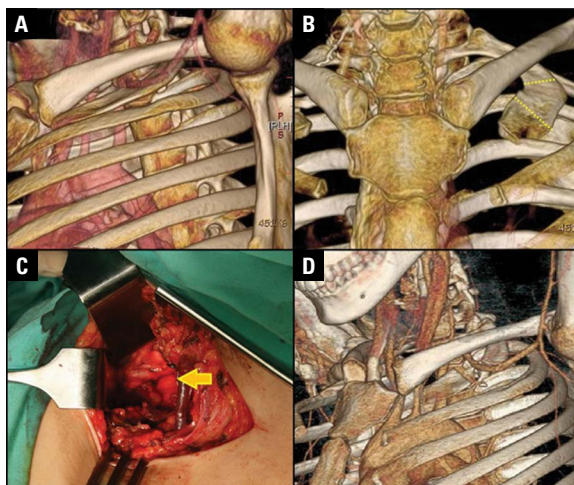
Figure 11. A. Preoperative computed tomography (CT) shows the first rib compressing the subclavian artery; **B.** Preoperative planning of the excision; **C.** Transaxillary first rib resection. at the level of the scalene tubercle (arrow) and myotomy; **D.** Postoperative CT shows partial resection of the first rib and the decompressed subclavian artery.
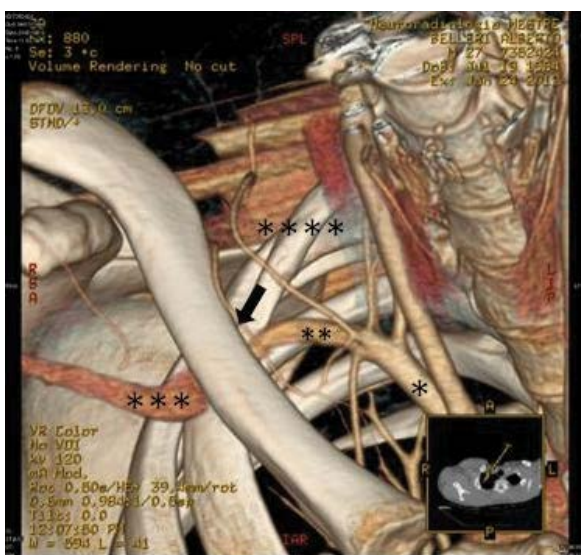
Figure 10. The contrast-enhanced computed tomography scan documents the stenotic effect of the subclavian artery (→) during the Adson test. In particular when the patient, while seated, rotates his head and elevates his chin to the side in which is suspected the syndrome, the compression on the subclavian artery by the cervical rib is increased determining a stenotic effect; *brachiocephalic trunk; ** pre-stenosis subclavian artery; ***post-stenosis subclavian artery; ****cervical rib.

Diagnosis

We can make the diagnosis by confirming a compromised circulation of the artery and identifying an anatomical factor responsible for arterial obstruction. Experiments were performed in compliance with the Italian laws and guidelines concerning the informed consent of patient (Dir. 2001/20/CE). A provocative test may suggest the diagnosis of arterial insufficiency (Fig. 10): 1) Adson test: if the patient, while seated, rotates his head and elevates his chin to the side where the syndrome appears localised causes his pulse to decreases or disappear, then the test is positive for vascular compression by anterior scalenus muscle or cervical rib (Fig. 8); 2) The overhand exercise test: the patient raises both arms overhead and quickly extends and flexes the fingers; if he fills pain, sense of weight, tingling and pallor appears in 20 seconds then the test is considered positive. Instrumental examinations useful for diagnosis are standard arteriography, MR or CT angiography, Doppler ultrasonography, which can be associated to postural manoeuvres to reveal the arterial impairment. The arteriography performed with the patient seated has more sensitivity than in supine position, in particular if he changes the position of the arms [7, 9, 17].

Management

It is necessary to identify the site of arterial compression and the surgery of resection of cervical or anomalous first rib and of scalene muscle release and arterial reconstruction (Fig. 11). Not all patients treated with cervical or anomalous first rib resection are able to return to their level of physical activity because there are often delays in treating chronic-pain syndrome [3].

RESULTS

Seventy-nine per cent of patients were included in the first two stages of nerve, artery, vein (NAV) staging (148 cases) and provided with physio-kinesiotherapy experienced good/excellent results, whilst the remaining 21% were transferred to the third stage. 33 patients that were included in the third and fourth stage underwent surgery with excellent results on vascular and sensory neuropathic disorders. However, the operations did not completely restore the hand fine motility due to the severe hypotrophy of the affected muscles. The retrospective analysis of our study showed that the tendon bands stretched between the sketch of the accessory rib and the first rib, associated with other factors (dominant limb, physical characteristics, prolonged limb abduction) are the most common cause of neurogenic TOS (N3 of the NAV staging). Indeed these malformations — which compress the lower primary trunk from below — can develop in a subtle way severe deficits in the hand motility, without causing particular pain or sensory disturbances.

DISCUSSION

Cervical rib and anomalous first rib are predisposing factors for the development of TOS, but in most patients more than an osseous abnormality must be present to determine symptoms. Often a neck trauma, either work-related or not, happens before the appearance of symptoms. The presence of a cervical rib or anomalous first rib, by itself, does not imply that surgery is necessary even with symptoms of disability and non-responsiveness to conservative therapy [1, 11, 15]. The diagnosis of neurogenic TOS should be made, above all, on the basis of clinical findings whether with or without any osseous abnormality. However, anomalous first ribs can determine arterial stenosis that can remain asymptomatic until thrombosis or embolisation occurs. Therefore, if neurogenic symptoms do not lead to the necessity of surgery, the patient must be evaluated and monitored with duplex scanning for stenosis or aneurysm formation. Although there aren't clinical trials comparing operative and non-operative therapies for TOS, common surgical interventions include excision of first rib, scalenectomy and lysis of fibrotic band (Fig. 9) [7, 13]. Excision of the cervical rib may be performed with or without the first rib, but often — if the first rib is not excised — there is a higher operation failure rate. The explanation for such better results (i.e. when the first rib and cervical rib are

both removed) is not obvious. The treatment of acute forms involves thrombolysis and anticoagulant therapy followed by the decompression of the thoracic outlet. Surgery is appropriate for true neurogenic TOS, vascular TOS and patients for whom conservative therapy fails. Operative intervention often gives good results [3].

Conflict of interest: None declared

REFERENCES

1. Bianchi E, Mancini P, De Vito S, et al. Congenital asymptomatic diaphragmatic hernias in adults: a case series. J Med Case Rep. 2013; 7: 125, doi: 10.1186/1752-1947-7-125, indexed in Pubmed: 23668793.
2. Busetto A, Fontana P, Zaccaria A, et al. Thoracic outlet syndrome: clinical staging. Italian Surg. 2004; 56(N1): 55–62.
3. Cavallotti C, Artico M, Cavallotti D. Occurrence of adrenergic nerve fibers and of noradrenaline in thymus gland of juvenile and aged rats. Immunol Lett. 1999; 70(1): 53–62, doi: 10.1016/s0165-2478(99)00127-3.
4. Dachling P. Diagnosis and surgical management of thoracic outlet syndrome. Techn Neurosurg. 2000; 6(1): 27–49, doi: 10.1097/00127927-200006010-00005.
5. Ferrante MA, Ferrante ND. The thoracic outlet syndromes: Part 1. Overview of the thoracic outlet syndromes and review of true neurogenic thoracic outlet syndrome. Muscle Nerve. 2017; 55(6): 782–793, doi: 10.1002/mus.25536, indexed in Pubmed: 28006844.
6. Huang JH, Zager EL. Thoracic outlet syndrome. Neurosurgery. 2004; 55(4): 897–902.
7. Hussain MA, Aljabri B, Al-Omran M. Vascular thoracic outlet syndrome. Semin Thorac Cardiovasc Surg. 2016; 28(1): 151–157, doi: 10.1053/j.semtcvs.2015.10.008, indexed in Pubmed: 27568153.
8. Illig KA, Rodriguez-Zoppi E, Illig KA, et al. The incidence of thoracic outlet syndrome. Ann Vasc Surg. 2021; 70(1): 263–272, doi: 10.1016/j.avsg.2020.07.029, indexed in Pubmed: 32771464.
9. Khun E, Lbus VGF, Bible E. Thoracic outlet syndrome. J Am Acad Orthop Surg. 2015; 23(4): 222–232.
10. Likes K, Dapash T, Rochlin DH, et al. Remaining or residual first ribs are the cause of recurrent thoracic outlet syndrome. Ann Vasc Surg. 2014; 28(4): 939–945, doi: 10.1016/j.avsg.2013.12.010, indexed in Pubmed: 24462539.
11. Likes K, Rochlin DH, Call D, et al. Coexistence of arterial compression in patients with neurogenic thoracic outlet syndrome. JAMA Surg. 2014; 149(12): 1240–1243, doi: 10.1001/jamasurg.2014.280, indexed in Pubmed: 25322469.
12. Nichols A. Diagnosis and management of thoracic outlet syndrome. Curr Sports Med Rep. 2009; 8(5): 240–249, doi: 10.1249/jsr.0b013e3181b8556d.
13. Raptis CA, Sridhar S, Thompson RW, et al. Imaging of the patient with thoracic outlet syndrome. Radiographics. 2016; 36(4): 984–1000, doi: 10.1148/rg.2016150221, indexed in Pubmed: 27257767.
14. Rochlin DH, Orlando MS, Likes KC, et al. Bilateral first rib resection and scalenectomy is effective for treatment of thoracic outlet syndrome. J Vasc Surg. 2014; 60(1): 185–190, doi: 10.1016/j.jvs.2014.01.034, indexed in Pubmed: 24709438.
15. Sanders RJ, Hammond SL. Management of cervical ribs and anomalous first ribs causing neurogenic thoracic outlet syndrome. J Vasc Surg. 2002; 36(1): 51–56, doi: 10.1067/mva.2002.123750, indexed in Pubmed: 12096257.
16. Seifert S, Sebesta P, Klenske M, et al. [Thoracic Outlet Syndrome]. Zentralbl Chir. 2017; 142(1): 104–112, doi: 10.1055/s-0042-121611, indexed in Pubmed: 28303559.
17. Spartalis E, Spartalis M, Tsilimigras D, et al. Extensive or partial first rib resection for thoracic outlet syndrome? The contribution of three-dimensional imaging to the preoperative planning and the postoperative evaluation. Clin Case Rep. 2018; 6(8): 1631–1632, doi: 10.1002/ccr3.1617.
18. Taviani M, Prandi M, Iurilli L, et al. Ourexperience with thoracic outlet syndrome. G Chir. 1996; 17(6-7): 329–331.
19. Vemuri C, McLaughlin LN, Abuirqeba AA, et al. Clinical presentation and management of arterial thoracic outlet syndrome. J Vasc Surg. 2017; 65(5): 1429–1439, doi: 10.1016/j.jvs.2016.11.039, indexed in Pubmed: 28189360.

ORIGINAL ARTICLE

VIA MEDICA

Musculus peroneus longus in foetal period

A. Karykowska[1], Z.A. Domagała[2] , B. Gworys[3]

[1]Department of Anthropology, Wroclaw University of Environmental and Life Sciences, Wroclaw, Poland
[2]Division of Anatomy, Department of Human Morphology and Embryology, Faculty of Medicine,
Wroclaw Medical University, Wroclaw, Poland
[3]Faculty of Health Science and Physical Education, The Witelon State University of Applied Sciences, Legnica, Poland

Background: The lateral compartment of the leg, due to its distal and concurrent superficial positioning, is a multiple trauma site. Detailed knowledge of compartimentum lateralis cruris (CLC) structure is crucial for physicians. Musculus peroneus longus (MPL) is located within the structures of the CLC most superficially. There is a lot of data on the morphology of the MPL but there is no publication analysing in detail its anatomy in the foetal period. The aim of the study was to determine the variability of metric and morphological parameters of MPL in a studied period of prenatal ontogenesis.

Materials and methods: The analysis included 207 human foetuses (101 males and 106 females) at calendar age from 113 to 222 days. The analysed material comes from the local anatomy collection. Foetuses were stored in typical preservation solutions. Access to the muscle was obtained on the basis of standard preparation techniques. The authors evaluated the metric parameters of the muscle showing the presence of variable dynamics of metric increments of the examined muscle in particular age classes.

Results: In the studied period of prenatal ontogenesis, MPLs of the foetuses increased by about 60% in the length and width dimension and by about 100% in the thickness dimension. The topography of the initial and final muscle attachment was also evaluated. Statistically significant dimorphic differences were found in some aspects of muscle attachment topography.

Conclusions: The analysis of the place of the origin and insertion of MPL showed a relatively large variety of these features. (Folia Morphol 2022; 81, 1: 124–133)

Key words: foetus, lateral compartment of the leg, dissection, fibularis longus muscle

INTRODUCTION

The lateral compartment of the leg (*compartimentum lateralis cruris*) is bounded by two fibrous intermuscular septa, which are attached to the crural fascia [3, 30]. It contains several important anatomical structures, which are of great importance for the mechanics of the foot [25]. The following muscles: *Musculus peroneus longus* and *Musculus peroneus brevis*, filling the compartment, are not only responsible for the pronation and plantar flexion of the foot, but they also stabilize the first ray of the foot in the toe-off phase of gait [4]. The lateral compartment of the leg,

Table 1. Basic metric data of the examined group of foetuses

Age class	Number of foeti	Age [g]	M$\bar{x}$m [g]	M$\bar{x}$f [mm]	L$\bar{x}$m [mm]	L$\bar{x}$f [mm]	Vtub$\bar{x}$m [mm]	Vtub$\bar{x}$f [mm]	C$\bar{x}$m [mm]	C$\bar{x}$f [mm]
5	69	18.80	211.47	255.77	212.56	219.94	182.08	188.38	182.08	188.38
6	78	22.49	397.28	429.64	263.21	263.82	185.15	189.06	185.15	189.06
7	40	25.83	580.50	524.95	300.61	292.50	208.83	207.50	208.83	207.50
8	13	30.62	615.13	712.00	322.25	335.00	217.00	229.60	217.00	229.60

M — body mass; L — body length; Vtub — vertex-tuberale length; C = CRL — crown-rump length; $\bar{x}$ — mean value interpolated at the centre of age class; f — female; m — male; age — average calendar age in weeks

due to its distal and concurrent superficial positioning, is a multiple trauma site, which may contribute to the occurrence of various clinical pathologies [17]. It is subject to a high risk of fractures of bones, which constitute its scaffolding, bruises, lacerations or stab wounds. One of the most serious consequences leg injuries is the compartment syndrome, which can be the result of injuries as well as of intensive physical activity. If untreated, it can lead to irreversible disturbances in the innervation and blood supply of the foot and leg. This may cause tissue necrosis [23, 27–29]. Detailed knowledge of *compartimentum lateralis cruris* structure is therefore significant not only for an anatomist but also for surgeons and traumatologists. Peroneus longus muscle (MPL) is located within the structures of the lateral compartment of the lower leg most superficially [21]. The proximal muscle attachment is wide, as fibres branch off in two groups: the proximal one, from the lateral condyle of the shin, capsule of tibiofibular joint and head of the fibula, and the distal one begins on the shaft of the fibula and the crural fascia. Proximal part of the muscle is divided into two compartments by the common fibular nerve (*nervus fibularis communis*), running in this area. In many anatomical publications, the more superficially positioned compartment is referred to as a superficial head, while the deeper part is defined as a deep head [3, 4]. The terminal tendon of the nerve lies in a gutter formed by the peroneus brevis muscle (*musculus fibularis brevis*), and just above the lateral malleolus of the tendon of both muscles they pass under the fibular retinaculum and penetrate the fibro-osseous canal, which allows the tendon to pass from the leg to the foot [21]. This is where the tendons cross. In the plantar region of foot the MPL is attached to the base of the first metatarsus and medial cuneiform bone. The terminal section of the muscle plays an extremely important role in supporting the plantar arch of foot [34]. There is a lot of data on the morphology of the described muscle

in the available literature [3, 4, 30], but there is no publication analysing in detail the anatomy of the MPL in the foetal period. The aim of the study was to determine the variability of metric and morphological parameters of *musculus peroneus longus* in a studied period of prenatal ontogenesis. In addition, the authors of the paper will determine the presence of possible dimorphic and bilateral differences.

MATERIALS AND METHODS

The analysis included 207 human foeti (101 males and 106 females) at calendar age from 113 to 222 days of foetal life. Only four foetuses of both sexes were analysed in the fourth month, and three foetuses in the ninth month. Due to the insufficient number in these classes, the mentioned foetuses were excluded from the metric analysis. The analysed foetal material is derived from the collection of the Department of Anatomy, Medicine Faculty, Wroclaw Medical University. The material was obtained from the maternity wards of local clinics as a result of preterm births and miscarriages in the years 1960–1996. Before conservation, the calendar and morphological age of each foetus were determined individually for each of them. To assess the morphological age of foeti, a multi-characteristic assessment method for the foetus age, was used [15, 16, 35]. If the difference between morphological and calendar age was more than 2 weeks, the foeti were determined as dysmorphic and excluded from the analysis. The foetuses are stored in an appropriate solid preservative solution containing ethanol, glycerol and formaldehyde in constant proportions in a room at a stable temperature. The way of storing foetuses did not change during the whole period of storage. The study excluded foetuses with visible developmental malformations and those that did not have complete clinical documentation. The reliability and scientific value of the collection used for research have been confirmed in many previously published studies [8, 10–12, 15, 20, 31, 32]. Basic data of the studied foetus population have been presented in Table 1.

125

Access to the muscle was obtained on the basis of standard preparation techniques. In the first stage, the skin and subcutaneous tissue were removed. Then the fascia was cut and the structures of *compartimentum lateralis cruris* were shown. MPL was cleaned from its top, at the head of the fibula up to the lateral malleolus canal. In the second stage, the terminal tendon of the studied muscle was prepared by removing the surface structures within the plantar region of foot. The morphological features of the examined muscle were evaluated after final visualisation of its whole structure. The data collected during the morphological evaluation were recorded in the form of schematic drawings. Photographs, which documented the research, were taken. The length and thickness of the muscle belly and the length of the muscle tendon were measured using digital calliper Mitutoyo – Absolute Digimatic 573-125-10, Mitutoyo Corp, Kawasaki, Japan. Each measurement was performed 3 times and the average value was taken into account for statistical analysis. All measurements were carried out with a foetus being positioned in a fixed, uniform manner on the measuring table. The obtained data was routed to MS Excel 2010, Microsoft Corp., Redmond, WA, USA. The obtained digital data were then statistically analysed using the Statistica PL, Tibco Software Inc., USA statistical package. The average values were adjusted to the middle of the age class according to the Legrange interpolation formula [5]. Aim of this statistical procedure was to achieve equal time intervals between successive age classes. This made it possible to precisely determine the growth rate of each of the analysed features. Two-factor ANOVA variance analysis was used to assess bilateral and dimorphic differences. In order to examine the differences between the quality features, the chi-square test of independence was used. For the analysed metric features, the rate of their growth was calculated using the formula: $\frac{b-a}{a} \times 100$, where 'a' is average value of the characteristic in the month of development, 'b' — average value of this characteristic in the following month of development. Work has a local bioethical commission acceptance KB-708/2017.

RESULTS

Metric evaluation

Length of the muscular belly and the length of terminal tendon of MPL (Table 2) were determined on the basis of preparation studies. In the case of the assessment of the length of the MPL belly, statistical

analysis (t-Student test) did not reveal any statistically significant bilateral differences in both the male (p = 0.416) and female (p = 0.337) genders. Additionally, ANOVA's two-factor analysis showed that among the analysed parameters only age, regardless of gender, significantly differentiated the MPL length (p < 0.001). At the same time, Tukey's post hoc test revealed the presence of a statistically significant difference between the MPL length in 5-month-old foetuses and foetuses in the remaining age classes for both male and female sex. The test did not reveal differences between foetuses of different sexes in the same age class. However, a statistically significant difference was found between 6- and 8-month foetuses in both sexes (Table 3).

The Student's t-test for the two dependent variables showed no statistically significant bilateral differences between male (p = 0.41) and female (p = 0.09) foetuses while evaluating the length of the final MPL tendon. The analysis of the relationship between sex and age of foetuses (ANOVA) and the dynamics of growth of the tendon length showed that only age significantly differentiated the length of the tendon (p < 0.001) regardless of the examined side. Additionally, the post hoc test revealed that there is a statistically significant difference between the length of the MPL tendon in 5-month-old foetuses and foetuses in other age classes. A difference was also observed between 6- and 8-month-old foetuses but only the male gender (Table 4).

The most intensive increase in the length of this muscle (belly and tendon) is characteristic for the period between 5 and 6 months of age. Period between 6 and 7 month of the intrauterine development demonstrates a decrease in the rate of growth by 70–80%. Re-acceleration of the growth rate takes place in the 8 month and it is about 1/3 of the value when compared to the first observed period.

The data on the thickness of the MPL belly are presented in Table 5. Statistical analysis carried out with the Student's t-test for the two dependent variables confirmed the absence of bilateral differences in the male sex (p = 0.70) and the presence of borderline statistical differences in the female sex (p = 0.049). Similarly to muscle length and tendon length of the MPL, its thickness varies only by age of the individuals regardless of body side (ANOVA; p = 0.000). Analysis of the maximum thickness of the MPL indicates that the most intensive growth rate is observed between 5 and 6 month of the foetal life and this is visible for

Table 2. Basic metric characteristics of *musculus peroneus longus* (MPL) in examined population

Age class	N	MPLL		MPLT	
		Right (SD)	Left (SD)	Right (SD)	Left (SD)
Male					
5	34	39.57 (6.12)	39.21 (1.33)	27.67 (0.99)	27.94 (5.73)
6	39	54.56 (7.34)	54.83 (1.24)	37.45 (0.93)	37.30 (5.21)
7	18	59.36 (7.26)	59.07 (1.83)	38.81 (1.37)	40.23 (5.67)
8	8	66.68 (5.42)	65.68 (2.75)	44.58 (2.05)	46.04 (6.41)
Female					
5	35	42.31 (8.31)	41.80 (1.32)	28.59 (0.98)	28.85 (6.31)
6	39	56.00 (7.70)	55.69 (1.24)	38.49 (0.93)	39.12 (6.02)
7	22	59.91 (9.96)	59.96 (1.83)	40.19 (1.24)	41.04 (6.37)
8	5	65.82 (7.67)	67.26 (2.75)	44.72 (2.60)	45.40 (5.01)

L — belly length; T — tendon length; SD — standard deviation

Table 3. Results of the post-hoc test (Tukey's test) for two-way ANOVA age to sex in the range of *musculus peroneus longus* belly length in the examined foetal group. The red numbers indicate statistically significant result.

Sex	Age	1	2	3	4	5	6	7	8
Right side		39.574	54.651	59.361	66.675	42.314	56.000	59.914	65.820
Male	5		0.000032	0.000032	0.000032	0.816700	0.000032	0.000032	0.000032
Male	6	0.000032		0.380128	0.041410	0.000032	0,994324	0,166184	0.045341
Male	7	0.000032	0.380128		0.325851	0.000032	0.787345	0.999998	0.710049
Male	8	0.000032	0.041410	0.325851		0.000032	0.048131	0.392693	0.999999
Female	5	0.816700	0.000032	0.000032	0.000032		0.000032	0.000032	0.000032
Female	6	0.000032	0.994324	0.787345	0.008131	0.000032		0.542008	0.046946
Female	7	0.000032	0.166184	0.999998	0.392693	0.000032	0,542008		0.777974
Female	8	0.000032	0.045341	0.710049	0.999999	0.000032	0.046946	0.777974	
Left side		39.209	54.828	59.067	65.675	41.803	55.687	59.964	67.260
Male	5		0.000032	0.000032	0.000032	0.864503	0.000032	0.000032	0.000032
Male	6	0.000032		0.542445	0.007889	0.000032	0.999716	0.205708	0.017520
Male	7	0.000032	0.542445		0.482301	0.000032	0.794361	0.999961	0.425621
Male	8	0.000032	0.007889	0.482301		0.000032	0.021118	0.634922	0.999965
Female	5	0.864503	0.000032	0.000032	0.000032		0.000032	0.000032	0.000032
Female	6	0.000032	0.999716	0.794361	0.021118	0.000032		0.440039	0.036944
Female	7	0.000032	0.205708	0.999961	0.634922	0.000032	0.440039		0.555593
Female	8	0.000032	0.017520	0.425621	0.999965	0.000032	0.036944	0.555593	

both sexes. Period between 6 and 7 month of a foetal development reveals the reduction of the growth rate by 50% to 75%. Between 7 and 8 month of the prenatal period development, the rate of growth of the characteristics decreases very rapidly. The decrease ranges from as much as up to 98%. It was only in the case of the right MPL in male foetus that growth rate remained at the same level as in the previous period. Detailed statistics (Tukey's post hoc test) are shown in Table 6.

Morphological evaluation
Proximal attachment

According to data from the previously published studies, based on an evaluation of the dissection materials, the proximal attachment of the MPL is located

Table 4. Results of the post-hoc test (Tukey's test) on *musculus peroneus longus* tendon length for the examined group. Results in red are statistically significant

Sex	Age	1	2	3	4	5	6	7	8
Right side		27.67	37.45	39.81	44.58	28.59	38.49	40.19	44.72
Male	5		0.000032	0.000032	0.000032	0.997982	0.000032	0.000032	0.000032
Male	6	0.000032		0.844296	0.033750	0.000032	0.993613	0.641422	0.143218
Male	7	0.000032	0.844296		0.530317	0.000032	0.993183	0.999999	0.706019
Male	8	0.000032	0.033750	0.530317		0.000032	0.122558	0.599782	1.000000
Female	5	0.997982	0.000032	0.000032	0.000032		0.000032	0.000032	0.000032
Female	6	0.000032	0.993613	0.993183	0.122558	0.000032		0.957691	0.316984
Female	7	0.000032	0.641422	0.999999	0.599782	0.000032	0.957691		0.765517
Female	8	0.000032	0.143218	0.706019	1.000000	0.000032	0.316984	0.765517	
Left side		27.94	37.30	40.23	46.04	28.85	39.12	41.04	45.40
Male	5		0.000032	0.000032	0.000032	0.998262	0.000032	0.000032	0.000032
Male	6	0.000032		0.654295	0.003243	0.000032	0.872867	0.247059	0.072549
Male	7	0.000032	0.654295		0.280427	0.000032	0.997859	0.999868	0.661700
Male	8	0.000032	0.003243	0.280427		0.000032	0.049874	0.443223	1.000000
Female	5	0.998262	0.000032	0.000032	0.000032		0.000032	0.000032	0.000032
Female	6	0.000032	0.872867	0.997859	0.049874	0.000032		0.923765	0.322431
Female	7	0.000032	0.247059	0.999868	0.443223	0.000032	0.923765		0.810350
Female	8	0.000032	0.072549	0.661700	1.000000	0.000032	0.322431	0.810350	

Table 5. Basic statistical data of *musculus peroneus longus* belly thickness

Age	N	Mean value (standard deviation)
Male, right		
5	34	1.31 (0.38)
6	39	2.09 (0.68)
7	18	2.41 (0.74)
8	8	2.81 (0.58)
Male, left		
5	34	1.35 (0.35)
6	39	2.02 (0.52)
7	18	2.52 (0.82)
8	8	2.51 (0.56)
Female, right		
5	35	1.50 (0.58)
6	39	2.14 (0.53)
7	22	2.57 (0.79)
8	5	2.60 (0.56)
Female, left		
5	35	1.53 (0.52)
6	39	2.03 (0.52)
7	22	2.36 (0.75)
8	5	2.38 (0.41)

on the lateral surface of the knee region. The original attachment of the muscle was being observed between the proximal part of the fibula and the proximal part of the tibia due to the course of the common fibular nerve in majority of the examined specimens. The site of the original attachment was found to be either very large, including the head of fibula, part of the shaft of fibula as well as the lateral condyle of tibia or very narrow, including only the fibula head. Based on anatomical observations, six basic types of primary muscle attachments were determined (Fig. 1):

— type I — head of the fibula, 1/2 superior of the shaft of the fibula, lateral condyle of the tibia;
— type II — head of the fibula, 1/2 superior of the shaft of the fibula;
— type III — head of the fibula, lateral tibia, superior 1/3 of the body of fibula
— type IV — head of the fibula, lateral tibia, superior 2/3 of the body of fibula;
— type V — head of the fibula, lateral condyle of the tibia;
— type VI — other locations not included within the aforementioned and remaining types of the original attachment.

Table 6. Results of the post-hoc test (Tukey's test) on *musculus peroneus longus* belly thickness for the examined group. Results in red are statistically significant

Sex	Age	1	2	3	4	5	6	7	8
Right side		1.31	2.09	2.41	2.81	1.50	2.14	2.57	2.60
Male	5		0.000033	0.000032	0.000032	0.894120	0.000032	0.000032	0.000243
Male	6	0.000033		0.607280	0.044574	0.000692	0.999977	0.062652	0.641840
Male	7	0.000032	0.607280		0.759939	0.000038	0.779637	0.990376	0.998376
Male	8	0.000032	0.044574	0.759939		0.000033	0.078102	0.977459	0.998673
Female	5	0.894120	0.000692	0.000038	0.000033		0.000178	0.000032	0.003537
Female	6	0.000032	0.999977	0.779637	0.078102	0.000178		0.133019	0.746058
Female	7	0.000032	0.062652	0.990376	0.977459	0.000032	0.133019		1.000000
Female	8	0.000243	0.641840	0.998376	0.998673	0.003537	0.746058	1.000000	
Left side		1.35	2.02	2.52	2.51	1.53	2.03	2.36	2.38
Male	5		0.000041	0.000032	0.000035	0.890278	0.000039	0.000032	0.003249
Male	6	0.000041		0.035664	0.314252	0.004389	1.000000	0.311993	0.879043
Male	7	0.000032	0.035664		1.000000	0.000032	0.039344	0.984605	0.999654
Male	8	0.000035	0.314252	1.000000		0.000233	0.327963	0.997880	0.999904
Female	5	0.890278	0.004389	0.000032	0.000233		0.003775	0.000033	0.032970
Female	6	0.000039	1.000000	0.039344	0.327963	0.003775		0.331978	0.886912
Female	7	0.000032	0.311993	0.984605	0.997880	0.000033	0.331978		1.000000
Female	8	0.003249	0.879043	0.999654	0.999904	0.032970	0.886912	1.000000	
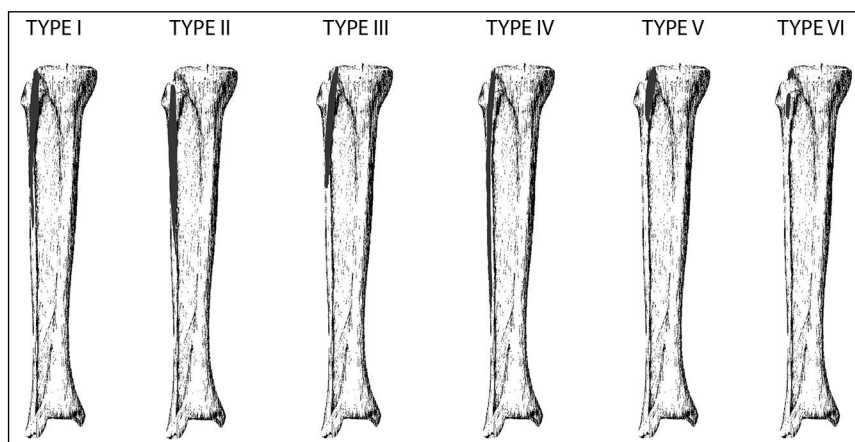
Figure 1. The main six types of fibularis longus muscle proximal attachments.

Statistical analysis (test for two structure parameters) did not reveal statistically significant dimorphic differences in the frequency of individual types of MPL proximal attachments on the right and left side ($p \geq 0.05$).

Distal attachment

Analysis of the distal part of the MPL has shown that in about 90% of cases the terminal attachments are located on the medial cuneiform bone and on the base of the first metatarsal bone. Three basic types of this attachment have been distinguished:

— type 1 — medial cuneiform bone with the base of the first metatarsal bone (Fig. 2);
— type 2 — base of the first metatarsal bone (Fig. 3);
— type 3— medial cuneiform bone (Fig. 4).

The remaining 10% of the population was characterised by a very variable terminal attachment including the surface of medial cuneiform bone, shaft

Figure 2. Type 1 of the distal attachment of the musculus fibularis longus; A — the base of the first metatarsal bone; B — medial cuneiform bone, female, right, 7 month.

Figure 3. Type 2 of the distal attachment of the musculus fibularis longus; female, right, 7 month.

Figure 4. Type 3 distal attachment of the musculus peroneus longus; male, right, 7 month.

Table 7. Distal attachment of the *musculus fibularis longus* typology. Type 4 constitutes a group of single unrelated attachment types

Distal attachment type	Right				Left			
	Male	Female	Total		Male	Female	Total	
			N	P			N	P
Type 1	77 (74.76%)	76 (73.08%)	153	0.34	70 (67.96%)	77 (74.04%)	147	0.51
Type 2	7 (6.80%)	10 (9.62%)	17	0.52	10 (9.71%)	18 (17.31%)	28	0.1259
Type 3	10 (9.71%)	14 (13.46%)	24	0.46	15 (14.56%)	5 (5.77%)	20	0.01
Type 4	9 (8.73%)	4 (3.84%)	13	0.31	8 (7.77%)	4 (3.85%)	12	0.02
All	103 (100%)	104 (100%)	207	–	103 (100%)	104 (100%)	207	–

of the first metatarsal bone and the navicular bone. For statistical purposes, this differentiated group was defined as type 4 of the terminal attachment of the MPL. The analysis did not reveal the presence of statistically significant differences in the location of terminal attachment of the MPL in the right limb. Analysis of the left lower limb revealed a significantly statistical difference in the occurrence of type 3 terminal attachment of the MPL — was more common in male foetuses (14.56%) than in female foetuses (5.77%). Statistically significant differences in type 4 were also found (Table 7).

DISCUSSION AND CONCLUSIONS

Musculus peroneus longus is of great clinical importance. Cases of its damage accompanied by the occurrence of the inter-fascial tightness syndrome have been frequently described [1, 18, 27, 29]. First of all, peroneus longus tendon autografts are commonly used in many orthopaedic procedures like deltoid ligament reconstruction [13] and medial patellofemoral ligament reconstruction [14] and anterior cruciate ligament reconstruction [24] (anterior half of the peroneus longus tendon). One of the reasons associated with clinical usefulness of the tendon is its length and its stable, unchangeable course, which has been shown in our study. Additionally, its attractiveness in terms of surgical procedures results from synergistic function of the MPL and peroneus brevis muscle.

When analysing the proximal part of the MPL, the most frequently pointed are the lateral condyle of the tibia and the head of fibula [7] as the site of the original attachment. According to Davda et al. [6] its origin is on the proximal 2/3 lateral side of fibula, anterior intermuscular septum and the lateral condyle of the tibia. The results obtained in this study also indicated that the site of the original attachment of

this muscle is quite varied. The original attachment was usually located on the head and the closer half of the fibula and on the lateral condyle of the tibia. This applies to the whole examined foetus cohort, which may imply that this feature does not show any significant dimorphic and bilateral differences. Evaluating the dynamics of the belly and MPL tendon development, the authors, who describe the leg muscles in the foetal period, present very diverse and contradictory data. For example Domagala et al. [9] when analysing the peroneus tertius, proved that as the foetus age increase, an increasingly longer belly and proportionally shorter tendon are being observed. According to the authors of the paper this is to be a result of physical activity of the foetus, which increases in utero with age. It must be emphasised that the study of Domagala et al. [9] includes the analysis of an atypical muscle within the anterior compartment of the leg and relatively large foetal material is examined by the authors. Within the MPL analysis, Albay and Candan [2] proves that the length of tendon increases rapidly in the third trimester. This work, however, is based on a much smaller study group and the material is divided into only three age classes (second trimester, third trimester, full time newborns). On the other hand, the results of our work indicate that the growth rate of both the belly and the MPL tendon is similar, the highest in the fifth to sixth month of life, whereupon it drops sharply to slightly increase in the last age class. It has not been proved that the dynamics of an increase in the tendon length has significantly changed in relation to the length of the belly.

From 5 month of the foetal life the MPL tendon in the examined foetuses proved to be very long. Its length is close to the length of the entire muscle. It was observed that the tendon begins deeply between the muscle fibre bundles, which has been confirmed

by the research of Bogacka et al. [4] carried out on adults. This tendon subsequently runs along the plantar region of foot and is usually attached to the base of the first metatarsal bone [24]. Shyamsundar et al. [26] suggest that the MPL attachment to the first metatarsal bone is most commonly observed and typical muscle termination. The authors claim that the connection observed between the tendon and the medial cuneiform bone is only a weak slip. According to our observations, the dominating attachment was the one connected within the medial cuneiform bone and the first metatarsal bone, but the distribution of fibres between the bones was either proportional or the majority of fibres were directed towards the plantar surface of the medial cuneiform bone. Similarly to our observations, Davda et al. [6] indicate the site of the muscle attachment on the closer part of the plantar surface of the medial cuneiform bone and on the base of the first metatarsal bone in a more precise manner. Despite the fact, the authors emphasize a relatively high variability of the terminal attachment. Moreover, a major interpersonal differentiation of this trait has been revealed by the foetal studies. In more than 70% of all examined individuals, the site of terminal attachment of the MPL was shown to be on the medial cuneiform bone and on the base of the first metatarsal bone. The remaining types are present in 30% of cases, so it may be concluded that the encountering any of them in practice is less likely.

Analysis of differences between average values of length, breadth and thickness of both muscles in successive age classes has shown that the growth rate of both muscles is very similar to that of the scapula [19]. The authors indicate a negative correlation with the length-width index of the scapula in foetuses, observed with age. This study has revealed that thickness increases most intensely, then as in the case of the scapula, it is followed by the width and finally the length.

The authors have described a great number of anomalies and variations within the peroneal muscles region. Example: a low-located muscle tummy, presence of a bone spur of the fibula penetrating into the muscles, a very extended peroneal trochlea, a very slack inferior peroneal retinaculum and many others [3, 22, 33]. However, in the examined sample, no aforementioned varieties or abnormalities in the course of peroneal muscles were found. It should therefore be concluded that the anomalies and varieties mentioned within the peroneal muscles, are

secondary. They do not result from developmental errors in the embryonic period, but suggest that they occur along with the motility of the lower limbs. Thus, they are rather the result of paragenetic or epigenetic and environmental factors.

Conflict of interest: None declared

REFERENCES

1. Aigner F, Longato S, Gardetto A, et al. Anatomic survey of the common fibular nerve and its branching pattern with regard to the intermuscular septa of the leg. Clin Anat. 2004; 17(6): 503–512, doi: 10.1002/ca.20007, indexed in Pubmed: 15300871.

2. Albay S, Candan B. Evaluation of fibular muscles and prevalence of accessory fibular muscles on fetal cadavers. Surg Radiol Anat. 2017; 39(12): 1337–1341, doi: 10.1007/s00276-017-1887-y, indexed in Pubmed: 28608130.

3. Bakkum BW, Russell K, Adamcryck T, et al. Gross anatomic evidence of partitioning in the human fibularis longus and brevis muscles. Clin Anat. 1996; 9(6): 381–385, doi: 10.1002/(SICI)1098-2353(1996)9:6<381::AID-CA4>3.0.CO;2-E, indexed in Pubmed: 8915617.

4. Bogacka U, Dziedzic D, Komarnitki I, et al. Anatomy of the long peroneal muscle of the leg. Folia Morphol. 2017; 76(2): 284–288, doi: 10.5603/FM.a2016.0054, indexed in Pubmed: 27714727.

5. Bożiłow W, Sawicki K. Metody badań zmienności cech anatomicznych człowieka podczas rozwoju prenatalnego i okołoporodowego. Akademia Medyczna, Wrocław 1980: 52–85.

6. Davda K, Malhotra K, O'Donnell P, et al. Peroneal tendon disorders. EFORT Open Rev. 2017; 2(6): 281–292, doi: 10.1302/2058-5241.2.160047, indexed in Pubmed: 28736620.

7. Didomenico LA, Cross DJ, Giagnacova A. Technique for utilization of an interference screw for split peroneus brevis tendon transfer in lateral ankle stabilization. J Foot Ankle Surg. 2014; 53(1): 114–116, doi: 10.1053/j.jfas.2013.09.016, indexed in Pubmed: 24239429.

8. Domagała Z, Domański J, Zimmer A, et al. Methodology of preparation of corrosive specimens from human placenta: A technical note. Ann Anat. 2020; 228: 151436, doi: 10.1016/j.aanat.2019.151436, indexed in Pubmed: 31704147.

9. Domagała Z, Gworys B, Kreczyńska B, et al. contribution to the discussion concerning the variability of the third peroneal muscle: An anatomical analysis on the basis of foetal material. Folia Morphol. 2006; 65(4): 329–36, indexed in Pubmed: 17171612.

10. Domagała Z, Gworys B, Porwolik K. Preliminary assessment of anatomical variability of nervus peroneus superficialis in the foetal period. Folia Morphol. 2003; 62(4): 401–403, indexed in Pubmed: 14655126.

11. Dudek K, Kędzia W, Kędzia E, et al. Mathematical modelling of the growth of human fetus anatomical structures. Anat Sci Int. 2017; 92(4): 521–529, doi: 10.1007/s12565-016-0353-y, indexed in Pubmed: 27393150.

12. Dudek K, Nowakowska-Kotas M, Kędzia A. Mathematical models of human cerebellar development in the fetal period. J Anat. 2018; 232(4): 596–603, doi: 10.1111/joa.12767, indexed in Pubmed: 29315634.

13. Ellis SJ, Williams BR, Wagshul AD, et al. Deltoid ligament reconstruction with peroneus longus autograft in flatfoot deformity. Foot Ankle Int. 2010; 31(9): 781–789, doi: 10.3113/FAI.2010.0781, indexed in Pubmed: 20880481.

14. Grunfeld R, Oh I, Flemister S, et al. Reconstruction of the deltoid-spring ligament. Tech Foot Ankle Surg. 2016; 15(1): 39–46, doi: 10.1097/btf.0000000000000108.

15. Gworys B, Domagała Z, Markocka-Maczka K. Development of the descending colon during the human foetal period. Folia Morphol. 2004; 63(2): 173–178, indexed in Pubmed: 15232772.

16. Gworys B, Domagala Z. The typology of the human fetal lanugo on the thorax. Ann Anat. 2003; 185(4): 383–386, doi: 10.1016/S0940-9602(03)80066-3, indexed in Pubmed: 12924478.

17. Herzog GA, Serrano-Riera R, Sagi HC. Traumatic proximal tibiofibular dislocation: a marker of severely traumatized extremities. J Orthop Trauma. 2015; 29(10): 456–459, doi: 10.1097/BOT.0000000000000348, indexed in Pubmed: 26397776.

18. Hiramatsu K, Yonetani Y, Kinugasa K, et al. Deep peroneal nerve palsy with isolated lateral compartment syndrome secondary to peroneus longus tear: a report of two cases and a review of the literature. J Orthop Traumatol. 2016; 17(2): 181–185, doi: 10.1007/s10195-015-0373-8, indexed in Pubmed: 26362782.

19. Kedzia A, Andrzejak R, Dudek K, et al. Analysis of human scapula morphometry in the fetal period. Adv Clin Exp Med. 2009; 18(3): 197–204.

20. Kędzia A, Ziajkiewicz M, Seredyn A, et al. Computer morphometric analysis of the palmaris longus muscle in the fetal period. Adv Clin Exp Med. 2009; 18(5): 437–47.

21. Olewnik Ł. Is there a relationship between the occurrence of frenular ligaments and the type of fibularis longus tendon insertion? Ann Anat. 2019; 224: 47–53, doi: 10.1016/j.aanat.2019.03.002, indexed in Pubmed: 30930196.

22. Patil V, Frisch NC, Ebraheim NA. Anatomical variations in the insertion of the peroneus (fibularis) longus tendon. Foot Ankle Int. 2007; 28(11): 1179–1182, doi: 10.3113/FAI.2007.1179, indexed in Pubmed: 18021587.

23. Rajasekaran S, Hall MM. Nonoerative management of chronic exertional comartment syndrome: a systematic review. Curr Sports Med Rep. 2016; 15: 191–198.

24. Rhatomy S, Asikin AI, Wardani AE, et al. Peroneus longus autograft can be recommended as a superior graft to hamstring tendon in single-bundle ACL reconstruction. Knee Surg Sports Traumatol Arthrosc. 2019; 27(11): 3552–3559, doi: 10.1007/s00167-019-05455-w, indexed in Pubmed: 30877316.

25. Sarig-Bahat H, Krasovsky A, Sprecher E. Evaluation of clinical methods for peroneal muscle testing. Physiother Res Int. 2013; 18(1): 55–62, doi: 10.1002/pri.1534, indexed in Pubmed: 22911954.

26. Shyamsundar S, Wazir A, Allen PE. Variations in the insertion of peroneus longus tendon-a cadaver study. Foot Ankle Surg. 2012; 18(4): 293–295, doi: 10.1016/j.fas.2012.05.003, indexed in Pubmed: 23093127.

27. Slabaugh M, Oldham J, Krause J. Acute isolated lateral leg compartment syndrome following a peroneus longus muscle tear. Orthopedics. 2008; 31(3): 272, doi: 10.3928/01477447-20080301-37, indexed in Pubmed: 19292237.

28. Imade S, Takao M, Miyamoto W, et al. Leg anterior compartment syndrome following ankle arthroscopy after maisonneuve fracture. J Arthrosc relat Surg. 2009; 25(2): 215–218, doi: 10.1016/j.arthro.2007.08.027, indexed in Pubmed: 19171284.

29. van Zantvoort APM, de Bruijn JA, Winkes MB, et al. Isolated chronic exertional compartment syndrome of the lateral lower leg: a case series. Orthop J Sports Med. 2015; 3(11): 2325967115617728, doi: 10.1177/2325967115617728, indexed in Pubmed: 26740955.

30. Wilke J, Engeroff T, Nürnberger F, et al. Anatomical study of the morphological continuity between iliotibial tract and the fibularis longus fascia. Surg Radiol Anat. 2016; 38(3): 349–352, doi: 10.1007/s00276-015-1585-6, indexed in Pubmed: 26522465.

31. Woźniak J, Kędzia A, Dudek K. Brachial plexus variations during the fetal period. Anat Sci Int. 2012; 87(4): 223–233, doi: 10.1007/s12565-012-0150-1, indexed in Pubmed: 22945314.

32. Wozniak S, Pytrus T, Kobierzycki C, et al. The large intestine from fetal period to adulthood and its impact on the course of colonoscopy. Ann Anat. 2019; 224: 17–22, doi: 10.1016/j.aanat.2019.02.004, indexed in Pubmed: 30914345.

33. Yammine K. The accessory peroneal (fibular) muscles: peroneus quartus and peroneus digiti quinti. A systematic review and meta-analysis. Surg Radiol Anat. 2015; 37(6): 617–627, doi: 10.1007/s00276-015-1438-3, indexed in Pubmed: 25638531.

34. Zanetti M, Pfirrmann CWA, Saupe N, et al. Anatomic variants associated with peroneal tendon disorders: MR imaging findings in volunteers with asymptomatic ankles. Radiology. 2007; 242(2): 509–517, doi: 10.1148/radiol.2422051993, indexed in Pubmed: 17255421.

35. Ziółkowski M, Gworys B, Kurlej W. Estimation of fetal age on the basis of certain measurements and ossification of the sternum. Folia Morphol. 1988; 47(1-4): 145–151, indexed in Pubmed: 3267621.

ORIGINAL ARTICLE

Paratenon of the cruciate ligaments of the knee: a macroscopic and histological study of human foetuses

J.H. Kim[1], N. Sugai[2], D. Suzuki[3], G. Murakami[4], H. Abe[5], J.F. Rodríguez-Vázquez[6], M. Yamamoto[7]

[1]Department of Anatomy, Jeonbuk National University Medical School, Jeonju, Korea
[2]Department of Rehabilitation and Physical Therapy, Hitshuji-ga-oka Hospital, Sapporo, Japan
[3]Division of Common Curriculum, Hokkaido Chitose College of Rehabilitation, Chitose, Japan
[4]Division of Internal Medicine, Cupid Clinic, Iwamizawa, Hokkaido, Japan
[5]Emeritus Professor of Akita University School of Medicine, Akita, Japan
[6]Department of Anatomy and Embryology, School of Medicine, Complutense University, Madrid, Spain
[7]Department of Anatomy, Tokyo Dental College, Tokyo, Japan

Background: The paratenon is a sheath-like connective tissue that allows the tendon to move with minimal friction. The careful removal of the paratenon along the cruciate ligaments is a critical step of knee surgery. Thus, orthopaedic surgeons and interventional radiologists consider the paratenon as a basic anatomical tissue along a ligament, not along a tendon.

Materials and methods: We performed macroscopic and histological observations of cruciate ligament-associated paratenons in 43 human foetuses.

Results: This tissue usually had a thick armour-like appearance that was distant from the infrapatellar fat pad. The anterior cruciate ligament, rather than the posterior ligament, was deeply embedded in the paratenon. The paratenon contained abundant arteries and veins and, at and near the crossing between the cruciate ligaments, had a well-developed venous plexus. Notably, there were abundant fused veins in the paratenon venous plexus, and prenatal knee movements (especially rotation) seemed to restrict its blood supply, leading to the development of a large cavity by way of advancing fusion of veins in the degenerating plexus. This unique manner of cavitation likely expanded the joint cavity.

Conclusions: Differences in knee movements in utero seemed to cause differences in the thickness of the paratenon among foetuses. New-borns might have limited knee flexion due to a mass-effect of the thick paratenon around the cruciate ligaments. A slight twisting or rotation at the knee may help to release the knee, because it can break the foetal paratenon and accelerate cavitation. (Folia Morphol 2022; 81, 1: 134–143)

Key words: paratenon, tendon sheath, cruciate ligament of the knee, histology, human foetus

---

Address for correspondence: Dr. J.H. Kim, Department of Anatomy, Jeonbuk National University Medical School, 20 Geunji-ro, Deokjin-gu, Jeonju, 54907, Republic of Korea, tel: 82-63-270-3097, fax: 82-63-274-9880, e-mail: 407kk@hanmail.net

INTRODUCTION

There is variation and some confusion in use of the term "paratenon" among clinicians. Benjamin et al. [1] provided concise definitions of the paratenon and its analogues as follows: the endotendon is a thin film of loose connective tissue providing a vascular route; the epitenon surrounds the tendon as a whole and is continuous with the endotendon; and the paratenon is a tendon sheath that has a different histology and is clearly separated from the tendon itself. These authors considered the paratenon of the Achilles tendon as the best example. Therefore, the paratenon is not usually continuous with the synovial lining of a joint; similarly, some bursas, such as the trochanteric bursa, do not communicate with the joint cavity.

The careful removal of the paratenon along the cruciate ligament is a critical step in knee surgery [3], and paratenon stripping is an important procedure in interventional radiology of the knee [14]. The paratenon of the knee refers specifically to a sheath of the ligament, in contrast to the other or more common use of this term to refer to a sheath of the Achilles tendon [8, 18, 19]. Clinicians commonly use the term "paratenonitis" to refer to inflammation of the outer layer of the tendon, regardless of whether the paratenon is lined by a synovium [12]. However, for knee surgeons and interventional radiologists, the paratenon is a basic anatomical tissue along a ligament, not along a tendon. In the knee joint, the synovial lining should cover the paratenon along the cruciate ligaments. Because the infrapatellar fat pad is the largest synovial plica (thin tissue fold) in the human body, it might communicate with the paratenon.

The general aim of this study was to describe the development and morphology of the paratenon along the cruciate ligaments of the knee in human foetuses. The cruciate ligaments develop in the interzone mesenchymal tissue, between the femur and tibia [5, 15, 16]. Thus, it is likely that the paratenon also develops from primary interzone tissue, rather than being divided from the established cruciate ligament. The specific aim of this study was to determine whether a synovial lining was present at the expanding joint cavity along and around the paratenon of the knee. Previous research showed that the cytoplasm-rich cells in foetal synovial tissues had a cuboidal appearance [9, 13].

MATERIALS AND METHODS

This study was performed in accordance with the provisions of the 2013 revision of the Declaration of Helsinki. For macroscopic observations, the left knees of 25 near-term foetuses (crow-rump length [CRL]: 272–310 mm; gestational age [GA]: 32–37 weeks) were examined. The patellar tendon was cut at the tibial attachment to reflect the patella and infrapatellar fat pad upward. During the reflection, an attachment of the fat pad to the femur was cut (if present). A slight dissection was performed along the cruciate ligaments, and photos were taken at each step using a Pentax K-1 camera with a 50–100 mm zoom lens.

For histological observations, sagittal sections of the unilateral knee from 8 midterm foetuses (CRL: 35–73 mm; GA: 8–12 weeks) and 10 near-term foetuses (CRL: 280–320 mm; GA: 33–39 weeks) were examined. The latter 10 specimens were not used for the macroscopic observations. All sections were stained with haematoxylin and eosin (H&E). Most histological photographs were taken using a Nikon Eclipse 80, but photographs at ultra-low magnification (objective lens less than ×1) were taken using a high-grade flat scanner with translucent illumination (Epson scanner GTX970).

The histological sections from 6 midterm foetuses were part of the large collection at the Department of Anatomy of the Universidad Complutense, Madrid, and were from miscarriages or ectopic pregnancies at the Department of Obstetrics of the University. Until 1980, the sections had been prepared and stained with H&E, Azan or silver impregnation. The used of these specimens for research was approved by the Ethics Committee of Complutense University (B08/374). The knees of near-term foetuses were part of the collection of the Department of Anatomy, Akita University, Japan and were donated by families to the Department in 1975–1985 and preserved in 10% w/w neutral formalin solution for more than 30 years. Data on these specimens included the date of donation and the number of gestational weeks, but not the name of the family, obstetrician, hospital, or reason for abortion. The use of these specimens for research was approved by the Akita University Ethics Committee (No. 1428).

The unilateral knees from the 10 near-term foetuses were divided, and the specimens were incubated at room temperature in Plank-Rychlo solution (AlCl$_2$/6H$_2$O, 7.0 w/v%; HCl, 3.6%; HCOOH, 4.6%) for 1 to 2 weeks. Routine procedures for paraffin-embedded histology were performed, and semiserial sections of knees were prepared at 0.1 mm intervals.
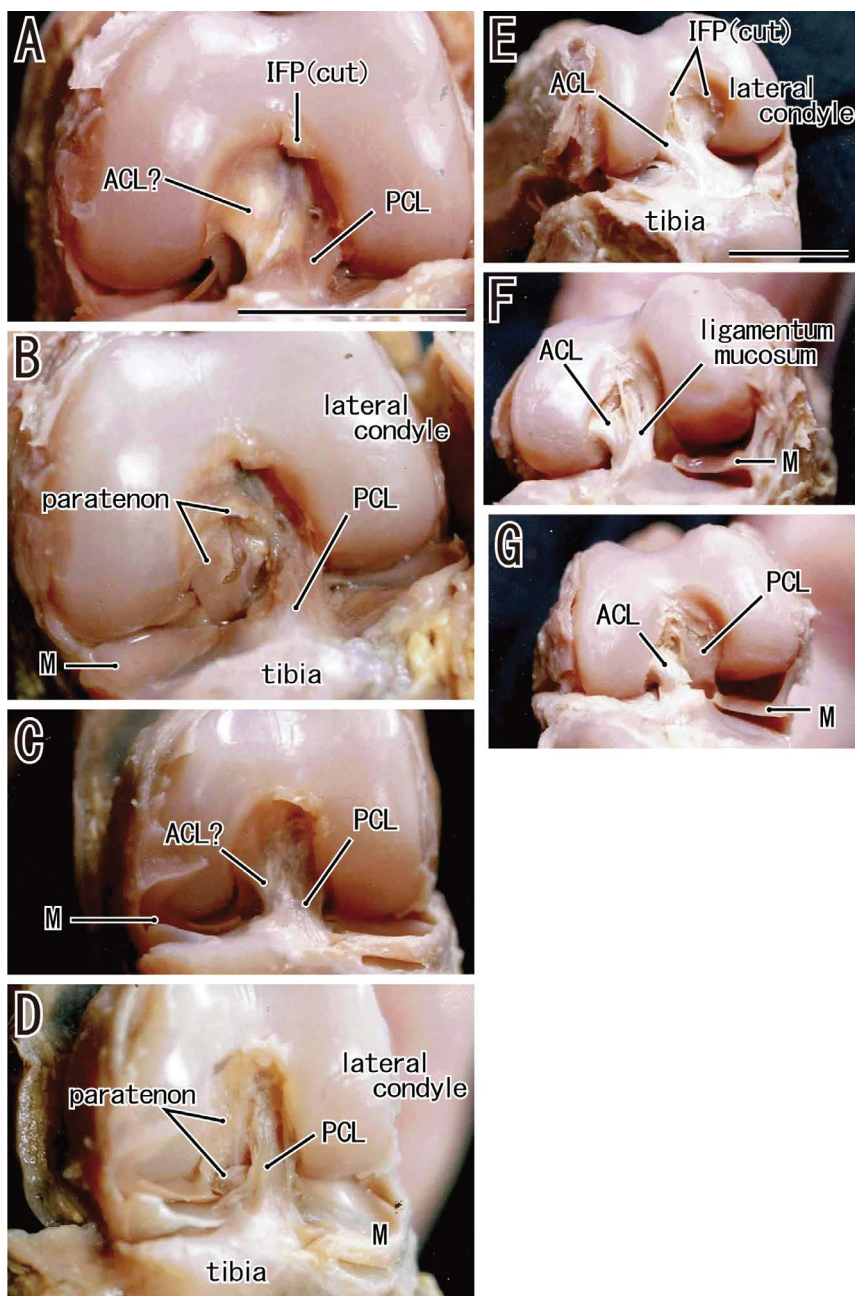
Figure 1. Anterior macroscopic views of the left knees of three near-term foetuses, with the patellas, infrapatellar fat pads, and patellar tendons removed; **A, B.** Foetus of 305 mm crow-rump length (CRL), approximately 36 weeks gestational age (GA); **C, D.** Foetus of 286 mm CRL, approximately 33 weeks GA; **E–G.** Foetus of 276 mm CRL, approximately 32 weeks GA. When the knee joint was opened, the infrapatellar fat pad was cut at the femoral attachment if present (infrapatellar fat pad [IFP] cut, panel A). The anterior cruciate ligaments (ACL) was entirely covered by a thick capsule-like paratenon (panel B), and the paratenon likely contained a feather-like structure (panel D). Panel E shows a rare example of a thin paratenon along the anterior ligament. The posterior cruciate ligament (PCL) accompanied a band-like tissue (ligamentum mucosum, panel F). Both ligaments were almost in parallel when the tibia was twisted (panel G); M — meniscus. Scale bar in panel A (5 mm) refers to panels A–D; scale bar in panel E (5 mm) refers to panels E–G.

RESULTS

Macroscopic observations

When we removed the patella and patellar tendon to open the knee joint from the anterior side, we also pulled off the infrapatellar fat pad from the joint cavity because it was attached to the patellar tendon at the inferior side of the patella. However, because a marginal part of the fat pad was attached to the femur, we cut it before taking photos (Fig. 1). The cruciate ligaments consistently had a smooth

surface (Fig. 1A, C, E). However, this surface was not usually of the ligament itself, but of the paratenon. Twenty-three of the 25 knees examined macroscopically had anterior cruciate ligaments (ACLs) that were entirely covered by capsule-like paratenons (Fig. 1B), and these sometimes contained feather-like structures attached to the anterior aspect of the ACL (Fig. 1D). Thus, in contrast to the first impression upon opening of the knee, the actual ACL was rarely exposed to the joint cavity (Fig. 1E). The ACL was evident in the anterior view in the other two knees (Fig. 1E, F). When the tibia was twisted, a crossing between the ACL and the posterior cruciate ligament (PCL) was released, and provided an almost parallel arrangement (Fig. 1G). This posture allowed us to determine whether a residual paratenon was present or absent after dissection.

The paratenon also covered the PCL, but was usually much thinner there than along the ACL. In 6 of 25 knees in which the paratenon was thick along the PCL, it had the appearance of another ligament that merged with the ACL at the tibial attachment (i.e. the ligamentum mucosum, Fig. 1F). Therefore, in these 6 knees, the paratenon of the PCL tended to be thicker on the lower side due to the antero-inferior course of the ligamentum mucosum. We found no correlation between the foetal age and gross morphology of the paratenon.

Histological observations

At midterm, an interzone mesenchymal tissue between the femur and tibia gradually disappeared (Fig. 2A). However, at 9 weeks GA, most parts of the ACL were embedded in the interzone tissue remnant (Fig. 2B). At that time, a joint cavitation advanced into the posterolateral part. Thus, along the PCL, the interzone tissue was limited to near the femoral attachment (Fig. 2C). Development of the infrapatellar fat pad was much delayed relative to the cruciate ligaments (Fig. 2B).

At near-term, we found various stages of paratenon development, and no clear correlation of stage with foetus age or size. Thus, the larger knees did not usually have a sheath- or armour-like paratenon, and also did not usually have a larger joint cavity. A candidate initial stage of the paratenon differentiation was present in the posterior side of the ACL (Fig. 3A, B). In this case, the enlarging joint cavity was surrounded by synovial plica-like tissues and by ligament-like tight tissues; the latter was apparently divided from the
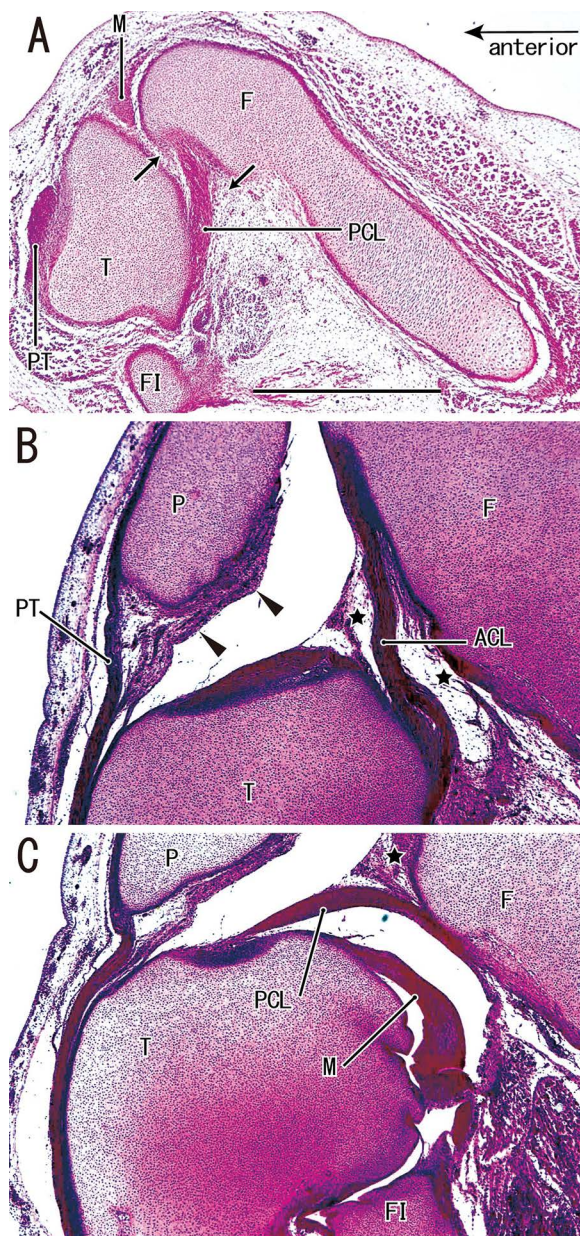
Figure 2. Sagittal sections of interzone mesenchymal tissues of the knee joints of two midterm foetuses; **A.** Foetus of 35 mm crow--rump length (CRL), approximately 8 weeks gestational age (GA); **B, C.** Foetus of 46 mm CRL, approximately 9 weeks GA. At 8 weeks, the posterior cruciate ligament (PCL) was embedded in interzone mesenchymal tissue (arrows in panel A) of the knee joint. The patella was present in more medial sections. At 9 weeks, the anterior cruciate ligament (ACL) was embedded in the interzone tissue remnant (stars in panel B) along almost the entire course. In contrast, along the PCL the loose tissue (star in panel C) was restricted near the femur (F). The infrapatellar fat pad was not developed (arrowheads in panel B); FI — fibula; M — meniscus; P — patella; PT — patellar tendon; T — tibia. Scale bar in panel A (1 mm) refers to all panels.

ACL with long tears (Fig. 3B). In contrast, an initial change was limited to an interzone tissue remnant that extended inferiorly along the PCL (Fig. 3C, D).

137
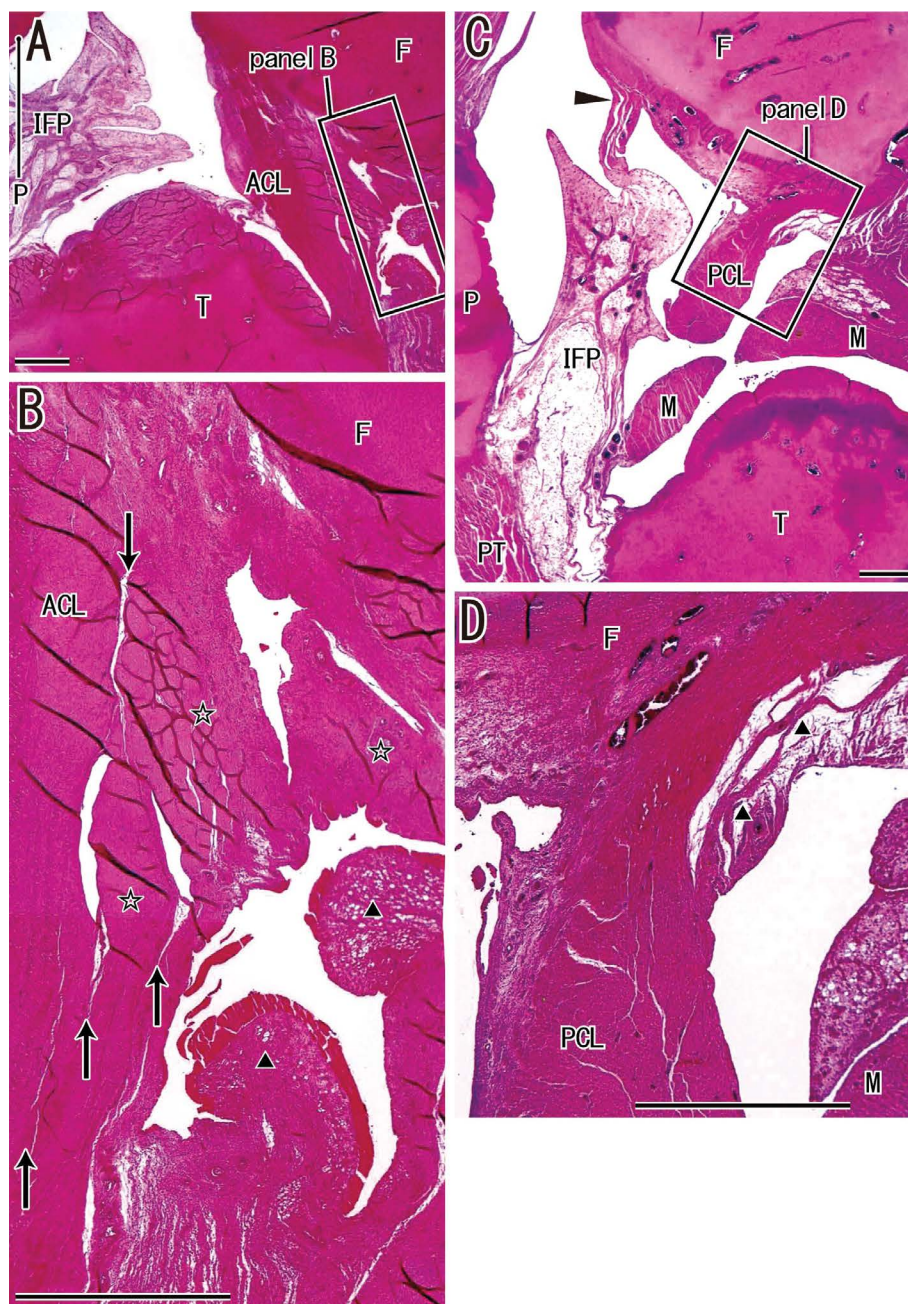
Figure 3. Sagittal sections of the initial differentiation of the paratenon along the cruciate ligaments of the knees of two near-term foetuses; **A, B.** Foetus of 270 mm crow-rump length (CRL), approximately 32 weeks gestational age (GA); **C, D.** Foetus of 282 mm CRL, approximately 33 weeks GA. Panels B and D provide magnified views of the delineated regions in panels A and C, respectively. An expanding joint space in the posterior side of the anterior cruciate ligaments (ACL) was surrounded by synovial fold-like tissues (triangles in panel B) and by ligament-like tight tissues (stars in panel B). The latter appear to be divided from the anterior ligament because of tears (arrows in panel B). In contrast, a loose tissue (triangles in panel D), corresponding to an interzone tissue remnant (Fig. 2C), extended inferiorly along the posterior cruciate ligament (PCL). The infrapatellar fat pad (IFP) was connected to the femur (arrowhead in panel C); F — femur; M — meniscus; P — patella; PT — patellar tendon; T — tibia. Scale bar in panel A (1 mm) refers to panels A and C; scale bar in panel B (1 mm) refers to panels B and D.

At the next stage (CRL 320 mm), the ACL accompanied a fatty tissue-rich paratenon or synovial plica around it (Fig. 4) or was embedded in a venous plexus-like paratenon (Fig. 6). These loose tissues contained abundant veins and several arteries. In contrast, the PCL accompanied the paratenon at and near the bony attachments. The infrapatellar fat pad was thick and long, and composed of a mesh of fibrous bands (less than 0.1 mm thick) that contained fatty tissues between the bands (Fig. 4C). The fat pad
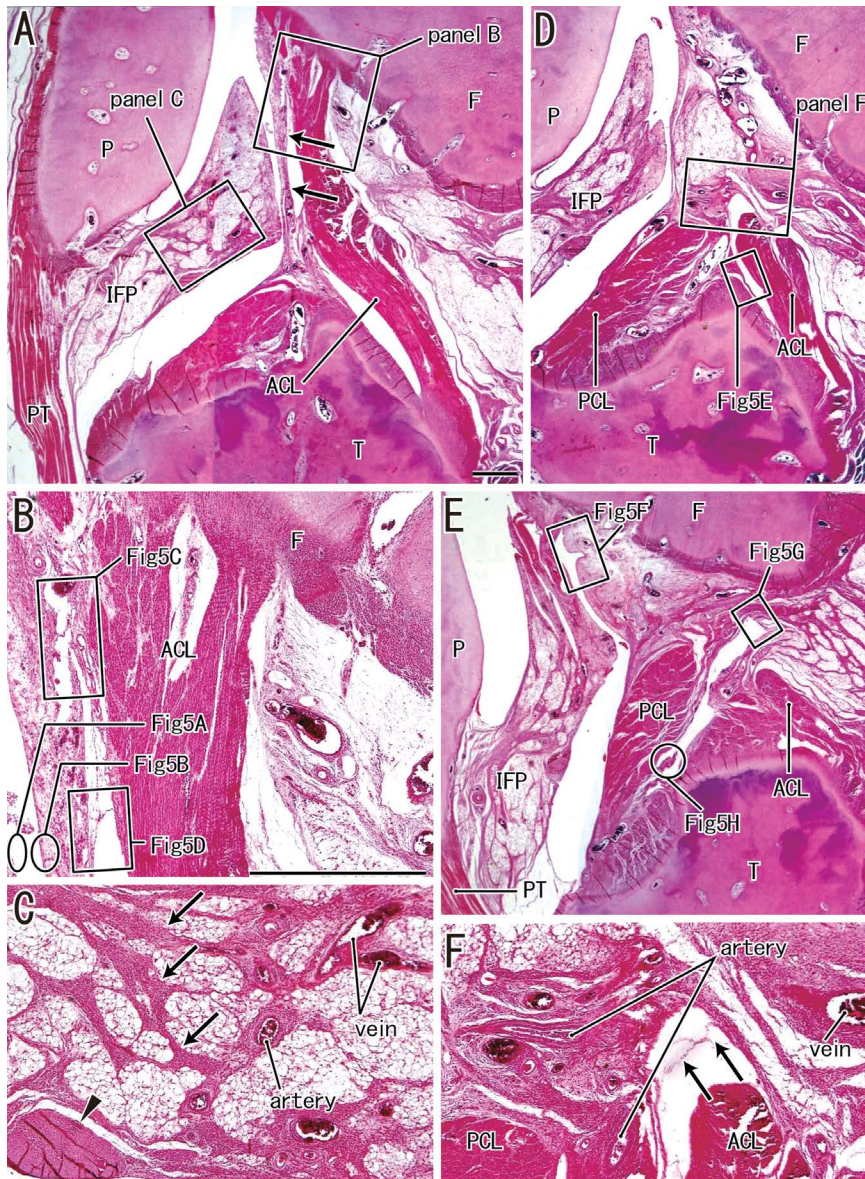
Figure 4. Sagittal sections of the fibro-adipose tissues of the paratenon at the knee in a near-term foetus; **A–F.** Foetus of 320 mm crow-rump length (CRL), approximately 39 weeks gestational age (GA). Panels A (most medial), D, and E (most lateral) show the anterior cruciate liga-ment (ACL) and posterior cruciate ligament (PCL) at low magnification. The ACL is separated from the infrapatellar fat pad (IFP) by a synovial plica (arrows in panel A). Panels B, C, and F provide magnified views of the delineated regions in panels A and B, and Figure 5 provides mag-nified views of the delineated regions in panels B and E. The femoral attachment of the anterior ligament (panel B) was sandwiched by loose tissues or paratenons. Panel C shows the infrapatellar fat pad, which consists of fatty tissues in a mesh of fibrous bands (arrows; < 0.1 mm thick). Some fat pads contained thick fibre bundles (arrowhead; > 0.3 mm thick). Panel F shows a site near the crossing of the cruciate ligaments, in which the arteries run near the ligaments. A cavity along the anterior ligament contained remnant fibres (arrows in panel F). F — femur; P — patella; PT — patellar tendon; T — tibia. Scale bar in panel A (1 mm) refers to panels A, D and E; scale bar in panel B (1 mm) refers to panels B, C and F.

surface and the paratenon surface to the joint cavity were lined by cuboidal cells (i.e. a primitive synovial lining, Fig. 5A, B, F). In contrast, flat cells lined a loose space along the ACL (Fig. 5C, D).

Notably, the cavity with flat lining cells continued to or communicated with the other non-lining spaces, which contained thin fibres (Figs. 4F and 5E) and/or fragmented tissues (Fig. 6C, D, G). Thus, at near-term, the drastic reconstruction of the paratenon was likely to occur with a cavitation along the ACL. Likewise, in the venous plexus-like paratenon (Fig. 7), vein fusion and degeneration provided a venous valve-like struc-
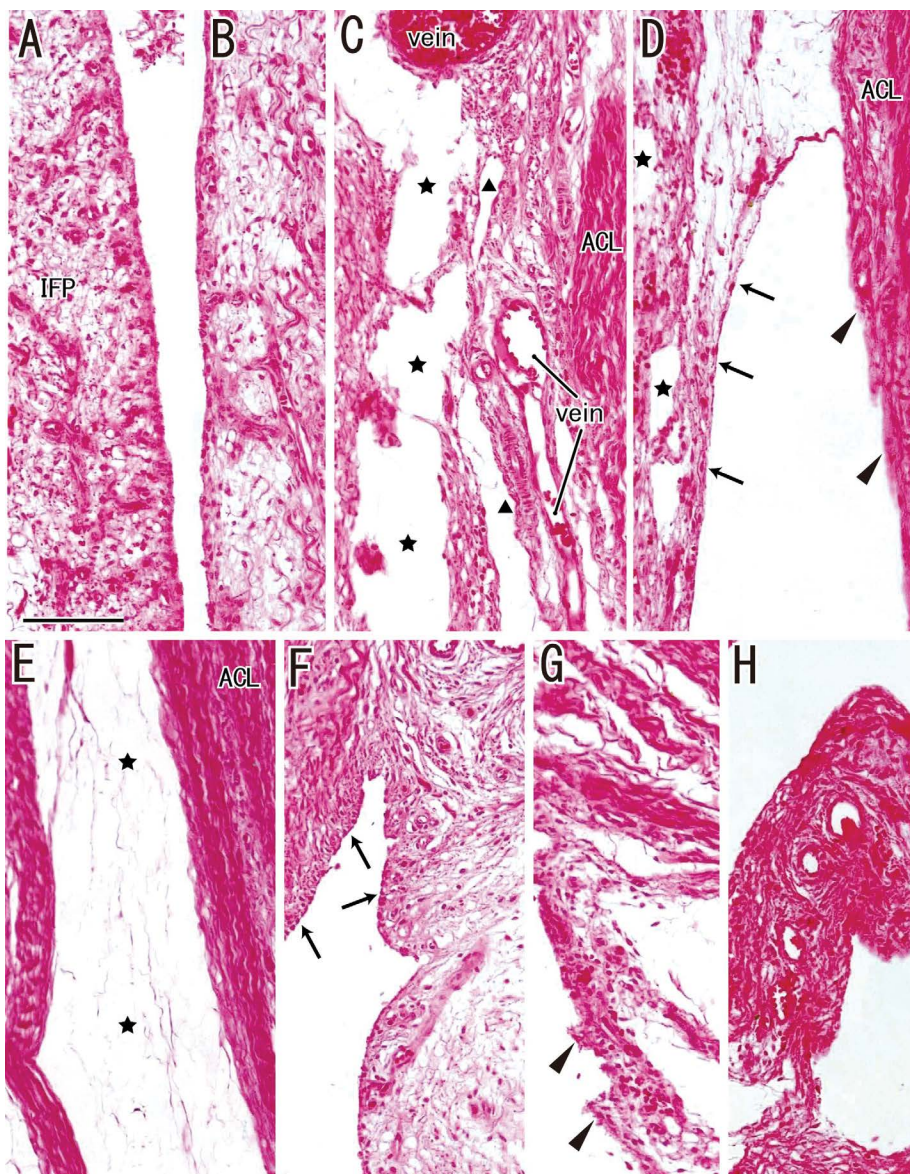
Figure 5. A–H. Higher magnification views of the fibro-adipose paratenon and synovium in a near-term foetus. Images are from delineated regions in panels B, D and E of Figure 4. Cuboidal and flat cells were mixed, and lined a surface of the infrapatellar fat pad (IFP, panel A) and a synovial plica along the anterior ligament (panel B). Along the anterior aspect of the anterior cruciate ligament (ACL) (panel C), there was a thick and long cavity without lining cells (stars) and two thin cavities with a lining of flat cells (triangles). At a site below panel C, a cavity in panel D was lined by flat cells (arrows) but was exposed to ACL fibres without lining (arrowheads). There were also small spaces with unclear lining cells (stars in panel D). Near the tibial attachment of the ACL (panel E), a cavity (stars) contained multiple remnant fibres. There was a cuboidal cell lining of the paratenon near the femoral attachment of the anterior ligament (arrows in panel F). In contrast, there were fragmented tissues without lining cells (arrowheads in panel G) near the femoral attachment of the posterior cruciate ligament (PCL). The PCL had a short synovial plica near the tibia (panel H). Scale bar in panel A (1 mm) refers to all panels.

ture (i.e. a degenerating venous endothelium, Fig. 7B–E). This morphology was quite different from an actual vein that was surrounded by a flat endothelial lining (Fig. 7A). Therefore, the venous fusion was similar to the process of joint cavitation *via* fusion of small spaces in degenerative tissues (Fig. 5C). These processes of the cavitation and venous reconstruction in the paratenon exposed the nearby arteries to the joint cavity (Figs. 4F and 6G).

DISCUSSION

The present study is apparently the first histological report of the paratenon of the knee in human foetuses. Because these ligament-associated
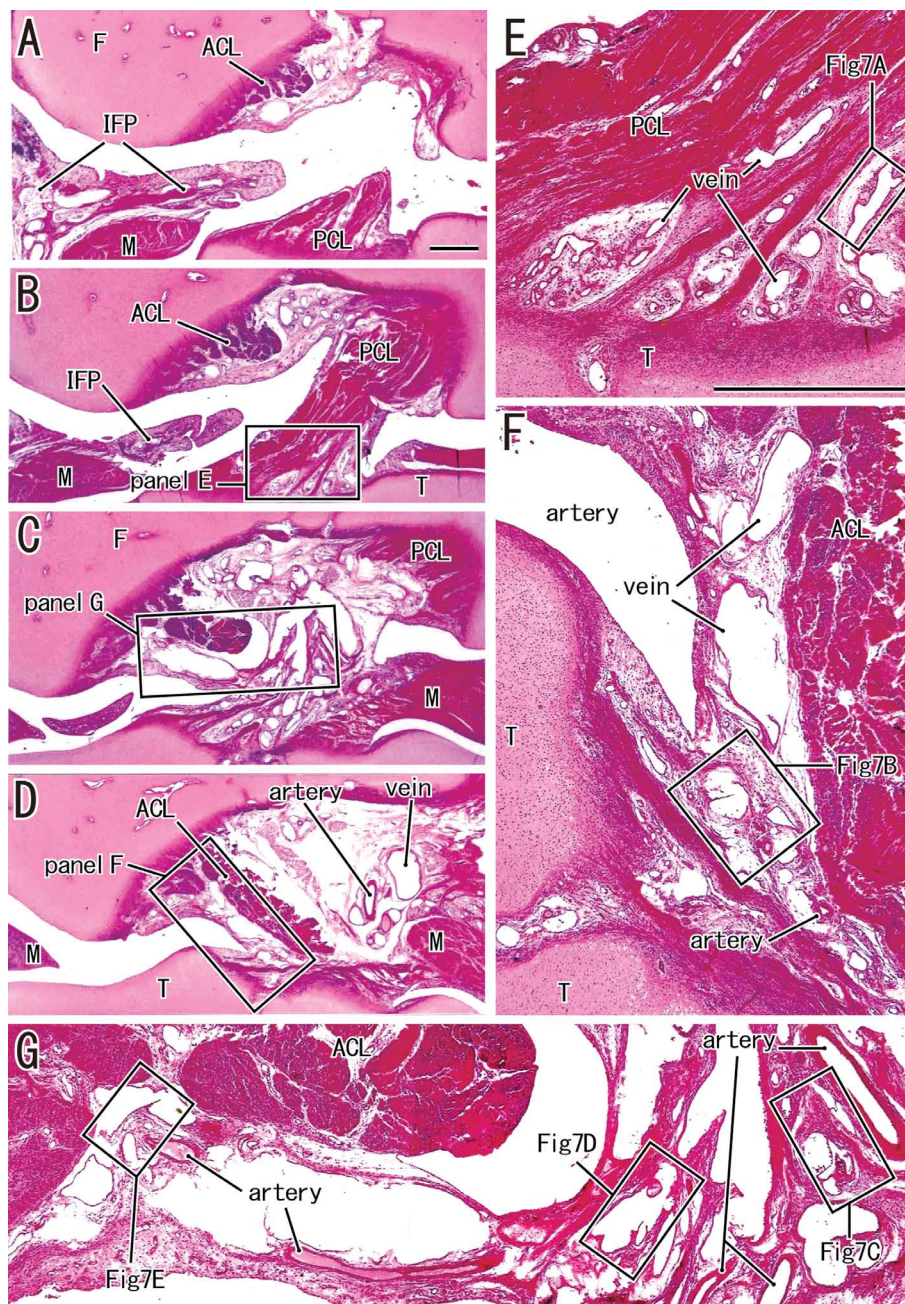
Figure 6. Sagittal sections of a vein-rich paratenon at the knee in a near-term foetus (280 mm crow-rump length, approximately 33 weeks gestational age); **A–D.** The anterior cruciate ligament (ACL) and posterior cruciate ligament (PCL) at low magnification, and panel A is the most medial view. Delineated areas in these panels are shown in panels **E–G** and Figure 7. The tibial attachment of the posterior ligament (panel E) contains abundant veins. In the anterior side of the anterior ligament (panel F), veins in the paratenon appear to be broken or degenerated (see also Fig. 7B). Near the crossing of the ACL and PCL (panel G), veins with irregular shapes form a plexus (see also Fig. 7C–E). F — femur; IFP — infrapatellar fat pad; M — meniscus; T — tibia. Scale bar in panel A (1 mm) refers to panels A–D; scale bar in panel E (1 mm) refers to panels E–G.

tissues are small and thin in midterm foetuses, we believe that the thick paratenons that we identified macroscopically in near-term foetuses (Fig. 1) likely developed from the interzone mesenchymal tissue between 13 and 31 weeks GA. In contrast to the development of a tight meniscus in the loose interzone tissue [4], a relatively loose paratenon did not have a definite shape during the prenatal period. However, in near-term foetuses, there was likely to be a drastic reconstruction of the paratenon, especially along the ACL. At this time, individual differences in the thickness of the paratenon became evident along the
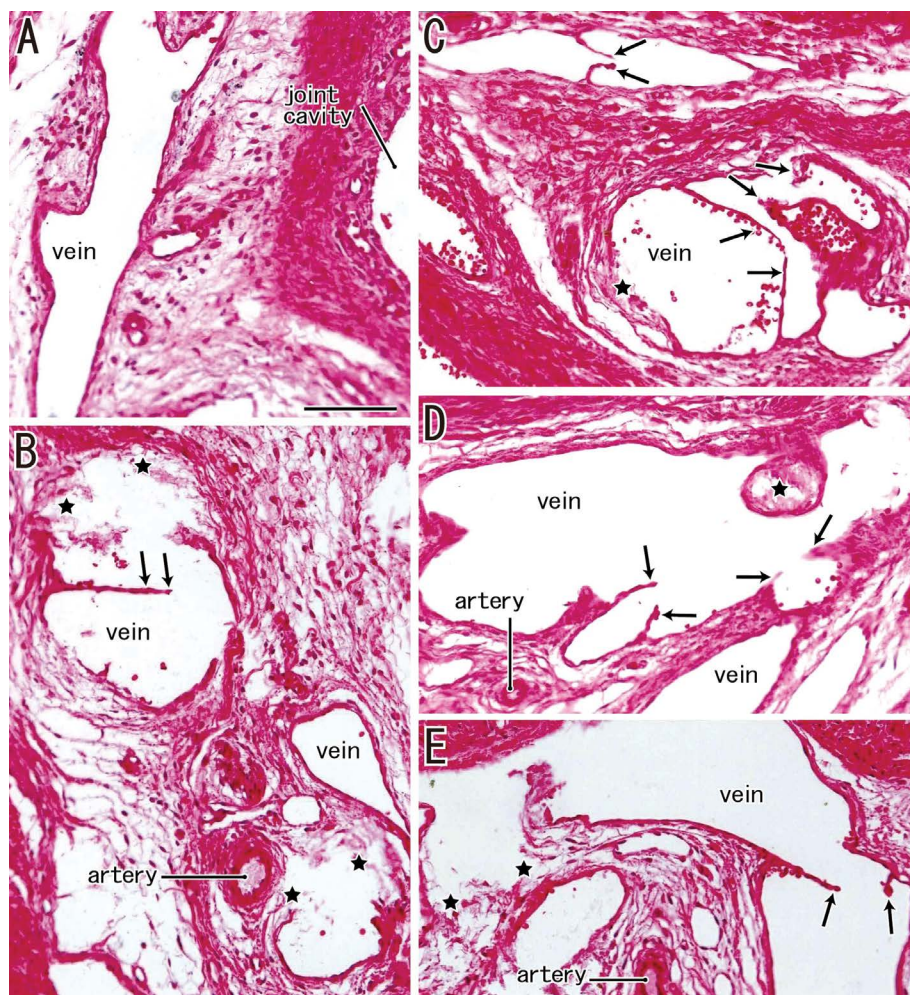
Figure 7. A–E. Higher magnification views of normal and specific veins in the paratenon of a near-term foetus. Images are from delineated regions in panels E–G of Figure 6. Panel A shows a flat endothelial cell lining of a vein that is clearly different from the synovial lining of the joint cavity (see also Fig. 5A, B). Veins in the paratenon of the cruciate ligaments (panels B–E) often have valve-like structures of the endothelium (arrows) and broken or degenerated endothelium (stars). Scale bar in panel A (0.1 mm) refers to all panels.

ACL, presumably due to differences in knee posture *in utero*. A slight twisting of the cruciate ligaments (i.e. a slight rotation at the knee) at this time probably pushed and interfered with enlargement of the paratenon. Actually, Katz et al. [10] reported greater external rotation of the tibia in babies after earlier delivery. We found two-types of histology: a fatty tissue-rich paratenon and a venous plexus-like paratenon. Because active cavitation in the paratenon was suggested in the venous plexus, it is unlikely that one type of paratenon could change into the other type. In both types, the paratenon contained abundant arteries and veins, especially at and near the crossing between the cruciate ligaments.

Notably, veins in the paratenon were likely to fuse and, because of limited blood supply from prenatal knee movements, the plexus seemed to degenerate.

In the degeneration in near-term knees, the advancing fusion of venous cavities seemed to provide a large cavity without the usual cuboidal synovial cell lining. This might be a unique manner of joint cavitation, although it is somewhat similar to the fusion of thyroid follicles in the aged thyroid because of abundant valve-like fragments of the follicle wall [20]. A similar fusion is also seen in circadian changes of the follicles although it is followed by re-division: the size of follicle drastically changes [21]. The unique cavitation in the paratenon venous plexus exposed the nearby arteries to the joint cavity (Figs. 4F and 6G), and these arteries should be degenerated. In near-term foetuses, we recently reported a close topographical relationship between the tributaries of the external vertebral venous plexus and recesses of the zygapophysial joint cavity [13]. A degenerating venous

plexus during joint cavitation might be a common method of development. Although we cannot deny the possibility that the present venous plexus-like paratenon is pathological, we are unaware of any evidence supporting this interpretation.

It is well known that knee joints undergo frequent movements *in utero* [6, 7, 11]. A baby usually has a knee flexion posture at birth. In new-borns and infants, stiffness at the knee is released from 21.4 to 3.3 degrees within the first 6 months [2]. This knee stiffness is apparently caused by a mass-effect of the thick paratenon armoured around the cruciate ligaments. A slight twisting or rotation at the knee is likely to release an infant's knee because it can break the paratenon and accelerate cavitation. Finally, we had a study limitation that we did not perform a MOVAT's pentachrome staining [17] for long-preserved specimens.

CONCLUSIONS

Differences in knee movements *in utero* seemed to cause differences in the thickness of the paratenon among foetuses. New-borns might have limited knee flexion due to a mass-effect of the thick paratenon around the cruciate ligaments. A slight twisting or rotation at the knee may help to release the knee, because it can break the foetal paratenon and accelerate cavitation.

Conflict of interest: None declared

REFERENCES

1. Benjamin M, Kaiser E, Milz S. Structure-function relationships in tendons: a review. J Anat. 2008; 212(3): 211–228, doi: 10.1111/j.1469-7580.2008.00864.x, indexed in Pubmed: 18304204.
2. Broughton NS, Wright J, Menelaus MB. Range of knee motion in normal neonates. J Pediatr Orthop. 1993; 13(2): 263–264, indexed in Pubmed: 8459024.
3. Chahla J, Moatshe G, Cinque ME, et al. Arthroscopic anatomic single-bundle anterior cruciate ligament reconstruction using bone-patellar tendon-bone autograft: pearls for an accurate reconstruction. Arthrosc Tech. 2017; 6(4): e1159–e1167, doi: 10.1016/j.eats.2017.04.001, indexed in Pubmed: 29354412.
4. Clark CR, Ogden JA. Development of the menisci of the human knee joint. Morphological changes and their potential role in childhood meniscal injury. J Bone Joint Surg Am. 1983; 65(4): 538–547, indexed in Pubmed: 6833331.
5. Gray DJ, Gardner E. Prenatal development of the human knee and superior tibiofibular joints. Am J Anat. 1950; 86(2): 235–287, doi: 10.1002/aja.1000860204, indexed in Pubmed: 15410671.
6. Higginbottom J, Bagnall KM, Harris PF, et al. Ultrasound monitoring of fetal movements. A method for assessing fetal development? . Lancet. 1976; 307(7962): 719–721, doi: 10.1016/s0140-6736(76)93092-0.
7. Humphrey T. Some correlations between the appearance of human fetal reflexes and the development of the nervous system. Progr Brain Res. 1964: 93–135, doi: 10.1016/s0079-6123(08)61273-x.
8. Huisman ES, Andersson G, Scott A, et al. Regional molecular and cellular differences in the female rabbit Achilles tendon complex: potential implications for understanding responses to loading. J Anat. 2014; 224(5): 538–547, doi: 10.1111/joa.12169, indexed in Pubmed: 24571598.
9. Isogai S, Murakami G, Wada T, et al. Which morphologies of synovial folds result from degeneration and/or aging of the radiohumeral joint: an anatomic study with cadavers and embryos. J Shoulder Elbow Surg. 2001; 10(2): 169–181, doi: 10.1067/mse.2001.112956, indexed in Pubmed: 11307082.
10. Katz K, Naor N, Merlob P, et al. Rotational deformities of the tibia and foot in preterm infants. J Pediatr Orthop. 1990; 10(4): 483–485, indexed in Pubmed: 2358486.
11. Katz K, Mashiach R, Bar On A, et al. Normal range of fetal knee movements. J Pediatr Orthop. 1999; 19(6): 739–741, indexed in Pubmed: 10573342.
12. Khan KM, Maffulli N, Coleman BD, et al. Patellar tendinopathy: some aspects of basic science and clinical management. Br J Sports Med. 1998; 32(4): 346–355, doi: 10.1136/bjsm.32.4.346, indexed in Pubmed: 9865413.
13. Kitamura K, Hayashi S, Jin ZWu, et al. Fetal cervical zygapophysial joint with special reference to the associated synovial tissue: a histological study using near-term human fetuses. Anat Cell Biol. 2021; 54(1): 65–73, doi: 10.5115/acb.20.265, indexed in Pubmed: 33594011.
14. Lalam RK, Winn N, Cassar-Pullicino VN. Interventional articular and para-articular knee procedures. Br J Radiol. 2016; 89(1059): 20150413, doi: 10.1259/bjr.20150413, indexed in Pubmed: 26682669.
15. Mérida-Velasco J, Sánchez-Montesinos I, Espín-Ferra J, et al. Development of the human knee joint ligaments. Anat Rec. 1997; 248(2): 259–268, doi: 10.1002/(sici)1097-0185(199706)248:2<259::aid-ar13>3.0.co;2-o.
16. McDermott L. Development of the human knee joint. Arch Surg. 1943; 46(5): 705, doi: 10.1001/archsurg.1943.01220110121021.
17. Movat HZ, More RH. The nature and origin of fibrinoid. Am J Clin Pathol. 1957; 28(4): 331–353, doi: 10.1093/ajcp/28.4.331, indexed in Pubmed: 13478538.
18. Shaw HM, Vázquez OT, McGonagle D, et al. Development of the human Achilles tendon enthesis organ. J Anat. 2008; 213(6): 718–724, doi: 10.1111/j.1469-7580.2008.00997.x, indexed in Pubmed: 19094187.
19. Stecco C, Corradin M, Macchi V, et al. Plantar fascia anatomy and its relationship with Achilles tendon and paratenon. J Anat. 2013; 223(6): 665–676, doi: 10.1111/joa.12111, indexed in Pubmed: 24028383.
20. Takayama T, Hirano-Kawamoto Ai, Yamamoto M, et al. Macrophage infiltration into thyroid follicles: an immunohistochemical study using donated elderly cadavers. Okajimas Folia Anat Jpn. 2016; 93(3): 73–80, doi: 10.2535/ofaj.93.73, indexed in Pubmed: 28216539.
21. Uchiyama Y, Oomiya A, Murakami G. Fluctuations in follicular structures of rat thyroid glands during 24 hours: fine structural and morphometric studies. Am J Anat. 1986; 175(1): 23–33, doi: 10.1002/aja.1001750104, indexed in Pubmed: 3953468.

ORIGINAL ARTICLE

Morphometric profile in foetuses and evolution of Achilles tendon

A. Waśniewska[1], Ł. Olewnik[2], M. Polguj[1]

[1]Department of Normal and Clinical Anatomy, Chair of Anatomy and Histology, Medical University of Lodz, Poland
[2]Department of Anatomical Dissection and Donation, Chair of Anatomy and Histology, Medical University of Lodz, Poland

Background: The Achilles tendon (AT) develops from the merge of the tendinous part of the gastrocnemius (GM) and soleus (SM) muscles. The AT is the structural base for the biomechanical work of the ankle joint. Understanding morphometry of the AT is crucial due to the tendon vulnerability to rupture and damage which requires further surgical repair and management. Despite its clinical significance, data concerning measurements of the AT in human foetuses are scare. The aim of our study was to assess the AT, GM and SM morphometry in human foetuses.
Materials and methods: Thirty-seven spontaneously-aborted human foetuses (17 male, 20 female) aged 18–38 weeks of gestation were examined. The morphometry of the GM, SM and AT were evaluated.
Results: No significant correlation between sex or side and size of the AT in human foetuses was observed. The only significant correlation was between sex and the length of the tendon of the SM; in 3rd trimester it was longer in male than in female. In 2nd trimester the SM muscle to tendon ratio was higher in female than in male.
Conclusions: There was no significant correlation between sex or side and size of the AT in human foetuses, probably due to scant muscle load during prenatal period. (Folia Morphol 2022; 81, 1: 144–149)

Key words: foetuses, Achilles tendon, calcaneal tendon, triceps suralis

INTRODUCTION

The Achilles tendon (AT), also known as calcaneal tendon, is the largest and the strongest tendon in human body [9, 14, 23]. The AT develops from the merge of the tendinous part of the gastrocnemius muscle (GM) and soleus muscle (SM) [2, 5, 9]. The GM and SM, that is beneath the GM, componentize the triceps surae or "calf" muscle [5, 7]. The triceps surae and the AT belong to superficial compartment of the calf [14]. The GM is composed of two heads, the medial and lateral. The medial head originates from the medial supracondylar line and adductor tubercle of the femur, and the lateral head originates from the posterior part of the lateral femoral condyle, posterior and superior to the lateral epicondyle [5]. The lateral head is smaller, shorter and extends in lesser degree than the medial head [5, 25]. The SM originates from the soleal line and the middle part of the border of the tibia, from the posterior surface of the head and proximal part of the shaft of the fibula, and from a fibrous band between these two bones [25]. The AT is supplied by the posterior tibial artery, the peroneal arteries and the tibial nerve [14]. The AT inserts to the calcaneal tuberosity, to its posterior-superior aspect [11, 26].

Address for correspondence: Dr. A. Waśniewska, Department of Normal and Clinical Anatomy, Chair of Anatomy and Histology, Medical University of Lodz, ul. Żeligowskiego 7/9, 90–752 Łódź, Poland, e-mail: ania.wasniewska@gmail.com

The AT is the structural base for the biomechanical work of the ankle joint [28]. The GM with the SM is the main plantar flexor of the ankle joint [14, 24]. The SM is also a powerful knee flexor [21]. It is not able to exert full power at both joints simultaneously, for example when the knee is flexed; GM is unable to generate as much force at the ankle [21]. The opposite is true when the ankle is flexed.

Multiple morphological variations were described in this area, whereas most of them concerns plantaris muscle, GM and SM, especially their attachments, number of heads or even presence [17, 20, 21].

Increasing interest in sport activity results in increasing number of tendon injuries [9]. Problems with tendons are dominated by the AT, among athletes as well as the general public [9, 11, 28]. Disorders of the AT might be traumatic and nontraumatic, e.g. tendinopathy, ruptures of the tendon and insertional tendinitis [18, 29, 30]. Congenital disorders of the AT may result in toe walking or equinus deformation in children [8]. Understanding morphometry of the AT is crucial due to the tendon vulnerability to rupture and damage which requires further surgical repair and management [11]. Previous studies compared the measurements of the AT i.a. between sexes or sides in adults and proposed that differences were more correlated with the muscle strength, rather than gender [13]. Despite its clinical significance, data concerns measurements of the AT in human foetuses are scare.

The aim of our study was to assess the AT, GM and SM morphometry in human foetuses. We hypothesize that there will not be significant correlation between sex or side and size of the AT in human foetuses because of scant muscle load during prenatal period.

MATERIALS AND METHODS

Thirty-seven spontaneously-aborted human foetuses (17 male, 20 female) aged 18–38 weeks of gestation were examined. The foetuses were obtained from spontaneous abortion after parental consent. The study was conducted in accordance with the cadaveric donation programme for both adults and foetuses and with the legal procedures in force in Poland. Their ages were determined on the basis of cranio-sacral and head measurements. Foetuses were divided into two groups according to trimester. Permission for the study was received from the Local Bioethic Committee (agreement no. RNN/218/20/KE).

Table 1. Detail measurements of muscles and tendon

Structure	Measurements
Gastrocnemius muscle	Length of the lateral head — distance from posterior part of the lateral femoral condyle to the end of its muscle part
	Length of the medial head — distance from posterior part of the medial femoral condyle to the end of its muscle part
	Length of the lateral tendon — distance from the end of its muscle part to the calcaneal tuberosity
	Length of the medial tendon — distance from the end of its muscle part to the calcaneal tuberosity
Soleus muscle	Length from its beginning at soleal line on tibia to the end of the muscle part
	Length of the tendon from the end of its muscle part to the calcaneal tuberosity
Achilles tendon	Width at the calcaneal tuberosity
	Thickness at the calcaneal tuberosity

A dissection of the leg and foot was performed by traditional techniques [15, 16, 18, 19]. Firstly GM was exposed by the subcutaneous tissue. Morphometric measurements of the lateral and medial head and the tendon of the GM were performed. Secondly GM was separated from the SM, then measurements of the muscle and tendon of the SM were performed. The thickness and width of the AT was measured at its insert to calcaneal tuberosity. Detailed measurements are characterized in Table 1 and Figure 1. Measurements were carried out with an electronic digital calliper (Mitutoyo Corporation, Kawasaki-shi, Kanagawa, Japan). Each measurement was performed twice with an accuracy of up to 0.01 mm.

### Ethical approval and consent to participate

The cadavers belonged to the Department of Anatomical Dissection and Donation, Medical University of Lodz.

Statistical analysis

The collected measurements of muscles and tendon were compared using the Statistica 13.1 software package (StatSoft, Cracow, Poland). The Mann–Whitney U test and the χ^2 test were used to compare nominal and contentious variables between two groups; the Shapiro–Wilk test was used to determine the normality of the distribution. The level of significance was 0.05.
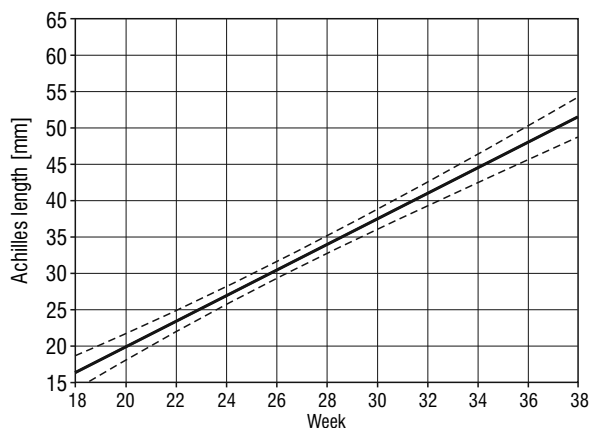
RESULTS

The mean length of medial head of GM was longer than lateral head in both second and third trimester
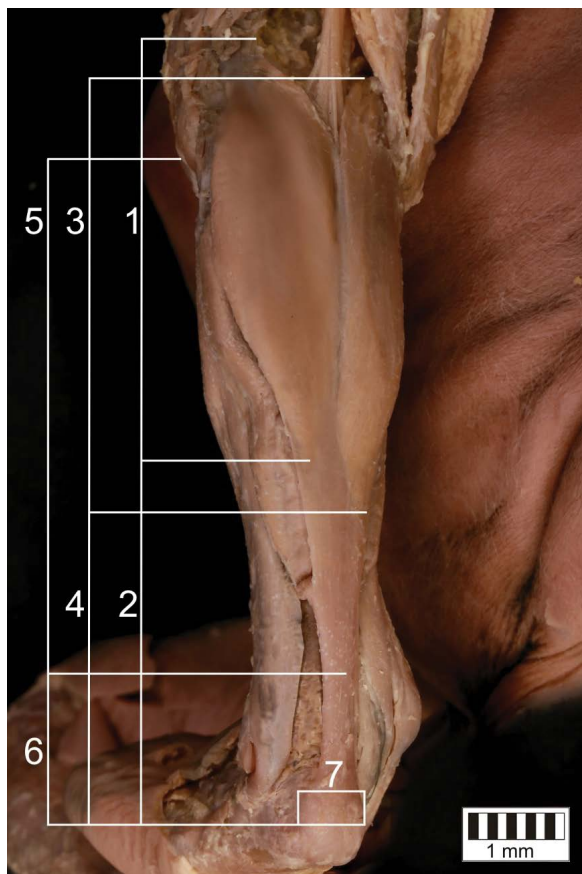
Figure 1. Detail measurements of muscles and tendon; 1 — length of the lateral head of the gastrocnemius muscle (GM); 2 — length of the lateral tendon of the GM; 3 — length of the medial head of the GM; 4 — length of the medial tendon of the GM; 5 — length of the muscle of the soleus muscle (SM); 6 — length of the tendon of the SM; 7 — thickness and width of the Achilles tendon.

Figure 2. Linear correlation between length of the Achilles tendon and week of gestation with 95% confidence interval.

(27.33 ± 6.04 mm vs. 29.46 ± 5.95 mm, p = 0.049; 45.84 ± 5.85 mm vs. 40.47 ± 5.9 mm, p = 0.036, respectively). The mean length of the tendon of the medial part of the GM was shorter than lateral part; however, statistical difference was observed only in second trimester of the gestation (second trimester: 24.92 ± ± 4.48 mm vs. 27.93 ± 4.29 mm, p < 0.001; third trimester: 42.22 ± 10.05 mm vs. 48.64 ± 90.1 mm, p = 0,113). In third trimester the mean length of muscle part of soleus was longer in male than in female, 62.98 ± 13.14 mm and 53.57 ± 2.57 mm, respectively. The mean length of tendon of SM in third trimester was also longer in male (24.83 ± 3.42 mm) than in female (18.95 ± 2.36 mm), what was significant, p = 0.045. The mean width and thickness of the AT was larger in male than in female in third trimester. The mean width and thickness of the AT in male was 8.26 ± 1.94 mm and 1.46 ± 0.28 mm,

in female 7.38 ± 0.31 mm and 1.33 ± 0.05 mm respectively. However in second trimester the mean width of the AT was larger in female (5.01 ± 1.5 mm) than in male (4.81 ± 1.12 mm). The mean thickness of the AT in second trimester was larger in male (1.07 ± 0.46 mm) than in female (1.01 ± 0.43 mm). In second trimester, the muscle to tendon ratio of the SM was significantly higher in female (2.75 ± 0.76 mm) than in male (2.29 ± 0.77 mm), p = 0.029. The detailed analyses of the performed measurements are presented in Figure 2 and Tables 2 and 3.

DISCUSSION

To best of our knowledge our investigation is the first study to analyse morphometric measurements of the AT in such numerous group of human foetuses, what may be useful as a basic research for future studies concerning the AT. The key result of our study was that there is no significant correlation between sex or side and size of the AT in human foetuses. The only significant correlation was between sex and the length of the tendon of the SM; in third trimester it was longer in male than in female (p = 0.045). In second trimester the SM muscle to tendon ratio was higher in female than in male (p = 0.029).

In order to understand the differences in the structure of such a complex tendon, it is necessary to understand the basics of embryology. In an 11 mm embryo the common flexor mass begins to show signs of differentiation into the muscle rudiments [3, 6]. In a 14 mm embryo the two muscle groups are fairly distinct: a superficial, proximolateral group for the GM SM, and plantaris muscle, and a deep, more medial group for the flexor hallucis longus,

Table 2. Measurements of the Achilles tendon, gastrocnemius muscle (GM) and soleus muscle (SM) in third trimester foetuses

Features (third trimester)	Sex			Body side		
	Male (n = 10)	Female (n = 2)	P	Left (n = 6)	Right (n = 6)	P
GM:						
LH muscle	41.61 ± 5.77	34.81 ± 2.54	0.144	39.57 ± 3.59	41.38 ± 7.85	0.619
LH tendon	49.58 ± 9.44	43.98 ± 6.18	0.449	48 ± 10.36	49.28 ± 8.38	0.818
MH muscle	46.38 ± 6.3	43.12 ± 1.12	0.498	44.12 ± 4.72	47.56 ± 6.78	0.331
MH tendon	44.24 ± 9.75	32.13 ± 3.22	0.124	43.39 ± 10.76	41.05 ± 10.14	0.706
SM:						
Muscle	62.98 ± 13.14	53.57 ± 2.57	0.354	59.68 ± 12.54	63.14 ± 13.31	0.652
Tendon	24.83 ± 3.42	18.95 ± 2.36	0.045	25.2 ± 4.32	22.50 ± 3.26	0.251
Achilles:						
Width	8.26 ± 1.94	7.38 ± 0.31	0.551	7.98 ± 2.06	8.24 ± 1.65	0.817
Thickness	1.46 ± 0.28	1.33 ± 0.05	0.559	1.47 ± 0.29	1.4 ± 0.25	0.639
GM LH to MH muscle	0.9 ± 0.07	0.81 ± 0.08	0.141	0.89 ± 0.04	0.87 ± 0.11	0.559
GM LH muscle to tendon ratio	0.86 ± 0.12	0.80 ± 0.17	0.615	0.85 ± 0.13	0.85 ± 0.14	0.983
GM MH muscle to tendon ratio	1.08 ± 0.18	1.35 ± 0.17	0.075	1.05 ± 0.18	1.19 ± 0.20	0.231
SM muscle to tendon ratio	2.6 ± 0.73	2.86 ± 0.49	0.650	2.42 ± 0.66	2.86 ± 0.69	0.281

LH — lateral head of gastrocnemius; MH — medial head of gastrocnemius

Table 3. Measurements of the Achilles tendon, gastrocnemius muscle (GM) and soleus muscle (SM) in second trimester foetuses

Features (second trimester)	Sex			Body side		
	Male (n = 24)	Female (n = 38)	P	Left (n = 31)	Right (n = 31)	P
GM:						
LH muscle	26.12 ± 4.97	28.07 ± 6.55	0.225	27.04 ± 5.31	27.61 ± 6.75	0.718
LH tendon	27.22 ± 3.86	28.36 ± 4.53	0.318	28.06 ± 4.16	27.80 ± 4.47	0.812
MH muscle	28.35 ± 5.42	30.13 ± 6.22	0.26	29.84 ± 5.37	29.09 ± 6.53	0.625
MH tendon	23.99 ± 3.42	25.48 ± 4.97	0.212	24.86 ± 4.57	24.97 ± 4.46	0.921
SM:						
Muscle	34.77 ± 5.44	37.24 ± 6.61	0.137	36.31 ± 6.30	36.31 ± 6.33	0.999
Tendon	16.3 ± 4.17	14.43 ± 4.19	0.096	14.72 ± 4.02	15.53 ± 4.48	0.465
Achilles:						
Width	4.81 ± 1.12	5.01 ± 1.5	0.586	4.87 ± 1.41	4.99 ± 1.34	0.734
Thickness	1.07 ± 0.46	1.01 ± 0.43	0.622	0.95 ± 0.43	1.11 ± 0.44	0.170
GM LH to MH muscle	0.93 ± 0.15	0.94 ± 0.15	0.891	0.91 ± 0.08	0.96 ± 0.19	0.150
GM LH muscle to tendon ratio	0.96 ± 0.17	1.01 ± 0.29	0.579	0.96 ± 0.15	1.01 ± 0.33	0.489
GM MH muscle to tendon ratio	1.19 ± 0.26	1.21 ± 0.27	0.889	1.22 ± 0.23	1.18 ± 0.29	0.587
SM muscle to tendon ratio	2.29 ± 0.77	2.75 ± 0.76	0.029	2.61 ± 0.7	2.54 ± 0.88	0.734

LH — lateral head of gastrocnemius; MH — medial head of gastrocnemius

flexor digitorum longus and popliteus, and tibialis posterior [3, 6]. The gastrocnemius group is connected with the blastema of the calcaneus and the two long flexor muscles with the flat aponeurotic "footplate" from which tendons extend to the blastema of the digits [3, 6]. The gastrocnemius-soleus group gradually spreads from its original lateral position towards the medial side of the leg to attain the tibial attachment, and the two heads of the GM develop during the second half of the second month, the

medial head attaining its attachment later than the lateral [3, 6]. The plantaris muscle seems to split off at a comparatively late stage from the lateral head of the GM [3, 6].

From an evolutionary point of view, the difference between morphology of the triceps surae in human and the other species is apparent [1]. Humans' bellies of GM are short, their tendon fuse with SM tendon and develop massive AT [1]. In herbivorous apes, the AT is absent or very short, thus their muscles of posterior leg extended to their tarsal bones [12]. Changes in lifestyle, like food supply, forced apes to adapt to this situation and evolve their anatomy [12]. Differences in food intake, correlate with differences in locomotion [1]. Gorillas, orangutans, bonobos and chimpanzees share a wide range of locomotor behaviours such as clambering and orthograde suspension, quadrupedalism, whereas modern humans are primarily bipeds [1, 7]. The longer ATs were observed in early hominis than in apes [12]. The key role in development of the AT was in fast locomotion, e.g. hunting, that is why the AT is more evolutionary advantage in athletes [12].

In Pang and Yings' [22] sonographic study, the cross sectional area of the AT was significantly higher in 50-year-old and older patients than in younger patients. Furthermore, in that study, the cross-sectional area of the AT in the dominant leg was significantly higher than that in the nondominant leg [22]. Also Ying et al. [31] noticed that the thickness of the AT for dominant leg in the both regularly exercise group and the irregularly exercise group, is significantly higher than in the nondominant leg. Moreover, in their study, the mean thickness of the AT in the regularly exercise group was significantly higher in comparison with the irregularly exercise group [31]. Previous studies noted that differences in mechanical properties of the AT between male and female is more correlated with the differences in muscle strength, rather than sex [13]. Probably due to that there were no significant differences in thickness or width of the AT between sexes or body sides in our research; the use of muscle in foetuses is minimal.

The medial head of the GM dominate in size and power over lateral head [5, 25]. This superiority of medial belly was also visible in our measurements. Kearns et al. [10] examined soccer players and compared them with moderate active and untrained college students. The thickness of the medial head of the GM of the dominant leg was significantly larger

in the soccer players than in others [10]. However, in our study, there was no positive correlation between muscle size and body side or sex. It might be also the result of the low muscle load in human foetuses.

Although the AT is the most powerful tendon in human body [9, 14, 23], it is very vulnerable to injuries [12, 28]. The "Achilles tendinitis" has formerly been used for describing any pain in the posterior region; however, nowadays vocabulary of disorders in this region of leg is more miscellaneous and precise [26]. We can differentiate inflammation of the AT with its adjacent structures, such as: paratenonitis, tendonitis and bursitis [18, 26, 29, 30]. Tendinosis, that is another AT disorder, is a noninflammatory process caused by fatty or mucinoid degeneration with a disorganisation in collagen structure [4, 26]. Ball or racquet sports or other athletic activity has been noted as a cause of the AT rupture up to 80% of cases [26, 27]. The high proneness of the AT, despite its enlargement, may raise us a question, what is the future of the AT? How thick, long and wide it will be in our descendants? Will it endure in its shape?

The present study does have some limitations. First of all, no sample size calculation was performed. Moreover, the abundance of group according to sex was not equal. However, the number of the human foetuses in our research was larger in comparison with previous studies.

CONCLUSIONS

There was no significant correlation between sex or side and size of the AT in human foetuses, probably due to scant muscle load during prenatal period. However, we still do not know how important is genetics and environment regarding the aetiopathology of the disorders of the AT. The vulnerability of the AT to injuries should motivate our efforts in carrying out research to better understand its complicated pathology and increase the effectiveness of its treatments.

Conflict of interest: None declared

REFERENCES

1. Aerts P, D'Août K, Thorpe S, et al. The gibbon's Achilles tendon revisited: consequences for the evolution of the great apes? Proc Biol Sci. 2018; 285(1880), doi: 10.1098/rspb.2018.0859, indexed in Pubmed: 29899076.
2. Ballal MS, Walker CR, Molloy AP. The anatomical footprint of the Achilles tendon: a cadaveric study. Bone Joint J. 2014; 96-B(10): 1344–1348, doi: 10.1302/0301-620X.96B10.33771, indexed in Pubmed: 25274919.

3. Boyle E, Mahon V, Diogo R. Muscles lost in our adult primate ancestors still imprint in us: on muscle evolution, development, variations, and pathologies. Curr Mol Biol Rep. 2020; 6(2): 32–50, doi: 10.1007/s40610-020-00128-x.

4. Calleja M, Connell DA. The Achilles tendon. Semin Musculoskelet Radiol. 2010; 14(3): 307–322, doi: 10.1055/s-0030-1254520, indexed in Pubmed: 20539956.

5. Dayton P. Anatomic, vascular, and mechanical overview of the achilles tendon. Clin Podiatr Med Surg. 2017; 34(2): 107–113, doi: 10.1016/j.cpm.2016.10.002, indexed in Pubmed: 28257668.

6. Diogo R, Siomava N, Gitton Y. Development of human limb muscles based on whole-mount immunostaining and the links between ontogeny and evolution. Development. 2019; 146(20), doi: 10.1242/dev.180349, indexed in Pubmed: 31575609.

7. Ferrero EM, Pastor JF, De Paz FF. Primates: Classification, Evolution and Behavior. In: Hughes E, Hill M (eds). Nova Science Publishers 2012: 1–70.

8. Gourdine-Shaw MC, Lamm BM, Herzenberg JE, et al. Equinus deformity in the pediatric patient: causes, evaluation, and management. Clin Podiatr Med Surg. 2010; 27(1): 25–42, doi: 10.1016/j.cpm.2009.10.003, indexed in Pubmed: 19963168.

9. Järvinen TAH, Kannus P, Maffulli N, et al. Achilles tendon disorders: etiology and epidemiology. Foot Ankle Clin. 2005; 10(2): 255–266, doi: 10.1016/j.fcl.2005.01.013, indexed in Pubmed: 15922917.

10. Kearns CF, Isokawa M, Abe T. Architectural characteristics of dominant leg muscles in junior soccer players. Eur J Appl Physiol. 2001; 85(3-4): 240–243, doi: 10.1007/s004210100468, indexed in Pubmed: 11560076.

11. Latiff S, Bidmos MA, Olateju OI. Morphometric profile of tendocalcaneus of South Africans of European ancestry using a cadaveric approach. Folia Morphol. 2021; 80(1): 196–203, doi: 10.5603/FM.a2020.0026, indexed in Pubmed: 32159844.

12. Malvankar S, Khan WS. Evolution of the Achilles tendon: The athlete's Achilles heel? Foot (Edinb). 2011; 21(4): 193–197, doi: 10.1016/j.foot.2011.08.004, indexed in Pubmed: 21900004.

13. Muraoka T, Muramatsu T, Fukunaga T, et al. Elastic properties of human Achilles tendon are correlated to muscle strength. J Appl Physiol (1985). 2005; 99(2): 665–669, doi: 10.1152/japplphysiol.00624.2004, indexed in Pubmed: 15790689.

14. O'Brien M. The anatomy of the Achilles tendon. Foot Ankle Clin. 2005; 10(2): 225–238, doi: 10.1016/j.fcl.2005.01.011, indexed in Pubmed: 15922915.

15. Olewnik Ł, Gonera B, Kurtys K, et al. A proposal for a new classification of the fibular (lateral) collateral ligament based on morphological variations. Ann Anat. 2019; 222: 1–11, doi: 10.1016/j.aanat.2018.10.009, indexed in Pubmed: 30408521.

16. Olewnik Ł, Karauda P, Gonera B, et al. Intramuscular innervation of plantaris muscle evaluated using a modified Sihler's staining protocol - Proposal for a new classification. Ann Anat. 2020; 230: 151504, doi: 10.1016/j.aanat.2020.151504, indexed in Pubmed: 32173561.

17. Olewnik Ł, Kurtys K, Gonera B, et al. Proposal for a new classification of plantaris muscle origin and its potential effect on the knee joint. Ann Anat. 2020; 231: 151506, doi: 10.1016/j.aanat.2020.151506, indexed in Pubmed: 32173563.

18. Olewnik Ł, Wysiadecki G, Podgórski M, et al. The plantaris muscle tendon and its relationship with the Achilles tendinopathy. Biomed Res Int. 2018; 2018: 9623579, doi: 10.1155/2018/9623579, indexed in Pubmed: 29955614.

19. Olewnik Ł, Wysiadecki G, Polguj M, et al. Anatomic study suggests that the morphology of the plantaris tendon may be related to Achilles tendonitis. Surg Radiol Anat. 2017; 39(1): 69–75, doi: 10.1007/s00276-016-1682-1, indexed in Pubmed: 27155667.

20. Olewnik Ł, Zielinska N, Karauda P, et al. A three-headed plantaris muscle: evidence that the plantaris is not a vestigial muscle? Surg Radiol Anat. 2020; 42(10): 1189–1193, doi: 10.1007/s00276-020-02478-8, indexed in Pubmed: 32382814.

21. Olewnik Ł, Zielinska N, Paulsen F, et al. A proposal for a new classification of soleus muscle morphology. Ann Anat. 2020; 232: 151584, doi: 10.1016/j.aanat.2020.151584, indexed in Pubmed: 32810614.

22. Pang BSF, Ying M. Sonographic measurement of achilles tendons in asymptomatic subjects: variation with age, body height, and dominance of ankle. J Ultrasound Med. 2006; 25(10): 1291–1296, doi: 10.7863/jum.2006.25.10.1291, indexed in Pubmed: 16998101.

23. Park SY, Khemani D, Nelson AD, et al. Rectal gas volume measured by computerized tomography identifies evacuation disorders in patients with constipation. Clin Gastroenterol Hepatol. 2017; 15(4): 543–552.e4, doi: 10.1016/j.cgh.2016.11.013, indexed in Pubmed: 27856363.

24. Patel NN, Labib SA. The achilles tendon in healthy subjects: an anthropometric and ultrasound mapping study. J Foot Ankle Surg. 2018; 57(2): 285–288, doi: 10.1053/j.jfas.2017.10.005, indexed in Pubmed: 29275904.

25. Pichler W, Tesch NP, Grechenig W, et al. Anatomic variations of the musculotendinous junction of the soleus muscle and its clinical implications. Clin Anat. 2007; 20(4): 444–447, doi: 10.1002/ca.20421, indexed in Pubmed: 17022026.

26. Schepsis AA, Jones H, Haas AL. Achilles tendon disorders in athletes. Am J Sports Med. 2002; 30(2): 287–305, doi: 10.1177/03635465020300022501, indexed in Pubmed: 11912103.

27. Soroceanu A, Sidhwa F, Aarabi S, et al. Surgical versus nonsurgical treatment of acute Achilles tendon rupture: a meta-analysis of randomized trials. J Bone Joint Surg Am. 2012; 94(23): 2136–2143, doi: 10.2106/JBJS.K.00917, indexed in Pubmed: 23224384.

28. Szaro P, Witkowski G, Smigielski R, et al. Fascicles of the adult human Achilles tendon — an anatomical study. Ann Anat. 2009; 191(6): 586–593, doi: 10.1016/j.aanat.2009.07.006, indexed in Pubmed: 19734029.

29. van Dijk CN, van Sterkenburg MN, Wiegerinck JI, et al. Terminology for Achilles tendon related disorders. Knee Surg Sports Traumatol Arthrosc. 2011; 19(5): 835–841, doi: 10.1007/s00167-010-1374-z, indexed in Pubmed: 21222102.

30. Weinfeld SB. Achilles tendon disorders. Med Clin North Am. 2014; 98(2): 331–338, doi: 10.1016/j.mcna.2013.11.005, indexed in Pubmed: 24559878.

31. Ying M, Yeung E, Li B, et al. Sonographic evaluation of the size of achilles tendon: the effect of exercise and dominance of the ankle. Ultrasound Med Biol. 2003; 29(5): 637–642, doi: 10.1016/s0301-5629(03)00008-5.

Prevalence and distribution of triticeal cartilage

E. Emre, R.F. Akkoc, M. Ogeturk

Department of Anatomy, Faculty of Medicine, Firat University, Elazig, Turkey

Background: The triticeal cartilage can be found in the lateral thyrohyoid ligament. The triticeal cartilage may exist in different shapes and locations, may be present unilaterally or bilaterally, or absent. The study aims to determine the prevalence, distribution, level, shape, and the degree of ossification of the triticeal cartilage by using three-dimensional computed tomography angiography (CTA).

Materials and methods: Computed tomography angiography images of 1450 patients (785 women and 665 men), obtained in the period from 1 January 2017 to 30 September 2019, were evaluated retrospectively. Any unilateral or bilateral presence or the absence of triticeal cartilage was recorded with its anatomical level, shape, and degree of ossification.

Results: At least one triticeal cartilage was found in the CTA images of 57.4% (833 out of 1450) patients. The prevalence was 51.3% in women (403 out of 785) and 64.7% in men (430 out of 665). Bilateral triticeal cartilages were more common compared to unilateral ones. Ossification was most commonly mild at a rate of 39.1%. A round-shaped triticeal cartilage was the most common form at a rate of 46.6%. Triticeal cartilage was detected at various intervertebral disc levels from the second and third cervical vertebrae to the level of the sixth cervical vertebra.

Conclusions: Triticeal cartilage is common in the Turkish population and it should receive substantial attention from clinicians because it can be confused with calcified plaques and fractures of the superior horn of the thyroid cartilage. Therefore, for appropriate diagnoses and treatment, it is important to know the prevalence of triticeal cartilage with its distribution, intervertebral disc levels of location, shapes, and ossification degrees. (Folia Morphol 2022; 81, 1: 150–156)

Key words: triticeal cartilage, computed tomography angiography, thyrohyoid complex, triticeal ossification

INTRODUCTION

Triticeal cartilage (TC) is a type of cartilage that can be found in the lateral thyrohyoid ligament. TC may exist unilaterally or bilaterally or may be absent [1, 3, 5, 11]. TC can be found at the level of the third and fourth cervical vertebrae which is in line with the carotid bifurcation, usually between the superior horn of the thyroid cartilage and the tip of the greater horn of the hyoid bone. TC is observed in the shape of wheat grain. The function of TC is yet to be established; however, some researchers suggest that TC strengthens the lateral thyrohyoid ligament [1, 3]. The theory of Wilson et al. [12] suggests that TC has no function in humans (Fig. 1).

Triticeal cartilage is composed of hyaline cartilage [7, 12]. As other laryngeal cartilages, TC tends to ossify, too. An ossified TC may be mistaken for calcified plaques in the carotid artery in panoramic radiogra-

Address for correspondence: Dr. M. Ogeturk, Department of Anatomy, Faculty of Medicine, Firat University, Elazig, Turkey,
e-mail: mgeturk@gmail.com
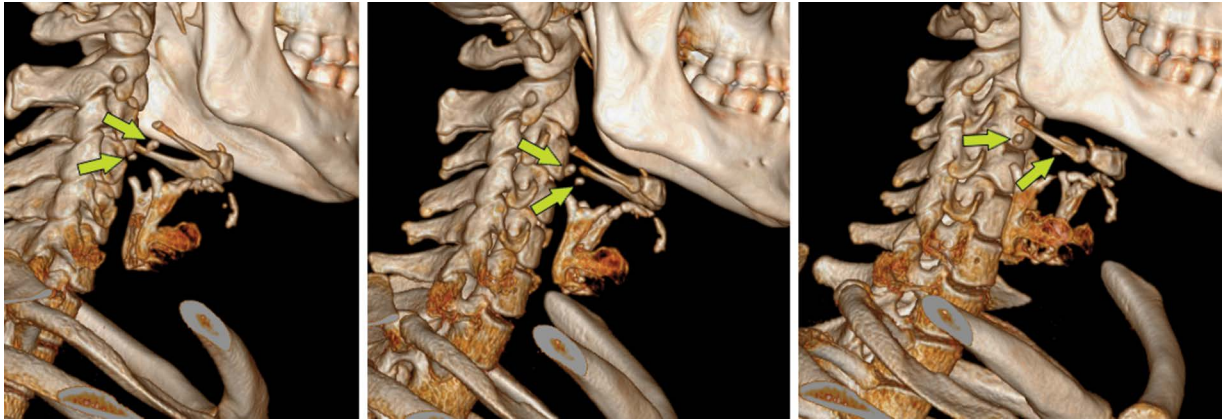
Figure 1. Three-dimensional reconstruction of computed tomographic angiography images. Yellow arrow demonstrates triticeous cartilage.

phy and computed tomography images, especially for calcified plaques at the carotid bifurcation level [1, 8, 10]. Furthermore, an ossified TC has been reported to be mistaken for the fractures of the superior horn of the thyroid cartilage [6]. An enlarged and ossified TC has been reported to cause dysphagia and odynophagia and to become symptomatic after endotracheal intubation [4]. Additionally, an enlarged TC has been reported to cause clinical symptoms similar to those of a foreign body [9].

To the best of our knowledge, there are no studies in the literature reporting the prevalence and distribution of TC by the level of location and gender. Therefore, the aim of this study has been to determine the frequency, distribution, location levels, shape, and the degree of ossification of TC and to reveal gender differences.

MATERIALS AND METHODS

Computed tomography angiography (CTA) images obtained in the period between 1 January 2017 and 30 September 2019 from 1643 individuals, who were 25 years old or older, were examined in the study. The CTA images of individuals who had pathological structures in the neck area and who underwent surgical interventions of the larynx or the CTA images with poor image quality were not included in the evaluation. The present study included 785 women and 665 men, making up 1450 individuals in total. The CTA images of these individuals were retrospectively evaluated. The age range of the individuals whose CTA images were evaluated was from 25 to 97 (mean ± ± standard deviation [SD] 63 ± 14) years.

The analyses of the CTA images, the degree of ossification, and the distribution of the shapes of TC were determined based on the study of Alqahtani et al. [3].

The calcification extent of TC was determined according to the study of Alqahtani et al. [3] and by comparing the calcification of TC to the density of the surrounding bone tissues in the CTA images. The calcification extent of TC was consulted by an experienced radiology specialist. Additionally, utilising the software used during the evaluation of angiography images, the exposure degrees of the images were adjusted. Thus, each image was evaluated using equivalent exposures.

In the CTA images, the unilateral or bilateral presence or the absence of TC, and the intervertebral disc levels of TC location were evaluated. The evaluations were performed independently by two researchers. Then, the data were compared accordingly. When an agreement could not be made, a third researcher evaluated the images again independently. The data were accepted valid when two researchers reached an agreement.

Statistical analysis

The statistical analyses were performed with the SPSS statistical package, version 22.0 (SPSS Inc., Chicago, IL, USA). The categorical values were summarised as numbers and percentages. The χ^2 test was used for comparing the categorical data between the groups. The level of statistical significance in all tests was accepted as $p < 0.05$.

RESULTS

The presence of at least one TC was found at rates of 51.3% in women (403 in 785), 64.7% in men (430 in 665), and 57.4% in the total study population (833

Table 1. Incidence of triticeal cartilage

Cartilago triticea	Women	Men	All subjects
None	382 (48.6%)	235 (35.3%)	617 (42.6)
Unilateral:			
Right	65 (8.3%)	53 (8)	118 (8.1)
Left	87 (11.1%)	68 (10.2)	155 (10.7)
Bilateral	251 (32%)	309 (46.5%)	560 (38.6)
Total	785 (100%)	665 (100%)	1450 (100%)

in 1450). The incidence of TC in the overall population and by gender has been presented in Table 1. Presence of TC in individual decades of life, broken down by gender, has been presented in Table 2. There was not statistically significant difference between the age groups and the incidence of TC in women, men, and regardless of gender.

Examination of the degree of ossification of TC revealed mild ossification in 39.1% of the study population and it was found out to be the most commonly seen ossification type. The least common type of ossification was the apparent ossification at a rate of 15.5%. The ossification degrees in the overall study population and distribution by gender have been presented in Table 3. While there was not a statistically significant relationship between the age groups and the degree of ossification (p > 0.05), a significant relationship was found between the ossification degrees and gender (p < 0.05). TC in women was more intensely ossified compared to men (Table 3). The degrees of ossification of TC have been shown in Figure 2.

A rounded TC was the most common form at a ratio of 40.6% and a spindle-shaped TC was the rarest form at a rate of 2.2% (Table 4). The shapes

of TC observed in the sagittal CTA images have been shown in Figure 3.

The fourth cervical vertebra was the most common level of TC location at a rate of 42.1% and the least common location level was the sixth cervical vertebra at a rate of 0.2% (Table 5). In the lateral thyrohyoid ligament, TC was detected at different intervertebral disc levels (Fig. 4).

DISCUSSION

Knowing the presence, structure (ossified or cartilage structure), and location levels of TC may be important for making a differential diagnosis across calcified arterial plaques, fractures of the superior horn of thyroid cartilage, and calcified soft tissue abnormalities. We think that such information will provide beneficial tools to clinicians when they examine the radiological images of the neck region. In the present study, the CTA images of the eligible individuals were retrospectively reviewed for the incidence, distribution, shapes, the intervertebral disc levels of location, and ossification degrees of TC. As a differentiation point, this study has been conducted on the CTA images from 1450 individuals, which is the largest population ever reported by similar studies in the literature.

Studies report the incidence of TC in the range from 13.5% to 68.1% as found in cadavers, autopsy cases, and CTA images from various populations [2, 3, 8, 11, 12]. The results of the present study are within this range and close to the upper limit. The studies reporting the incidence of ossification of TC on panoramic radiographs [1, 5] were not included in the evaluation because they neither reflected the prevalence of ossified TC nor the precise prevalence.

Table 2. Incidence of triticeal cartilage (TC) in age groups

Age groups [years]	Women		Men		All subjects	
	N	Subjects with TC (%)	N	Subjects with TC (%)	N	Subjects with TC (%)
25–34	31	16 (51.6%)	17	8 (47.1%)	48	24 (50%)
35–44	78	39 (50%)	48	34 (70.8%)	126	73 (57.9%)
45–54	149	77 (51.77%)	91	55 (60.4%)	240	132 (55%)
55–64	198	103 (52%)	158	108 (68.4%)	356	211 (59.3%)
65–74	190	100 (52.6%)	203	132 (65%)	393	232 (59%)
75–84	121	60 (49.6%)	122	74 (60.7%)	243	134 (55.1%)
≥ 85	18	8 (44.4%)	26	19 (73.1%)	44	27 (61.4%)
P		P = 0.994		P = 0.377		P = 0.760

Table 3. Ossification degrees of triticeal cartilage

	Ossification degrees				
	Cartilago triticea	**Mild triticeal ossification**	**Moderate triticeal ossification**	**Apparent triticeal ossification**	**Total**
Women:					
Right	57 (18%)	88 (27.9%)	100 (31.6%)	71 (22.5%)	316 (100%)
Left	45 (13.3%)	121 (35.8%)	91 (26.9%)	81 (24%)	338 (100%)
Total	102 (15.6%)	209 (32%)	191 (29.2%)	152 (23.2%)	654 (100%)
Men:					
Right	107 (29.6%)	167 (46.1%)	54 (14.9%)	34 (9.4%)	362 (100%)
Left	117 (31%)	169 (44.8%)	61 (16.2%)	30 (8%)	377 (100%)
Total	224 (30.3%)	336 (45.5%)	115 (15.6%)	64 (8.6%)	739 (100%)
All subjects:					
Right	164 (24.2%)	255 (37.6%)	154 (22.7%)	105 (15.5%)	678 (100%)
Left	162 (22.8%)	290 (40.5%)	152 (21.2%)	111 (15.5%)	715 (100%)
Total	326 (23.4%)	545 (39.1%)	306 (22%)	216 (15.5%)	1393 (100%)

Figure 2. Sagittal (**A**, **C**, **E**, **G**) and axial (**B**, **D**, **F**, **H**) planes showing a variety of ossification intensities in cartilago triticea in the computed tomography angiography images. Arrows demonstrates cartilago triticea (**A**, **B**), mild triticeal ossification (**C**, **D**), moderate triticeal ossification (**E**, **F**), apparent triticeal ossification (**G**, **H**).

The incidence of having bilateral TC was reported to be higher than having a unilateral one in many studies investigating the incidence and distribution [3, 5, 6, 8, 11]. This finding is consistent with the results of the present study. On the other hand, Wilson et al. [12] reported in their study on cadavers that the incidence of unilateral TC was higher than the incidence of bilateral TC.

Our findings, suggesting that the prevalence of TC is significantly higher in men than in women, support the results reported by previous studies [3, 6, 11]. However, Wilson et al. [12] reported that the prevalence of TC was not significantly different between the genders.

As reported in previous studies, no correlations were found between the degrees of ossification of TC and the age [3, 11]. In this study, a 28-year-old man was observed having a markedly ossified TC, whereas a 91-year-old woman was found to have an unossified bilateral TC.

153

Table 4. Distribution of triticeal cartilage by shape

	Shape							
	Round	**Oval**	**Spindle**	**Elongated**	**Rectangular**	**Teardrop**	**Triangular**	**Total**
Women:								
Right	165 (52.2%)	108 (34.2%)	8 (2.5%)	7 (2.2%)	4 (1.3%)	19 (6%)	5 (1.6%)	316 (100%)
Left	166 (49.1%)	115 (34%)	13 (3.8%)	9 (2.7%)	8 (2.4%)	19 (5.6%)	8 (2.4%)	338 (100%)
Total	331 (50.6%)	223 (34.1%)	21 (3.2%)	16 (2.4%)	12 (1.9%)	38 (5.8%)	13 (2%)	654 (100%)
Men:								
Right	113 (31.2%)	153 (42.3%)	5 (1.3%)	39 (10.8%)	13 (3.6%)	14 (3.9%)	25 (6.9%)	362 (100%)
Left	121 (32.1%)	134 (35.5%)	5 (1.3%)	43 (11.4%)	12 (3.2%)	42 (11.2%)	20 (5.3%)	377 (100%)
Total	234 (31.7%)	287 (38.8%)	10 (1.3%)	82 (11.1%)	25 (3.4%)	56 (7.6%)	45 (6.1%)	739 (100%)
All subjects:								
Right	278 (41.0%)	261 (38.5%)	13 (1.9%)	46 (6.8%)	17 (2.5%)	33 (4.9%)	30 (4.4%)	678 (100%)
Left	287 (40.2%)	249 (34.8%)	18 (2.5%)	52 (7.3%)	20 (2.8%)	61 (8.5%)	28 (3.9%)	715 (100%)
Total	565 (40.6%)	510 (36.6%)	31 (2.2%)	98 (7%)	37 (2.7%)	94 (6.7%)	58 (4.2%)	1393 (100%)
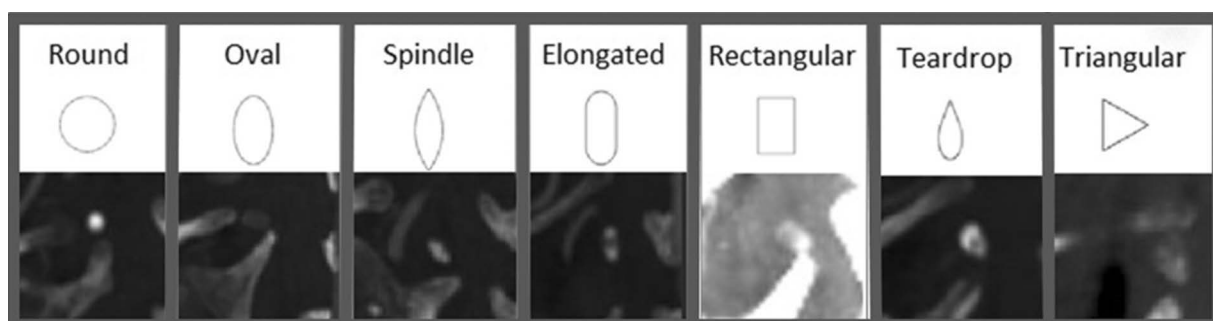
Figure 3. Various shapes of cartilago triticea in sagittal computed tomography angiography images.

Table 5. Triticeal cartilage's distribution by the level of location

	Level								
	C 2–3	**C 3**	**C 3–4**	**C 4**	**C 4–5**	**C 5**	**C 5–6**	**C 6**	**Total**
Women:									
Right	3 (0.9%)	65 (20.6%)	71 (22.5%)	134 (42.4%)	34 (10.8%)	9 (2.8%)	–	–	316 (100%)
Left	5 (1.5%)	70 (20.7%)	83 (24.6%)	134 (39.6%)	35 (10.4%)	11 (3.2%)	–	–	338 (100%)
Total	8 (1.2%)	135 (20.6%)	154 (23.5%)	268 (41%)	69 (10.6%)	20 (3.1%)	–	–	654 (100%)
Men:									
Right	–	31 (8.6%)	83 (22.9%)	154 (42.6%)	68 (18.8%)	20 (5.5%)	3 (0.8%)	3 (0.8%)	362 (100%)
Left	2 (0.5%)	33 (8.7%)	93 (24.7%)	165 (43.8%)	61 (16.2%)	21 (5.6%)	2 (0.5%)	–	377 (100%)
Total	2 (0.3%)	64 (8.7%)	176 (23.8%)	319 (43.2%)	129 (17.4%)	41 (5.5%)	5 (0.7%)	3 (0.4%)	739 (100%)
All subjects:									
Right	3 (0.4%)	96 (14.2%)	154 (22.7%)	288 (42.5%)	102 (15.1%)	29 (4.3%)	3 (0.4%)	3 (0.4%)	678 (100%)
Left	7 (1%)	103 (14.4%)	176 (24.6%)	299 (41.8%)	96 (13.4%)	32 (4.5%)	2 (0.3%)	–	715 (100%)
Total	10 (0.7%)	199 (14.3%)	330 (23.7%)	587 (42.1%)	198 (14.2%)	61 (4.4%)	5 (0.4%)	3 (0.2%)	1393 (100%)
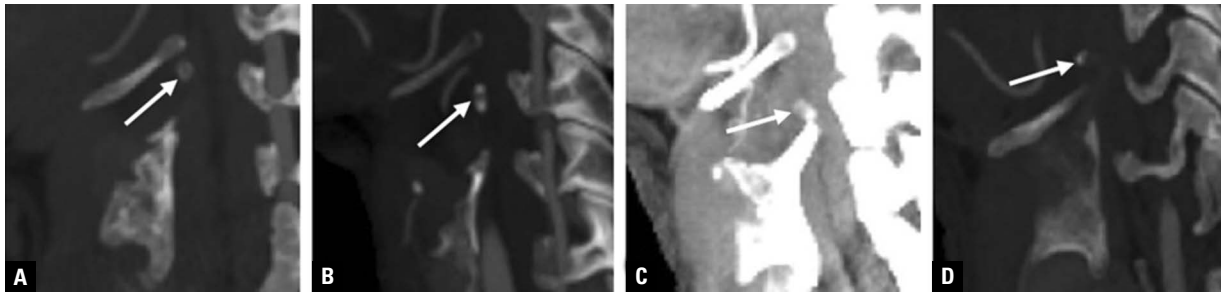
Figure 4. Arrows demonstrates the triticeal cartilage is seen in the upper (**A**), middle (**B**) and lower (**C**) positions as well as being observed at atypical sites (e.g. above cornu majus; **D**) in the lateral thyrohyoid ligament.

A study on CTA images conducted by Alqahtani et al. [3] reported that mild ossification of TC was the most common form of ossification, while the least common form of ossification was apparent ossification. Alqahtani et al. [3] reported that they determined less intense degrees of ossification in men and more pronounced ossification in women. This result is consistent with the findings of our study. However, another study on CTA images conducted by Vatansever et al. [11] from our country found that mild ossification of TC was the least common and that the apparent ossification was the most common. Furthermore, Vatansever et al. [11] reported that there was not a relationship between ossification and gender.

Alqahtani et al. [3] evaluated shapes of TC in CTA images and reported that TC was found in various shapes including round, oval, spindle, elongated, rectangular, teardrop, and triangular forms. The study conducted by Vatansever et al. [11] reported that the oval shape of TC was the most common at a rate of 42.5% and the teardrop shape was the least common at a rate of 2.8%. In the present study, the oval-shaped TC was the most common form after the round shape at a rate of 36.6%. The teardrop shape of TC was determined as the least common form at a rate of 6.7% after the spindle and triangular-shaped ones.

Triticeal cartilage is not found on the same axis and plane even in people with bilateral TC. It may be located in different places within the thyrohyoid ligament. Moreover, TC has been reported to be observed at higher levels than the location of the greater horn of the hyoid bone in some people [3]. Such findings are consistent with our results. Furthermore, there are several reports stating that TC is usually located at the level of the third or fourth cervical vertebrae [1, 3, 12]. Similar to such reports, in our study, 80.1% of TC was found at the level of the third and fourth

cervical vertebrae. To the best of our knowledge, no prevalence studies about the intervertebral disc level location of TC have been conducted and reported in the literature. This is the first study, reporting the prevalence and distribution of TC according to the level of location by gender and in the total population regardless of gender (Table 5).

The prevalence and morphology of TC vary from one population to another [2, 3, 8, 11, 12]. Although this study was conducted in a large population, it is limited to the geographical structure of the population and some ethnic features might have been reflected in the prevalence rates. Indeed, some differences are observed between the results of the present study and the first study from Turkey. We believe that these differences might have occurred because the present study included CTA images of individuals from overall Turkey, whereas, the first study in the literature evaluated CTA images of individuals from only one geographical region of Turkey [11].

CONCLUSIONS

When CTA and panoramic radiographic images are examined, clinicians should always note that TC can be mistaken for calcified plaques in the carotid artery and the fractures of the superior horn of the thyroid cartilage. Furthermore, care should be exercised in identifying this anatomical structure because the presence of an enlarged and ossified TC is associated with dysphagia, odynophagia, and clinical symptoms of foreign bodies in the respective location. Establishing the prevalence, distribution, intervertebral disc levels of location, various possible shapes, and ossification degrees of TC is critical to make an accurate diagnosis and conduct a proper treatment.

Conflict of interest: None declared

REFERENCES

1. Ahmad M, Madden R, Perez L. Triticeous cartilage: prevalence on panoramic radiographs and diagnostic criteria. Oral Surg Oral Med Oral Pathol Oral Radiol Endod. 2005; 99(2): 225–230, doi: 10.1016/j.tripleo.2004.06.069, indexed in Pubmed: 15660097.

2. Ajmani ML. A metrical study of the laryngeal skeleton in adult Nigerians. J Anat. 1990; 171: 187–191, indexed in Pubmed: 2081705.

3. Alqahtani E, Marrero DE, Champion WL, et al. Triticeous cartilage CT imaging characteristics, prevalence, extent, and distribution of ossification. Otolaryngol Head Neck Surg. 2016; 154(1): 131–137, doi: 10.1177/0194599815615350, indexed in Pubmed: 26556461.

4. Alsarraf R, Mathison S, Futran N. Symptomatic presentation of an enlarged, ossified triticeal cartilage. Am J Otolaryngol. 1998; 19(5): 339–341, doi: 10.1016/s0196-0709(98)90010-2, indexed in Pubmed: 9758185.

5. Aoun G, Nasseh I. Calcified triticeous cartilage detected on digital panoramic radiographs in a sample of lebanese population. J Clin Imaging Sci. 2018; 8: 16, doi: 10.4103/jcis.JCIS_11_18, indexed in Pubmed: 29770264.

6. Di Nunno N, Lombardo S, Costantinides F, et al. Anomalies and alterations of the hyoid-larynx complex in forensic radiographic studies. Am J Forensic Med Pathol. 2004; 25(1): 14–19, doi: 10.1097/01.paf.0000113931.49721.e4, indexed in Pubmed: 15075682.

7. Flynn W, Vickerton P. Anatomy, head and neck, larynx cartilage. StatPearls Publishing, Treasure Island (FL) 2020.

8. Joshi MM, Joshi SD, Joshi SS. Prevalence and variations of cartilago triticea. Int J Anat Res. 2014; 2: 474–477.

9. Mesa MM, Villarreal SM. Symptomatic presentation of calcified triticeal cartilage. Acta Otorrinolaringol Esp. 2009; 60(1): 75–76, doi: 10.1016/s2173-5735(09)70104-8.

10. Tamura T, Inui M, Nakase M, et al. Clinicostatistical study of carotid calcification on panoramic radiographs. Oral Dis. 2005; 11(5): 314–317, doi: 10.1111/j.1601-0825.2005.01125.x, indexed in Pubmed: 16120119.

11. Vatansever A, Demiryürek D, Tatar I, et al. The triticeous cartilage — redefining of morphology, prevalence and function. Folia Morphol. 2018; 77(4): 758–763, doi: 10.5603/FM.a2018.0034, indexed in Pubmed: 29611161.

12. Wilson I, Stevens J, Gnananandan J, et al. Triticeal cartilage: the forgotten cartilage. Surg Radiol Anat. 2017; 39(10): 1135–1141, doi: 10.1007/s00276-017-1841-z, indexed in Pubmed: 28314939.

ORIGINAL ARTICLE

Macroanatomical and morphometric study on the skull bones of Aksaray Malakli dogs

R. İlgün[1], Z. Özüdoğru[1], O. Karabulut[2], M. Can[3]

[1]Department of Anatomy, Faculty of Veterinary Medicine, Aksaray University, Aksaray, Turkey
[2]Department of Biometrics, Faculty of Veterinary Medicine, Aksaray University, Aksaray, Turkey
[3]Department of Anatomy, Faculty of Veterinary Medicine, Balıkesir University, Balıkesir, Turkey

Background: The skull is an important anatomical structure to discern dog breeds and wolves from dogs. For this purpose, skull morphology and some morphometric measurements of Malakli dogs, a local breed in the Aksaray region, were examined.
Materials and methods: Thirty-two distances were measured and seven ratios calculated in nine skulls of adult dogs. In our study, different morphological features and statistical findings that were not revealed by taking measurements from 32 distinct anatomical points of Aksaray Malakli dog skull bones were determined in accordance with the literature.
Results: Processus zygomaticus was found to be long and pointed in the Aksaray Malakli dogs. The results of morphometric analysis were as follows: facial index value 107.68 ± 4.98, nasal index value 19.61 ± 3.25, cranial index value 56.17 ± ± 2.52, basal index value 30.57 ± 1.30, skull index 54.68 ± 3.01, palatal index I value 56.76 ± 1.89 and palatal index II value 59.83 ± 2.23.
Conclusions: It can be concluded form the present investigation that the neurocranium length, facial index, cranial index, basal index, skull index, and palatal index values were statistically different from other dog breeds. (Folia Morphol 2022; 81, 1: 157–163)

Key words: neuroanatomy, macroanatomy, morphometric, cranial index

INTRODUCTION

Aksaray Malakli dogs are large guarding dogs and their name comes from the Aksaray region in Turkey where they come from. According to the findings in the genetic studies on dog breeds, it is reported that mastiff-type dogs may be a different breed due to their genetic similarity to Akbaş, Kars and Kangal shepherd dogs [2–4]. Aksaray Malakli dog has a grey-coloured, large body and drooping lips. The paws are bigger and thicker than the Kangal dog, which breeders mostly compare. However, it is reported that Aksaray Malakli dog is not preferred in herd management, because it is not resistant to cold climate and because of the saggy nature of its lips; it drains the mouth, salivates while drinking water and it is tired quickly after guarding the herd [2, 3, 5, 18, 26, 27]. The skull is an important anatomical structure to discern dog breeds [1, 9, 11, 12, 28], Kangal and Malakli dogs [10, 18, 21], Tarsus Çatalburun dog [17], German wolfdog [19, 20], and grey wolf [14]. It has been found that there are many studies on skull morphology and morphometry in lynx [7], red fox [22], vulpes [25] and golden jackal [15]. In our study, the measurements taken from 32 anatomical points of

Address for correspondence: R. İlgün, PhD, Department of Anatomy, Faculty of Veterinary Medicine, Aksaray University, Aksaray, Turkey, Postal code: 68100, tel: +903822882863, e-mail: rilgun1980@hotmail.com; rilgun2017@gmail.com
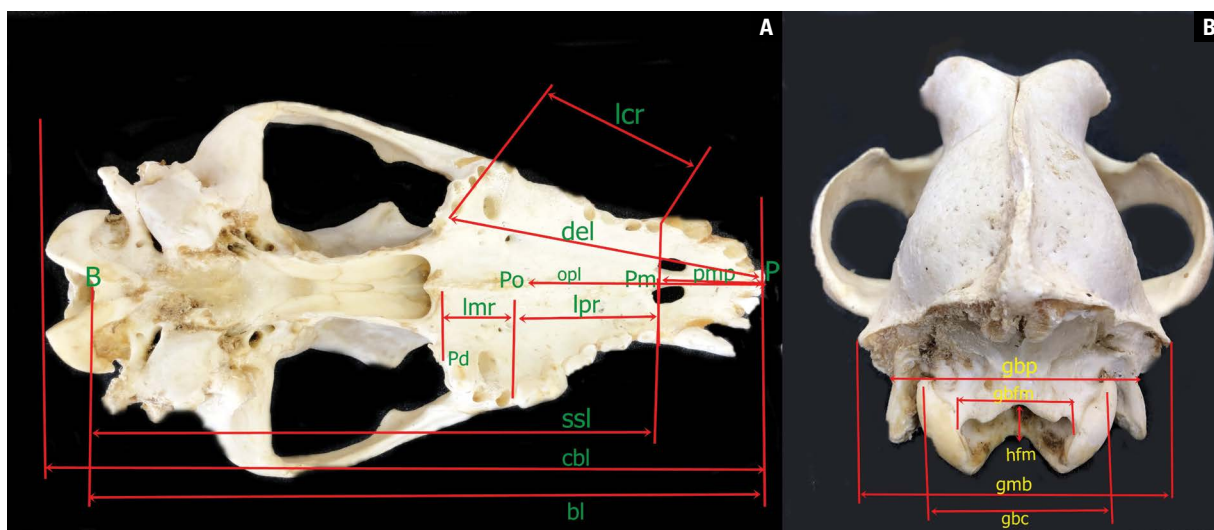
Figure 1. Measurements of the skull of Aksaray Malakli dog; **A.** Ventral view; **B.** Caudal view; Akmlk — Aksaray Malakli dog; pl — profile length; cbl — condylobasal length; bl — basal length; ssl — short skull length; pmp — premolare–prosthion; nl — neurocranium length; vl — viscerocranium length; mfl — median frontal length; unl — upper neurocranium length; fcl — facial length; ais — akrokranion-infraorbitale of one side; gll — greatest length of the lacrimal; gln — greatest length of the nasals; slfl — short lateral facial length; fabo — from the aboral border of one occipital condyle to the infraorbitale of the same side; del — dental length; opl — oral palatal length; llp — lateral length of the premaxilla; lcr — length of the cheektooth row (measured along the alveoli); lmr — length of the molar row (measured along the alveoli on the buccal side); lpr — length of the premolar row (measured along the alveoli on the buccal side); giho — greatest inner height of the orbit; gmb — greatest mastoid breadth; gbc — greatest breadth of the occipital condyles; gbp — greatest breadth at the bases of the paraoccipital processes; gbfm — greatest breadth of the foramen magnum; hfm — height of the foramen magnum; gncb — greatest neurocranium breadth; lbbo — least breadth between the orbits; gbap — greatest breadth across the premaxillae; infl — distance between two infraorbitals; grpb — greatest palatal breadth.

Aksaray Malakli dog skull bones were compared with other dog breeds by making statistical calculations in line with the literature information. The results of the examination were compared with other carnivores. Significant differences were detected.

The aim of this study was to assess Aksaray Malakli dog skulls morphometrically in detail. By doing so, we hope to contribute to the international morphology database on dog breeds.

MATERIALS AND METHODS

Sample collection and processing

The skulls of 9 Aksaray Malakli dogs, aged 4–5 years old, regardless of the difference in weight and gender, that had died of various reasons at the Veterinary Health and Practice and Research Centre of Aksaray University Veterinary Faculty between 2015 and 2019, were used in this study.

Skulls were harvested and cleaned according to a standard protocol [13, 24]. In short, this protocol consisted of boiling the skinned skull in 5–10% NaHC0$_3$ for 1 day, cleaning from soft tissue manually thereafter, then immersing in a 10% hydrogen peroxide solution for 2–3 days. Skulls were prepared for measurements after maceration [24].

Morphometry

In the literature, there are reports on skull measurements. Simoens et al. [23] (Peking dog), Onar [19] (German wolfdog), Onar et al. [21] (Kangal dog) reported measurement locations and methods applied. Of the 44 measurement points reported in the literature [19, 20, 23], 32 measurement points that are prominent in the Aksaray Malakli dog were selected. Thirty-two measurements were made with a digital calliper (A Brand, 200 mL, Germany). Seven index ratios were calculated. The calculation methods used in the Kangal dog morphometry study [21] were applied. One measurement was taken from each skull (Figs. 1, 2). In the measurements, the average of both sides of the skull was taken. Images were taken with a camera (Canon CE500). The nomenclature used in this study is according to Nomina Anatomica Veterinaria [16].

Statistical analysis

Statistical significance of skull measurements was evaluated. Correlation test was used to determine whether there is a relationship between the variables and if so, in which direction and to what extent. The mean, standard deviation and correlation values of
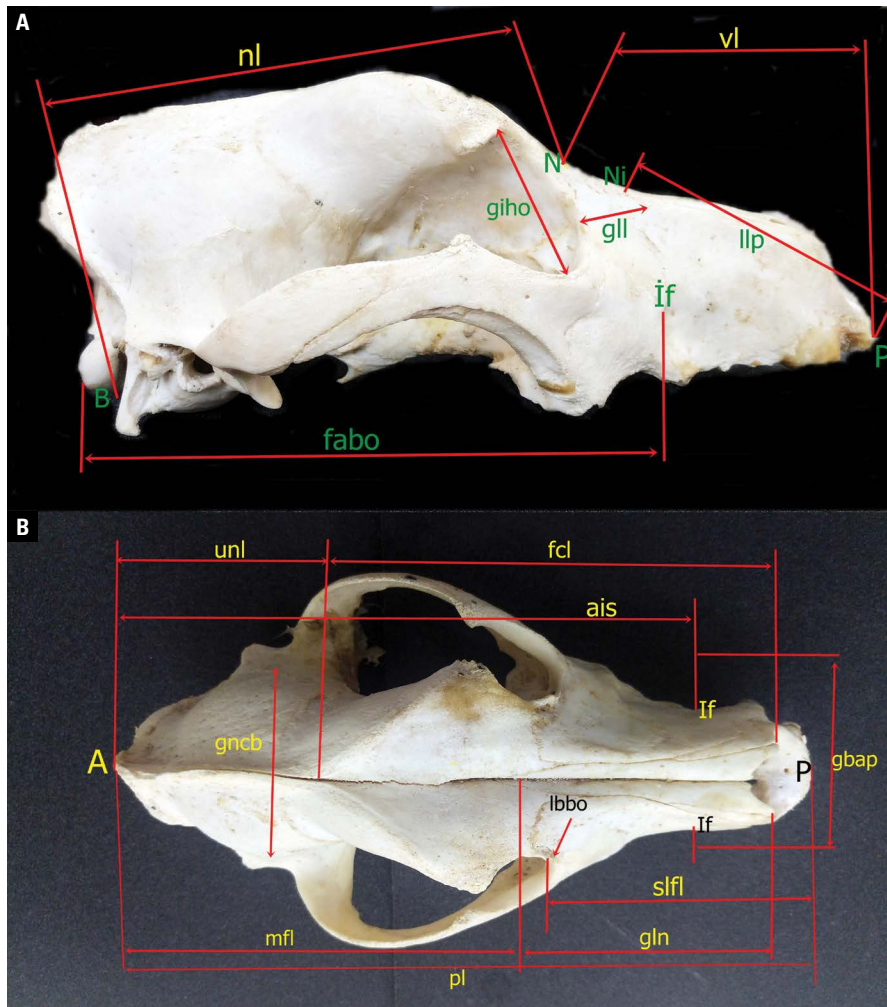
Figure 2. Measurements of the skull of Aksaray Malakli dog; **A.** Lateral view; **B.** Dorsal view; abbreviations — see Figure 1.

all measurements obtained were determined in the SPSS (18.0) version programme [6].

RESULTS

According to the macroanatomical findings in the Aksaray Malakli dog skull, the os frontale and os parietale were prominent. The os temporale was located laterally on the skull bone. The foramen was prominent towards the infraorbital cranial. Tuber faciale was not prominent. Processus zygomaticus of Aksaray Malakli dog was found to be tall and sharp. It was determined that the foramen magnum of os occipitale was surrounded by oval condyli occipitales, and the processi jugulares were curved ventrally. A thick arcus zygomaticus was prominent on the sides of the cranial bones (Figs. 1, 2). The relevant mean and standard deviation values of the craniofacial indices of the Aksaray Malakli dog's skull are shown

in Table 1. The calculated cranial indices in Aksaray Malakli dogs were as follows: facial index 107.68 ± ± 4.98, nasal index 19.61 ± 3.25, cranial index 56.17 ± ± 2.52, basal index 30.57 ± 1.30, skull index 54.68 ± ± 3.01, palatal index I 56.76 ± 1.89, and palatal index II 59.83 ± 2.23. Average and standard deviation values of the Aksaray Malakli dog's skull morphometric parameters are shown in Table 2.

Condylobasal length of Aksaray Malakli dog was 227.03 ± 12.63 mm, basal length 214.80 ± 10.93, neurocranium length 139.43 ± 3.37 mm, upper neurocranium length 67.66 ± 13.54 mm, facial length 154.76 ± 18.48 mm, height of the foramen magnum 20.09 ± 2.05. The greatest inner height of the orbit was measured as 37.16 ± 1.60 mm (Table 1).

According to the correlation analysis of the Aksaray Malakli dog skull measurements, profile length (pl) and condylobasal length (cbl), short skull length

Table 1. Craniofacial indices of Aksaray Malakli dog skulls (Akmlk) (n = 9)

Akmlk	Facial index	Nasal index	Cranial index	Basal index	Skull index	Palatal index I	Palatal index II
Mean ± SD	107.68 ± 4.98	19.61 ± 3.25	56.17 ± 2.52	30.57 ± 1.30	54.68 ± 3.01	56.76 ± 1.89	59.83 ± 2.23

Facial index — maximum zygomatic width × 100/viscerocranial length; Nasal index — greatest breadth across the nasals × 100/greatest length of the nasals; Cranial index — maximum width of the neurocranium × 100/cranial length; Basal index — maximum width of neurocranium × 100/basal length; Skull index — maximum zygomatic width × 100/skull length; Palatal index I — greatest breadth of the palate × 100/median palatal length; Palatal index II — greatest breadth of the palate × 100/palatal length; SD — standard deviation

Table 2. Mean values of 32 morphometric parameters in Aksaray Malakli dog skulls (n = 9)

Parameters	Mean ± SD
pl	245.78 ± 15.35
cbl	227.03 ± 12.63
bl	214.80 ± 10.93
ssl	143.95 ± 22.38
pmp	69.17 ± 14.18
nl	139.43 ± 3.37
vl	114.39 ± 3.93
mfl	135.06 ± 12.55
unl	67.66 ± 13.54
fcl	154.76 ± 18.48
ais	177.65 ± 8.34
gll	40.95 ± 3.79
gln	85.74 ± 5.49
slfl	115.67 ± 4.68
fabo	158.95 ± 7.29
del	117.00 ± 5.97
lcr	77.51 ± 3.73
lmr	48.47 ± 5.19
lpr	36.02 ± 3,09
giho	37.16 ± 1.60
gmb	83.58 ± 3.68
gbc	46.57 ± 3.79
gbp	64.27 ± 3.90
gbfm	19.88 ± 2.20
hfm	20.09 ± 2.05
gncb	58.36 ± 3.77
lbbo	58,10 ± 4.54
gbap	45.57 ± 5.20
infl	51.74 ± 4.27
grpb	79.78 ± 4.69
llp	69.66 ± 8.44
opl	110.73 ± 12.55

SD — standard deviation; rest abbreviations — see Figure 1

(ssl), facial length (fcl), from the aboral border of one occipital condyle to the infraorbitale of the same side (fabo), basal length (bl), ssl, fcl, length between cbl

and bl, upper neurocranium length (unl) and fabo, bl to fabo, premolare–prosthion (pmp) length and oral palatal length (opl), there was a very strong positive correlation between fcl length and fabo length, neurocranium length (nl) and length of the molar row (lmr), and the greatest breadth across the premaxillae (gbap) and the distance between two infraorbitals (infl). On the other hand, it was found that there is a strong negative correlation between ssl length and pmp length (Table 3).

DISCUSSION

Atalar et al. [1] reported that the dorsal part of the neurocranium, which forms the skull, consists of frontal and parietal bones in wolves and foxes, and the lateral part of the temporal bone. Similar findings were detected in the Aksaray Malakli dog.

Karan et al. [11, 12] reported that foramen infraorbitale was shaped narrow and oval in dogs, and tuber faciale was absent. Similar to the literature [11, 12], there was no tuber faciale in our study, but the foramen infraorbital was in a deep pit.

In the study, the facial index of the Aksaray Malakli dog was found to be 107.68 ± 4.98. The facial index was reviewed in literature reviews in collie [8, 21] and Russian wolfhound dogs [8, 21] at 81, in German shepherd [8, 21], beagle [8, 21] and setter [8, 21] dogs at 111, and in Boston terrier [8, 21] and Pekingese dogs [8, 21] at 215. The facial index of Aksaray Malakli dog according to index values that of collie [8, 21], Russian wolfhound [8, 21], German shepherd [8, 21], beagle [8, 21] and setter [8, 21], and lower than that of Boston terrier [8, 21] and Pekingese [8, 21] dogs.

In our study, the cranial index value of Aksaray Malakli dog was 56.17 ± 2.52. It was reported at 48 in Collie and Russian wolfhound, 57 in German shepherd, beagle and setter dogs, and 81 in Boston terrier and Pekingese dogs [8, 21]. It was calculated as 73.24 in German wolfdog [20] and 71.28 in golden jackal [15]. Cranial index value of Aksaray Malakli dog was higher than that of collie [8, 21] and Russian wolfhound [8, 21] dogs, German wolfdog [19], golden jackal [15], German shepherd [8, 21], and

Table 3. Correlation values of different skull measurements in the Aksaray Malakli dog (n = 9)

pl	cbl	0.948***	**bl**	ssl	0.852*	**mfl**	unl	0.840*	**fcl**	ais	0.890**
	bl	0.956***		vl	0.779*		fcl	0.916**		fabo	0.970***
	ssl	0.962***		mfl	0.814*		ais	0.972***		del	0.765*
	pmp	−0.784*		unl	0.914**		fabo	0.853*		opl	−0.784*
	mfl	0.927**		fcl	0.949**		opl	−0.874**		giho	0.904**
	unl	0.919**		ais	0.822*		giho	0.788*		gmb	0.904**
	fcl	0.994***		gln	−0.779*		gmb	0.763*		gbc	0.891**
	ais	0.907**		fabo	0.949***	**ais**	fabo	0.850*		gbfm	0.793*
	gln	−0.786*		del	0.904**		opl	−0.817*		gbap	0.787*
	fabo	0.972***		giho	0.943**		giho	0.771*		infl	0.889**
	del	0.777*		gmb	0.955**		gmb	0.770*	**gbfm**	hfm	0.872**
	opl	−0.795*		gbc	0.931**	**gln**	fabo	−0.794*		gncb	0.829*
	giho	0.888**		gbp	0.899**		gncb	−0.849*		infl	0.757*
	gmb	0.901**		gbfm	0.789*		gbap	−0.822*	**del**	lcr	0.901**
	gbc	0.872*		gbap	0.796*	**slfl**	lcr	0.755*		lpr	0.822*
	gbfm	0.790*		infl	0.873**		lpr	0.797*		giho	0.853*
	gbap	0.779*	**pmp**	Nl	0.834*		grpb	0.901***		gmb	0.856*
	infl	0.863*		mfl	−0.782*	**fabo**	del	0.810*		gbc	0.782*
cbl	bl	0.980***		Fcl	−0.771*		giho	0.853*		gbp	0.848*
	ssl	0.850*		opl	0.963***		gmb	0.846*		gbap	0.773*
	vl	0.838*		Llp	0.926**		gbc	0.897**		infl	0.791*
	mfl	0.822*		lmr	0.912**		gbp	0.763*	**nl**	opl	0.784*
	unl	0.966***		hfm	−0.824*		gbap	0.840*		llp	0.862*
	fcl	0.955**	**ssl**	pmp	−0.920**		infl	0.886**		lmr	0.982***
	ais	0.836*		mfl	0.912**	**lpr**	giho	0.759*	**vl**	unl	0.763*
	fabo	0.966***		unl	0.858*		gbc	0.797*		fcl	0.802*
	del	0.905**		Fcl	0.955**		lbbo	0.767*		lcr	0.840*
	lcr	0.823*		ais	0.882**		gbap	0.847*		lpr	0.887**
	lpr	0.819*		gln	−0.802*		infl	0.891**		giho	0.879**
	giho	0.945**		fabo	0.939**		grpb	0.759*		gmb	0.841*
	gmb	0.915**		opl	−0.905**	**giho**	gmb	0.947***		gbc	0.812*
	gbc	0.925**		lmr	−0.755*		gbc	0.910**		infl	0.886**
	gbp	0.837*		gmb	0.781*		gbp	0.859*	**llp**	lmr	0.935**
	gbap	0.816*		gbc	0.771*		infl	0.814*	**hmf**	gncb	0.843*
	infl	0.898**		hfm	0.762*	**gmb**	gbc	0.889**	**gncb**	gbap	0.756*
lcr	lpr	0.937**		gbap	0.779*		gbp	0.866*	**lbbo**	gbap	0.862*
	giho	0.797*		infl	0.827*		gbfm	0.869*	**gbap**	infl	0.953***
	infl	0.773*	**opl**	Llp	0.898**		gbap	0.762*			
	grpb	0.760*		lmr	0.877**		infl	0.877**			

Abbreviations — see Figure 1; *p < 0.05, **p < 0.01, ***p < 0.001

beagle [8, 21]. It was observed to be lower than setter [8, 21], Boston terrier [8, 21] and Pekingese [8, 21] dogs.

Khosravi et al. [14] reported basal index value in grey wolf was 60.56 ± 3.99 and cranial index value was 60.66 ± 2.94, whereas Onar et al. [22] evaluated basal index value in red foxes as 37.75 and 35.34, and cranial index value as 62.37 and 57.92. It was observed in our Aksaray Malakli dog that the basal index value

was 30.57 ± 1.30 and the cranial index value was 56.17 ± 2.52 — lower than grey wolf [14] and red fox [22].

Onar et al. [21] reported the skull index value as 64.00 in husky du labrador dog, 63.00 in pointer dog, 60.17 in St. Bernard dog, and Khosravi et al. [2012] as 53.13 ± 3.35 in grey wolf. In another study, it was reported that in red foxes [22] it was calculated as 52.52 and 52.53. The skull index value of Aksaray Malakli dog was found to be 54.68 ± 3.01 — higher than that of grey wolf [14] and red fox [22] while it was lower than husky du labrador dog, pointer dog and St. Bernard dog [21].

Onar et al. [22] evaluated the palatal index I value as 56.52 and 54.11, and the palatal index II value as 57.95 and 55.10 in their study in red foxes. The palatal index I value of Aksaray Malakli dog was 56.76 ± 1.89, and the palatal index II value was 59.83 ± 2.23 — higher than red foxes.

In the literature studies, condylobasal length measurement was reported as 215.76 ± 12.22 in grey wolf [14], basal length measurement was 206.79 ± ± 11.13 mm, and in this study, condylobasal length of Aksaray Malakli dog was 227.03 ± 12.63 mm and basal length value was 214.80 ± 10. According to these evaluations, the condylobasal length and basal length of Aksaray Malakli dog was longer than that of grey wolf [14].

In the study, the length of neurocranium in Aksaray Malakli dog was determined as 139.43 ± 3.37 mm. This measurement value was reported to be 74.21 ± ± 8.91 in grey wolf [14]. According to the measurement values, it was determined that the length of neurocranium of Aksaray Malakli dog was longer than that of grey wolf [14].

In the skulls of the Aksaray Malakli dog examined, the upper neurocranium length was 67.66 ± 13.54 mm. In the literature studies, upper neurocranium length measurement was reported to be 58.56 ± 5.99 mm in grey wolf [14]. Our investigation material revealed that Aksaray Malakli dog's upper neurocranium length is longer than grey wolf [14].

İlgün and Özkan [10] reported greatest inner height of the orbit as 31.06 ± 1.15 mm in Kangal dog. In our research material of Aksaray Malakli dog, this height was measured as 37.16 ± 1.60 mm. According to the measurement values, the greatest inner height of the orbit of the Aksaray Malakli dog was longer than the Kangal dog [10].

In our study, the height of the foramen magnum of Aksaray Malakli dog was measured as 20.09 ± ± 2.05 mm. In the study of İlgün and Özkan [10] on Kangal dog, the height of the foramen magnum is reported as 24.86 ± 0.59 mm. The height of the foramen magnum of Aksaray Malakli dog was found to be shorter than the Kangal dog.

CONCLUSIONS

According to the results of the study, it is thought that the skull measurements and index calculations of Aksaray Malakli dog will contribute to the creation of a databank in racial discrimination. It is also thought to provide resources for specialists working in different disciplines such as anatomy, morphology, osteo-archeology and can be used in determining the taxonomic classification of carnivorous species. However, it was concluded that more sample studies are needed to obtain more absolute data on the relationships between statistical parameters.

Conflıct of ınterest: None declared

REFERENCES

1. Atalar Ö, Üstündağ Y, Yaman M, et al. Comparative anatomy of the neurocranium in some wild carnivora. J Anim Vet Adv. 2009; 8: 1542–1544.
2. Atasoy F, Kanlı O. Türk çoban köpeği kangal. 2. Baskı, Ankara. Medisan Yayınevi, 2005. No: 60.
3. Atasoy F, Uğurlu M, Özarslan B, et al. Halk elinde yetiştirilen Akbaş köpeklerinde canlı ağırlık ve vücut ölçüleri. Ankara Univ Vet Fak Derg. 2011; 58(3): 213–215, doi: 10.1501/ vetfak_0000002477.
4. Atasoy F. Türk Mastifi Köpeklerin morfolojik ve genetik özelliklerinin belirlenmesi ve bu köpeğin Tanıtılması. 1.Baskı, Ankara: Medisan Matbaacılık 2011.
5. Atasoy F, Erdoğan M, Özarslan F, et al. Malaklı Karabaş köpeklerde bazı morfolojik ve genetik özellikler. Ankara Üniv Vet Fak Derg. 2014; 61(2): 125–132, doi: 10.1501/ vetfak_0000002616.
6. Büyüköztürk Ş. Sosyal Bilimlerde Veri Analizi El Kitabı. Pegem Yayınevi, Ankara 2011.
7. Dayan MO, Gürbüz İ, Demiraslan Y, et al. Craniometric Measurements of the Male Eurasian Lynx from Turkey. Anim Vet Sci. 2017; 5(1): 15, doi: 10.11648/j. avs.20170501.13.
8. Evans HE, Christensen GC. The skeletal system [skull]. In: Miller's Anatomy of the Dog. Evans HE ed. 3rd ed. Chapter 1. W.B. Saunders, Philadelphia 1993: 6–49.
9. Figueirido B, Pérez-Claros J, Hunt R, et al. Body mass estimation in amphicyonid carnivoran mammals: a multiple regression approach from the skull and skeleton. Acta Palaeontologica Polonica. 2011; 56(2): 225–246, doi: 10.4202/app.2010.0005.

10. İlgün R, Özkan ZE. Aksaray Malaklı Köpeği ile Kangal Köpeği Neurocranium ve Splanchnocranium Kemiklerinin Bazı Osteometrik Ölçümlerinin Karşılaştırılmalı Olarak İncelenmesi. F Ü Sağ Bil Vet Derg. 2015; 29: 157–161.

11. Karan M, Aydın A, Timurkaan S, et al. Bazı carnivorlarda viscerocranium'un karşılaştırmalı makroanatomik incelenmesi. F Ü Sağ Bil Vet Derg. 2015; 19: 99–102.

12. Karan M, Timurkaan S, Ozdemir D, et al. Comparative macroanatomical study of the neurocranium in some carnivora. Anat Histol Embryol. 2006; 35(1): 53–56, doi: 10.1111/j.1439-0264.2005.00659.x, indexed in Pubmed: 16433674.

13. Keneisenuo K, Choudhary OP, Priyanka P, et al. Applied anatomy and clinical significance of the maxillofacial and mandibular regions of the barking deer (Muntiacus muntjak) and sambar deer (Rusa unicolor). Folia Morphol. 2021; 80(1): 170–176, doi: 10.5603/FM.a2020.0061, indexed in Pubmed: 32491187.

14. Khosravi R, Kaboli M, Imani J, et al. Morphometric variations of the skull in the Gray Wolf (Canis lupus) in Iran. Acta Theriologica. 2012; 57(4): 361–369, doi: 10.1007/s13364-012-0089-6.

15. Monfared AL. Macroanatomical investigation of the skull of Golden Jackal [Canis aureus] and its clinical Application during Regional Anethesia. Global Veterinaria. 2013; 10: 547–550, doi: 10.5829/idosi.gv.2013.10.5.7298.

16. Nomina Anatomica Veterinaria [NAV]. International Comitte on Veterinary Gross Anatomical Nomenclature. General assembly of the World Association of Veterinary Anatomists. Fifth Edition Gent. Published by the Editorial Committee Hannover [Germany] Columbia. MO [U.S.A.] Ghent [Belgium]. Sapporo [Japan]. 2012.

17. Oğrak Y, Yoldaş A, Uroseviç M, et al. Some morphological traits of Tarsus Çatalburun breed of Turkish hunting dog. Eurasian J Vet Sci. 2014; 30(1): 25–25, doi: 10.15312/eurasianjvetsci.201415912.

18. Oğrak Y, Öztürk N, Akın D, et al. Comparison various body measurements of Aksaray Malakli and Kangal Dogs. J Istanbul Vet Sci. 2018; 2(3): 86–91, doi: 10.30704/http-wwww-jivs-net.462546.

19. Onar V. A morphometric study on the skull of the German shepherd dog (Alsatian). Anat Histol Embryol. 1999; 28(4): 253–256, doi: 10.1046/j.1439-0264.1999.00202.x, indexed in Pubmed: 10488631.

20. Onar V, Kahvecioğlu KO, Mutuş R, et al. Alman Kurt Köpeklerinde Mandibulanın Morfometrik Analizi [Morphometric Analysis Of The Mandible In German shepherd Dogs]. Vet Anim Sci. 1999; 23: 329–334.

21. Onar V, Pazvant S, Özcan S. Skull typology of adult male Kangal dogs. Anat Histol Embryol. 2001; 30(1): 41–48, doi: 10.1046/j.1439-0264.2001.00292.x.

22. Onar V, Belli O, Owen P. Morphometric examination of red fox (vulpes vulpes) from the van-yoncatepe necropolis in Eastern Anatolia. Int J Morphol. 2005; 23(3), doi: 10.4067/s0717-95022005000300011.

23. Simoens P, Poels P, Lauwers H. Morphometric analysis of the foramen magnum in Pekingese dogs. Am J Vet Res. 1994; 55(1): 34–39, indexed in Pubmed: 8141494.

24. Taşbaş M, Tecirlioğlu S. Maserasyon tekniği üzerinde araştırmalar. J Faculty Vet Med. 1966; 12: 324–30.

25. Tserendorj M, Reading RP, Buuveibaatar B, et al. Comparative Craniometric Measurements of Two Sympatric Species of Vulpes in Ikh Nart Nature Reserve, Mongolia. Mongol J Biol Sci. 2018; 18(1), doi: 10.22353/mjbs.2018.16.03.

26. Yılmaz O. Türk kangal [Karabaş] Köpeği 4.Baskı. İstanbul: Bilge Kültür Sanat Yayınevi. 2018.

27. Yılmaz O, Ertuğrul M. Türkiye yerli köpek ırk ve tipleri. Igdır Univ J Ins Sci Tech. 2012; 02: 99–106.

28. Zinoviev AV. Study of the medieval dogs from novgorod, Russia (X-XIV century). Int J Osteoarchaeol. 2010; 22(2): 145–157, doi: 10.1002/oa.1191.

ORIGINAL ARTICLE

VIA MEDICA

A comparative study on the morphology, radiography and computed tomography of the skull bones of barking deer (*Muntiacus muntjak*) and sambar deer (*Rusa unicolor*)

K. Keneisenuo[1] , O.P. Choudhary[1] , P.C. Kalita[1] , S. Duro[2], A. Kalita[1], P.J. Doley[1] ,
R.S. Arya[3], S. Debroy[1], P. Priyanka[4]

[1]Department of Veterinary Anatomy and Histology, College of Veterinary Sciences and Animal Husbandry,
Central Agricultural University (I), Selesih, Aizawl, Mizoram, India
[2]Faculty of Veterinary Medicine, Agricultural University of Tirana, Tirana, Albania
[3]Department of Veterinary Pathology, College of Veterinary Sciences and Animal Husbandry,
Central Agricultural University (I), Selesih, Aizawl, Mizoram, India
[4]Department of Veterinary Microbiology, College of Veterinary Sciences and Animal Husbandry,
Central Agricultural University (I), Jalukie, Peren, Nagaland, India

Background: There is scanty information on the skull morphology of barking and sambar deer; thus the present study was designed to provide information on morphology, radiography and computed tomography (CT) of the skull bones of both deer species.
Materials and methods: The study was conducted on 12 skulls of adult barking deer (n = 6) and sambar deer (n = 6) of either sex (n = 3 males and n = 3 females) collected from Aizawl Zoological Park, Aizawl, Mizoram. The skulls of both species were macerated as per the standard maceration techniques.
Results: The skull bones of both deer species were divided into a neurocranium and a viscerocranium. The neurocranium was comprised of occipital, sphenoid, temporal, frontal, parietal, interparietal and ethmoid bones. The viscerocranium consisted of nasal, lacrimal, zygomatic, maxilla, incisive, palatine, pterygoid, vomer, mandible, turbinates and hyoid bones. The cranial cavity was oval and elongated caudally. The orbit was round, complete in barking deer; however, it was oval, complete in sambar deer. The facial tuberosity was present caudal to infraorbital foramen and dorsally at superior third premolar tooth in barking deer whereas dorsally at the superior first molar tooth in sambar deer. The infraorbital foramina were small, elliptical and placed at the level of the superior first premolar tooth. The alveolus for a canine tooth was present rostrally in the maxilla of both species. Turbinates bones were visible and mandibular symphysis remained unossified on radiographs and CT in both species. The radiographs of both species showed that the nasal canal was divided by the nasal septum. The CT scan demonstrated the paranasal, frontal and maxillary sinuses.
Conclusions: The present study is important in the comparative anatomy of ruminant species and may help the wildlife forensic officials to identify and differentiate the bones of these two species from those of other domestic and wild small ruminants. (Folia Morphol 2022; 81, 1: 164–174)

Key words: barking deer, sambar deer, skulls, morphology, radiography, computed tomography

---

INTRODUCTION

The barking deer, also recognised as Indian Muntjac (*Muntiacus muntjak*) is a cervid species indigenous to South and South-east Asia and has been classified on the International Union for Conservation of Nature (IUCN) red-list as 'Least concern' [22]; and is protected under Schedule III of Indian Wildlife Protection Act, 1972. This species is named barking deer due to its bark-like sound [1, 13]. Among all the signals used in intra-specific and inter-specific communication, vocalisation has been the primary means of communication for the species living in dense forest habitats [17]. They are moderately small tropical deer with a solitary lifestyle [1, 11, 14] and extensive natural distribution, ranging throughout a large part of Southeast Asia [11, 16]. The body length of muntjacs varies from 89 to 135 cm long and their height ranges from 38 to 66 cm tall with an average weight of 22 to 16 kg [7]. They are regarded as the most primitive of all living cervidae [15]. The male of barking deer has small antlers projected from the long body hair enveloped pedicles above their eyes, whereas the female has tiny bony knobs. The barking deer may kill the prey by hitting with forelegs and biting using their canines [9].

The sambar deer, also known as sunda sambar (*Rusa unicolor*) is a large cervid species that is indigenous to the Indian subcontinent, Southern China, and Southeast Asia [12]. This deer species has been categorised by the IUCN red-list as 'vulnerable' due to a decrease in their population year by year [10, 23] and is protected under Schedule-III of the Indian Wildlife Protection Act, 1972. In general, they attain a height of 100–160 cm at the shoulder and may weigh 100 to 550 kg. The head and body length of sambar deer varies from 162–270 cm, with a 22–35 cm tail [2]. They inhabit both gentle sloping and steep forested hillsides. They preferably reside near cultivated areas such as gardens and plantations, thick forests, swamp forests and move between higher altitudes during summer and lower, more sheltered areas in winter [15, 18].

Several studies on gross morphology, radiography and computed tomography (CT) of skull bones have been undertaken in many domestic and wild small ruminant species such as goats [3, 20], sheep [6, 8, 21] and deer species, i.e. chital, blackbuck and chinkara [4, 5, 19] in an attempt to give baseline anatomical information.

There is scanty information on the morphology, radiography and CT of skull bones of barking deer and sambar deer. Therefore, the present study has been delineated for determining the morphology, radiography and CT of skull bones of barking and sambar deer.

MATERIALS AND METHODS

The present study was conducted at Aizawl from March 2019 to June 2020. Twelve skulls of adult barking deer (n = 6) and sambar deer (n = 6) of either sex (n = 3 males and n = 3 females) were collected. The age of barking deer and sambar deer used for skull collection were in the range of 3 to 4 years and 6 to 8 years, respectively. All procedures involving sample collection were conducted as per the Institutional Animal Ethics Committee (IAEC), College of Veterinary Sciences and Animal Husbandry, Aizawl, Mizoram.

Skulls were collected from the Aizawl Zoological Park, Aizawl, Mizoram, after obtaining official permission from the Principal Chief Conservator of Forest (PCCF) and Chief Wildlife Warden, Government of Mizoram vide letter no. A.22011/5/2017-CWLW/91, dated 15.03.2019. The collected skulls were macerated as per the standard hot water maceration technique [9] after excavating out from the graveyard located at the site of the Aizawl Zoological Park, Aizawl, Mizoram. After maceration, skulls were soaked in 4% hydrogen peroxide for three days in a sealed container until bones appeared clean and whitish [9]. Finally, processed skulls were sun-dried for three days and utilised for the studies.

The gross morphological studies on skull bones were carried out at the Department of Veterinary Anatomy and Histology, College of Veterinary Sciences and Animal Husbandry, Selesih, Aizawl and Aizawl Zoological Park under the supervision of the zoo officials. The skull bones radiography was carried out by the Allengers-325 X-ray machine (200 mA) and CT scan by Siemens Somatom Emotion instrument (270 mA) at Diagnostic Division Radiology and Imaging, Mizoram Health Care, Aizawl, Mizoram.

The present study was designed to provide information on the morphological, radiographic and CT of the barking and sambar deer skull and provide baseline morphological information. The obtained morphological results of both species were compared with the other domestic and wild small ruminants as per the available literature.
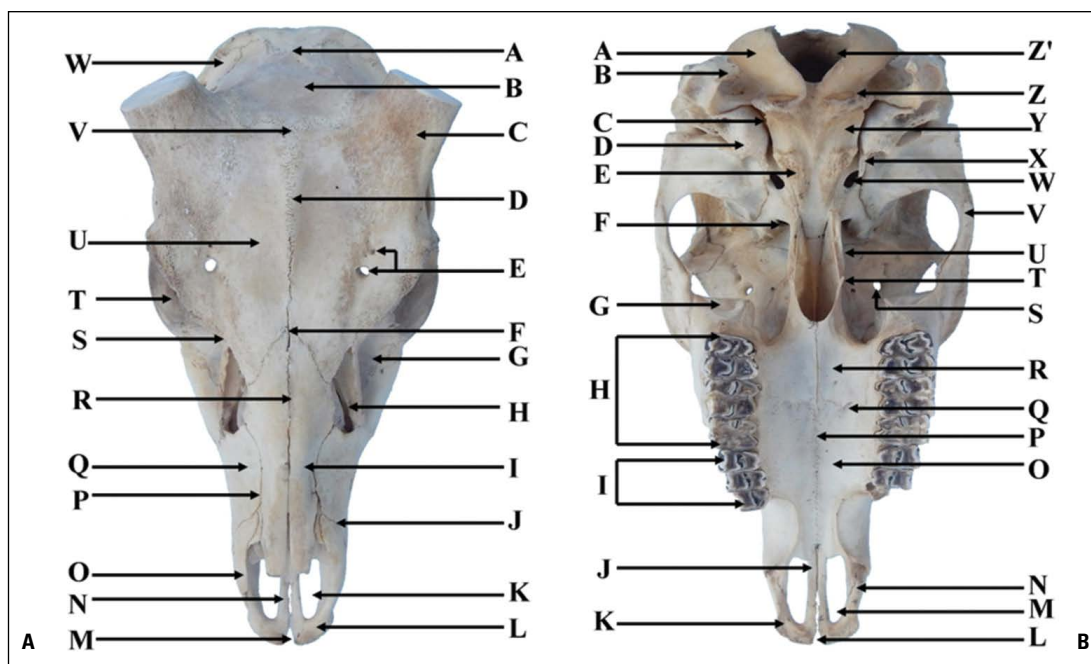
Figure 1. A. Dorsal view of the skull of male sambar deer showing lambdoid suture (A); interparietal bone (B); cornual process (C); interfrontal suture (D); supraorbital foramen (E); nasofrontal suture (F); preorbital fossa (G); nasolacrimal fissure (H); nasal bone (I); maxilloincisive suture (J); palatine fissure (K); body of incisive bone (L); interincisive fissure (M); palatine process of incisive bone (N); nasal process of incisive bone (O); nasomaxillary suture (P); maxilla bone (Q); internasal suture (R); frontolacrimal suture (S); orbit (T); frontal bone (U); frontoparietal suture (V); parietal (W); **B.** Ventral view of the skull of sambar deer showing occipital condyle (A); paracondylar or paramastoid process (B); jugular foramen (C); tympanic bulla (D); muscular tubercle (E); foramen orbitorotundum (F); lacrimal bulla (G); superior first, superior second and superior third molar tooth (H); superior first, superior second and superior third premolar tooth (I); palatine process of incisive bone (J); body of the incisive bone (K); interincisive fissure (L); palatine fissure (M); nasal process of incisive bone (N); maxillary process of palatine bone (O); median palatine suture (P); major palatine foramen (Q); horizontal part of palatine bone (R), supraorbital foramen (S); pterygoid hamulus (T); pterygoid bone (U); zygomatic arch (V); foramen ovale (W); muscular process (X); basilar part of occipital bone (Y); ventral condyloid fossa (Z); foramen magnum (Z').

RESULTS

The skulls of barking and sambar deer (Fig. 1A, B) were elongated and dolichocephalic. The skull bones of both deer species were divided into a neurocranium and a viscerocranium. The neurocranium was comprised of occipital, sphenoid, temporal, frontal, parietal, interparietal and ethmoid bones. The viscerocranium consisted of nasal, lacrimal, zygomatic, maxilla, incisive, palatine, pterygoid, vomer, mandible, turbinates and hyoid bones.

The morphology of individual skull bones (Fig. 1–7A, B) of both species has been compared as per the literature available for other domestic and wild small ruminants. The interspecies comparison has elaborated in the manuscript's discussion section.

DISCUSSION

Skull as a whole

The dorsal surface of the skull in both species was formed by parietal, interparietal, frontal, nasal and incisive bones as reported earlier in kagani goat [20], chital [19] and blackbuck [4].

While viewing from the lateral surface, the zygomatic process of temporal bone did not join with the zygomatic process of the frontal bone in both species as mentioned in chital [19], blackbuck [4] and Bardhoka sheep [6].

The orbit was located rostrolaterally and composed of frontal bone dorso-caudally with zygomatic bone ventro-caudally and lacrimal bone rostrally. It was round and complete in barking deer as mentioned earlier in goat of Mizoram [3]. The orbit was complete and oval in sambar deer as reported in chinkara [20]. The greatest contribution in the formation of bony orbit was by frontal bones as compared to zygomatic and lacrimal bones as mentioned in kagani goat [20], chital [19], blackbuck [4], chinkara [20] and Bardhoka sheep [6]. The orbital rim was circular as reported earlier in blackbuck [4]. The orbit joined with the cranial cavity *via* ethmoidal foramen, optic
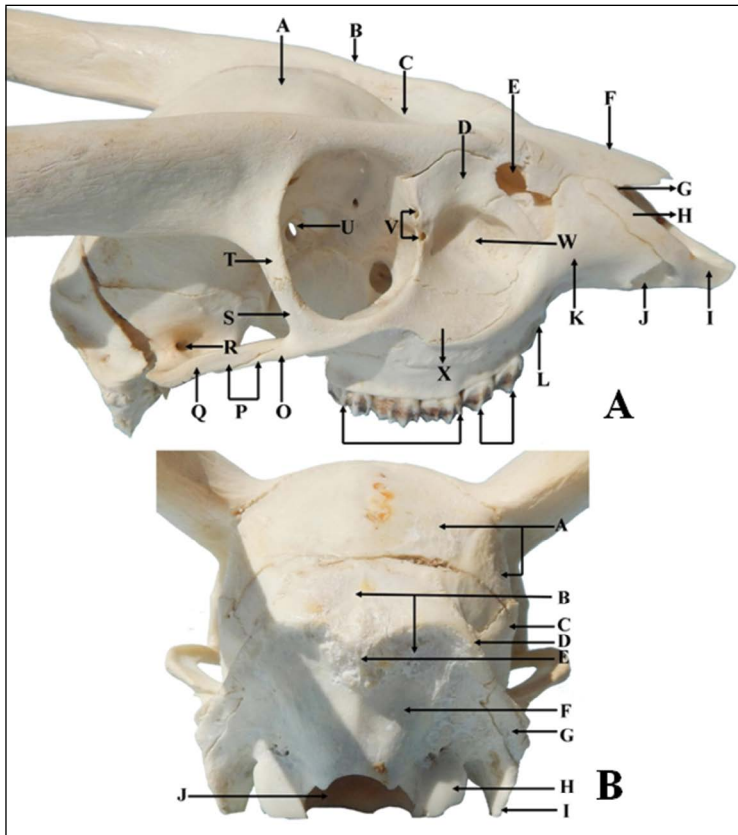
Figure 2. A. Dorsolateral view of the skull of male barking deer showing frontal bone (A); frontal crest (B); shallow concavity on rostral part of frontal bone (C); lacrimal bone (D); nasolacrimal fissure (E); nasal bone (F); nasoincisive fissure (G); incisive bone (H); nasal process of incisive bone (I); alveolus for upper canine tooth (J); maxilla bone (K); alveolus for superior first premolar tooth (L); second superior and third superior premolar tooth (M); first superior, second superior and third superior molar tooth (N); temporal process of zygomatic bone (O); zygomatic arch (P); zygomatic process of temporal bone (Q); tempora orifice of temporal meatus (R); frontal process of zygomatic bone (S); zygomatic process of frontal bone (T); optic foramen (U); lacrimal foramen (V); preorbital fossa (W); zygomatic bone (X); **B.** Nuchal view of the skull of male barking deer showing parietal bone (A); squamous part of occipital bone (B); temporal bone (C); nuchal crest (D); external occipital protuberance (E); lateral part of occipital bone (F); mastoid process of temporal bone (G); occipital condyle (H); paracondylar/paramastoid process (I); foramen magnum (J).
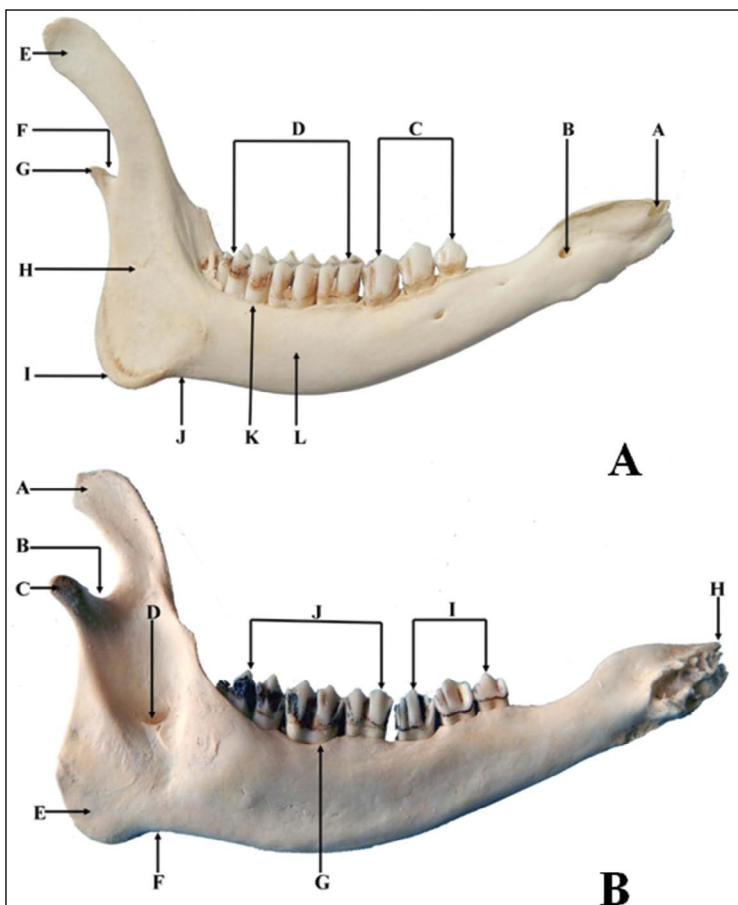
Figure 3. A. Lateral view of mandible of barking deer showing alveolar socket for incisors tooth (A); mental foramen (B); inferior first, inferior second and inferior third premolar tooth (C); inferior first, inferior second and inferior third molar tooth (D); coronoid process/head/height of mandible (E); incisures of mandible (F); condyloid process/condylar process (G); ramus of the mandible (H); mandibular angle (I); notch for facial artery and vein (J); alveolar border (K); body of mandible (L); **B.** Medial view of mandible of barking deer showing coronoid process/head//height of mandible (A); incisure of mandible (B); condyloid process/condylar process (C); mandibular foramen (D); mandibular angle (E); notch for facial artery and nerve (F); alveolar border (G); alveolar socket for incisors tooth (H); inferior first, inferior second and inferior third premolar tooth (I); inferior first, inferior second and inferior third molar tooth (J).
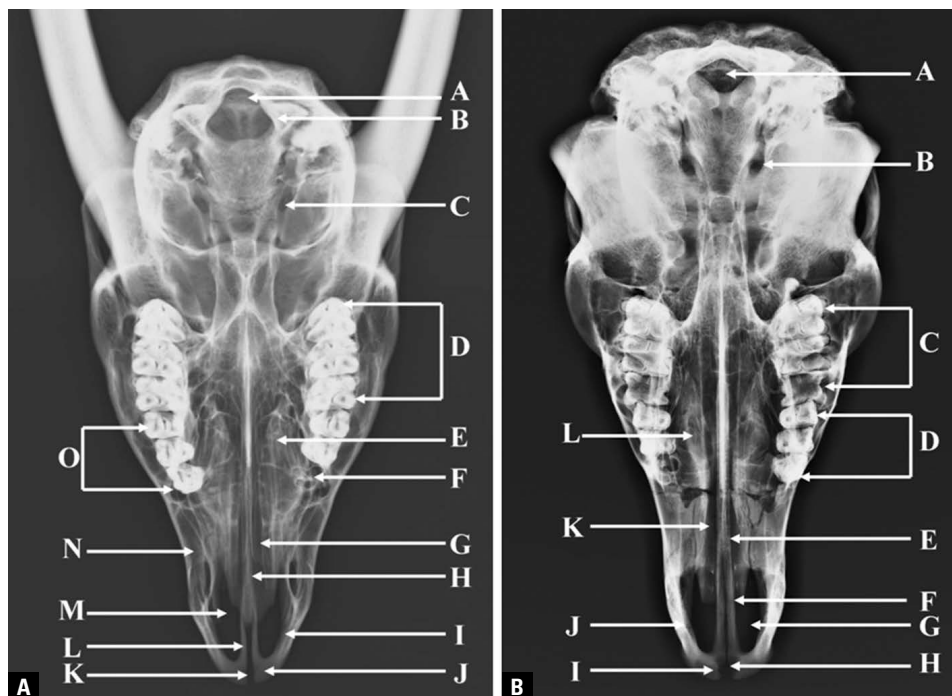
Figure 4. A. Radiograph of dorsal view of the skull of male barking deer showing foramen magnum (A); occipital condyle (B); foramen ovale (C); superior first, superior second and superior third molar tooth (D); turbinate bone (E); alveolar socket of superior first premolar tooth (F); nasal canal (G); vomer bone (H); nasal process of incisive bone (I); body of incisive bone (J); interincisive fissure (K); palatine process of incisive bone (L); palatine fissure (M); pre-orbital fossa (N); superior first, superior second and superior third premolar tooth (O); **B.** Radiograph of dorsal view of the skull of male sambar deer showing foramen magnum (A); foramen ovale (B); superior first, superior second and superior third molar tooth (C); superior first, superior second and superior third premolar tooth (D); vomer bone (E); palatine process of incisive bone (F); palatine fissure (G); interincisive fissure (H); body of incisive bone (I); nasal process of incisive bone (J); nasal canal (K); turbinate bone (L).

foramen and foramen orbitorotundum as in chital [19], blackbuck [4] and chinkara [20].

In both species, the cranial cavity was ovoid and elongated caudally as mentioned in blackbuck [4] and goat [3]. The cranial cavity roof was formed by the frontal, occipital, interparietal and parietal bones. The floor was made up of the basioccipital and sphenoid bones. The cranial cavity's lateral wall was constituted by occipital, parietal, temporal and frontal bones in the barking and sambar deer as reported earlier in chital [19] and blackbuck [4]. The nasal cavity wall was made up of a cribriform plate of the ethmoid that separated the nasal cavity from the cranium, which was even noticed in chital [19] and blackbuck [4]. A cerebral fossa was noticed dorso-lateral to internal acoustic meatus as reported in chital [19] and blackbuck [4].

In barking and sambar deer, the nasal cavity was a longitudinal passage that expanded *via* the upper part of facial bone. This cavity was separated into two halves: right and left by median septum nasi as recorded earlier in chital [19] and blackbuck [4]. The lateral wall was formed by the maxilla, incisive and perpendicular part of palatine bones as reported earlier in chital [19] and blackbuck [4]. The nasal cavity floor was lengthy compared to its roof as mentioned earlier in blackbuck [4].

The total numbers of teeth in barking and sambar deer were 34 with an upper canine tooth in maxilla bone. The upper jaw carried the superior 3 premolars and molars and the lower jaw presented 3 incisors, 1 canine, 3 inferior premolars and 3 molars, respectively. However, the total numbers of teeth were 32 due to the absence of an upper canine tooth in chital [19] and blackbuck [4].

Neurocranium

Os occipitale

The occipital bone was observed in the caudal surface of the skull in both species and consisted of basilar part, squamous part and lateral parts as reported earlier in chital [19], blackbuck [4] and chinkara [20]. The basilar part was short and wide in barking and sambar deer as described in blackbuck [4]. The
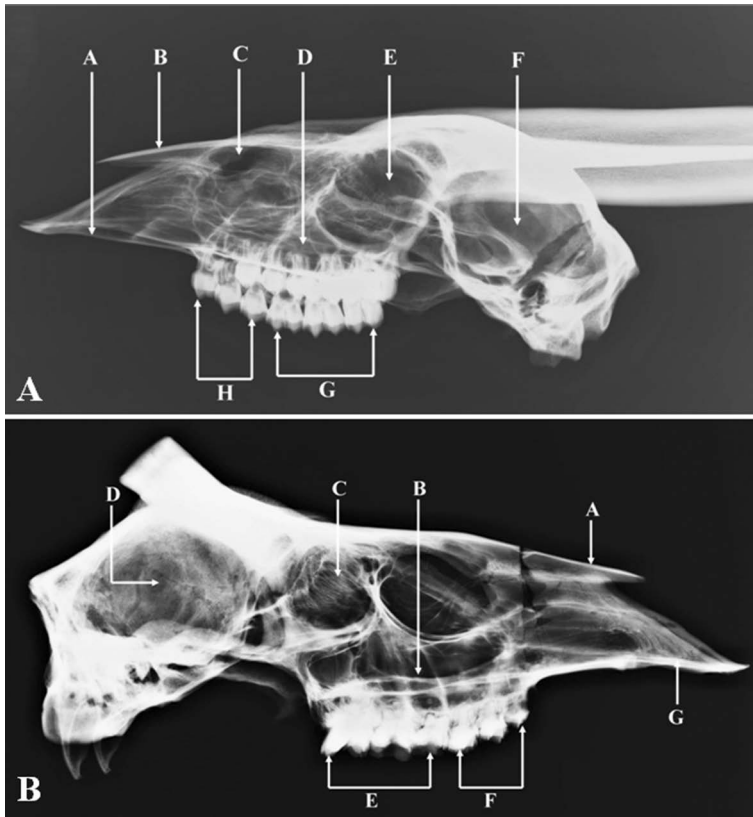
Figure 5. A. Radiograph of lateral view of the skull of male barking deer showing incisive bone (A); nasal bone (B); turbinate bone (C); maxillary sinus (D); orbit (E); cranial cavity (F); superior first, superior second and superior third molar tooth (G); superior first, superior second and superior third premolar tooth (H); **B.** Radiograph of lateral view of the skull of male sambar deer showing nasal bone (A); maxillary sinus (B); orbit (C); cranial cavity (D); superior first, superior second and superior third molar tooth (E); superior first, superior second and superior third premolar tooth (F); incisive bone (G).
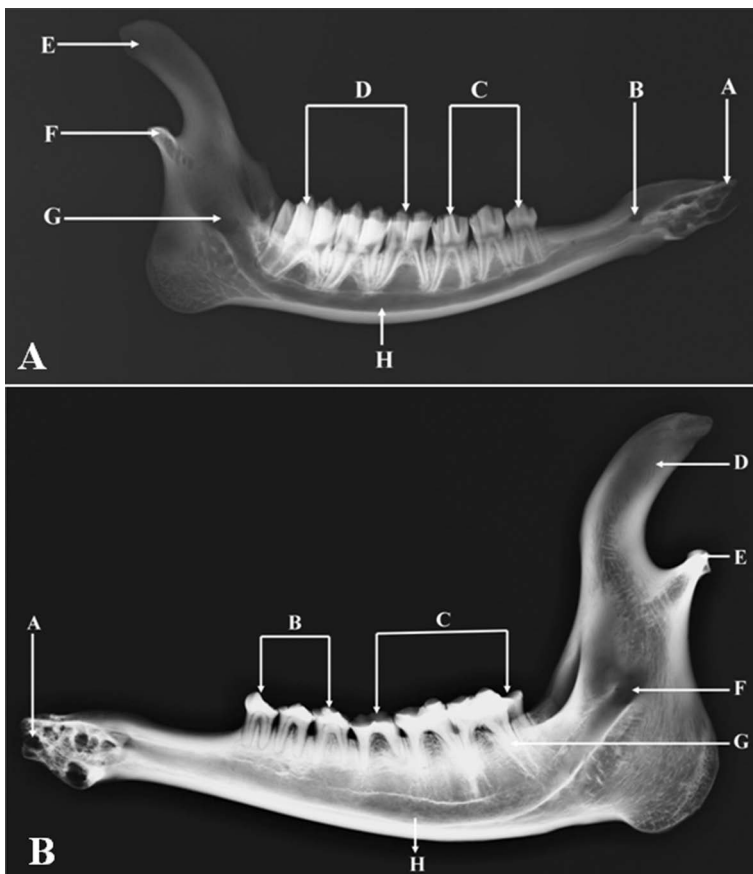
Figure 6. A. Radiograph of lateral view of the mandible of barking deer showing root of the lateral alveolar tooth (A); mental foramen (B); inferior first, inferior second and inferior third premolar tooth (C); inferior first, inferior second and inferior third molar tooth (D); height/head/coronoid process of mandible (E); condylar process (F); mandibular foramen (G); mandibular canal (H); **B.** Radiograph of medial view of the mandible of sambar deer showing root of the lateral alveolar tooth (A); inferior first, inferior second and inferior third premolar tooth (B); inferior first, inferior second and inferior third molar tooth (C); height/head/coronoid process of mandible (D); condylar process (E); mandibular foramen (F); root of teeth (G); mandibular canal (H).

Figure 7. A. Computed tomography scan of the head region of the barking deer showing frontal bone (A), frontal sinus (B), nasal septum (C), maxillary sinus (D), nasolacrimal duct (E), ethmoturbinates with ethmoidal conchae (F) and mandibular canal (G); **B.** Computed tomography scan of the head region of the sambar deer showing frontal bone (A), frontal sinus (B), nasal septum (C), maxillary sinus (D), nasolacrimal duct (E), ethmoturbinates with ethmoidal conchae (F) and mandibular canal (G).

jugular foramen (Fig. 1B) was located on either side of the basilar part, adjacent to the tympanic bullae. The muscular tubercle was found in the basilar portion of the occipital bone in both species. The squamous part was quadrilateral in both species as reported in blackbuck [4], whereas it was pentagonal in kagani goat [20]. The lateral parts of the occipital bones formed the lateral borders of the foramen magnum in both species. The nuchal crest was less prominent in barking and sambar deer as reported in blackbuck [4]. In both species, the external occipital protuberance was a median triangular projection for attachment of nuchal ligament as noted earlier in chital [19] and blackbuck [4]. The paramastoid processes were thin, prismatic and projected ventrally in barking and sambar deer as noticed earlier in chital [19], blackbuck [4] and chinkara [20]. The lateral parts of the occipital bone formed the lateral borders of the foramen magnum in both species. The lateral parts consisted of occipital condyles with the condylar process. Lateral to the condylar processes, paracondylar processes were present in both species as reported in chital [19] and blackbuck [4]. The hypoglossal canal (canalis nervi

hypoglossi) was located between the paracondylar and condylar processes in both species. The foramen magnum was huge and almost oval as mentioned in chital [19], goat of Mizoram [3], chinkara [20] and Bardhoka sheep [6].

Os sphenoidale

In barking and sambar deer, the sphenoid bone was single. It was located between the basilar portion of the occipital bone and ethmoid bone rostrally as reported in chital [19] and blackbuck [4]. It formed the cranial cavity floor and was composed of two parts: presphenoid rostrally and postsphenoid caudally. The orbital fissure and round foramen (foramen rotundum) unite to form foramen orbitorotundum as mentioned in chital [19] and blackbuck [4]. The oval foramen was formed completely by the sphenoid bone as described earlier in blackbuck [4].

Os temporale

The temporal bone was paired, irregular in shape in both species. The temporal bone formed the lateral wall of the cranium. This bone was situated between

parietal bone dorsally, frontal bone cranially, sphenoid bone ventrally and occipital bone caudally as reported in chital [19] and blackbuck [4]. These bones consisted of three parts, namely: the squamous (*pars squamosa*), petrous parts (*pars petrosa*) and tympanic part (*pars typmpanica*). The squamous portion of the temporal bone was shell-like and the petrous portion was placed in between the occipital caudally and parietal cranially and was overlapped exteriorly by squamous temporal bone as mentioned in chital [19] and blackbuck [4]. The zygomatic process of temporal bone did not articulate with the zygomatic process of frontal bone as mentioned in goat of Mizoram [3]. The articular tubercle was present; however, it was absent in chital [19]. The hyoid process was short rod-shaped in both species, projected downwards and onwards beneath the external auditory processes. The mastoid process was present in both species but was absent in chital [19] and blackbuck [4]. The tympanic bulla was huge in both species as mentioned in chital [19] and blackbuck [4]. The temporal fossa was deep and well developed in both species as reported earlier in kagani goat [20], blackbuck [4] and Bardhoka sheep [6].

Os frontale

The frontal bone was paired and irregular and slightly rectangular in both deer species. The caudal portion of the external surface of these bones was convex with the suppressed cranial part, which was also mentioned in chital [19] and blackbuck [4]. In both species, these bones joined with parietal bone at the frontoparietal suture, caudally and rostrally to nasal bones at the nasofrontal suture. The supraorbital foramen was placed in a supraorbital groove near the orbit's medial margin, similar to the findings in chital [19] and blackbuck [4]. However, it was in the supraorbital groove of the medial brim of the orbit in chinkara [20]. The frontal sinus was merged to the frontal bone as noted earlier in chital [19] and blackbuck [4].

Os parietale

The parietal bone in both species was paired and composed the dorsolateral wall of the cranial cavity. It was bordered by the occipital bone caudally and frontal bone rostrally in both species as reported in chital [19] and blackbuck [4].

Os interparietale

In barking and sambar deer, the interparietal bone was unpaired, wide, quadrilateral and situated between occipital and parietal bone as reported in chital [19] and blackbuck [4]. It contributed to the formation of the cranial cavity roof as also reported earlier in chinkara [20].

Os ethmoidale

In both species, the ethmoid bone was single and placed in between the cranial and nasal cavity as noticed in chital [19], blackbuck [4] and chinkara [20]. Ethmoid bones merged with presphenoid caudally, vomer and palatine bones rostro-ventrally and with frontal bones dorso-rostrally, which was parallel to the findings in chital [19], blackbuck [4] and chinkara [20]. It was composed of the cribriform plate, labyrinth and the perpendicular plate as discussed earlier in chital [19] and blackbuck [4]. In both deer species, it carried an ethmoidal foramen placed in an orbital plate of frontal bone as reported earlier in chital [19] and blackbuck [4]. In contrast, the same foramen was located entirely in the frontal bone in chinkara [20].

Viscerocranium
Os nasale

In barking and sambar deer, the nasal bone (Fig. 1A) was pair of bone articulated rostrally with incisive bone and caudally with the frontal bone as reported earlier in chital [19] and blackbuck [4]. In both species, the nasal bones constituted the larger part of the roof of the nasal cavity. The rostral extremity of these bones was separated into two by a notch. The posterior extremity of the paired nasal bone presented with a notch composed of the rostral part of frontal bones resembled the observations in chital [19] and blackbuck [4].

Os lacrimale

In both species, the lacrimal bone (Fig. 2A) was paired. These bones superiorly articulated with frontal and nasal bones, ventrally with maxilla bone and caudally with the malar bone as described in chital [19]; however, the lacrimal bone connected with frontal bones superiorly, maxilla bones ventrally, malar bones caudally and palatine bone beneath and beyond in blackbuck [4]. The larger and smaller parts of lacrimal bones were combined together along the orbital rim. A lacrimal bulla was noted in both species as described in chital [19] and blackbuck [4]. These bones also presented a deep nasolacrimal fissure in both species as reported in Bardhoka sheep [6], but it was much deeper in sambar deer. In both species,

very deep and prominent depression or fossa called lacrimal fossa for lodgement of the preorbital gland as described in Bardhoka sheep [6] and these fossae were deeper in sambar deer.

Os zygomaticum

In both species, the zygomatic bone was paired and situated between lacrimal above and maxilla beneath and in front as reported earlier in blackbuck [4]. These bones were curved crest-like, around the infraorbital margin continuing to the maxilla bone as also reported in chital [19] and blackbuck [4]. The orbital surface of the zygomatic bone was smaller than the lateral surface in both species similar to findings in chital [19] and blackbuck [4]. The frontal process of the zygomatic bones articulated with the zygomatic process of the frontal bones, as mentioned in chital [19] and blackbuck [4].

Os maxillare

In barking and sambar deer, the maxilla (Fig. 2A, B) was irregular and placed between the nasal and incisive bones. The facial tuberosity was present caudal to the infraorbital foramen as elucidated in blackbuck [4] and Bardhoka sheep breed [6]. This tuberosity was present dorsally at the superior third premolar tooth in barking deer as also discussed in chital [19], goat [3]; and was dorsally at the superior first molar tooth in sambar deer, which was also noted in Bardhoka sheep [6]. However, the same was placed at the junction of fourth and fifth cheek teeth in kagani goat [20] and was at the level of fifth cheek tooth in Mehraban sheep [8]. A small, elliptical infraorbital foramen was placed at the level of the superior first premolar tooth as mentioned in chital [19], while the infraorbital foramen was oval-shaped and placed in maxilla bone dorsally and oriented rostrally at the level of second cheek tooth in chinkara [20] and was located at the level of the first molar in Bardhoka sheep [6]. The facial crest was found in both the deer species; however, it was very prominent in Mehraban sheep [8]. The facial tuberosity was observed dorsally at the superior third premolar in barking deer as reported earlier in chital [19] and goat [3]. In contrast, it was placed dorsally at the superior first molar tooth in the sambar deer, which was just caudal to infraorbital foramen in chital [19], blackbuck [4] and Bardhoka sheep [6]. In other studies, it was found to be at the intersection of fourth and fifth cheek teeth in kagani goat [20], at the level of fifth cheek tooth in sheep [8].

The facial crest caudally extended from facial tuberosity to the facial surface of the zygomatic bone. In both species, the alveolar border presented 6 alveoli for the superior 3 premolar and superior 3 molar as also noted in chital [19] and blackbuck [4]. The palatine process (*Processus palatinus*) was a thin plate that forms the rostral part of the basis of hard palate as reported in blackbuck [4].

Os incisivum

In both species, the incisive bone (Fig. 2A) was a paired bone, thin and wide plate as also reported in chital [19]. It did not carry any alveolus for upper teeth and presented a dental pad as in chital [19] and blackbuck [4]. The nasal process of incisive bone was joined to the nasal bone. The palatine process was a thin plate that composed the rostral part of the basis of the hard palate in barking and sambar deer, which was also recorded in chital [19] and blackbuck [4]. The palatine fissure was wide and elongated. Both species also presented nasoincisive incisure as also noticed in Bardhoka sheep [6].

Os palatinum

In the barking and sambar deer, the palatine bone (Fig. 1B) was a paired bone and visualised in the ventral surface of the skull between the maxilla, sphenoid and pterygoid bones. The horizontal plate of palatine bones was extensive, whereas the same was narrow in chital [19] and blackbuck [4]. The two major palatine foramina were perforated on the palatine bone as reported earlier in chital [19] and blackbuck [4]. In contrast, it was placed on the intersection of the horizontal plate of palatine bone and the palatine process of the maxilla in chinkara [20]. In both deer species, the transverse palatine suture was "V" shaped and serrated, lying over the greater palatine foramina as reported in kagani goat [20].

Vomer

In barking and sambar deer, the vomer was an unpaired bone. It remained fused with the incisive, maxilla and sphenoid bone and did not articulate with the palatine bone as mentioned in chital [19] and blackbuck [4]. The cranial third of these bones fitted into the nasal crest of the maxilla in both species that was also recorded in chital [19] and blackbuck [4]. However, the laminae of the vomer bone terminated at the junction of palatine processes of maxilla and palatine processes of incisive bones in Bardhoka sheep [6].

Os pterygoideum

In both species, the pterygoid was a paired bone. These bones (Fig. 1B) were thin bony plates and placed between the sphenoid and horizontal plate of the palatine bone. The pterygoid hamulus in both species was a hook-shaped process as reported in chital [19] and blackbuck [4].

Mandibula

In both species, the mandible was a paired bone consisted of a body and a ramus. The mandibular symphysis (Fig. 3; 6A, B) remained unossified as mentioned in chital [19] and blackbuck [4]. The medial surface of the mandibular symphysis displayed large interdigitating septa in both species that entered into large mediolateral depressions of the opposing mandible. The mandibular corpus was moderately curved when placed on a flat surface and did not join the surface at each extremity. In barking and sambar deer, an incisive part of the body remained elevated from the ground, resembling to chital [19] and blackbuck [4]. The mandible also presented 6 alveoli for inferior 3 premolar teeth and inferior 3 molar teeth in both species as reported in chital [19] and blackbuck [4]. The mandible also presented 8 alveoli for canine and incisors as mentioned earlier in chital [19]. In both deer species, the mental foramen, an external opening of the mandibular canal was located in the fossa placed at junction with the body of the mandible as stated in chital and blackbuck [4, 19]. The mental foramina in sambar deer were exceptionally large and in most cases elongated but were complete spheres in the barking deer. The mandibular foramina were oval or elongated in sambar and barking deer. The mandibular tuberosity was absent, which was also similar to chital [19]. The caudal and perpendicular part of the mandible (ramus) was the non-tooth bearer part as reported in chinkara and [20] blackbuck [4]. In the barking and sambar deer, the articular extremity or caudal extremity contained the condylar process and coronoid process with an intervening notch. The coronoid process was curved caudally and caudodorsally expanded above the condyle and formed the tallest point of the bone that was the same as observed in chital [19] and blackbuck [4]. The head of the condylar process of the mandible was transversely elongated as reported earlier in chital [19] and blackbuck [4].

Ossa turbinata

In barking and sambar deer, the turbinate bones (Fig. 4A, B) were paired, very fine, scroll-like, complex bony plates located vertically in the nasal cavity attached to the lateral wall of the nasal cavity. These bones arose from dorsal and lateral walls of ethmoid bones in both deer species. Turbinate bones were visible on radiographs and CT in both species. There were paired dorsal and paired ventral turbinates on each edge of the nasal cavity as recorded in chital [19] and blackbuck [4].

Os hyoideum

The hyoid bone was an unpaired bone and its morphology was similar to the domestic and wild small ruminant species such as goat of Mizoram, chital and blackbuck [3, 4, 19].

Radiographic study

The radiograph of skull bones of barking and sambar deer (Fig. 4–6A, B) showed the dolichocephalic type and elongated as mentioned in blackbuck [4]. The nasal canal was divided by a nasal septum similar to chital [19]. The cranial cavity was visibly recognised with the foramen magnum located along its caudoventrally as reported in chital [19]. The ventrodorsal aspect was more appropriate for the vomer, nasal septum, nasal cavity, premolar and molar teeth. The dorsoventral view showed better visualisation of the vomer, palatine and maxillary sinuses that was also noticed in blackbuck [4]. The occipital condyles and foramen magnum were also clearly recognized in both species as reported in sheep [21] and blackbuck [4].

Computed tomography study

The CT (Fig. 7A, B) scan of skull bones of both species clearly showed the paranasal, frontal and, maxillary sinuses. A thick bony septum (nasal septum) completely separated the left and right frontal sinus, and a thin incomplete bony septum divided the maxillary sinus into rostral and caudal compartments as was recorded in chital [19].

The frontal sinuses of both species were roughly triangular in outline with its base located medially and the same was also reported in chital [19]. These sinuses were air-filled cavities formed by the evagination of frontal bones into the nasal cavity. The frontal sinus was bounded by frontal bone dorsally, medial wall of the orbit ventrolaterally, cranium caudoventrally

and turbinates rostroventrally and continued directly to the caudal maxillary side. A thick midline bony septum (nasal septum) completely divided both left and right frontal sinuses as also mentioned in chital [19]. The frontal sinus presents rostral and caudal compartments extended to the cornual processes in barking and sambar deer.

In both species, the maxillary sinuses were an air-filled cavity formed by the evagination of maxillary, lacrimal and zygomatic bones as also reported in chital [19]. These sinuses directly communicated with the nasal cavity. The lateral wall of the maxillary sinus was comprised of the maxilla, lacrimal and zygomatic bones, while the alveolar part of the maxilla formed the floor or ventral wall. The frontal sinus was bounded by the maxilla, ventral turbinate and the lateral mass of ethmoid bone, medially. A thin incomplete bony septum divided the sinuses into two compartments that are cranial and caudal and this septum angled caudally oblique with the varied position in its rostral aspect, generally over the roots of second and third molar teeth and the same was also described in chital [19].

CONCLUSIONS

The skull morphology derived in the present study can help the wildlife forensic officials, researchers, clinicians and surgeons in giving better knowledge about the different anatomical structures present on the skull bones and its comparative observation between various domestic and wild small ruminants.

Conflict of interest: None declared

REFERENCES

1. Adnyane IKM, Zuki ABZ, Noordin MM, et al. Morphological study of the infraorbital gland of the male barking deer, muntiacus muntjak. African J Biotech. 2011; 10(77): 17891–17897, doi: 10.5897/ajb10.2634.
2. Boitani L. Simon & Schuster's guide to mammals. Simon & Schuster/Touchstone Books, New York, USA 1984.
3. Choudhary OP, Priyanka P, Kalita PC, et al. A morphometrical study on the skull of goat (capra hircus) in mizoram. Int J Morphol. 2020; 38(5): 1473–1478, doi: 10.4067/s0717-95022020000501473.
4. Choudhary OP, Singh I. Morphogical and radiographic studies on the skull of Indian blackbuck (Antilope cervicapra). Int J Morphol. 2016; 16(2): 775–783, doi: 10.4067/S0717-95022020000501473.
5. Din S, Masood S, Zaneb H, et al. Gross and Clinical Anatomy of the Skull of Adult Chinkara (Gazella bennettii). Pak J Zool. 2020; 52(5), doi: 10.17582/journal.pjz/20190207070209.
6. Gündemir O, Duro S, Jashari T, et al. A study on morphology and morphometric parameters on skull of the Bardhoka autochthonous sheep breed in Kosovo. Anat Histol Embryol. 2020; 49(3): 365–371, doi: 10.1111/ahe.12538, indexed in Pubmed: 32022341.
7. Ilyas O, Khan JA. Food habits of barking deer (Muntiacus muntjak) and goral (Naemorhedus goral) in Binsar Wildlife Sanctuary, India. Mammalia. 2003; 67(4), doi: 10.1515/mamm-2003-0406.
8. Karimi I, Onar V, Pazvant G, et al. The cranial morphometric and morphologic characteristics of Mehraban sheep in western Iran. Global Vet. 2011; 6(2): 111–117.
9. Keneisenuo K, Choudhary OP, Kalita PC, et al. Comparative morphometrical studies on the skull bones of barking deer (Muntiacus muntjak) and sambar deer (Rusa unicolor). Anat Histol Embryol. 2021; 50(3): 500–511, doi: 10.1111/ahe.12653, indexed in Pubmed: 33423310.
10. Leslie D. Rusa unicolor (Artiodactyla: Cervidae). Mammalian Species. 2011; 43: 1–30, doi: 10.1644/871.1.
11. Long JL. Introduced mammals of the world: their history, distribution and influence. CSIRO Publishing, Collingwood Victoria, Australia 2003.
12. Medway L. The wild mammals of Malaya. Oxford University Press, London, UK 1969.
13. Miazi OF, Miah G, Bilkis T, et al. Phenotypic and reproductive parameters of barking deer under management condition of chittagong zoo. Int J Genet Genomics. 2016; 4(5): 40–44, doi: 10.11648/j.ijgg.20160405.11.
14. Mishra HR. The ecology and behaviour of chital (Axis axis) in the Royal Chitawan National Park, Nepal with comparative studies of hog deer (Axis porcinus), sambar (Cervus unicolor) and barking deer (Muntiacus muntjak). Ph.D. Thesis, Edinburgh, University, Edinburgh, 1982.
15. Nowak RM. Walker's Mammals of the world. 6th edn. The Johns Hopkins University Press, Baltimore, London, UK 1999.
16. Ohtaishi N, Gao Y. A review of the distribution of all species of deer (Tragulidae, Moschidae and Cervidae) in China. Mammal Rev. 1990; 20(2-3): 125–144, doi: 10.1111/j.1365-2907.1990.tb00108.x.
17. Oli MK, Jacobson HA. Vocalizations of barking deer (Muntiacus muntjak) in Nepal. Mammalia. 1995; 59(2), doi: 10.1515/mamm.1995.59.2.179.
18. Payne J, Francis C, Phillips KA. A field guide to the mammals of Borneo. The Sabah Society with WWF Malaysia, Malaysia 1985.
19. Ramswarup. Gross anatomical studies on the bones of the skull in chital (Axis axis). M.V.Sc. Thesis. Rajasthan University of Veterinary and Animal Sciences, Bikaner, Rajasthan, India, 2011.
20. Sarma K. Morphological and Craniometrical Studies on the Skull of Kagani Goat (Capra hircus) of Jammu Region. Int J Morphol. 2006; 24(3), doi: 10.4067/s0717-95022006000400025.
21. Sarma K. Suri S Kalita A. Gross anatomical studies on the skull of local sheep of Jammu region. Indian J Anim Sci. 2007; 77(10): 999–1001.
22. Timmins RJ, Duckworth JW, Hedges S. Muntiacus muntjak. The IUCN red list of threatened species. International Union for Conservation of Nature and Natural Resources, 2016.
23. Timmins RJ, Kawanishi K, Giman B, et al. Rusa unicolor. The IUCN red list of threatened species. IUCN, 2015.

VIA MEDICA

ORIGINAL ARTICLE

Bone dehiscences of medial orbital wall on computed tomography and assessment of terminological errors in literature

M. Kaya[1], F. Cankal[2], I. Tekdemir[3]

[1]Department of Radiology, Gazi University School of Medicine, Ankara, Turkey
[2]Department of Anatomy, Ankara Medipol University School of Medicine, Ankara, Turkey
[3]Department of Anatomy, Ankara University School of Medicine, Ankara, Turkey

Background: The objective of this study is to investigate the position and frequency of dehiscences in the medial orbital wall and to reveal that dehiscences and orbital adipose tissue hernias are distinct entities.

Materials and methods: Two hundred-thirty medial orbital walls of 115 patients with a preliminary diagnosis of headache and sinusitis but without active ethmoidal sinusitis were examined by computer tomography in the axial plane. Two separate radiologists assessed continuity of the medial orbital wall and orbital fat tissue herniation in ethmoid cells. The medial orbital wall was divided into four quadrants and the dehiscence distribution was evaluated.

Results: Bone defects were detected in 71 (30.9%) patients in 230 orbital medial wall reviews of 115 patients (59 males, 56 females). Eight (3.5%) of these cases (4 male, 4 female) had herniation of the orbital adipose tissue into the ethmoid sinus. Of the 108 dehiscences, 47 were localised in the posterior upper quadrant. A statistically significant difference was found in the dehiscence distribution according to the quadrants. No significant relationship was found among age, gender, side of dehiscence and frequency of dehiscence.

Conclusions: Dehiscences in the posterior upper quadrant are more common in the medial orbital wall. Although bone dehiscences in the medial orbital wall and the herniation of the orbital fat tissue are two different entities, they are used interchangeably in most of the literature and in radiological reporting. (Folia Morphol 2022; 81, 1: 175–182)

Key words: dehiscence, herniation, medial orbital wall, computed tomography

INTRODUCTION

The bone structures that constitute the orbital medial wall are the lateral or orbital face of the lacrimal bone, the frontal process of the maxillary bone, the lamina papyracea (LP) of the ethmoid bone, and the corpus of the sphenoid bone [10]. Paranasal sinuses are air-filled spaces located within the facial and skull bones where many variations are seen [18]. Especially medial orbital wall bone structures are very thin and dehiscences are common [25]. Meloni et al. [14] re-

ported a high prevalence rate of dehiscence in lamina papyracea as 32%.

Dehiscences in the bone structure are important for the intraorbital and intracranial spread of paranasal sinus infections [4]. It is also a facilitating condition for complications that can be seen during functional endoscopic sinus surgery (FESS) [15]. During FESS, various complications such as bleeding, blindness and even skull base defect can develop [1].

A properly performed computed tomography (CT) for paranasal sinuses provides detailed information about the sinonasal anatomy and its variations [2]. After a detailed investigation of the literature we tried to highlight the confusion about the terminological errors in publications about medial orbital wall discontinuities. In addition, we examined the frequency and localisations of medial orbital wall dehiscences in patients who underwent paranasal sinus CT examination with a pre-diagnosis of sinusitis but did not have active ethmoidal sinusitis.

MATERIALS AND METHODS

Five hundred paranasal sinus CT scans with pre-diagnosis of sinusitis and headache have been analysed by Picture Archiving and Communication Systems. Forty-eight patients with a history of surgery and/or major trauma and 26 patients with movement artefacts that impaired the medial orbital wall assessment were removed from the study sample. In addition, 311 patients with active sinusitis that could interfere with the evaluation of the medial orbital wall by affecting air-bone contrast were excluded from the study (Fig. 1). The study group consisted of 115 patients (59 males, 56 females) between 12 and 88 years of age who were previously thought to have had sinusitis but active ethmoid sinusitis was not detected by the CT scan.

Imaging studies were performed in a private medical imaging centre between 07/2017 and 01/2018 using a GE brand IQ model spiral device with 32 detectors, and 130 kV voltage and 80–120 mAs values in accordance with the bone protocol. CT images were taken in the axial plane with a cross-section thickness of 2.5 mm and evaluated together with sagittal and coronal reformatted images.

This retrospective study involving human participants was in accordance with the ethical standards of the institutional and national research committee and with the 1964 Helsinki Declaration and its later amendments or comparable ethical standards. Informed consent was waived because of the retro-
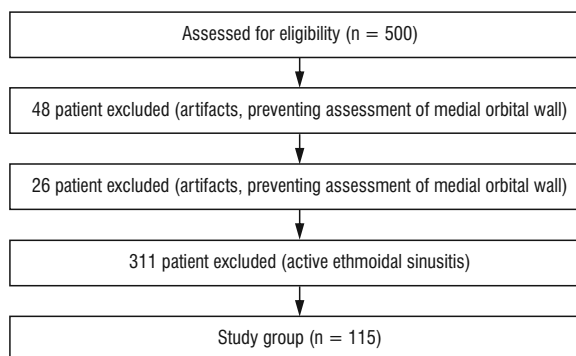
Figure 1. Flowchart shows study population and patient selection process.

spective nature of the study and the analysis used anonymous clinical data.

Two hundred-thirty orbital walls of 115 patients were examined in the axial plane and the discontinuity of bone density belonging to the bone structure between the orbital adipose tissue and ethmoid air was investigated. If bone discontinuities detected in the axial plane could be confirmed in the coronal or sagittal plane, they were accepted as a defect/gap. Findings were recorded for all patients, and cases were identified as defect/gap when two independent radiologists agreed. The medial orbital wall was divided into four as the anterior upper, anterior lower, posterior upper, posterior lower quadrant, and the distribution of dehiscence according to the quadrants was recorded.

Anterior and posterior dehiscences have been reported in the classification of dehiscence in literature and basal lamella separating the anterior and posterior ethmoid cells is considered as a border [14]. A classification of four quadrants, as we did in this report, has not been done before. The bone structures that constitute the medial orbital wall are the orbital face of the lacrimal bone, the frontal process of the maxillary bone, the LP of the ethmoid bone, and the corpus of the sphenoid bone.

Although the four-quadrant classification is not based on the bone margins, it can be said the anterior upper quadrant is formed by the frontal process of the maxillary bone, the upper 1/3 part of the lacrimal bone and the anterior part of the lamina papyracea superior 1/2 section. The anterior lower quadrant is formed by the lacrimal process of the maxillary bone, the lower 2/3 part of the lacrimal bone and the anterior part of the LP inferior 1/2 section. The

posterior upper quadrant is formed by the posterior part of the LP superior 1/2 section and part of the sphenoid bone corpus. The posterior lower quadrant is formed by the posterior part of the LP inferior 1/2 section and part of the sphenoid corpus.

Statistical analysis

Patients with dehiscence were evaluated with the Spearman rho correlation coefficient test in terms of age, gender and dehiscence's being on the right or left side. The dehiscence frequencies according to the quadrants were analysed using the χ^2 test. SPSS version 22 software (IBM Corporation NY, USA) was used when performing statistical analyses and the level of significance was set at alpha = 0.05.

RESULTS

Bone defects were detected in 71 (30.9%) of 230 orbital medial walls of 115 patients (59 male, 56 female). Some orbital medial walls had more than one defect and the total number of dehiscences was 108. A total of 108 dehiscences were detected, including 8 in the right anterior upper quadrant, 10 in the right anterior lower quadrant, 23 in the right posterior upper quadrant, 15 in the right posterior lower quadrant, 10 in the left anterior upper quadrant, 7 in the left anterior lower quadrant, 24 in the left posterior upper quadrant, and 11 in the left posterior lower quadrant (Fig. 2). Eight of the total orbital medial walls (3.5%) had herniation of the orbital adipose tissue into the ethmoid sinus.

While no dehiscence was found in 60 patients, 16 patients had dehiscence on both the right and left sides. Dehiscence was observed in 23 patients on the right side and 16 patients on the left side.

When classified as right and left, there were 32 bone defects on the right orbital medial wall, while there were no bone defects on 83 orbital medial walls. While there were 39 bone defects on the left orbital medial wall, there were no bone defects on 76 orbital medial walls.

The mean age was 39.957, median age 39 years and the standard deviation was 15.871. The age distribution between men and women was homogeneous.

There was no significant relationship between age, sex, dehiscence on the right or left side, and the frequency of dehiscence (r in range of 0.074–0.211 p > 0.05). A statistically significant difference was found in the dehiscence distribution according to the quadrants (χ^2 test, p < 0.05; Tables 1–4).
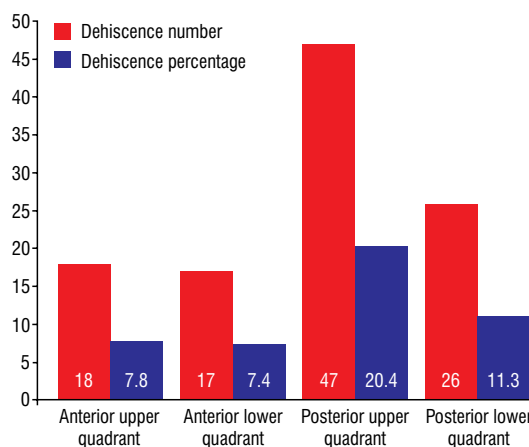
Figure 2. Distribution of dehiscences by quadrants.

Table 1. Prevalence of medial orbital wall dehiscences

	Computed tomography images	
	115 patients, n (%)	230 sides, n (%)
Medial orbital wall dehiscences	55 (47.8%)	71 (30.9%)

Table 2. The localisation of medial orbital wall dehiscences as right- and left-sided

Medial orbital wall dehiscences	Positive CT images 115 patients, n	Negative CT images 115 patients, n
Right	32	83
Left	39	76

CT — computed tomography; n — number of patients

DISCUSSION

The dehiscences in the medial orbital wall were firstly included in the German work which we can translate as the past and present of the University of Vienna Human Anatomy Museum written by Prof. Dr. Joseph Hyrtl in 1869. It is an inventory study of the museum; Hyrtl used the same term for bone defects in various anatomical structures in more than thirty locations in this work [8].

Prof. Dr. Emil Zuckerkandl, one of Hyrtl's students, who would be much more famous than Hyrtl himself in the future, also mentioned the existing dehiscences for many bones in his work titled "Normale und pathologische Anatomie der Nasenhöhle und ihrer pneumatischen Anhänge" published in 1882. Zuckerkandl used the term of dehiscence, which was also mentioned by

Table 3. Bilateral and unilateral distributions of medial orbital wall dehiscences

	Right medial orbital wall positive dehiscences CT images, n	Right medial orbital wall negative dehiscences CT images, n
Left medial orbital wall positive dehiscences CT images, n	16 (14% bilateral positive)	16 (14% left unilateral positive)
Left medial orbital wall negative dehiscences CT images, n	23 (20% right unilateral positive)	60 (52% bilateral negative)

CT — computed tomography; n — number of patients

Table 4. Spearman rank correlation coefficient analysis between age, gender, side and dehiscence

Spearman's rho	Gender	Age	Right	Left
Gender:				
r	1.000	–0.74	–0.133	0.036
p		0.429	0.158	0.669
Age:				
r		1.000	0.087	0.059
p			0.353	0.533
Right:				
r			1.000	0.211
p				0.024
Left:				
r				1.000
p				

Hyrtl before, for dehiscence in the medial orbital wall, stated that he saw this defect in various localisations of the medial orbital wall in 14 cases. Zuckerkandl also gave information about these dehiscences in the same work with very successful drawings [26].

American surgeon Howard A. Lothrop who studied at the University of Vienna for 2 years, stated that dehiscence in the frontal sinus as "the defects described as dehiscences by Zuckerkandl" in his article titled "The Anatomy and Surgery of the Frontal Sinus and Anterior Ethmoidal Cells", which was published in 1898. He stated that there was no frontal sinus dehiscence in his study, he found only two dehiscences in the LP in the 250 orbital walls of 125 cadavers, and this situation had no clinical significance [12].

The famous Hungarian otorhinolaryngology professor Adolf Onodi reported that there was an increase in the spread of sinus infections due to congenital and acquired bone defects, and he defined anterior frontal, posterior frontal, cribriform, maxillary, optic and sphenoid dehiscences in 1909 in his study of "oculo-orbital, intracranial and cerebral complications of paranasal sinus diseases". He emphasized the parallelism of these findings with Zuckerkandl, Mouret, Lindt, Castex, Cisneros, Jacques, Merlin, Gilmaertz and Spee and their importance in the spread of infection.

In the same article, he examined the thinness of the bones and stated that the cribriform plate was the thinnest bone, while drawing attention to the LP [17].

In 1911, Thomas J. Harris first used the term "Zuckerkandl dehiscence" in his article titled "Atypical mastoiditis — its cause, pathology, symptomatology and diagnosis" published in the journal of Laryngoscope [6]. However, he used this term (Zuckerkandl dehiscence) for dehiscences in the temporal bone and cited it as one of the spreading paths of the periostitis seen in latent mastoiditis.

Teatini et al. [23], in their article titled "Computed tomography of the ethmoid labyrinth and adjacent structures" performed in 1987, stated that dehiscences in LP were not frequent but their number increased after polyposis. In our opinion, this is one of the rare studies where the term dehiscence is used correctly. In the figure of the polyposis case presented in the study, dehiscences in the bone structure are clearly seen and herniation is not available.

In our literature review, we have noticed that the term of dehiscence is used synonymously with protrusion and herniation.

Meloni et al. [14] stated that they found a dehiscence rate of LP at 32% and only 6% had posterior ethmoid localisation in a radiological anatomy study involving 100 patients and emphasized the surgical importance of anatomic variations of ethmoid labyrinth and sphenoid sinus. Meloni et al. [14] reported the highest dehiscence rate of LP as 32% in 1992 in the literature and this number is the closest value to our study. These dehiscences are 23% anterior, 6% posterior, and 2% affecting both. Meloni et al. [14] state that these defects are very common in very thin bone structures, which possibly occur as previous or already existing diseases, or sometimes develop spontaneously. In both cases, incomplete ossification or excessive pneumatisation is shown as the reason for this. In this study, Meloni et al. [14] reports bone dehiscences around the internal acoustic canal, maxillary nerve, and Vidian nerve as well as the dehiscences in LP. The reason for the high dehiscence

rates is probably because the researchers interpret the excessive thinning of the bone plate as a dehiscence. Although there are no patients with active ethmoidal sinusitis in our study group, previous sinusitis can also cause excessive thinning of the bone plate, which we interpret as dehiscence.

Moulin et al. [16] reported that six dehiscences, which they found in the 783 CT scans, always involved the external wall of the ethmoid bulla and the posterior part of the ethmoid bone was preserved. Similar to previous literature, they stated that there was no dehiscence in the posterior of basal lamella [16]. While Moulin et al. [16] explained the dehiscence rate as 0.8%, they stated that they might be confused with infectious, tumoural or post-traumatic lesions. This implies that all six patients had a fatty mass protrusion view associated with orbital fat through a gap. It was reported that in one patient, dehiscence affected the lacrimal bone; in no case the ethmoid bulla was completely filled. Again, in the same study, the term 'gap' was used several times instead of dehiscence.

The embryogenesis of congenital LP dehiscences is uncertain. Since ethmoid cells are formed by the invagination of the olfactory pit epithelium, the holes in the LP can occur as the olfactory pit epithelium goes beyond the lateral limit of the facial embryonic mesenchyme (overextension). However, cadaveric studies and the bulge towards the medial, which Zuckerkandl defined in LP, conflict with this explanation [16].

Han et al. [5] prefer the term 'prolapse' instead of dehiscence because 70% of the orbital adipose tissue herniations have displacement or bowing in the bone. In the same study, although it was not statistically significant, it was stated that the age-related degeneration or subclinical minor traumas may be plausible explanation in congenital dehiscence or orbital medial bone wall weaknesses, by drawing attention to the frequency rate increasing with age [5].

In a major review article called "Ophtalmic complications of the endoscopic sinus surgery", Bhatti and Stankiewicz [1] shares the illustration of cutting by aspirating the medial rectus muscle into the sinus although a powered cutting instrument does not enter into the orbita in a dehiscence case without an apparent herniation in the orbital medial wall and stated that the cutting surgical tool can cause damage to the medial rectus muscle without entering the orbita in dehiscence cases [1].

In the case report in which the dehiscence in LP was explained with magnetic resonance findings, Makariou et al. [13] stated that herniation containing orbital adipose tissue and medial rectus muscle accompanying the defect in LP caused complaints of diplopia and blurred vision and they reported that it would be beneficial to know the presence of this anatomic malformation in order to decrease the risks for complications such as globe and extraocular muscle damage, haematoma, cerebrospinal fluid leak, intracranial infection or intracranial injury during FESS [13].

In the study in which Meyers and Valvassori [15] evaluated the anatomical variations of the paranasal sinus with the surgical perspective, they suggest that LP was firstly examined from the anterior to the posterior for proper defect in terms of critical surgical information obtained from axial CT images. Meyers and Valvassori [15] use the terms 'protrusion', 'herniation' and 'dehiscence' in similar meanings in the study in which they stated that they found two herniations in 400 patients [15].

Kitaguchi et al. [9] stated that they found 1.4% dehiscence in their study on 315 patients and that all dehiscences were at the level of anterior ethmoid sinus. Seeley et al. [20] reported a bilateral anterior LP dehiscence case in 2010.

In a case report published by Lim et al. [11] in 1999, they stated that that the CT findings in 57-year--old woman with the complaints of nasal obstruction, postnasal discharge and clear rhinorrhoea and without a history of previous nasal surgery or trauma was reported as normal by the radiologist and, in the subsequent evaluation, herniating orbital fat and part of medial rectus muscle could be clearly seen on the medial orbital wall. Lim et al. [11] stated that lamina papyracea dehiscences and accompanying orbital adipose tissue protrusions were previously reported to occur due to congenital or posttraumatic causes, but protrusion without a gap in the medial orbital wall was reported for the first time. In our study, one patient had protrusion bordered by bone structure without gap in the medial orbital wall.

After the widespread use of CT, detailed imaging of the ethmoid bone has increased especially and also publications about the topic have increased in the literature in recent years. The cases in which the orbital contents have shown herniation into the ethmoid sinus have been generally considered as dehiscence. However, it has been observed that the presence of

dehiscence has not met the requirement of a herniation in dissection studies since Lothrop [12].

In some publications over the past 20 years, dehiscences on the medial wall of the orbita have been defined as "Zuckerkandl dehiscence" [3, 7, 19, 21, 22].

In the case report "Concomitant bilateral orbital and brain abscess" conducted by Huang et al. [7] in 2003, they referred to Zuckerkandl's own work written in 1892 and stated that dehiscences in LP were also called the Zuckerkandl dehiscence.

In 2008, Shoja et al. [21] described the scientist's life and studies in the article "Emil Zuckerkandl", and they said that the fissures in the ethmoid bone were called Zuckerkandl dehiscence.

In 2014, a paediatric case presentation titled "Bilateral orbital complications of paediatric rhinosinusitis" by Singh et al. [22] and another article "Imaging for Headache: What the neuroradiologist looks for" by Bricker and Stultz [3], it was reported that dehiscences in lamina papyracea were known as the Zuckerkandl dehiscence.

In 2014, Ozdemir and Elmas [19] carried the phrase Zuckerkandl dehiscence to the title of their article as "Recurrent sinusitis and periorbital cellulitis secondary to congenital Zuckerkandl dehiscence".

As can be seen, there is confusion in the medical literature in terms of both the distinction between dehiscence and herniation, and naming the defects in lamina papyracea as Zuckerkandl dehiscence.

In the literature, we have noticed that different authors use the terms of dehiscence, protrusion, herniation, prolapse, or even ingression for the herniation of orbital content into the ethmoid sinus [24]. In our opinion, the dehiscences that are not accompanied by orbital adipose tissue herniation in LP and those accompanied by orbital adipose tissue herniation are different entities (Figs. 3–5). Although the subject of which entity is more risky during FESS needs to be investigated; the presence of herniation accompanying the dehiscence can be a more risky situation in LP, which is mostly a thin structure, compared to the presence of only dehiscence. Therefore, we think that defining the herniation that accompanies dehiscence as only a dehiscence is an inadequate explanation.

Lamina papyracea dehiscences observed on CT are not uncommon, but misinterpretation is possible depending on quality of CT images. We agree with Meloni et al. [14] that there is no difference in terms of the vulnerability of the bone that is thin enough to be interpreted as a true dehiscence or

Figure 3. Dehiscence of medial orbital wall on axial plane computed tomography (most likely incomplete ossification).
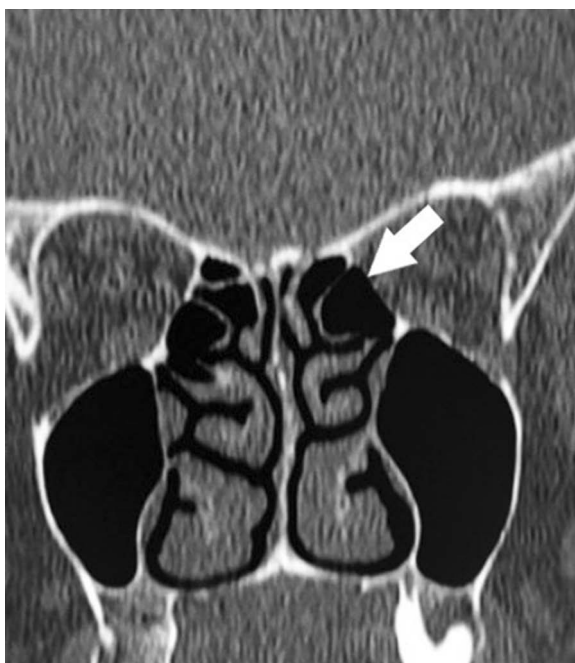
Figure 4. Dehiscence of medial orbital wall on coronal plane computed tomography (most likely incomplete ossification).

dehiscence in CT. The point we want to emphasize is that the introduction of orbital content into the ethmoid sinus, which can be expressed in protrusion/
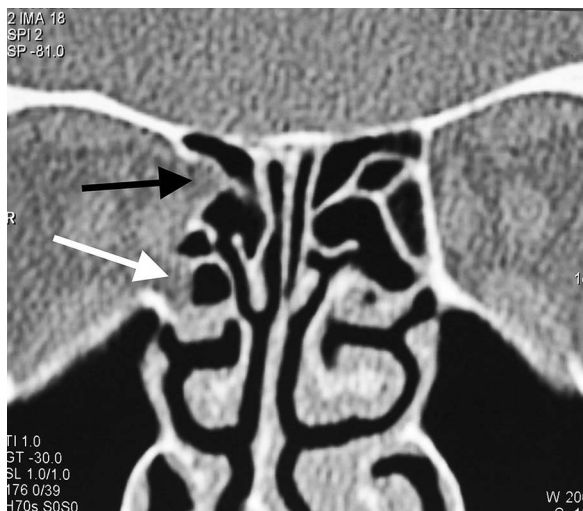
Figure 5. Orbital adipose tissue herniated from two separate localisations to the ethmoid sinus; black arrow — orbital adipose tissue herniated from superior; white arrow — orbital adipose tissue herniated from inferior.

Figure 6. Bone plus orbital fat protrusion without dehiscence on the medial orbital wall, which Lim defined in 1999 and we observed in one case.

prolapse/herniation, or otherwise, is not the same thing with the situation that does not accompany such changes and has been called dehiscence since 1869. In other words, the situation that we express as dehiscence in lamina papyracea does not always occur with herniation.

Therefore, using the term "dehiscence" for gaps and defects while interpreting the images and using the term "herniation" for the entry of the orbital content into the ethmoid sinus accompanied by de-

hiscence will eliminate the confusion of situations. In addition, the terms of "protrusion" or "bone protrusion" or "bone and orbital fat protrusion" will be more explanatory for the definition of protrusion without dehiscence in the medial orbital wall, which was reported by Lim et al. [11], and such an image is already seen in one of our patients (Fig. 6). In our opinion, calling the LP dehiscence 'Zuckerkandl dehiscence' will be a preference that may cause misunderstandings rather than specifying the situation.

In our study, the rate of dehiscence (loss of bone continuity) without herniation was found to be higher than in most of the research. There may be three explanations for this high rate of dehiscence. First, the inability to distinguish the low-density bone structure below a certain thickness in our CT examinations. Second, the excessive thinning of the medial orbital wall caused by the previous sinusitis in our study group. Third, the fact that most of the research only defines orbital adipose tissue herniations as dehiscence may be the explanation for our high rate of dehiscence. It was thought that these interpretations could be checked by microdissection of samples with dehiscence in cadaver specimens undergoing CT.

CONCLUSIONS

As a result, we believe that radiologists should investigate the presence of medial orbital wall dehiscence whether there is a herniation or not, during the interpretation of paranasal sinus CT, and they should pay strict attention to the correct use of the words "herniation, dehiscence/gap, protrusion" in their comments and studies.

Conflict of interest: None declared

REFERENCES

1. Bhatti M, Stankiewicz J. Ophthalmic complications of endoscopic sinus surgery. Surv Ophthalmol. 2003; 48(4): 389–402, doi: 10.1016/s0039-6257(03)00055-9.
2. Bolger WE, Butzin CA, Parsons DS. Paranasal sinus bony anatomic variations and mucosal abnormalities: CT analysis for endoscopic sinus surgery. Laryngoscope. 1991; 101(1 Pt 1): 56–64, doi: 10.1288/00005537-199101000-00010, indexed in Pubmed: 1984551.
3. Bricker A, Stultz T. Imaging for headache: what the neuroradiologist looks for. Otolaryngol Clin North Am. 2014; 47(2): 197–219, doi: 10.1016/j.otc.2013.10.009, indexed in Pubmed: 24680489.
4. Dankbaar JW, van Bemmel AJM, Pameijer FA. Imaging findings of the orbital and intracranial complications of acute bacterial rhinosinusitis. Insights Imaging. 2015;

6(5): 509–518, doi: 10.1007/s13244-015-0424-y, indexed in Pubmed: 26253983.

5. Han M, Chang K, Min Y, et al. Nontraumatic prolapse of the orbital contents into the ethmoid sinus: Evaluation with screening sinus CT. Am J Otolaryngol. 1996; 17(3): 184–189, doi: 10.1016/s0196-0709(96)90058-7.

6. Harris TJ. Atypical mastoiditis — its cause, pathology, symptomatology and diagnosis. Laryngoscope. 1911; 21(7): 775–783, doi: 10.1288/00005537-191107000-00005.

7. Huang SF, Lee TJ, Lin KL. Concomitant bilateral orbital and brain abscesses--unusual complications of pediatric rhinosinusitis. Chang Gung Med J. 2005; 28(1): 51–55, indexed in Pubmed: 15804149.

8. Hyrtl J. Vergangenheit und Gegenwart des Museums für Menschliche Anatomie an der Wiener Universität. Wilhelm von Braumüller, Wien 1869.

9. Kitaguchi Y, Takahashi Y, Mupas-Uy J, et al. Characteristics of dehiscence of lamina papyracea found on computed tomography before orbital and endoscopic endonasal surgeries. J Craniofac Surg. 2016; 27(7): e662–e665, doi: 10.1097/SCS.0000000000003005, indexed in Pubmed: 27536917.

10. Lang J, Schäfer K. [Ethmoidal arteries: origin, course, regions supplied and anastomoses]. Acta Anat (Basel). 1979; 104(2): 183–197, indexed in Pubmed: 442972.

11. Lim JC, Hadfield PJ, Ghiacy S, et al. Medial orbital protrusion: a potentially hazardous anomaly during endoscopic sinus surgery. J Laryngol Otol. 1999; 113(8): 754–755, doi: 10.1017/s0022215100145116, indexed in Pubmed: 10748855.

12. Lothrop HA. IV. The anatomy and surgery of the frontal sinus and anterior ethmoidal cells. Ann Surg. 1898; 28(5): 611–638, indexed in Pubmed: 17860649.

13. Makariou E, Patsalides A, Harley E. Dehiscence of the lamina papyracea: MRI findings. Clin Radiol Extra. 2004; 59(5): 40–42, doi: 10.1016/j.cradex.2003.12.003.

14. Meloni F, Mini R, Rovasio S, et al. Anatomic variations of surgical importance in ethmoid labyrinth and sphenoid sinus. A study of radiological anatomy. Surg Radiol Anat. 1992; 14(1): 65–70, doi: 10.1007/BF01628046, indexed in Pubmed: 1589850.

15. Meyers RM, Valvassori G. Interpretation of anatomic variations of computed tomography scans of the sinuses: a surgeon's perspective. Laryngoscope. 1998; 108(3): 422–425, doi: 10.1097/00005537-199803000-00020, indexed in Pubmed: 9504618.

16. Moulin G, Dessi P, Chagnaud C, et al. Dehiscence of the lamina papyracea of the ethmoid bone: CT findings. Am J Neuroradiol. 1994; 15(1): 151–153, indexed in Pubmed: 8141047.

17. Onodi A, Goldstein MA. The oculo-orbital, intracranial and cerebral complications of diseases of the nasal accessory sinuses. Laryngoscope. 1909; 19(11): 801–822, doi: 10.1288/00005537-190911000-00001.

18. Onodi A. Die Stirnhöhle: Beiträge Zur Topographisch — chirurgischen Anatomie Und Zur Lehre Von Den Erkrankungen Der Stirnhöhle. Alfred Hölder, Wien 1909.

19. Ozdemir O, Elmas B. Recurrent Sinusitis and Periorbital Cellulitis Secondary to Congenital Zuckerkandl Dehiscence. MOJ Immunology. 2014; 1(5), doi: 10.15406/moji.2014.01.00027.

20. Seeley MJ, Waterhouse DR, Shetty S, et al. Boundary issues: a case of nontraumatic bilateral dehiscence of the lamina papyracea. Arch Otolaryngol Head Neck Surg. 2010; 136(1): 88–89, doi: 10.1001/archoto.2009.196, indexed in Pubmed: 20083785.

21. Shoja MM, Tubbs RS, Loukas M, et al. Emil Zuckerkandl (1849-1910): anatomist and pathologist. Ann Anat. 2008; 190(1): 33–36, doi: 10.1016/j.aanat.2007.09.001, indexed in Pubmed: 18342140.

22. Singh SK, James E, Sabarigirish K, et al. Bilateral orbital complications of paediatric rhinosinusitis. Med J Armed Forces India. 2014; 70(1): 68–72, doi: 10.1016/j.mjafi.2012.11.015, indexed in Pubmed: 24623951.

23. Teatini G, Simonetti G, Salvolini U, et al. Computed tomography of the ethmoid labyrinth and adjacent structures. Ann Otol Rhinol Laryngol. 2016; 96(3): 239–250, doi: 10.1177/000348948709600301.

24. Wang Y, Zhang YJ, Zhu HH. [Effect of lamina papyracea ingression on orbito-ocular complications after functional endoscopic sinus surgery]. Zhonghua Er Bi Yan Hou Tou Jing Wai Ke Za Zhi. 2016; 51(8): 589–592, doi: 10.3760/cma.j.issn.1673-0860.2016.08.006, indexed in Pubmed: 27625128.

25. Yang YX, Lu QK, Liao JC, et al. Morphological characteristics of the anterior ethmoidal artery in ethmoid roof and endoscopic localization. Skull Base. 2009; 19(5): 311–317, doi: 10.1055/s-0028-1115323, indexed in Pubmed: 20190940.

26. Zuckerkandl E. Normale und pathologische Anatomie der Nasenhöhle und ihrer pneumatischen Anhange. DMW — Deutsche Medizinische Wochenschrift. 2009; 8(23): 328–329, doi: 10.1055/s-0029-1196610.

ORIGINAL ARTICLE

The use of hyoid bone dimensions in age and sex estimation in a Turkish population: a cone-beam computed tomography study

E. Köse[1], D. Göller Bulut[2]

[1]Department of Oral and Maxillofacial Radiology, Faculty of Dentistry, Aydın Adnan Menderes University, Aydın, Turkey
[2]Department of Oral and Maxillofacial Radiology, Faculty of Dentistry, Bolu Abant İzzet Baysal University, Bolu, Turkey

Background: The aim of the study was to determine sex and age from hyoid bone morphology on cone-beam computed tomography (CBCT).
Materials and methods: The study sample comprised 130 CBCT images. Eight different measurements were performed for each hyoid bone. Fusion conditions were assigned to each side of the hyoid bone separately as; unfused, partially fused, and totally fused.
Results: The hyoid length, width of the left proximal end and stature variables showed sexual dimorphism in all hyoid fusion types (p < 0.05). In young adult age group, a significant difference was found between sex and fusion types (p = 0.025). The body length (81.35%) and stature measurements (76.25%) contributed most significantly to sex estimation.
Conclusions: Patient's CBCT scans which enable reproducible and reliable measurements for bone tissues can be used for forensic procedures. Hyoid bone measurements with CBCT are useful methodology for age and sex estimation in forensic sciences with high predictive accuracy. (Folia Morphol 2022; 81, 1: 183–189)

Key words: age estimation, hyoid bone fusion, hyoid bone measurement, sex estimation

INTRODUCTION

Sex identification is an important forensic and archaeological procedure [1, 20]. Comparison of ante mortem and post mortem records and examination of bones have a crucial role for identification [20, 21]. Pelvis, skull and long bone measurements are usually used for sex estimation [20]. But these bones may be damaged — burned and fragmented — because of disasters. In such cases, determined sex is usually used as an estimation of other biological features like age and ancestry. Thus, another method using

other bones should be established for cases where the pelvis, skull and long bones are unavailable [21].

The hyoid bone originates from the branchial arches and arch cartilages [7]. It is a solitary bone without any bony articulations [5, 9]. It has muscles, ligaments and fascia attachments from cranium, mandible and pharynx that provide physiological functions; including speaking, breathing, swallowing and keeping the upper airway open during sleep [6, 7, 11, 15]. The hyoid bone has distinct morphological features that allow forensic researchers to quickly

---

identify it. U-shaped bone lies anteriorly to fourth cervical vertebra in adults and is composed of a body, two greater cornua and two lesser cornua [5, 7, 15]. These cornua which are directed postero-laterally are attached to the body by synchondrosis [15]. Some hyoid bones show a diarthrodial structure and have a gap between body/cornua bone articulation [10].

Measurements of hyoid bone and the degree of fusion between hyoid bone and greater cornua might be helpful in age and sex estimation. Several studies including cadavers, photographs, and radiographs have used hyoid bone for sex estimation [1, 7, 11, 15]. Among these techniques, radiological assessment is important for age calculation and sex estimation. It is simple, easily applicable and non-invasive method, and can be evaluated in living individuals as well as in the dead. Cone-beam computed tomography (CBCT) is a radiological imaging system that provides three-dimensional visualisation of the anatomical structures and gives realistic measurements. While there are studies evaluating hyoid bone for age and sex estimation, no study has been found that examine sexual dimorphism of hyoid bone measurements of living patients in a contemporary Turkish population with CBCT images.

The aim of this study was to evaluate the fusion between hyoid body and cornua, and hyoid bone measurements in sex estimation and aging using CBCT images.

MATERIALS AND METHODS

In this retrospective study, CBCT images, which were performed because of patients' dental problems, from database of oral and maxillofacial radiology department of Aydın Adnan Menderes University were used. The study was approved by the local ethical committee (No: 2020/36). For this study, 650 CBCT scans from lower jaw that were performed between October 2014 and February 2019 were visually inspected. Fractures and acquired or congenital abnormalities of hyoid bone were excluded from study. Images with whole hyoid bone structure visible and without any artefacts were included. According to inclusion and exclusion criteria, a total of 130 CBCT scans were selected for the study. The CBCT scans were obtained using standard exposure parameters and patient positioning protocols (field of view: 20 × 10 cm and 20 × 15 cm, resolution: 0.2–0.4 mm, 80–84 kVp, 8–12 mA) with a CBCT unit (Planmeca promax 3D Max, Helsinki, Finland). Romexis version 4.6.2. software (Planmeca, Helsinki, Finland) was used for hyoid bone measurements. Inter- and intra-observer

rates were calculated by re-evaluating 30 randomly selected subset data (15 males and 15 females). The original author examined and measured all scans and the subset data. Co-author examined and measured the subset data to assess interobserver error. Coefficient of reliability (R) and relative technical error of measurements (rTEM, %) were calculated. R value > 0.75 was considered sufficiently exact which reveals the quantity of the between-subject variance free of measurement errors [25]. The acceptance ranges of rTEM for intraobserver errors and interobserver errors were < 1.5% and < 2.0%, respectively [24].

Axial, sagittal, coronal and oblique views were investigated. All of the measurements were made from axial images that were obtained and corrected with slice-by-slice tracing of coronal and sagittal images. Eight measurements were performed for each hyoid bone as below:
— Hyoid width (Hyd-W) — linear distance between the most distal points of the greater cornua of the hyoid (Fig. 1A);
— Body length (B-L) — linear distance between the right and left most lateral surfaces of the hyoid body (Fig. 1A);
— Hyoid length (Hyd-L) — perpendicular length from the most anterior surface of the hyoid body to the line that links the most lateral points of the greater cornua of the hyoid body (Fig. 1B);
— Width of the left proximal end (LP-W) and right proximal end (RP-W) maximum width of the proximal end of the left and right greater cornua (Fig. 1C);
— Diameter of the left distal end (LD-D) and right distal end (RD-D) maximum diameter of the distal end of the left and right greater cornua (Fig. 1C);
— Hyoid bone length sum of distances (stature): bilateral linear distance between the most distal point of greater cornua and middle point of proximal surface of greater cornua, and bilateral linear distance between middle point of distal surface of hyoid body and the most proximal point of hyoid bone (Fig. 1D).

Fusion conditions were assigned to each side of the hyoid bone separately. The smallest distance between the greater cornua and hyoid body on each side was assessed and following three grades defined as below:
— Unfused — there is a space between the nearest points of the hyoid body and greater cornua without any contact (Fig. 2A);
— Partially fused — there is a line with lower intensity between partially fused body and greater cornua. Fusion is not uniform (Fig. 2B);
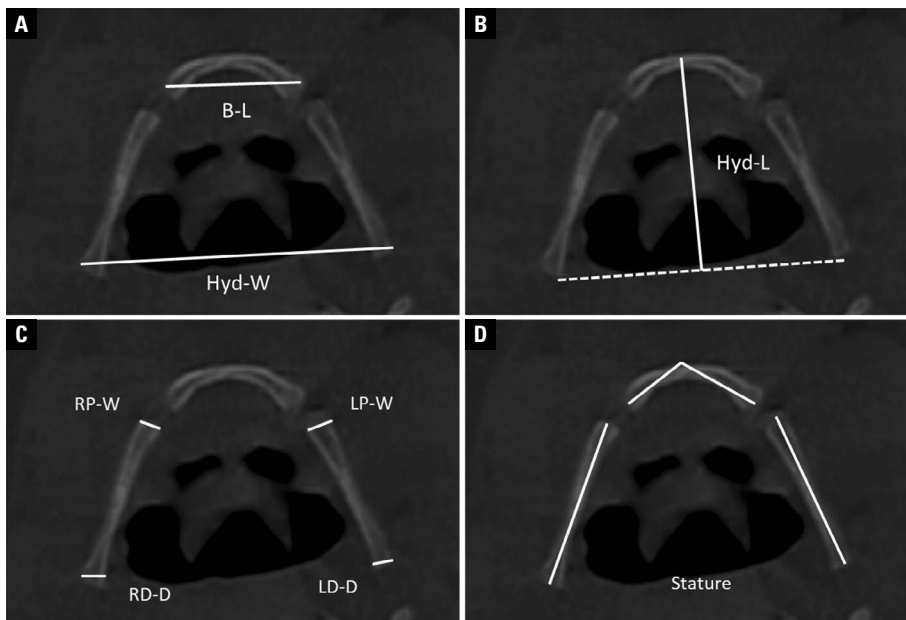
Figure 1. Measurements of hyoid bone; **A**. B-L — body length; Hyd-W — hyoid width; **B**. Hyd-L — hyoid length; **C**. RP-W — width of the right proximal end; RD-D — diameter of the right distal end; LP-W — width of the left proximal end; LD-D — diameter of the left distal end; **D**. Stature: total length of hyoid.

Figure 2. Fusion conditions of hyoid; **A**. Unfused; **B**. Partial fused; **C**. Totally fused.

— Totally fused — there is a uniform fusion without any space between the hyoid body and greater cornua. A line of fusion may be visible or invisible as one continuous structure (Fig. 2C).

Statistical analysis

Statistical analyses were done on a personal computer using SPSS (IBM Statistical Package for the Social Sciences Statistics; New York, ABD) version 21.0 computer software. Means, standard deviations, and ranges of all hyoid bone measurements were calculated according to age. The normality was assessed using the Shapiro-Wilk test. The mean differences between the sexes in the all hyoid measurement data were assessed using two-sample independent t-test. The association of fusion types with sex and age groups were analysed with χ^2 test and Pearson

correlation. Statistically significant level was considered at a p value of < 0.05.

Univariate discriminant function analysis for sex classification was used for all measurements. Then stepwise discriminant function analysis was used to find most accurate sex classification. Function at group centroids were calculated, sectioning points for each measurements were calculated by adding group centroids and dividing their total by 2. Wilk's lambda was calculated. Correct prediction rates were calculated by the leave-one-out cross validation test.

RESULTS

Table 1 demonstrates the R and rTEMs values. The R values ranged from 0.96 to 0.99. The rTEMs values for interobserver and intraobserver errors ranged

Table 1. The coefficient of reliability (R) and the relative technical error of measurement (rTEM) (n = 30)

Variable	Intraobserver		Interobserver	
	R	rTEM	R	rTEM
Hyd-W	0.96	1.54%	0.96	1.24%
B-L	0.98	1.32%	0.96	1.85%
Hyd-L	0.99	1.45%	0.97	1.63%
RD-D	0.99	1.03%	0.98	1.25%
RP-W	0.98	0.88%	0.97	1.12%
LD-D	0.99	1.35%	0.99	1.54%
LP-W	0.98	1.66%	0.96	1.36%
Stature	0.96	1.08%	0.96	1.94%

Hyd-W — hyoid width; B-L — body length; Hyd-L — hyoid length; RD-D — diameter of the right distal end; RP-W — width of the right proximal end; LD-D — diameter of the left distal end; LP-W — width of the left proximal end

from 1.03% to 1.88% and from 1.12% to 1.94%, respectively. The mean, standard deviation, and ranges of all hyoid bone measurements according to gender were shown in Table 2. There were significant differences between sexes for all measurements except the LD-D (p = 0.437). There is no significant difference in the mean age of genders (p = 0.123). No significant difference was found between RD-D and LD-D, RP-W and LP-W (p = 0.448 and p = 0.700, respectively).

The measurement means and standard deviations according to fusion types for males and females in the population are shown in Table 3. The mean age of subjects in all hyoid fusion types showed no difference with regard to sex. Outcomes of the two-sample independent t-test for sexual differences between genders are shown in Table 4. The Hyd-L, LP-W and stature variables showed sexual dimorphism in all hyoid fusion types.

Types of fusion according to sex and age groups are presented in Table 5. In young adult age group, a significant difference was found between sex and fusion types (p = 0.025), although there were no significant difference in adults and < 20 years groups (p = 0.068 and p = 0.150, respectively). The results of univariate discriminant function analyses for the hyoid bone measurements are shown in Table 6. The B-L (81.35%) and stature measurements (76.25%) contributed most significantly to sex estimation.

DISCUSSION

In forensic science, it is important that measurements made on any structure be reproducible and reliable. Additionally, measurements should be identified and explained clearly to understand definition [14]. Several studies have used hyoid bone measurements for sex and age estimation. Most of these studies included direct bone measurements or pictures of hyoid bones extracted from autopsies or anatomical collections [1, 11, 12, 14, 15, 22, 23]. Some of studies focused on two-dimensional computed tomography images from databases [7, 21] or X-ray films with various projections [17]. In this study, measurements of hyoid bone were performed on CBCT images which were made by two observers and intra-observer and inter-observer reliability was found to be high. This shows that the measurements made on the CBCT image of the hyoid bone are reproducible and reliable.

In this study, the mean age of the patients with fused hyoid bone was found to be higher than the unfused and partial fused hyoid bone. In previous studies [8, 18, 21], it was reported that the ossification of the hyoid bone increased with age. This finding is

Table 2. Descriptive statistic results for age and measurements of all hyoid bones and comparison using t tests

	Male		Female		P value	Total	
	Mean ± SD	Range	Mean ± SD	Range		Mean ± SD	Range
Age [years]	33.04 ± 13.42	15–55	35.29 ± 15.20	14–55	0.123	34.37 ± 14.49	14–55
Hyd-W	45.20 ± 5.62	35.40–58.00	42.32 ± 4.64	28.60–54.50	0.001*	43.50 ± 5.15	28.60–8.00
B-L	23.75 ± 2.49	18.20–28.70	20.39 ± 2.12	13.20–24.70	< 0.001*	21.77 ± 2.81	13.20–28.70
Hyd-L	37.74 ± 4.00	30.20–46.40	32.28 ± 3.01	26.40–37.50	< 0.001*	34.52 ± 4.36	26.40–46.40
RD-D	3.38 ± 0.73	2.00–4.80	3.11 ± 0.55	2.10–4.50	0.017*	3.22 ± 0.64	2.00–4.80
RP-W	3.52 ± 0.77	2.10–4.90	2.83 ± 0.51	2.00–4.10	< 0.001*	3.11 ± 0.72	2.00–4.90
LD-D	3.32 ± 0.83	2.00–5.00	3.22 ± 0.71	2.00–5.20	0.437	3.26 ± 0.76	2.00–5.20
LP-W	3.42 ± 0.79	2.00–5.10	2.94 ± 0.51	1.80–4.10	< 0.001*	3.13 ± 0.68	1.80–5.10
Stature	86.30 ± 7.38	73.00–103.00	76.73 ± 6.84	60.40–90.40	< 0.001*	80.65 ± 8.48	60.40–103.00

SD — standard deviation; Hyd-W — hyoid width; B-L — body length; Hyd-L — hyoid length; RD-D — diameter of the right distal end; RP-W — width of the right proximal end; LD-D — diameter of the left distal end; LP-W — width of the left proximal end

Table 3. Descriptive statistic results for the measurements of hyoid bones according to fusion types

	Sex	Unfused hyoid		Partially fused hyoid		Fused hyoid	
		Mean	SD	Mean	SD	Mean	SD
Age (years)	Total	35.96	14.65	33.7	15.17	39.75	16.01
Hyd-W	Male	46.86	3.05	44.93	6.46	44.13	1.50
	Female	39.54	5.45	42.99	4.17	42.33	2.05
	Total	42.59	5.83	43.76	5.25	43.23	1.96
B-L	Male	22.82	1.46	24.34	2.46	21.60	2.63
	Female	17.71	2.10	20.97	1.69	21.06	0.90
	Total	19.84	3.15	22.30	2.61	21.33	1.89
Hyd-L	Male	37.38	2.23	38.28	4.48	34.93	0.63
	Female	29.97	2.32	32.94	2.97	31.33	2.06
	Total	33.05	4.35	35.06	4.47	33.13	2.37
RD-D	Male	3.26	0.50	3.42	0.82	3.30	0.23
	Female	2.92	0.47	3.17	0.56	2.96	0.50
	Total	3.06	.50	3.27	0.69	3.13	0.41
RP-W	Male	3.18	0.61	3.63	0.78	3.43	0.91
	Female	2.47	0.34	2.92	0.53	2.83	0.36
	Total	2.76	.58	3.20	0.72	3.13	0.73
LD-D	Male	3.82	0.91	3.24	0.80	3.03	0.59
	Female	2.51	0.34	3.36	0.64	3.46	1.03
	Total	3.05	0.91	3.31	0.71	3.25	0.83
LP-W	Male	3.48	0.29	3.57	0.79	2.36	0.49
	Female	2.65	0.13	2.93	0.51	3.7	0.22
	Total	3.00	.46	3.18	0.71	3.05	0.80
Stature	Male	82.38	6.32	88.10	7.49	81.50	2.72
	Female	72.78	8.99	77.77	6.21	75.90	3.74
	Total	76.78	9.20	81.86	8.41	78.70	4.27

SD — standard deviation; Hyd-W — hyoid width; B-L — body length; Hyd-L — hyoid length; RD-D — diameter of the right distal end; RP-W — width of the right proximal end; LD-D — diameter of the left distal end; LP-W — width of the left proximal end

Table 4. Sexual dimorphisms in the population

	Un-fused hyoids				Partially fused hyoids				Fused hyoids			
	MD [mm]	t-value	DF	p-value	MD [mm]	t-value	DF	p-value	MD [mm]	t-value	DF	p-value
Hyd-W	7.13	3.82	22	0.001*	1.93	1.78	94	0.078	1.80	1.72	10	0.115
B-L	5.10	6.60	22	< 0.001*	3.37	7.94	94	< 0.001*	0.53	0.46	10	0.649
Hyd-L	7.40	7.81	22	< 0.001*	5.33	7.01	94	< 0.001*	3.60	4.08	10	0.002*
RD-D	0.33	1.64	22	0.114	0.25	1.78	94	0.078	0.33	1.45	10	0.176
RP-W	0.70	3.61	22	0.002*	0.71	5.29	94	< 0.001*	0.60	1.49	10	0.167
LD-D	1.30	4.90	22	< 0.001*	–0.12	–0.82	94	0.410	-0.43	–0.89	10	0.394
LP-W	0.82	9.27	22	< 0.001*	0.64	4.80	94	< 0.001*	–1.36	–6.18	10	< 0.001*
Stature	9.59	2.89	22	0.008*	10.32	7.33	94	< 0.001*	5.60	2.96	10	0.014*

*Statistical significance level is p < 0.05; MD — mean difference; DF — degrees of freedom; Hyd-W — hyoid width; B-L — body length; Hyd-L — hyoid length; RD-D — diameter of the right distal end; RP-W — width of the right proximal end; LD-D — diameter of the left distal end; LP-W — width of the left proximal end

consistent with the results of this study. Consistent with the results of previous studies [5, 14, 19, 21, 23], the mean values of all measurements of hyoid bone in all fusion types except LD-D were higher in males than females. Similarly, Logar et al. [14] reported that there was no significant difference between the sexes on the average of the maximum height of the upper end of the both left and right cornua.

Table 5. Male and female and fusion types with regard to age groups

Age groups	Sex	Fusion types			P-value
		1 (non-fusion)	2 (partial fusion)	3 (fusion)	
< 20 years	Male	24 (85.0%)	6 (15.0%)	–	0.150
	Female	22 (55.0%)	14 (35.0%)	4 (10.0%)	
	Total	59 (71%)	20 (25.0%)	4 (5.0%)	
Young adult (20–30 years)	Male	24 (75%)	2 (6.2%)	6 (18.8%)	0.025*
	Female	48 (92.4%)	2 (3.8%)	2 (3.8%)	
	Total	72 (85.7%)	4 (4.8%)	8 (9.5%)	
Adult (31–55 years)	Male	26 (72.2%)	4 (11.1%)	6 (16.7%)	0.068
	Female	58 (90.6%)	–	6 (9.4%)	
	Total	84 (84.0%)	4 (4.0%)	12 (12.0%)	

*Statistical significance level is $p < 0.05$

Table 6. Discriminant functions for all hyoid bones in the population

	Group centroid		Sectioning point	Wilks' lambda	Eigenvalue	Canonical correlation	Correct prediction rates (%)		
	Male	Female					Male	Female	Overall
Hyd-W	0.342	−0.237	0.052	0.924	0.082	0.275	29.6	84.6	57.1
B-L	0.871	−0.603	0.134	0.652	0.533	0.590	70.4	92.3	81.35
Hyd-L	0.933	−0.646	0.143	0.620	0.612	0.616	59.3	87.2	73.25
RD-D	0.252	−0.174	0.036	0.957	0.045	0.207	22.2	89.7	55.95
RP-W	0.643	−0.445	0.099	0.775	0.291	0.475	51.9	87.2	69.55
LP-W	0.441	−0.305	0.068	0.880	0.136	0.347	40.7	79.5	60.1
Stature	0.800	−0.554	0.123	0.690	0.450	0.557	70.4	82.1	76.25

Since the left distal diameter is not statistically significant, it is not included in the model. Hyd-W — hyoid width; B-L — body length; Hyd-L — hyoid length; RD-D — diameter of the right distal end; RP-W — width of the right proximal end; LP-W — width of the left proximal end

All measurements except RD-D of unfused hyoid bone measurements showed sexual dimorphism in present study. B-L, Hyd-L, RP-W, LP-W and stature measurements of partially fused hyoid bone and Hyd-L, LP-W and stature measurements of fused hyoid bone showed sexual dimorphism. Although Reesink et al. [17] did not find any significant sex difference in the length of the cornu major, in our study Hyd-W of unfused hyoid bone measurements showed sexual dimorphism consisted with D'Anastasio et al. [2] and Shimizu et al. [18]. In the studies of Leksan et al. [13] and Shimizu et al. [18] B-L in males was significantly longer than that in females in all age groups which is concordant with our unfused and partially fused hyoid bone measurements. This means that discriminant function equations obtained from parameters showing sexual dimorphism can be used for sex determination.

In this study, B-L and Hyd-L showed a high prediction rate. Similarly, in the study of Torimitsu et al. [21] and Urbanová et al. [23], Hyd-L and B-L showed

the highest level of sexual dimorphism. In addition, Pollard et al. [16] and Mukhopadhyay [15] previously reported that the female hyoid bones were generally large; therefore, the total anteroposterior length was reported to be more useful in predicting sex than Hyd-W. In this study, B-L achieved a successful sexual prediction rate of > 80%. Considering these results, it can be said that sex can be predicted even when there is no bone other than hyoid bone.

With the introduction of CBCT in dentistry, there has been an improvement in the ability to analyse bone structures in three-dimensional imaging [3]. Multiplanar images obtained from all planes were used to evaluate bone morphology. One-to-one measurements of bone structures can be made on sections formed in desired thickness and desired plane. Today, CBCT is an easily accessible and easily acquired imaging system with a relatively low radiation dose. It can be obtained from individuals so that measurements in the images can be used to estimate age and gender in forensic cases [4].

CONCLUSIONS

In this study, hyoid bone showed important morphologic changes and differences according to age and sex which can be useful in forensic science for age and sex estimation with high predictive rates. Imaging hyoid bone with CBCT is simple, easily applicable and very reproducible methodology. So, in forensic medicine, accurate measurements and evaluation can be performed by CBCT in living individuals with lower radiation dose. To support the results of the study, new studies are needed in which the distribution of sex is equal and the age groups are similar and with volume measurements.

Conflict of interest: None declared

REFERENCES

1. Balseven-Odabasi A, Yalcinozan E, Keten A, et al. Age and sex estimation by metric measurements and fusion of hyoid bone in a Turkish population. J Forensic Leg Med. 2013; 20(5): 496–501, doi: 10.1016/j.jflm.2013.03.022, indexed in Pubmed: 23756521.
2. D'Anastasio R, Viciano J, Di Nicola M, et al. Estimation of sex from the hyoid body in skeletal individuals from archeological sites. Homo. 2014; 65(4): 311–321, doi: 10.1016/j.jchb.2014.01.002, indexed in Pubmed: 24767538.
3. da Costa ED, Roque-Torres GD, Brasil DM, et al. Correlation between the position of hyoid bone and subregions of the pharyngeal airway space in lateral cephalometry and cone beam computed tomography. Angle Orthod. 2017; 87(5): 688–695, doi: 10.2319/022217-133.1, indexed in Pubmed: 28686091.
4. El-Shal O, Shaaban A. Evaluation of different mandibular measurements by cone beam computed tomography as a forensic age & gender determination tools. Al-Azhar D J. 2019; 6(4): 445–452, doi: 10.21608/adjg.2019.7749.1098.
5. Fakhry N, Puymerail L, Michel J, et al. Analysis of hyoid bone using 3D geometric morphometrics: an anatomical study and discussion of potential clinical implications. Dysphagia. 2013; 28(3): 435–445, doi: 10.1007/s00455-013-9457-x, indexed in Pubmed: 23456326.
6. Feng X, Todd T, Hu Y, et al. Age-related changes of hyoid bone position in healthy older adults with aspiration. Laryngoscope. 2014; 124(6): E231–E236, doi: 10.1002/lary.24453, indexed in Pubmed: 24227680.
7. Fisher E, Austin D, Werner HM, et al. Hyoid bone fusion and bone density across the lifespan: prediction of age and sex. Forensic Sci Med Pathol. 2016; 12(2): 146–157, doi: 10.1007/s12024-016-9769-x, indexed in Pubmed: 27114259.
8. Gupta A, Kohli A, Aggarwal NK, et al. Study of age of fusion of hyoid bone. Leg Med (Tokyo). 2008; 10(5): 253–256, doi: 10.1016/j.legalmed.2008.03.002, indexed in Pubmed: 18442944.
9. Ha JG, Min HJ, Ahn SH, et al. The dimension of hyoid bone is independently associated with the severity of obstructive sleep apnea. PLoS One. 2013; 8(12): e81590, doi: 10.1371/journal.pone.0081590, indexed in Pubmed: 24312562.
10. Kanetaka H, Shimizu Y, Kano M, et al. Synostosis of the joint between the body and greater cornu of the human hyoid bone. Clin Anat. 2011; 24(7): 837–842, doi: 10.1002/ca.21183, indexed in Pubmed: 21538567.
11. Kim DI, Lee UY, Park DK, et al. Morphometrics of the hyoid bone for human sex determination from digital photographs. J Forensic Sci. 2006; 51(5): 979–984, doi: 10.1111/j.1556-4029.2006.00223.x, indexed in Pubmed: 17018072.
12. Kindschuh SC, Dupras TL, Cowgill LW. Determination of sex from the hyoid bone. Am J Phys Anthropol. 2010; 143(2): 279–284, doi: 10.1002/ajpa.21315, indexed in Pubmed: 20853481.
13. Leksan I, Marcikić M, Nikolić V, et al. Morphological classification and sexual dimorphism of hyoid bone: new approach. Coll Antropol. 2005; 29(1): 237–242, indexed in Pubmed: 16117329.
14. Logar CJ, Peckmann TR, Meek S, et al. Determination of sex from the hyoid bone in a contemporary White population. J Forensic Leg Med. 2016; 39: 34–41, doi: 10.1016/j.jflm.2016.01.004, indexed in Pubmed: 26817970.
15. Mukhopadhyay PP. Morphometric features and sexual dimorphism of adult hyoid bone: a population specific study with forensic implications. J Forensic Leg Med. 2010; 17(6): 321–324, doi: 10.1016/j.jflm.2010.04.014, indexed in Pubmed: 20650421.
16. Pollard J, Piercecchi-Marti MD, Thollon L, et al. Mechanisms of hyoid bone fracture after modelling: evaluation of anthropological criteria defining two relevant models. Forensic Sci Int. 2011; 212(1-3): 274.e1–274.e5, doi: 10.1016/j.forsciint.2011.06.020, indexed in Pubmed: 21764532.
17. Reesink EM, Immerseel AV, Brand R, et al. Sexual dimorphism of the hyoid bone? Int J Osteoarchaeol. 1999; 9(5): 357–360, doi: 10.1002/(sici)1099-1212(199909/10)9:5<357::aid-oa494>3.0.co;2-j.
18. Shimizu Y, Kanetaka H, Kim YH, et al. Age-related morphological changes in the human hyoid bone. Cells Tissues Organs. 2005; 180(3): 185–192, doi: 10.1159/000088247, indexed in Pubmed: 16260865.
19. Soltani S, Aghakhani K, Fallah F. Sex prediction potential of hyoid metric measurements in Iranian adults. Leg Med (Tokyo). 2017; 25: 6–10, doi: 10.1016/j.legalmed.2016.12.010, indexed in Pubmed: 28457512.
20. Teke HY, Duran S, Canturk N, et al. Determination of gender by measuring the size of the maxillary sinuses in computerized tomography scans. Surg Radiol Anat. 2007; 29(1): 9–13, doi: 10.1007/s00276-006-0157-1, indexed in Pubmed: 17171233.
21. Torimitsu S, Makino Y, Saitoh H, et al. Determination of sex on the basis of hyoid bone measurements in a Japanese population using multidetector computed tomography. Int J Legal Med. 2018; 132(3): 907–914, doi: 10.1007/s00414-017-1728-x, indexed in Pubmed: 29098386.
22. Urbanová P, Hejna P, Zátopková L, et al. The morphology of human hyoid bone in relation to sex, age and body proportions. Homo. 2013; 64(3): 190–204, doi: 10.1016/j.jchb.2013.03.005, indexed in Pubmed: 23648280.
23. Urbanová P, Hejna P, Zátopková L, et al. What is the appropriate approach in sex determination of hyoid bones? J Forensic Leg Med. 2013; 20(8): 996–1003, doi: 10.1016/j.jflm.2013.08.010, indexed in Pubmed: 24237807.
24. Ward RE, Jamison PL. Measurement precision and reliability in craniofacial anthropometry: implications and suggestions for clinical applications. J Craniofac Genet Dev Biol. 1991; 11(3): 156–164, indexed in Pubmed: 1761648.
25. Weinberg SM, Scott NM, Neiswanger K, et al. Intraobserver error associated with measurements of the hand. Am J Hum Biol. 2005; 17(3): 368–371, doi: 10.1002/ajhb.20129, indexed in Pubmed: 15849702.

ORIGINAL ARTICLE

VIA MEDICA

The influence of the morphometric parameters of the intercondylar notch on occurrence of meniscofemoral ligaments

M. Minic[1] , I. Zivanovic-Macuzic[1] , M. Jakovcevski[1], M. Kovacevic[1] ,
S. Minic[2], D. Jeremic[1]

[1]Department of Anatomy, Faculty of Medical Sciences, University of Kragujevac, Serbia
[2]College of Applied Health Sciences, Ćuprija, Serbia

Background: The purpose of this study was to examine the existence of correlation between the morphometric parameters of the intercondylar notch of the femur and the occurrence of meniscofemoral ligaments (MFLs) and if there is any relationship in the running angle (RA) value between narrowed and normal sized intercondylar notch.

Materials and methods: Coronal, sagittal and horizontal magnetic resonance (MR) images of 90 patients with specified exclusion criteria were included in this study. The χ^2 test was used for statistical analysis. In our research either one or both MFLs were identified in 70 (77.8%) of the 90 coronal MR images. In normal sized intercondylar notch, MFLs was seen in 39 (43.3%) cases and on 31 (34.4%) MR images with narrowed intercondylar notch.

Results: A significant correlation was established between the occurrence of the MFL and morphometric parameters of the intercondylar notch (p < 0.05). In normal sized intercondylar notch, 12 posterior meniscofemoral ligaments (pMFLs) of type I were detected (RA value 42°), 8 of type II (RA value 33°), 5 of type III (RA value 23°) and two were of indeterminate type, whilst 10 anterior meniscofemoral ligaments (aMFLs) were of type I (RA value 39°), 7 of type II (RA value 31°), 2 of type III (RA value 25°) and the remaining 6 were indeterminate. In narrowed intercondylar notch, 10 ligaments of pMFLs were of type I (RA value 30°), 8 of type II (RA value 25°), 5 of type III (RA value 20°), 10 ligaments of aMFLs were of type I (RA value 35°) and 9 were indeterminate. Statistically significant differences in the value of the running angle of pMFL type I and of type II were evaluated between two groups with different shaped intercondylar notch (p < 0.05).

Conclusions: The results shown in our study may be useful in medical clinical practice, reconstructive surgery, interpretation of knee MR images as well as genetic research. (Folia Morphol 2022; 81, 1: 190–195)

Key words: intercondylar notch, meniscofemoral ligament, knee and magnetic resonance

Address for correspondence: Dr. I. Zivanovic-Macuzic, Department of Anatomy, Faculty of Medical Sciences, University of Kragujevac, Kragujevac, Serbia, e-mail: ivanaanatom@yahoo.com

INTRODUCTION

The intercondylar notch (IN) is located on the posterior side of the distal part of the femur between the lateral and medial condyle. The roof of the notch is built by the distal extremity of the femur while its distal and posterior borders are marked by distal surface of condyles [20]. Anderson et al. [4] found that the females have a smaller IN dimensions compared to males but they found no difference in shape of the notch. Based on morphometric parameters of IN, Hutchinson et al. [14] defined two types of IN, U-shaped and A-shaped notch, while Tanzer and Lenczner [21] considered narrowed IN, as A-shaped and IN with normal with as U-shaped notch.

The variation in morphology of the femur is associated with increased risk for ligament injury. Of the ligaments in the knee joint, the anterior cruciate ligament (ACL) is the most commonly injured [19, 20, 25]. Intercondylar notch dimensions are considered as a significant predictive risk factor for ACL injury [5]. The meniscofemoral ligaments (MFLs) connect the posterior horn of the lateral meniscus to the intercondylar aspect of the medial femoral condyle, or to the posterior cruciate ligament [23]. There are two types of MFLs, depending on their position in relation to the posterior cruciate ligament (PCL). According to Amis et al. [1] the ligament of Humphry (anterior meniscofemoral ligament [aMFL]) passes anterior to the PCL and attaches distally, close to the articular cartilage. The ligament of Wrisberg (posterior meniscofemoral ligament [pMFL]) passes posterior to the PCL and attaches proximally, close to the roof of the IN [1, 2]. The aMFL is tense in knee flexion, while the pMFL is tense in knee extension. [9]. One MFL is present in 93% of specimens, whilst both ligaments co-exist more frequently in younger specimens [10, 11, 24]. According to earlier anatomical studies their incidence may range from 35% to 76% [12]. The attachments of those two ligaments are separated, which supports the theory that those are two separate structures and not, as was previously thought, two branches of the same ligament [15]. The other study suggests that they may degenerate with age [18]. It has previously been demonstrated that additional resection of the MFL further destabilised the knee joint, as well as significantly increased anterior tibial translation [8, 17].

In literature data, depending on the location of the attachment, there are three types of MFLs: 1) the ligament of type I, inserted into the medial femoral condyle and separated from the PCL; 2) the ligament of type II, attached to the proximal portion of the PCL; 3) the ligament of type III, attached to the distal portion of the PCL [7]. Cho et al. [7] defined the running angle of the MFL as the angle between the line connecting the distal surfaces of medial and lateral femoral condyles and the long axis of the MFL. The relationship between morphometric parameters of the IN and the running angle value was reported [7]. However, the influence of the morphometric parameters of the IN on the value of the running angle is poorly described in literature. On the other hand, this information could be relevant in predicting the risk of MFLs rupture and their degeneration.

The aim of this study was to determinate occurrence of MFLs depending on the IN morphometry, to examine incidence of single and both MFLs as well the absence of MFLs, to evaluate statistically significant difference between the different type of IN and finally to determinate influence of its morphology on the value of the running angle.

MATERIALS AND METHODS

The study included magnetic resonance (MR) images of 90 patients (48 males and 42 females), aged from 20 to 60 (44.68 ± 10.52) receiving a 1.5-T knee scan at our radiologic institute after the approval from ethics committee, which were taken in the period from 2010 to 2017. All MR examinations were performed on 1.5-T MR unit (Siemens Area AG, model syngo MR E11, with NUMARIS/4 software, Siemens software packages). The knee was placed in neutral position in an extremity coil. Coronal images were obtained using conventional spin-echo techniques (time to echo: 8.7 ms, repetition time: 3080 ms, field of view: 190 × 190 mm, section thickness: 3.5 mm, with 1 mm gap, voxel size: 0.6 × 0.6 × 3.5 mm). Additionally, for the measurements, we used ImageJ 1.50 g software (National Institutes of Health, USA). The following exclusion criteria were defined:
— inadequate quality of the images;
— fracture or dysplasia of the distal femur;
— previous arthroscopy or open surgery;
— osteoarthritic changes of the IN;
— varus or valgus deformity of the knee.

The following parameters on horizontal images (Fig. 1) were measured: the width of the lateral and medial femoral condyle, the notch width (NW), the total width of the distal femur. The cross section (a) on which measurements were conducted was determined on sagittal MR images, based on the vertical
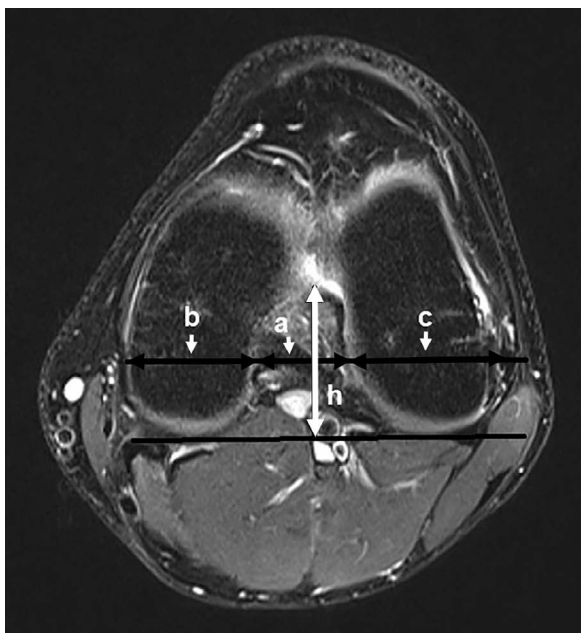
Figure 1. Intercondylar notch — A-shaped. The notch width (a), width of the medial femoral condyle (b), width of the lateral femoral condyle (c) and the notch height (h — white line with arrow on both ends) on axial magnetic resonance image in a 30-year-old man.
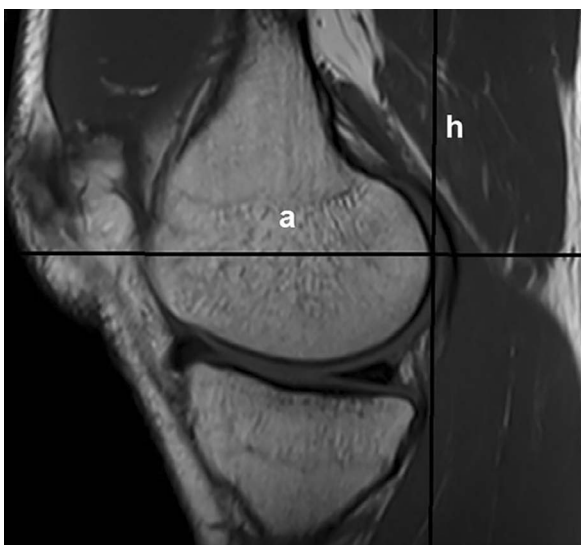
Figure 2. Cross section (a) passes through the most posterior point of the lateral and medial condyle (h — vertical line) on sagittal magnetic resonance image.

line (h) which passes through the most posterior point of the lateral and medial condyle (Fig. 2). At this level, on axial images, the measurements were done on the line which passes through the popliteal groove. The width of the medial femoral condyle (b) and the width of the lateral femoral condyle (c) were measured as the distance between the external and

internal margins of each condyle and the NW was measured as the distance between the inner most margins of femoral condyles (a). Also, the notch height (ICH) was measured on the line perpendicular to the line constructed through the most posterior point of the lateral and medial condyle of the femur, as a distance between the apex of the IN and the intersection of above mentioned lines (h) (Fig. 1).

The notch width index (NWI) — the ratio between the NW and the total width of the distal femur, was calculated. The values of the NWI of 0.270 or more were considered as normal, while values of 0.269 or less were considered as below normal [3]. Notch shape index (NSI) was defined as the ratio between the NW and the ICH. The values of the NSI of 0.532 or less indicate on stenosed type of the IN [22]. We measured the running angle of the MFL as the angle between the line connecting the distal surfaces of medial and lateral femoral condyles and the long axis of the MFL on coronal images, using in literature described method (Fig. 3) [7]. Authors have noted no significant difference in the value of the running angle between the ligament of Humphery and the ligament of Wrisberg [7], so we used these criteria for both ligaments.

All measurements were done by two independent investigators. No significant difference was found in comparison of their measurements. In order to avoid bias, the measurements were repeated by both examiners after 3 weeks on the same, randomly selected 50 MR images. The results were compared by Cohen kappa coefficient, with kappa values over the 0.8 for all measurement, which suggest very good intra- and interobserver agreement.

Statistical analysis

The statistical differences between the presence and absence MFLs as well as prevalence of A- or U-shaped IN on MR images were evaluated by χ^2 tests. A p value of less than 0.05 was regarded as statistically significant.

For every metric variable the mean, standard deviation and range were displayed. The normal distribution was tested with the Kolmogorov-Smirnov test, as well as visually through a Gaussian distribution curve over the histogram of the respective data. The homogeneity of variances was ensured through a non-significant Levene's test. For normally distributed, metric variables, differences between the groups were tested for significance with Student's t-test. In

Figure 3. A. Coronal magnetic resonance image shows the meniscofemoral ligament (arrow); **B.** The running angle of the meniscofemoral ligament as the angle between the distal surfaces of medial and lateral condyles and long axis of the meniscofemoral ligament on coronal magnetic resonance images.

the case of non-normally distributed, metric variables, the Mann-Whitney U-test was used instead.

RESULTS

According to NWI and NSI criteria we found U-shaped IN in 46 (51.2%) analysed coronal MR images and A-shaped IN in 44 (48.8%) (Table 1). There was no significant difference in incidence between the groups (p > 0.05). The MFLs was identified in 70 (77.8%) of the 90 coronal MR images scans. In group with U-shaped IN, MFLs was observed in 39 (43.3%) cases and in 31 (34.4%) cases in the group with A-shaped IN. There was a significant difference in MFLs occurrence between the groups with A- and U-shaped IN (p < 0.05).

U-shaped. The pMFL was seen alone in 30.4% (14) of cases, while aMFL was observed alone in 26.1% (12). Both ligaments were visible in 28.3% (13) while neither was found in 15.2% (7) cases. Among the pMFL, 12 ligaments were of type I (average running angle [RA] value 42°), 8 of type II (average RA value 33°), 5 of type III (average RA value 23°) and 2 were classified as indeterminate type, whilst 10 ligaments of aMFL were of type I (average RA value 39°), 7 of type II (average RA value 31°), 2 of type III (average RA value 25°) and the remaining 6 were indeterminate. Statistically significant difference in the value of the RA was observed between the types

Table 1. Mean magnetic resonance images measurements of the distal femur

	Intercondylar notch	
	U-shaped (n = 46)	A-shaped (n = 44)
Intercondylar notch width [mm]	21.23 ± 2.28	19.98 ± 1.75
Intercondylar notch height [mm]	36.77 ± 1.67	37.95 ± 1.43
Total width of distal femur [mm]	76.27 ± 7.10	76.45 ± 6.23
Notch shape index	0.577 ± 0.021	0.526 ± 0.018
Notch width index	0.278 ± 0.023	0.261 ± 0.012

(p < 0.05). No significant differences in the value of the RA between the pMFL and aMFL were noted (p > 0.05).

A-shaped. In A-shaped IN single pMFL was detected in 27.3% (12) of cases and the single aMFL ligament was observed in 18.2% (8). Both ligaments were found in 25% (11) while neither was found in 29.5% (13). Statistically significant difference in the MFLs not detected group was observed between the A and U form of IN (p < 0.05). Among the pMFLs, 10 ligaments were of type I (average RA value 30°), 8 of type II (average RA value 25°), 5 of type III (average RA value 20°), while 10 ligaments of aMFLs were of type I (average RA value 35°) and 9 were indeterminate. Statistically significant differences in the value of the running angle were noted between the type I and type II (p < 0.05).

Table 2. Incidence of the meniscofemoral ligaments (MFLs) and the values of its running angle (RA) in U-shaped and A-shaped intercondylar notch (IN)

Ligament (n)	U (n)	A (n)	U-shaped IN		A-shaped IN		P
			MFL type (n)	RA value (°)	MFL type (n)	RA value (°)	
Posterior MFL (50)	27	23	Type I (12)	42 ± 3.9	Type I (10)	30° ± 2.6	p < 0.05*
			Type II (8)	33 ± 2.3	Type II (8)	25° ± 2.2	p < 0.05*
			Type III (5)	23 ± 2.5	Type III (5)	20° ± 1.6	p > 0.05
			ID type (2)	–	ID type (/)	–	
Anterior MFL (44)	25	19	Type I (10)	39 ± 2.7	Type I (10)	35° ± 2.5	p > 0.05
			Type II (7)	31 ± 2.5	Type II (/)	–	
			Type III (2)	25 ± 1.2	Type III (/)	–	
			ID type (6)	–	ID type (9)	–	

*Statistically significant difference; U — normal sized intercondylar notch; A — narrowed intercondylar notch; ID — indeterminate type of MFL

Statistically significant differences in the value of the running angle of pMFL type I, between U- and A-shaped IN was observed (p < 0.05, Table 2).

DISCUSSION

Earlier studies of the MFLs pointed different incidence of the aMFL and pMFL. The differences can be also found between the MR images and cadaveric studies. Herzog et al. [13] found that the MR images measurements were the closest to directly measured in the cadaver. Gupte et al. [10] conducted MR images study in which 93% specimens contained at least one MFL. The aMFL was present in 74%, and the pMFL in 69%. Both ligaments were present in 50%. Bintoudi et al. [6] found the MFLs in 37% of cases, while in 7.6% of cases MFLs were absent. In MR images study performed by Cho et al. [7] the pMFL was identified in 90% of cases and aMFL was observed in 17%. Both ligaments were visible in 15% cases and neither was seen in 7.5%. Kusayama et al. [16] showed the MFL with incidences of 100% and that 46% of the specimens had both MFLs, 23% had only aMFL and the remaining 31% had a pMFL. Röhrich et al. [18] reported that the MFL exists in incidences of 94%, aMFL in incidences of 71% as was the incidence of pMFL (71%) and both MFLs was seen in 47% cases. The incidence of pMFL was higher than incidence of aMFL in most MR images studies. In anatomical studies in the literature, incidences range from 35% to 76% for the presence of at least one MFL [12].

In accordance with other authors, we found MFLs in 70 coronal MR images (77.8%), only aMFL was observed in 20.3% of cases, pMFL in 37.14%, both ligaments were present in 34.2% while in 20.3% MFLs was absent. The results presented in this paper are totally in

agreement to the findings of the most studies. However, the authors showed incidence of MFL independent of IN morphology. In our MR images study, we created two IN groups, according to NWI and NSI criteria, U- and A-shaped notch group. In group with U-shaped IN, we observed at least one MFL with incidence of 84%, while in A-shaped IN group incidence was 70.4%. Occurrence of MFLs obtained in our study is lower in narrowed notch compared with normal sized notch. This probably demonstrates that anatomical changes in this region could have an influence on development and anatomical characteristic of these ligaments. Because of the limitation of the resolution of MR imaging, 15 of the 44 aMFLs, and 2 of the 50 pMFLs did not present details at MR imaging. Similar misreading was noted in literature data [7]. The report of Cho et al. [7] showed that the average running angle was 35° in the type I, 30° in the type II and 27° in the type III. In our study, the average running angle was a little higher in the normal sized IN. The lower value of the running angle in A-shaped IN may be explained by descending medial IN wall, combined with lower ligaments attachment [25]. Statistically significant difference was found in the value of the running angle of pMFL type I, between U- and A-shaped IN. The running angle modification may be associated with narrowing of the IN, so further studies are needed to investigate this correlation.

CONCLUSIONS

After conducting the research, we found significant correlation between the IN morphometry and presence or absence of the MFLs as well as the running angle value. The data obtained in our study may be useful in medical clinical practice (reconstructive surgery), interpretation of knee MR images or genetic

research. Our results suggest that it is possible to determine which patient have narrower IN based on the running angle value. Further study is needed to determine if a correlation exists between morphometry of IN and the value of the running angle.

Conflict of interest: None declared

REFERENCES

1. Amis AA. The biomechanics of ligaments. In: Jenkins DHR (ed.). Ligament injuries and their treatment. Chapman and Hall, London 1985: 3–28.
2. Amis AA, Gupte CM, Bull AMJ, et al. Anatomy of the posterior cruciate ligament and the meniscofemoral ligaments. Knee Surg Sports Traumatol Arthrosc. 2006; 14(3): 257–263, doi: 10.1007/s00167-005-0686-x, indexed in Pubmed: 16228178.
3. Al-Saeed O, Brown M, Athyal R, et al. Association of femoral intercondylar notch morphology, width index and the risk of anterior cruciate ligament injury. Knee Surg Sports Traumatol Arthrosc. 2013; 21(3): 678–682, doi: 10.1007/s00167-012-2038-y, indexed in Pubmed: 22552619.
4. Anderson AF, Lipscomb AB, Liudahl KJ, et al. Analysis of the intercondylar notch by computed tomography. Am J Sports Med. 1987; 15(6): 547–552, doi: 10.1177/036354658701500605, indexed in Pubmed: 3425782.
5. Balgovind SR, Raunak B, Anusree A. Intercondylar notch morphometrics in Indian population: an anthropometric study with magnetic resonance imaging analysis. J Clin Orthop Trauma. 2019; 10(4): 702–705, doi: 10.1016/j.jcot.2018.07.001, indexed in Pubmed: 31316241.
6. Bintoudi A, Natsis K, Tsitouridis I. Anterior and posterior meniscofemoral ligaments: MRI evaluation. Anat Res Int. 2012; 2012: 839724, doi: 10.1155/2012/839724, indexed in Pubmed: 23019526.
7. Cho JM, Suh JS, Na JB, et al. Variations in meniscofemoral ligaments at anatomical study and MR imaging. Skeletal Radiol. 1999; 28(4): 189–195, doi: 10.1007/s002560050499, indexed in Pubmed: 10384988.
8. Frank JM, Moatshe G, Brady AW, et al. Lateral meniscus posterior root and meniscofemoral ligaments as stabilizing structures in the ACL-deficient knee: a biomechanical study. Orthop J Sports Med. 2017; 5(6): 2325967117695756, doi: 10.1177/2325967117695756, indexed in Pubmed: 28660229.
9. Moran CJ, Poynton AR, Moran R, et al. Analysis of meniscofemoral ligament tension during knee motion. Arthroscopy. 2006; 22(4): 362–366, doi: 10.1016/j.arthro.2005.09.023, indexed in Pubmed: 16581447.
10. Gupte CM, Smith A, McDermott ID, et al. Meniscofemoral ligaments revisited. Anatomical study, age correlation and clinical implications. J Bone Joint Surg Br. 2002; 84(6): 846–851, doi: 10.1302/0301-620x.84b6.13110, indexed in Pubmed: 12211675.
11. Gupte CM, Bull AMj, Thomas RD, et al. A review of the function and biomechanics of the meniscofemoral liga-

ments. Arthroscopy. 2003; 19(2): 161–171, doi: 10.1053/jars.2003.50011, indexed in Pubmed: 12579149.
12. Heller L, Langman J. The menisco-femoral ligaments of the human knee. J Bone Joint Surg Br. 1964; 46: 307–313, doi: 10.1302/0301-620X.46B2.307, indexed in Pubmed: 14167639.
13. Herzog RJ, Silliman JF, Hutton K, et al. Measurements of the intercondylar notch by plain film radiography and magnetic resonance imaging. Am J Sports Med. 1994; 22(2): 204–210, doi: 10.1177/036354659402200209, indexed in Pubmed: 8198188.
14. Hutchinson MR, Ireland ML. Knee injuries in female athletes. Sports Med. 1995; 19(4): 288–302, doi: 10.2165/00007256-199519040-00006, indexed in Pubmed: 7604201.
15. Kaplan EB. The lateral meniscofemoral ligament of the knee joint. Bull Hosp Joint Dis. 1956; 17(2): 176–182, indexed in Pubmed: 13413392.
16. Kusayama T, Harner CD, Carlin GJ, et al. Anatomical and biomechanical characteristics of human meniscofemoral ligaments. Knee Surg Sports Traumatol Arthrosc. 1994; 2(4): 234–237, doi: 10.1007/BF01845594, indexed in Pubmed: 8536047.
17. Ohori T, Mae T, Shino K, et al. Complementary function of the meniscofemoral ligament and lateral meniscus posterior root to stabilize the lateral meniscus posterior horn: a biomechanical study in a porcine knee model. Orthop J Sports Med. 2019; 7(1): 2325967118821605, doi: 10.1177/2325967118821605, indexed in Pubmed: 30719478.
18. Röhrich S, Kainberger F, Hirtler L. Evaluation of age-dependent morphometrics of the meniscofemoral ligaments in reference to the posterior cruciate ligament in routine MRI. Eur Radiol. 2018; 28(6): 2369–2379, doi: 10.1007/s00330-017-5128-x, indexed in Pubmed: 29322332.
19. Shelbourne KD, Davis TJ, Klootwyk TE. The relationship between intercondylar notch width of the femur and the incidence of anterior cruciate ligament tears. A prospective study. Am J Sports Med. 1998; 26(3): 402–408, doi: 10.1177/03635465980260031001, indexed in Pubmed: 9617403.
20. Stijak L, Malis M, Maksimović R, et al. [The influence of the morphometric parameters of the intercondylar notch on rupture of the anterior cruciate ligament]. Vojnosanit Pregl. 2012; 69(7): 576–580, doi: 10.2298/vsp101224012s, indexed in Pubmed: 22838168.
21. Tanzer M, Lenczner E. The relationship of intercondylar notch size and content to notchplasty requirement in anterior cruciate ligament surgery. Arthroscopy. 1990; 6(2): 89–93, doi: 10.1016/0749-8063(90)90004-w, indexed in Pubmed: 2363786.
22. Tillman MD, Smith KR, Bauer JA, et al. Differences in three intercondylar notch geometry indices between males and females: a cadaver study. Knee. 2002; 9(1): 41–46, doi: 10.1016/s0968-0160(01)00135-1, indexed in Pubmed: 11830380.
23. Tomczyk J, Rachalewski M, Bianek-Bodzak A, et al. Anatomical variations of knee ligaments in magnetic resonance imaging: pictorial essay. Folia Morphol. 2019; 78(3): 467–475, doi: 10.5603/FM.a2019.0004, indexed in Pubmed: 30664231.
24. Yamamoto M, Hirohata K. Anatomical study of the menisco-femoral ligaments of the knee. Kobe J Med Sci. 1991; 37((4-5)), indexed in Pubmed: 1803135.
25. Zhang C, Zhang X, Fang Z, et al. The correlation between common 2D femoral notch parameters and 3D notch volume: a retrospective MRI study. BMC Musculoskelet Disord. 2019; 20(1): 146, doi: 10.1186/s12891-019-2530-3, indexed in Pubmed: 30954066.

ORIGINAL ARTICLE

Evaluating the relation between the elongated styloid process and the ponticulus posticus using cone-beam computed tomography

S. Shahidi[1], M. Hasani[1], M. Khozaei[2]

[1]Department of Oral and Maxillofacial Radiology, School of Dentistry, Shiraz University of Medical Sciences, Shiraz, Iran
[2]School of Dentistry, Shiraz University of Medical Science, Shiraz, Iran

Background: Ponticlus posticus (PP) as a one of the cervical vertebra variations brings about symptoms similar to Eagle syndrome. This study aimed to determine the relationship between elongated styloid process (ESP) and PP in a group of Iranian patients using cone-beam computed tomography (CBCT) images.

Materials and methods: The CBCT images of 349 patients (118 males and 231 females; mean age: 32.53 ± 14.143) were involved in this study. The atlas vertebra was investigated for the presence and classification of PP (partial or complete) in sagittal views. Also, the styloid process was evaluated for the presence of ESP in reconstructed panoramic and three-dimensional images. Data were analysed using Mann-Whitney test, Fisher's exact test, and Chi-square test to assess the relationship between the presence of PP and ESP with regard to age and gender.

Results: Ponticulus posticus was observed in 24.5% of patients with ESP and 31.98% of patients without ESP. There was no significant relationship between the presence of PP and ESP ($p = 0.198$). Twenty-five patients with ESP showed PP; cases of ESP with either side and opposite side PP were 7.84% and 1.96%, respectively. Cases of bilateral ESP and PP were predominant (14.70%). The mean age of patients with bilateral ESP and PP was higher than others. There was no significant difference between males and females ($p = 0.456$).

Conclusions: Considering the prevalence and characteristics of PP in the case and control groups, there was no significant relationship between PP and ESP. (Folia Morphol 2022; 81, 1: 196–202)

Key words: elongated styloid process, ponticulus posticus, cone-beam computed tomography

INTRODUCTION

The styloid process is a cylindrical projection from the inferior part of the petrous temporal bone, with an average length of 20–30 mm. If ossification of the stylohyoid ligament exceeds 30 mm in length, it is considered to be elongated. The incidence of elongated styloid process (ESP) is controversial. Pre-vious studies have reported incidence rates of 0.09% to 54% in different populations [7, 14, 15, 17, 19]. Eagle syndrome is significant clinical condition due to ESP. It is associated with several complications, such as, dysphagia, recurrent throat pain, foreign body sensation, otalgia, tinnitus, globus sensation, cervical pain, headache, pain on neck rotation, dizzi-
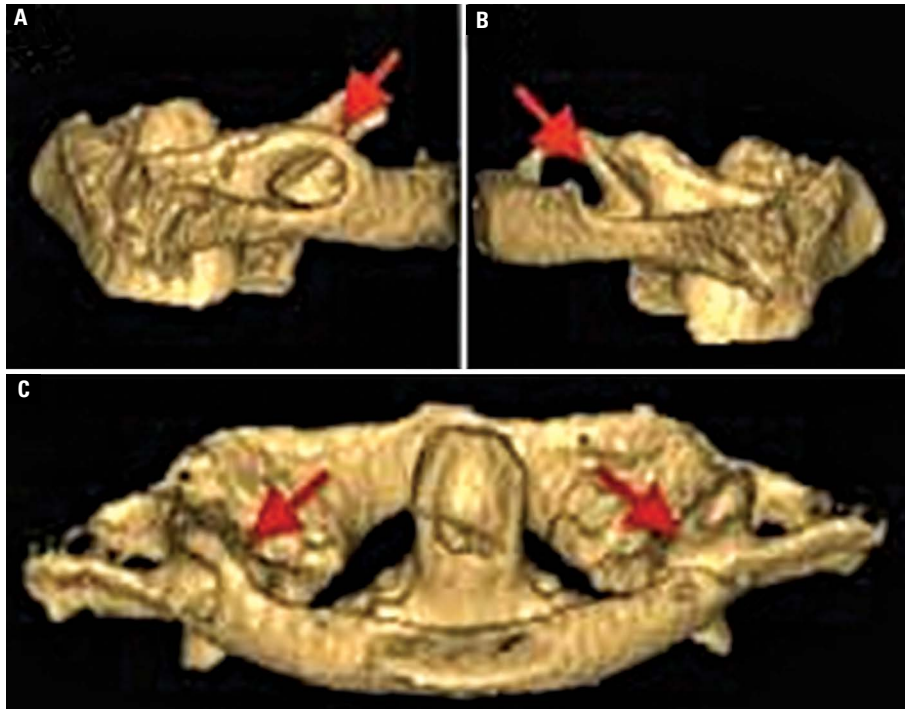
Figure 1. Three-dimensional images show ponticulus posticus on extracted atlas vertebra, with one side complete and the other side partial; **A.** Left-side view; **B.** Right-side view; **C.** Rear view.

ness, cerebral ischaemia, and vertigo [7, 11, 20]. Clinicians are conscious about this medical disorder [1]. On the other hand, one of the cervical vertebra variations brings about similar symptoms like Eagle syndrome [3, 12].

The first cervical vertebra of the spine, known as the atlas vertebra, is composed of an anterior and a posterior arch. The posterior arch contains a groove on its superior surface for the vertebral artery and consists of two lateral masses. This cervical vertebra has several variations, including ponticulus posticus (PP). PP is an osseous anomaly of the atlas vertebra, manifesting as a partial or complete calcified bridge. It is located between the lateral masses and over the vertebral groove of the posterior arch of the atlas (Fig. 1) [2]. Exact aetiology of PP is unknown; however, it may be congenital or age-related as a result of degeneration associated with aging [16].

Ponticulus posticus, with a prevalence rate of 1–46%, is not a rare anomaly. In Western countries, its prevalence ranges from 5.1% to 37.8% [8, 12, 16, 21, 24]. In the Iranian population, the frequency of PP has been estimated at 20.6% [10]. PP may be associated with conditions, such as migraine without aura, headache, cervical pain, diplopia, neck pain, shoulder

pain, hearing loss, vertebrobasilar insufficiency, visual disorders, speech and swallowing problems, and vertigo [3–6, 8, 9, 16, 21, 24].

Some of these complications are common between PP and ESP, such as headache, cervical pain, speech and swallowing problems, and vertigo [4, 5, 23]. Considering common symptoms, more investigation about any possible relation between ESP and PP can be beneficial.

A previous study established a significant relationship between the presence of PP and ESP and, PP was found in 21.6% of patients [22]. This study only evaluated the frequency of PP in patients with ESP and did not consider patients without ESP. However, there is little evidence to confirm this relationship. Therefore, the present study aimed to evaluate the relationship between ESP and the presence of PP using cone-beam computed tomography (CBCT) images in the case and control groups as well as to assess the effects of gender and age on PP and ESP occurrence.

MATERIALS AND METHODS

This retrospective study surveyed the CBCT images of patients from the archives of the Dental School of Shiraz University of Medical Sciences, Shiraz, Iran. The patients were referred to the Dental School Clinic
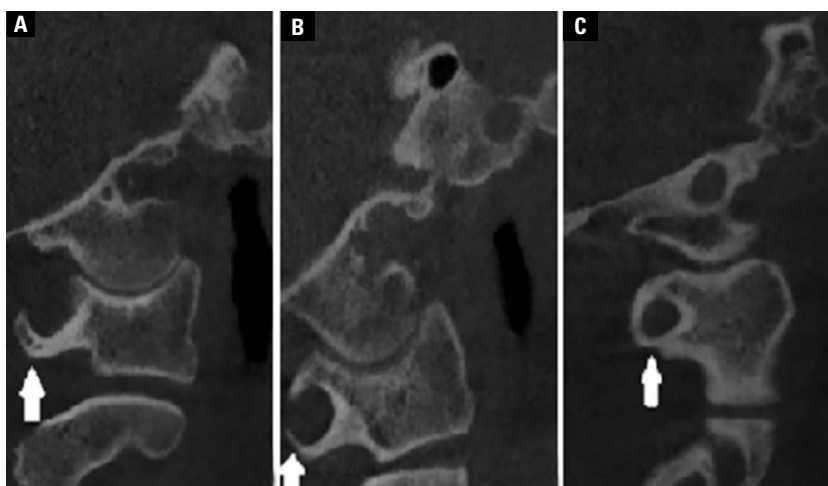
Figure 2. Sagittal cone-beam computed tomography views present; **A.** Without ponticulus posticus (PP); **B.** Partial PP; **C.** Complete PP.

between April 2017 and December 2019 because of different dentofacial problems. Informed contest was taken from patients or their guardians before CBCT examination for probable use in future studies. This study was approved by the Ethics Committee of Shiraz University of Medical Sciences (#IR.SUMS.DENTAl. REC.1399.058). On the other hand, images that could not clearly represent the first cervical vertebra or the apex of styloid process were excluded. Finally, 188 out of 537 images were excluded. In the study group, the CBCT images of 349 patients (118 males and 231 females) were inspected carefully for the presence of PP and ESP.

The CBCT images were acquired using a CBCT system, equipped with a flat panel detector (New Tom VGi, QR srl, Italy). The following parameters were applied for acquiring the images: 110 kVp; total exposure time of 1.8 s; and fields of view of 15 cm × 12 cm and 15 cm × 15 cm. Also, the electrical current (mA) was adjusted automatically for each patient. The subjects were positioned with the Frankfurt plane parallel to the floor. The CBCT images were analysed in NNT version 8.0. For PP assessments, sagittal images were applied. The PP images were categorized as partial or complete, according to their completeness. In the complete type, there was a steady bridge between the lateral mass and the posterior arch, whereas the partial type did not extend fully from the posterior lateral mass to the posterior tubercle (Fig. 2). Images with PP were also categorised as unilateral and bilateral.

To assess styloid process, reconstructed panoramic and three-dimensional images were examined. Styloid
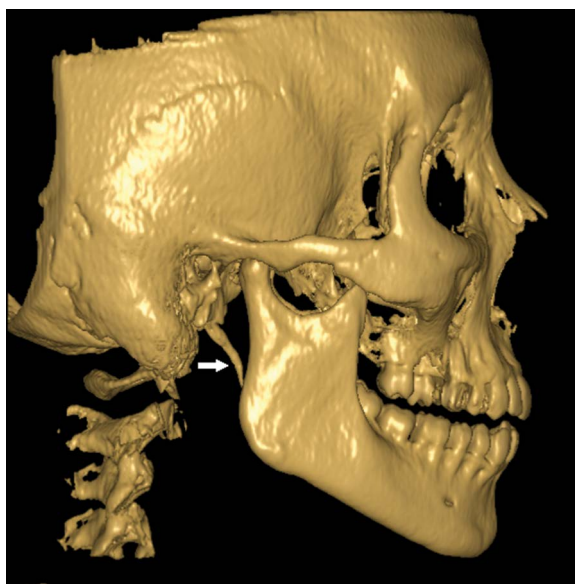
Figure 3. A three-dimensional image of the elongated styloid process in cone-beam computed tomography image.

process length from where it leaves the tympanic plate of the temporal bone to tip of the process was measured. Styloid process longer than 30 mm was considered to be ESP (Fig. 3). Images with ESP were categorised as unilateral or bilateral. Age and sex were also determined in both groups. The ESP cases were categorised into four groups: group 1 — cases with ESP, but without PP; group 2 — cases with simultaneous ESP and PP on either side; group 3 — cases with bilateral ESP and PP concurrently; and group 4 — cases with ESP and PP on the opposite sides. The

Table 1. Classification of the case group regarding elongated styloid process (ESP) and ponticulus posticus (PP)

Groups	Coexistence of ESP and PP	N		Total (%)	Mean age	Standard deviation
		Female	Male			
1	ESP without PP	54	23	77 (75.50%)	34.57	11.684
2	ESP and PP on either side	5	3	8 (7.84%)	34.13	13.622
3	Bilateral ESP and PP	10	5	15 (14.70%)	40.25	12.221
4	ESP and PP on the opposite sides	2	0	2 (1.96%)	31.00	2.828

Table 2. Classification of the control group regarding elongated styloid process (ESP) and ponticulus posticus (PP)

Groups	ESP and PP status	N		Total (%)	Mean age	Standard deviation
		Female	Male			
1	No ESP and no PP	105	63	168 (68.02%)	30.52	15.907
2	No ESP with PP on either side (or bilaterally)	55	24	79 (31.98%)	33.82	12.738

control group was also categorised into two groups: group 1 — no ESP and no PP; and group 2 — no ESP but with PP on either side or both sides.

Statistical analysis

Statistical analysis was performed in SPSS for Windows version 23.0 (SPSS Inc., Chicago, IL, USA). Data were analysed using Mann-Whitney test, Fisher's exact test, and χ^2 test to assess the relationship between the presence of PP and ESP. The relationship between these variables was also assessed with respect to age and gender. The level of statistical significance was set at $p < 0.05$.

RESULTS

The study group consisted of 118 (33.81%) males and 231 (66.19%) females, with the mean age of 32.53 ± 14.143 years (total age range: 3–81 years; age range of males: 5–70 years; and age range of females: 3–81 years). The mean age of patients without ESP was 31.55 years (standard deviation [SD] = = 14.89), while the mean age of patients with ESP was 34.89 years (SD = 11.886).

Out of 349 patients, ESP was observed in 102 (29.2%) patients, including 13 (12.75%) ESPs on the left side, 15 (14.70%) ESPs on the right side, and 74 (72.55%) bilateral ESPs. There was no significant difference regarding the prevalence of ESP between males (31/118; 26.3%) and females (71/231; 30.7%) ($p = 0.456$). Bilateral ESP was detected in 51 (50%) female patients, while unilateral ESP was found in 20 (19.61%) female patients. On the other hand,

bilateral ESP was found in 23 (22.55%) male patients, and unilateral ESP was detected in 8 (7.84%) male patients ($p = 0.667$).

As mentioned earlier, the case group was divided into four subgroups (Table 1). Group 1 included cases without PP (n = 77, 75.50%), with the mean age of 34.57 years; this group comprised the majority of cases. Also, 25 patients with ESP showed PP. Cases of bilateral ESP and PP (group 3) were predominant. Group 2 and group 4 included cases of either side and opposite side ESP and PP (n = 10, 9.80%). The results showed that the number of female patients with PP was higher than males (17 vs. 8). The control group was also categorized into two groups (Table 2). The control group with PP (group 2) comprised 79 (31.98%) patients, with the mean age of 33.82 years. The results showed that the number of female patients with PP was higher than males (55 vs. 24).

There was no significant relationship between the presence of PP and ESP ($p = 0.198$). Table 3 presents the analysis of PP and ESP in patients regarding the mean age and gender. The mean age of the patients with ESP and PP was higher than that of the control group. Also, the highest mean age (40.25 ± 12.221 years) was reported in cases of bilateral ESP and PP. Considering gender, there was no significant difference between males and females.

DISCUSSION

Ponticulus posticus is an important anomaly of the atlas vertebra [4, 6, 12]. It is associated with complications that have negative effects on the indi-

Table 3. Analysis of the prevalence of the elongated styloid process (ESP) and ponticulus posticus (PP) considering gender and age

ESP	PP							
	Absent				**Present**			
	Female	**Male**	**Mean age**	**Standard deviation**	**Female**	**Male**	**Mean age**	**Standard deviation**
Absent	105	63	30.52	15.907	55	24	33.76	12.256
Present	54	23	34.57	11.684	17	8	35.88	12.686

vidual's quality of life, such as migraine without aura, headache, cervical pain, neck pain, shoulder pain, vertebra-basilar insufficiency, visual disorders, and speech and swallowing problems [3, 4, 6, 8, 9, 12, 16, 24]. The importance of PP is not only because of its clinical effects, but is also related to the insertion of lateral mass screws in this area that is a common treatment for atlas fixation in cases of atlantoaxial instability. If surgeons do not pay particular attention to the presence of PP, they may insert a screw into PP that may result in vertebral artery injuries, fractures, screw weakening, or even death [6, 24].

According to the literature, PP is a significant and common radiographic finding in the nevoid basal cell carcinoma syndrome [13]. Moreover, some studies have shown an association between PP and Barré-Lieou syndrome; however, there is little evidence to confirm this relationship [9]. Some complications, such as headache, cervical pain, speech disorders, and swallowing problems, are common between PP and ESP. However, only one previous study considered the presence of PP in patients with ESP [22]. In the present study, CBCT images were analysed to determine the relationship between the presence of PP and ESP. Based on the results, the case group with ESP included 77 (75.50%) patients without PP, 5 (4.90%) patients with PP on the left side, 3 (2.94%) patients with PP on the right side, 15 (14.70%) patients with bilateral ESP and PP, and 2 (1.96%) patients with opposite-side PP. Based on the results, the number of patients with bilateral ESP and PP was higher than that of patients with ESP and PP on one side. In the current study, in the control group (n = 247). 168 (68.02%) patients showed no PP, 11 (4.45%) patients showed PP on the left side, 8 (3.24%) patients showed PP on the right side, and 60 (24.29%) patients had bilateral PP. Overall, PP was not found in the majority of patients in the control group.

There was no significant relationship between the presence of ESP and PP with regard to laterality (p = 0.198).

The only 1 study investigated the relationship between PP and ESP and reported a significant association between the presence of PP and ESP [22]. Unlike our study, Sekerci et al. [22] did not include a control group to evaluate the presence of PP in patients without ESP. The mean age of the case group in the present study and the study by Sekerci et al. [22] was almost similar. The present study showed that the majority of patients in the case group had bilateral ESP, which is consistent with the results reported by Sekerci et al. [22] However, the prevalence of PP in their study (39.3%) was higher than the present study (29.8%). It should be noted that the current research and the mentioned study used CBCT images for the evaluation of patients [22]. Therefore, the discrepancy between the results can be related to different ethnicities of the study groups.

Moreover, the incidence rate of ESP in the study by Sekerci et al. [22] was estimated at 21.5%, which is close to the present study (29.2%). Based on our results, although the number of female patients was higher than that of male patients in the groups, the relationship between gender and PP was not significant (p = 0.460). In line with the present findings, previous studies did not report a significant relationship between PP and gender [2, 10, 16, 18, 24], whereas Sekerci et al. [22] reported a higher number of male patients than females.

In the current study, the mean age of the patients with ESP and PP was higher than that of the control group. But there was no significant difference between case and control groups. The highest mean age (40.25 ± 12.221 years) was reported in cases of bilateral ESP and PP. There was a significant correlation between the grade of PP completeness and age; in other words, with increasing age, partial PP on the right side tended to become more complete. Some studies have shown that the prevalence of PP increases with age, while some studies found no significant relationship between PP and age [18, 21]. Therefore, further longitudinal research may better

represent this relationship. Overall, the prevalence of PP alone (29.8%) is somehow similar to the prevalence of isolated ESP (29.2%). Although these structures were not rare in the study population, their coexistence was not confirmed.

CONCLUSIONS

The prevalence and characteristics of PP and ESP were evaluated in an Iranian population to assess the relationship between the presence of PP and ESP using CBCT images. According to the results, no significant relationship was found between PP and ESP. The mean age of patients with bilateral ESP and PP was higher than others. Also, a higher prevalence of PP was reported among female patients in both case and control groups.

This study was a retrospective study that did not examine the patients, and there was no information about the patients' symptoms. Therefore, it is recommended to investigate the clinical status of these patients in future studies. Also, further assessment of different racial and ethnic groups can provide us with more reliable results.

REFERENCES

1. Ayyildiz VA, Senel FA, Dursun A, et al. Morphometric examination of the styloid process by 3D-CT in patients with Eagle syndrome. Eur Arch Otorhinolaryngol. 2019; 276(12): 3453–3459, doi: 10.1007/s00405-019-05602-6, indexed in Pubmed: 31435729.
2. Bayrakdar IS, Miloglu O, Altun O, et al. Cone beam computed tomography imaging of ponticulus posticus: prevalence, characteristics, and a review of the literature. Oral Surg Oral Med Oral Pathol Oral Radiol. 2014; 118(6): e210–e219, doi: 10.1016/j.oooo.2014.09.014, indexed in Pubmed: 25457896.
3. Bayrakdar IŞ, Miloğlu Ö, Yeşiltepe S, et al. Ponticulus posticus in a cohort of orthodontic children and adolescent patients with different sagittal skeletal anomalies: a comparative cone beam computed tomography investigation. Folia Morphol. 2018; 77(1): 65–71, doi: 10.5603/FM.a2017.0075, indexed in Pubmed: 28832088.
4. Bayrakdar IŞ, Yasa Y, Duman ŞB, et al. Cone beam computed tomography evaluation of ponticulus posticus in patients with cleft lip and palate: a retrospective radio-anatomic study. Folia Morphol. 2018; 77(1): 72–78, doi: 10.5603/FM.a2017.0076, indexed in Pubmed: 28832089.
5. Buyuk SK, Sekerci AE, Benkli YA, et al. A survey of ponticulus posticus: Radiological analysis of atlas in an orthodontic population based on cone-beam computed tomography. Niger J Clin Pract. 2017; 20(1): 106–110, doi: 10.4103/1119-3077.178916, indexed in Pubmed: 27958256.
6. Chitroda PK, Katti G, Baba IA, et al. Ponticulus posticus on the posterior arch of atlas, prevalence analysis in symptomatic and asymptomatic patients of gulbarga population. J Clin Diagn Res. 2013; 7(12): 3044–3047, doi: 10.7860/JCDR/2013/6795.3847, indexed in Pubmed: 24551723.
7. Elimairi I, Baur DA, Altay MA, et al. Eagle's syndrome. Head Neck Pathol. 2015; 9(4): 492–495, doi: 10.1007/s12105-014-0599-4, indexed in Pubmed: 25537830.
8. Geist JR, Geist SMRY, Lin LM. A cone beam CT investigation of ponticulus posticus and lateralis in children and adolescents. Dentomaxillofac Radiol. 2014; 43(5): 20130451, doi: 10.1259/dmfr.20130451, indexed in Pubmed: 24785819.
9. Giri J, Pokharel PR, Gyawali R. How common is ponticulus posticus on lateral cephalograms? BMC Res Notes. 2017; 10(1): 172, doi: 10.1186/s13104-017-2494-z, indexed in Pubmed: 28454552.
10. Hasani M, Shahidi S, Rashedi V, et al. Cone beam CT study of ponticulus posticus: prevalence, characterictics. Biomed Pharmacol J. 2016; 9(3): 1067–1072, doi: 10.13005/bpj/1050.
11. Hamedani S, Dabbaghmanesh MH, Zare Z, et al. Relationship of elongated styloid process in digital panoramic radiography with carotid intima thickness and carotid atheroma in Doppler ultrasonography in osteoporotic females. J Dent (Shiraz). 2015; 16(2): 93–99, indexed in Pubmed: 26046104.
12. Kim KH, Park KW, Manh TH, et al. Prevalence and morphologic features of ponticulus posticus in Koreans: analysis of 312 radiographs and 225 three-dimensional CT scans. Asian Spine J. 2007; 1(1): 27–31, doi: 10.4184/asj.2007.1.1.27, indexed in Pubmed: 20411149.
13. Leonardi R, Santarelli A, Barbato E, et al. Atlanto-occipital ligament calcification: a novel sign in nevoid basal cell carcinoma syndrome. Anticancer Res. 2010; 30(10): 4265–4267, indexed in Pubmed: 21036751.
14. Mayrink G, Figueiredo EP, Sato FR, et al. Cervicofacial pain associated with Eagle's syndrome misdiagnosed as trigeminal neuralgia. Oral Maxillofac Surg. 2012; 16(2): 207–210, doi: 10.1007/s10006-011-0276-7, indexed in Pubmed: 21720752.
15. Mendelsohn AH, Berke GS, Chhetri DK. Heterogeneity in the clinical presentation of Eagle's syndrome. Otolaryngol Head Neck Surg. 2006; 134(3): 389–393, doi: 10.1016/j.otohns.2005.10.046, indexed in Pubmed: 16500433.
16. Nv A, Avinash M, Srivijayanand KS, et al. Congenital osseous anomalies of the cervical spine: occurrence, morphological characteristics, embryological basis and clinical significance: a computed tomography based study. Asian Spine J. 2019; 13(4): 535–543, doi: 10.31616/asj.2018.0260, indexed in Pubmed: 30866614.

17. Ozdemir MB, Okunak M, Koseler A, et al. An ancient anatomic variation: bilateral elongated styloid process of cranium. Ital J Anat Embryol. 2013; 118(2): 184–188, indexed in Pubmed: 25338408.

18. Pérez I, Chávez A, Ponce D. Frequency of ponticulus posticus in lateral cephalometric radiography of Peruvian patients. Int J Morphol. 2014; 32(1): 54–60, doi: 10.4067/s0717-95022014000100010.

19. Politi M, Toro C, Tenani G. A rare cause for cervical pain: Eagle's syndrome. Int J Dent. 2009; 2009: 781297, doi: 10.1155/2009/781297, indexed in Pubmed: 20339566.

20. Salega S, Fabra M. First evidence of elongated styloid process in two female archaeological individuals from Córdoba hills, Argentina (late Holocene). Int J Osteoarchaeol. 2018; 28(4): 458–463, doi: 10.1002/oa.2665.

21. Saleh A, Gruber J, Bakhsh W, et al. How common is the ponticulus posticus?: a computed tomography based analysis of 2917 patients. Spine (Phila Pa 1976). 2018; 43(8): E436–E441, doi: 10.1097/BRS.0000000000002400, indexed in Pubmed: 28885291.

22. Sekerci AE, Soylu E, Arikan MP, et al. Is there a relationship between the presence of ponticulus posticus and elongated styloid process? Clin Imaging. 2015; 39(2): 220–224, doi: 10.1016/j.clinimag.2014.11.016, indexed in Pubmed: 25497077.

23. Shakibaei Z, Tohidi E, Salemi F, et al. Prevalence of stylohyoid ligament calcification on panoramic radiographs in an iranian population. J Dent Mat Tech. 2015; 4(1): 21–28, doi: 10.22038/jdmt.2014.3803.

24. Sharma V, Chaudhary D, Mitra R. Prevalence of ponticulus posticus in Indian orthodontic patients. Dentomaxillofac Radiol. 2010; 39(5): 277–283, doi: 10.1259/dmfr/16271087, indexed in Pubmed: 20587651.

VIA MEDICA

ORIGINAL ARTICLE

Morphometric analysis of three-rooted mandibular first molars in a Slovene population: a macroscopic and cone-beam computed tomography analysis

L. Strmšek[1], I. Štamfelj[1, 2]

[1]Department of Dental Diseases and Dental Morphology, Faculty of Medicine, University of Ljubljana, Slovenia
[2]Department of Operative Dentistry and Endodontics, University Medical Centre Ljubljana, Ljubljana, Slovenia

Background: This study examined the root morphology of mandibular first molars (MFMs) with radix entomolaris (RE), which presents diagnostic and therapeutic challenges for clinicians.

Materials and methods: A total of 17 three-rooted MFMs were taken from a collection of extracted teeth. Root lengths and levels of furcations were measured with a digital calliper. The pulp floor configuration, root canal systems, and RE canal curvatures were evaluated using the cone-beam computed tomography scans.

Results: Radix entomolaris was either located disto-lingually, with its coronal portion fixed to the distal root (n = 16) or mid-lingually (n = 1). A literature search identified four additional cases of MFMs with RE located mid-lingually. In the present study, RE was significantly (p ≤ 0.001) shorter than the distal root (DR) and the mesial root, on average by 2.04 mm and 3.15 mm, respectively. The level of the distal furcation was significantly (p = 0.003) lower than that of the mesiodistal furcation, on average by 1.39 mm. The average divergence angle formed by the cervical portions of the RE and DR canals was 53.14°. All RE canals were severely curved (> 25°) in buccolingual direction. The RE orifice was located slightly disto-lingually to considerably mesio-lingually from the DR orifice.

Conclusions: The traditional assumption of a disto-lingually located RE needs to be changed, even though this is the most prevalently found variant of this anatomy. The additional variant includes the presence of a mid-lingually located RE, which has implications for the endodontic access cavity design. (Folia Morphol 2022; 81, 1: 203–211)

Key words: *radix entomolaris*, supernumerary root, dental morphology, dental anthropology, odontometrics

INTRODUCTION

The root complex of the mandibular first molar (MFM) possesses two roots: a mesial root (MR) and a distal root (DR). However, a third root may be present on the lingual side of the tooth or very rarely on the buccal side of the tooth [30]; the former is named *radix entomolaris* (RE) and the latter *radix paramolaris* (RP).

The prevalence of RE shows a distinctive pattern of geographic variation [23]. Also, this root appears to be more frequent in individuals affected by Turner syndrome than in healthy individuals [17]. In North and East Asians and Eskimo-Aleuts, this trait reaches a prevalence of > 20%, which sets them apart from all other human populations. By contrast, it rarely occurs in Western Eurasian, Sub-Saharan African, New Guinean, Melanesian, and Indian populations (< 5%). A recent radiographic study reported a prevalence of 2.36% (95% confidence interval [CI] 1.61–3.42%) for the Slovene population [27]. As such, RE is among the traits used for ancestry estimation in the context of forensic dental profiling. A recently developed web-based application rASU-DAS estimates the ancestry of unknown individuals based on their suite of tooth crown and root traits, including RE [22]. In contrast, RP seems to be rare in all human populations [5].

Apart from their role in forensic anthropology, RE and RP represent a diagnostic and therapeutic challenge in clinical dentistry, particularly in oral surgery, endodontics and periodontology. First, these roots are prone to fracture during the extraction of the tooth. Second, they may be the cause of endodontic treatment failure if not identified, properly instrumented and filled. Third, their presence may contribute to localised periodontal destruction, which is probably related to the increased complexity of furcation morphology [13]. As a result of all these factors, three-rooted MFMs are lost in significantly younger patients than their two-rooted counterparts [8].

Knowledge of the morphological characteristics of three-rooted MFMs is essential for improving the success rate of various treatments and reducing the frequency of procedural complications. In the previous decade, cone-beam computed tomography (CBCT), spiral computed tomography (SCT) and micro-computed tomography (micro-CT) have been used to analyse several morphometric aspects of such teeth, including pulp chamber geometry, root canal configuration, root canal curvature and odontometric variables [9, 10, 16, 20, 25]. However, until now, few studies have addressed the morphology of three-rooted MFMs in European populations [4, 5, 16]. Thus, this study aimed to analyse the morphometric aspects of the external and internal anatomy of three-rooted MFMs extracted from dental patients in Slovenia.

MATERIALS AND METHODS

Extracted teeth

The Faculty of Medicine of the University of Ljubljana houses a collection of extracted teeth donated by Slovene dentists. The collection presently includes 17 three-rooted MFMs (11 right and 6 left). All of them have a lingually-located supernumerary root (RE). The teeth and their supernumerary roots were identified by the present authors. For most teeth, there was no data on the patients' gender, age, ethnic background, and the reasons for extractions.

Macroscopic analysis of the external dental morphology

The following observations and measurements were recorded:
— Position of RE: the teeth were grouped into four types (A, B, C, AC) according to the classification described by Carlsen and Alexandersen [4]. Types A and B refer to an RE that is located directly lingually in relation to the DR, which consists of two components (divided by a longitudinal furrow) or a single component, respectively. Type C refers to an RE that is located directly lingually in relation to the MR, and the intermediate type AC to an RE that is located exactly midway between the MR and DR;
— Curvature and relative length of RE: the teeth were grouped into five types (I, II, III, small type, and conical type) according to the classifications described by Ribeiro and Consolaro [19] and Song et al. [24];
— Level of root apex: distance from the apex to the cemento-enamel junction (CEJ) was measured along the tooth axis. Measurements were made for all three roots;
— Level of root furcation: distance from the lowest level of furcation to the CEJ measured along the tooth axis. The furcation between the MR and DR (mesio-distal furcation) and the furcation between the RE and DR (distal furcation) were measured, respectively;
— RE's degree of separation (in relation to the DR) was determined according to Carlsen [3]: the furco-apical extension of the DR was divided by its cervico-apical extension.

All measurements were made with a digital calliper with a resolution of 0.01 mm (ABS Digimatic, Mitutoyo, Japan).
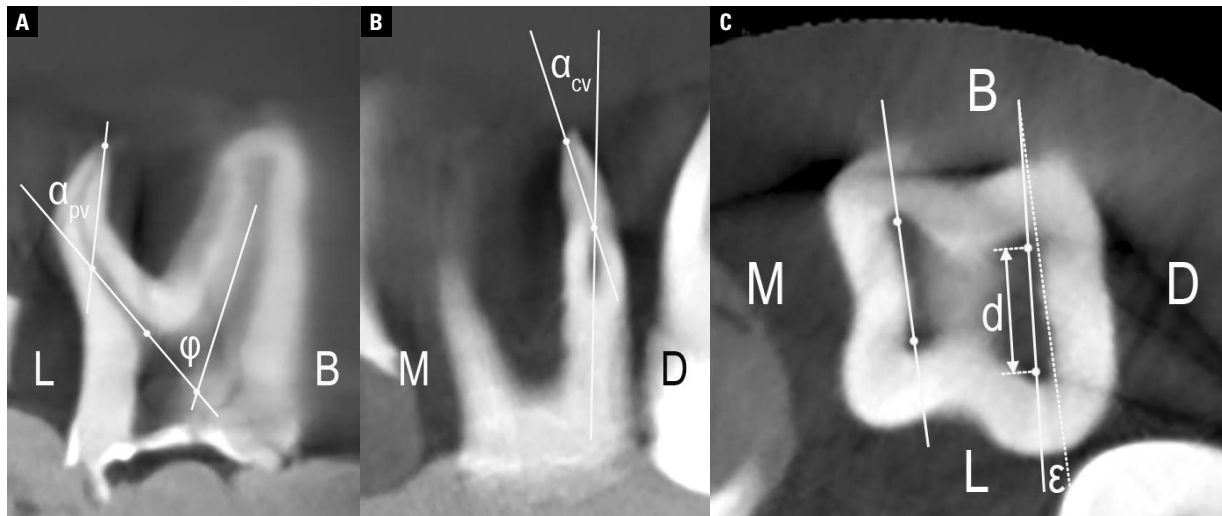
Figure 1. Cone-beam computed tomography images of the extracted mandibular first molar demonstrating measurements in a proximal view (**A**), clinical view (**B**), and on the pulp chamber floor (**C**); φ — angle of divergence of the *radix entomolaris* (RE) canal in relation to the distal root canal; α_{pv} — angle of curvature of the RE canal in proximal view; α_{cv} — angle of curvature of the RE canal in clinical view; d — distance between distal root canal orifices; ε — angle formed by lines through both mesial and both distal root canal orifices; L — lingual; B — buccal; M — mesial; D — distal.

CBCT analysis of the internal dental morphology

The CBCT images of the extracted teeth were taken with a Veraviewepocs 3D R100 device (Morita, Kyoto, Japan). The operating parameters were 8 mA, 90 kV, field of view 42.6 mm × 43.0 mm, slice thickness 1.0 mm, and voxel size 0.125 mm³. The obtained images were analysed using i-Dixel One Volume Viewer 2.0.0 software (Morita, Kyoto, Japan).

The following observations and measurements were recorded:
— Configuration of the root canal system: the canal configuration in each root was determined and recorded by Vertucci's method [29];
— Divergence of the RE canal (in relation to the DR canal): the angle formed by lines running through the cervical portions of the RE and DR canals was measured (Fig. 1A);
— Curvature of the RE canal: the root canal curvature was measured for a proximal view (PV) (Fig. 1A) and a clinical view (CV) (Fig. 1B) using the technique described by Schneider [21]. The RE canal curvature was classified as follows: straight (< 10°), moderate (10–25°), severe (> 25°);
— Position of the RE canal orifice (in relation to the DR canal orifice): a line was drawn between the centres of the RE and DR canal orifices and the inter-orifice distance (d) was measured using the geometric measurement module of the software (Fig. 1C). The angle (ε) formed by the lines con-

necting both mesial and both distal orifices was also measured (Fig. 1C). The position of the RE canal orifice was displayed in a coordinate system with the origin in the DR canal orifice and a horizontal axis parallel with the line connecting both mesial orifices. The RE canal orifice coordinates were calculated from the measured parameters ($x = d \times \cos\varepsilon$, $y = d \times \sin\varepsilon$).

Data analysis

All measurements were made independently by both authors, and the average was used for data analysis. A t test was applied to examine any statistically significant difference between the lengths of both main roots and RE, between the levels of mesio-distal and distal furcations, and between the RE canal curvature in CV and PV. A p-value of < 0.05 was considered significant.

Literature search

A literature search for articles on MFMs with RE published until August 2019 was conducted using a PubMed database search. The following keywords were used: 'three-rooted mandibular first molar', 'radix entomolaris', 'disto-lingual root', 'additional distal root', and 'extra distal root'. Papers were retrieved and screened for three-dimensional (3D) pictures of MFMs with RE (photographs of extracted teeth and 3D reconstructed CBCT, SCT and micro-CT images of teeth). Cases
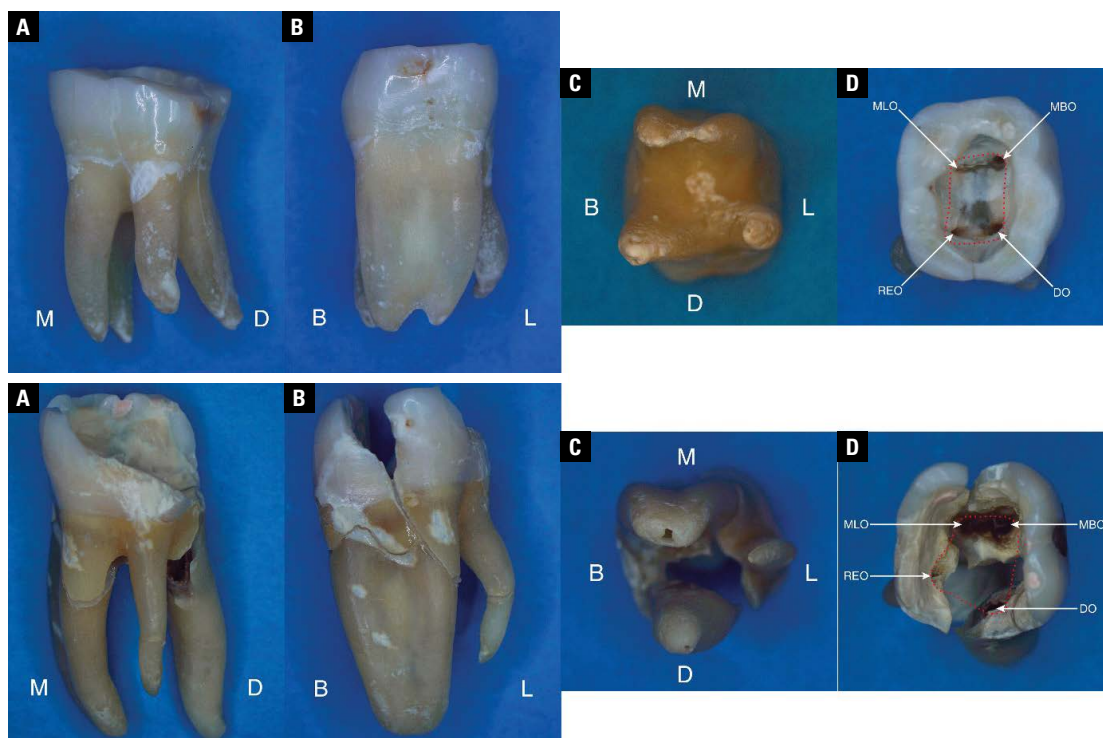
Figure 2. Right permanent mandibular first molars with type A morphology (upper row) and type AC morphology (lower row). Both specimens are displayed from the lingual side (**A**), mesial side (**B**), apical side (**C**), occlusal side (**D**); M — mesial; D — distal; B — buccal; L — lingual; MLO — mesio-lingual canal orifice; MBO — mesio-buccal canal orifice; REO — *radix entomolaris* canal orifice; DO — distal root canal orifice. The red dotted line indicates the shape of the pulp floor.

of teeth depicted only two-dimensionally (periapical radiographs, CT slices) were excluded. Reference lists were checked to identify any other relevant articles.

On the selected pictures, the following observations were recorded:

— Position of RE: the teeth were grouped into four types (A, B, C, AC) according to the classification described by Carlsen and Alexandersen [4];

— Relative length of RE: it was recorded whether RE was shorter or longer than half of the length of the associated DR;

— RE's separation: it was recorded whether RE was separate or non-separate in relation to the DR.

All pictures were independently evaluated by both authors. Disagreements were resolved by joint evaluation.

RESULTS

Macroscopic analysis of the external dental morphology

We were able to sort the examined teeth into types A (n = 16) and AC (n = 1) defined by Carlsen and Alexandersen [4]. In type A, the cervical part of the RE was fused with the DR, whereas in type AC the RE was located exactly midway between the MR and DR (Fig. 2). The only tooth with AC morphology was extracted from a 22-year-old female patient of Slovene origin after unsuccessful endodontic treatment. It was undoubtedly an MFM, since all three mandibular molars were present in the tooth row before extraction.

Table 1 shows the distribution of teeth according to the curvature and relative length of the RE [7, 14, 24]. The average levels of the root apexes and root furcations can be seen in Table 2. The RE was significantly (p = 0.001) shorter than the DR, with an average difference of 2.04 mm (range 0.07–3.50 mm). It was also significantly (p < 0.001) shorter than the MR, with an average difference of 3.15 mm (range 1.60–4.95 mm). The level of the distal furcation was significantly (p = 0.003) lower than that of the mesio-distal furcation with an average difference of 1.39 mm (range 0–6.22 mm). All three roots separated at the same level in 4 MFMs (3 of type A and 1 of type AC). In type A, RE's degree of separation, in relation to the DR, varied from 0.30 to 0.85 with an average value of 0.64.

Table 1. Curvature and relative length of the *radix entomolaris*, scored according to the classifications of Ribeiro and Consolaro (1997) and Song et al. (2010)

Reference	Country	Method	N	Conical type	Small type	Type I	Type II	Type III
Song et al. [24]	Korea	CBCT	358	5 (1.4%)	9 (2.5%)	29 (8.1%)	170 (47.5%)	145 (40.5%)
Kim et al. [14]	Korea	CBCT	507	–	8 (1.6%)	39 (7.7%)	141 (27.8%)	319 (62.9%)
De Moor et al. [7]	Belgian	ET, CE	18	–	–	2 (11.1%)	5 (27.8%)	11 (61.1%)
Present study	Slovenia	ET	14	0 (0%)	0 (0%)	1 (7.1%)	3 (21.4%)	10 (71.4%)

N — number of three-rooted mandibular first molars; type I — straight and parallel to the distal root; type II — straight, but lingually tilted; type III — lingually tilted, and buccally curved; Small type — shorter than half the length of the distal root, Conical type — cone-shaped extension without root canal; CBCT — cone-beam computed tomography, ET — extracted teeth, CE — clinical evaluation during the endodontic treatment

Table 2. Levels of root apexes and furcations from the cementoenamel junction

Structure	Sample size	Minimum [mm]	Maximum [mm]	Mean [mm]	P
Mesial root	15	12.24	16.75	14.38 (14.09)	< 0.001
Distal root	15	9.82	14.85	12.30 (13.64)	0.001
Radix entomolaris	12	8.60	12.87	11.10	
Mesio-distal furcation	16	2.02	4.85	3.37	0.003
Distal furcation	16	2.60	9.59	4.77	

Numbers in parentheses indicate average root lengths for two-rooted mandibular first molars extracted from dental patients in Slovenia [15].

CBCT analysis of the internal dental morphology

The RE and DR of the examined MFMs exhibited Vertucci type I root canal system (only one DR with type III canal system was the exception). The MR showed a more variable canal configuration; however, the prevailing anatomy was type IV (10 cases), followed by type II (4 cases). The 3-2-1 canal system was observed in one case. The canal configuration in the remaining two MRs could not be determined.

Divergence of the RE canal, in relation to the DR canal varied from 30.90° to 75.58° with a mean value of 53.14°. All RE canals contained a primary curvature in the buccal direction; in one tooth, there was also a secondary apically-located curvature in the opposite, i.e. lingual, direction. In PV, all RE canals were classified as severely curved. In CV, however, only one severely curved RE canal was found. Statistical analysis showed that the average RE canal curvature was significantly (p < 0.001) greater in PV than in CV (Table 3).

The average inter-orifice distance from the RE canal to the DR canal was 3.59 mm (range 2.39–4.50 mm). The RE canal orifice was located disto-lingually to mesio-lingually from the DR canal orifice (Fig. 3). In the mesio-distal direction, its position varied from 1.44 mm mesially (type AC morphology) to 0.61 mm distally from the DR canal orifice.

Table 3. Curvature of the *radix entomolaris* root canals

View	Sample size	Minimum [o]	Maximum [o]	Mean [o]	P
Proximal	8	30.71	69.61	48.48	< 0.001
Clinical	8	0.00	39.10	10.04	
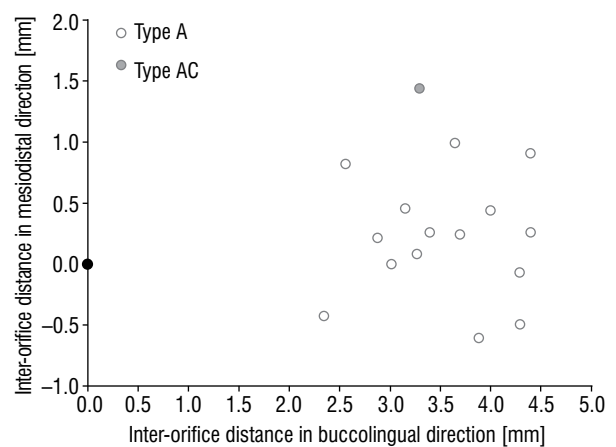
Figure 3. Position of the *radix entomolaris* canal orifice in relation to the distal root canal orifice. The centre of the distal root canal orifice represents the origin of the coordinate system (black circle). The horizontal coordinate axis runs parallel to the line connecting root canal orifices in the mesial root. All teeth are represented as they were from the right side.

Table 4. Summary of the mandibular first molars with mid-lingually located *radix entomolaris* (type AC morphology according to the classification of Carlsen and Alexandersen [4])

Tooth (FDI-notation)	Age [years]	Gender	Country	Ethnicity	Method	Relative length	Reference
46	NS	Male	Canada	Inuit	ET	< 1/2	Turner [28]
46	NS	Male	Canada	Inuit	ET	< 1/2	Turner [28]
46	NS	NS	Senegal	Wolof	ET	< 1/2	Sperber and Moreau [26]
46	NS	NS	Brazil	NS	Micro-CT	> 1/2	Souza-Flamini et al. [25]
46	22	Female	Slovenia	Caucasian	ET	> 1/2	Present study

NS — not specified; ET — extracted tooth; micro-CT — three dimensional model of the tooth, produced from micro-computed tomography scans. The relative length indicates whether *radix entomolaris* was shorter (< 1/2) or longer (> 1/2) than half of the length of the associated distal root

Literature search

The literature search identified 29 relevant papers with 3D pictures of 58 MFMs with RE (39 right and 19 left). Type A morphology was identified in 54 MFMs; in three of them, RE was non-separate in relation to the DR [4, 18]. RE shorter than half of the length of the associated DR was observed in one tooth [14]. Type AC morphology was identified in four mandibular first molars [25, 26, 28]; data on these teeth are summarised in Table 4. In three of them, RE was shorter than half of the length of the associated DR.

DISCUSSION

The material available for this study was small (17 MFMs with RE), which is a characteristic problem when studying relatively rare root traits in small ethnic areas, such as Slovenia. This is also due to the decreasing availability of extracted teeth for research purposes, which is associated with the decline in the prevalence of caries and advances in dental care in this country. Nevertheless, the teeth were well preserved, and it was possible to perform most of the observations and measurements. Moreover, in one MFM, the RE was located exactly midway between the MR and DR, corresponding to type AC as defined by Carlsen and Alexandersen [4]. A tooth with such morphology has not been found even in much larger collections of extracted teeth, e.g. in the Copenhagen and Amsterdam collections that together included 87 MFMs with RE [4, 30].

Our finding challenges the widespread belief that RE in MFMs invariably appears disto-lingually, with its coronal portion fixed to the DR (type A variant) [1, 3, 4]. Various positional terms (disto-lingual root, supernumerary disto-lingual root, disto-lingual extra root, additional distal root and extra distal root) have almost completely replaced the more common

term 'RE' in the recent dental and anthropological literature. According to the results of our literature search, only four MFMs with type AC morphology have been documented (Table 4). Surprisingly, none of the authors mentioned that this was an unusual root morphology of the MFM. In three of these teeth, RE was shorter than half of the length of the distal root. The ethnic origin of individuals with type AC MFMs was variable; however, the present study appears to provide the first description of such a tooth in an ethnic European individual.

A small number of documented MFMs with type AC morphology probably reflects the rarity with which they occur. An additional reason might be that such teeth are discarded by oral surgeons, because it is even less possible to extract them in one piece than their more prevalent type A counterparts. In our case, the tooth was extracted in several fragments that were collected and later glued together and only then the unusual root morphology became apparent. Fortunately, the lingual side of the root trunk was not damaged during extraction, and it was possible to register the position of RE in the root complex with certainty.

In our study, the RE was always longer than half the length of the DR (short and conical types absent) and most frequently (71.4% of the teeth) tilted lingually and curved buccally (type III). A Belgian study of extracted and endodontically treated teeth [8] and a Korean CBCT-based study [15] yielded comparable results; however, another Korean CBCT-based study [26] reported similar frequencies of types II and III (Table 1).

It is often claimed in the literature that the RE is shorter than the MR and DR; however, numerical data have been presented by only a few authors. In the examined MFMs, the RE was on average 2.04 mm shorter than the DR and 3.15 mm shorter than the

MR. Both differences were statistically significant (p ≤ 0.001). Our results are in line with studies on three-rooted MFMs extracted from Taiwanese [6] and Chinese patients [10]. The former reported that the RE was significantly shorter than the DR with an average of 1.48 mm. In the later, RE was significantly shorter than both DR and MR with an average of 0.88 mm and 1.54 mm, respectively. A CBCT study in Korea has shown that MFMs with RE shorter than half of the length of the associated DR represent around 4% of all cases [24]. Therefore, in MFMs, the RE mostly appears as a well-formed root approaching the length of both main roots. In the present study, the average lengths of the MR and DR were similar to those reported for two-rooted MFMs extracted from dental patients in Slovenia [15] (Table 2). These findings are of clinical significance when determining working lengths during the endodontic treatment.

Knowledge of the distal furcation level plays a significant role when planning periodontal treatment, especially because it is not possible to detect this furcation with conventional radiography. In four of the examined MFMs (3 type A and 1 type AC), RE separated from the root trunk at the same level as both main roots, forming a trifurcation. These teeth would be suitable for resection of RE in the case of furcation involvement, because a 'normal' two-rooted morphology could be established in this manner. In the remaining 13 MFMs, the RE separated from the DR apically from the mesio-distal furcation. Therefore, distal furcation would become periodontally involved later in the disease process when the amount of periodontal tissue support may not be sufficient to allow RE resection. The level of the distal furcation was significantly (p = 0.003) lower than that of the mesio-distal furcation, with an average of 1.39 mm. These results are concordant with those obtained in a Chinese study [10]. Moreover, the RE's degree of separation, in relation to the DR, varied considerably (from 0.30 to 0.85). Our literature search indicates that, in extreme cases, a complete fusion (degree of separation 0) between the RE and DR may also occur [4, 18].

In Asian populations, the root canal anatomy of the MFMs with and without RE has been comparatively studied *in vivo* using CBCT [32], and *in vitro* using micro-CT [9] or the method of canal staining and root clearing [11, 12]. The MR predominantly contained type IV (29–94%) and type II (2–31%) canal configurations in both, the two- and three-rooted molars. In contrast, the DR less frequently contained two canals in the three-rooted molars (5–14%) as in the two-rooted molars (28–36%). These results, together with those from our study, indicate that the occurrence of the RE is associated with a tendency for simplification of the canal system in the DR, but not in the MR.

In all examined MFMs, the RE canal was severely curved (> 25°) bucco-lingually, which is in accordance with previous studies that established a severe bucco-lingual curvature of the RE canal in 90.5% to 100% of the examined MFMs [6, 9, 20]. This pronounced curvature of the RE canal has to be taken into consideration during root canal instrumentation, because it increases the risk of complications such as over-straightening with strip perforations or instrument fractures. Yu et al. [33] showed that a significantly greater incidence of instrument separation, lateral perforation, and underfill was associated with the RE canal than with other root canals in MFMs. Also, our study showed that there was a considerable lingual inclination of the RE canal, ranging from 30.90° to 75.58°. Therefore, the endodontic instruments have to be inserted into the RE canal from the buccal side. Worthy of note is that the two clinically relevant morphometrical characteristics of RE (buccolingual curvature and lingual inclination) cannot be visualised using conventional two-dimensional radiography.

Several authors measured the distance on the pulp floor between the orifices of the DR and RE canals. For teeth extracted from Chinese patients they reported the average inter-orifice distance of 2.93 mm [8], for those extracted from Korean patients of 3.77 mm [14], and for those extracted from Brazilian patients of 3.20 mm [25] and 3.93 mm [20]. A comparable average value of 3.59 mm was determined in the present study. However, in the above-mentioned studies, the position of the RE canal orifice, in relation to the DR canal orifice, has not been investigated, although it has implications for the endodontic access cavity design. We were able to demonstrate the positional continuity between the RE canal orifices located slightly disto-lingually and those located considerably mesio-lingually from the canal in the DR. Based on literature review, Abella et al. [2] suggested that the disto-lingual corner of the access cavity should extend more lingually to facilitate the localisation and access to the RE canal. To this we can add that in MFMs with type AC morphology the extension should be directed mesio-lingually (as seen in Fig. 2).

The radiographic identification of a disto-lingually located RE (type A) may be a challenging task, because this root is mostly situated in the same bucco-lingual plane as the DR. Therefore, the additional 25° mesial radiograph is essential in such cases [31]. In MFMs with mid-lingually located RE (type AC), overlapping with the DR is less likely, which makes it easier to identify by using periapical radiography. The absence of overlapping between the RE and DR appears to be the only sign indicating type AC morphology on a straight periapical radiograph. CBCT overcomes these limitations and allows a reliable distinction between both morphological types of RE.

The absence of MFMs with RP in our material is not unexpected, given the rarity with which they occur. Such a tooth was not found among 1954 MFMs from the Amsterdam collection of extracted teeth [30], nor was it found on CBCT scans of 116 Brazilian dental patients [20]. However, one MFM with a separate RP and four MFMs with unseparated RP and MR were identified in the Copenhagen collection of extracted teeth [5].

CONCLUSIONS

Mid-lingual position of a RE is a rare but clinically significant anatomic variation of MFMs. This variation needs to be identified during endodontic treatment so that appropriate adjustments to the access opening can be made, and thorough debridement of the additional root canal can be accomplished. From a periodontal viewpoint, such a tooth is suitable for resection of the RE in the case of furcation involvement. This study disputes the previous assertion that an RE in MFMs always occurs on the lingual side of the main distal root. Replacement of the more inclusive term 'RE' with positional terms stating the distal position of the additional root (disto-lingual/additional distal/extra distal root) is hardly appropriate in light of the presented findings. Regardless of the RE position in the root complex, the clinician should anticipate that its root canal exhibits a lingual tilt and a severe curve toward the buccal, which cannot be detected readily on conventional radiographs.

Conflict of interest: None declared

REFERENCES

1. Abella F, Mercadé M, Duran-Sindreu F, et al. Managing severe curvature of radix entomolaris: three-dimensional analysis with cone beam computed tomography. Int Endod J. 2011; 44(9): 876–885, doi: 10.1111/j.1365-2591.2011.01898.x, indexed in Pubmed: 21671948.
2. Abella F, Patel S, Durán-Sindreu F, et al. Mandibular first molars with disto-lingual roots: review and clinical management. Int Endod J. 2012; 45(11): 963–978, doi: 10.1111/j.1365-2591.2012.02075.x, indexed in Pubmed: 22681628.
3. Carlsen O. Dental morphology. Munksgaard, Copenhagen 1987.
4. Carlsen O, Alexandersen V. Radix entomolaris: identification and morphology. Scand J Dent Res. 1990; 98(5): 363–373, doi: 10.1111/j.1600-0722.1990.tb00986.x, indexed in Pubmed: 2293344.
5. Carlsen O, Alexandersen V. Radix paramolaris in permanent mandibular molars: identification and morphology. Scand J Dent Res. 1991; 99(3): 189–195, doi: 10.1111/j.1600-0722.1991.tb01884.x, indexed in Pubmed: 1871529.
6. Chen G, Yao H, Tong C. Investigation of the root canal configuration of mandibular first molars in a Taiwan Chinese population. Int Endod J. 2009; 42(11): 1044–1049, doi: 10.1111/j.1365-2591.2009.01619.x, indexed in Pubmed: 19825040.
7. De Moor RJG, Deroose CA, Calberson FLG. The radix entomolaris in mandibular first molars: an endodontic challenge. Int Endod J. 2004; 37(11): 789–799, doi: 10.1111/j.1365-2591.2004.00870.x, indexed in Pubmed: 15479262.
8. Gu Y, Lu Q, Wang H, et al. Root canal morphology of permanent three-rooted mandibular first molars — part I: pulp floor and root canal system. J Endod. 2010; 36(6): 990–994, doi: 10.1016/j.joen.2010.02.030, indexed in Pubmed: 20478452.
9. Gu Y, Lu Q, Wang P, et al. Root canal morphology of permanent three-rooted mandibular first molars: Part II — measurement of root canal curvatures. J Endod. 2010; 36(8): 1341–1346, doi: 10.1016/j.joen.2010.04.025, indexed in Pubmed: 20647093.
10. Gu Y, Zhou P, Ding Y, et al. Root canal morphology of permanent three-rooted mandibular first molars: Part III. An odontometric analysis. J Endod. 2011; 37(4): 485–490, doi: 10.1016/j.joen.2011.01.013, indexed in Pubmed: 21419295.
11. Gulabivala K, Aung TH, Alavi A, et al. Root and canal morphology of Burmese mandibular molars. Int Endod J. 2001; 34(5): 359–370, doi: 10.1046/j.1365-2591.2001.00399.x, indexed in Pubmed: 11482719.
12. Gulabivala K, Opasanon A, Ng YL, et al. Root and canal morphology of Thai mandibular molars. Int Endod J. 2002; 35(1): 56–62, doi: 10.1046/j.1365-2591.2002.00452.x, indexed in Pubmed: 11853239.
13. Huang RY, Lin CD, Lee MS, et al. Mandibular disto-lingual root: a consideration in periodontal therapy. J Periodontol. 2007; 78(8): 1485–1490, doi: 10.1902/jop.2007.060419, indexed in Pubmed: 17668967.
14. Kim Y, Roh BD, Shin Y, et al. Morphological characteristics and classification of mandibular first molars having 2 distal roots or canals: 3-dimensional biometric analysis using cone-beam computed tomography in a korean population. J Endod. 2018; 44(1): 46–50, doi: 10.1016/j.joen.2017.08.005, indexed in Pubmed: 29033084.
15. Krobot J. Velikost stalnih zob pri prebivalcih Slovenije — raziskava ekstrahiranih zob [Undergraduate thesis in Slovene]. Ljubljana: University of Ljubljana; 2020. University of Ljubljana Repository.
16. Martins JNR, Marques D, Mata A, et al. Root and root canal morphology of the permanent dentition in a Caucasian

population: a cone-beam computed tomography study. Int Endod J. 2017; 50(11): 1013–1026, doi: 10.1111/iej.12724, indexed in Pubmed: 27883205.

17. Midtbø M, Halse A. Root length, crown height, and root morphology in Turner syndrome. Acta Odontol Scand. 1994; 52(5): 303–314, doi: 10.3109/00016359409029043, indexed in Pubmed: 7825400.

18. Quackenbush LE. Mandibular molar with three distal root canals. Endod Dent Traumatol. 1986; 2(1): 48–49, doi: 10.1111/j.1600-9657.1986.tb00123.x, indexed in Pubmed: 3457702.

19. Ribeiro FC, Consolaro A. Importancia clinica y antropologica de la raiz distolingual en los molars inferiors permanentes. Endodoncia. 1997; 15(2): 72–78.

20. Rodrigues CT, de Oliveira-Santos C, Bernardineli N, et al. Prevalence and morphometric analysis of three-rooted mandibular first molars in a Brazilian subpopulation. J Appl Oral Sci. 2016; 24(5): 535–542, doi: 10.1590/1678-775720150511, indexed in Pubmed: 27812625.

21. Schneider S. A comparison of canal preparations in straight and curved root canals. Oral Surg, Oral Med, Oral Pathol. 1971; 32(2): 271–275, doi: 10.1016/0030-4220(71)90230-1.

22. Scott G, Pilloud M, Navega D, et al. rASUDAS: a new web-based application for estimating ancestry from tooth morphology. Forensic Anthropol. 2018; 1(1): 18–31, doi: 10.5744/fa.2018.0003.

23. Scott GR, Turner II CG, Townsend GC. The anthropology of modern human teeth. Dental morphology and its variation in recent and fossil Homo sapiens. 2nd ed. Cambridge University Press, Cambridge 2018.

24. Song JS, Choi HJ, Jung IY, et al. The prevalence and morphologic classification of distolingual roots in the mandibular molars in a Korean population. J Endod. 2010; 36(4): 653–657, doi: 10.1016/j.joen.2009.10.007, indexed in Pubmed: 20307739.

25. Souza-Flamini LE, Leoni GB, Chaves JF, et al. The radix entomolaris and paramolaris: a micro-computed tomographic study of 3-rooted mandibular first molars. J Endod. 2014; 40(10): 1616–1621, doi: 10.1016/j.joen.2014.03.012, indexed in Pubmed: 25260733.

26. Sperber GH, Moreau JL. Study of the number of roots and canals in Senegalese first permanent mandibular molars. Int Endod J. 1998; 31(2): 117–122, doi: 10.1046/j.1365-2591.1998.00126.x, indexed in Pubmed: 9868938.

27. Strmšek L, Štamfelj I. The prevalence of three-rooted permanent mandibular first molars in the population of Slovenia. Anthropol Noteb. 2019; 25(3): 69–75.

28. Turner CG. Three-rooted mandibular first permanent molars and the question of American Indian origins. Am J Phys Anthropol. 1971; 34(2): 229–241, doi: 10.1002/ajpa.1330340207, indexed in Pubmed: 5572604.

29. Vertucci F. Root canal anatomy of the human permanent teeth. Oral Surg Oral Med Oral Pathol. 1984; 58(5): 589–599, doi: 10.1016/0030-4220(84)90085-9.

30. Visser JB. Beitrag zur Kenntnis der menschlichen Zahnwurzelformen. Hilversum: Buchdruckerei, Rotting 1948.

31. Wang Q, Yu G, Zhou XD, et al. Evaluation of x-ray projection angulation for successful radix entomolaris diagnosis in mandibular first molars in vitro. J Endod. 2011; 37(8): 1063–1068, doi: 10.1016/j.joen.2011.05.017, indexed in Pubmed: 21763895.

32. Wang Y, Zheng QH, Zhou XD, et al. Evaluation of the root and canal morphology of mandibular first permanent molars in a western Chinese population by cone-beam computed tomography. J Endod. 2010; 36(11): 1786–1789, doi: 10.1016/j.joen.2010.08.016, indexed in Pubmed: 20951288.

33. Yu G, Ye L, Huang D. [Clinical investigation of radix entomolaris in mandibular first molars]. Hua Xi Kou Qiang Yi Xue Za Zhi. 2012; 30(3): 259–261, indexed in Pubmed: 22768762.

VIA MEDICA

ORIGINAL ARTICLE

Morphometric analysis of the apical foramina in extracted human teeth

M.Z. Manva[1] , S. Sheereen[2] , M.K. Hans[3], R. Alroomy[1] , S.K. Mallineni[4, 5]

[1]College of Dentistry, Restorative Dental Sciences, Majmaah University, Al-Majmaah, Kingdom of Saudi Arabia
[2]College of Dentistry, Department of Preventive Dental Sciences, Dar Al Uloom University, Riyadh, Saudi Arabia
[3]Geetanjali Dental and Research Institute, Conservative Dentistry and Endodontics, Udaipur, Rajasthan, India
[4]Department of Preventive Dental Science, College of Dentistry, Majmaah University, Al-Majmaah, Saudi Arabia
[5]Centre for Transdisciplinary Research (CFTR), Saveetha Institute of Medical and Technical Sciences, Saveetha Dental College, Saveetha University, Chennai, Tamil Nadu, India

Background: The aim of the study was to analyse the morphology of the apical foramen in permanent maxillary and mandibular human teeth.

Materials and methods: The anatomic parameters include shapes (rounded, oval, uneven, flat and semilunar) and location (centre, buccal/labial, lingual/palatal, mesial, and distal) of the apical foramina was evaluated. The shapes and locations of apical foramen were analysed based on tooth type (central incisor, lateral incisor, canine, premolars, and molars) arch type (maxillary and mandibular), and position (anterior and posterior). All the teeth were investigated for the apical foramina shape and location using a stereomicroscope at a magnification of 10×. Descriptive statistics performed using SPSS (Version 21.0, IBM, NY, USA) at p value less than 0.05.

Results: The common shape of apical foramina was round (65%) and location was centre (32%). The frequency of deviation of apical was 68% in overall teeth. Apical foramina in maxillary anterior teeth showed more deviation while posterior teeth in mandibular teeth. The most common shape of apical foramina was round (65.1%) followed by (31%) and flat and semilunar shapes are very rare in studied subjects.

Conclusions: The most frequent direction of deviation is the distal surface, followed by the mesial surface. The variation is more common in mandibular posterior teeth, while maxillary posteriors showed the least difference. The commonest shape of the apical foramen is of a round shape, followed by the oval. The oval shape of the apical foramen is most frequent with central incisors. (Folia Morphol 2022; 81, 1: 212–219)

Key words: apical foramina, morphology, location, shape, root, stereomicroscope

INTRODUCTION

The success of the root canal treatment includes effective mechanical preparation as well as chemical cleansing of the pulp space and its complete filling with an inert substance. Root canal morphology of teeth specifically in the apical third is a judgmentally significant factor during the endodontic treatment. It is very essential to envision and to have a thorough

anatomic knowledge of the tooth before root canal treatment [1]. Cautious radiographic examination and evaluation of the tooth is mandatory and Arora and Tewari [3] reported that the angled radiographs could offer the inclusive evidence of root canal morphology. Moreover, the regular radiographs may not reveal the comprehensive anatomic picture of the tooth including root as they are two-dimensional images of a three-dimensional structure [13]. The majority of the clinicians used an apical constriction as an endpoint for biomechanical preparation of the endodontic therapy. Clinically it is very difficult to establish or locate the apical constriction and apical foramen; a few prior reported studies postulated that the radiographic apex is more dependable as an endpoint [12]. The radiographic apex is the tip of the root determined by radiographs; however, the tip of the root identified morphologically is considered as anatomical apex [3, 5, 7]. Dissimilarities in the location of the radiographic apex in relation to the anatomic apex might be the result of various root morphology and radiographic distortion [14]. Prior studies have often established that the position of the apical foramen is not always located at the root apex or centre of the apex. If the apical foramen is found away from the centre it is considered as deviated and it could be distal, mesial, lingual/palatal, and labial/buccal. The occurrence of deviation of the apical foramen ranges between 46% and 92% [6, 16]. It has been described and it is assumed that the apical foramina is round, although studies showed that shape can vary from round to oval [18] or other shapes such as uneven, semilunar, and flat. It has been reported that it is very imperative to be aware of the occurrence of apical foramina in various ethnic groups and its anatomical variations. Numerous studies had reported diverse tendencies in the location and shapes of the apical foramina amongst the different ethnicities [2, 4, 8, 26]. The prior reported studies focused on either maxillary teeth or mandibular teeth and anterior and posterior teeth. The distribution of shapes and location of apical foramina based on tooth type was not clearly discussed in the published literature. Therefore, the present study was aimed to analyse the morphology of shapes and locations of the apical foramen in permanent maxillary and mandibular human teeth based on arch, position and tooth type.

MATERIALS AND METHODS

Extracted human teeth were used in the present in-vitro study. The teeth with completely formed apices without any form of pathological defects were included in the study while teeth with pathological defects such as fracture, hypercementosis, root resorption (internal or external), without crowns and etc., teeth with single root of multi rooted teeth were excluded from the study. Thirty specimens of each tooth type (i.e., central incisors, lateral incisor, canine, 1st and 2nd premolars, 1st and 2nd molars) were involved in the study. All the specimens were cleaned manually from the build-up of calculus and remnants of periodontal tissues and were stored in containers filled with saline. The teeth were dried with cotton and compressed gauge, and the apical areas were stained with graphite (Apsara Platinum Extra Dark Pencils) to facilitate the identification of the apical foramen of each root. The largest diameter with opening found at the root apex was denoted as the apical foramen. Containers with number code labelled individually were used to keep the teeth separate. The specimens were mounted on a glass slide (long axis of the teeth are parallel to the glass slab) to calculate anatomic parameters. A stereomicroscope was used to examine the apical foramina at $10\times$. The parameters of apical foramen evaluated were the shapes (rounded, oval, uneven, flat, and semilunar), location (centre, buccal, lingual, mesial, and distal) of the apical foramen of each tooth used for analysis (Figs. 1, 2). In maxillary first premolars and both maxillary and mandibular molars number of roots were considered for the analysis. It was considered as the deviation of apical foramina when a large portion of the major apical foramen ($\geq 50\%$) was not located at the centre. The shape and location of apical foramen in maxillary and mandibular arch were evaluated. The distribution of apical foramina-based teeth position (anterior and posterior) also evaluated .The overall distribution of apical foramina of each tooth in the entire sample was considered for final analysis. Descriptive statistics done using SPSS (version 21.0, IBM, NY, USA), and $p < 0.05$ was considered statistically significant with 95% confidence interval.

RESULTS

In the present study the total number of apical foramen evaluated were 696 (maxillary: 377 and mandibular: 319) of 420 teeth. The commonest shape found in all evaluated apical foramen was round shape (65.1%) followed by oval shape (31.0%) (Fig. 3). The round shape of apical foramen was more common in mandibular teeth (68.2%) than the maxil-
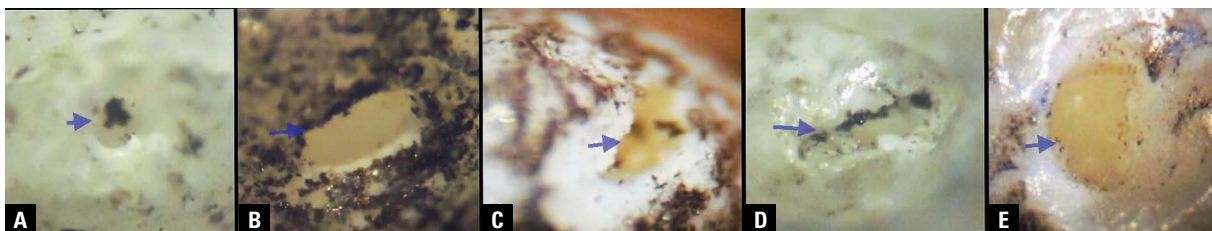
Figure 1. Shapes of apical foramina round (**A**), oval (**B**), semilunar (**C**), flat (**D**), and uneven (**E**) in the study.
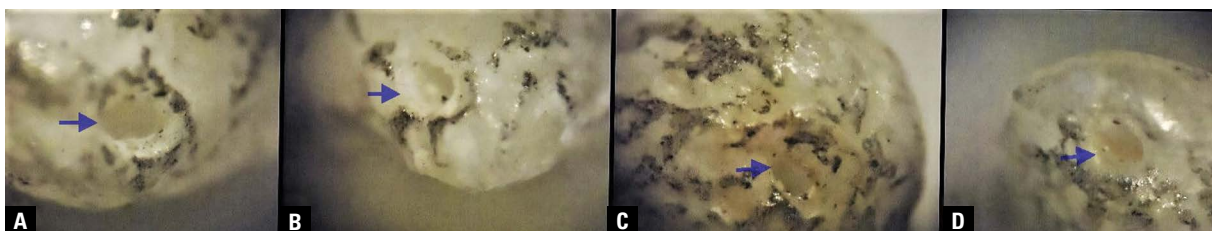
Figure 2. Deviations of the apical foramen lingually (**A**), buccally (**B**), mesially (**C**), and distally (**D**).
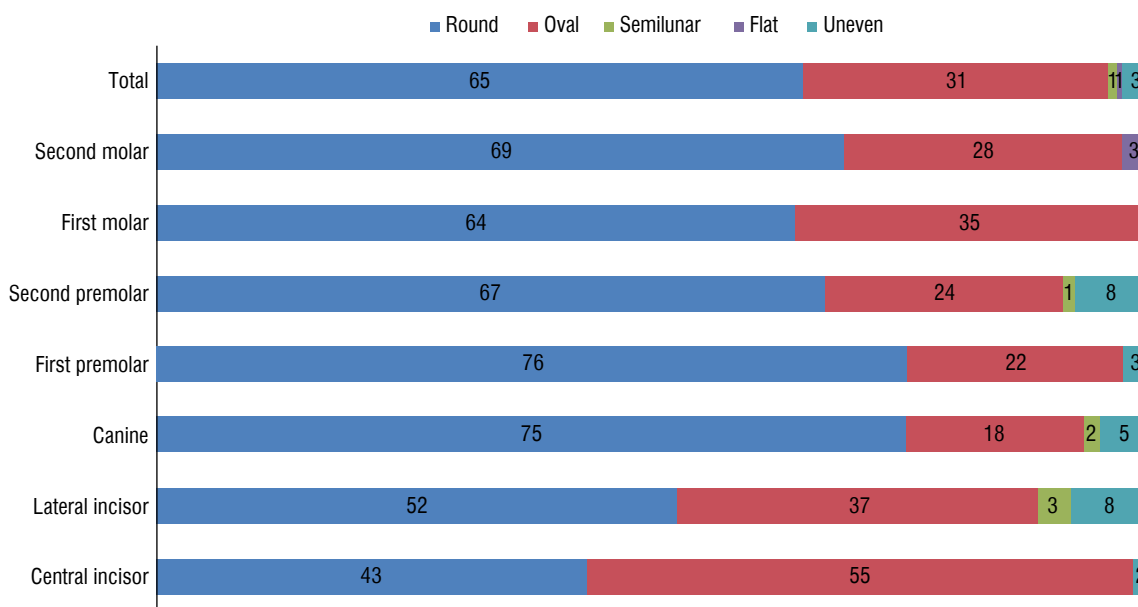
Figure 3. Distribution of shapes based on tooth type (%).

lary teeth (62.3%). On the other hand oval shape was more common in maxillary teeth (32.4%) than mandibular teeth (29.6%). The flat shape of apical foramen was only reported in maxillary teeth. The commonest shape of apical foramen for mandibular central incisors was oval with 53.3%. The commonest shape was round in both anterior (57%) and posterior teeth (68%) (Table 1). The round shaped apical foramen was slightly more in mandibular anterior teeth (29.9%) than the maxillary anterior teeth (27.2%) shown in

Figure 4. Among the posterior teeth, maxillary posterior teeth reported more of round shaped apical foramen (36.1%) than the mandibular teeth (31.6%).

The commonest location of the apical foramen was centre (31.6%) and the second commonest location of apical foramina distal (18.2%) (Fig. 5). Apical foramen residing in the centre was reported more in roots of maxillary teeth (33.2%) while it was 29.8% in roots mandibular teeth, this suggests higher deviation of apical foramen in mandibular

Table 1. Distribution of shapes of apical foramina (%) in anterior and posterior teeth in both the arches

Shapes	Anterior		Posterior	
	Maxillary	Mandibular	Maxillary	Mandibular
Round	27.2	29.9	36.1	31.8
Oval	18.5	17.9	17.2	11.9
Semilunar	0	1.6	0.2	0
Flat	0	0	0.8	0
Uneven	3.3	1.6	1.8	0.2
Total	49	51	56.1	43.9

Table 2. Distribution of location of apical foramina (%) in anterior and posterior teeth in both the arches

Location	Anterior		Posterior	
	Maxillary	Mandibular	Maxillary	Mandibular
Distal	7.1	4.3	9.4	11.3
Mesial	9.2	6.0	9.4	8.8
Buccal/labial	6.0	16.3	8.4	6.7
Palatal/lingual	13.6	7.6	9.2	4.6
Centre	13.1	16.8	19.7	12.5
Total	49	51	56.1	43.9
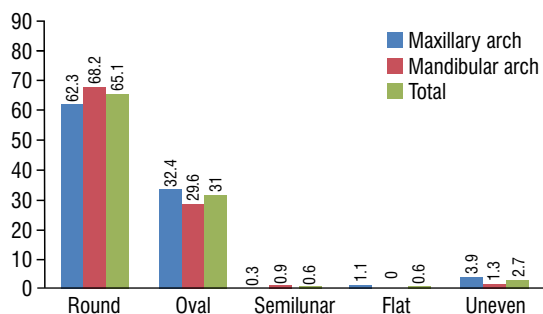
Figure 4. Distribution of shape of apical foramina in roots of maxillary and mandibular teeth.

Table 3. Distribution of deviation of apical foramina location (%) in anterior and posterior teeth in both the arches

Arch	Anterior		Posterior		P
	Centre	Deviation	Centre	Deviation	
Maxillary	3.6	86.4	19.5	80.5	< 0.05
Mandibular	16.8	83.2	12.5	87.5	

dibular teeth (20.7%) while roots of maxillary teeth showed palatal deviation of apical foramen (19.1%), which is summarised in Table 2. Table 3 represents the percentage of commonest location of apical foramen as well the percentage of deviation among anterior and posterior teeth. In anterior teeth the deviation is more in maxillary arch with 86.4% while in posterior teeth it was more with mandibular arch with 87.5%.

teeth (70.2%) the results were statistically significant (p < 0.05). The deviation of apical foramen was commonly reported in distal location in roots man-
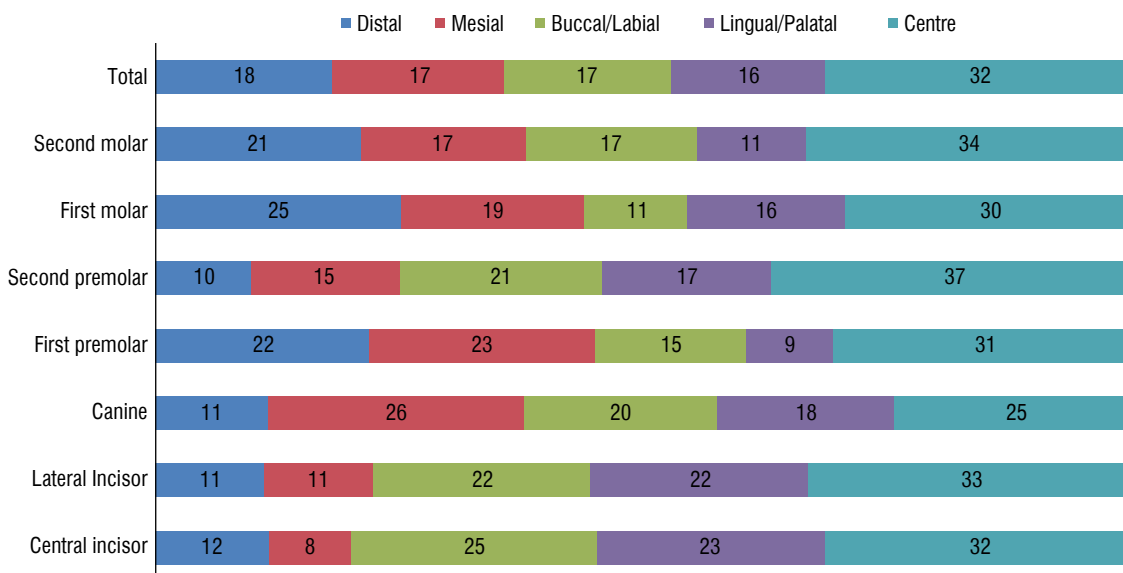
Figure 5. Distribution of location of apical foramina based tooth type (%).

Table 4. Distribution of shape of the apical foramina (%) in total sample

Shapes	Central incisor	Lateral incisor	Canine	First premolar	Second premolar	First molar	Second molar	Total
Round	3.7	4.7	6.6	8.5	8.9	18.3	14.2	65.1
Oval	4.7	3.3	1.6	2.4	3.1	10.1	5.7	31
Semilunar	0	0.3	0.2	0	0.2	0	0	0.6
Flat	0	0	0	0	0	0	0.6	0.6
Uneven	0.2	0.7	0.4	0.3	1	0.2	0	2.7
Total	8.6	9.1	8.8	11.2	13.2	28.6	20.5	696 (100)

Table 5. Distribution of location of the apical foramina (%) in total sample

Location	Central incisor	Lateral incisor	Canine	First premolar	Second premolar	First molar	Second molar	Total
Distal	1	1	1	2.4	1.3	7.2	4.3	18.2
Mesial	0.7	1	2.3	2.6	2	5.3	3.4	17.4
Buccal/labial	2.2	2	1.7	1.7	2.7	3	3.6	17
Lingual/palatal	2	2	1.6	1	2.3	4.6	2.3	15.8
Centre	2.7	3	2.2	3.4	4.9	8.5	6.9	31.6
Total	8.6	9.1	8.8	11.2	13.2	28.6	20.5	696 (100)

Over all common shapes was round in the roots of lateral incisors (4.7%), canine (6.6%), first premolar (8.5%), second premolar (8.9%), first molar (18.3%) and second molar (14.2%) while oval shape (4.7%) was common in central incisors roots that evaluated (Table 4). The frequent location of apical foramina in roots of anterior teeth was in the maxillary arch was palatal (13.6%) while centre location (16.8%) of apical foramina was common in mandibular teeth followed by labial (16.3%). The frequent location of apical foramina in the roots of posterior teeth was in the maxillary arch was centre (19.7%) followed by mesial and digital (9.4%), while centre (12.5%) location followed by digital (11.3%) in mandibular teeth (Table 5). The common location of apical foramina was centre in both maxillary and mandibular teeth (Fig. 6). The frequent deviation of apical foramina was observed in maxillary canine and very less frequently found in Maxillary second premolars (Fig. 7).

DISCUSSION

Changes in the apex's shape and location are possible under specific influences on the tooth include occlusion, adjacent drifting tooth, and pressure exerted by the tongue [24]. These subsequent changes lead to the changes in the alveolar bone around the
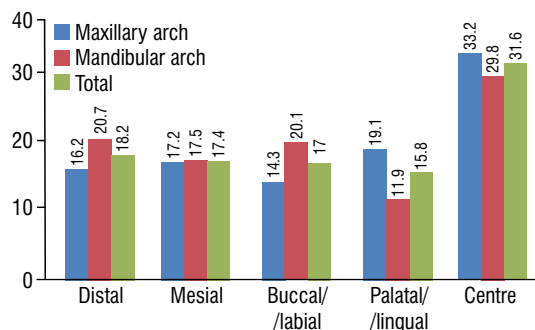
Figure 6. Distribution of location of apical foramina in roots of maxillary and mandibular teeth.
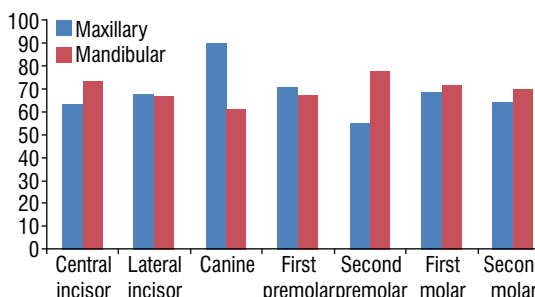
Figure 7. Distribution of deviation of apical foramina in roots based on the arch.

tooth. This might lead to resorption on the cemental wall of the apical foramen may be due to the exerted

pressure is inevitable. Apparently, this results in the foramen's deviation that alters from the radiographic root apex [4]. Anatomy, of course, is the foundation of the art and science of healthcare. There is a need to have knowledge of the microscopic and topographic anatomy of the dental apex [12].

The anatomic parameter examined in the present study was the shape and location of the apical foramen. It was evident that the frequent location was centre and the topical shape was round. The shapes of apical foramina in the present study were classified as round (65.1%), oval (31%), uneven (2.7%), semilunar (0.6%), and flat (0.6%). Flat shaped apical foramen was evident only in maxillary second molars teeth and not existent in any mandibular tooth type. Semilunar shaped apical foramina were evident in maxillary second premolars and mandibular lateral incisor, and canine while uneven apical foramina was not evident in second molars of both maxillary and mandibular teeth. All the tooth types found to have commonly round shaped apex more and only in central incisors where oval shaped apical foramina are frequently evident. These findings from the present study were in agreement with Chinese study [21] and Brazilian study [19]. The Chinese study examined 1282 teeth photographed by the XTL-2 photstero microscope and found 94% of an apical foramen in the study sample with a round shape [21]. On the other hand the Brazilian study found 52.9% of apical foramen was with a round shape of 1331 root specimens were evaluated. In contrast, a few prior studies [3, 10] found that the oval-shaped apical foramina are very common. A German study [16] reported that 71% of an apical foramen in the maxillary molars showed an oval shape, while it was evident in 53% of the roots of the mandibular molar teeth. In the present study, only 29% of 696 the apical foramen was of oval shape while 17% for maxillary posteriors and 12% for mandibular molars. An Indian study [3] reported that the commonest shape of apical foramen to be an oval shape (81%) of 800 extracted maxillary and mandibular posterior teeth in a stereomicroscopic study. On the other hand, a Korean study [10] inspected 60 mandibular molars and found that the frequent shape of the apical foramen was an oval shape (69.9%). However, the results from these three studies were not compared with the present study because the present study analysed all the teeth types. The Brazilian study [19] allocated their sample into incisors, canines, premolars, and molars groups, respectively,

for the maxillary and mandibular arches. The authors found that the maxillary molars group showed the maximum number of apical foramina with a round shape (67.6%). In comparison, the maxillary premolars group showed the maximum number of apical foramen with an oval shape (33.7%). On the other hand, in the present study, we found that the mandibular canine group showed a maximum of apical foramen with a round shape (77.8%). In comparison, the maxillary incisors group showed a maximum of apical foramen with an oval shape (46.7%). The German study [16] separated the specimens into four groups include mandibular first molar, mandibular second molars, maxillary first molar, and maxillary second molars. These German authors [16] found the maxillary first molar group showed more number of the oval-shaped apical foramen (74%), while the maximum round-shaped apical foramen was found in mandibular molars (44%).

The most common location of apical foramen was observed at the centre (31.6%) of 696 roots (420 teeth) in the present study, followed by distal location (18.2%). These results are in agreement with previous studies performed on the apical foramina of human teeth [18, 23]. Martos et al. [18] concluded that the commonest location of apical foramen was the centre for all evaluated groups of specimens. The results were similar to the present study except for the maxillary canine and mandibular incisors group, which showed the commonest location as lingual and buccal, respectively. A South Indian study [9] reported that 84% of evaluated roots of maxillary central incisor, 75% of the maxillary lateral incisor, and 15% of maxillary canine showed apical foramen location to be in the centre. The authors analysed only 285 roots of maxillary anterior teeth. A Brazilian study [23] investigated 84 maxillary central incisors and found that 25% of specimens with the apical foramen location in the centre. Teo et al. [25] found the apical foramens in 54.3% of the 635 maxillary central incisors Similar findings were reported by previous published studies [27, 28]. An Iranian stereoscopic analysis of 100 maxillary central incisors found 17% of apical foramen location was in the centre [22]. A Japanese study found that 16.7% of central incisors and cuspids and 6.7% of lateral incisors have a location of an apical foramen in the centre of 90 maxillary anterior teeth [20]. In the present study, only 36.7% of maxillary central incisors, 33.3% of maxillary lateral incisors, and 10% of maxillary canines showed apical

217

foramen in the centre. Another Japanese study investigated 510 maxillary central incisors and found 55% of an apical foramen in the apex [11]. In the present study, only 36.7% of maxillary central incisors, 33.3% of maxillary lateral incisors, and 10% of maxillary canines showed apical foramen in the centre. The deviation was almost 70% in anterior teeth and 67% in posterior teeth. Moreover, we have analysed the shapes and locations for the entire sample to draw the percentage of each shape and location based on tooth type. These results are first of its kind hence not compared with any of the studies published earlier. A Croatian study [17] studied the apical foramen of all anterior teeth and found that 41% of central incisors, 40% of the lateral incisors, and 38.5% of canines showed apical foramen in the centre of the apex. In the present study, 31.7% of central incisors, 33.3% of the lateral incisors, and 24.6% of canines showed apical foramen located in the centre of the apex. The Iranian study [22] found that the roots of 137 maxillary second premolars found that in the maxillary second premolar. In the present study, 29% of maxillary first premolars, 45% of maxillary second premolars, 32.5% of mandibular first premolars, and 22.8% of mandibular second premolars showed apical foramen with a central location. In the present study, 23.7% of permanent molars roots present the location of an apical foramen in the centre while it was almost similar for the distal location, with 23.4%.

The clinical determination of the apical foramina is based on the clinicians' tactile sensitivity and the subjective understanding of the radiographs. The instrumentation and obturation filling should not extend beyond the apical foramen considered as effective endodontic treatment [26]. In some instances, the buccal position of apical foramina may result in over instrumentation. There is an association between the root apex and the apical foramen, which normally does not coincide [15, 25–28]. The apical foramina are very small in size, but the relatively significant anatomical variation of apical micromorphology cannot be evident in two-dimensional imaging. There is a need to use supplementary methods like an operating microscope, electronic methods and three-dimensional imaging.

CONCLUSIONS

Anatomical knowledge of apical foramina is very essential for the success of endodontic treatment. The commonest shape of the apical foramen is of a round shape, followed by the oval. The oval shape of the apical foramen is most frequent with central incisors. The common location of apical foramina was centre in all teeth and the most frequent direction of deviation is the distal surface, followed by the mesial surface. The variation is more common in mandibular posterior teeth, while maxillary posteriors showed the least difference.

Ethical clearance

Acknowledgements

Conflict of interest: None declared

REFERENCES

1. Abarca J, Zaror C, Monardes H, et al. Morphology of the physiological apical foramen in maxillary and mandibular first molars. Int J Morphol. 2014; 32(2): 671–677, doi: 10.4067/S0717-95022014000200048, indexed in Pubmed: 25937698.
2. Al-Qudah AA, Awawdeh LA. Root canal morphology of mandibular incisors in a Jordanian population. Int Endod J. 2006; 39(11): 873–877, doi: 10.1111/j.1365-2591.2006.01159.x, indexed in Pubmed: 17014525.
3. Arora S, Tewari S. The morphology of the apical foramen in posterior teeth in a North Indian population. Int Endod J. 2009; 42(10): 930–939, doi: 10.1111/j.1365-2591.2009.01597.x.
4. Asna M, Nouri M, Mozayyeni MA, et al. Evaluation of apical foramen situation by anatomic apex and diagnostic value of radiography on determination of its location (A stereo microscopic study). J Dent Sch. 2004; 22: 361–368.
5. Basrani B, Revah S, Robinson C. Ubicacion del foramen apical. Rev Asoc Odontol Argent. 1997; 85: 230–232.
6. Cheung GSP, Yang J, Fan B. Morphometric study of the apical anatomy of C-shaped root canal systems in mandibular second molars. Int Endod J. 2007; 40(4): 239–246, doi: 10.1111/j.1365-2591.2007.01193.x, indexed in Pubmed: 17284270.
7. ElAyouti A, Weiger R, Löst C. The ability of root ZX apex locator to reduce the frequency of overestimated radiographic working length. J Endod. 2002; 28(2): 116–119, doi: 10.1097/00004770-200202000-00017, indexed in Pubmed: 11833683.
8. Gulabivala K, Opasanon A, Ng YL, et al. Root and canal morphology of Thai mandibular molars. Int Endod J. 2002;

35(1): 56–62, doi: 10.1046/j.1365-2591.2002.00452.x, indexed in Pubmed: 11853239.

9. Jain P, Balasubramanian S, Sundaramurthy J, et al. Position of apical foramina in permanent maxillary anterior teeth representative of an Indian population: An in vitro Study. J Int Oral Health. 2017; 9(6): 279, doi: 10.4103/jioh.jioh_132_17.

10. Jeong H, Park Sj, Park SH, et al. Morphology of the apical root canal system in Korean mandibular first molar. J Korean Academy Conservative Dentistry. 2009; 34(2): 137, doi: 10.5395/jkacd.2009.34.2.137.

11. Kasahara E, Yasuda E, Yamamoto A, et al. Root canal system of the maxillary central incisor. J Endod. 1990; 16(4): 158–161, doi: 10.1016/S0099-2399(06)81962-X, indexed in Pubmed: 2074404.

12. Kuttler Y. Microscopic investigation of root apexes. J Am Dent Assoc. 1955; 50(5): 544–552, doi: 10.14219/jada.archive.1955.0099, indexed in Pubmed: 14366934.

13. Mallineni SK, Anthonappa RP, King NM. Reliability of horizontal and vertical tube shift techniques in the localisation of supernumerary teeth. Eur Arch Paediatr Dent. 2016; 17(6): 455–460, doi: 10.1007/s40368-016-0253-9, indexed in Pubmed: 27848203.

14. Mallineni SK, Jayaraman J, Wong HM, et al. Dental development in children with supernumerary teeth in the anterior region of maxilla. Clin Oral Investig. 2019; 23(7): 2987–2994, doi: 10.1007/s00784-018-2709-2, indexed in Pubmed: 30374829.

15. Manva MZ, Alroomy R, Sheereen S, et al. Location and shape of the apical foramina in posterior teeth: an in-vitro analysis. Surg Radiol Anat. 2021; 43(2): 275–281, doi: 10.1007/s00276-020-02601-9, indexed in Pubmed: 33200273.

16. Marroquín BB, El-Sayed MAA, Willershausen-Zönnchen B. Morphology of the physiological foramen: I. Maxillary and mandibular molars. J Endod. 2004; 30(5): 321–328, doi: 10.1097/00004770-200405000-00005, indexed in Pubmed: 15107643.

17. Martić D, Prpić-Mehicić G, Simeon P, et al. Morphometrical analysis of main and accessory canals in apical root portion of frontal teeth. Coll Antropol. 1998; 22 Suppl: 153–159, indexed in Pubmed: 9951157.

18. Martos J, Ferrer-Luque CM, González-Rodríguez MP, et al. Topographical evaluation of the major apical foramen in permanent human teeth. Int Endod J. 2009; 42(4): 329–334, doi: 10.1111/j.1365-2591.2008.01513.x, indexed in Pubmed: 19220517.

19. Martos J, Lubian C, Silveira LF, et al. Morphologic analysis of the root apex in human teeth. J Endod. 2010; 36(4): 664–667, doi: 10.1016/j.joen.2010.01.014, indexed in Pubmed: 20307741.

20. Mizutani T, Ohno N, Nakamura H. Anatomical study of the root apex in the maxillary anterior teeth. J Endod. 1992; 18(7): 344–347, doi: 10.1016/s0099-2399(06)80486-3.

21. Pi X, Li C, Chen Z. [The micro-anatomy and clinical significance of the apical foramen in 1,282 permanent teeth]. Zhonghua Kou Qiang Yi Xue Za Zhi. 1996; 31(5): 294–295, indexed in Pubmed: 9592259.

22. Rahimi S, Shahi S, Yavari HR, et al. A stereomicroscopy study of root apices of human maxillary central incisors and mandibular second premolars in an Iranian population. J Oral Sci. 2009; 51(3): 411–415, doi: 10.2334/josnusd.51.411, indexed in Pubmed: 19776508.

23. Souza R, Figueiredo J, Colombo S, et al. Location of the apical foramen and its relationship with foraminal file size. Dental Press Endod. 2014; 1(1): 64–68, doi: 10.14436/2178-3713.1.1.064-068.oar.

24. Teng F, Du FY, Chen HZ, et al. Three-dimensional analysis of the physiologic drift of adjacent teeth following maxillary first premolar extractions. Sci Rep. 2019; 9(1): 14549, doi: 10.1038/s41598-019-51057-4, indexed in Pubmed: 31601925.

25. Teo CS, Chan NC, Loh HS. The position of the apical foramen of the permanent incisors. Aust Dent J. 1988; 33(1): 51–55, doi: 10.1111/j.1834-7819.1988.tb00628.x, indexed in Pubmed: 3044307.

26. Wasti F, Shearer AC, Wilson NH. Root canal systems of the mandibular and maxillary first permanent molar teeth of south Asian Pakistanis. Int Endod J. 2001; 34(4): 263–266, doi: 10.1046/j.1365-2591.2001.00377.x, indexed in Pubmed: 11482136.

27. Wolf TG, Anderegg AL, Yilmaz B, et al. Root canal morphology and configuration of the mandibular canine: a systematic review. Int J Environ Res Public Health. 2021; 18(19): 10197, doi: 10.3390/ijerph181910197, indexed in Pubmed: 34639498.

28. Wolf TG, Kim P, Campus G, et al. 3-Dimensional analysis and systematic review of root canal morphology and physiological foramen geometry of 109 mandibular first premolars by micro-computed tomography in a mixed swiss-german population. J Endod. 2020; 46(6): 801–809, doi: 10.1016/j.joen.2020.03.002, indexed in Pubmed: 32303349.

ORIGINAL ARTICLE

A golden ratio for foramen magnum: an anatomical pilot study

T. Ulcay[1] , B. Kamaşak[1] , Ö. Görgülü[2] , A. Uzun[3] , K. Aycan[1]

[1]Department of Anatomy, Faculty of Medicine, Kırşehir Ahi Evran University, Kırşehir, Turkey
[2]Department of Biostatistics, Faculty of Medicine, Kırşehir Ahi Evran University, Kırşehir, Turkey
[3]Department of Anatomy, Faculty of Medicine, Ondokuz Mayıs University, Samsun, Turkey

Background: The foramen magnum (FM) is an important landmark because of its close relationship to key structures such as the brainstem and spinal cord, an extension of the medulla oblongata. Because of the similarity in their shape, the existence of a relationship between cranial length and anteroposterior diameter of the FM, and between cranial width and transverse diameter of the FM may reveal the magnificent harmony of the skull and FM. Based on this idea, we investigated the existence of this harmony in skulls that we used in our study.

Materials and methods: In this study, 60 adult dry skulls belonging to the Turkish population were examined. The anteroposterior and transverse diameters of the foramen magnum and the length and width of the skull were measured. Measurements were made directly on the skull using a digital sliding calliper. New indices and ratios were applied with those measurements.

Results: Our study suggests that FM width and FM length could be estimated by using the cranial length and cranial width measurements in the skull by accepting the mean of these coefficients (4.62) as the golden ratio. The average of the coefficients of cranial width to FM width ratio (4.62 ± 0.35 [95% CI: 4.52–4.70]) and the average of the coefficients of cranial length to the FM length ratio (4.62 ± 0.50 [95% CI: 4.49–4.76]) were found to be equal to each other. In order to check the accuracy of this hypothesis, FM width and FM lengths were estimated with the help of new equations.

Conclusions: In the present study, the ratio between the anteroposterior and transverse diameters of both FM and the cranium was estimated at 4.62, indicating a magnificent harmony between cranial and subcranial structures. With this ratio, it is easy to estimate FM's size based on simple cranial measurements.
(Folia Morphol 2022; 81, 1: 220–226)

Key words: anthropometry, foramen magnum, occipital bone, skull base

INTRODUCTION

The human occipital bone, like that of most other mammals, is ontogenetically and functionally unique when compared to other bones of the cranium. It is one of the first bones of the skull to develop and consists anatomically of four parts surrounding the

foramen magnum (FM): the basilar, squamous, and two condylar parts [3]. The FM is an important landmark because of its close relationship to key structures such as the brainstem and spinal cord, an extension of the medulla oblongata. The FM also transmits the vertebral and spinal arteries, tectorial membranes, and alar ligaments. Thus, the FM is of particular interest to clinicians, such as radiologists, neurosurgeons, or skull-base surgeons [5, 10]. The anterior border of the FM is formed by the basilar process of the occipital bone, the lateral borders by the left and right ex-occipitals, and the posterior border is formed by the supra-occipital part of the occipital bone [7].

Anatomical knowledge of FM is important for understanding several pathologic conditions as well as for planning surgical procedures [13]. For instance, the length and breadth of the FM is clinically relevant in patients with achondroplasia; the cervicomedullary junction may be compressed as a result of marked FM stenosis, resulting in neurologic manifestations [21]. In addition, the knowledge of the dimensions and shape of the FM has important clinical implications in the prognosis and treatment of various neurological pathologies like Arnold Chiari syndrome, and posterior cranial fossa lesions [23, 26]. As in FM meningioma resection, in transcondylar surgical approach to FM, anatomical features of the FM and variations in condylar resections to expose FM have been taken into consideration in various studies [8, 24]. Wanebo et al. [27] stated that longer FM anteroposterior diameters permitted greater contralateral surgical exposure for condylar resection. Thus, understanding of the anatomical features, dimensions, shape types, variations and morphometry of the FM is essential for accurate diagnosis and treatment of these pathologies.

Also variations of the shape of FM have got diagnostic, clinical and radiological importance. The morphological variants of the shapes of FM: round, shape, egg, tetragonal, oval, irregular, hexagonal and pentagonal shapes [5, 9].

Additionally, many authors have reported the usefulness of the FM in gender determination [6, 11, 16, 18]. In 1982, Teixeira [25] revealed the basic osteometric data of the two main diameters of the human FM regarding gender, age, height, ethnic origin and secular disposition.

Despite its particular clinical importance, only a few anatomical reports on FM are available in the literature. These reports are generally on measurement of the current size of FM [10, 21, 23], determination

of its shape [5, 23], gender differences [7, 11, 25], ethnic differences [6, 18], dimensions in other mammals [14] and relationship to the intra-cranial volume [1].

However, the relationship between the FM and cranial dimensions were not fully analysed so far. The similarity in shape between the skull and FM may suggest a relationship between cranial length and anteroposterior diameter of FM and between cranial width and transverse diameter of FM. Those relations may reveal the magnificent harmony of the skull and FM. Based on this idea, we investigated this harmony's existence in 60 skulls that we used in our study. In other words, our study aims to investigate the possible relationship between cranial length and the anteroposterior diameter of the FM (in the sagittal plane) and between the cranial width and the transverse diameter of the FM (in the coronal plane).

MATERIALS AND METHODS

In the present study, 60 dry skulls of human adults from the Turkish population were examined. The exact age and sex of the skulls have not been determined. The different shapes of the FM were macroscopically noted and classified as two semicircle, oval, round, egg, tetragonal, pentagonal, hexagonal and irregular shapes. The shapes were determined after the discussion with team of three members in order to avoid observational bias. The number and incidence of each type in the studied skull was registered and tabulated. The anteroposterior and transverse diameters of the FM were measured using digital sliding callipers (Mitutoyo) with 0.1 mm precision. The anteroposterior diameter was measured from the end of the anterior border (basion) to the end of the posterior border (opisthion). The transverse diameter was measured from the point of maximum concave on the right edge to the maximum concave on the left edge (Fig. 1A).

The length of the skull was assumed as the distance between the glabella (g) and opisthocranion (g-op). The skull width was measured between the two most remote points (eurion-eurion) located on the right and the left side of the skull (eu-eu) (Fig. 1B).

In the present study, new indices were determined from measurements of the FM and skull. Measurements in the coronal and sagittal planes were used to determine these indices. While the measurements in the coronal plane were used to calculate the foramen magnum width-cranial width (FMW-CW) index, the measurements in the sagittal plane were used to
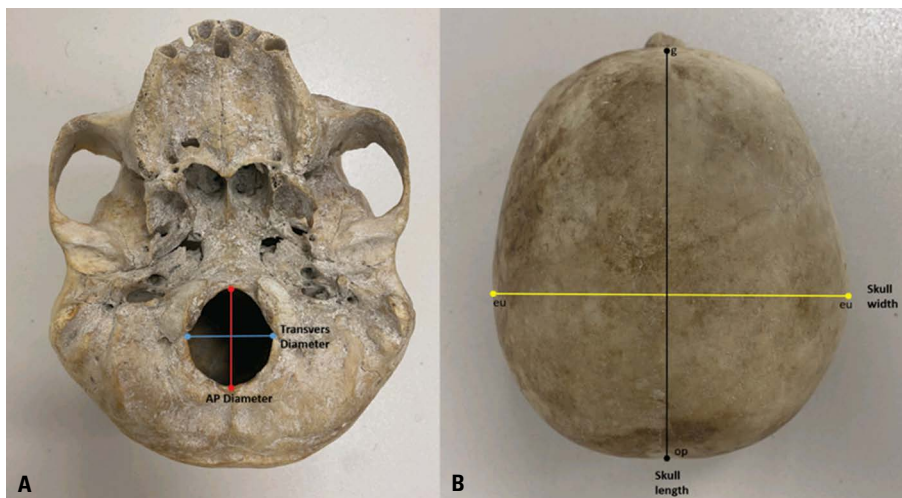
Figure 1. A, B. Antero-posterior (AP) and transverse diameters of foramen magnum and skull measurements.

calculate the foramen magnum length-cranial length (FML-CL) index.

$$FMW\text{-}CW\ index = \frac{FMW}{CW} \times 100 \qquad (\text{equation-1})$$

$$FML\text{-}CL\ index = \frac{FML}{CL} \times 100 \qquad (\text{equation-2})$$

When calculating the cranial index (cranial width/cranial length × 100) and FM index (FM width/FM length × 100), the ratio of width measurements to length measurements is always taken. From this point of view, it was thought that the ratio of equation-1 (width index) and equation-2 (length index) to each other might be an indicator of the magnificent harmony in the skull.

Statistical analysis

Statistical analysis of the study data was performed using SPSS version 21.0 software for Windows (IBM SPSS Statistics for Windows, Version 21.0. Armonk, NY: IBM Corp., USA). Normality assumption was tested using Kolmogorov-Smirnov and Shapiro-Wilk tests. The assumption of homogeneity of variances was tested with the Levene's test. Data was expressed as mean ± standard deviation (SD) and number (n). Independent t-test was used to the comparison of the groups in the study. In all statistical tests, p value < 0.05 was considered to indicate accepted to be statistically significant.

RESULTS

When we compared the width index (equation-1) and the length index (equation-2), those two indices, surprisingly, were approximately equal (1.01).

Within the scope of this equation, as a result of the measurements we made from 60 human skulls, the average of the coefficients of cranial width to FM width ratio (4.62 ± 0.35 [95% confidence interval: 4.52–4.70]) and the average of the coefficients of cranial length to FM length ratio (4.62 ± 0.50 [95% confidence interval: 4.49-4.76]) were found to be equal to each other. The relationship between these coefficients calculated in 60 skulls was found to be statistically insignificant (p > 0.05) (Table 1).

In our study, it was suggested that FM width (28.14 ± 1.77 mm) and FM length (35.81 ± 7.56 mm) can be estimated by using the cranial length (162.45 ± ± 6.20 mm) and cranial width (129.45 ± 4.99 mm) measurements in the skull by accepting the mean of these coefficients (4.62) as the golden ratio. In order to check the accuracy of this hypothesis, FM width and FM lengths were estimated with the help of equation-3 and equation-4.

$$FM\ Width = \frac{Cranial\ Width}{4.62} \qquad (\text{equation-3})$$

$$FM\ Lenght = \frac{Cranial\ Lenght}{4.62} \qquad (\text{equation-4})$$

There was no statistically significant difference between the measured (observed values) FM width and estimated FM width (p > 0.05). Similarly, there was no statistically significant difference between the measured (observed values) FM length and estimated FM length values (p > 0.05) (Table 1).

Eight different shapes were observed for the FM. Type, quantity and frequency of these are shown in Figure 2 and Table 2. In our study, the occipital condyle was not observed to protrude into the FM in any of the skulls.

Table 1. Descriptive statistics of variables and group comparisons

	Mean ± SD	95% CI (lower-upper)	P value
Cranial width	129.45 ± 4.99	117.0–138.0	–
Cranial length	162.45 ± 6.20	151.0–178.5	
Cranial width/FM width	4.62 ± 0.35	4.52–4.70	0.889
Cranial length/FM length	4.62 ± 0.50	4.49–4.76	
FM width (observed values)	28.14 ± 1.77	27.68–28.60	0.640
FM width (prediction values)	28.01 ± 1.07	27.74–28.29	
FM length (observed values)	35.81 ± 7.56	33.85–37.76	0.513
FM length (prediction values)	35.16 ± 1.34	34.81–35.50	

CI — confidence interval; FM — foramen magnum; SD — standard deviation
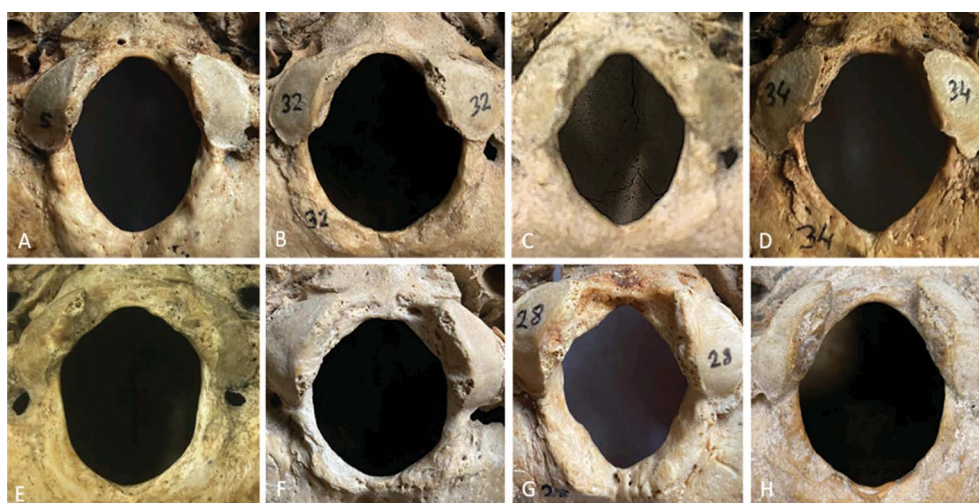
Figure 2. Different shape types of the foramen magnum; **A.** Oval; **B.** The hole formed by the combination of two semicircles; **C.** Tetragonal; **D.** Pentagonal; **E.** Hexagonal; **F.** Round; **G.** Irregular; **H.** Egg-shaped.

Table 2. Frequency of different shapes of foramen magnum (FM) (n = 60)

Different shapes of FM	Number	Frequency (%)
Oval	12	20
Two semicircle	10	16.67
Tetragonal	6	10
Pentagonal	5	8.33
Hexagonal	5	8.33
Round	4	6.67
Irregular	10	16.67
Egg	8	13.33
Total	60	100

DISCUSSION

The foramen magnum is an important cranial structure with far-reaching implications for various fields of study. Most of the morphometric studies of the FM took into account the transverse and sagittal diameters as well as the area occupied by the foramen edge. Similarly, regarding the morphology of FM, the FM index (aspect ratio between sagittal and transverse diameters) has been largely the only measurable parameter used to evaluate the shape of the FM. This study is unique in that the FM index and dimensions are predicted from basic cranial index and measurements.

Rooppakhun et al. [20], in their study on computed tomography images of 91 Thai skulls, found the mean value of the cranial length of male skulls as 173.09 ± 4.74 mm, and the average value of FM length of the same skulls as 36.78 ± 2.14 mm. The ratio between these two lengths is 4.70 and it can be seen that it is within the confidence interval specified

223

Table 3. Comparison of observed and predicted values with the literature

Studies	Gender	N	Equation-1/ /Equation-2	Equation-3 (FMW)		Equation-4 (FML)	
				Prediction values [mm]	Observed values [mm]	Prediction values [mm]	Observed values [mm]
Rooppakhun et al. [20]	Male	56	1.00	31.20	30.71	37.47	36.78
(Thai skulls)	Female	35	0.99	30.48	28.90	35.75	34.29
Burdan et al. [4]	Male	142	1.03	32.32	32.98	39.23	37.06
(Caucasian skulls)	Female	171	0.93	31.22	30.95	37.36	35.47
Mahakkanukrauh et al. [17]	Male	100	1.02	31.26	30.63	37.37	35.72
(Thai skulls)	Female	100	1.02	30.02	28.89	35.50	33.44
Ramamoorthy et al. [19]	Male	43	0.87	28.79	31.3	38.59	36.6
(Indian skulls)	Female	27	0.89	27.71	30.7	36.90	36.5
Present study (Turkish skulls)	–	60	1.01	28.01	28.14	35.16	35.81

FMW — foramen magnum width; FML — foramen magnum length

in our study. In the same study, cranial width and FM width were found to be 144.13 ± 5.45 mm and 30.71 ± 2.05 mm, respectively. The ratio between the widths is 4.69 and it is within the confidence interval in our study. In females, they reported the mean values of cranial and FM lengths as 165.15 ± ± 6.61 mm and 34.29 ± 2.35 mm, respectively. In addition, Rooppakhun et al. [20] reported the mean values of cranial width and FM width of female skulls as 140.83 ± 5.40 mm and 28.90 ± 1.89 mm, respectively. In females, the ratio between both cranial and FM lengths (4.81) and the ratio between cranial and FM widths (4.87) is very close to this range, although not within the confidence interval in our study. And according to the results of Rooppakhun et al. [20], the ratio of equation-1 (width index) and equation-2 (length index) to each other is approximately equal in both males and females (equation-1/equation-2 = 1.00 for males, 0.99 for females) (Table 3). In this respect, our work is fully compatible with the study of Rooppakhun et al. [20].

The study of Burdan et al. [4] on computed tomography images of 313 Caucasian individuals reported the cranial length and width values of males as 181.22 ± 7.53 mm and 149.33 ± 6.57 mm, respectively, and 172.59 ± 8.79 mm and 144.22 ± 7.61 mm for females, respectively. In the same study, the length and width values of FM were reported as 37.06 ± 3.07 mm and 32.98 ± 2.78 mm in males, 35.47 ± 2.60 mm and 30.95 ± 2.71 mm in females, respectively. According to these results, it was determined that the ratio of cranial width to FM width in both males

and females was within the confidence interval in our study (males: 4.53, females: 4.65). The ratio of cranial length to FM length was found very close to the confidence interval in both genders (male: 4.89, female: 4.86). According to the results of Burdan et al. [4], the ratio of equation-1 (width index) and equation-2 (length index) to each other was slightly lower in females, but the result obtained in males was consistent with our study. Our results were consistent with the results of males, while a little deviation in female (equation-1/equation-2 = 1.03 for males, 0.93 for females) (Table 3).

Mahakkanukrauh et al. [17], in their study on 200 Thai dried skulls (100 male, 100 female), reported cranial length and width values as 164.02 ± 6.76 mm, 138.68 ± 5.33 mm in females and 172.64 ± 6.23 mm, 144.44 ± 5.69 mm in males, respectively. Mahakkanukrauh et al. [17] reported the average length and width values of FM as 33.44 ± 2.03 mm and 28.89 ± 1.84 mm in females, 35.72 ± 2.41 mm and 30.63 ± 1.81 mm in males respectively. According to these reported measurements, it was determined that the ratio of cranial width to FM width in males was within the confidence interval in our study and very close to the confidence interval in females (male: 4.72, female: 4.80). The ratio of cranial length to FM length was very close to the confidence interval in both genders (male: 4.83, female: 4.90). And according to the results of Mahakkanukrauh et al. [17], the ratio of equation-1 (width index) and equation-2 (length index) to each other were equal in both males and females (equation-1/equation-2 = 1.02 for males,

Table 4. Comparison of different shapes of foramen magnum (FM) with the previous reports

Different shapes of FM	Singh et al. [23] (n)	Chethan et al. [5] (n)	Govsa et al. [9] (n)	Sharma et al. [22] (n)	Current study (n)
Oval	33.3% (40)	15.1% (8)	7.93% (30)	16% (8)	20% (12)
Two semicircle	–	–	23.28% (88)	–	16.67% (10)
Tetragonal	16.6% (20)	18.9% (10)	25.66% (97)	12% (6)	10% (6)
Pentagonal	13.3% (16)	3.8% (2)	4.23% (16)	8% (4)	8.33% (5)
Hexagonal	16.6% (20)	5.61% (3)	16.67% (63)	8% (4)	8.33% (5)
Round	13.3% (16)	22.6% (12)	3.97% (15)	22% (11)	6.67% (4)
Pear	6.6% (8)	–	–	–	–
Irregular	–	15.1% (8)	4.50% (17)	18% (9)	16.67% (10)
Egg	–	18.9% (10)	13.75% (52)	16% (8)	13.33% (8)
Total	100% (120)	100% (53)	100% (352)	100% (50)	100% (60)

1,02 for females) (Table 3). In this respect, our work is fully compatible with the study of Mahakkanukrauh et al. [17].

The proportions obtained from the reported width values in the study of Ramamoorthy et al. [19] on 70 Indian adult skulls were lower than the current study and literature for both genders. Ramamoorthy et al. [19] reported cranial length and width values as 170.5 ± 6.84 mm, 128 ± 6.15 mm in females and 178.3 ± 8.13 mm, 133 ± 6.22 mm in males, respectively. They reported the average length and width values of FM as 36.5 ± 2.43 mm and 30.7 ± 3.00 mm in females, 36.6 ± 3.16 mm and 31.3 ± 3.16 mm in males, respectively. According to these results, it was determined that the ratio of cranial width to FM width was found close to the confidence interval in both genders (male: 4.25, female: 4.17). The ratio of cranial length to FM length was found within the confidence interval in females and very close confidence interval in males (males: 4.87, females: 4.67). To the results of Ramamoorthy et al. [19], the ratio of equation-1 (width index) and equation-2 (length index) to each other was slightly lower in both genders (equation-1/equation-2 = 0.87 for males, 0.89 for females) (Table 3).

Some studies have focused on exploring external factors while FM takes its final form (the effect of sleeping position on the final form of FM in children under 5 years of age) [28]. Also some studies have evaluated the protrusion of occipital condyle and variations of the surrounding structures of the FM. Avcı et al. [2] reported that the occipital condyle protruded into the FM in 57% of the skulls examined.

Several researches have been made on the shape of the FM on the craniovertebral intersection. The most frequently observed FM type was reported as oval shaped by Singh et al. (33.3%) [23], Avcı et al. (58%) [2] and Henríquez-Pino et al. (87.3%) [12], as round shaped by Chethan et al. (22.6%) [5] and Sharma et al. (22%) [22], as tetragonal shaped by Govsa et al. (25.66%) [9]. In the present study, oval shape was the most common shape of the FM (20%) (Fig. 2, Table 4).

CONCLUSIONS

In the present study, the ratio between the anteroposterior and transverse diameters of both FM and the cranium is 4.62, indicating a magnificent harmony between cranial and subcranial structures. With this ratio, it is very easy to estimate the size of FM from basic cranial measurements.

Our research was conducted on 60 skulls; thus, it should be treated as a pilot study. We investigated the relationship between head length and width values and FM dimensions. We found that some data in the literature support this hypothesis. Besides, we calculated the rates we determined using the average values of the studies in the literature. However, similar studies should be carried out on material from various populations. Therefore, we suggest that the FM's anatomic and morphometric evaluation showed a significant difference between various parameters, so further comparative studies are required. Repeated anatomical observations deepen existing knowledge, help overcome the subjective aspect in the description made by individual researchers, and can be useful for practitioners [29].

REFERENCES

1. Acer N, Sahin B, Ekinci N, et al. Relation between intracranial volume and the surface area of the foramen magnum. J Craniofac Surg. 2006; 17(2): 326–330, doi: 10.1097/00001665-200603000-00020, indexed in Pubmed: 16633182.
2. Avci E, Dagtekin A, Ozturk AH, et al. Anatomical variations of the foramen magnum, occipital condyle and jugular tubercle. Turk Neurosurg. 2011; 21(2): 181–190, doi: 10.5137/1019-5149.JTN.3838-10.1, indexed in Pubmed: 21534200.
3. Bernard S, Loukas M, Rizk E, et al. The human occipital bone: review and update on its embryology and molecular development. Childs Nerv Syst. 2015; 31(12): 2217–2223, doi: 10.1007/s00381-015-2870-8, indexed in Pubmed: 26280629.
4. Burdan F, Szumiło J, Walocha J, et al. Morphology of the foramen magnum in young Eastern European adults. Folia Morphol. 2012; 71(4): 205–216, indexed in Pubmed: 23197139.
5. Chethan P, Prakash KG, Murlimanju BV, et al. Morphological analysis and morphometry of the foramen magnum: an anatomical investigation. Turk Neurosurg. 2012; 22(4): 416–419, doi: 10.5137/1019-5149.JTN.4297-11.1, indexed in Pubmed: 22843456.
6. El-Atta HA, Abdel-Rahman R, El-Hawary G, et al. Sexual dimorphism of foramen magnum: An Egyptian study. Egypt J Foren Sci. 2020; 10(1), doi: 10.1186/s41935-019-0167-x.
7. Gapert R, Black S, Last J. Sex determination from the foramen magnum: discriminant function analysis in an eighteenth and nineteenth century British sample. Int J Legal Med. 2009; 123(1): 25–33, doi: 10.1007/s00414-008-0256-0, indexed in Pubmed: 18553095.
8. George B, Lot G, Boissonnet H. Meningioma of the foramen magnum: a series of 40 cases. Surg Neurol. 1997; 47(4): 371–379, doi: 10.1016/s0090-3019(96)00204-2.
9. Govsa F, Ozer MA, Celik S, et al. Three-dimensional anatomic landmarks of the foramen magnum for the craniovertebral junction. J Craniofac Surg. 2011; 22(3): 1073–1076, doi: 10.1097/SCS.0b013e3182107610, indexed in Pubmed: 21586947.
10. Gruber P, Henneberg M, Böni T, et al. Variability of human foramen magnum size. Anat Rec (Hoboken). 2009; 292(11): 1713–1719, doi: 10.1002/ar.21005, indexed in Pubmed: 19777568.
11. Günay Y, Altinkök M. The value of the size of foramen magnum in sex determination. J Clin Forensic Med. 2000; 7(3): 147–149, doi: 10.1054/jcfm.2000.0430, indexed in Pubmed: 16083665.
12. Henríquez-Pino J, Cricenti SV, Didio LJ. Morphometry of the foramen magnum and its relationship to skull types on Brazilian individuals. Rev Chil Anat. 1995; 13: 159–164.
13. Di Ieva A, Bruner E, Haider T, et al. Skull base embryology: a multidisciplinary review. Childs Nerv Syst. 2014; 30(6): 991–1000, doi: 10.1007/s00381-014-2411-x, indexed in Pubmed: 24740442.
14. Ilgun R, Ozkan ZE. Comparative study of some osteometric measurements of the neurocranium and splanchnocranium bones in Aksaray Malaklı and Kangal dogs. Fırat University Veterinary Journal of Health Sciences. 2015; 29(3): 157–161.
15. Iwanaga J, Singh V, Ohtsuka A, et al. Acknowledging the use of human cadaveric tissues in research papers: Recommendations from anatomical journal editors. Clin Anat. 2021; 34(1): 2–4, doi: 10.1002/ca.23671, indexed in Pubmed: 32808702.
16. Madadin M, Menezes RG, Al Saif HS, et al. Morphometric evaluation of the foramen magnum for sex determination: a study from Saudi Arabia. J Forensic Leg Med. 2017; 46: 66–71, doi: 10.1016/j.jflm.2017.01.001, indexed in Pubmed: 28157592.
17. Mahakkanukrauh P, Sinthubua A, Prasitwattanaseree S, et al. Craniometric study for sex determination in a Thai population. Anat Cell Biol. 2015; 48(4): 275–283, doi: 10.5115/acb.2015.48.4.275, indexed in Pubmed: 26770879.
18. Manoel C, Prado FB, Caria PHF, et al. Morphometric analysis of the foramen magnum in human skulls of brazilian individuals: its relation to gender. Braz J Morphol Sci. 2009; 26(2): 104–108.
19. Ramamoorthy B, Pai MM, Prabhu LV, et al. Assessment of craniometric traits in South Indian dry skulls for sex determination. J Forensic Leg Med. 2016; 37: 8–14, doi: 10.1016/j.jflm.2015.10.001, indexed in Pubmed: 26519924.
20. Rooppakhun S, Surasith P, Vatanapatimakul N, et al. Craniometric study of Thai skull based on three-dimensional computed tomography (CT) data. J Med Assoc Thai. 2010; 93(1): 90–98, indexed in Pubmed: 20196417.
21. Samara O, Amarin J, Badran D, et al. Morphometric analysis of the foramen magnum. Int J Morphol. 2017; 35(4): 1270–1275, doi: 10.4067/s0717-95022017000401270.
22. Sharma S, Sharma A, Modi B, et al. Morphometric evaluation of the foramen magnum and variation in its shape and size: a study on human dried skull. Int J Anat Res. 2015; 3(3): 1399–1403, doi: 10.16965/ijar.2015.246.
23. Singh A, Agarwal P, Singh A. Morphological and morphometric study of foramen magnum in dry human skull and its clinical significance. Int J Anat Radiol Surg. 2019; 8(3): AO10–AO12, doi: 10.7860/IJARS/2019/41319:2488.
24. Spektor S, Anderson GJ, McMenomey SO, et al. Quantitative description of the far-lateral transcondylar transtubercular approach to the foramen magnum and clivus. J Neurosurg. 2000; 92(5): 824–831, doi: 10.3171/jns.2000.92.5.0824, indexed in Pubmed: 10794297.
25. Teixeira WR. Sex identification utilizing the size of the foramen magnum. Am J Forensic Med Pathol. 1982; 3(3): 203–206, doi: 10.1097/00000433-198209000-00003, indexed in Pubmed: 7148772.
26. Ulutabanca H, Acer N, Küçük A, et al. Chiari type I malformation with high foramen magnum anomaly. Folia Morphol. 2015; 74(3): 402–406, doi: 10.5603/FM.2015.0059, indexed in Pubmed: 26339825.
27. Wanebo JE, Chicoine MR. Quantitative analysis of the transcondylar approach to the foramen magnum. Neurosurgery. 2001; 49(4): 934–41; discussion 941, doi: 10.1097/00006123-200110000-00027, indexed in Pubmed: 11564256.
28. Zdilla MJ, Russell ML, Bliss KN, et al. The size and shape of the foramen magnum in man. J Craniovertebr Junction Spine. 2017; 8(3): 205–221, doi: 10.4103/jcvjs.JCVJS_62_17, indexed in Pubmed: 29021672.
29. Żytkowski A, Tubbs R, Iwanaga J, et al. Anatomical normality and variability: Historical perspective and methodological considerations. Trans Res Anat. 2021; 23: 100105, doi: 10.1016/j.tria.2020.100105.

V M
VIA MEDICA

C A S E   R E P O R T

Anatomical variations of the superficial ulnar artery: case series observed on historical specimens prepared by Ludwik Karol Teichmann

E. Clarke[1], J. Skrzat[2], M. Mazur[2], A. Musiał[2], J. Sienkiewicz[2], M. Radek[3], M. Polguj[1], G. Wysiadecki[1]

[1]Department of Normal and Clinical Anatomy, Chair of Anatomy and Histology, Medical University of Lodz, Poland
[2]Department of Anatomy, Jagiellonian University Medical College, Krakow, Poland
[3]Department of Neurosurgery, Spine and Peripheral Nerve Surgery, Medical University of Lodz, University Hospital WAM-CSW, Lodz, Poland

Background: This report presents a series of cases representing variant origin and course of the ulnar artery, namely the superficial ulnar artery (SUA), observed during the review of collection of historical specimens prepared in the 19th century by the prominent Polish anatomist Ludwik Karol Teichmann and his collaborators, exhibited in the Anatomy Museum of Jagiellonian University Medical College.
Results: Three distinct variants of the SUA were found on anatomical specimens of the upper limb with arteries injected by using Teichmann's method. In case no. 1, the SUA originated from the brachial artery slightly above the interepicondylar line of the humerus. This aberrant vessel gave off the common interosseous artery in the upper half of the cubital fossa and then ran superficially to the bicipital aponeurosis and over the muscles arising from the medial epicondyle of the humerus. The cases no. 2 and 3 involved two similar variants of the superficial artery in which the common interosseous artery arose from the radial artery. In the unique case no. 4, the SUA arose from the radial artery.
Conclusions: The SUA shows diverse anatomy regarding its topography and blood supply territory. Orthopaedic, hand, and plastic surgeons should be aware of anatomic variations of the SUA both in planning and in conducting surgeries of the upper limb. (Folia Morphol 2022; 81, 1: 227–233)

Key words: anatomic variation, arteries, brachial artery, common interosseous artery, radial artery, superficial ulnar artery, ulnar artery, superficial brachioulnoradial artery

INTRODUCTION

In the upper limb, the brachial artery is typically divided into two terminal branches; the radial and ulnar artery, at the level of the cubital fossa and slightly below the interepicondylar line of the humerus (Fig. 1) [16, 28]. The radial artery courses under the cover of the brachioradialis muscle, turns back at the wrist below some slender tendons that go to the thumb and passes through the 1st metacarpal space to the palmar surface of the hand to form the deep palmar arch [16, 19–22, 28]. The ulnar artery gives off the common interosseous artery and passes deep to the
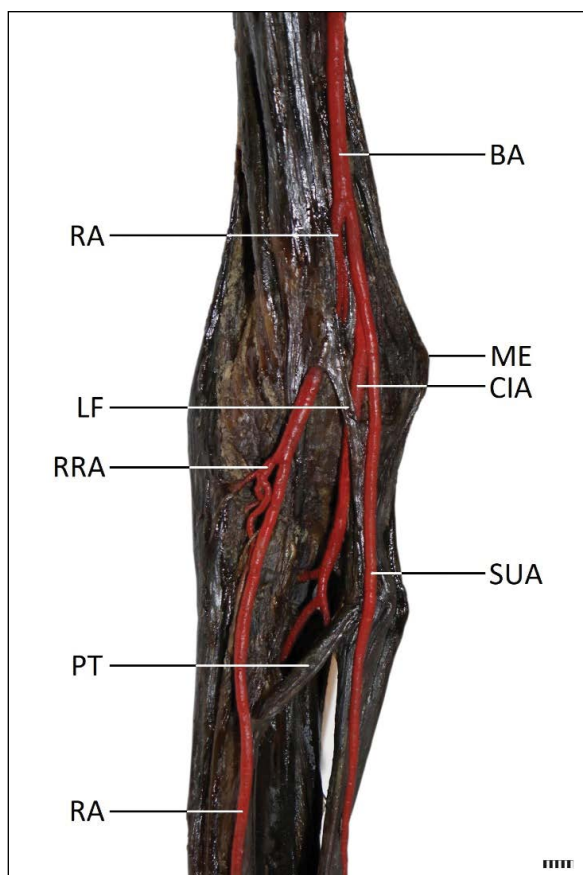
Figure 1. Variant of the superficial ulnar artery (SUA). Specimen described as case no. 1. Anterior view to the specimen of the right upper limb. The SUA originates from the brachial artery slightly above the interepicondylar line of the humerus. This aberrant vessel gives common interosseous artery in the upper half of the cubital fossa and then ran superficially to the bicipital aponeurosis (lacertus fibrosus) and over the muscles arising from the medial epicondyle of the humerus. In the lower third of the forearm, aberrant (superficial) ulnar artery followed its typical course. On this specimen the radial artery shows typical morphology. Scale bar shows 10 mm; BA — brachial artery; CIA — common interosseous artery; LF — lacertus fibrosus; ME — medial epicondyle; PT — pronator teres muscle; RA — radial artery; RRA — radial recurrent artery.

ulnar head of the pronator teres muscle as well as under the flexor digitorum superficialis muscle. At the wrist, the ulnar artery runs superficially to the flexor retinaculum and terminates as the superficial palmar arch on the palmar surface of the hand [16, 19–22, 28]. Diverse variations of this arrangement may be observed; however, most of the anomalies involve the radial artery [3, 10–12, 14, 19–22, 30, 32]. The superficial ulnar artery (SUA) is an anatomical variation in which the ulnar artery courses superficial to the flexors of the forearm. Such atypical vessel may arise directly from axillary, brachial or superficial brachial

artery [1–9, 13, 14, 17–26, 31–33]. The incidence of this anatomical variation in adults ranges between 0.67% and 7% [14, 20–23].

Research on the anatomical variations of blood vessels flourished between the 18th and 20th centuries [9, 14, 19–22, 27, 29]. In this report, we described a series of cases representing various origin and course of the SUA. All those anatomical variations were observed during the review of collection of historical specimens prepared in 19th century by prominent Polish anatomist Ludwik Karol Teichmann [15] and his collaborators, exhibited in the Anatomy Museum of Jagiellonian University Medical College. Novelty of the study was in-depth anatomical description and a comparison of three different variants of the SUA located exclusively in the cubital fossa and forearm. The course, topography and branching pattern of those aberrant vessels were traced. The issue of classification and anatomical terminology was also discussed in the context of observed cases. Thus, our report may supplement anatomical description of the SUA existing in anatomical literature. It is especially true regarding the origin of the common interosseous artery, ulnar recurrent branches and formation of the superficial palmar arch in presence of this aberrant artery. As the anatomical variations of the arterial system in upper limbs may be a challenging clinical issue, this report may help to better understand in detail the diverse anatomy of the SUA, including its topography and blood supply territory.

CASE REPORT

Three distinct anatomical variants of the SUA were found on selected historical dry anatomical specimens of the upper limb, being a part of the collection presented in the Anatomy Museum (originally Theatrum Anatomicum) of Jagiellonian University Medical College. All those specimens varied regarding branching pattern and distribution of the main arterial trunks. Teichman introduced advances in techniques of the corrosion casting by developing mass for cold injections [15]. Using cold mass to prepare anatomical specimens did not damage the tissues. Teichman's mass applied to inject blood vessels was obtained using glass putty. The obtained images of the blood vessels were a very accurate reflection of true anatomical relationships. The diameters of radial and SUAs were measured at the level of the wrist to facilitate comparison of contribution of those vessels in hand blood supply. The measurements of external diameter
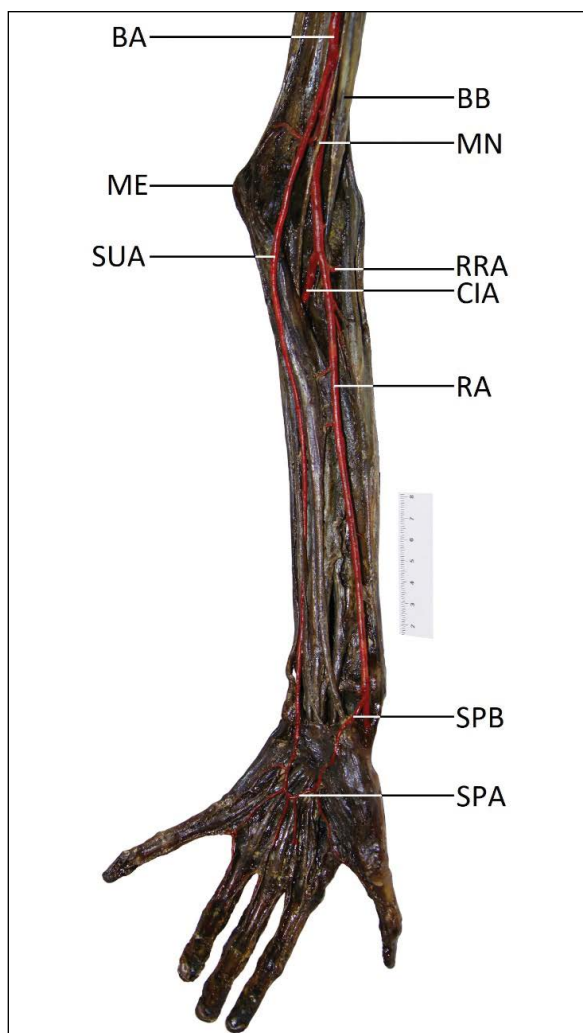
Figure 2. Variant of the superficial artery in which the common interosseous artery arise from the radial artery. Specimen described as case no. 2. Anterior view to the specimen of the left upper limb. In this case, the superficial ulnar artery (SUA) runs superficially to the flexors of the forearm and obtains position typical for the ulnar artery in the lower third of the forearm; BA — brachial artery; BB — biceps brachii muscle (tendon); CIA — common interosseous artery; ME — medial epicondyle; MN — median nerve; RA — radial artery; RRA — radial recurrent artery; SPA — superficial palmar arch; SPB — superficial palmar branch of the radial artery.

of those arterial trunks were taken with a Digimatic Calliper (Mitutoyo Corporation, Kawasaki-shi, Kanagawa, Japan). Measurements were performed by two independent researchers. Each measurement was repeated twice and an average was calculated as final result, with an accuracy of two decimal places.

Case 1

In this case (specimen of the right upper limb), the SUA originated from the brachial artery above the cubital fossa, i.e. 51.5 mm proximally to the interepicondylar line of the humerus (Fig. 1). This aberrant vessel gave off common interosseous artery in the upper half of the cubital fossa, just at the level of the interepicondylar line. The common interosseous artery ran deep to the bicipital aponeurosis (Fig. 1) and gave off the ulnar recurrent arteries. The SUA ran superficially to the bicipital aponeurosis (lacertus fibrosus) and over the muscles arising from the medial epicondyle of the humerus (Fig. 1). No ulnar recurrent arteries were found on this specimen. In the lower third of the forearm (141 mm below the medial epicondyle, with a forearm length of 276 mm), aberrant (superficial) ulnar artery followed a typical course (Fig. 1). On this specimen the radial artery was typical. It ran under the bicipital aponeurosis, gave off radial recurrent artery and took the course along the lateral border of the brachioradialis muscle. The diameters of the SUA and the radial artery at the level of the wrist were 2.43 mm and 3.19 mm, respectively. The hand was removed on this specimen, so the palmar arches couldn't be assessed.

Case 2 and 3

Both cases involved similar variants of the arterial pattern of the upper limb, in which the SUA was present, while the common interosseous artery arose from the radial artery (Fig. 2). In case no. 2 (specimen of the left upper limb), the SUA originated from brachial artery in the lower third of the arm, 65.5 mm above the interepicondylar line of the humerus (Fig. 2). In the case no. 3 (specimen of the left upper limb), the SUA originated from the brachial artery, slightly (7.2 mm) above the level of the interepicondylar line of the humerus. Thus, in both cases, the division of the brachial artery into the terminal branches (in this variant the terminal branches were radial and SUAs) was located in the distal arm, above the typical level. In both cases, the common interosseous artery branched off the radial artery (Fig. 2). It may be assumed that in this variant of the forearm arterial supply, the common interosseous artery replaced missing ulnar artery of typical location with respect to its muscular branches to the forearm flexors. On its course in the forearm, the SUA ran superficially to the flexors of the forearm and obtained position typical for the ulnar artery, i.e. between the flexor carpi ulnaris and flexor digitorum superficialis, in the lower third of the forearm (Fig. 2). In case no. 2, the typical
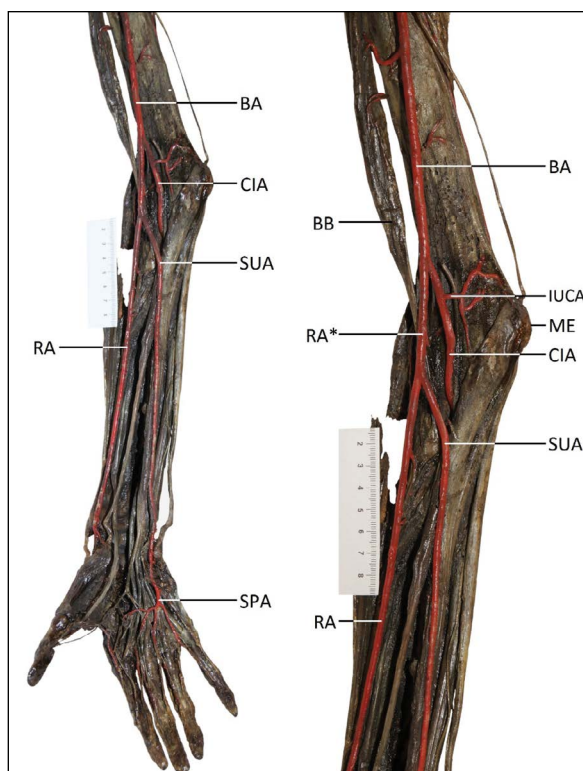
Figure 3. The superficial ulnar artery (SUA) arising from the radial artery (RA). Specimen described as case no. 4. Anterior view of the specimen of the right upper limb. The right side of this figure shows general view, the left side shows magnification of the anterior surface of the distal arm and proximal forearm. The brachial artery (BA) is divided into the radial and common interosseous artery (CIA). The CIA resembles incomplete ulnar artery, it gives a single steam of the ulnar recurrent artery, and supplies flexors of the forearm, however, its territory does not involve the hand. In the lower half of the cubital fossa, the SUA branches off from the RA. This aberrant vessel crosses obliquely anterior group of the forearm muscles. At the level of wrist, it obtains a typical position for the ulnar artery; BB — biceps brachii muscle; IUCA — inferior ulnar collateral artery (anastomotica magna artery); ME — medial epicondyle; RA* — initial part of radial artery (resembling superficial brachioulnoradial artery); SPA — superficial palmar arch.

position was obtained 164 mm below the medial epicondyle of the humerus (with forearm length of 267 mm), while in the case no. 3 the normal position was obtained 182 mm below the medial epicondyle of the humerus (with the forearm length of 243 mm). The diameters of the SUA and the radial artery at the level of the wrist were accordingly 2.11 mm and 3.15 mm in the case no. 2, while the same diameters measured in the case no. 3 were 2.65 mm for the SUA and 2.95 mm for the radial artery. In both cases, the SUA contributed to blood supply of the hand; however, some differences in formation of the superficial palmar arch were found between those two cases.

In the case no. 2, the superficial palmar arch was of closed radio-ulnar type, in which contribution from the SUA formed an anastomosis with the superficial palmar branch of the radial artery (Fig. 2). In the case no. 3, the superficial palmar arch was also radio-ulnar type (both radial and ulnar artery contributed to its formation). However, the arch was opened in this case with no anastomosis between the parts of the arch formed by the superficial palmar branch of the radial artery and SUA. In the case no. 3, the territory of the radial artery involved the princeps pollicis artery and the first metacarpal space, while the SUA has given off the common digital arteries to the second, third and fourth metacarpal spaces.

Case 4

In this rare case of the forearm arterial pattern observed on specimen of the right upper limb, the SUA arose from the radial artery. The brachial artery was divided 36.6 mm above interepicondylar line of the humerus into the radial artery and common interosseous artery (Fig. 3). The common interosseous artery gave off the inferior ulnar collateral artery and then supplied flexor muscles of the forearm. However, its blood supply territory did not involve the hand. The radial artery showed a typical course. However, in the lower half of the cubital fossa, 26 mm below the interepicondylar line of the humerus, the SUA branched off from the radial artery (Fig. 3). This aberrant vessel crossed obliquely anterior group of the forearm muscles. Only at the level of wrist, it obtained a position typical for the ulnar artery and joined the Guyon's canal (fibro-osseous tunnel extending from the transverse carpal ligament at the proximal aspect of the pisiform to the origin of the hypothenar muscles at the hook of hamate). The SUA in this case terminated in the incomplete superficial palmar arch (with no superficial palmar branch of the radial artery contributing to its formation). This variant may also be called the "ulnar type" of the superficial palmar arch. The princeps pollicis artery arose from the radial artery in this specimen. The diameters of the SUA and the radial artery at the level of the wrist were 2.91 mm and 3.34 mm, respectively.

DISCUSSION

Outline of embryology

According to the classic "sprouting" theory, the arteries of the developing upper limb arise successively from a single trunk of the axial artery [27]. However,
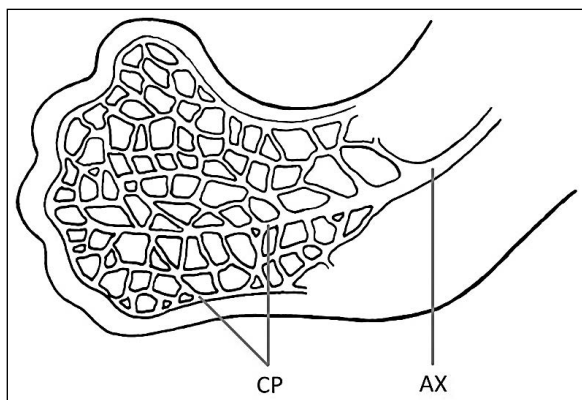
Figure 4. Capillary plexus (CP) in the developing upper limb; AX — axial artery differentiated within the arm region (precursor trunk for the brachial artery). This figure is a modification of the drawing taken from Wysiadecki et al. (2017) under the terms of the Creative Commons Attribution 4.0 International License (https://creativecommons.org/licenses/by/4.0/), which permits unrestricted use, distribution, and reproduction in any medium.

based on recent theories, the precursor trunks for the main arteries of the upper limb develop from the primitive capillary plexus forming "vascular labyrinth" (Fig. 4). Based on this model it may be presumed that the dominant vascular channels in the developing upper limb gradually differentiate as a result of capillary remodelling. This remodelling may continue until the formation of the muscular membrane in the developing arteries [20–22]. Thus, an aberrant course of some arteries may result from plexiform appearance of the upper limb arteries during early stages of the ontogenesis. This model may also be useful to explain unusual variations of the definitive arterial pattern that occasionally occur during arterial development [20–22]. Examples of the results of such an atypical development of the ulnar artery have been presented in this report.

Variants and classification of the SUA

The SUA may originate at a variable level: within the axillary fossa or in the arm or in the cubital fossa [1–9, 13, 14, 17–26, 31–33]. It may provide an accessory ulnar recurrent artery, radial recurrent artery, or interosseous artery. However, in some variants of the SUA the ulnar recurrent or/and the common interosseous arteries may arise from the radial artery. Thus, different arterial patterns involving the presence of the SUA were described in the medical literature [1–9, 13, 14, 17–26, 31–33]. It should be emphasized, however, that there are difficulties in classification of individual variants of the SUA. Our case no. 1 resem-

bles a situation where the typical termination of the brachial artery is shifted upwards. The initial segment of the SUA gives off the common interosseous artery, which is similar to typical anatomical relationships.

Another pattern, i.e. bifurcation of the brachial artery into a common radial–interosseous trunk and SUA, was described by Narayanan and Murugan [18]. This variant resembles cases no. 2 and 3 described in our report. However, based on the classification provided by Bergman et al. [3], this pattern may also be described as the radial origin of the common interosseous artery. Such classification was applied in our report. A different view for classification of this pattern was presented by Shankar and Veeramani [26], who stated that when the superficial artery is present, the brachial artery commonly terminates as the radial and common interosseous artery. Another way in which Gruber [9] and Rodríguez-Niedenführ et al. [21] describe the presence of the SUA in the forearm is partial duplication of the ulnar artery. According to those authors, partial duplications of the ulnar artery involves the presence of two vessels — the superficial ulnar artery reaching the palm and the rudimentary "normal" ulnar artery, sending of the ulnar recurrent artery, the common interosseous arteries and terminating as small muscular branches to the forearm flexor muscles. However, as Rodríguez-Niedenführ et al. [21] stress, many authors who reported the SUA, have observed the origin of the ulnar recurrent artery from the interosseous arteries, but they did not consider such variant as a duplication.

Based on the review of existing literature, we did not find a case of a radial origin of the SUA. Only the radial origin of the median artery was reported [3]. However, in the light of recent classifications [20–22], our case no. 4 may resemble the superficial brachioulnoradial artery. Rodríguez-Niedenführ et al. [21] define the superficial brachioulnoradial artery as "a superficial brachial artery branching at the elbow level into the radial and ulnar arteries coursing over the superficial forearm flexors and coexisting in the whole arterial pattern of the limb with a normal brachial artery that continues as the common interosseous trunk". The incidence of this variant ranges from 0.13% to 1.47% [17, 21]. However, the superficial brachioulnoradial artery most often arises from the proximal half of the brachial artery and bifurcates proximal to the interepicondylar line of the humerus [1, 2, 20–22]. In our case, the common trunk for the radial and SUA took origin in the distal quarter

of the forearm (36 mm above the interepicondylar line of the humerus) and undergo division below the interepicondylar line of the humerus. Thus, double classification may be applied regarding this case.

The SUA, when present, terminates by joining the normal position in distal part of the forearm and hand [1–9, 13, 14, 17–26, 31–33]. In most cases, however, the radial artery seems to be the dominant vessel in the distal forearm and, consequently, constitutes the major source of vascularisation to the hand [12, 14, 16, 20–22]. In all our cases the SUA was less dominant at the level of the wrist. The SUA may also be accompanied by anomalies of the palmar arches or forearm muscles [31–33].

Clinical significance

The SUA which runs beneath the skin may become vulnerable to iatrogenic or self-inflicted injuries [1, 4–8, 14, 17, 23–25, 31]. Presence of the SUA may influence vascular and reconstructive procedures as well as evaluation of angiographic examination [1, 4–8, 14, 17, 23–25, 31]. An unexpected atypical artery, running superficially, may also be a cause of complications during medical procedures, because incidental damage of such a vessel may cause distal limb ischaemia [14, 23].

Reports regarding the presence of SUA in a variety of clinical situations occasionally occur in medical literature. For example, Salunke et al. [23] reported a case of 22-year-old male who had sustained a glass cut injury to his right forearm and bleeding from the damaged radial artery. During revision of the wound, a large but intact superficial artery was found on the ulnar side of the surgical site. The diagnosis of SUA was confirmed in this case based on ultrasound Doppler examination and clinical assessment of the absence of the ulnar artery in its normal position [23]. Chin and Singh [5] conclude, based on their clinical experience, that SUA may cause a potential hazard in patients with difficult venous access. Those authors stress close relations of the SUA to the basilic vein which cause, that this aberrant artery may be at risk of unintended vascular puncture. They describe a case of a 53-year-old former heroin addict (which caused venous access difficulties), to gain intravenous access, a "non-pulsatile superficial vessel" was found in the right ventro-medial forearm, that resembled a venous channel. However, during an attempt at cannulation, blood was observed to flow rapidly up into the intravenous fluid tubing [5]. The cannulated

vessel was identified as SUA. Chin and Singh [5] stress, that presence of the aberrant SUA should be kept in mind when the venous access is performed in the antecubital fossa or on the ventro-medial aspect of the forearm. Schonauer et al. [24], in turn, stress that SUA is a rare finding but shows significant surgical implications. When properly diagnosed, the presence of the SUA may also help during reconstructive surgeries; the SUA flap may be an excellent solution for soft tissue reconstruction [7, 24].

Salunke et al. [23] proposed a series of clinical recommendations to reduce the risk of complications when dealing with unexpected vascular variations. Those recommendations involve: using of intraoperative Doppler ultrasound during reconstructive and orthopaedic procedures, tracing arterial vessels at their normal anatomical location while using neurovascular structures as landmarks and careful preoperative assessment of the vascular anatomy.

Limitations of the study

There are some limitations as a result of the time and method of the specimen creation. For instance, not all branches of the common interosseous artery could be traced because it was impossible to reach the deeper muscle layers without damaging of the specimens. However, so far researchers refer to historical sources that still may be an inspiration for in-depth research on anatomical variations [3, 9, 14, 19, 21, 22]. Finally, the analysis of anatomical variations can contribute to obtaining an actual, not idealised image of the inside of the human body, which is crucial in everyday clinical practice [34].

CONCLUSIONS

The SUA shows diverse anatomy regarding its topography and blood supply territory. It may originate from the brachial artery in the lower third of the arm. It may give off the common interosseous artery, however in some instances the common interosseous may arise from the radial artery. The ulnar recurrent branches may also be absent. In rare cases the superficial ulnar may arise below the interepicondylar line of the humerus, from the radial artery. The blood supply territory of the SUA may thus be highly variable.

lymphatic system, described haemin crystals ("Teichmann's crystals") and introduced numerous advances in techniques of the anatomical preparations.

Conflict of interest: None declared

REFERENCES

1. Ariyo O, Fenderson B. A variant of the classical superficial brachioulnoradial artery: morphology and clinical significances. Surg Radiol Anat. 2016; 38(6): 751–753, doi: 10.1007/s00276-015-1605-6, indexed in Pubmed: 26831325.
2. Atlasi MA. A brachioulnoradial artery: a short report. Surg Radiol Anat. 2014; 36(1): 99–101, doi: 10.1007/s00276-013-1126-0, indexed in Pubmed: 23645170.
3. Bergman RA, Afifi AK, Miyauchi R. Illustrated Encyclopedia of Human Anatomic Variation: Opus II: Cardiovascular System: Arteries: Upper Limb. 2015. https://www.anatomyatlases.org/AnatomicVariants/Cardiovascular/Text/Arteries/Ulnar.shtml.
4. Casal D, Pais D, Toscano T, et al. A rare variant of the ulnar artery with important clinical implications: a case report. BMC Res Notes. 2012; 5: 660, doi: 10.1186/1756-0500-5-660, indexed in Pubmed: 23194303.
5. Chin KJ, Singh K. The superficial ulnar artery: a potential hazard in patients with difficult venous access. Br J Anaesth. 2005; 94(5): 692–693, doi: 10.1093/bja/aei548, indexed in Pubmed: 15814810.
6. D'Costa S, Shenoy BM, Narayana K. The incidence of a superficial arterial pattern in the human upper extremities. Folia Morphol. 2004; 63(4): 459–463, indexed in Pubmed: 15712144.
7. Devansh A. Superficial ulnar artery flap. Plast Reconstr Surg. 1996; 97(2): 420–426, doi: 10.1097/00006534-199602000-00022, indexed in Pubmed: 8559826.
8. Fadel RA, Amonoo-Kuofi HS. The superficial ulnar artery: development and surgical significance. Clin Anat. 1996; 9(2): 128–132, doi: 10.1002/(SICI)1098-2353(1996)9:2<128::AID-CA5>3.0.CO;2-D, indexed in Pubmed: 8720787.
9. Gruber W. Über die Arteria mediana antibrachii superficialis, Arteria ulnaris antibrachii superficialis und Duplicität der Arteria ulnaris. Arch Anat Physiol Wisen Med. 1867: 668–687.
10. Haładaj R, Wysiadecki G, Dudkiewicz Z, et al. The high origin of the radial artery (brachioradial artery): its anatomical variations, clinical significance, and contribution to the blood supply of the hand. Biomed Res Int. 2018; 2018: 1520929, doi: 10.1155/2018/1520929, indexed in Pubmed: 29992133.
11. Haładaj R, Wysiadecki G, Polguj M, et al. Hypoplastic superficial brachioradial artery coexisting with atypical formation of the median and musculocutaneous nerves: a rare combination of unusual topographical relationships. Surg Radiol Anat. 2019; 41(4): 441–446, doi: 10.1007/s00276-019-02183-1, indexed in Pubmed: 30652211.
12. Haerle M, Häfner HM, Dietz K, et al. Vascular dominance in the forearm. Plast Reconstr Surg. 2003; 111(6): 1891–1898, doi: 10.1097/01.PRS.0000057529.76413.D7, indexed in Pubmed: 12711949.
13. Mannan A, Sarikcioglu L, Ghani S, et al. Superficial ulnar artery terminating in a normal ulnar artery. Clin Anat. 2005; 18(8): 602–605, doi: 10.1002/ca.20150, indexed in Pubmed: 16187323.
14. McCormack LJ, Cauldwell EW, Anson BJ. Brachial and antebrachial arterial patterns; a study of 750 extremities. Surg Gynecol Obstet. 1953; 96(1): 43–54, indexed in Pubmed: 13015348.
15. Musiał A, Zarzecki M, Gryglewski R, et al. Ludwik Karol Teichmann (1823-1895). Folia Med Cracov. 2017; 57(4): 41–54, doi: 10.24425/118114.
16. Nasr AY. The radial artery and its variations: anatomical study and clinical implications. Folia Morphol. 2012; 71(4): 252–262, indexed in Pubmed: 23197145.
17. Natsis K, Papadopoulou AL, Paraskevas G, et al. High origin of a superficial ulnar artery arising from the axillary artery: anatomy, embryology, clinical significance and a review of the literature. Folia Morphol. 2006; 65(4): 400–405, indexed in Pubmed: 17171623.
18. Narayanan S, Murugan S. Bifurcation of brachial artery into a common radial-interosseous trunk and superficial ulnar artery: a rare variation. Anat Sci Int. 2018; 93(3): 400–403, doi: 10.1007/s12565-017-0427-5, indexed in Pubmed: 29277855.
19. Quain R. Anatomy of the arteries of the human body. Taylor and Walton, London 1844: 326–337.
20. Rodríguez-Niedenführ M, Burton GJ, Deu J, et al. Development of the arterial pattern in the upper limb of staged human embryos: normal development and anatomic variations. J Anat. 2001; 199(Pt 4): 407–417, doi: 10.1046/j.1469-7580.2001.19940407.x, indexed in Pubmed: 11693301.
21. Rodríguez-Niedenführ M, Vázquez T, Nearn L, et al. Variations of the arterial pattern in the upper limb revisited: a morphological and statistical study, with a review of the literature. J Anat. 2001; 199(Pt 5): 547–566, doi: 10.1046/j.1469-7580.2001.19950547.x, indexed in Pubmed: 11760886.
22. Rodríguez-Niedenführ M, Vázquez T, Parkin I, et al. Arterial patterns of the human upper limb: update of anatomical variations and embryological development. Eur J Anat. 2003; 7(S1): 21–28.
23. Salunke AA, Nambi GI, Dhanwate AD, et al. Superficial ulnar artery: Clinical recommendations to avoid iatrogenic complications due to variation in arterial system. Niger Med J. 2014; 55(3): 276–277, doi: 10.4103/0300-1652.132071, indexed in Pubmed: 25013265.
24. Schonauer F, Marlino S, Turrà F, et al. Superficial ulnar artery perforator flap. J Craniofac Surg. 2014; 25(5): 1870–1871, doi: 10.1097/SCS.0000000000001061, indexed in Pubmed: 25102397.
25. Senanayake KJ, Salgado S, Rathnayake MJ, et al. A rare variant of the superficial ulnar artery, and its clinical implications: a case report. J Med Case Rep. 2007; 1: 128, doi: 10.1186/1752-1947-1-128, indexed in Pubmed: 17988391.
26. Shankar N, Veeramani R. Bilateral superficial ulnar arteries with an unusual arterial arch in the forearm. Int J Anat Var (IJAV. 2009; 2: 24–26.
27. Singer E. Embryological pattern persisting in the arteries of the arm. Anat Rec. 1933; 55(4): 403–409, doi: 10.1002/ar.1090550407.
28. Standring S. Gray's Anatomy: The Anatomical Basis of Clinical Practice. Churchill Livingstone, Edinburgh, London 2016.
29. Von Ha. Anatomical description of the arteries of the human body. Thomas B Wait, Boston, MA 1813.
30. Wysiadecki G, Polguj M, Haładaj R, et al. Low origin of the radial artery: a case study including a review of literature and proposal of an embryological explanation. Anat Sci Int. 2017; 92(2): 293–298, doi: 10.1007/s12565-016-0371-9, indexed in Pubmed: 27631096.
31. Yadav PS, Ahmad QG, Shankhdhar VK, et al. Absence of the palmaris longus is a warning sign for avoiding the superficial ulnar artery 'trap'. Indian J Plast Surg. 2013; 46(1): 149–150, doi: 10.4103/0970-0358.113738, indexed in Pubmed: 23960326.
32. Yalcin B, Kocabiyik N, Yazar F, et al. Arterial variations of the upper extremities. Anat Sci Int. 2006; 81(1): 62–64, doi: 10.1111/j.1447-073X.2006.00110.x, indexed in Pubmed: 16526599.
33. Yazar F, Kirici Y, Ozan H, et al. An unusual variation of the superficial ulnar artery. Surg Radiol Anat. 1999; 21(2): 155–157, doi: 10.1007/s00276-999-0155-1, indexed in Pubmed: 10399219.
34. Żytkowski A, Tubbs R, Iwanaga J, et al. Anatomical normality and variability: Historical perspective and methodological considerations. Transl Res Anat. 2021; 23: 100105, doi: 10.1016/j.tria.2020.100105.

VIA MEDICA

C A S E   R E P O R T

Transantral intraseptal sinuous canal

M.C. Rusu⬤, C. Bichir, A.D. Vrapciu

Division of Anatomy, Faculty of Dental Medicine, "Carol Davila" University of Medicine and Pharmacy, Bucharest, Romania

The sinuous canal is an anatomically well-defined intramural canal of the maxillary sinus (MS) folded within the antral walls. Commonly, its first, infraorbital part, courses within the antral roof, while its second, transverse facial part courses below the infraorbital foramen within the anterior antral wall. While retrospective files of patients that were scanned in cone-beam computed tomography (CBCT) for different dental medical purposes were observed randomly, a peculiar variant of the sinuous canal was noticed and further documented. The respective canal origin was far posterior in the infraorbital groove and the canal coursed through the MS embedded within an incomplete oblique septum dividing the antrum into anterosuperior and posteroinferior chambers. Then the sinuous canal continued with the transverse facial segment. As the sinuous canal contains the superior anterior alveolar nerve and artery, major suppliers of the frontal teeth, it is recommended to document in CBCT a possible transantral, and not intramural, course of it, especially when surgical or endoscopic corridors through the MS are planned. (Folia Morphol 2022; 81, 1: 234–236)

Key words: superior anterior alveolar nerve, infraorbital nerve, infraorbital canal, maxillary sinus

INTRODUCTION

The canalis sinuosus (CS) diverts from the infraorbital canal (IOC) allowing passage for the anterior superior alveolar nerve (ASAN) and anterior superior alveolar artery (ASAA) that branch from the infraorbital neurovascular bundle [8, 9]. Forming in the roof of the maxillary sinus (MS) and usually ending at the base of the anterior nasal spine, it has an anteromedial direction through the maxillary walls, passing inferior to the infraorbital foramen (IOF) [13].

The double curvature along the course of the canal is what attributed the term "sinuosus" to its name. Usually, it tunnels from the IOC through the orbital floor (the primary segment of the CS) to reach the anterior antral wall where it takes a sharp turn downward and medial to reach the nasal lateral wall,

in front of the anterior end of the inferior concha. From there it angles again, following the contour of the anterior nasal aperture, towards the anterior nasal spine [4].

Although its passage is described as a sinuous path folded to the maxillary walls all the way from the IOC to the anterior maxillary region, the CS can have a more direct path through a MS septum. To our knowledge, an intraseptal, transantral variant of the CS has not been reported before.

Taking into consideration the clinical implications of damaging the ASAN during surgical procedures such as Caldwell-Luc, sinus floor elevation, and antrostomy, surgical interventions in the posterior maxillary region require detailed knowledge of maxillary sinus anatomy and possible anatomical variations [6].
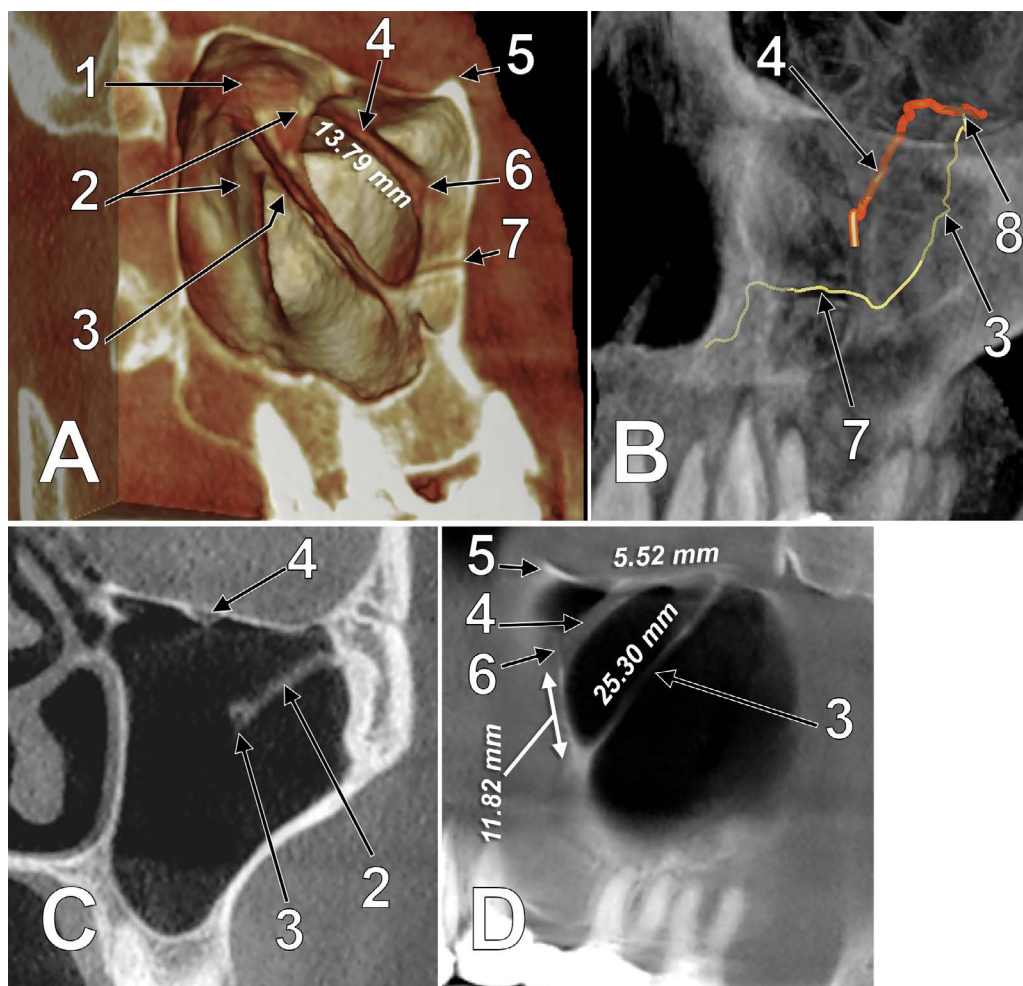
Figure 1. Transantral canalis sinuosus embedded within an incomplete intrasinus septum; **A.** Three-dimensional volume rendering, postero--infero-medial view of the left maxillary sinus; **B.** Three dimensional volume rendering, anterior view of the left maxilla, digitally reconstructed canals; **C.** Planar coronal cut of the left maxillary sinus; **D.** Digital orthopantomogram of the left maxillary sinus; 1 — infraorbital groove; 2 — incomplete oblique septum; 3 — transantral course of the first segment of the canalis sinuosus, from the infraorbital groove to the anterior antral wall; 4 — infraorbital canal; 5 — infraorbital margin; 6 — infraorbital foramen; 7 — intramural transverse facial segment of the canalis sinuosus; 8 — canalis sinuosus' origin from the infraorbital groove. Measurements were taken on sagittal cuts and applied in the figures.

CASE REPORT

During an evaluation on cone-beam computed tomography (CBCT) archived files, a unilateral transantral course of the CS was found in a 56-year-old female patient. As described in previous studies, the CBCT patient file was scanned with an iCat CBCT machine (Imaging Sciences International; Hatfield, PA, USA) with the settings: resolution 0.250 pixels/inch, field of view 130 mm, and image matrix size 640 × 640 pixels [9, 10]. By using the iCatVision software, the CBCT data were exported as a single uncompressed DICOM file, which was further analysed using the Planmeca Romexis Viewer 3.5.0.R software. The patient had given written informed consent for all medical data to be used for research and teaching purposes, provided the protection of the identity is maintained.

The right side presented no abnormal pattern of the CS, and a single antral septum was noticed in the maxillary sinus. On the left side, endosinus anatomy was different (Fig. 1). Two antral septa were found, one attached to the sinus roof below the infraorbital groove (IOG), and another one below the first, that ended on the MS floor in the premolar area. Both septa were located in the same anatomical plane having an anteroinferior direction. A transantral course of the left IOC was found in the superior septum. Within the inferior septum, another canal coursed from the IOG, through the MS, to the anterior antral wall where it continued beneath the IOF with a transverse course. This was therefore assessed as CS with the first segment being equally transantral and intraseptal.

DISCUSSION AND CONCLUSIONS

It is considered that the CS "has been little explored and many practitioners have no knowledge of its presence and location" [1] and that "many surgeons do not know much about this anatomical structure" [4].

The CS prevalence ranges between studies from 15.7% to 100%, and in a recent CBCT study [1], it was found that only 54.14% of patients presented bilateral CS. This implies that although the CS is a well-described anatomical structure, its presence is not easily traceable.

Anatomical transantral passage is not uncommon knowledge, as it has been presented before for other structures like the IOC [2]. Still, to the authors' knowledge, a transantral variant of the CS has not been described yet. Even more peculiar, the canal is situated in the bony confinement of a septum, making it insidious to clinicians in the absence of a complex radiological investigation.

The maxillary sinus septa are of interest, especially when performing surgical procedures such as sinus lift [5] or even Le Fort I osteotomy [11]. These barriers of cortical bone can arise from the antral floor or walls as primary or secondary septa to partially or completely separate the sinus into two or more cavities [7]. As secondary septa appear based on progressive pneumatisation of the MS in edentulous patients, in this case, both septa that have been found could be regarded as primary ones.

In endonasal endoscopic approaches of transmaxillary-transantral surgical intervention routes, large portions of the medial antral wall, as well as other bony structures along the way, might be removed. The purpose is to gain access to the posterior maxillary sinus wall in the attempt of removing lesions in the pterygopalatine fossa [3] or to approach the Meckel's cave [12].

Because of it being featured as a small, poorly recognised bony canal, the CS usually gets acknowledged when postsurgical complications such as haemorrhage, pain, anaesthesia, and paraesthesia appear [4]. Therefore, in surgical procedure planning, the transantral variant of CS should be taken into account, and careful evaluation of three-dimensional radiological investigation of the antral septa is recommended.

Conflict of interest: None declared

REFERENCES

1. Aoki R, Massuda M, Zenni LT, et al. Canalis sinuosus: anatomical variation or structure? Surg Radiol Anat. 2020; 42(1): 69–74, doi: 10.1007/s00276-019-02352-2, indexed in Pubmed: 31606782.
2. Cârstocea L, Rusu MC, Pascale C, et al. Three-dimensional anatomy of the transantral intraseptal infraorbital canal with the use of cone-beam computed tomography. Folia Morphol. 2020; 79(3): 649–653, doi: 10.5603/FM.a2019.0109, indexed in Pubmed: 31617577.
3. Cavallo L, Messina A, Gardner P, et al. Extended endoscopic endonasal approach to the pterygopalatine fossa: anatomical study and clinical considerations. Neurosurgical Focus. 2005; 19(1): 1–7, doi: 10.3171/foc.2005.19.1.6.
4. Gurler G, Delilbasi C, Ogut EE, et al. Evaluation of the morphology of the canalis sinusous using cone-beam computed tomography in patients with maxillary impacted canines. Imaging Sci Dent. 2017; 47(2): 69–74, doi: 10.5624/isd.2017.47.2.69, indexed in Pubmed: 28680842.
5. Jung J, Park JS, Hong SJ, et al. Axial triangle of the maxillary sinus, and its surgical implication with the position of maxillary sinus septa during sinus floor elevation: a CBCT analysis. J Oral Implantol. 2020; 46(4): 415–422, doi: 10.1563/aaid-joi-D-18-00229, indexed in Pubmed: 32315428.
6. Krennmair G, Ulm C, Lugmayr H. Maxillary sinus septa: incidence, morphology and clinical implications. J Craniomaxillofac Surg. 1997; 25(5): 261–265, doi: 10.1016/s1010-5182(97)80063-7, indexed in Pubmed: 9368861.
7. Maestre-Ferrín L, Galán-Gil S, Rubio-Serrano M, et al. Maxillary sinus septa: a systematic review. Med Oral Patol Oral Cir Bucal. 2010; 15(2): e383–e386, doi: 10.4317/medoral.15.e383, indexed in Pubmed: 19767706.
8. Rusu MC, Iacov-Crăiţoiu MM, Săndulescu M, et al. Constant features of the adult maxillary bone in the site of the premaxillary suture: the sutura notha, Macalister's foramina, Parinaud's canal, and the second angle of the canalis sinuosus of Wood Jones. Rom J Morphol Embryol. 2019; 60(4): 1097–1103, indexed in Pubmed: 32239084.
9. Rusu MC, Săndulescu M, Bichir C, et al. Combined anatomical variations: The mylohyoid bridge, retromolar canal and accessory palatine canals branched from the canalis sinuosus. Ann Anat. 2017; 214: 75–79, doi: 10.1016/j.aanat.2017.07.006, indexed in Pubmed: 28823708.
10. Rusu MC, Sava CJ, Ilie AC, et al. Agger nasi cells versus lacrimal cells and uncinate bullae in cone-beam computed tomography. Ear Nose Throat J. 2019; 98(6): 334–339, doi: 10.1177/0145561319840836, indexed in Pubmed: 31012345.
11. Samsudin AbR, Qabbani A, Wahbi S. Le fort i osteotomy complicated by presence of maxillary sinus septa. J Craniofac Surg. 2020 [Epub ahead of print], doi: 10.1097/SCS.0000000000006650, indexed in Pubmed: 32604301.
12. Van Rompaey J, Suruliraj A, Carrau R, et al. Meckel's cave access: anatomic study comparing the endoscopic transantral and endonasal approaches. Eur Arch Otorhinolaryngol. 2014; 271(4): 787–794, doi: 10.1007/s00405-013-2581-2, indexed in Pubmed: 23771278.
13. von Arx T, Lozanoff S. Anterior superior alveolar nerve (ASAN). Swiss Dent J. 2015; 125(11): 1202–1209, indexed in Pubmed: 26631255.

VIA MEDICA

CASE REPORT

Two cases of combined anatomical variations: maxillofacial trunk, vertebral, posterior communicating and anterior cerebral atresia, linguofacial and labiomental trunks

M.C. Rusu[1] , A.M. Jianu[2], M.D. Monea[2], A.C. Ilie[3]

[1]Division of Anatomy, Faculty of Dental Medicine, "Carol Davila" University of Medicine and Pharmacy, Bucharest, Romania
[2]Department of Anatomy, Faculty of Medicine, "Victor Babeş" University of Medicine and Pharmacy, Timişoara, Romania
[3]Department of Functional Sciences, Discipline of Public Health, Faculty of Medicine, "Victor Babes" University of Medicine and Pharmacy, Timisoara, Romania

Background: Commonly, arterial anatomic variants are reported as single entities. However, different such variants can occur in a single patient.
Materials and methods: During a retrospective study of computed tomography angiograms of 52 adult patients, 2 cases were found with unilateral maxillofacial trunks. In each case different other anatomic variants were documented.
Results: The maxillofacial trunk in the first case was associated with bilateral posterior kinks of the internal carotid artery which passed beyond the transverse processes of the atlas vertebra and indented and displaced the internal jugular veins. Common carotid origins of the superior thyroid arteries were found, as well as a high origin of the contralateral facial artery. In the second case a plethora of variants were associated with a unilateral maxillofacial trunk: 1) direct oc-cipital-vertebral arterial anastomosis; 2) ipsilateral atresia of the distal vertebral artery and of the A1 segment of the anterior cerebral artery; 3) bilateral atresia of posterior communicating arteries; 4) linguofacial and labiomental trunks; 5) terminal trifurcation of the external carotid artery.
Conclusions: The arterial anatomical variants of the head and neck should be carefully documented prior to specific surgical and interventional procedures, as well as for understanding the compensatory anatomical pathways of circulatory insufficiencies. (Folia Morphol 2022; 81, 1: 237–246)

Key words: vertebral artery, carotid artery, circle of Willis, maxillary artery, facial artery

INTRODUCTION

The external (ECA) and the internal (ICA) carotid arteries are the terminal branches of the common carotid artery (CCA), leaving it in the carotid triangle of neck [32], typically at the level of the upper border of the thyroid cartilage.

The ECA further sends off its collateral branches: the superior thyroid artery (StA), lingual artery (LA),

facial artery (FA), ascending pharyngeal artery (APA), occipital artery (OA) and posterior auricular artery (PAA). Commonly, the ECA divides terminally into the maxillary (MA) and superficial temporal (STA) arteries. Rarely, the ECA could trifurcate terminally, the third added branch being either the middle meningeal artery (MMA), or the transverse facial artery (TFA) [31].

Different common trunks could result after the fusion of the ECA branches, such as the thyrolingual, linguofacial and thyrolinguofacial trunks [4, 20]. The maxillofacial trunk (MFT) is an extraordinary arterial variation in man [28]. Although few authors were quoted by Pretterklieber et al. [28] for listing this last arterial variation, they did not provide supportive evidence [4, 15]. In the online "Illustrated Encyclopedia of Human Anatomic Variation" Bergman et al. [3] documented that the origin of the MA is constant and very rarely it leaves the FA to course upwards into the infratemporal fossa.

The posterior cerebral circulation is supplied by the vertebrobasilar system of arteries. The vertebral arteries (VAs) commonly join in the posterior cranial fossa to form the basilar artery (BA). This later supplies the circle of Willis, as the ICAs also do. Cerebral insufficiencies could result if anatomical variant lead to an incomplete circle of Willis, but they could be compensated by ECA-to-VA anastomoses.

It was therefore aimed at documenting a retrospective lot of computed tomography (CT) angiograms for the MFT variant and whether, or not, other anatomic variations are associated with it.

MATERIALS AND METHODS

The anatomic variations reported here were found during a retrospective study of CT angiograms from 52 adult patients, a 68-year-old female patient (case 1) and a 57-year-old male patient (case 2). For the CT studies an iodine radiocontrast agent (Ultravist 370 mg/mL) was injected in the brachial vein, followed by 20 mL saline medium. The CT was performed with a 32-slice scanner (Siemens Multislice Perspective Scanner), using a 0.6 mm collimation and reconstruction of 0.75 mm thickness with 50% overlap for multiplanar and three-dimensional volume rendering technique [31]. The arterial variants were documented with the Horos software. The research was conducted ethically in accordance with The Code of Ethics of the World Medical Association (Declaration of Helsinki). Informed consent for anonymous use of the data with scientific purposes was signed

Table 1. Anatomic variations encountered in the 2/52 cases found with maxillofacial trunks

Anatomic variation	Case 1	Case 2
Maxillofacial trunk	U	U
ICA folded into the IJV	B	–
CCA origin of the StA	B	–
Os stylo-hyale	B	–
High origin (C2) of the facial artery	U	–
CB origin of the StA	–	B
Os cerato-hyale	–	B
Occipital-to-vertebral arterial anastomosis	–	U
Terminal trifurcation of the ECA	–	U
Aberrant course of the STA		
Aplasia of the distal segment of the VA	–	U
Aplasia of the A1 segment of the ACA	–	U
Aplasia of the posterior communicating artery	–	B
Linguofacial trunk	–	U
Labiomental trunk	–	U

ACA — anterior cerebral artery; B — bilateral; CB — common carotid artery bifurcation; CCA — common carotid artery; ECA — external carotid artery; ICA — internal carotid artery; IJV — internal jugular vein; STA — superficial temporal artery; StA — superior thyroid artery; U — unilateral; VA — vertebral artery

by patients. The manuscript was tacitly approved by the responsible authorities where the work was carried out.

RESULTS

Two of the 52 (3.8%) cases presented each the exceptionally rare arterial variation — unilateral MFT. Moreover, in each case different other rare variations were found and are listed in Table 1.

Case 1: Left maxillofacial trunk

In this first case, the right CCA bifurcation was posterior to the tip of the greater horn of the hyoid bone, at 1.28 cm deep to the gonial angle (Fig. 1), at the level of the 3rd cervical vertebra. Prior to its bifurcation the CCA was sending off the StA, which originated above the greater horn of the hyoid bone and coursed inferiorly, over that bone. Immediately as the respective ECA left the carotid bifurcation it gave off from its anterior side the LA of which initial segment was coiled and continued inferiorly towards the greater horn. Above the origin of the LA, at the level of the 2nd cervical vertebra, three major vessels had parapharyngeal posterior kinks, folded into each other: the ECA, ICA and the internal jugular vein (IJV) (Fig. 1). These kinks were at
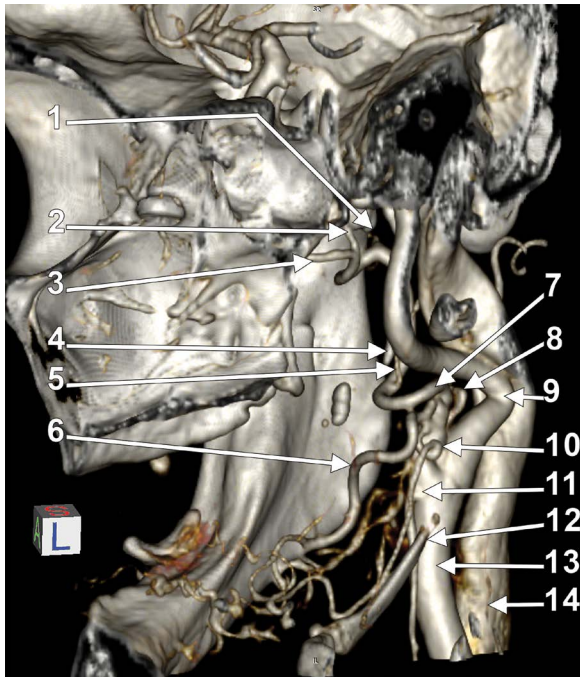
Figure 1. Three dimensional volume renderisation, infero-medial view, right side (case 1); 1 — superficial temporal artery; 2 — middle meningeal artery; 3 — maxillary artery; 4 — os stylo-hyale; 5 — posterior auricular artery; 6 — facial artery; 7 — external carotid artery; 8 — occipital artery; 9 — posterior kink of the internal carotid artery; 10 — coiled lingual artery; 11 — origin of the superior thyroid artery; 12 — greater horn of the hyoid bone; 13 — common carotid artery; 14 — internal jugular vein.
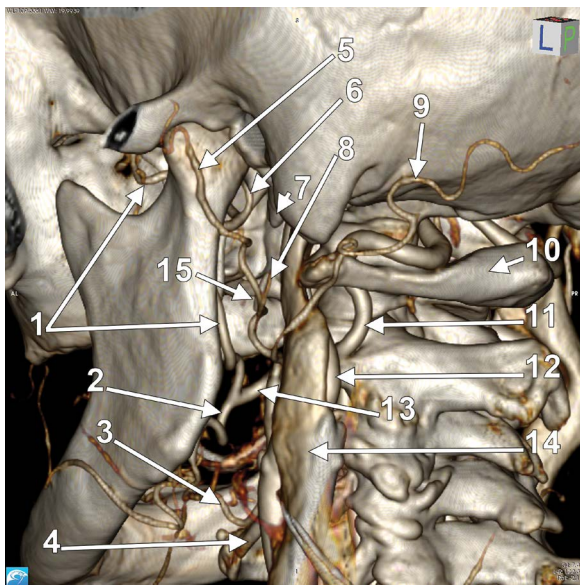
Figure 2. Three dimensional volume renderisation, postero-infero-lateral view, left side. The maxillofacial trunk (case 1); 1 — maxillary artery; 2 — facial artery; 3 — lingual artery; 4 — greater horn of the hyoid bone; 5 — superficial temporal artery; 6 — middle meningeal artery; 7 — os tympano-hyale; 8 — posterior auricular artery; 9 — occipital artery; 10 — atlas vertebra; 11 — vertebral artery; 12 — posterior kink of the internal carotid artery; 13 — maxillofacial trunk; 14 — internal jugular vein; 15 — os stylo-hyale.

1.78 cm postero-medial to the mandibular ramus, and the kinks of the ICA and IJV were posterior to the frontal plane of the transverse processes of the axis vertebra. From the ECA's posterior kink left a posterior branch — the OA, and an anterior one — the FA. The FA originated at 2.18 cm postero-infero-medially to the mandibular foramen. Then, the FA turned laterally in front of the styloglossus muscle and further descended infero-laterally between the styloglossus and the medial pterygoid to reach the inferior border of the mandible. In that course the FA was placed between the parotid and submandibular glands. Above the anterior loop of the FA was an anterior loop of the ECA which turned laterally also in front of the styloglossus and gave off the PAA. After the PAA emerged the medial side of the ECA it ascended on its inner side. The ECA continued in the retromandibular fossa and bifurcated terminally postero-medial to the mandibular neck into the STA and MA. The MA coursed into the infratemporal fossa deep to the inferior head of the lateral pterygoid muscle.

On the left side (Figs. 2, 3) the CCA bifurcated postero-superiorly to the tip of the respective greater horn of the hyoid bone, at the level of the 3rd cervical vertebra. The StA left the anterior side of the CCA, prior to its bifurcation. At 35 mm distally from its origin, the left ECA sent off a posterior branch — the OA, a medial one — the APA, and an anterior one — the LA. Then the ECA continued vertically for another 59 mm, being located antero-medially to a large posterior kink of the ICA which, in turn, was folded into the medial side of the IJV to get posterior to the frontal plane through the transverse process of the 2nd cervical vertebra. The left ECA divided terminally into the STA and MFT at 1.47 cm deep to the gonial angle. The STA initially looped anteriorly in the parapharyngeal space, then it continued posteriorly and passed behind the *os stylo-hiale* to enter the parotid space. At that level the STA gave off the PAA.

The MFT looped anteriorly and then reached laterally the medial pterygoid muscle to bifurcate into an ascending branch — the MA, and a descending one — the FA. The MA ascended posterior to the medial pterygoid muscle, on the medial side of the posterior mandibular border. Above the medial pterygoid muscle the MA reached the inferior head of the lateral pterygoid muscle and continued deep to it with a normal course.

239
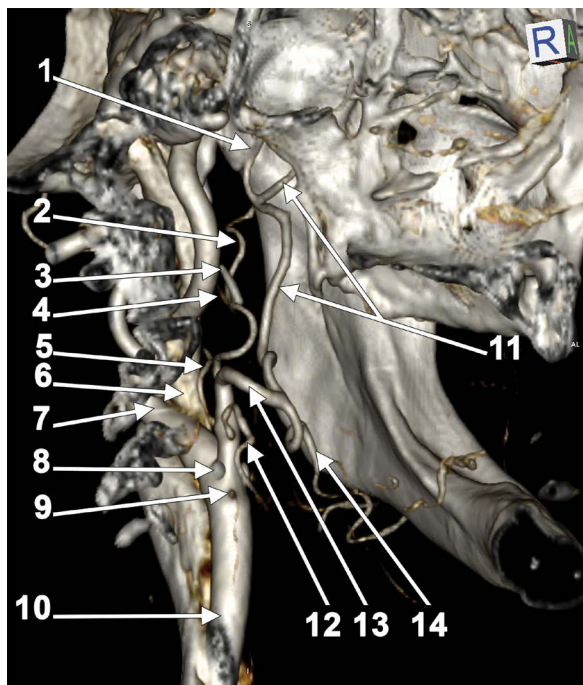
Figure 3. Three dimensional volume renderisation, infero-medial view, left side. The maxillofacial trunk (case 1); 1 — middle meningeal artery; 2 — superficial temporal artery; 3 — os stylo-hyale; 4 — posterior auricular artery; 5 — ascending pharyngeal artery; 6 — internal jugular vein; 7 — posterior kink of the internal carotid artery; 8 — tip of the greater horn of the hyoid bone; 9 — origin of the superior thyroid artery; 10 — common carotid artery; 11 — maxillary artery; 12 — lingual artery; 13 — maxillofacial trunk; 14 — facial artery.

Figure 4. Three dimensional volume renderisation, infero-lateral view, left side (case 2). The occipital-to-vertebral anastomosis. Terminally trifurcated external carotid artery. Linguofacial arterial trunk; 1 — transverse facial artery; 2 — internal carotid artery; 3 — occipital artery; 4 — linguofacial trunk; 5 — facial artery; 6 — external carotid artery; 7 — lingual artery; 8 — superior thyroid artery; 9 — superficial temporal artery; 10 — styloid process; 11 — internal jugular vein; 12 — descending branch of the occipital artery; 13 — occipital-to-vertebral arterial anastomosis; 14 — vertebral artery; 15 — maxillary artery.

Case 2: Right maxillofacial trunk

In the second case reported here there were found different unilateral combinations of anatomic variants.

On the left side the CCA had a high terminal bifurcation, which was at mid distance between the greater horn of the hyoid bone and the angle of mandible, at the level of the C3-C4 disc. From that bifurcation left off the StA. From the ECA first left the APA. Then the ECA sent off an anterior linguofacial trunk and the posteriorly directed OA, and continued deep to the gonial angle where it gave off the PAA. Then it passed beneath the tip of the styloid process with a medio-lateral course, to continue lateral to it till it reached the postero-lateral side of the neck of mandible (Fig. 4). Here it trifurcated terminally into the STA, MA and TFA (Fig. 4). The OA continued towards the occipital region where it sent off the descending branch. That branch further continued with a thinned and kinked anastomotic arch which joined the left VA into the intervertebral space between the transverse

processes of the 2nd and 3rd cervical vertebrae (Fig. 4). The VA was further observed in the posterior cranial fossa and was noticed the aplasia of its distal segment (Fig. 5). The left VA was not contributing to the BA. Instead, it continued as left posterior inferior cerebellar artery (Fig. 5). When the circle of Willis was carefully observed it was also noticed the aplasia of the A1 precommunicating segment of the left anterior cerebral artery (ACA) (Fig. 5). The posterior communicating arteries were also absent. Therefore, the respective circle of Willis appeared incompetent.

On the right side the CCA had also a high terminal bifurcation, at the level of the C3-C4 disc. Such as on the opposite side the StA left the CCA bifurcation. Then, from the right ECA were leaving the LA and the OA (Fig. 6). The LA's initial segment was coiled medially to the initial segments of the ECA and ICA. Then, the ECA divided terminally immediately beneath the gonial angle into an anterior MFT and the STA (Fig. 7).

On that side was found an *os cerato-hyale* located beneath the tip of the styloid process (Fig. 6). The STA crossed posteriorly that *os cerato-hyale* and
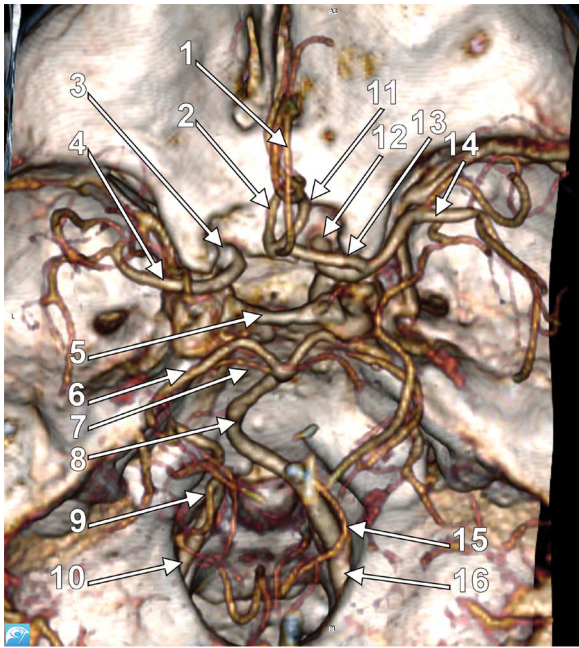
Figure 5. Three dimensional volume renderisation, superior view of the skull base (case 2). Aplasia of the A1 segment of the left cerebral artery. Aplasia of the left distal vertebral artery; 1 — left pericallosal artery; 2 — left anterior cerebral artery; 3 — left internal carotid artery; 4 — left middle cerebral artery; 5 — dorsum sellae; 6 — left posterior cerebral artery; 7 — left superior cerebellar artery; 8 — basilar artery; 9 — left posterior inferior cerebellar artery; 10 — left vertebral artery; 11 — right anterior cerebral artery; 12 — right internal carotid artery; 13 — A1 segment of the right anterior cerebral artery; 14 — right middle cerebral artery; 15 — right posterior inferior cerebellar artery; 16 — right vertebral artery.

Figure 6. Three dimensional volume renderisation, anterior view, right side. Origin of the maxillofacial trunk (case 2); 1 — coronoid process; 2 — superficial temporal artery; 3 — maxillary artery; 4 — facial artery; 5 — submandibular artery; 6 — maxillofacial trunk; 7 — common carotid artery; 8 — pterygoid plexus; 9 — internal carotid artery; 10 — styloid process; 11 — internal jugular vein; 12 — pharyngeal plexus; 13 — os cerato-hyale; 14 — vertebral artery; 15 — lingual artery; 16 — superior thyroid artery; 17 — greater horn of the hyoid bone.

continued laterally posterior to the mandibular ramus, crossing it at 1.13 cm above the gonial angle. It sent off the PAA and ascended laterally to the posterior border of the mandibular ramus (Fig. 7), behind the masseter muscle, with the superficial temporal vein on its lateral side. The STA gave off the TFA which ascended on masseter at the level of the mandibular notch and coronoid process. The STA continued laterally to the neck of mandible, covered by the superficial part of the parotid gland. It further ascended over the temporomandibular joint and posterior zygomatic root in the temporal region. The STA divided terminally at pterion into the frontal and parietal branches.

The respective right MFT trifurcated at the tip of the *os cerato-hyale* into inferior, middle and superior branches (Fig. 6). The inferior one was a glandular submandibular artery. The middle one was an ascending MA. The superior one was the FA. The FA initially descended below the inferior border of the mandible

then it continued laterally to the body of mandible where it sent off a labiomental trunk (Fig. 8). The MA had an initial ascending course, first being posterior to the medial pterygoid muscle, then passing through it to reach the *sulcus colli* postero-superior to the mandibular foramen, at the inferior border of the lateral pterygoid muscle. From this level it continued superficially to the lateral pterygoid with a normal antero-superior course, intermingling with veins of the pterygoid plexus (Fig. 7).

When the right ICA was observed above the skull base (Fig. 5) was noticed that the A1 segment of the right ACA was sending the A2 segments of both ACAs. The left pericallosal artery was leaving the A2 segment of the left ACA immediately after this latter originated from the A1 segment of the opposite ACA.

241

DISCUSSION

The embryonic maxillofacial trunk

During embryogenesis of the pharyngeal system six paired aortic arches develop bilaterally between primitive ventral and dorsal aortae [21]. The dorsal remnants of the first embryonic aortic arch coalesce with the hyoid artery which emerges the second aortic arch to form the hyostapedial artery [31]. From that latter emerge the primitive supraorbital artery and the embryonic maxillofacial trunk [31]. This embryonic trunk will give rise to infraorbital and mandibular branches and ultimately connects to the ECA, which is a derivative of the ventral aortic system [21, 31]. Commonly, the embryonic maxillofacial trunk becomes the definitive MA [25]. The primitive FA arises from the ECA and it could be speculated here that if the ECA origin of the FA glides cranially on the primitive maxillofacial trunk, the adult MFT would result. On other hand, if the primitive maxillofacial trunk, which is a dorsal aortic derivative, fuses with the FA bud, and not with the primitive ECA, it could also result the adult MFT. Nevertheless, if the initial segment of the definitive MA fails to insert on the ECA, it could be replaced by the ascending palatine artery from the FA, as documented in [28].

The maxillofacial trunk in human adult

The adult MFT appears as the common trunk of ECA origin of the MA and FA. This is different of the embryonic maxillofacial trunk which is the primordium of the definitive MA. Seemingly, Quain (1844) [29] was the first who reported an adult MFT, which was found once in 302 cases.

Pretterklieber et al. [28] reported a case with bilateral MFTs which were dissected in an 88-year-old adult male. The MA had, such as in the 2 cases reported here, two parts: an ascending one, followed by a pterygoid one. Dissections allowed the observation that the ascending part of the MFT-emerged MA ran straight upwards, covered by the posterior margin of the mandibular ramus and by the medial pterygoid muscle; further, the MA pierced that muscle between a tendinous dorsal and a fleshy ventral portion, to continue within the infratemporal fossa. On both sides the pterygoid part of the variant MA coursed deep to the inferior head of the lateral pterygoid muscle. In the present study, while in case 1 the MA ran deep to the lateral pterygoid muscle, in case 2 it was superficial to the respective muscle.

Figure 7. Three dimensional volume renderisation, postero-infero--lateral view, right side. Origin of the maxillofacial trunk (case 2); 1 — internal carotid artery; 2 — styloid process; 3 — posterior auricular artery; 4 — occipital artery; 5 — vertebral artery; 6 — internal jugular vein; 7 — transverse facial artery; 8 — superficial temporal artery; 9 — maxillofacial trunk; 10 — facial artery; 11 — lingual artery.

Figure 8. Three dimensional volume renderisation, infero-lateral view, right side (case 2). The labiomental trunk; 1 — superficial temporal artery; 2 — superficial temporal vein; 3 — occipital artery; 4 — internal jugular vein; 5 — facial artery; 6 — transverse facial artery; 7 — facial vein; 8 — labiomental trunk.

Different from humans, the MFT is a common phylogenetic trait and is a common finding in lagomorphs with extremely enlarged medial pterygoid and masseter muscles [28]. Therefore, a MFT in man should not be regarded as an atavism but as an ontogenetic adaptation of the arterial anatomy to enlarged masseter and medial pterygoid muscles [28].

The linguofacial trunk

The linguofacial trunk is a well-known possibility of variation in which the LA and FA could emerge from the ECA [12]. The incidence of the linguofacial trunk has been reported being 7% [2], 7.5% [26], 10% [5], 18% [20], 20% [7, 40], or 21% [24].

The labiomental trunk

The anatomy of the FA was recently reviewed, being documented that the inferior labial artery it either branches at the cheilion and courses along the vermilion border of the inferior lip, or it branches below the cheilion and courses along the labiomental crease as an horizontal labiomental artery [17], such as in the case 2 reported here. The inferior labial artery and the horizontal labiomental artery are the main arteries used in the lower lip pedicle [18].

Kinked internal carotid arteries

As Paulsen et al. [27] documented, in most descriptions the cervical part of the ICA runs a straight course to the base of skull. However, in 12/282 preparations (4.2%) kinks of the ICA were found [27]. These were documented for their relation with the pharyngeal wall, being found that in female patients the ICA kinks come in relation with the pharyngeal wall in 3.33% of cases [27]. Details on the uni- or bilateral evidence of such kinked ICAs were blurred by the material and methods that were used [27]. In case 1 were found bilaterally symmetrical antero--posterior kinks of the ICAs which were extended posterior to a frontal plane through the transverse processes of the atlas vertebra. Moreover, they were either indenting medially, or displacing posteriorly the adjacent IJV. Such morphological variant brings the ICA and the IJV posterior to the vertebral vessels, this being important in spine and back surgery. As kinking of an artery is the angulation of arterial segments, it is often associated with stenosis [39]. A kinked ICA could be clinically significant and cause cerebral infarction [39]. Few reports detailed previously the IJV extrinsic compression caused by ICA compression [19].
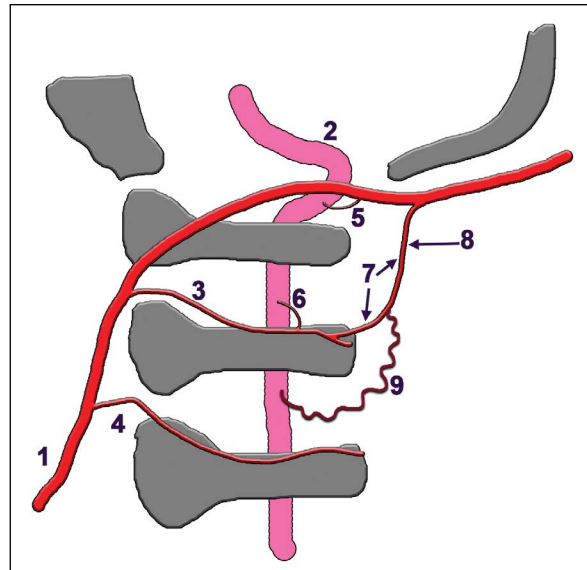
Figure 9. Drawing of a left lateral view updating the occipital-vertebral anastomotic pattern of Lasjaunias et al. [16]; 1 — occipital artery; 2 — vertebral artery; 3 — posterior muscular branch of the 2nd intervertebral space; 4 — posterior muscular branch of the 3rd intervertebral space; 5 — anastomotic channel of the 1st (atlantooccipital) space; 6 — anastomotic channel of the 2nd space; 7 — posterior arch of Lasjaunias; 8 — descending branch of the occipital artery (Nomina Anatomica); 9 — anastomotic channel of the 3rd space (case 2).

The IJV stenosis is characterized by a series of non--specific symptoms determined by blood flow obstruction [19].

Incompetent circle of Willis

As in case 2 the A1 segment of the left anterior cerebral artery, as well as both, left and right, posterior communicating arteries were also absent, the circle of Willis was regarded as an incompetent one. To that unfavourable anatomical disposition was added the distal aplasia of the left VA (Fig. 9).

Aplasia of the A1 segment of the anterior cerebral artery and bilateral aplasia of the posterior communicating artery

The aplasia of the A1 segment of the left anterior cerebral artery was found in case 2. Thus both distal parts of the anterior cerebral arteries were supplied from the contralateral ICA. This is a rare finding, but the most frequently observed variation of the anterior cerebral artery [37]. Lippert and Pabst [20] indicated this variant to occur in 10% of cases, Carels et al. [6] found it in 10.5%, but Uchino et al. (2006) [37] observed it in just 5.6% of cases.

243

Lippert and Pabst [20] also indicated an incidence of 10% of the bilateral aplasia or hypoplasia of both posterior communicating arteries. The bilateral posterior communicating artery atresia was listed as a variation in the configuration of the circle of Willis by Jinkins [14]. The unilateral aplasia of the posterior communicating artery was found in 3.5% of cases [9]. Alpers et al. [1] reported a prevalence of 0.6% of the unilateral absence of the posterior communicating artery. Saeki and Rhoton [33] credited Alpers et al. [1] for the incidence of the absent posterior communicating but in "Bergman's Comprehensive Encyclopedia of Human Anatomic Variation" [4] this anatomic variation was attributed to Saeki and Rhoton [33]. As it appears, in Bergman's Encyclopedia the possible bilateral absence of the posterior communicating arteries was not documented.

Distal aplasia of the vertebral artery

Interestingly, on the side with the occipital-vertebral anastomotic channel (case 2) the distal part of that left VA was aplastic, thus it was not contributing to the formation of the BA, but it ended supplying the posterior inferior cerebellar artery. Such a unilateral aplastic distal VA was reported with an incidence of 4.6% in asymptomatic persons by use of magnetic resonance imaging, while it has been reported as 0.2% of cases after use of cerebral angiography [23].

The occipital-vertebral arterial anastomosis

In the 4–5 mm embryos, a pair of neural arteries supply the hindbrain and anastomose with the ICA system through trigeminal, otic, hypoglossal and proatlantal arteries [8]. These are ventro-dorsal anastomotic arteries or cervical somatic arteries [16]. The proatlantal (cervical somatic) arteries persist until the VAs develop [8]. Two types of proatlantal arteries are described: type 1, when the proatlantal artery arises from the ICA and courses above the atlas vertebra to enter the foramen magnum and join the VA, and type 2, which leaves the ECA and joins the VA outside the skull [8]. Different possibilities of regression of the proatlantal arteries determine the variation of the OA origin, either from the ECA, or from the ICA, or from the VA [16, 36, 38].

In the present study was found, among other variations, an anastomotic channel between the descending branch of the OA and the VA in the 3rd intervertebral space (C2-C3 space). This should not be unusual, as in the anatomical and neuroradio-

logical literature is admitted that the OA and VA are anastomosed, usually by muscular anastomotic channels [16].

According to Lasjaunias et al. [16], from the ascending (cervico-occipital) portion of the OA two posterior muscular branches arise and project in the 2nd and 3rd intervertebral spaces, respectively. The branch of the 2nd space anastomoses with the VA by an anastomotic channel of the 2nd space [16]. Further, from the horizontal (occipital) portion of the OA arise: (a) a direct anastomotic channel of 1st space, which anastomoses with the VA in that atlantooccipital space and (b) a posterior arch (descending branch) that anastomoses with the anastomotic channel of the 2nd space.

Therefore, the anastomotic channel that was found here uniting the descending branch of the OA with the VA in the 3rd space appears as a novel finding to be added to the morphological pattern that was suggested by Lasjaunias et al. [16] (Fig. 9).

If the occipital-vertebral anastomotic channel of the 3rd intervertebral space is regarded as a part of a general arterial picture (Fig. 10) it appears that it could play a certain role in supplying the ipsilateral middle cerebral artery with blood from the VA, thus it compensates the ipsilateral absent posterior communicating artery. However, on the opposite side the arterial anatomy indicates that the VA supplies both posterior cerebral arteries and the ICA supplies the ipsilateral middle and anterior cerebral arteries, as well as the contralateral anterior cerebral one.

Richter [30] found in 25/30 cases segmental branches from the VA to the muscles of the neck, which supports the theory of Lasjaunias et al. [16]. Richter [30] observed filling of the OA that occurred once during vertebral angiography. Additionally he observed in 2 cases of ICA thrombosis the possibility of a compensatory occipital-vertebral flow [30]. In such a case with ICA thrombosis, Richter [30] found multiple small occipital-vertebral connections [10]. Schechter [34] observed in a retrospective study of 1000 cerebral angiograms just 8 cases with occipital-vertebral anastomosis. This author demonstrated on angiograms small anastomotic pathways linking the vertebral system with the descending branch of the OA and discussed they can function in either direction, carotid-to-vertebral or vertebral-to-carotid [34]. Occipital-vertebral anastomoses built-up by muscular branches of the 2nd and 3rd intervertebral space ensured an ipsilateral ECA supply of the cer-
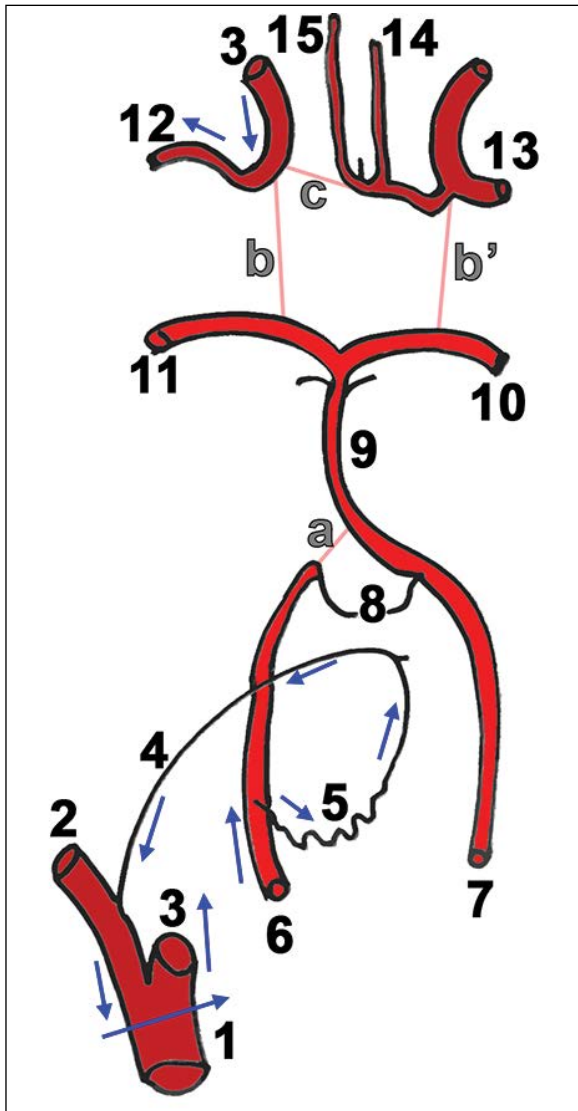
Figure 10. Diagram of the arterial variation (superior view) in case 2. The ipsilateral vertebral-to-middle cerebral artery pathway is indicated with arrows; 1 — left common carotid artery; 2 — left external carotid artery; 3 — left internal carotid artery; 4 — left occipital artery; 5 — occipital-vertebral anastomotic channel of the 3rd intervertebral space; 6 — left vertebral artery; 7 — right vertebral artery; 8 — posterior inferior cerebellar arteries; 9 — basilar artery; 10 — right posterior cerebral artery; 11 — left posterior cerebral artery; 12 — left middle cerebral artery; 13 — right middle cerebral artery; 14 — right anterior cerebral artery; 15 — left anterior cerebral artery; thin lines indicate the aplastic arteries: a — distal left vertebral artery; b, b' — posterior communicating arteries; c — left A1 segment of the anterior cerebral artery.

ebral circulation in a case with occluded ICA [13]. The anastomotic channel of the 3rd space was also tortuous, such as in the present report.

Anastomoses of the carotid and vertebrobasilar systems exist or become apparent in different pathological conditions (occlusions, arteriovenous malformations) [13]. The possibility for the occipital-verte-

bral anastomoses being constitutive was supported by a series of four cases with such direct anastomoses in the 1st (atlantooccipital space), when just two of these were associated with VA occlusion, the other two being not related neither to ECA, nor to VA occlusion [35]. Rarely, the occipital-vertebral anastomosis is symptomatic (syncope, vertebrobasilar insufficiency) due to a vertebral steal phenomenon through the anastomotic channel [11]. The occipital-vertebral anastomoses are infrequently visualised on angiographies, although they are not uncommon [22]. In the 2nd case reported here the occipital-vertebral anastomosis was seemingly of benefit to compensate the aplasia of different arterial suppliers of the circle of Willis.

CONCLUSIONS

The arterial anatomical variants of the head and neck should be carefully documented prior to specific surgical and interventional procedures, as well as for understanding the compensatory anatomical pathways of circulatory insufficiencies.

Conflict of interest: None declared

REFERENCES

1. Alpers BJ, Berry RG, Paddison RM. Anatomical studies of the circle of Willis in normal brain. AMA Arch Neurol Psychiatry. 1959; 81(4): 409–418, doi: 10.1001/archneurpsyc.1959.02340160007002, indexed in Pubmed: 13636509.
2. Anangwe D, Saidi H, Ogeng'o J, et al. Anatomical variations of the carotid arteries in adult Kenyans. East Afr Med J. 2008; 85(5): 244–247, doi: 10.4314/eamj.v85i5.9619, indexed in Pubmed: 18814535.
3. Bergman RA, Afifi AK, Miyauchi R. Illustrated encyclopedia of human anatomic variation: Opus II: Cardiovascular system: Arteries: Head, neck, and thorax. Maxillary artery. 2013. https://www.anatomyatlases.org/AnatomicVariants/Cardiovascular/Text/Arteries/Maxillary.shtml.
4. Bergman RA, Tubbs RS, Shoja MM, Loukas M. Bergman's comprehensive encyclopedia of human anatomic variation. John Wiley & Sons, Hoboken, New Jersey 2016.
5. Cappabianca S, Scuotto A, Iaselli F, et al. Computed tomography and magnetic resonance angiography in the evaluation of aberrant origin of the external carotid artery branches. Surg Radiol Anat. 2012; 34(5): 393–399, doi: 10.1007/s00276-011-0926-3, indexed in Pubmed: 22215429.
6. Carels K, Cornelissen SA, Robben D, et al. Smaller caliber of the internal carotid artery in patients with ipsilateral aplasia of the A1 segment of the anterior cerebral artery: a study with CTA. Acta Neurol Belg. 2018; 118(2): 297–302, doi: 10.1007/s13760-018-0935-7, indexed in Pubmed: 29721852.
7. Devadas D, Pillay M, Sukumaran TT. A cadaveric study on variations in branching pattern of external carotid

artery. Anat Cell Biol. 2018; 51(4): 225–231, doi: 10.5115/acb.2018.51.4.225, indexed in Pubmed: 30637155.

8. Gumus T, Onal B, Ilgit ET. Bilateral persistence of type 1 proatlantal arteries: Report of a case and review of the literature. AJNR Am J Neuroradiol. 2004; 25: 1622–1624, indexed in Pubmed: 15502152.

9. Gunnal SA, Farooqui MS, Wabale RN. Anatomical variability of the posterior communicating artery. Asian J Neurosurg. 2018; 13(2): 363–369, doi: 10.4103/ajns.AJNS_152_16, indexed in Pubmed: 29682035.

10. Hackett ER, Wilson CB. Congenital external carotid-vertebral anastomosis. A case report. Am J Roentgenol Radium Ther Nucl Med. 1968; 104(1): 86–89, doi: 10.2214/ajr.104.1.86, indexed in Pubmed: 5672781.

11. Harada J, Kuwayama N, Nishijima M, et al. Symptomatic occipital-vertebral anastomosis — a case report. Interv Neuroradiol. 2000; 6(4): 317–320, doi: 10.1177/159101990000600406, indexed in Pubmed: 20667210.

12. Herrera-Núñez M, Menchaca-Gutiérrez JL, Pinales-Razo R, et al. Origin variations of the superior thyroid, lingual, and facial arteries: a computed tomography angiography study. Surg Radiol Anat. 2020; 42(9): 1085–1093, doi: 10.1007/s00276-020-02507-6, indexed in Pubmed: 32488410.

13. Holodny AI. Supply of the unilateral circulation of the brain by an occipital artery anastomosis — a case report. Angiology. 2005; 56(1): 93–95, doi: 10.1177/000331970505600113, indexed in Pubmed: 15678262.

14. Jinkins JR. Atlas of neuroradiologic embryology, anatomy, and variants. Lippincott Williams & Wilkins, Philadelphia 2000.

15. Krmpotić-Nemanić J. Anatomie, Variationen und Mißbildungen der Gefäße im Kopf- und Halsbereich (Erläuterungen zum Referat). Archives Of Oto-Rhino-Laryngology. 1978; 219(2): 285–305, doi: 10.1007/bf00463786.

16. Lasjaunias P, Théron J, Moret J. The occipital artery. Anatomy — normal arteriographic aspects — embryological significance. Neuroradiology. 1978; 15(1): 31–37, doi: 10.1007/BF00327443, indexed in Pubmed: 643171.

17. Lee HJ, Won SY, O J, et al. The facial artery: a comprehensive anatomical review. Clin Anat. 2018; 31(1): 99–108, doi: 10.1002/ca.23007, indexed in Pubmed: 29086435.

18. Lee SH, Lee HJ, Kim YS, et al. What is the difference between the inferior labial artery and the horizontal labiomental artery? Surg Radiol Anat. 2015; 37(8): 947–953, doi: 10.1007/s00276-015-1447-2, indexed in Pubmed: 25724940.

19. Li M, Su C, Fan C, et al. Internal jugular vein stenosis induced by tortuous internal carotid artery compression: two case reports and literature review. J Int Med Res. 2019; 47(8): 3926–3933, doi: 10.1177/0300060519860678, indexed in Pubmed: 31304848.

20. Lippert H, Pabst R. Arterial variations in man: Classification and frequency. Springer 1985.

21. McEachen JC, Obrzut M, Bokhari SJ. A rare combination of carotid artery congenital abnormalities: understanding the embryology and clinical associations. Emerg Radiol. 2009; 16(5): 411–414, doi: 10.1007/s10140-008-0756-8, indexed in Pubmed: 18682997.

22. Miyachi S, Negoro M, Sugita K. The occipital-vertebral anastomosis as a collateral pathway: Hemodynamic patterns-case report. Surg Neurol. 1989; 32(5): 350–355, doi: 10.1016/0090-3019(89)90138-9.

23. Morimoto K, Nagahata M, Ono S, et al. Incidence of unilateral distal vertebral artery aplasia: evaluation by combining basiparallel anatomic scanning-magnetic resonance imaging (BPAS-MRI) and magnetic resonance angiography. Jpn J Radiol. 2009; 27(3): 151–155, doi: 10.1007/s11604-008-0313-0, indexed in Pubmed: 19412683.

24. Natsis K, Raikos A, Foundos I, et al. Superior thyroid artery origin in Caucasian Greeks: A new classification proposal and review of the literature. Clin Anat. 2011; 24(6): 699–705, doi: 10.1002/ca.21181, indexed in Pubmed: 21438023.

25. Osborn AG. Diagnostic cerebral angiography. 2nd ed. Lippincott Williams & Wilkins, Philadelphia, PA 1999.

26. Ozgur Z, Govsa F, Ozgur T. Assessment of origin characteristics of the front branches of the external carotid artery. J Craniofac Surg. 2008; 19(4): 1159–1166, doi: 10.1097/SCS.0b013e3180690252, indexed in Pubmed: 18650752.

27. Paulsen F, Tillmann B, Christofides C, et al. Curving and looping of the internal carotid artery in relation to the pharynx: frequency, embryology and clinical implications. J Anat. 2000; 197 (Pt 3): 373–381, doi: 10.1046/j.1469-7580.2000.19730373.x, indexed in Pubmed: 11117624.

28. Pretterklieber ML, Krammer EB, Mayr R. A bilateral maxillofacial trunk in man: an extraordinary anomaly of the carotid system of arteries. Acta Anat (Basel). 1991; 141(3): 206–211, doi: 10.1159/000147123, indexed in Pubmed: 1755281.

29. Quain R. The anatomy of the arteries of the human body. Taylor and Walton, London 1844.

30. Richter HR. Collaterals between the external carotid artery and the vertebral artery in cases of thrombosis of the internal carotid artery. Acta Radiol. 1953; 40(2-3): 108–112, doi: 10.3109/00016925309176574, indexed in Pubmed: 13114009.

31. Rusu MC, Măru N, Rădoi PM, et al. Trifurcated external carotid artery and complete gamma-loop of its maxillary branch. Surg Radiol Anat. 2019; 41(2): 231–234, doi: 10.1007/s00276-018-2142-x, indexed in Pubmed: 30483866.

32. Rusu MC, Vasilescu A, Nimigean V. A rare anatomic variant: the lateral position of the external carotid artery. Int J Oral Maxillofac Surg. 2006; 35(11): 1066–1067, doi: 10.1016/j.ijom.2006.04.001, indexed in Pubmed: 16828540.

33. Saeki N, Rhoton AL. Microsurgical anatomy of the upper basilar artery and the posterior circle of Willis. J Neurosurg. 1977; 46(5): 563–578, doi: 10.3171/jns.1977.46.5.0563, indexed in Pubmed: 845644.

34. Schechter MM. The occipital-vertebral anastomosis. J Neurosurg. 1964; 21: 758–762, doi: 10.3171/jns.1964.21.9.0758, indexed in Pubmed: 14210007.

35. Suzuki S, Kuwabara Y, Karasawa S. [The developmental mechanism of occipital-vertebral anastomosis (author's transl)]. No To Shinkei. 1980; 32: 69–79, indexed in Pubmed: 7356852.

36. Tanaka Y, Hara H, Momose G, et al. Proatlantal intersegmental artery and trigeminal artery associated with an aneurysm. Case report. J Neurosurg. 1983; 59(3): 520–523, doi: 10.3171/jns.1983.59.3.0520, indexed in Pubmed: 6886766.

37. Uchino A, Nomiyama K, Takase Y, et al. Anterior cerebral artery variations detected by MR angiography. Neuroradiology. 2006; 48(9): 647–652, doi: 10.1007/s00234-006-0110-3, indexed in Pubmed: 16786350.

38. Uchino A, Saito N, Mizukoshi W, et al. Anomalous origin of the occipital artery diagnosed by magnetic resonance angiography. Neuroradiology. 2011; 53(11): 853–857, doi: 10.1007/s00234-010-0825-z, indexed in Pubmed: 21174081.

39. Vannix R, Joergenson EJ, Carter R. Kinking of the internal carotid artery. Am J Surg. 1977; 134(1): 82–89, doi: 10.1016/0002-9610(77)90288-4.

40. Zümre O, Salbacak A, Ciçekcibaşi AE, et al. Investigation of the bifurcation level of the common carotid artery and variations of the branches of the external carotid artery in human fetuses. Ann Anat. 2005; 187(4): 361–369, doi: 10.1016/j.aanat.2005.03.007, indexed in Pubmed: 16163849.

VM VIA MEDICA

C A S E   R E P O R T

An extremely rare complete bilateral duplication of inferior vena cava in a male cadaver: anatomy, embryology and clinical relevance

S. Shaheen[1], K.I. Alyahya[1], A.F. El Fouhil[1], E.E.A. Salama[1], M. Atteya[1], F. Elshaer[2], H. Darwish[1]

[1]Clinical Anatomy Lab., Department of Anatomy, College of Medicine, King Saud University, Riyadh, Saudi Arabia
[2]King Khalid University Hospital, King Fahad Cardiac Centre, King Saud University, Riyadh, Saudi Arabia

The study presented an extremely rare case of real complete bilateral duplication of inferior vena cava (IVC) in a male cadaver which has never been reported before. Both IVC had approximately the same diameter. The right IVC drained into the right atrium; the left IVC continued as hemiazygos vein and drained into the superior vena cava. Three anastomotic venous channels, a cranial preaortic, a middle and a caudal retroaortic, joined both vessels. Multiple variations in the way of drainage of posterior intercostal veins, on both sides, were also present. The present report invalidates an old classification defining the two vessels when joined at the level of the renal veins as complete bilateral duplication of IVC. Although the presence of combination of venous variations is extremely rare, awareness of such variations is essential for clinical and surgical procedures to avoid misdiagnosis and surgical complications. (Folia Morphol 2022; 81, 1: 247–253)

INTRODUCTION

In human anatomy, inferior vena cava (IVC) is the largest single vein in the body which is responsible for the majority of venous return, as it drains the blood from the lower extremities and the abdominopelvic viscera. IVC is formed by the union of the common iliac veins anterior to the fifth lumbar vertebral body (L5) approximately 2.5 cm to the right of midline. It ascends on the right side of the body to the level of eighth thoracic vertebra (T8), and passes through the diaphragm to drain into the right atrium [30]. Because of the complexity of its developmental stages, IVC may be presented with numerous anatomical forms and variations [3, 21]. Congenital anomalies of IVC

were first described in 1793 [1]. They are nowadays increasingly recognised in asymptomatic patients due to the more frequent use of non-invasive imaging techniques [15, 21]. Duplication of IVC is a relatively uncommon condition with a reported incidence of 0.2–3% [4, 5, 9, 15, 18, 20].

Herein we present a case of an extremely rare variant of a duplicated IVC associated with other vessel anomalies in a male cadaver. In addition to the anatomical description, the development of veins with special reference to that of IVC as well as the previous reports for duplication of IVC are reviewed. An explanation of the underlying embryological changes is proposed. The clinical relevance of IVC variants is also discussed.

CASE REPORT

During a routine anatomy dissection for undergraduate medical students, in the Department of Anatomy, College of Medicine, King Saud University, Riyadh, Saudi Arabia, an abnormal left large vein was found to the left of the abdominal aorta in the posterior abdominal wall of an adult male cadaver. The anatomical variant was outlined from its beginning distally and traced to its termination proximally. The venous channels in relation to such variant were checked for associated anomalies. The two common iliac veins were joined by a large anastomotic venous channel of approximately 1.5 cm in width and 2 cm in length, at the level of L5. They continued upwards as two separate vessels (right and left IVC) of approximately 1.6 cm in width, each. At the level of L4, both IVC were interconnected by a transverse venous channel, of approximately one cm in width and 2 cm in length, posterior to the abdominal aorta. At the level of L3, both IVC were reconnected by another transverse anastomotic channel of approximately 1.2 cm in width and 1.2 cm in length, posterior to the abdominal aorta. At the level of the renal veins (L2), a third narrower and longer anastomotic channel, of about 0.5 cm in width and 5 cm in length, crossed anterior to the abdominal aorta and connected the right and left IVC. On the right side, one renal vein drained into the right IVC. On the left side, two renal veins, a superior and an inferior, drained into the left IVC. The right suprarenal vein and right testicular vein drained into the right IVC proximal and distal to right renal vein, respectively. The left suprarenal vein and left testicular vein drained into the left superior renal vein. The left IVC, preserving the same width (1.6 cm), continued in the thoracic cavity as the hemiazygos vein, anterior to the thoracic vertebrae. At the level of T4, the hemiazygos vein arched transversally from the left to the right, anterior to the bifurcation of the trachea to drain into the superior vena cava (SVC). A short accessory hemiazygos vein connected the arch of hemiazygos vein to the left brachiocephalic vein. The azygos vein, significantly smaller than the hemiazygos vein, arose from the right IVC, between the middle and cranial anastomotic venous channels distal to the right testicular vein, and ran upwards, from the right to the left side, to the thoracic cavity where it joined the hemiazygos vein, at the level of T6. The right IVC followed its normal course and drained into the right atrium of the heart. The posterior intercostal veins, on both sides, were checked for variations in
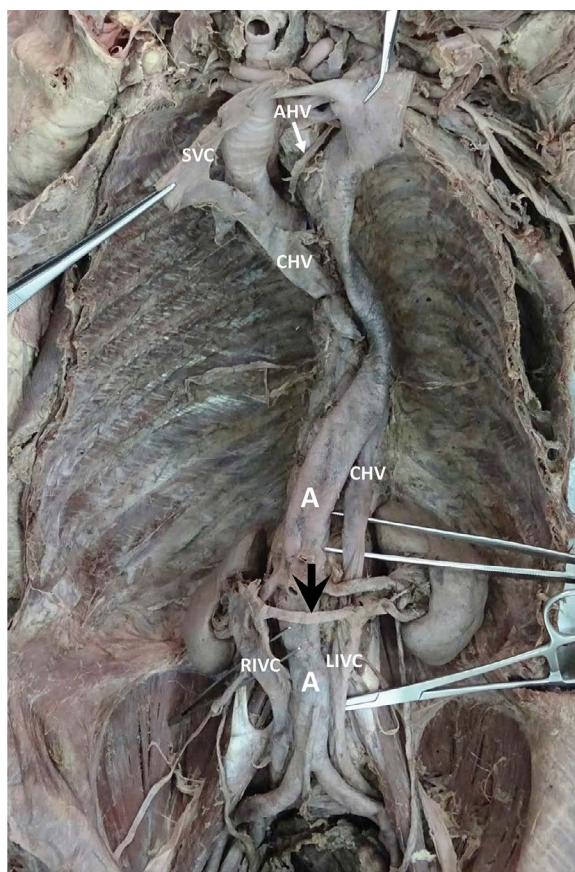
Figure 1. Gross appearance of the duplicated inferior vena cava; RIVC — right inferior vena cava; LIVC — left inferior vena cava; A — aorta; CHV — continuous hemiazygos vein; AHV — accessory hemiazygos vein; SVC — superior vena cava; arrow — preaortic anastomosis.

the way of their drainage. The right 11th, 10th, 9th and 8th posterior intercostal veins drained into the small azygos vein. The right 7th and 6th posterior intercostal veins drained into the hemiazygos vein. The right 5th and 4th posterior intercostal veins drained into the arch of the hemiazygos vein. The right second and third posterior intercostal veins united to form the right superior intercostal vein which also drained into the arch of the hemiazygos vein. The left posterior intercostal veins from 11th to 7th drained into the hemiazygos vein. The left posterior intercostal veins from 6th to 4th drained into the accessory hemiazygos vein (Figs. 1–5).

DISCUSSION

Initially, at the fourth week of intra-uterine life, the anterior cardinal veins (ACV) and posterior cardinal veins (PCV) drain cranial and caudal parts of the embryo, respectively. They join the common cardinal
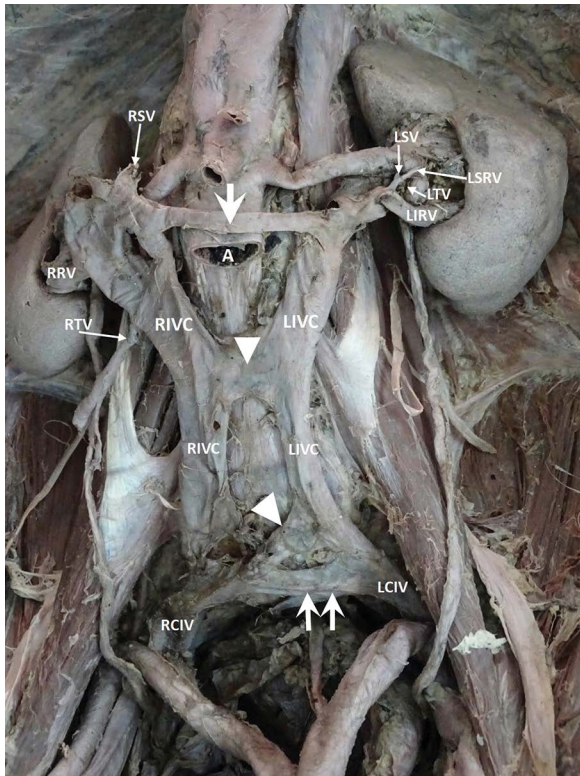
Figure 2. Gross appearance of the duplicated inferior vena cava after partial dissection of the abdominal aorta (A); RIVC — right inferior vena cava; LIVC — left inferior vena cava; RCIV — right common iliac vein; LCIV — left common iliac vein; RRV — right renal vein, RSV — right suprarenal vein; RTV — right testicular vein; LSRV — left superior renal vein, LIRV — left inferior renal vein; LSV — left suprarenal vein; LTV — left testicular vein; CHV — continuous hemiazygos vein; arrow — preaortic anastomosis; arrowhead — retroaortic anastomosis; Double arrows — anastomosis between common iliac veins.

Figure 3. The abnormal way of drainage of the right posterior intercostal veins from 2 to 11. The arch of continuous hemiazygos vein (CHV) and the superior vena cava (SVC) are reflected to the left; A — aorta; AV — azygos vein; LK — left kidney; RK — right kidney; RSIV — right superior intercostal vein.

veins (CCV) and form a symmetrical system. The right brachiocephalic vein is formed by the right ACV; the left brachiocephalic vein by the anastomosis between right and left ACV; and the superior vena cava by both right ACV and right CCV. During the sixth and seventh weeks of intrauterine life, the subcardinal and supracardinal veins, gradually replace and supplement PCV. The only adult derivatives of PCV are the root of the azygos vein and the common iliac veins. The subcardinal veins form the stem of left renal vein, the suprarenal and gonadal veins; the supracardinal veins form the azygos and hemiazygos veins. The right renal vein and the remaining of the left renal vein are formed by an anastomosis between the subcardinal and supracardinal veins. Finally, the IVC is formed by the fusion of four different segments; a hepatic segment derived from the right vitelline vein, a prerenal segment derived from the right subcardinal vein,

a renal segment derived from the subcardinal-supracardinal anastomosis, and a postrenal segment from the right supracardinal vein [17].

Duplication of IVC has been reported previously in several forms. The most common form is one in which two distinct IVC arise from each iliac vein [22]. Usually, the left IVC ends at the level of the renal veins, crossing anterior to the abdominal aorta to join the right IVC [7, 15, 18]. This variation was defined by Natsis et al. [18] as "complete bilateral duplication of IVC" because it comprised both renal and infrarenal segments of IVC. They further subdivided it into three types; major (type I) with two bilateral symmetrical trunks and a preaortic trunk of the same diameter [24, 28], minor (type II) with two bilateral symmetrical trunks but smaller in diameter in comparison to the preaortic trunk [27, 31], and asymmetrical (type III) with three trunks asymmetric in size [8, 13]. The term
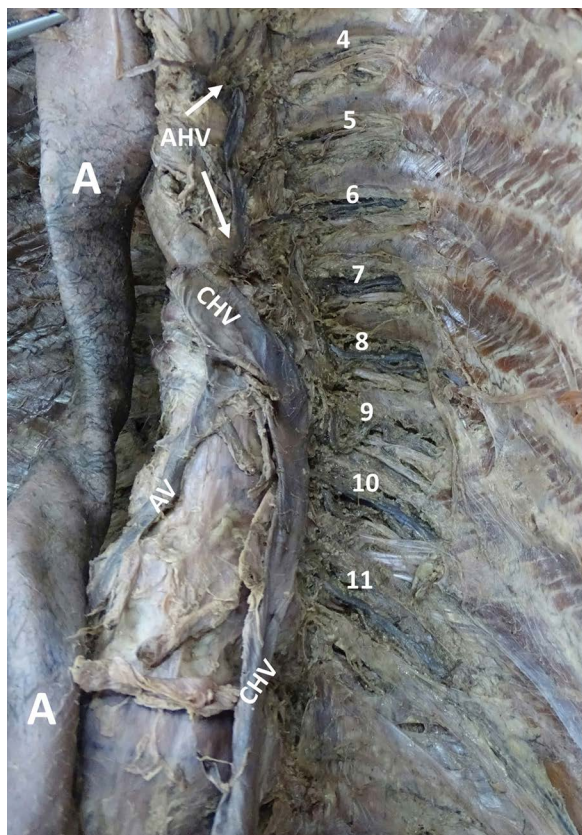
Figure 4. The abnormal way of drainage of the left posterior intercostal veins from 4 to 11; A — aorta; AHV — accessory hemiazygos vein; CHV — continuous hemiazygos vein; AV — azygos vein.

Figure 5. Schematic illustration of the duplicated inferior vena cava, abnormal azygos system and abnormal way of drainage of posterior intercostal veins; RIVC — right inferior vena cava; LIVC — left inferior vena cava; RCIV — right common iliac vein; LCIV — left common iliac vein; RRV — right renal vein, RSV — right suprarenal vein; RTV — right testicular vein; LSRV — left superior renal vein, LIRV — left inferior renal vein; LSV — left suprarenal vein; LTV — left testicular vein; CHV — continuous hemiazygos vein; AHV — accessory hemiazygos vein; SVC — superior vena cava; AV — azygos vein; arrow — preaortic anastomosis; arrowhead — retroaortic anastomosis; double arrows — anastomosis between common iliac veins.

"incomplete bilateral duplication" was referred to cases where the left IVC is smaller in diameter and empties into the left renal vein [10]. Other reported forms of duplication of IVC included double IVC with retroaortic right renal vein and hemiazygos continuation of the IVC [2, 4, 9, 21], and double IVC with retroaortic left renal vein and azygos continuation of the IVC [6, 21]. In cases of hemiazygos continuation, right IVC joins right renal vein which passes behind the aorta to join the left IVC that ascends as hemiazygos vein and either joins the rudimentary azygos vein in the thorax or the coronary vein of the heart through a persistent left SVC or continues as accessory hemiazygos vein to drain into the left brachiocephalic vein. In cases of azygos continuation, left IVC joins left renal vein which runs behind the aorta to join the right IVC that continues as azygos vein and drains into SVC. Petik [21] also reported a case of both continuous azygos and hemiazygos veins joining together supradiaphragmatically and draining into SVC.

The present case also reported multiple variations in the way of drainage of the posterior intercostal veins, on both sides. Normally, the right posterior intercostal veins, from 11th to 4th, drained into the azygos vein, while the right second and third posterior intercostal veins unite to form the right superior intercostal vein which drains into the arch of the azygos vein. On the left side, the posterior intercostal veins from 11th to 9th drained into the hemiazygos vein, while those from 8th to 4th drained into the accessory hemiazygos vein [30]. In the present study, the small azygos vein received only the right posterior intercostal veins, from 11th to 8th; the continuous hemiazygos vein received the 7th and 6th right posterior intercostal veins; and the large arch of the continuous hemiazygos vein received the right 5th and 4th posterior intercostal veins, as well as, the right superior

intercostal vein. On the left side, posterior intercostal veins from 11th to 7th drained into the continuous hemiazygos vein and those from 6th to 4th drained into the accessory hemiazygos vein. Variations in the azygos venous system were previously reported in few literatures. An underdeveloped hemiazygos vein was described associated with abnormal drainage of left posterior intercostal veins into the azygos vein [19, 23]. However, the multiple variations in the way of drainage of posterior intercostal veins, on both sides, described in the present case have never been reported before. Furthermore, the present study was the first to report a case of duplicated IVC associated with multiple variations in the way of drainage of posterior intercostal veins.

The present case possesses a complex combination of venous variations that, to the best of the authors' knowledge, has never been reported before. We report a case of duplicated IVC where both vessels, of same diameter, continue into the thorax; the right IVC drains into the right atrium and the left IVC continues as hemiazygos vein, joins the right IVC through the azygos vein, joins the left brachiocephalic vein through the accessory hemiazygos vein and finally drains into SVC. The present report invalidates the classification of Natsis et al. [18] and presents a "real complete bilateral duplication of IVC". The present report also describes, for the first time, three large anastomotic channels between right and left IVC; a cranial preaortic, a middle and a caudal retroaortic. Furthermore, an explanation for the variations found in the case is suggested and illustrated in Figure 4. Variations are mostly due to persistence of a large portion of the left supracardinal vein, the supracardinal anastomoses and additional portions of the left PCV, left CCV and left ACV. The left IVC with its hemiazygos continuation is mainly formed by the left supracardinal vein with small contributions from subcardinal supracardinal anastomosis, left PCV, left CCV and left ACV, while its terminal arch is derived from an anastomosis between the two ACV. The rudimentary azygos vein and the two retroaortic anastomotic channels are derived from supracardinal anastomoses; the preaortic anastomotic channel from the subcardinal supracardinal anastomosis; the accessory hemiazygos from the left ACV. The left superior renal vein together with left suprarenal and left testicular veins are derived from the left subcardinal vein, while the left inferior renal vein from the subcardinal supracardinal anastomosis. The right

IVC together with its associated veins have a normal development (Fig. 6).

Because it is the principal vein draining all the intra-abdominal and pelvic organs, it is vital for surgeons, radiologists and clinicians to be aware of IVC normal anatomy as well as its variations. Most of cases of double IVC are asymptomatic and are discovered incidentally during abdominal imaging or during cadaveric dissections as in the present case. This is likely due to the compensation of adequate venous blood return to the heart created by the deep venous collateral systems [18]. Awareness of double IVC along with other vessels variations will help to eliminate the risk of haemorrhage, misdiagnosis or life-threatening complications during abdominal and thoracic surgeries and the risk of recurrent embolism during the placement of an IVC filter in vascular interventional procedures. In addition, awareness of such variations is necessary to prevent misinterpretation of aberrant vessels as paravertebral lymph nodes enlargement or mediastinal masses [6].

Inferior vena cava malformations were also reported to be a predisposing factor to deep vein thrombosis (DVT), especially in young patients. Accordingly, IVC anomalies should be alerted and excluded by clinicians if a young patient presented with an idiopathic DVT, especially when the intrathoracic hemiazygos or azygos systems are dilated in the diagnosed case [12]. Duplication of IVC has been reported to be associated with symptomatic venous thrombosis of lower extremities and with recurrent pulmonary thromboembolism [26].

Several double IVC case reports described associated abnormalities in the renal and gonadal vessels. Duplicated renal veins were reported to be more frequent on the right side as a result of persistence of anastomoses on that side and their regression on the left side [11]. In contrast to such reports, the present study reported duplication of the left renal vein resulting from an unusual persistence of the subcardinal supracardinal anastomosis on the left side. In the literature, anomalies on the left side included retroaortic and circumaortic left renal veins [18]. Anatomical variations in gonadal vessels were mainly in the form of duplications of testicular [31] or ovarian [25] veins, and they were more common on the left side [18]. Moreover, in patients with duplicated IVC, the left kidney is often lower in position than the right kidney due to the pull by the left IVC on the left renal vein [13, 16]. These venous abnormalities have led
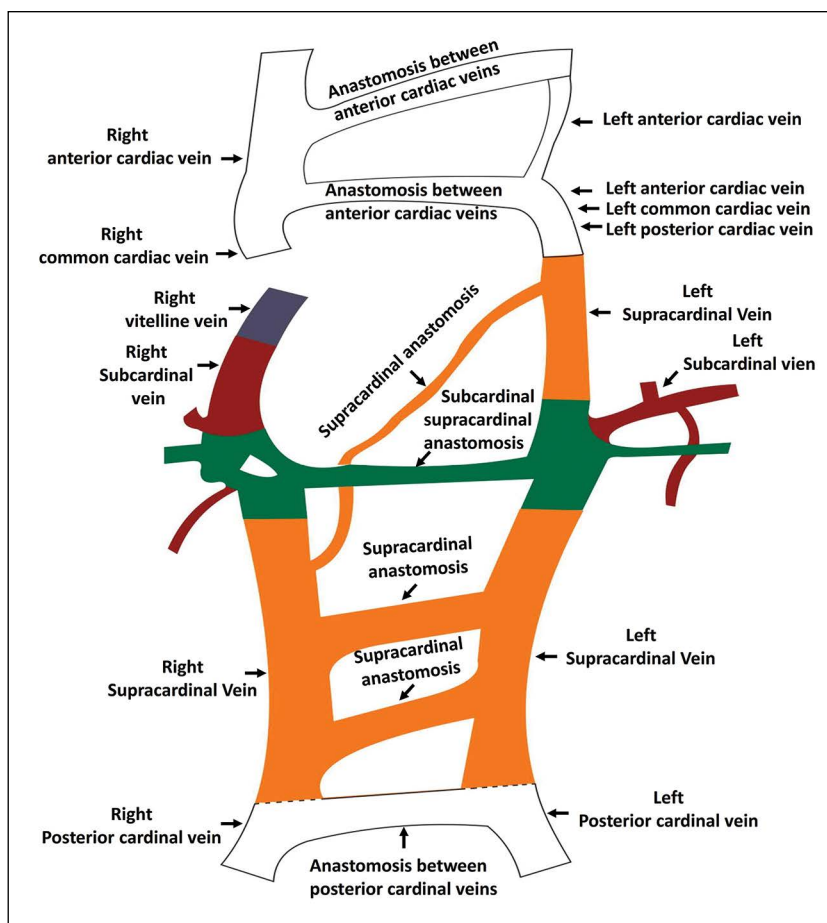
Figure 6. Schematic diagram suggesting the origins of the duplicated vena cava and the associated vessel anomalies; white — anterior, posterior and common cardinal veins; orange — supracardinal veins; red — subcardinal veins; green — subcardinal supracardinal anastomosis; blue — right vitelline vein.

to urogenital complications including obstruction of the ureter [29]. An atypical origin and course of the gonadal arteries might be associated with vascular and developmental variations of the kidneys [14]. Kidneys with bilateral multicystic changes were reported in cases of duplication of IVC [31]. The presence of the multicystic kidney might coincide with a high incidence of hydronephrosis and infections of the upper urinary tract and might result in deterioration of late renal function and secondary hypertension. Duplication of the IVC associated with vascular variations of the kidneys and gonads are important not only from the developmental point of view, but also have important clinical implications. These anomalies can manifest various clinical symptoms and can affect the approach to surgical procedures. The presence of duplication of the IVC poses hazards during abdominal aortic surgery. The double renal arteries, renal arterial origin of the testicular arteries and atypical

drainage of the testicular veins increase the complexity of renal transplantation and lead to a higher percentage of transplant failures. Thus, familiarity with these anatomical anomalies is vital for vascular surgeons and urologists to reduce the risk of serious haemorrhage during surgical treatment and to avoid operative complications [31].

CONCLUSIONS

In conclusion, the present report presents an extremely rare complete duplication of IVC. Preoperative diagnosis of the IVC anomalies through accurate use of detailed imaging modalities would reduce the complication rate and would also help in planning a proper treatment as placement of preventive IVC filters. Finally, care should be taken during routine medical dissections and hopefully, the present case report will create the awareness that surely enlighten the academic fields.

REFERENCES

1. Abernethy J. Account of two instances of uncommon formation, in the viscera of the human body. Philos Trans R Soc London. 1993; 83: 59–66, doi: 10.1098/rstl.1793.0010.
2. Artico M, Lorenzini D, Mancini P, et al. Radiological evidence of anatomical variation of the inferior vena cava: report of two cases. Surg Radiol Anat. 2004; 26(2): 153–156, doi: 10.1007/s00276-003-0192-0, indexed in Pubmed: 14600789.
3. Banerjee A, Maharana S, Anil Kumar I. Duplication of the inferior vena cava – report of a rare congenital variation. IJAV. 2012; 5: 141–143.
4. Bass JE, Redwine MD, Kramer LA, et al. Spectrum of congenital anomalies of the inferior vena cava: cross-sectional imaging findings. Radiographics. 2000; 20(3): 639–652, doi: 10.1148/radiographics.20.3.g00ma09639, indexed in Pubmed: 10835118.
5. Chen H, Emura S, Nagasaki S, et al. Double inferior vena cava with interiliac vein: a case report and literature review. Okajimas Folia Anat Jpn. 2012; 88(4): 147–151, doi: 10.2535/ofaj.88.147, indexed in Pubmed: 22645906.
6. Coco D, Cecchini S, Leanza S, et al. Inferior vena cava duplication: incidental case in a young woman. Case Rep Radiol. 2016; 2016: 3071873, doi: 10.1155/2016/3071873, indexed in Pubmed: 27217964.
7. Ghandour A, Partovi S, Karuppasamy K, et al. Congenital anomalies of the IVC-embryological perspective and clinical relevance. Cardiovasc Diagn Ther. 2016; 6(6): 482–492, doi: 10.21037/cdt.2016.11.18, indexed in Pubmed: 28123970.
8. Itoh M, Moriyama H, Tokunaga Y, et al. Embryological consideration of drainage of the left testicular vein into the ipsilateral renal vein: analysis of cases of a double inferior vena cava. Int J Androl. 2001; 24(3): 142–152, doi: 10.1046/j.1365-2605.2001.00286.x, indexed in Pubmed: 11380703.
9. Kandpal H, Sharma R, Gamangatti S, et al. Imaging the inferior vena cava: a road less traveled. Radiographics. 2008; 28(3): 669–689, doi: 10.1148/rg.283075101, indexed in Pubmed: 18480478.
10. Khaledpour C, Matanovic P, Rienäcker J, et al. An abdominal aortic aneurysm (AAA) in combination with duplication of the inferior vena cava (IVC), the right renal artery (RRA) and the right renal vein (RRV). Surg Radiol Anat. 1990; 12(1): 73–76, doi: 10.1007/BF02094132, indexed in Pubmed: 2345901.
11. Kudo FA, Nishibe T, Miyazaki K, et al. Left renal vein anomaly associated with abdominal aortic aneurysm surgery: report of a case. Surg Today. 2003; 33(8): 609–611, doi: 10.1007/s00595-003-2536-0, indexed in Pubmed: 12884099.
12. Lamparello BM, Erickson CR, Kulthia A, et al. Congenital anomaly of the inferior vena cava and factor V Leiden mutation predisposing to deep vein thrombosis. Vasc Health Risk Manag. 2014; 10: 609–613, doi: 10.2147/VHRM.S66283, indexed in Pubmed: 25395858.
13. Lewis SJ. Observations on a double inferior vena cava: A case report with a literature review. Clin Anat. 1992; 5(3): 227–233, doi: 10.1002/ca.980050307.
14. Machnicki A, Grzybiak M. Variations in testicular arteries in fetuses and adults. Folia Morphol. 1997; 56(4): 277–285, indexed in Pubmed: 9635363.
15. Malaki M, Willis AP, Jones RG. Congenital anomalies of the inferior vena cava. Clin Radiol. 2012; 67(2): 165–171, doi: 10.1016/j.crad.2011.08.006, indexed in Pubmed: 22070941.
16. McNeil JC, Whipp KP, Lambert HW. Unique variant of a double inferior vena cava with interiliac communication: Review of clinical and surgical relevance. Int J Anat Var. 2016; 9: 35–38.
17. Moore K, Persaud T. The Developing Human. Clinically Oriented Embryology. 7th ed. Elsevier Science, USA 2003.
18. Natsis K, Apostolidis S, Noussios G, et al. Duplication of the inferior vena cava: anatomy, embryology and classification proposal. Anat Sci Int. 2010; 85(1): 56–60, doi: 10.1007/s12565-009-0036-z, indexed in Pubmed: 19330283.
19. Ozdemir B, Aldur MM, Celik HH. Multiple variations in the azygos venous system: a preaortic interazygos vein and the absence of hemiazygos vein. Surg Radiol Anat. 2002; 24(1): 68–70, doi: 10.1007/s00276-002-0008-7, indexed in Pubmed: 12197015.
20. Perumal S, Subramaniam S. Missing inferior vena cava: report of a rare case. Int Surg J. 2019; 6(6): 2201, doi: 10.18203/2349-2902.isj20192393.
21. Petik B. Inferior vena cava anomalies and variations: imaging and rare clinical findings. Insights Imaging. 2015; 6(6): 631–639, doi: 10.1007/s13244-015-0431-z, indexed in Pubmed: 26373648.
22. Pineda D, Moudgill N, Eisenberg J, et al. An interesting anatomic variant of inferior vena cava duplication: case report and review of the literature. Vascular. 2013; 21(3): 163–167, doi: 10.1177/1708538113478731, indexed in Pubmed: 23518845.
23. Seema, Singh M. Multiple variations of the azygos venous system: a case report. Int J Anat Var. 2013; 6: 34–35.
24. Senecail B, Lefevre C, Person H, et al. Radiologic anatomy of duplication of the inferior vena cava: a trap in abdominal imaging. A report of 8 cases. Surg Radiol Anat. 1987; 9(2): 151–157, doi: 10.1007/BF02086600, indexed in Pubmed: 3120333.
25. Takagi T, Nozaka Y, Ohsawa T. Double superior venae cavae with bilateral inferior venae cavae. Kaibogaku Zasshi. 1982; 57(1): 9–14, indexed in Pubmed: 7090729.
26. Tamizifar B, Seilani P, Zadeh MR. Duplication of the inferior vena cava and thrombosis: A rare case. J Res Med Sci. 2013; 18(10): 911–913, indexed in Pubmed: 24497866.
27. Tohno Y, Tohno S, Azuma C, et al. One case of the double inferior venae cavae found in a Japanese man. J Nara Med Assoc. 2006; 57(6): 193–197.
28. Wagner J, Bogusch G. An abnormal pattern of blood vessels in the retroperitoneal space with a duplicated inferior vena cava in an adult: a case report. Surg Radiol Anat. 1993; 15(3): 201–205, doi: 10.1007/BF01627706, indexed in Pubmed: 8235963.
29. Wang LT, Lo HC, Yu DS, et al. Ureteral obstruction caused by a duplicated anomaly of inferior vena cava. Int J Urol. 2005; 12(9): 842–844, doi: 10.1111/j.1442-2042.2005.01171.x, indexed in Pubmed: 16201983.
30. Williams PL, Bannister H, Berry MM, Collins P, Dyson M, Dussek JE, Fergusson MWJ. eds. Gray's Anatomy. 38th ed. Churchill Livingstone, London 1995.
31. Xue HG, Yang CY, Asakawa M, et al. Duplication of the inferior vena cava associated with other variations. Anat Sci Int. 2007; 82(2): 121–125, doi: 10.1111/j.1447-073X.2006.00153.x, indexed in Pubmed: 17585569.

VIA MEDICA

C A S E   R E P O R T

Unusual variability of the superficial venous system of the upper limb and its consequences for deep venous system

Z.M. Ziętek[1, 2]

[1]Department of General Surgery and Transplantology, Pomeranian Medical University, Szczecin, Poland
[2]Department of Normal and Clinical Anatomy, Pomeranian Medical University, Szczecin, Poland

In our report we would like to present a variation of the two main superficial veins of the upper limb. In 21 (88%) explored upper limbs, the venous system showed a pattern similar to that presented in the anatomical textbook. However, in 4 (12%) others venous patterns differed from those already described. Especially in one of them the variant of the veins of the upper limb distinctly contrasted with the others. In that case, the basilic and cephalic vein, instead of the normal course to the arm where they should bypass the elbow pit, unexpectedly merged into one and formed one of the two brachial veins. Towards the axillary cavity it ran laterally over the entire arm regardless of the second brachial vein. In the armpit cavity, instead of connecting with the second one, it gave rise to an independent second vein — the accessory axillary vein. This uniqueness was based on that, independently from deep venous system, the superficial one formed their own net. The accessory axillary vein and the second brachial vein were completely formed by two main superficial veins: the basilic and cephalic vein. By describing this case we wanted to emphasize that in any surgical procedure on the upper limbs, especially on the venous system, there is a certain probability of encountering this anatomical variation. Another conclusion is that the catalogue of patterns of the venous system of the upper limb seems to be endless. (Folia Morphol 2022; 81, 1: 254–257)

Key words: venous system, upper limb, anatomical variation, surgery

INTRODUCTION

The nature of the human body inspires from the dawn of mankind to the present day. Despite new alternative methods, the anatomical dissection still remains the golden standard in the study of the anatomy of the human body [7]. Searching of new patterns or variations of structures of the human body is the most important challenge for every anatomist [10, 12]. Former postulates of clinicians addressed to anatomists, encouraging them to continue exploration of human body, have not lost their relevance [6, 8, 12].

Variations in the venous pattern of the upper limb are very common. Conventional textbooks describe the anatomy of the venous system of the upper limb as two layouts [11]. The first one is called superficial or superfascial and the second one — deep or subfascial. These are not independent systems, but the existing anastomoses between them provide blood

Figure 1. The unique pattern of veins of the left upper limb — the veins are blue; 1 — basilic vein; 2 — cephalic vein; 3 — "superficial" brachial vein — pulled up by probe; 4 — "deep" brachial vein — pulled up by probe; 5 — radial artery — pulled up by a garter; 6 — ulnar artery — pulled up by a garter; 7 — "superficial" axillary vein; 8 — "deep" axillary vein; 9 — brachial artery — pulled up; 10 — axillary artery; 11 — singular radial vein; 12 — singular ulnar vein; for the clarity of photography — the nervous system was missed.

flow from the superficial to the deep system, which ultimately delivers blood to the heart. The superficial system is represented by two main veins: the basilic vein and cephalic vein. At the level of the forearm and arm both these veins run along the inner and lateral side of the upper limb. Finally, in the middle of the arm, the basilic vein connects to one of the brachial veins and the cephalic vein joins the axillary vein in the deltopectoral triangle. The deep system consists of veins accompanying the arteries, whose names come from the accompanying arteries. Usually, in this system, there are two veins which run along one artery, except of the axillary and subclavian vein [7, 9]. The number of anatomical variants of the veins of the upper limb seems countless. There are reports of new discovered variants of the veins of the upper limb constantly. Continuous update increases the number of anatomical variants of the veins of the upper limb. Updating these patterns is especially important in vascular procedures [6, 7].

CASE REPORT

During preparation of one of the upper limbs for the educational purposes an unusual pattern of superficial and deep veins system was noticed.

As can be seen on the photography of the left upper limb was observed the unusual pattern of the basilic and cephalic vein (Fig. 1). Basically, the cephalic and basilic vein runs up along both side of forearm. Then, both veins enter the arm, avoiding the area of the cubital fossa but in our case they ran directly to the elbow pit where unexpected they both fused to form one of two main brachial veins. For this publication it was called superficial brachial vein. As can be seen on Figure 1 the second brachial vein has been formed fully separately by the veins of the deep system.

According to classical textbooks both brachial veins, near the armpit should join together to create singular axillary vein. As can be seen, each of brachial veins ran separately along the whole arm up to the axillary cavity. They both became axillary veins and ran, still separately, upwards. The axillary vein, which was formed by the superficial brachial vein, was named the accessory axillary vein.

One has an irresistible impression when looking at the photograph that the blood flowing from the upper limb rolls along two independent vessel systems. One system runs superficially, independently of the arteries, up to the axillary cavity, the other one is located deeper and accompanies the arteries of the

upper limb. This pattern of blood circulation in the upper limbs seems to be unique and has not been published so far.

The work was approved by the Local Ethics Committee of Pomeranian Medical University in Szczecin.

DISCUSSION

The traditional anatomy texts offer a lot of description of the upper arm veins and are particularly abundant in regards to their variations [6, 8, 12].

Bardeleben [2] was one of the first authors to provide a systematic nomenclature of the veins of the upper limbs and their topography. He also described about 36 varieties. However, in none of them was a description similar to the presented case [2]. Also the detailed classification of the superficial and deep upper limb veins is given by Vazquez et al. [14]; however, among these 11 variants there is also no description similar to the presented case.

Although the literature describes some types of anatomical variants of the veins of the upper limb, we have established that this pattern has not yet been published [1, 6, 8–10]. It has been found a report which describes an anatomical variant of the basilic and cephalic vein that is slightly similar to our case. But in their case the deep system was joined with the superficial system in the cubital fossa [11]. The occurrence of accessory axillary vein is estimated quite high, over 50%. Charpy [3] was the first to describe this variability, but there were no similar descriptions to the presented case. Similarly, Gusmao and Prates [5] in their observations noted that the basic branches forming the accessory axillary vein originated from the deep vessel system, which sometimes received the branches from the superficial system. The authors did not encounter the accessory axillary vein formed exclusively by the veins from superficial system [5]. Unlike the basilic vein, which is characterized by some topographic instability, many reports indicate a fairly stable course of the cephalic vein [10, 12]. However, several variants of the cephalic vein have been already described. Del Sol et al. [4] and Ukoha et al. [13] in their research indicated six pattern varieties of the vein course in the area of the ulnar fossa; however, none of the given variants was similar to ours. It may be another proof that variability of the cephalic vein is not a rare phenomenon, as it is supposed to be [1, 10, 12]. Some authors have emphasized the importance of identifying some variants of cephalic vein for surgical procedures, especially vascular or orthopaedic [8, 10].

They especially point out some procedures, such as creation of arteriovenous fistulas, where transposition of veins in some variants could increase the risk of complications [1, 8]. Some authors suggest vein mapping before surgery to minimise the risk of some complications resulting from unexpected variants [1].

The presence of two large veins in the axillary cavity was demonstrated by ultrasound examination in patients undergoing vascular procedures. The authors regarded one of these veins as the accessory axillary vein. At this point, should be emphasized the importance of radiologic tools in anatomical exploration on the living. However, the authors concluded that anatomical dissection should be the basis for transferring the new anatomical pattern to other descriptions, e.g. radiological.

The above conclusion can be seen when editing radiological or surgical atlases. Therefore, cross-sectional studies should be still continued.

CONCLUSIONS

The catalogue of patterns of the upper limb venous system seems to be unlimited and should therefore be constantly updated. During each vascular surgery the probability of anatomical and topographic variability of the venous system of the upper limb should be taken into account.

Conflict of interest: None declared

REFERENCES

1. Anaya-Ayala JE, Younes HK, Kaiser CL, et al. Prevalence of variant brachial-basilic vein anatomy and implications for vascular access planning. J Vasc Surg. 2011; 53(3): 720–724, doi: 10.1016/j.jvs.2010.09.072, indexed in Pubmed: 21144691.
2. Bardeleben K. Die Hauptvene des Armes, vena capitalis brachii. Jenaische Zeitschrift 1880, 586-606 mit Tafeln XXVIII.
3. Charpy A. Systeme veineux. Veines du membre superieur. Traite d'anatomie humaine. Chapter IV. 1903: 904–924.
4. Del Sol M, Mardones LM, Bustos JE. Venous formations in the cubital fossa of Mapuche. Bioscopy study. Int J Morph. 2007; 23: 885–894.
5. Gusmao LC, Prates JC. Anatomical study of the accessory axillary vein. Surg Radiol Anat. 1992; 14(2): 131–136, doi: 10.1007/BF01794889, indexed in Pubmed: 1641737.
6. Kaiser CL, Anaya-Ayala JE, Ismail N, et al. Unrecognized basilic vein variation leading to complication during basilic vein transposition arteriovenous fistula creation: case report and implications for access planning. Eur J Vasc

Endovasc Surg. 2010; 39(5): 627–629, doi: 10.1016/j. ejvs.2010.01.011, indexed in Pubmed: 20172752.

7. Lee HS, Song YR, Kim JK, et al. Anatomical variants of upper arm veins on preoperative mapping venography for hemodialysis access in Korean adults. J Vasc Access. 2019; 20(3): 270–275, doi: 10.1177/1129729818803870, indexed in Pubmed: 30306819.

8. Loukas M, Myers CS, Wartmann ChT, et al. The clinical natomy of the cephalic vein in the deltopectoral triangle. Folia Morphol. 2008; 67(1): 72–77, indexed in Pubmed: 18335417.

9. Mikuni Y, Chiba S, Tonosaki Y. Topographical anatomy of superficial veins, cutaneous nerves, and arteries at venipuncture sites in the cubital fossa. Anat Sci Int. 2013; 88(1): 46–57, doi: 10.1007/s12565-012-0160-z, indexed in Pubmed: 23131916.

10. Radkowski CA, Richards RS, Pietrobon R, et al. An anatomic study of the cephalic vein in the deltopectoral shoulder approach. Clin Orthop Relat Res. 2006; 442: 139–142, doi: 10.1097/01.blo.0000181146.78434.da, indexed in Pubmed: 16394752.

11. Sadeghi A, Setayesh Mehr M, Esfandiari E, et al. Variation of the cephalic and basilic veins: A case report. J Cardiovasc Thorac Res. 2017; 9(4): 232–234, doi: 10.15171/jcvtr.2017.40, indexed in Pubmed: 29391938.

12. Sandhu NPS, Sidhu DS. Mid-arm approach to basilic and cephalic vein cannulation using ultrasound guidance. Br J Anaesth. 2004; 93(2): 292–294, doi: 10.1093/bja/aeh179, indexed in Pubmed: 15194622.

13. Ukoha UU, Oranusi CK, Okafor JI, et al. Patterns of superficial venous arrangement in the cubital fossa of adult Nigerians. Niger J Clin Pract. 2013; 16(1): 104–109, doi: 10.4103/1119-3077.106777, indexed in Pubmed: 23377482.

14. Vazquez T, Sanduo J. Veins of the upper limb. Bergman's Comprehensive Encyclopedia of Human Anat Variation. Ed: Tubbs RS, Shoja MM, Loukas MM. Willey Pub 2016: 826–830.

LETTER TO THE EDITOR

Epiligament or paratenon is more appropriate for describing the enveloping tissue of the cruciate ligaments of the human knee?

G.P. Georgiev

Department of Orthopaedics and Traumatology, University Hospital Queen Giovanna – ISUL, Medical University of Sofia, Bulgaria

I read with interest the article by Kim et al. [5] on description of a macroscopic and histological observations of the paratenon (PT) of the cruciate ligament in 43 human foetuses — "Paratenon of the cruciate ligaments of the knee: a macroscopic and histological study of human foetuses." The authors described PT with a thick armour-like appearance distant from the infrapatellar fat pad. According to them the anterior cruciate ligament (ACL) is more deeply embedded in the PT compared to the posterior cruciate ligament. The PT is presented by abundant arteries and veins especially at and near the crossing between the ligaments and had a well-presented venous plexus.

However, I would like to make my modest comments about the enveloping tissue of the knee ligaments. I do not agree with the author's statement that the tissue around the cruciate ligaments should be termed PT. Firstly, when describing the tissue around ligament structure is more logically and accurately to use the term epiligament (EL) [epi- (Greek — on or upon); ligament (Latin — ligare, to bind)] [2]. In 1990, Bray et al. [1] in their article "Fine vascular anatomy of adult rabbit knee ligaments" defined for the first time the term EL. Nowadays, the morphology of the EL of the ACL in human knee has been described in details by Georgiev et al. [3, 4]. After describing the EL morphology of the ACL and comparing it to medial collateral ligament of the knee, the authors formulate and propose a new theory about the ACL healing failure. Also I could not agree that the careful removal of the PT along the cruciate ligaments is a critical step of knee surgery. There is no such an orthopaedic technique and why should we remove the EL in intact ACL as we know that the main blood supply to the ligament is localized in its EL tissue. Third, I could not accept the statement that the orthopaedic surgeons and interventional radiologists consider the PT as a basic anatomical tissue along a ligament, not along a tendon. When and why the clinicians accept that the PT is part of ligament structure? As I pointed out, the description of the structure should be included in its name.

In conclusion, I consider that the term PT should be directed only to the tendon. Its usage for describing of the ACL enveloping tissue will provoke embarrassment and could mislead the readers.

Acknowledgements

Conflict of interest: None declared

REFERENCES

1. Bray RC, Fisher AW, Frank CB. Fine vascular anatomy of adult rabbit knee ligaments. J Anat. 1990; 172: 69–79, indexed in Pubmed: 2272910.
2. Georgiev GP, Iliev A, Kotov G, et al. Light and electron microscopic study of the medial collateral ligament epiligament tissue in human knees. World J Orthop. 2017; 8(5): 372–378, doi: 10.5312/wjo.v8.i5.372, indexed in Pubmed: 28567340.

Address for correspondence: G.P. Georgiev, MD, PhD, Department of Orthopaedics and Traumatology, University Hospital Queen Giovanna – ISUL, Medical University of Sofia, 8, Bialo More Str., BG 1527 Sofia, Bulgaria, tel: +359884 493523, e-mail: georgievgp@yahoo.com

3. Georgiev GP, Kotov G, Iliev A, et al. A comparative study of the epiligament of the medial collateral and the anterior cruciate ligament in the human knee. Immunohistochemical analysis of collagen type I and V and procollagen type III. Ann Anat. 2019; 224: 88–96, doi: 10.1016/j.aanat.2019.04.002, indexed in Pubmed: 31022516.

4. Georgiev GP, Landzhov B, Kotov G, et al. Matrix metalloproteinase-2 and -9 expression in the epiligament of the medial collateral and anterior cruciate ligament in human knees: A comparative study. Cureus. 2018; 10(11): e3550, doi: 10.7759/cureus.3550, indexed in Pubmed: 30648082.

5. Kim JH, Sugai N, Suzuki D, et al. Paratenon of the cruciate ligaments of the knee: a macroscopic and histological study of human foetuses. Folia Morphol. 2022; 81(1): 134–143, doi: 10.5603/FM.a2021.0003, indexed in Pubmed: 33511626.

FOLIA MORPHOLOGICA

CONTENTS

←

Cover picture: Sagittal sections of interzone mesenchymal tissues of the knee joints of two midterm foetuses; A. Foetus of 35 mm crow--rump length (CRL), approximately 8 weeks gestational age (GA). For details see: J.H. Kim et al., Folia Morphol 2022; 81, 1: 134–143.